annual progress report

2009

PROPULSION MATERIALS

U.S. DEPARTMENT OF ENERGY | Energy Efficiency & Renewable Energy

U.S. Department of Energy
Office of Vehicle Technologies
1000 Independence Avenue S.W.
Washington, DC 20585-0121

FY 2009

Progress Report for Propulsion Materials

Energy Efficiency and Renewable Energy
Office of Vehicle Technologies
Advanced Materials Technologies

Patrick B. Davis **Program Manager, OVT**
Carol L. Schutte **Team Leader, Advanced Materials Technologies**
Jerry L. Gibbs **Technology Manager**

January 2010

CONTENTS

INTRODUCTION

Propulsion Materials R&D: Enabling Technologies to Meet Vehicle Technologies Program Goals

The Department of Energy's (DOE's) Office of Vehicle Technologies (OVT) is pleased to introduce the *FY 2009 Annual Progress Report for the Propulsion Materials Research and Development Program*. Together with DOE national laboratories and in partnership with private industry and universities across the United States, the program continues to engage in research and development (R&D) that provides enabling materials technology for fuel-efficient and environmentally friendly commercial and passenger vehicles.

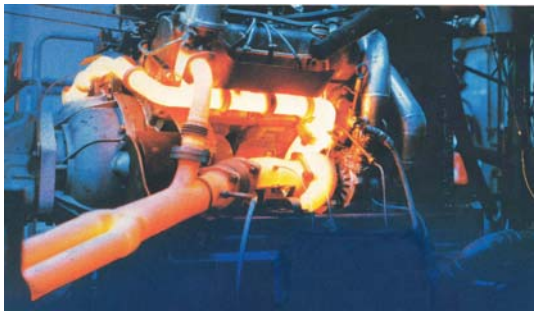

This introduction summarizes the objectives, progress, and highlights of the program in FY 2009. The Propulsion Materials R&D Program has supported the Vehicle Technologies Program since its inception. In research areas where industry views the risks as too high and uncertain, the Vehicle Technologies Program conducts long-term research, development, and demonstration activities that bring the technology to a stage of maturity such that industry can undertake the final commercialization stages. In order to provide more effective support to the program's stakeholders and participants, the former Automotive Propulsion Materials and Heavy Vehicle Propulsion Materials R&D programs were combined in FY 2007 into a single Propulsion Materials R&D program.

The Propulsion Materials program is a partner and supporter of the (OVT) Hybrid and Vehicle Systems, Energy Storage, Power Electronics and Electrical Machines, Advanced Combustion Engines, and Fuels and Lubricants R&D programs. Projects within the Propulsion Materials Program address materials concerns that directly impact the critical technical barriers in each of these programs—barriers such as fuel efficiency, thermal management, emissions reduction, and reduced manufacturing costs. The program engages only the barriers that involve fundamental, high-risk materials issues.

Enabling Technologies

The Propulsion Materials program focuses on enabling and innovative materials technologies that are critical in improving the efficiency of advanced engines. The program provides enabling materials support for combustion, hybrid, and power electronics development, including the following:

- Materials for low-temperature combustion, for example, homogenous-charge compression-ignition
- Materials for hydrogen engine fuel systems (is this still relevant?)
- Materials for 55% thermal efficiency heavy-duty diesel engines
- Materials for waste-heat recovery via thermoelectric modules, with potential 10% increase in fuel efficiency
- Materials technologies for efficient and effective reduction of tailpipe emissions, including diesel particulate filters, catalyst characterization and testing, and exhaust-gas recirculation (EGR) coolers
- Materials technologies for electric and hybrid-electric vehicles, including advanced power electronics materials and electric motors
- Materials for alternate-fuels vehicles, including materials compatibility and corrosion

The program supports these core technology areas by providing materials expertise, testing capabilities, and technical solutions for materials problems. The component development, materials processing, and characterization that the program provides are enablers of the successful development of efficient and emissions-compliant engines.

Program Organization

The Propulsion Materials Program consists of five R&D projects which support the OVT propulsion technologies. Each project consists of several related R&D agreements.

- Materials for Electric and Hybrid Drive Systems
  - Develop materials appropriate for power electronics, electric motors and other hybrid system applications

- Combustion System Materials
  - Develop materials for HCCI engines and fuel injection systems

- Materials for High Efficiency Engines
  - Develop materials for efficient engine components, such as valve-train components, fuel injectors, and turbochargers

- Materials for Control of Exhaust Gases and Energy Recovery Systems
  - Develop materials for exhaust aftertreatment and waste heat recovery applications
- Materials by Design
  - Adopt a computational materials – atomic-scale characterization protocol to develop advanced materials for NO_x catalysts, lithium-ion batteries, thermoelectric generators, and electric motors

R&D Projects and Agreements are evaluated annually using strategic objectives. Agreements are evaluated on relevance to OVT objectives and supported team's priorities, strength of industrial support for the activity, and perceived value of the R&D activity to the OVT Program. In order to keep the program fresh and up-to-date, over 10% of agreements are retired annually. New projects are selected in accordance with identified Office of Vehicle Technologies needs, for example:

- Advanced Combustion Team
  - Internal combustion engine materials
  - Thermoelectric materials
  - Catalysts and aftertreatment materials
  - Materials for engine sensors

- Hybrid Electric Systems Team
  - Power electronics materials
  - Materials for energy storage
  - Materials for electric motors

- Fuels Team
  - Alternative fuels materials compatibility

Selected Highlights:

Materials for Electric and Hybrid Drive Systems

The goal of the Automotive Power Electronic and Electric Machines (APEEM) Program is to reduce the size, weight, and volume of the power electronics without increasing the cost or reducing the reliability. Many, if not most, technical barriers are directly linked to the contemporary material limitations of subcomponents found within devices that comprise inverters, converters, and motors. The material limitations include:

- Insufficient temperature capability
- Excessive thermal insulations
- Excessive electrical insulation
- Insufficient power density in permanent magnets
- Insufficient bandgap

Many of these issues are already being addressed in the Vehicle APEEM Program, but there is interest in additional means to overcome some of those materials limitations through the application of advanced materials science and engineering. In 2008 modeling and analysis of a new concept for a direct-cooled power electronics substrate were conducted by R&D staff of the Oak Ridge National Laboratory (ORNL). The probability of survival was predicted to be greater than 99.999%. The direct-cooled ceramic substrate could be of interest for use in hybrid vehicle inverters because it has the potential to substantially reduce both the volume and weight of the inverter. The concept was recently patented (#2009/0231812), and a schematic from that patent is shown in Fig. 1. The patent describes cooling a three-dimensional, direct metallization layer in a PED. To enable sufficient cooling, coolant flow channels are formed within the ceramic substrate. The direct metallization layer (typically copper) may be bonded to the ceramic substrate, and semiconductor chips (such as IGBT and diodes) may be soldered or sintered onto the direct metallization layer to form a power electronics module. Multiple modules may be attached to cooling headers that provide in-flow and out-flow of coolant through the channels in the ceramic substrate. The modules and cooling header assembly are preferably sized to fit inside the core of a toroidal shaped capacitor.

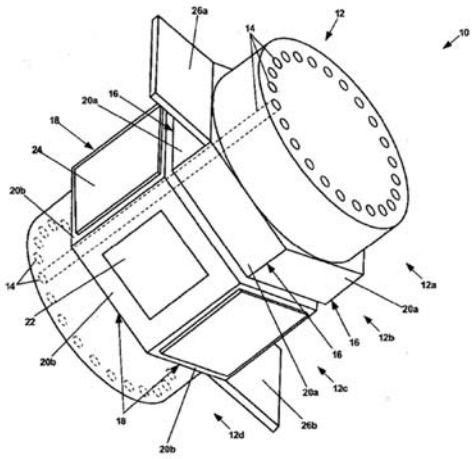

Figure 1. Schematic of the patented direct-cooled ceramic substrate (#2009/0231812).

Barriers to the deployment of new power electronic (PE) components in automotive applications include weight, size, reliability and cost. One approach to reduce the weight of the PE system is to use direct cooling from existing air conditioning systems using R134a refrigerant. This would reduce the weight of the power electronics system by eliminating the need for a separate cooling system. However, direct contact 2-phase cooling necessitates the evaluation of the PE compatibility with and reliability in the coolant. An effort

at ORNL is developing the laboratory methodology to evaluate the degradation of power electronics materials by evaporative liquids. In addition, a database indicating performance boundaries for standard materials and for several candidate coolants is being established.

A laboratory test system, shown in Fig. 2, which was designed and built in FY 2008, allows for high current flow and shaping of the wave form. Testing has been performed using a square wave of one or two seconds on and one or two seconds off to drive 10 to 40 amperes through 0.4 mm (400 microns) diameter aluminum wire shown in Fig. 2. The apparatus allows for condensation and recycle of the evaporated liquid, data recording and visual observation of the boards during testing. The test methodology that involves pulsing of the PE circuit at appropriate power levels and exaggerated cycle times allows for changes in power-on and power-off times. As such, it facilitates accelerated testing without changes in the failure mode(s) that would be observed in service. Further, the methodology allows for an evaluation of the effect of nucleate boiling on the failure mechanism(s).

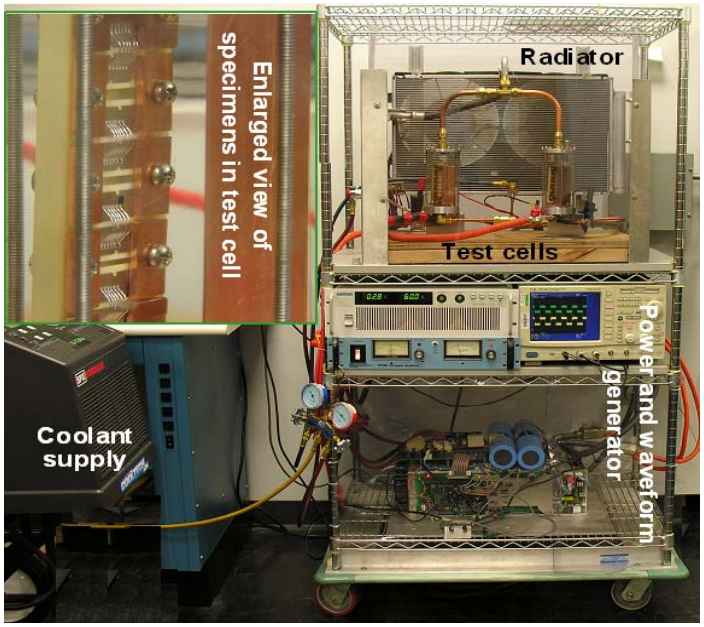

Figure 2. Two circuit boards are shown within their glass enclosures, which are in front of the condensing cooling radiator. Below this is shown the wave form shaping system and the high current power supply.

The use of vehicles with electric drive, which could reduce our oil dependence, will depend on lithium-ion batteries. But there are questions about the supply of lithium. The maximum demand for lithium and other materials was estimated by Argonne National Laboratory (ANL) assuming electric-drive vehicles expand their market share rapidly, estimating material demand per vehicle for four battery chemistries. This R&D effort was co-funded with the Energy Storage Program. Total demand for the United States is based on market shares from an Argonne scenario that reflects high demand for electric-drive vehicles, and total demand for the rest of the world is based on a similar International Energy Agency scenario. Total material demand is then compared to estimates of production and reserves, and the quantity that could be recovered by recycling, to evaluate the adequacy of supply. In the case of materials for lithium-ion batteries, it appears that even an aggressive program of vehicles with electric drive can be supported for decades with known supplies, if recycling is instituted. However, reliance on pure electrics could eventually strain supplies of lithium and cobalt.

Combustion System Materials

Researchers at the Argonne National Laboratory (ANL) are developing a methodology for reducing the diameters of fuel injector orifices to 50 μm by applying material to the internal diameter (ID) of the orifice. Micro-orifices should improve fuel distribution, increase efficiency, and reduce emissions in compression-ignition, direct-injection (CIDI) engines.

Several candidate methods are being evaluated and developed. Development of the electroless-nickel (EN) aqueous-based plating process has been advanced to the stage where commercial nozzles were treated and characterized with an advanced phase-contrast x-ray imaging technique, which confirmed uniform coating deposition along the orifice. Preparations were initiated to fabricate multi-sized orifices (50 and 125 μm) on a commercial nozzle. The plating process has been optimized, and analysis of the coating uniformity on sibling nozzles confirmed that the coating was uniformly deposited along the orifices. Figure 3 illustrates excellent results for EN plating of a commercial fuel-injector tip.

Researchers at the Lawrence Livermore National Laboratory (LLNL) are continuing to develop an inexpensive, rapid-response, high-sensitivity and selective electrochemical sensor for oxides of nitrogen (NOx) for compression-ignition, direct-injection (CIDI) exhaust gas monitoring. Because the need for a NOx sensor is fairly recent and the performance requirements are extremely challenging, most are still in the development phase. Currently, there is only one type of NOx sensor that is sold commercially, and it seems unlikely to meet more stringent future emission requirements.

Work at LLN L in FY 2009 has focused on more advanced NOx sensor prototypes that incorporate an alumina substrate with an imbedded heater and modifications for improving mechanical stability. An advance to the Au wire sensor has been made by moving to (La0.85Sr0.15)0.98Mn (LSM) metal-oxide based electrodes directly attached to the alumina substrate (Fig 4). In addition to excellent stability and sufficient tolerance towards temperature cycling, the LSM prototype also exhibited stable high-frequency (1 kHz) oxygen selectivity, and this permits compensating for oxygen cross-sensitivity and improving sensor accuracy. Furthermore, the LSM prototype has undergone continuous testing in a variety of oxygen, water, and NOx conditions for 3120 h and still showed good NOx sensitivity.

Researchers at the Pacific Northwest National Laboratory (PNNL) are continuing the characterization and development of piezoelectric materials for service in fuel injectors for hydrogen gas. PNNL's approach includes evaluation of failure modes for piezoelectric actuators in hydrogen gas, development of a model for hydrogen diffusion, absorption and damage in piezoelectric ceramics, and development of methods for controlling or remediating the hydrogen damage to prolong actuator life, measurement of the friction and wear characteristics of injector materials in hydrogen environments, measuring the performance of piezoelectric actuators and actuator materials in hydrogen environments, and development of a design approach to hydrogen injectors based on material behavior and performance in hydrogen. The project has addressed the issues of lubrication and wear resistance by exploring the use of nanotechnology. In nanolaminate structures, the alternating layers result in improved mechanical properties, such as strength, hardness, and toughness. Many nanoscale layers with alternating composition or crystal phase create the nanolaminate structure. These structures work to improve upon the mechanical properties of the component materials. Magnetron sputtering was used to produce these coatings of four different nanolaminate systems with excellent results. Figure 5 illustrates the uniform nature of the coatings.

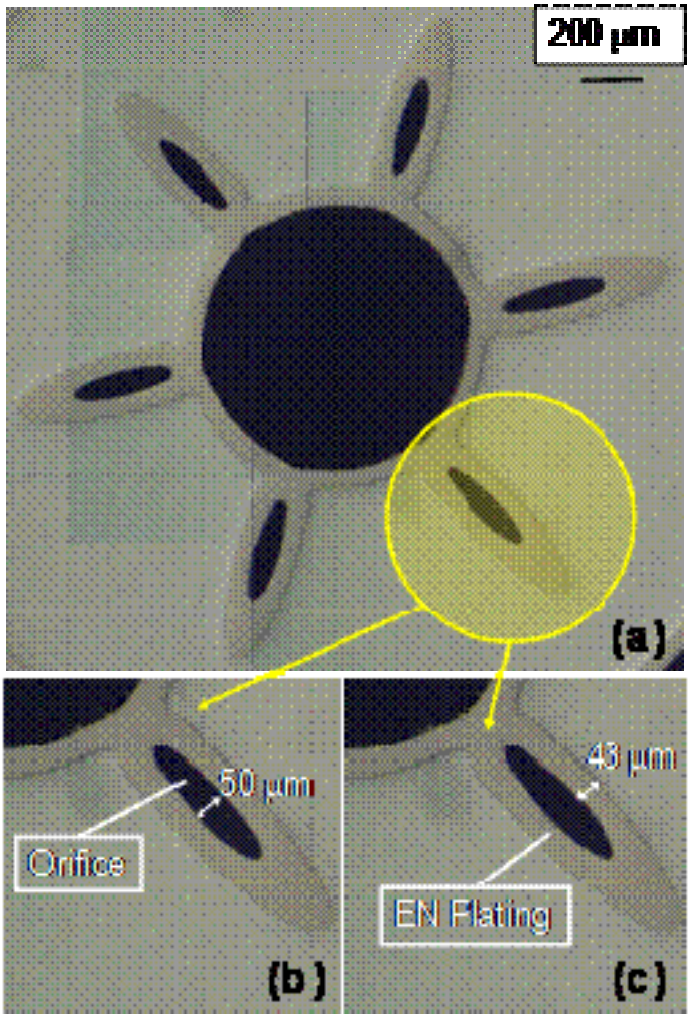

Figure 3 – Microscope images showing (a) coating uniformity for all orifices, (b) orifice reduction, and (c) coating thickness within the orifice

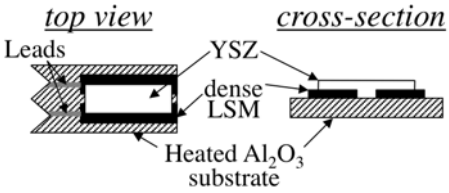

Figure 4. Schematic of more advanced NO_x prototype sensors using dense LSM as the sensing electrode.

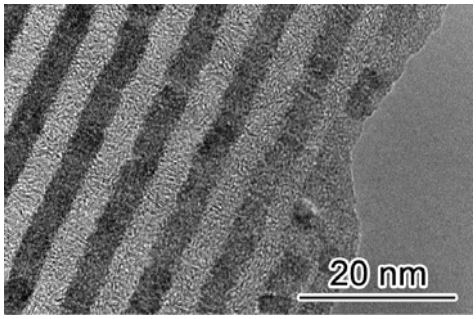

Figure 5: TEM Micrograph Showing the Uniform Nature of the Laminate Layers.

The use of HCCI combustion will subject engine components to significantly higher temperatures and pressures. The temperatures for diesel engines will reach over 1600°F, and pressure may reach >2000 psi, Such severe engine operating conditions will require a significant improvement in materials performance in order to take advantage of the HCCI engine concept. An R&D project at ORNL deals with identifying materials requirements for HCCI engines for automotive and truck applications and the development of advanced, yet cost-effective, materials through computational design. The approach is described in Table 1.

Table 1. ORNL materials-by-design toolbox

Modeling	Experimentation	Characterization
Thermodynamic modeling of material properties vs. alloy composition	Ultra-high-gauss magnetic stabilization of alloy steels	Advanced microscopy techniques
Neural-network modeling of diverse, nonlinear materials properties and process variations	Low-temperature gas carburization of finished components	X- ray and neutron scattering
Detailed microstructure based empirical modeling	Ability to produce small quantities of materials and fabricate them into test bars for property measurements	Surface and bulk property measuring techniques
Non-equilibrium modeling of solidified structures	and production of prototype components by a variety of methods, including sand and	
Extrapolation of properties from simple alloy systems to complex systems using interaction parameters	die casting, extrusion, forging and rolling	

In 2009 several commercial alloys that have the required fatigue properties at 870^{o}C for use in valve applications were identified using fully reversed fatigue tests and rotating beam fatigue tests. Computational thermodynamics models were used to identify alternate, lower-cost compositions, small batches of alloys were prepared, and tensile properties of selected alloys were evaluated. Performance of the experimental alloys is encouraging and will be optimized in 2010.

Materials for High Efficiency Engines

R&D agreements for high-efficiency engines are either driven by industry needs for specific classes of components, or by the invention of new methods of processing materials or new alloys which can be exploited to respond to the needs of industry for new materials for high-efficiency engines. The R&D efforts in this Project involve materials development for valve-train materials, turbochargers, exhaust-gas recirculation (EGR) systems and fuel systems. In addition, processing-driven efforts include those which exploit new technologies in joining, shock peening, friction-stir processing, and processing specifically of titanium alloys. An engine test cell and dedicated diesel engine have been made available for testing advanced materials and components. Highlights from those efforts are shown below:

Researchers at ORNL are developing means of friction and wear reduction in diesel engines**.** This effort used a three-pronged approach to understand and model the wear-oxidation-deformation processes involved in exhaust valve wear. A high-temperature repetitive-impact diesel engine valve material testing system, completed last year, was used to generate mechanically-mixed metal-oxide layers like those observed on valves. Research on Fe-, Ni-, and Co-based alloys demonstrated that prior abrasion damage affects the ability of contacting surfaces to form protective scales at high temperatures. A model for the effects of abrasive wear, deformation, and high-temperature frictional contact on exhaust valves and seats was developed; it involves the conjoint effects of deformation and abrasion of mechanically-mixed oxide layers. To provide data for the valve wear model, the friction coefficient was measured as a function of temperature up to 850^{o} C for a commercial exhaust valve material against a seat material. In addition, a new ASTM standard is being completed for measuring the friction of candidate materials for piston rings and cylinder liners under engine-conditioned lubricants.

A cooperative research and development agreement (CRADA) between Caterpillar, Inc. and ORNL has addressed the wear and failure modes of current on-highway heavy-duty diesel exhaust valves and seats, and then evaluated changes in seat-insert processing and advanced exhaust-valve alloys that will enable higher temperature capability, as well as better performance and durability. The need for such upgraded valve-seat alloys is driven by the demands to meet new emissions and fuel economy requirements, which then continue to push diesel exhaust component temperatures higher.

Caterpillar has provided and analyzed the baseline wear and mechanical behavior characteristics of engine-exposed valves and seats, and similar exposure of those components to laboratory simulation-rig testing at Caterpillar**.** Caterpillar completed upgrading and expansion of its thermo-mechanical valve & seat-insert test rig facility (Fig. 6). ORNL completed more in-depth characterization and microanalysis of those valves and seats over the past year. The oxidation-enhanced sub-surface degradation of the valve-seating surface of standard Pyromet 31V valves, based on micro-characterization and root-cause analyses, was identified. These analyses provided the basis for modifying seat processing last year. Caterpillar's valve seat supplier produced modified seats, and confirmed reduced wear rates with testing at Caterpillar. ORNL and Caterpillar identified several commercial Ni-based superalloy upgrade candidates, based on these analyses, and worked with the valve supplier to obtain new materials for critical mechanical testing and valve prototyping.

Figure 6. Thermo-mechanical valve and seat-insert test rigs for simulating high-temperature wear and performance of exhaust valves and seats for diesel engines, at the Caterpillar Technical Center. Caterpillar completed expanding facility from one to three test rigs this year, and began wear-testing of new modified seat-inserts.

EGR cooler fouling has been identified as a significant issue with diesel engines. As the exhaust gas flows through the EGR cooler, particulate matter will migrate from the hot exhaust gas to the cooled heat exchanger surface forming a porous deposit that has a thermal conductivity comparable to Styrofoam making it a nearly ideal thermal insulator. As the thickness of the deposit increases, the effectiveness of the EGR system goes down due to the inability to cool the exhaust gas. This is known as cooler fouling (see, for example, Figure 7). ORNL has assembled an advisory board from industry specialists from nine diesel engine companies and initiated an effort in mid-year to evaluate the phenomenon and provide characterization data to enable models which may lead to improved coolers. A GM 1.9 L engine on a Drivven controller has been purchased for this effort and is operational in standard and PCCI modes. A sampler system that will allow for the formation of controlled particulate matter deposits on model cooler tubes has been made available as well. Seven companies have provided eleven representative (half-useful-life) EGR coolers for analysis. Deposits have been analyzed using a variety of experimental techniques to identify common features that will help to guide future research. In 2010 the exhaust sampler system will be used to generate particulate matter deposits that will be aged in controlled conditions using a bench-flow reactor so as to evaluate the effect of water, hydrocarbon and cycling on deposit properties. In addition, the characterization of deposits from the industry-provided coolers will be completed.

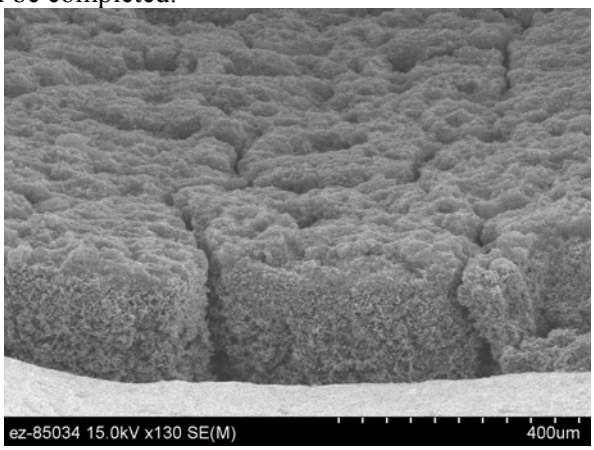

Fig 7. Fracture surface of an industry-supplied EGR cooler showing the structure of the particulate-matter deposits.

In order to improve fuel efficiency while controlling emissions, diesel engine designers have raised the pressures imposed on the fuel injectors. Repetitive pressurization exceeding 25,000 psi could stress the walls of the tips of the fuel injector nozzles above the endurance limit, leading to fatigue cracking and fracture. The consequences of these events can significantly affect engine performance, and the ability of nozzle materials to resist these effects becomes extremely important. Researchers at ORNL and Caterpillar are working to ensure the durability of high-pressure fuel injector nozzle materials through a three-pronged approach: (a) metallurgical characterization and hole metrology, (b) residual stress measurements of material near of spray holes, and (c) fatigue testing of smooth and notched specimens, dry and in the presence of fuel. Fatigue testing was performed on uniform diameter gage specimens in an MTS 810 servo-hydraulic machine at a frequency of 20 Hz. A two-stage fatigue life diagram (Fig. 8) was observed with clear separation in the fatigue lifetime of specimens that failed due to surface crack initiation (s_{max} > 900 MPa) and subsurface crack initiation (s_{max} < 900 MPa). The fatigue lifetimes for the two separate failure modes are separated by nearly two orders of magnitude. The multi-stage S-N curve has practical implications for design in that the endurance limit for conventional failure lifetimes (<10^6) is about 900 MPa, but is reduced to below 800 MPa if the ultra-high cycle regime failures (10^6-10^9) are considered.

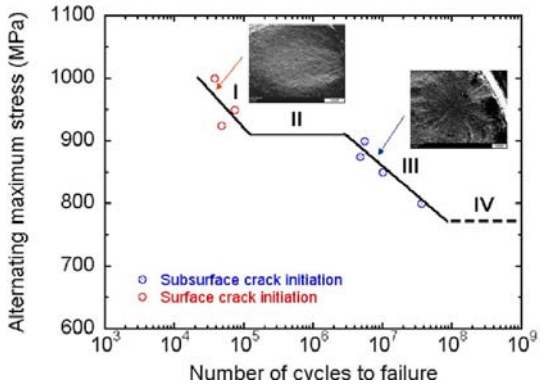

Figure 8. Two-stage fatigue life diagram for an alloy steel that is used in fuel injectors.

The use of piezoelectric multilayer actuators (PMLAs) as diesel fuel injectors has the potential to reduce injector response time, provide greater precision and control of the fuel injection event, and lessen energy consumption. Compared to conventional solenoid operation of an injector, the alternative use of a PMLA can enable precise rate shaping of the entire injection cycle that accurately controls injection timing and fuel quantity. Piezoelectric multilayer actuators (or piezo-stacks) fuel injectors contain a solid-state ceramic actuator (or "piezostack") that converts electric energy into linear motion precisely controlling the needle's opening and closing. This capability results in an engine with outstanding performance, improved fuel economy, low noise, and low emissions. Though their use is very attractive for the reasons mentioned above, uncertainty continues to exist over how reliable piezo-actuated fuel injectors will be in the challenging environment of a heavy diesel vehicle engine. Though piezoelectric function is the obvious primary function of lead zirconate titanate (PZT) ceramic PMLAs for fuel injectors, their reliability can be a performance and life limiter because the PZT ceramic within them is brittle, lacks high strength, and may exhibit fatigue susceptibility. That brittleness and relatively low strength can be overcome with proper probabilistic component design methodology. A cooperative agreement (CRADA) between ORNL and Cummins Engines Co. undertakes the reliability characterization of candidate PMLAs used in these fuel injectors and the piezoceramics used in the PMLAs. The products manufactured by Kinetic Ceramics, Inc. (KCI) and EPCOS have been the focuses of the CRADA.

Testing and characterization were focused on the candidate piezoceramics and piezo stacks that are currently considered in the use of heavy diesel engine fuel system in the first year of CRADA between ORNL and Cummins, Inc. Extensive mechanical tests were conducted on the KCI PZT by both BoR and 4-point bend fixtures in both the as-extracted and as-received. Strength limiters were characterized using the fractography. Electric field effect and temperature effect on the flexure strengths were studied and evaluated at the same time. Responses of EPCOS piezo stacks were conducted with both the breakdown and fatigue observed. Locating a safe working envelop of operation to appropriately drive a piezo actuator appears to be a main challenge for the application. With the careful prefatigue tests, this project was able to identify the operational parameters for subsequent accelerated fatigue testing. Work in the coming year will be directed more on introducing the environmental factors into the test matrix.

Caterpillar, Inc. and PNNL are investigating friction stir processed components that can enable energy-efficient combustion strategies. FSP produces selected, graded structures that have shown increased strength and durability in fatigue. Surface modification through FSP may have an opportunity to address some emerging material problems seen in very high combustion pressure systems such as HCCI engines. Additionally, the process allows for the incorporation of particulate into the surface, potentially selectively modifying the properties of materials to alter the thermal environment for increased thermal efficiency (see, for example, Fig. 9). Experimental work to date on aluminum systems has shown significant increases in fatigue lifetime and stress-level performance in aluminum-silicon alloys using friction processing alone, and ongoing work has shown the potential to create new mechanically mixed alloys of aluminum and carbon nanotubes and fibers that may provide unique thermal fatigue resistant surface regions to fatigue failure prone CIDI engine components. Future work includes quantifying property improvements and fabrication of prototype parts for engine durability testing.

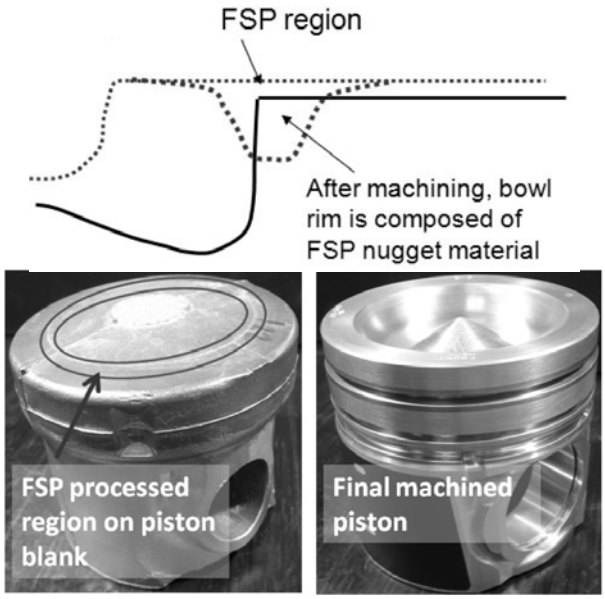

Figure 9. Cast Piston Blank (The area in the bowl rim after machining will be friction stir processed for improved microstructure

A CRADA agreement between ORNL and Caterpillar, Inc. to improve diesel engine performance, efficiency, and emissions through the application of materials-enabled technologies was initiated. The demands of meeting new emissions and fuel economy goals are continuing to push heavy-duty diesel engine components to higher temperatures and pressures and improved durability. Engine manufacturers have recognized several key needs that need to be addressed in order for heavy duty diesel engines to achieve an national efficiency goal of 55% by the year 2012. These include 1) improved structural materials to accommodate higher cylinder pressures and temperatures (associated with advanced combustion methodologies), 2). improved thermal management and waste heat recovery technologies, 3) improved durability, 4) improved transient performance, and 5) better aftertreatment performance. These needs address barriers associated with high parasitic losses, high-efficiency clean combustion and thermal management of the cylinder and exhaust. Caterpillar provided ORNL with two 600 hp motoring dynamometers and C15 ACERT engine. Caterpillar (working with ORNL) will develop and provide components to be evaluated on the engine platform. ORNL engine research staff will evaluate the engine performance with emphasis on combustion diagnostics, optimization and modeling. Materials scientists at ORNL will examine material performance and provide guidance to materials development. The test cell, control room, cooling water, ventilation, and bedplates and other infrastructure were all completed and installed.

The engine was mounted and aligned with the dynamometer as shown in Fig. 10. The engine and exhaust system were instrumented for temperature and pressure measurement. This instrumentation is necessary to perform the detailed thermodynamic analysis necessary to identify areas of potential efficiency gains. The engine and dynamometer were successfully commissioned in April and the engine was operated according to the Caterpillar break-in cycle to degreen the engine.

Figure 10. Photograph showing mounted engine and dynamometer. The control room is on the other side of the wall on the left of the photograph and behind the dynamometer.

Materials for Control of Exhaust Gases and Energy Recovery Systems

The development of new emission-treatment catalytic systems is still largely dominated by trial and error, which is often slow and expensive. A knowledge gap between theory and experiment has been a major contributing factor: traditional computational approaches have been significantly simplified in comparison to real materials, and experimental studies, especially on emission treatment catalysts, have primarily focused on fully formulated systems that can treat engine-out emissions in vehicles. Researchers at the Oak Ridge National Laboratory are developing a protocol that combines the power of theory and experiment for atomistic design of catalytically active sites that

can contribute directly to complete catalyst system suitable for technical deployment. The protocol includes theoretical modeling of catalyst systems via density functional theory (DFT), synthesis of experimental catalyst systems, exposure of catalysts under simulated operating conditions (including an ex-situ reactor which permits duplication of the reaction conditions in a bench-top reactor and facilitates high-resolution scanning transmission electron microscopy), and characterization of the catalyst performance and changes that occur in the catalysts during operation.

The theoretical modeling is based on DFT studies of Pt supported on θ-alumina. We have completed the study of single atoms of Pt, Pd, Au, and Ag supported on the 010 surface of θ-alumina. We have initiated the DFT study of larger clusters of Pt supported on θ-alumina. Our experimental studies suggest that CO oxidation is identical on both Pt supported on γ-alumina and θ-alumina. This suggests that the catalyst site structure is probably identical in both catalysts. Experimentally, we have synthesized a series of Pt clusters/particles of different sizes supported on γ-alumina and evaluated the catalysts NO oxidation activity. We monitored the microstructural changes throughout the NO oxidation process to correlate microstructure and activity. We have also carried out a preliminary study of HC oxidation processes.

Guided by the theoretical models and experimental results of the study, we anticipate that we will initiate work on the synthesis of a new set of catalyst materials with higher durability in FY10.

The durability of diesel particulate filters (DPFs) is being evaluated by research staff at the Oak Ridge National Laboratory and Cummins, Inc. via application of probabilistic design tools, nondestructive evaluation, and refinement and use of lifetime-prediction models. Mechanical and thermal shock characterization test procedures developed earlier were employed to measure properties in cordierite, aluminum titanate and mullite DPF materials. In ASTM round robin testing, the strengths of the SiC DPF materials were a least a factor of three stronger than those of the cordierite. Correcting the moment of inertia for the empty channels resulted in a factor of 2 increase in all strengths (Fig. 11). The Young's modulus of the aluminum titanate varied from the core to the rim with the rim region being stiffer. Finally, dynamic fatigue testing showed that the mullite DPF material has excellent resistance to the susceptibility of slow crack growth. The aluminum titanate material possessed a lot of strength variability requiring more testing before a conclusion can be drawn.

Materials by Design

Researchers at the Oak Ridge National Laboratory materials are developing design strategies for thermoelectric materials based on first principles calculations of electronic, vibrational and transport properties to identify potentially low cost, high performance thermoelectric materials suitable for application in vehicles. New insights into thermoelectric materials performance have emerged from density functional calculations in conjunction with transport theory. Promising directions for new thermoelectrics based on PbSe (Fig. 12) and on the use of materials with both heavy and light bands were found. These results suggest new opportunities for developing high performance lower cost thermoelectrics for vehicular waste heat recovery.

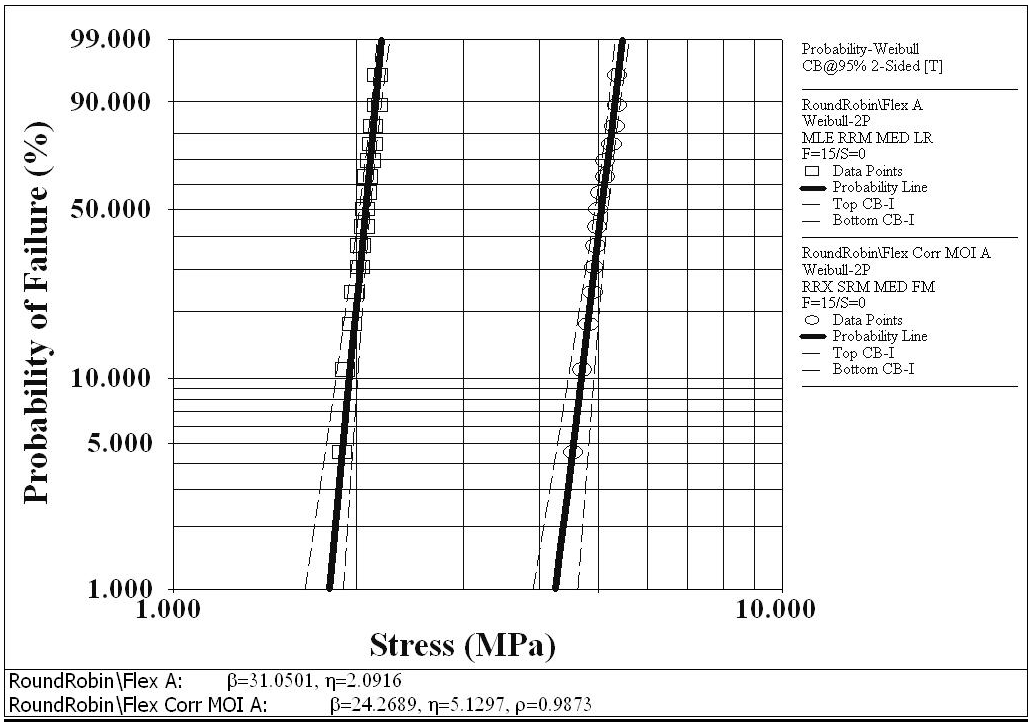

Figure 11: The effect of correcting for moment of inertia (right most data) on the Weibull parameters of a cordierite honeycomb specimen. Correcting for the wall architecture leads to computation of the wall strength of the honeycomb.

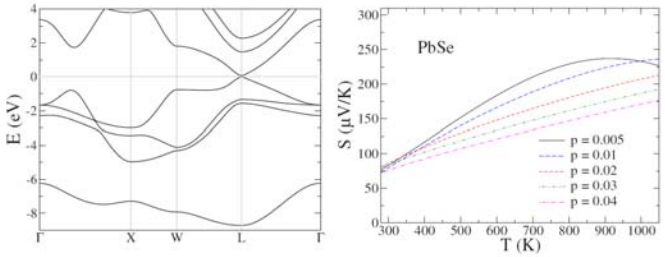

Figure 12: Band structure including spin-orbit interactions (left) and calculated thermopower as a function of temperature and doping (right) for p-type PbSe. Note that the thermopower in the temperature regime relevant to waste heat recovery does not decrease as rapidly as might be expected with doping.

Because of their unusual structural, mechanical, and tribological properties, superhard, nanocrystalline coatings can have an immediate and far-reaching impact on numerous advanced transportation applications. They can also be used to overcome toxic emission problems associated with exhaust gas recirculation in diesel engines. Durability of hard coatings is a critical property. The durability is determined by the surface adhesion energy, but is the result, in a large part, of the residual stresses that form as a result of materials, and processing parameters such as deposition bias voltage, ion flux, and temperature.

The approach for an effort at Argonne National Laboratory to characterize nanocrystalline coatings is to use the high-brilliance X-rays produced by the Advanced Photon Source (APS) at

ANL, and a microfocus beam, to measure the residual stresses/strains of MoN based thin films and commercial coatings such as ZrN and TiC as a function of depth from the surface through the interface to the substrate. Subsequently, residual stress profiles will be correlated with the film processing conditions, and the resulting film/substrate adhesion and the films tribological properties. ANL has applied cross-section x-ray micro-diffraction technique to study depth-resolved residual strain in two commercial coatings: ZrN and TiC, deposited on steel substrates. These coatings were fabricated using two different processing conditions. The nano-indentation technique has been demonstrated as a tool for establishing the variability in the mechanical properties of the coating as a function of the location from the edges to the center of the coatings (Fig. 13). To determine the adhesion energy of the coatings, a scratch tester has been procured and installed.

The remainder of this report communicates the progress achieved during FY 2007 under the Propulsion Materials Program. It consists of annual progress contributions from the several R&D Agreements that make up each of the five overarching R&D Projects that are highlighted above. The R&D contributions provide an overview of the critical work being conducted to develop enabling materials technologies for high-efficiency passenger and commercial vehicles, including goals, barriers, progress to date, and future plans

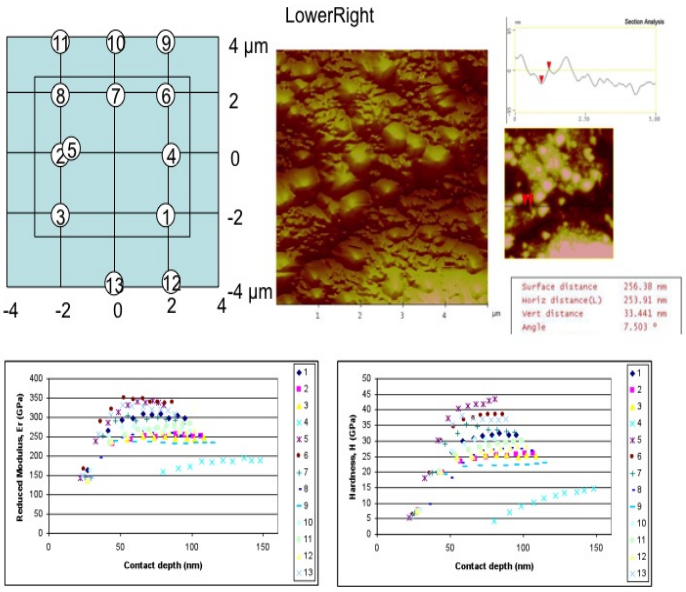

Figure 13. Location of nano-indents on ZrN coating and the measured elastic moduli and hardness values.

Carol L. Schutte
Team Leader, Advanced Materials Technologies
Office of Vehicle Technologies
Energy Efficiency and Renewable Energy

Jerry L. Gibbs
Technology Manager
Office of Vehicle Technologies
Energy Efficiency and Renewable Energy

Project 18516 - Materials for Electric and Hybrid Drive Systems

Agreement 16307 - Modeling/Testing of Environmental Effects on Automotive PE Devices

*A. A. Wereszczak, H. -T. Lin, and O. M. Jadaan**
Ceramic Science and Technology Group
Oak Ridge National Laboratory
P.O. Box 2008, MS 6068, Bldg. 4515
Oak Ridge, TN 37831-6068
(865) 576-1169; fax: (865) 574-6098; e-mail: wereszczakaa@ornl.gov
* *University of Wisconsin-Platteville, Platteville, WI*

DOE Technology Manager: Jerry L. Gibbs
(202) 586-1182; fax: (202) 586-1600; e-mail: jerry.gibbs@ee.doe.gov
ORNL Technical Advisor: D. Ray Johnson
(865) 576-6832; fax: (865) 574-6098; e-mail: johnsondr@ornl.gov

Contractor: Oak Ridge National Laboratory, Oak Ridge, Tennessee
Prime Contract No.: DE-AC05-00OR22725

Objectives

- Understand the complex relationship between environment (e.g., temperature, stress, etc.) and the performance and reliability of the material constituents within automotive power electronic devices (PEDs) and in supportive systems through materials characterization and modeling.
- Seek and identify alternative materials and architectures internal to PEDs and their supportive systems that will improve reliability, enable higher temperature operation, lessen weight, and decrease volume.

Approach

- Develop alternative means of thermal management of PEDs.
- Mechanically evaluate the strength of (brittle) semiconductor chips and apply Weibull distribution statistics.
- Evaluate the thermal management effectiveness of PEDs and seek means to achieve improvements that will enable reliability improvement and higher temperature usage.

Accomplishments

- Received patent for direct-cooled ceramic substrate concept applicable to PEDs. Enables reduction of both mass and volume of inverters for hybrid vehicles. Collaboration with APEEM Program and NTRC.
- Mechanically characterized silicon and silicon carbide semiconductor chips with respect to failure initiation occurring at edges and Weibull effective lengths. Enables improved reliability analysis.
- Characterized numerous properties of neodymium iron boride ($Nd_2Fe_{14}B$) permanent magnetic materials from motors from different makes of hybrid cars. Collaboration with APEEM Program and NTRC.

Future Direction

- Combine thermal modeling and diffusivity experiments on multilaminate structures from PEDs to estimate interfacial thermal losses and enable more accurate thermal modeling and management.
- Refine direct-cooled substrate designs for additional improvement of thermal management of PEDs.
- Continue to dissect failed PEDs to identify failure initiation locations and associations to material degradation.
- Establish collaboration with transportation-based PED OEM or PED end-user.

Introduction

Research performed under the FreedomCAR and Vehicle Technologies Program's Vehicle Systems subprogram seeks to lessen technical and cost barriers and enable development that will benefit advanced vehicles such hybrid electric vehicles. Weight, volume, and cost targets for the power electronics and electrical machines subsystems of the traction drive system in those vehicles must be attained to achieve success. Research areas include more powerful novel traction motor designs, more efficient and higher temperature-capable inverter technologies, reduced footprint and weight of converters, more effective thermal control and packaging technologies, and motor/inverter concepts.

Many, if not most, technical barriers are directly linked to the contemporary material limitations of subcomponents found within devices that comprise inverters, converters, and motors. For automotive power electronic devices (PEDs), contemporary material limitations include insufficient temperature capability, excessive thermal insulation, and excessive electrical insulation (i.e., generates excessive heat).

This project's objectives are to understand the complex relationship between environment (e.g., temperature, stress, etc.) and automotive power electronic PED performance through materials characterization and modeling, and identify alternative material constituents and architectures that will improve their reliability and enable their operation at higher temperatures without compromise to electronic function.

Results

The description of this year's progress is divided into three sections. They are completion of the development of a direct-cooled ceramic substrate, the mechanical evaluation of silicon and silicon carbide semiconductors, and the characterization of permanent magnetic materials. The ceramic substrate and permanent magnetic material efforts involved direct collaborations with ORNL/NTRC projects in the APEEM program. All three efforts directly or indirectly support this project's primary two objectives of understanding reliability as a function of environment (e.g., temperature, stress) and the search for improved PED architectures that will improve thermal management

Direct-Cooled Ceramic Substrate

Thermal and thermomechanical modeling support was provided to ORNL/NTRC's R. Wiles, K. Lowe, and C. Ayers throughout the development of a direct-cooled ceramic substrate concept. It was recently patented (#2009/0231812), and a schematic from that patent is shown in Fig. 1. The patent describes cooling a three-dimensional, direct metallization layer in a PED. To enable sufficient cooling, coolant flow channels are formed within the ceramic substrate. The direct metallization layer (typically copper) may be bonded to the ceramic substrate, and semiconductor chips (such as IGBT and diodes) may be soldered or sintered onto the direct metallization layer to form a power electronics module. Multiple modules may be attached to cooling headers that provide in-flow and out-flow of coolant through the channels in the ceramic substrate. The modules and cooling header assembly are preferably sized to fit inside the core of a toroidal shaped capacitor.

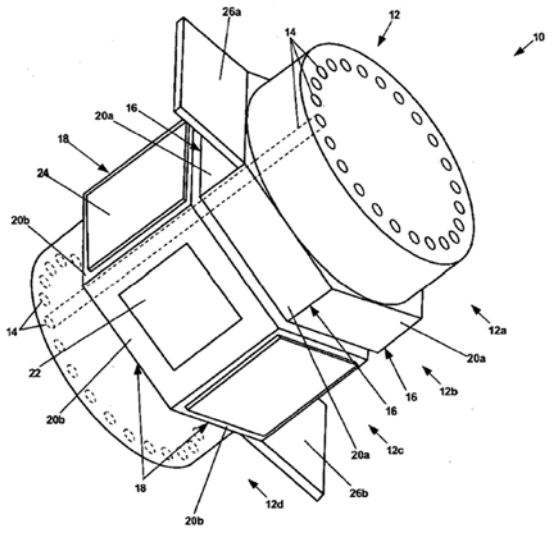

Figure 1. Schematic of the patented direct-cooled ceramic substrate (#2009/0231812).

Si and SiC Semiconductor Strength: Edge Effects

This effort focused on the strength testing and effective length evaluations of two different mechanical testing configurations designed to specifically promote failure initiation at edges of silicon (Si) and silicon carbide (SiC) chips. The effective length estimation enables estimations of failure-stress size scaling that is inherent to brittle materials.

The two test configurations are shown in Fig. 2. They are used to subject the 10x10x0.25 mm silicon and silicon carbide plates to three-point-bending or

anticlastic bending. Because these chips are so highly polished, the presumption was that edge-located flaws would be more apt to cause fracture than any present surface flaws.

The produced stress distributions for each of the two loading configurations are shown in Fig. 3. The manner in which the effective length for each was determined is shown as well. The resulting effective length as a function of Weibull modulus for each is shown in Fig. 4. The functions shown in Fig. 4 enable strength-size-scaling for the same strength-limiting flaw type.

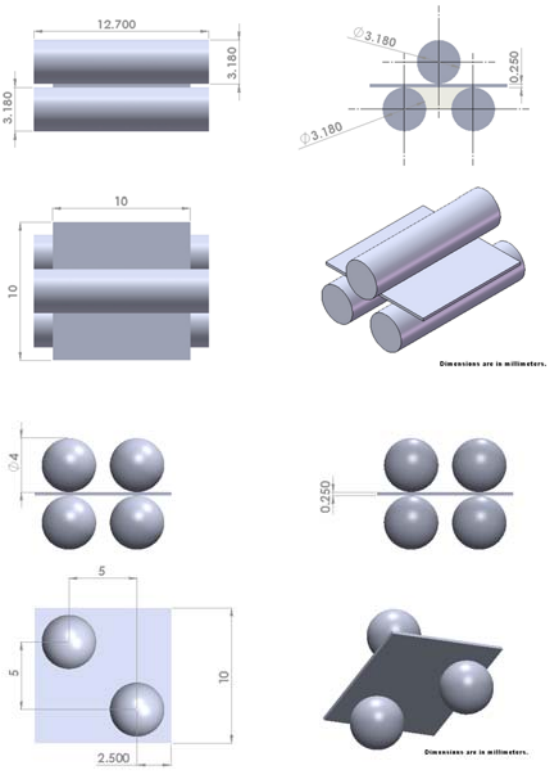

Figure 2. Two test configurations were sought to measure strength of the Si and SiC chips when edge-located flaws limit strength. Three-point (top) and anticlastic bending (bottom) configurations shown.

$$L_{e,3-point} = \frac{2L}{m+1}$$

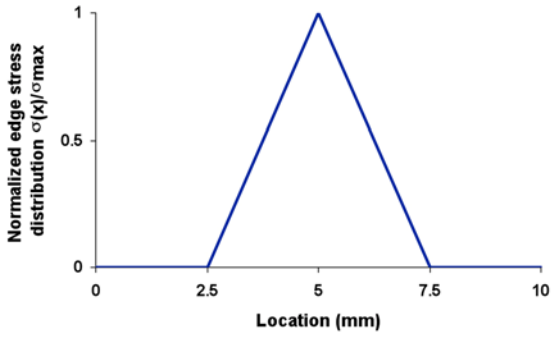

$$L_{e,AC} = 4\left[\int_0^{x1}\left(\frac{\sigma_{bottom\_edge}(x)}{\sigma_{\max}^{m}}\right)^{m} dx + \int_{x1}^{10}\left(\frac{\sigma_{top\_edge}(x)}{\sigma_{\max}^{m}}\right)^{m} dx\right]$$

σ(x) expressions obtained by fitting 9th order polynomials to curves below

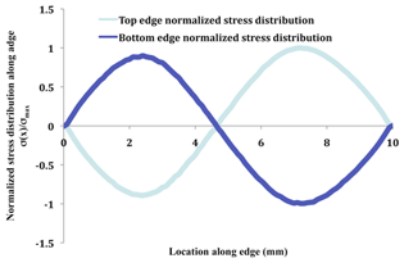

Figure 3. Resulting stress distributions along edges of the three-point-bend (top) and anticlastic bending (bottom) configurations.

There are advantages and disadvantages to each method. The three point-bending is the simplest configuration; however, it samples the least amount of edge length for flaws, and if there's differences in the surface condition of both sides of the chip and orientation (which is true for both for the silicon chips and the latter true for the silicon carbide chips), then up to four combinations of test sets need to be generated. The advantage of the anticlastic bending is that it establishes the shown stress profile in Fig. 3 on all eight edges, and therefore, if there were a weakest side among them, then in principal, this test method would exploit that. The disadvantages are the Hertzian contact stresses caused by the four balls need to be managed so not to cause the failure initiation, and the produced stress state at failure is somewhat complex making fractography somewhat challenging.

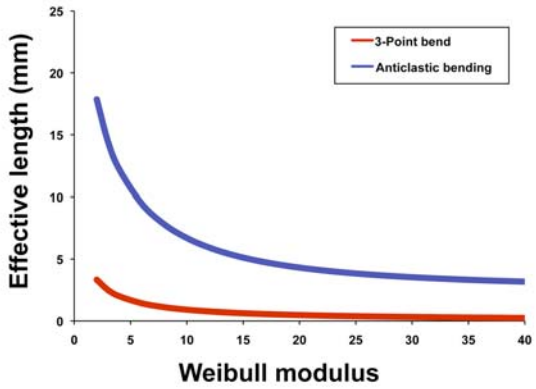

Figure 4. Effective length as a function of Weibull modulus for the two configurations.

Examples of results strength distributions are shown in Figs. 5-6. Failure stress anisotropy was evident from the three point bending of SiC as shown in Fig. 5. Unfortunately the supplier of the Si did not mark anisotropy of the provided die, so there was not record available to study anisotropy in Si (which is expected to exist). Because anticlastic bending subjects all 8 edges to tensile stress, the unknown of orientation in the Si chips does not inhibit testing. A comparison of anticlastic bending failure stress of the Si and SiC chips is shown in Fig. 6 with a higher characteristic failure stress (but more scatter) existing with the SiC chips.

Fractography of the Si and SiC strength test specimens is challenging. Because these specimens (chips) were single crystals, almost all specimens twinned during mechanical loading (3-pt and anticlastic bendings), and their patterns hinder the identification of the failure location. Work is ongoing.

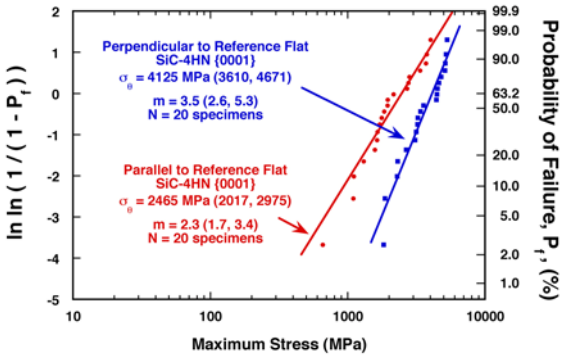

Figure 5. Failure stress anisotropy in SiC as exploited by three-point bending.

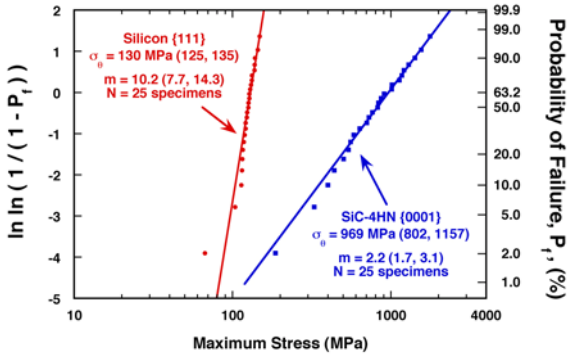

Figure 6. Anticlastic bending results comparing Si and SiC.

Permanent Magnetic Materials

Characterization and measurement of properties of permanent magnet materials (PMM) were performed. The PMM was neodymium iron boride ($Nd_2Fe_{14}B$ or NdFeB for short) and came from motors from a Toyota Camry, Lexus, and Prius (PMMs provided by ORNL/NTRC's T. Burress).

Microstructures shown on fracture surfaces of each of the three PMMs are shown in Fig. 7. For the specimen preparation to examine in them in the scanning electron microscope (SEM), a small volume of material was required otherwise its magnetic field interfered with the SEM imaging.

The measured properties and interpretation of their results are summarized as follows:

- CTE. The coefficient of thermal expansion (CTE) in this class of PMM is anisotropic (transversely isotropic). Due to the thin-plate geometry of the supplied materials, and the need to have a relatively long specimen for measurement, the CTE of only the in-plane orientation was measured. A dual-rod dilatometer was used for the measurement against a sapphire standard. The average CTE between 25-125°C was -4.1, -4.9, and -4.3 x 10^{-6}/°C for the materials from the Camry, Lexus, and Prius motors, respectively. A negative CTE in this orientation is typical for this material. Given an estimated ± 10% error in the CTE values, the PMMs from these three motors are equivalent or even identical.
- Density. 7.61 g/cm^3 for the Camry material, 7.54 g/cm^3 for the Lexus material, and 7.58 g/cm^3 for the Prius material.

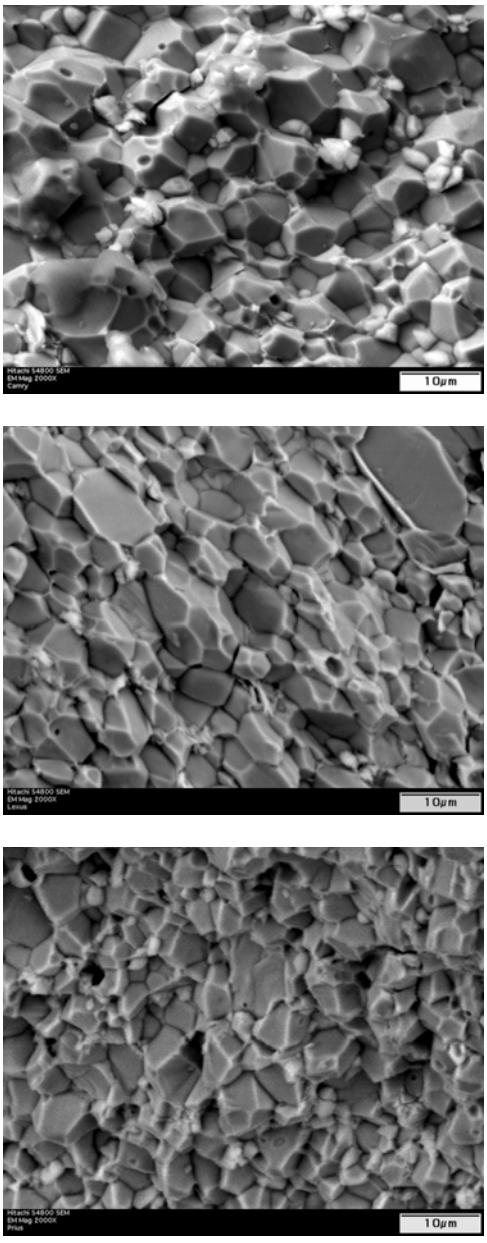

Figure 7. Microstructures of the PMM from the motor of a Camry (top), Lexus (middle), and Prius (bottom) hybrid vehicle.

- E and ν. A resonant ultrasound spectroscope (RUS) was used to measure the elastic modulus (E) and Poisson's ratio (ν) of the three NdFeB materials. The elastic modulus was measured to be 160, 165, and 164 GPa for the Camry, Lexus, and Prius NdFeBs, respectively. With an estimated 5% error in measurement, the elastic moduli can be concluded to be equivalent. The Poisson's ratios were 0.240, 0.259, and 0.245 for the Camry, Lexus, and Prius materials.
- Hardness. The average Knoop hardness of each of the three NdFeBs was measured using a 1-kg force according to ASTM C1326. They were 5.93 ± 0.15, 5.83 ± 0.09, and 5.95 ± 0.13 GPa for the Camry, Lexus, and Prius NdFeBs, respectively. Ten indents comprised each average value and the shown ± values are one standard deviation.
- Phase analysis. X-ray diffraction of each of the three NdFeBs was performed. Only the tetragonal $Nd_2Fe_{14}B$ phase (PDF# 39-473) was identified in all three materials.
- Elemental analysis. Semi-quantitative energy dispersive x-ray fluorescence (XRF) and energy dispersive spectroscopy (EDS) were performed on all three materials. The technique cannot identify low atomic number elements (e.g., boron). The XRF indentified 53 wt% Fe and 47 wt% Nd for the Camry material, 49% Fe and 51% Nd for the Lexus, and 60% Fe and 40% Nd for the Prius. XRF did not detect any other elements. EDS identified Fe and Nd too.

Based on the equivalence of each measured property or characteristic, these three PMMs could be identical.

Conclusions

A new concept for a direct-cooled ceramic substrate for use with PEDs was developed and patented. It enables effective thermal management with reduced weight and space.

The mechanical strength of Si and SiC semiconductors was measured and interpreted with respect to failure initiation (i.e., strength-limitation) being limited by the quality of the edge preparation. This brittle-material-testing approach, and the generated results, enables probabilistic reliability analysis and design optimization with respect Si's and SiC's strength distributions.

Numerous properties were measured of neodymium iron boride permanent magnetic materials from motors from Toyota Camry, Lexus, and Prius hybrids. Equivalence of properties of all three suggests they could be the same materials.

Agreement 16305 - Solder Joint of High Performance Power Electronics: Materials-by-Design

G. Muralidharan and Andrew Kercher
Materials Science and Technology Division
(865)574-428; fax: (865) 574-4357; e-mail: muralidhargn@ornl.gov

Burak Ozpineci
Engineering Science and Technology Division
(865) 241-4329; fax: (865) 574-9329; e-mail: ozpinecib@ornl.gov

Scott Leslie
Powerex Inc
(724) 925-4482; fax: (724) 925-4468; email:sleslie@pwrx.com

DOE Technology Manager: Jerry L. Gibbs
(202) 586-1182; fax: (202) 586-1600; e-mail: jerry.gibbs@ee.doe.gov
ORNL Technical Advisor: D. Ray Johnson
(865) 574-4556; fax: (865) 241-0411; e-mail: stintondp@ornl.gov

Contractor: Oak Ridge National Laboratory, Oak Ridge, Tennessee
Prime Contract No.: DE-AC05-00OR22725

Objectives

- Evaluate the reliability of high temperature solders for use in power electronic packages subject to thermal cycling
- Identify material property characteristics that would impact long-term reliability of solder joints to enable materials-by-design approach

Approach

- Evaluate the degradation in solder joint properties due to thermal cycling and steady state aging
- Evaluate the effect of solder joint compositions and hence the mechanical and physical properties on solder joint property degradation.

Accomplishments

- Solder joints consisting of one Au-Sn and one Sn-Ag solder capable of 200^{o}C operation were fabricated between Si dies or SiC dies and DBC substrates
- Thermal cycling between 200^{o}C and 5^{o}C have been carried out in representative joints and damage evolution has been followed using high resolution X-ray radiography
- Steady state aging has been completed on Au-Sn solders with exposure up to 1500 hours to understand the extent of microstructural evolution

Future Direction

- Effect of solder mechanical properties on reliability will be assessed using finite element modeling
- Mechanical property degradation of the solder joints will be quantified
- Properties and reliability of sintered joints will be evaluated and compared with solders

Introduction

Development of next generation hybrid and electric propulsion vehicles depend on the availability of high efficiency, lower cost, lower weight and lower volume, power electronic components and subsystems. These future power electronic systems need to operate reliably for 15 years at junction temperatures of 200°C in contrast to current maximum junction temperatures of about 125°C for such packages. Thus, there is a significant need to understand the effect of higher temperatures on power electronic components and subsystems.

Electronic packaging is a multidisciplinary technology which takes additional complications in power electronics due to the advanced thermal management that is required for packaging of such devices. Functions of an electronic package can be classified into a few categories:

1. Electrical interconnection (providing electrical path for power and signals)
2. Thermal interconnections (providing thermal path for the heat dissipated by the parts)
3. Electrical insulation (providing integrity of the electrical signals)
4. Environmental protection (providing protection of the parts and assembly from damage during handling and from the environment, especially moisture)
5. Mechanical support (providing mechanical support, rigidity, and ductility)

Typical packages used for devices consist of multiple elements. In designing a package for electronic devices to operate at high temperatures in harsh environmental conditions, a few important factors have to be considered:

1. Heat dissipation to keep the temperatures at safe operating levels.
2. Materials used must be stable at the higher temperatures and be able to maintain their properties during prolonged exposure to these temperatures and harsh environments
3. Thermal stresses caused by thermal expansion mismatches between the devices and various package elements including the substrate must be mitigated
4. Thermal shock resistance will be needed to withstand thermal cycling during service

Elements of a typical high-temperature package: Figure 1 shows a cross-section of a typical state-of-the-art packaging technology used for packaging SiC devices. Functions of several key elements are outlined below along with the materials requirements.

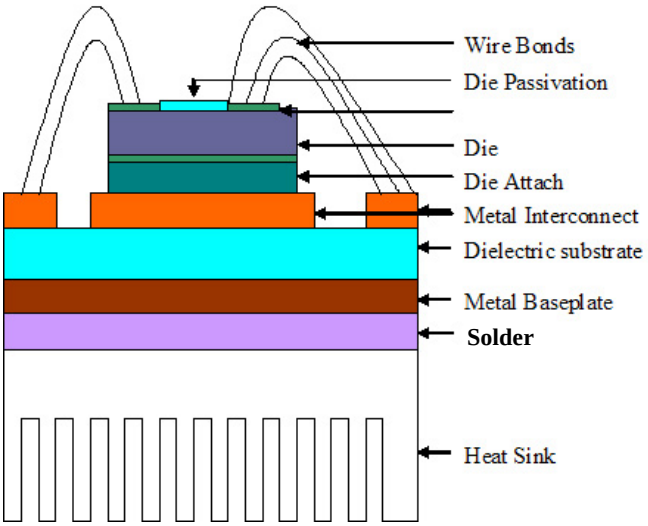

Figure 1. Schematic of a typical high temperature package

***Substrate*:** The key part of the package is the insulating dielectric substrate which has an electrically conductive metallization bonded to it on one surface. The insulating substrate can be either Al_2O_3 or AlN with the metallization layer being copper (as in Direct Bonded Copper (DBC)) or Au. Since SiC devices are designed to operate at high temperatures and high voltages, it is critical that the substrates remain thermally and mechanically stable, while retaining their dielectric properties to desired temperatures.

The metallization layer provides an electrical path between the multiple active and passive devices that may be bonded to the same substrate, and between the packaged devices and the external circuit. It is important that the metallization layer has good bonding with the substrate, retains its good electrical conductivity at high temperatures along with minimum tendency for the formation of intermetallic compounds. In addition, it is desirable that the metallization layer possesses good environmental resistance, and resistance to electromigration. As a rule of thumb, the melting temperature must at least be 1.5 times the operating temperature (in Kelvin) to prevent any diffusion related problems such as creep and electromigration.

Although the substrate is electrically insulating, it is desirable that its thermal conductivity be high to enable efficient dissipation of heat away from the SiC die. Hence AlN which has a higher thermal conductivity than Al_2O_3 is preferred from a thermal management perspective. Another important factor is the difference in the coefficient of thermal expansion between the device and the substrate. Larger differences in the coefficient of thermal expansions cause larger thermal stresses. Both Al_2O_3 and AlN have a thermal expansion coefficient that compares well with that of SiC.

Wire bonds: Electrical path from the device to the package is achieved through the use of one or more wire-bonds. These are typically aluminum wire bonds that are thermo-sonically bonded to the bond-pads on the device and to the metallization layer. Multiple wires are used for high current applications and to reduce stray inductance. It is known that wire-bonds are one of the weakest links within all the packaging elements.

***Die-attach*:** The device or die is mechanically bonded to the metallization layer through the use of a die attach. A die attach material should have the following properties:

1. Good adhesion with both the die and the substrate to that no debonding or delamination occurs
2. Self-resilience to provide good stress relaxation behavior so that the internal stresses are reduced to low levels
3. High thermal conductivity so that the heat dissipated from the power chip and the thermal expansion difference between the die and the substrate can be minimized
4. An appropriate processing temperature and good thermal stability to fit the typical process hierarchy
5. Good corrosion resistance
6. Good reworkability

Although organic materials have been used as die-attaches for packaging Si-based devices, these materials have limited applications in packages designed for temperatures of 200^{o}C. Many different kinds of materials have been explored for potential use in die-attach applications. High melting point solders, such as gold-tin, gold-germanium; gold-indium, as well as Au-Ag-Si transient liquid phase bonding, gold thermo-compression bonding and thick-film materials have been considered in previous work. Thus, the choice of appropriate die-attach materials is critical in achieving desired operating temperatures and performance, including the reliability. Another important issue with the use of increased operating temperature is that devices will have to tolerate deeper thermal cycles. The stresses from mismatched coefficients of thermal expansion (CTE) increase with larger thermal cycles and so the potential for fatigue failure is greater with high-power devices. Since metallic brazes have a relatively large thermal expansion, there is a large expansion mismatch with the SiC device and the substrate (such as AlN, Al_2O_3, or Si_3N_4), thus generating large thermal stresses and hence resulting in premature failure during thermal cycling.

Since solder joints and wire bonds serve as pathways for electrical connection to and from electronic devices used in hybrid and electric vehicles, failure of these solder joints and wire bonds will result in catastrophic failures of critical electronic components and hence systems used in these automobiles. Thus, there is a significant need to study the failures of electronic packages induced by metallurgical changes of solder joints and wire bonds. The focus of this work is to understand factors related to the reliability of a die attach solder joint used in power packages and to help understand factors that affect the selection of the appropriate solder material for reliable high temperature operation.

Task 1. Evaluate the reliability of selected commercially available packages. This task will be accomplished through interactions with industrial partners actively involved in the fabrication of power packages. It should be noted that there are no power packages currently available commercially for use at temperatures of 200^{o}C. Hence this part of the work will be performed on commercially available packages that can operate at the highest temperature currently feasible. The key concept behind this task is to understand the reliability of packages that are currently commercially available for high temperature use. This would establish a baseline to help compare the performance of alternate higher temperature solders in terms of expected lifetime. Since failures are induced in solder joints and other components by combination of temperatures, and stresses it is anticipated that reliability will be evaluated using steady state exposures to high temperatures and thermal cycling between temperature extremes as specified by JEDEC standards. Electrical properties will be measured as a function of thermal cycles to understand the impact of thermal cycling on electrical properties.

Task 2. Evaluate the reliability of joints prepared from selected high temperature solders. In this task, in collaboration with industrial partners, we will identify compositions of solders that have the potential to be used in a package capable of operating at a temperature of 200°C. Single solder joints will be fabricated and will be representative of die attach region in power packages. These joint will be subjected to steady state high temperature exposure and thermal cycling as in Task 1 to understand the evolution of microstructure and defects. The effect of solder melting temperature, and solder physical and mechanical properties on the lifetime observed during thermal cycling will be evaluated. This will eventually result in the identification of solder joint compositions and properties that will result in reliable high temperature packages. It should be noted that current reliability testing of plastic packages using JEDEC standards is limited to a high temperature of about 150°C. Standards to evaluate accelerated testing using thermal cycling representative of exposure to 200°C have not been established at this time. It is anticipated that knowledge gained from this work will assist in the establishment of such standards.

Task 3. Characterize microstructural evolution in solder joints subject to thermal cycling: Microstructural evolution occurs in solder joints during high temperature exposure. Coarsening of solder joint microstructures takes place during high temperature due to accelerated diffusion, and interdiffusion results in the formation of intermetallic compounds. Furthermore, combination of stresses and high temperatures results in creep deformation and combined creep/fatigue of solder joints resulting in the formation of voids. Characterization of microstructure of joints will be carried out using a combination of optical microscopy, x-ray radiography, ultrasonics and other techniques. Emphasis in this task is to understand the effect of high temperature exposure and thermal cycling on the evolution of defects and ultimately the failure of the functionality of the solder joint.

Extensive interaction with industrial partners will occur during all three tasks. Discussion with industrial partners is expected to help in the selection and fabrication of solder joints relevant to the industry. Results obtained in this work on the reliability data can be effectively transferred to industrial partners. It is anticipated that this work will ultimately help in the identification of appropriate solder joint compositions and fabrication of packages with optimum reliability.

Results

Solder Joint Fabrication

In collaboration with Powerex Inc., two solder joint compositions – 80Au-20Sn (T_m=280°C) and Sn-3.5Ag (T_m=221°C) were downselected for reliability evaluation in FY2009. Initial reliability testing of solder joints were carried out with solder joints prepared between silicon dies and DBC substrates. 2.5 mm x 2.5 mm silicon dies with Ti/Ni/Au metallization were mounted on a metallized AlN DBC substrate with the metallization consisting of a medium phosphorus (6-12%) Nickel layer followed by a flash Au layer on the surface. To understand the void content in the solder joint, high resolution x-ray radiography was carried out on selected specimens in the as-received condition. Figure 1 shows a typical Au-Sn solder joint prepared in collaboration with Powerex Inc. and a corresponding high resolution x-ray image of the joint showing voids present within the solder joint.

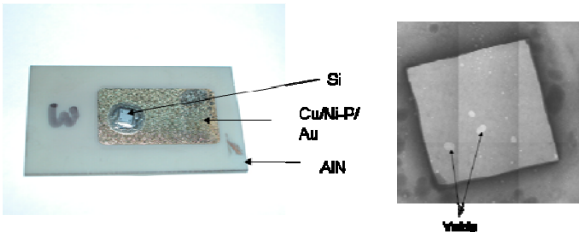

Figure 1. Typical Image and High Resolution X-ray Radiograph of Processed Au-Sn Solder Joint.

Reliability of solder joints were evaluated using thermal cycling between 200°C and 5°C with hold times of 30 minutes at 200°C and 5 minutes at 5°C. This thermal profile was selected since it represented exposure to the maximum proposed operating temperatures of 200°C on the higher end for prolonged periods of time as would be typical of uninterrupted operation at these temperatures. Figure 2 shows a typical thermal profile used in these experiments. The effect of thermal cycling on damage evolution within the solder joints was followed using high resolution X-ray radiography. Effect of steady state exposure on the microstructure of the solders is also being evaluated using steady-state aging at 200°C for times up to 3000 hours.

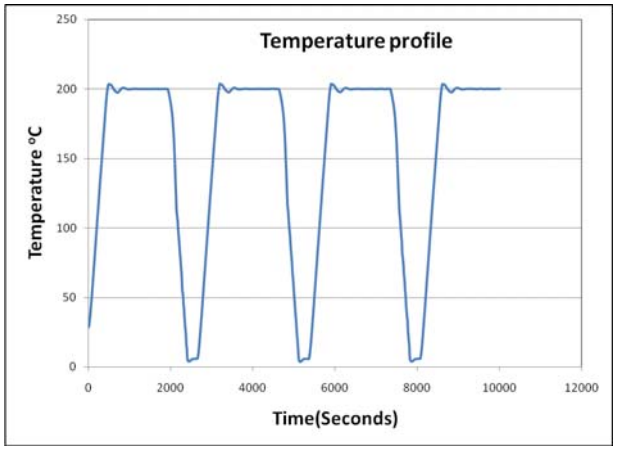

Figure 2. Typical thermal cycling profile used in the reliability testing of solder joints.

Thermal cycling of Au-Sn solder joints

Figure 3 shows the evolution of damage on a Au-Sn solder joint subject to thermal cycling using conditions depicted in figure 2. Note that cracking of the silicon die occurs very early in the thermal cycling process. This suggests that Au-Sn solder joints may not be appropriate for use in attaching silicon to DBC substrates and further work on joints between silicon and DBC was suspended. However, there was a need to understand the behavior of joints between SiC and DBC substrates subject to similar thermal cycling conditions. 2.0 mm x 2.0 mm SiC dies were mounted on a metallized AlN DBC substrate with the metallization consisting of a medium phosphorus (6-12%) Nickel layer followed by a flash Au layer on the surface. These joints are being subject to the thermal cycles shown in figure 2. Results obtained to-date suggests that such joints are able to sustain thermal cycling WITHOUT cracking of the SiC die. Further thermal cycling will be carried out to understand evolution of the damage in these solder joints and to understand the initiation of failure.

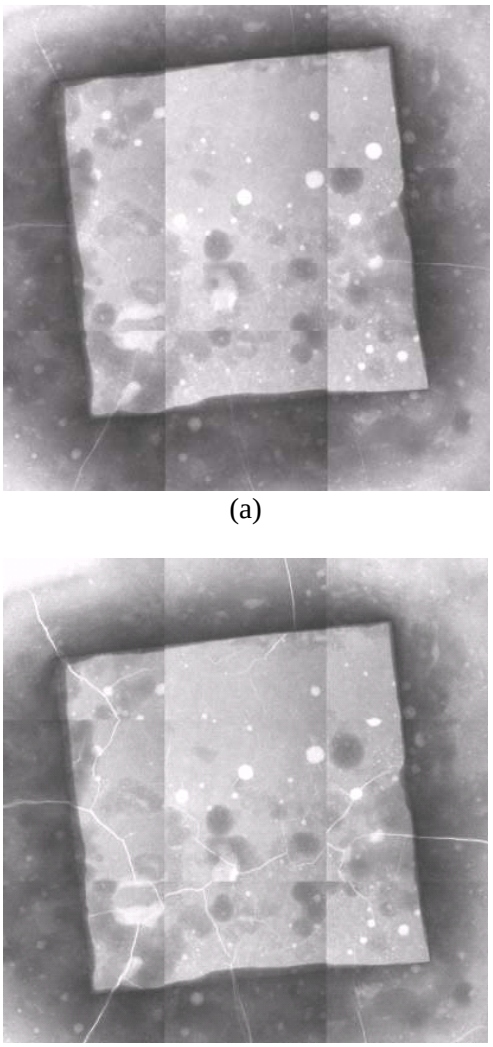

(a)

(b)

Figure 3. (a) High resolution X-ray radiography from a Au-Sn solder joint in the as-processed condition. Note the presence of voids within the solder joint. (b) High resolution X-ray radiography from the same Au-Sn solder joint after thermal cycling. Note the presence of cracks within the silicon die that has been formed due to the cyclic stresses in the thermal cycling process.

Thermal Cycling of Sn-Ag solder joints

2.5 mm x 2.5 mm silicon dies with Ti/Ni/Au metallization were mounted on a metallized AlN DBC substrate with the metallization consisting of a medium phosphorus (6-12%) Nickel layer followed by a flash Au layer on the surface using Sn-Ag solder joints. Figure 4 shows the results of thermal cycling on the high resolution X-ray radiograph obtained from the samples. Note that significant damage has been introduced due to thermal cycling but the joint has not failed mechanically even after 3000 thermal cycles. Future work will evaluate the strengths of these joints as a function of thermal cycling.

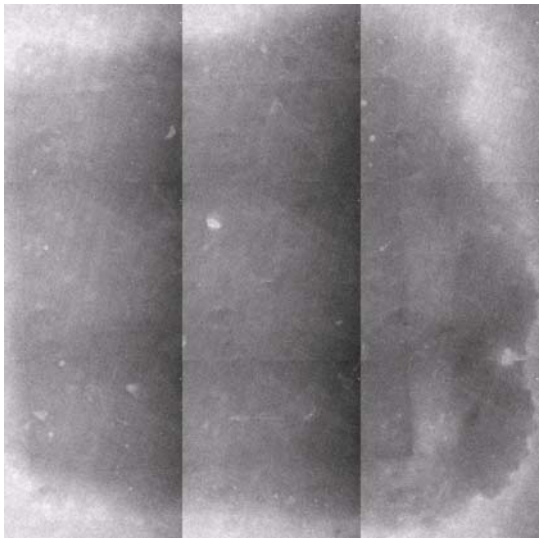

(a)

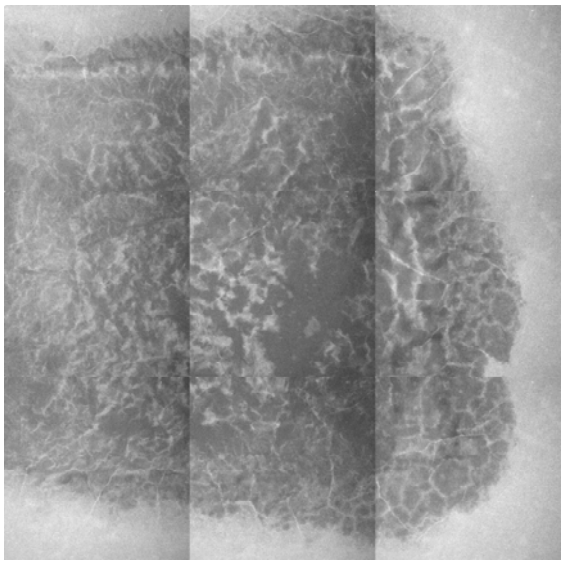

(b)

Figure 4. (a) High resolution X-ray radiography from a Sn-Ag solder joint in the as-processed condition. Note the presence of voids within the solder joint. (b) High resolution X-ray radiography from the same Sn-Ag solder joint after 3000 thermal cycles. Note the significant damage that has been introduced within the solder joint due to thermal cycling.

Steady- State Aging of Au-Sn Joints

In addition to thermal cycling tests, effect of thermal aging on microstructure is being evaluated in Au-Sn and Sn-Ag joints. Figure 5 shows the microstructure of Au-Sn solder joints in the as-received and after exposure to 200^{o}C for 1500 hours. Qualitative comparison shows very little increase in size of microstructural features. Quantitative comparisons will be pursued this year.

Conclusions

- Stresses introduced during thermal cycling of Au-Sn solder joints between Si and DBC results in cracking of the silicon die
- Preliminary evaluation of Au-Sn solder joints between SiC and DBC substrates show that SiC dies may resist cracking under similar thermal cycling conditions
- Sn-Ag joints show progressive degradation during thermal cycling but do not show complete mechanical failure when subject to as many as 3000 thermal cycles.

Publications/Presentations

None at this time

(a)

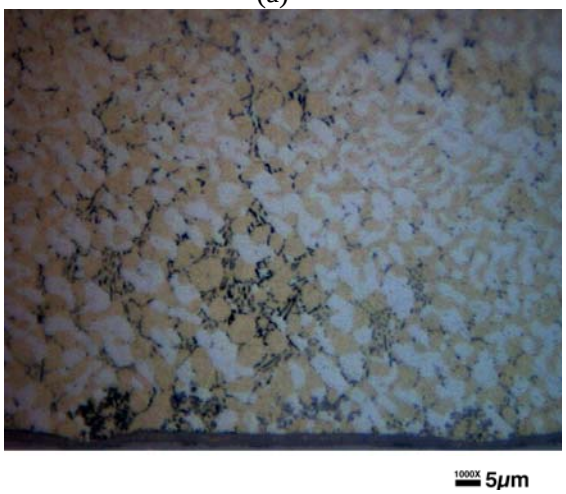

(b)

Figure 5. Effect of Steady State Aging at 200°C on the microstructure of Au-Sn solder joints (a)As processed, and (b) 1500 hours of aging at 200°C

Agreement 16306 - Power Electronics Materials Compatibility

D. F. Wilson, B. L Armstrong, C. W. Ayers and S. J. Pawel
Oak Ridge National Laboratory
P.O. Box 2008, MS 6063, Bldg. 4515
Oak Ridge, TN 37831-6068
(865)241-5862; fax: (865) 574-4913; e-mail: armstrongbl@ornl.gov

DOE Technology Manager: Jerry L. Gibbs
(202) 586-1182; fax: (202) 586-1600; e-mail: Jerry.gibbs@ee.doe.gov
ORNL Technical Advisor: D. Ray Johnson
(865) 576-6832; fax: (865) 574-6098; e-mail: johnsondr@ornl.gov

Contractor: Oak Ridge National Laboratory, Oak Ridge, Tennessee
Prime Contract No.: DE-AC05-00OR22725

Objectives

- Develop the methodology to map the materials compatibility space of power electronic materials in their operating environment.
- Validate the methodology for accelerated evaluation of power electronic devices.
- Populate a materials-coolant performance database.

Approach

- Establish methodology and build a test apparatus based on power pulsing an electronic component while it is immersed in coolant.
- Evaluate degradation mechanisms using analytical tools.

Accomplishments

- Built a test apparatus based on power pulsing an electronic component while immersed in coolant.
- Developed a flexible accelerated testing methodology.
- Methodology allows for expression of failure modes.

Future Direction

- Refine methodology for accelerated testing.
- Evaluate additional coolant effects and begin development of a database indicating performance boundaries.

Introduction

The use of evaporative cooling for power electronics (PE) has grown significantly in recent years as power levels and related performance criteria have increased. As service temperature and pressure requirements are expanded, there is concern among the Original Equipment Manufacturers (OEMs) that the reliability of electrical devices will decrease due to degradation of the electronic materials that come in contact with the liquid refrigerants. Potential forms of degradation are expected to include corrosion of thin metallic conductors as well as physical/chemical deterioration of thin polymer materials and/or the interface properties at the junction between dissimilar materials in the assembled components.

Barriers to the deployment of new power electronic components in automotive applications include weight, size, reliability and cost. One approach to reduce the weight of the PE system is to use direct cooling from existing air conditioning systems using R134a refrigerant. This would reduce the weight of the power electronics system by eliminating the need for a separate cooling system. However, direct contact 2-phase cooling necessitates the evaluation of the PE compatibility with and reliability in the coolant. This project will develop the laboratory methodology to evaluate the degradation of power electronics materials by evaporative liquids. In addition, a database indicating performance boundaries for standard materials and for several candidate coolants will be established.

Results

Test Methodology

A laboratory test system, shown in Fig. 1, which was designed and built in FY 2008, allows for high current flow and shaping of the wave form. Testing has been performed using a square wave of one or two seconds on and one or two seconds off to drive 10 to 40 amperes through 0.4 mm (400 microns) diameter aluminum wire shown in Fig. 2. The apparatus allows for condensation and recycle of the evaporated liquid, data recording and visual observation of the boards during testing.

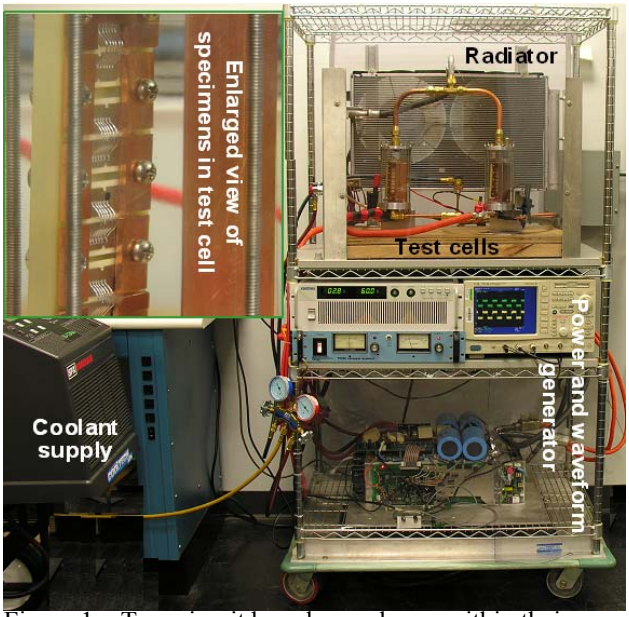

Figure 1. Two circuit boards are shown within their glass enclosures, which are in front of the condensing cooling radiator. Below this is shown the wave form shaping system and the high current power supply.

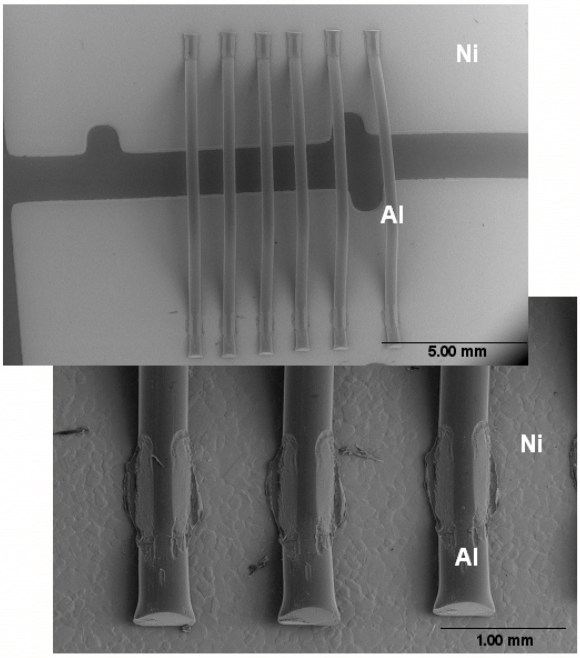

Figure 2. Scanning electron (SE) images of the typical appearance of six-wire test circuit. The bond regions show uniform contact area and deformation associated with the bonding process.

The test methodology that involves pulsing of the PE circuit at appropriate power levels and exaggerated cycle times allows for changes in power-on and power-off times. As such, it facilitates accelerated testing without changes in the failure mode(s) that would be observed in service. Further, the methodology allows for an evaluation of the effect of nucleate boiling on the failure mechanism(s).

Evaluations

In order to have a qualitative measure of the stressing of the wires during testing, one wire bond board was modified to allow for temperature measurement. A thermocouple was epoxied within a groove cut into the back layer of one of the boards in the vicinity of the wires on the front side. Figure 3 shows the oscilloscope trace of a test at 180 amps using two second on and four second off cycle through the series circuit. This equates to 30 amps through each 400 μm (15 mil) wire. The actual temperature being recorded is not representative of the true temperature being experienced by the aluminum wires because of the insulation provided by the board between the wires and the thermocouple, and the cooling effect from evaporative cooling. However, the observed 3°C differential between the highest and lowest temperatures during the cycle (purple trace in Figure

3), which is smaller than that actual being experienced by the wires, is indicative of the stress being placed on the wires.

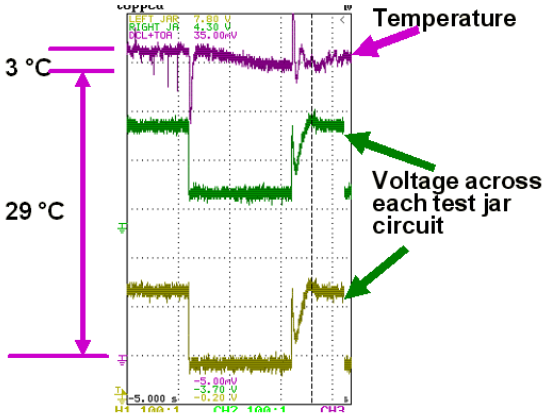

Figure 3. Oscilloscope trace of a 180 amps test through the series circuit. This is equivalent to 30 amps through each 400 µm (15 mil) wire.

Examination of the wires, after 690,570 cycles of one second on and one second off that drove 10 amperes through each wire revealed no observable environmental effects. However, after operations at 240 amps (40 amps through each 400 micron diameter wire) with 2 seconds on and 2 seconds off cycles, changes were observed at the crown of wires on the two cards at the bottom of the test cells. These cards were removed for destructive analyses. Figure 4 presents a low magnification image of the wires on one of the boards.

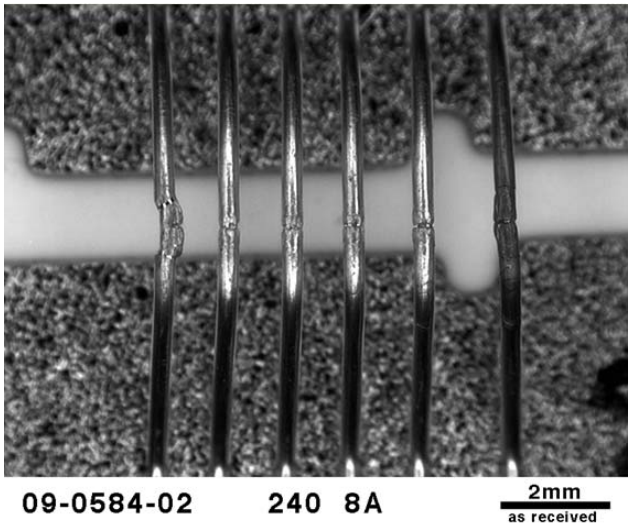

Figure 4. Aluminum wires showing changes that occurred at their crowns.

At higher magnification, significant deformation of the wires at the crowns is seen, as presented in Figures 5 and 6. Also, as shown in Figure 6, a large pore develops in the damaged crown region.

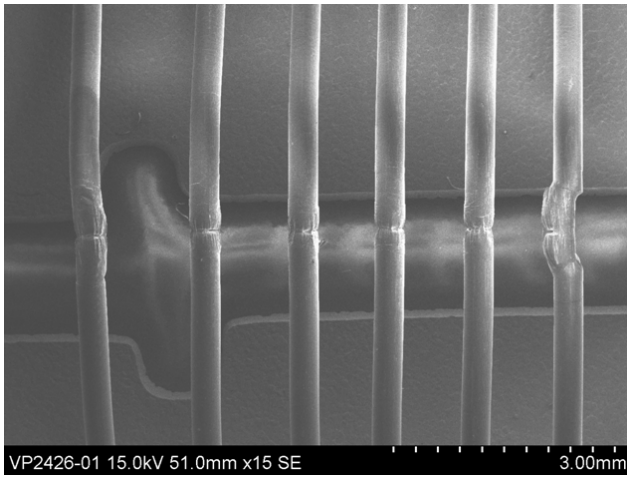

Figure 5. SEM image showing deformation and large pores on the aluminum wires.

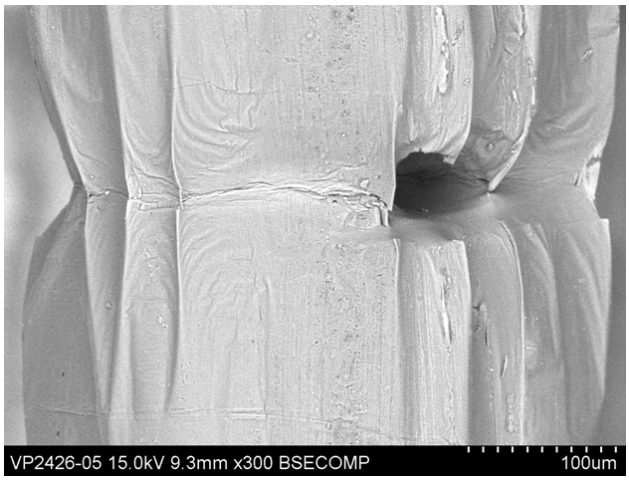

Figure 6. SEM image showing details of the typical deformation and large pore observed on the aluminum wire.

Subsequent to SEM analyses, wires were metallographically mounted and polished. As shown in Figure 7, there is a significant change in grain size and structure from the bond region to the crown of the wire as a result of this testing. Near the bond region, the structure consists of small diameter, elongated grains that is consistent with wire drawing. Moving along the wire toward its crown, increasing grain size is observed until at the crown, very large equiaxed grains that are consistent with recrystallization and grain growth from high temperature excursions present themselves. This recrystallization and grain growth results in few grains

across the diameter of the aluminum wire at the crown, as shown in Figure 7.

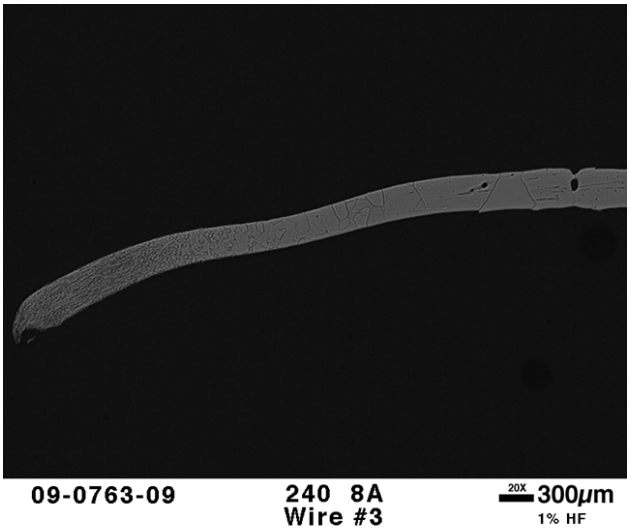

Figure 7. Polished cross section of aluminum wire showing the change in grain size and structure from the bond point (left) to the crown (right).

Conclusions

The adopted testing methodology is allowing for an expression of failure modes that would be observed in service. Further, it is facilitating accelerated testing.

Acknowledgements

The authors would like to thank Steven Campbell for all his work assembling and running the test apparatus.

Agreement 13295 - Development of Improved Powder for Bonded Permanent Magnets (co-funded with Project 19026 – Electrical Machines Research)

Principal Investigator: Iver E. Anderson
Materials and Engineering Physics Program
Ames Laboratory, Iowa State University
Ames, IA 50011
Voice: 515- 294-9791; Fax: (515) 294-8727; E-mail: andersoni@ameslab.gov

DOE Technology Manager (Propulsion Materials): Jerry L. Gibbs
(202) 586-1182; fax: (202) 586-1600; e-mail: jerry.gibbs@ee.doe.gov

DOE Technology Development Manager: Susan A. Rogers
Voice: 202-586-8997; Fax: 202-586-1600; E-mail: Susan.Rogers@ee.doe.gov

---

Objectives

- Increase the maximum operating temperature from about 125˚C to 180-200˚C and improve the environmental stability of permanent magnet (PM) materials to enable high volume manufacturing of advanced electric drive motors with improved operating characteristics and lifetime.
- Reduce the overall manufacturing cost of traction motors and enable a new generation of machine designs by developing magnets that can be formed efficiently into net-shapes or molded in-place as motor component assemblies with high magnetic energy density to conserve valuable materials.

Approach

- Develop enhanced control of nucleation and growth of nano-crystalline structure in rapidly solidified magnet alloy powders to reduce processing cost and to minimize annealing requirements.
- Attempt development of anisotropic (aligned cellular or single crystal) magnetic microstructures in particulate of mixed Rare Earth (MRE)-Fe-B alloys to make large gains in bonded magnet properties.
- Explore prospects for anisotropic sintered permanent magnets from the MRE-Fe-B alloys using transient liquid phase sintering or extrinsic additives for consolidation of aligned high strength (fully dense) magnets for high temperatures.
- Implement recommendations from analysis of total manufacturing cost for advanced electric drive motors that called for increased effort on anisotropic particulate for bonded MRE permanent magnets and other RE magnet types, e.g., sintered, which utilized improved tolerance to high operating temperatures.
- Formulate new research thrust on non-RE permanent magnets of sufficient magnetic strength and resistance to demagnetization for vehicle traction motor applications that include high operating temperatures.

Major Accomplishments

- Reviewed recommendations and initiated research emphasis on anisotropic sintered and bonded RE permanent magnets, consistent with the independent analysis that was received of the total manufacturing cost for advanced electric drive motors in appropriately designed interior PM rotor electric machines.
- Developed a milling process for chill cast ingots of MRE magnet alloys that involves hydrogen charging/decrepitation (HD), inert atmosphere (glove box) handling, and conventional ball milling to produce desirable powders for sintering with an average particle size of ~3μm and a reduced oxygen

content, allowing excess rare earth in the alloy to be significantly reduced for enhancing the energy product.

- Coupled a new high temperature sintering and annealing process with a previous MRE magnet alloy that was developed for melt spun isotropic magnets, employing chill casting and HD milling, to produce magnets with a density of 7.35 g/cm^3 and an energy product of 25.4 MGOe, demonstrating the importance of achieving LPS conditions, albeit at a high temperature, to achieve enhanced densification and improved magnetic properties.
- Discovered a segregated type of "core-shell" 2-14-1 phase structure upon microstructural examination of the 2-14-1 grains of intrinsic (unmodified) sintered MRE magnet samples (with Y-enrichment as a shell or rim on each grain) that appears to increase the negative temperature coefficient of the magnetic properties of MRE sintered anisotropic magnets, which is a critical problem to solve to make this type of magnet useful.
- Initial results of studies with extrinsic sintering additions showed that Al appears to be the most promising additive when used for controlled solid-state transformation (forming Al-Fe intermetallic phase) bonding at a low temperature (<600˚C) that leaves residual Al phase in the interparticle region, but more work with Al coated magnet particulate or thin Al flake is needed to investigate this concept.
- Concluded from a review of literature that 3 approaches should be pursued for making anisotropic nano-crystalline particulate for high strength anisotropic bonded MRE magnets, including a modified melt spinning method with low heat extraction rate and reduced thickness, a devitrification method that imposes a large temperature gradient on the ribbon during crystallization, and a devitrification method with a uni-axial pressure gradient on ribbon samples during crystallization, with initial experiments in-progress on each.
- Completed plans and submitted invitations to University of Maryland, Brown University, University of Nebraska, and Oak Ridge National Laboratory to attend the first Ames Lab workshop entitled "Beyond Rare Earth Magnets" that will be held on November 5-6, 2009.

Future Directions

- Conduct a special invited workshop to identify productive directions for research in high performance non-rare earth permanent magnets with the planned research team that will lead to development of a detailed action plan for the project.
- Select viable processing approach for anisotropic sintered MRE permanent magnets from either intrinsic or extrinsic sintering methods and demonstrate potential for high-energy product and reduced temperature coefficients for operation up to 200C.
- Compare promising approaches for generating anisotropic nano-crystalline particulate that can be used in anisotropic MRE bonded magnets to decide on top two methods for further investigation and to obtain an estimate of the potential for increased magnetic strength over isotropic bonded magnets.

Technical Discussion

Executive Summary

The efficient use of energy for personal transportation is of prime concern for the Department of Energy. In addition, the Clean Air Act requires the implementation of the best available technology to reduce automotive emissions while promoting efficient use of non-renewable liquid transportation fuels. The work outlined here is aimed at the rapid growth of internal combustion/electric hybrids, plug-in hybrids, and full electric vehicles, powered by batteries or fuel cells, through improvements in

the efficiency and durability of electric drive systems, consistent with APEEM program goals.

By this means, the use of non-renewable liquid transportation fuels will be greatly diminished or, eventually, completely eliminated.

For FY 2009, this project was expected to develop the materials and processes needed to fabricate high performance, RE permanent magnets that can be used for traction motors with an internal PM rotor design. While the APEEM program provided the largest portion of the total funding for this work in FY 2009, the Propulsion Materials program also provided significant support, consistent with the dual research emphasis and potential benefits of the work. To meet performance and cost goals for advanced electric drive motors, it is essential to improve the alloy design and processing of PM powders and the process for producing finished RE magnets, incorporating either direct in-rotor magnet molding or net shape magnet fabrication and insertion of the magnets in each rotor. The fully developed RE PM material must be suitable for elevated temperature (180-200˚C) operation to minimize motor cooling needs, where increased high temperature magnetic performance is a critical advantage over current commercial RE magnet material.

Ames Lab has developed a MRE magnet alloy design for high temperature operation that may be implemented at a first level of advantage with nano-crystalline isotropic flake particulate using conventional isotropic bonded magnet processing methods and a high temperature polymer. A second level of advantage may be realized if this high temperature MRE magnet alloy flake particulate is protected with an oxidation resistant surface coating by a batch process that was developed in this project. A third level of advantage may be realized for isotropic bonded magnets, if the high temperature magnet alloy can be translated successfully to a fine spherical isotropic powder production process based on inert gas atomization with and in situ protective powder coating. This third level of manufacturing advantage is derived from reduced molding pressures and enhanced performance and reliability for isotropic bonded MRE magnets, through increased magnetic powder loading and reduced irreversible magnetic losses from oxidation and corrosion.

According to the recommendations of an industry expert report that was commissioned by this project, anisotropic magnet development of the MRE alloys could provide further advantages over any of the isotropic MRE magnet developments that were cited above. First, if anisotropic nano-crystalline fine particulate can be produced so that polymer bonded MRE magnets can be in-rotor molded and magnetized in-place to the desired field pattern, it should be possible to achieve 4X multiplication of the magnetic torque, compared to similar isotropic bonded MRE magnets. As one of the targets of our current MRE magnet study, these high-energy bonded magnets may be strong enough to meet the 2015 APEEM goals for traction motor volume and weight, along with a significant manufacturing cost reduction and high temperature advantage. Second, if anisotropic sintered magnets can be fully consolidated from aligned micron-sized single crystal particles of the MRE magnet alloy by liquid phase sintering with an intrinsic or extrinsic phase, it should be possible to achieve the same maximum magnetic torque of today's RE sintered magnets, but with a higher operating temperature. As the other target of our current MRE magnet study, these anisotropic sintered magnets with maximum energy product certainly will support the 2015 APEEM goals for traction motor volume and weight, with the added advantage of high temperature operation.

In the final quarter of FY 2009, the project was requested to expand beyond the study of RE permanent magnets to take up the search for non-RE permanent magnets that would have sufficient magnetic strength to power advanced traction drive motors for vehicle applications with volume and weight requirements consistent with APEEM goals. The key driver for this new research thrust is the ability to regain free market conditions for magnet component supplies, in contrast to the apparent monopolistic situation for RE supplies. The growing problem with RE availability at an acceptable price is

compounded by the many new applications for RE materials, including high demand for RE magnets for electrical generators in wind turbines. Thus, planning was begun for a non-RE permanent magnet research thrust.

Introduction

Rare Earth permanent magnets based on $RE_2Fe_{14}B$ intermetallic compounds, with $Nd_2Fe_{14}B$ as a prototype, have had a large technological impact because of their unsurpassed (demonstrated) magnetic energy density. Over the past 30 years, extensive research has been performed to develop and improve the magnetic properties and technological benefits of these RE magnetic compounds. Commercially, two classes, anisotropic sintered (microcrystalline) and isotropic polymer bonded (nano-crystalline) $Nd_2Fe_{14}B$ magnets have been successfully developed. It should be noted that anisotropic sintered $Nd_2Fe_{14}B$ magnets are used in current hybrid vehicle systems with interior PM motor designs that require high magnetic torque, but that this magnet class and magnetic torque-dominated motor design have been judged (by at least one of the OEM partners) to be impractical for very large scale mass production at reduced cost. Also, a higher operating temperature was requested for future traction motors (and magnets) to tolerate a planned increase in cooling loop temperature. Thus, the opportunity was recognized to use new motor designs that utilize an enhanced reluctance torque, and, as such, are well suited to the reduced (but still sufficient, potentially) magnetic flux available from anisotropic bonded magnets or sintered magnets, especially if the high temperature tolerance of the MRE magnet alloy could be retained. Because there was uncertainty about the technical feasibility and the total manufacturing cost advantage for the new type of drive motor system from this revolutionary shift in magnet type and motor design, a cost analysis of this situation was commissioned from an industry expert (Dr. Peter Campbell) and the report was obtained at the end of FY 2008.

Thus, the Campbell report "System Cost Analysis for an Interior Permanent Magnet Motor" was analyzed and its recommendations were implemented in earnest during FY 2009. The report evaluated the range of viable Rare Earth (RE) permanent magnet materials for an IPM motor. The report considered existing RE permanent magnet materials and the effects of possible future developments in this area. Motor costs were estimated for an annual production run of 200,000 units. The analysis considered key processing steps and evaluated alternative magnet shapes. Costs associated with RE permanent magnet raw materials, processing, and motor assembly and manufacturing methods were estimated. Mechanical stresses and thermal requirements were considered in the evaluation. The report found that there are two viable alternatives for IPM motors, which meet the FreedomCar goals. Both of these involve anisotropic magnets and emphasize the significance of the development of magnet compositions with mixed RE (MRE) alloys to give tolerance for high magnet operating temperatures. The first type that was recommended for development is based on conventional anisotropic sintered magnets, but based on our MRE alloy design, while the second type is based on anisotropic bonded MRE magnets. The full report is available from the US Office of Scientific and Technical Information (OSTI) (http://www.osti.gov/bridge/product.biblio.jsp?query_id=0&page=0&osti_id=940187).

Approach

As a result of the Campbell report, research efforts were directed toward anisotropic magnets with efforts focusing on both sintered and bonded magnets. Since the most conventional approach to anisotropic magnets is through the crushing and sintering route, the majority of our initial effort focused on this route. It should be mentioned that sintered magnets should have the highest energy density and that commercial $Nd_2Fe_{14}B$ (2-14-1) magnets in sintered form are used widely in hybrid automobiles, today. The report states that the advantage of sintered magnets made from the new MRE alloys for motor performance could be significant at

increased operating temperature. However, the report notes that the current manufacturing processes used for making the sintered magnets and for assembling the motors have room for improvement in terms of efficiency and cost. For Nd-based 2-14-1 sintered magnets, it is necessary to produce single grain particles in the range of 1-3μm, to align and compact them in a magnetic field, locking in the alignment, to densify the compact by liquid phase sintering (LPS), and to anneal the magnet microstructure, maximizing coercivity. Unlike traditional $Nd_2Fe_{14}B$ magnets where a low melting ternary eutectic reaction that involves $Nd_2Fe_{14}B$ and $Nd_{1+\mu}Fe_4B_4$ phases forms a low melting Nd-rich liquid for LPS and provides a non-magnetic grain boundary phase after sintering, there is no low melting reaction in the $MRE_2Fe_{14}B$ system that involves the 2-14-1 phase and is near the stoichiometric composition. Therefore, in order to make LPS for $MRE_2Fe_{14}B$ practical, 1) the composition of $MRE_2Fe_{14}B$ alloys must be adjusted to promote a sufficient melting reaction, or, 2) some suitable extrinsic sintering aids must added to obtain a liquid phase that permits LPS processing.

Alternatively, the report states that anisotropic bonded magnets made from the high temperature compatible MRE alloys could offer a sufficient magnetic energy density and a significantly reduced manufacturing cost, especially if "molding in-place" can be used to form finished rotors. The energy product of an anisotropic bonded magnet can, in principal, be three to four times that of an isotropic bonded magnet. While the energy product of an anisotropic bonded magnet will never be more than 70% of that of an anisotropic sintered magnet, these magnets may offer the most significant advantages in terms of mechanical stability, corrosion resistance, and manufacturing simplicity, i.e., lower cost. In addition they allow much more flexibility in tailoring the direction of the magnetic flux, add to efficient use of the flux. Of course, to produce an anisotropic bonded magnet with greatly enhanced performance, anisotropic nano-crystalline powders of the MRE magnet alloys must be developed that can be used in the bonding process. Recognizing that the challenge of producing such powders has been investigated since the discovery of $Nd_2Fe_{14}B$ magnets, the phase relationships of the new MRE alloys (containing more "heavy" RE elements) may provide some advantage in terms of suppression of the free Fe phase over the previous Nd-based alloys. Thus, the development of anisotropic nano-crystalline MRE-Fe-B particulate also has been pursued during this period.

Results

Fine powder production for sintered MRE magnets

Based on our initial work on isotropic magnet alloys for bonded magnets, the alloy composition $[Nd_{0.45}(Y_6Dy_1)_{1/7*0.55}]_{16.6}Fe_{76.7}B_{6.7}$ (WT212) was selected because of its excellent high temperature properties. This WT212 magnet alloy also lacks Zr and C additions that previously were needed to stabilize a nano-crystalline structure, desirable for bonded isotropic magnets. As described above for Nd-based sintered magnets, the initial stage for production of sintered MRE magnets was the production of 1 to 3 μm powders of the 2-14-1 magnet alloy. The production of fine sized particulate was challenging due to the reactivity of the $MRE_2Fe_{14}B$ material. In contrast to the normal experimental situation, making large quantities of material is much easier than making small gram batches since in a large batch a small fraction of the sample may be sacrificed to clean up the atmosphere in the container. In addition, it was necessary to optimize many factors in the ball milling process to obtain fine particles. Initial experiments focused on conventional crushing and ball milling. Factors such as milling time, ball size and media to material ratio were studied.

The alloy ingots were first crushed into ~5mm chunks then further reduced to an average size of ~75μm using a mortar and pestle in a N_2 atmosphere glove box. The resulting powder was then placed in a ball mill jar in the glove box. This improved process greatly reduced the oxygen content during powder processing. The first ball milling studies were conducted using large balls and resulted in an average particle

size for WT212 of 7.2 μm after 70 hr ball milling using large balls. The size was larger than the required size of 3μm single grains for 2-14-1. If the ball milling time was further increased, the distribution of size became narrower. However, the average size was not reduced significantly. Moreover, long term milling times resulted in more contamination. Therefore, studies for optimizing the grinding media size distribution and the ratio of powder to grinding media were conducted.

As the particle size was refined by adjusting the milling parameters, automated optical particle size analysis of milled powders was found to produce ambiguous results. As a consequence, direct observation of these powders by scanning electron microscopy (SEM) was employed to explain the results. These observations revealed that the automated particle analyzer greatly overestimated the actual particle size due to agglomeration of the fine particles into larger clusters. Therefore, only the SEM results are considered to be valid. From SEM micrographs of WT213 powders milled for 18h, the size for primary particles was less than 3μm, although there existed a small number of particles whose size was larger than 3μm. On closer observation, most of those larger particles were agglomerates of many smaller particles. Therefore, the average size for the sample milled for 18h was ~ 3μm.

In addition to conventional ball milling, we also studied the use of a much higher energy ball milling process using a SPEX mill. Preliminary particle size analysis results indicated that the average size after milling for 3 and 5 hrs was 14.7 and 15.4 um, respectively. A longer milling time seemed to have resulted in a larger average size, indicating that powder particles are cold-welded together when powder reaches a critical size under the current milling conditions. Cold welded particles would not be single grained and so would not be suitable for our application. However, these SPEX milling results must be only considered as preliminary, since SEM measurements were not conducted to verify the automated particle size analysis results, as discussed above.

Although a grinding procedure using a conventional ball mill had been developed that produced the required size distribution, the oxygen contamination of the samples was higher than desired. In an effort to control oxygen content, the initial coarse grinding was replaced by hydrogen decrepitation (HD). In this process, the ingots were placed in a stainless steel container that was evacuated and filled with hydrogen at a pressure of 3bar. The samples remained under the 3 bar hydrogen pressure for 3-6h. After 4h of HD at 3 bar, SEM examination of the resulting powder showed that the average particle size was less than 20μm. This powder was then transferred to a roller ball mill jar and the jar was filled with cyclohexane or toluene and the grinding medium. This process was performed in a glove box so that the powder was not exposed to air. The post-HD powder was milled in the conventional ball mill for 16h. The average particle size was reduced to ~3μm, as desired. As a result of this process that suppressed RE oxidation and achieved the desired particle size, the amount of excess rare earth in the alloy could be significantly reduced; this in turn resulted in higher energy products due to an enhanced volume fraction of the 2-14-1 phase.

Sintering process development for MRE magnets

Intrinsic sintering: Unlike traditional $Nd_2Fe_{14}B$ magnets where a Nd-rich phase is in equilibrium with $Nd_2Fe_{14}B$ and $Nd_{1+\mu}Fe_4B_4$ phases forming a low melting (650-680˚C) ternary eutectic for LPS and providing a non magnetic grain boundary phase, there is no built in low melting reaction in the $MRE_2Fe_{14}B$ system, as mentioned above. Since the equilibrium phase diagram for the $MRE_2Fe_{14}B$ magnet alloy seems to be dominated by the majority Dy and Y components, the melting behavior of near-stoichiometric alloys, slightly RE-rich, follow the ternary diagram reported for Dy-Fe-B. Thus, DSC measurements, for example, of composition WT220 $[Nd_{0.45}(Y_3Dy_1)_{1/4*0.55}]_{2.8}Fe_{14}B_{1.1}$ revealed two melting reactions with onset temperatures of 725˚C and 1220°C. The 725°C corresponds to the lowest melting reaction in the MRE magnet alloys that involve the RE-rich phase and it

apparently is not consistent with an equilibrium phase distribution, while the 1220°C event is the peritectic melting of the 2-14-1 phase. The sintering and annealing temperatures for materials without secondary grain boundary pinning additions, e.g., Zr and C, were determined from these two onset temperatures. In general, the higher the sintering temperature is for this type of near-stoichiometric 2-14-1 alloy, the higher will be the density of the sintered sample, which will have a higher saturation magnetization. However, a higher sintering temperature also may result in larger grains, resulting in a reduction of coercivity. Selection of an optimum annealing temperature (post-sintering) should result in an improved microstructure that further increases coercivity due to stress relief, re-distribution of liquid phase at grain boundaries, and other processes.

Samples for sintering experiments were prepared by aligning and securing this aligned state in the powders in a transverse magnetic field of 1.8 T. In the initial experiments the powders were manually pre-compacted under the field and then further compacted in a hydraulic press after removal from the magnetic field. In later experiments, an apparatus that allowed the hydraulic pressing to be performed in the magnetic field was used. Following alignment and compaction, the pellets were wrapped in tantalum foil and sintered in a high vacuum (10^{-6} torr) furnace that was fitted for sample quenching.

Initial results of the sintering experiments appeared to be closely linked to the improvements in the process for producing the required 3μm single grain particles, i.e., as oxidation of the powder was reduced the magnetic properties were improved. In experiments conducted after full development of the HD and milling process, two samples of composition WT220 were sintered at 1080°C for 2hrs and 1130°C for 1hr, respectively, and then both were annealed at 650°C for 2hrs. The densities of the two sintered samples were measured to be 7.10 and 7.35 g/cm^3, respectively, where 7.4 g/cm^3 is approximately full density. The higher sintering temperature, 1130°C, resulted in higher M_r (remanent magnetization) and H_c (coercivity), and thus

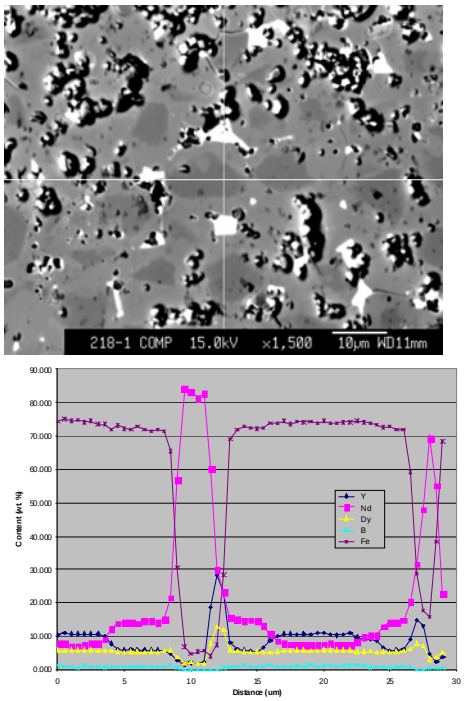

Figure 1. Backscattered SEM image (top) and WDS analysis (white horizontal line) of the sintered alloy WT218.

higher $(BH)_{max}$ (energy product) than the sample sintered at 1080°C, i.e., 25.4 MGOe, and 21.9 MGOe, respectively. This suggests that full densification is critical to obtaining the best magnetic properties. Unfortunately, the results for high temperature magnetic properties showed that the sintered samples had higher negative temperature coefficients of remanence and coercivity compared to those of samples of similar composition made by melt spinning. It was also noticed that the sample sintered at 1130°C had greater negative temperature dependence than the sample sintered at 1080°C, indicating that increased density of samples may improve room temperature magnetic properties, but degrade high temperature magnetic properties.

Microstructural examination of the sintered samples (Fig. 1) showed that the 2-14-1 grains have formed a type of "core-shell" phase structure after sintering at 1100-1150°C. In the

two types of regions in this structure, Nd-rich 2-14-1 was located at the center as a core, while Y-rich 2-14-1 was located outside as a shell, with the Dy level was constant throughout each grain. Therefore, it appeared that when a uniform compact of $MRE_2Fe_{14}B$ phase grains is sintered at high temperature, segregation of the rare earth elements within each 2-14-1 grain occurs. It was not clear why and how the segregation of the 2-14-1 phase occurred and if it can be suppressed, and this is still under investigation. However, it appeared obvious that increased segregation contributed to a strong negative temperature dependence of the sintered magnets, because Y-rich 2-14-1 located on the outside layer of the 2-14-1 grains would have a lower anisotropic field and result in a lower magnetic field reversal, i.e., coercivity. Consequently, in order to develop sintered MRE magnets with high performance, it is critical to solve this segregation problem.

In order to identify the sources of the segregation, microstructures of compositions over a wide range of MRE-rich alloys; WT218 $[Nd_{0.45}(Y_3Dy_1)_{1/4*0.55}]_{3.5}Fe_{14}B_{1.1}$, WT220 $[Nd_{0.45}(Y_3Dy_1)_{1/4*0.55}]_{2.8}Fe_{14}B_{1.1}$, and WT216 $[Nd_{0.45}(Y_3Dy_1)_{1/4*0.55}]_{2.5}Fe_{14}B_{1.1}$, have been studied. All of the samples exhibited rare earth segregation in the 2-14-1 phase, indicating that the segregation is independent of the RE enrichment. In an additional study, sintered magnets were prepared using a dual alloy approach, where a 2-14-1 alloy with a ternary combination of rare earths, Nd-Y-Dy, was mixed with a 2-14-1 alloy with a binary combination of rare earths, Nd-Y or Y-Dy. Initial composition profile results within grains and near grain boundaries for sintered magnets made from a dual mixture of ternary Nd-Y-Dy and binary Y-Dy were determined by wavelength dispersive spectroscopy (WDS) and significant segregation was observed in these samples. Further studies are underway to clarify the origin of the segregation and to determine if it can be suppressed.

While studies of the origin of the segregation continue, an alternative approach to the magnet preparation is being investigated in hopes of avoiding the segregation. In this approach, the final composition is obtained by the blending and co-sintering of two types of alloy particles whose average composition is the desired MRE magnet alloy. One of the alloys, $[Y_{0.5}Dy_{0.5}]_{2.5}Fe_{14}B$ (WT231), does not contain a low melting eutectic while the other Nd-rich alloy, $Nd_{10}Fe_{14}B$ (WT232) does. The hypothesis involved in this approach is that the liquid from melting of the Nd rich phase particles will uniformly wet the prior particle boundaries at the temperature of the Nd-Fe-B ternary eutectic. This should provide densification at a significantly lower temperature than our current process. Following densification that was expected to be rapid, diffusion should slowly eliminate the compositional gradients.

Powders of the two alloys were prepared separately using the same casting and HD process described above. The powders were then blended together. Two blended compositions were prepared, one with 10wt% of the Nd-rich alloy and the other with 20wt% of the Nd-rich alloy. The samples were aligned, compacted, and then sintered. The samples were sintered at temperatures of 1100 and 1150°C for 1 hour. Preliminary evaluation of these samples has been completed. Unfortunately, the data indicates that the anticipated densification at lower temperature did not occur and that a sintering temperature of 1150 °C is still required to approach full density. However, the sample sintered at a higher temperature obtains not only a higher density, but also a higher coercivity and lower negative temperature coefficient of coercivity. Further, the sample that contains the 10wt%Nd-rich alloy exhibited a lower H_c but higher B_r and $(BH)_{max}$ than the 20wt% of Nd-rich alloy sample. However, the coefficient of B_r for that sample is also higher, while the coefficient of H_c is slightly lower. The explanation of these results will require further microstructural studies to see if it is useful.

Extrinsic sintering additions: An alternative approach to the intrinsic sintering approach is the addition of an extrinsic sintering aid. Three techniques of increasing complexity are being used to study potential extrinsic liquid phase sintering aids. They are

1. Liquid phase diffusion couple – Single Interface

This technique gave a rapid evaluation of the compatibility of the candidate sintering aid with the magnet alloy, in this case WT-201, $[Nd_{0.45}(Y_2Dy_1)_{1/3*0.55}]_2Fe_{14}B$. A piece of melt-spun ribbon of the proposed sintering aid was placed on top of a polished disk of magnet alloy, sealed in a Ta can and annealed slightly above the melting temperature of the ribbon. The resulting piece was then cross-sectioned and viewed under the SEM with compositional analysis using EDS.

2. Liquid phase diffusion couple – Double Interface

This technique was designed to determine how well the candidate sintering aid wets the magnet alloy. Wetting is required to provide the capillary action that causes densification in LPS. In this case a ribbon of the sintering aid was held between two disks of magnet alloy in a boron nitride clamp. Annealing and analysis was the same as above.

3. Sintered Compact

This is a critical test of sintering. Magnet particulate of less than 45μm in size was mixed with roughly 10-50% by volume of equal sized sintering aid material in a Turbula blending system and pressed into a pellet. After annealing, the density, magnetic properties, and microstructure of the resulting pellet were determined.

Two types of extrinsic sintering aid candidates were considered with technique 1. The first contained only elements that are present in the parent magnet alloy. Adding these alloys can result in a tailored distribution of phases while reducing the chance of unwanted reactions. We have studied the iron-neodymium eutectic using the single interface method. The eutectic composition was chosen in order to achieve a low melting point. The sample was cross-sectioned and imaged. The compositions of the phases at the interface were studied both in the SEM and with our electron microprobe using WDS analysis that is more sensitive than energy dispersive spectroscopy (EDS). Two primary regions were seen in the region that was molten during annealing. One phase appeared to be an iron-neodymium mixture with a stoichiometry close to Fe_3Nd. Fe_3Nd is not stable in the iron-neodymium phase diagram. However, 3-1 phase is present in the dysprosium-iron system. It is possible that the dysprosium present in the substrate alloy is allowing a 3-1 phase to form. The other phase appeared to be a highly porous Nd eutectic phase mixture, as expected, that was oxidized during polishing. While this alloy appeared promising, it had one significant

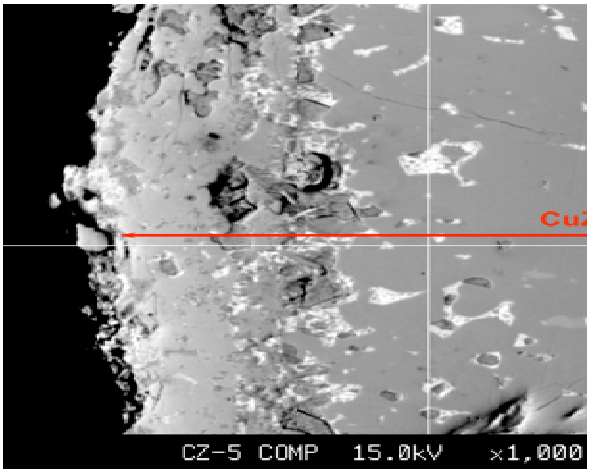

Figure 2. SEM Image of Cu- 35.5% Zr interface with $RE_2Fe_{14}B$ magnet alloy.

drawback in the easy oxidation of the Nd part of the eutectic. As in normal Nd-Fe-B, this will result in corrosion problems.

The second type of candidate sintering aids for liquid phase sintering contained elements that are not in the magnet alloy. While this may allow tailoring of the interface, there is a large potential for unwanted reactions. An example of this type of aid is Cu-35.5Zr (wt.%). This alloy is a glass former. It was thought that the corrosion resistance of the glass would provide a good interconnect for the magnet particles. Additionally, Zr is used in magnet alloys in order to refine grain structure. At 885ºC, the melting temperature of this composition is slightly higher than the optimum temperature. Once more the single interface diffusion (method 1) was used. Analysis of the reaction

layer (Fig. 2) showed a considerable amount of nearly pure iron surrounded by a neodymium copper mixture. Zirconium was only present in the surface layer (~25μm). Using WDS measurements the phases were more accurately described. Copper was seen nearly 80μm from the surface, indicating significant diffusion into the magnet material. While the copper did not appear to become a part of the matrix, the rare-earth/iron/boron ratios appeared to change in the region of Cu diffusion. This region changed from a $RE_2Fe_{14}B$ phase to a RE_2Fe_{17} phase. Near the interface, the presence of ZrB_2 explained this transformation. Due to these reactions, this alloy was not feasible to use as a sintering aid. However, similar alloys may still be used.

Another attractive extrinsic sintering aid prospect is aluminum, which is simple to incorporate as a particulate in a blended sample or allows the possibility of individually coating each magnetic powder particle using well-established industrial processes. Al also offers the prospect of either a transient liquid phase sintering process that stops when the Al is completely consumed by interparticle compound formation or an activated (exothermic) solid-state sintering process at lower temperatures that can leave residual Al as a ductile interparticle phase. In the initial investigation to determine the reaction temperatures of Al with our alloy, a sample was sintered in our differential scanning calorimeter (technique 3). A 50:50 (% by volume) mixture of MQP-11-HTP magnet alloy flake particulate and aluminum powder was pressed and placed in the DSC. The sample was ramped to 700°C and cooled back to room temperature. Two exothermic reactions were observed. The first, milder, reaction started at 570°C and a second, more intense, reaction started at 638°C. Both reactions appeared to be irreversible. In a second experiment a sample was pressed and taken to 598°C. Both samples were crushed and x-ray diffraction patterns were obtained. In the sample ramped to 598°C, the phases $RE_2Fe_{14}B$ and α-Al can be seen. While in the sample taken to the higher temperature, $RE_2Fe_{14}B$ and $NdAl_8Fe_4$ are observed. It appears that the higher temperature reaction is a liquid state reaction that complete consumes the Al, while the lower temperature reaction is a solid-state reaction, as expected. SEM analysis using EDS confirmed the above results with the additional finding that the low temperature (solid-state) sintered sample also showed presence of the phase Al_3Fe.

A double interface diffusion couple (technique 2) between Al and WT201, a simple stoichiometric Nd-based 2-14-1 magnet alloy, was made to test the low temperature (diffusion rate) limit of the solid-state reaction to determine if it was suitable for interparticle bonding without complete Al consumption. The diffusion couple was prepared by placing a piece of Al foil between two polished wafers of a drop-cast and annealed ingot of the magnet alloy. The assembly was placed in a boron nitride clamp. The diffusion couple was heat treated in a vacuum furnace which was ramped to 572°C and then quenched. The diffusion couple was then sectioned and polished, then submitted for electron microprobe (WDS) analysis. Line scans across the interface are currently being analyzed.

In further studies of aluminum as a sintering aid, magnet powders of MRE-based compositions $[Nd_{0.45}(Y_2Dy_1)_{1/3*0.55}]_{2.5}Fe_{14}B$ and $[Nd_{0.45}(Y_2Dy_1)_{1/3*0.55}]_{2.8}Fe_{14}B$, with higher RE content, were prepared by hydrogen decrepitation of strip cast alloy, followed by ball milling in cyclohexane. The average particle size of the milled powder of both alloys was approximately 3μm. The particulate of composition $[Nd_{0.45}(Y_2Dy_1)_{1/3*0.55}]_{2.5}Fe_{14}B$ was dried in a low vacuum environment and mixed with 10 vol.% gas atomized (high purity) Al powder (dia.<10μm) in a Turbula powder mixing system. The resulting blended sample was aligned and pressed into a dense compact in a magnetic field of 1.5T. For comparison, a second sample of the RE-enriched, $[Nd_{0.45}(Y_2Dy_1)_{1/3*0.55}]_{2.8}Fe_{14}B$, particulate, without an Al addition, also was aligned and pressed into a dense compact in a magnetic field of 1.5T. The resulting pellet of composition $[Nd_{0.45}(Y_2Dy_1)_{1/3*0.55}]_{2.8}Fe_{14}B$ was sintered in a vacuum furnace at 1130°C for one hour then quickly removed from the heating zone. The pellet of blended composition $[Nd_{0.45}(Y_2Dy_1)_{1/3*0.55}]_{2.5}Fe_{14}B$ + Al was sintered

with the extrinsic sintering aid in a vacuum furnace at 580°C for one hour and slowly cooled. The magnetic properties of the aligned and sintered magnets were measured parallel and perpendicular to the alignment direction. The intrinsically sintered sample showed good room temperature properties, typical of similar unannealed samples. However, the low temperature extrinsically sintered compact displayed soft magnetic properties.

One obvious reason for the apparent lack of retained anisotropy was the very limited distribution of the relatively large Al powders in the aligned and pressed sample and the planned avoidance of the Al melting excursion. The lack of Al melting probably limited the possible bonding (solid-state phase transformation) reaction to a very small fraction of the available 3μm magnetic particulate in the compact. Thus, when exposed to a reversed magnetic field in the SQUID magnetometer, the unbonded particles may have simply shifted position, losing the initial aligned orientation and exhibiting a soft magnetic behavior. While detailed studies of the extrinsically (Al aided) sintered sample is underway to verify this mechanism, further plans were set in motion to perform an improved test of the solid state sintering approach assisted by the Al (extrinsic) addition. It was decided to pursue physical vapor deposition (vacuum) coating of magnetic alloy particulate with Al to ensure availability of the Al phase on all surfaces during the solid-state reaction and to try the technique 3 test again, using a similar low sintering temperature. This improved initial condition should also permit the low temperature bonding procedure to be tested for its capability to produce smooth 2-14-1 phase grain boundaries for enhanced coercivity.

Particulate production for anisotropic MRE bonded magnets

In preparation for beginning efforts to produce anisotropic powders for bonded magnets an extensive review of the literature has been undertaken to identify what has been tried and what is known about the formation of anisotropic powders. Four different approaches have been tried previously to produce anisotropic powders. The only method currently employed to create anisotropic particulate on a commercial basis is known as the HDDR (hydrogenation, decomposition, desorption, recombination) process. It involves exposing a chill cast ingot of magnet material to an elevated pressure hydrogen atmosphere at high temperature, followed by evacuation and a diffusion anneal. While this produces anisotropic powders, they have extremely poor thermal stability and high (negative) temperature coefficients of coercivity and remanence. Other researchers have considered methods of improving this stability, but HDDR powders also exhibit poor environmental stability. Magnequench also produced commercial anisotropic magnet powders in the past by reprocessing scrap bulk isotropic (fully crystallized) magnets by a hot open die forging method. However, this process for making "MQ-III" particulate was only viable when their production process yielded large numbers of scrap magnets, a highly undesirable situation. The most desired powder for anisotropic bonded magnets would consist of polycrystalline particles of 30-50μm size that each contain crystallographically aligned 200nm grains. While it is possible to produced texture ribbons by controlling rapid solidification, the typical grain size is larger than acceptable for coercivity.

In 1987, Dadon et al. [1] determined that by melt spinning onto an uncooled copper wheel rotating at 19m/s, a large degree of anisotropy could be created. The wheel side of the ribbon exhibited significant texturing, with the c-axis of the 2-14-1 grains perpendicular to the surface. These grains were very small at the surface. Near the center of the ribbon, the grains grew and maintained anisotropy, but were greatly increased in size. Unfortunately, the solidification beyond the central zone, commonly called the "free" (unchilled) side resulted in equi-axed (unaligned) grains. The origin of the extended texture that grew beyond the chilled (wheel side) surface was later attributed by Kramer and McCallum [2] as a secondary nucleation effect induced by a fine distribution of α-Fe phase. Unfortunately these materials have very low coercivity that is attributed to the relatively poor alignment and

large grain size of the overall (through-thickness) microstructure for this rapidly solidified ribbon material, producing strong coupling between grains. Since the grain size is significantly below that of sintered magnets, this suggests an approach aimed at modifying the grain boundary phases to stabilize extended growth of fine aligned grains may work, along with promoting thinner ribbons. From this motivation, a modification of the conventional melt spinning approach, away from extremely rapid solidification, was attempted, involving use of a modified quench wheel surface to reduce thermal conductivity, but to maintain high wheel speeds. Microstructural and magnetic analysis of the resulting ribbon particulate from the initial experiments is in progress to determine the prospects for this approach.

Various attempts at inducing texture during solid-state crystallization (devitrification) of ribbons in the amorphous state also have been tried. Basically, a unique crystallization direction must be defined during growth of the crystal embryos in an "over-quenched" ribbon, contrary to the typical isotropic crystallization annealing process. Two new approaches that may be investigated are crystallizing in a magnetic field or under an applied temperature gradient. At the beginning of this project, a collaboration with Argonne National Lab was formed and attempts were made to anneal amorphous ribbon samples in an applied field of 8T. Unfortunately, the crystallization temperature is well above the Curie temperature and so that the magnetic force available for grain alignment from the external applied field was very low and no significant texture was observed. This also was attributed to the existence of randomly oriented crystalline embryos in the as-quenched material, which appear to be very difficult to eliminate. The imposition of a large temperature gradient on the ribbon during crystallization may also lead to anisotropic material; however, a large temperature gradient is difficult to achieve across a thin ribbon, but may be possible in the 2-14-1 phase due to its very poor thermal conductivity. Methods involving radiant heating and forced cooling are being considered.

At the current time, experiments also have begun where amorphous precursor ribbon samples are crystallized under uni-axial pressure. Based on the work of W. Barclay Kamb [3], the favored crystallization and growth directions should be the directions with the highest elastic constants. In the case of $Nd_2Fe_{14}B$, these directions are the 110-type directions. Starting amorphous ribbon material of $Nd_2Fe_{14}B$ + 3% TiC that was melt-spun at 25 m/s in 1/3 atm. of He was selected for the initial test of the pressure induced anisotropic growth concept in a magnet alloy that should suppress effectively the formation of random crystal embryos. Differential scanning calorimetry was performed on the resulting ribbon and a strong crystallization peak was observed. Based on the data gathered from the DSC, a small amount of the ribbon was annealed in a vacuum furnace at 625°C for 12 minutes under a 10^{-6} Torr atmosphere in order to crystallize the sample. X-ray diffraction was conducted on both the annealed and as-spun samples. The as-spun ribbon showed no significant crystallinity, while the annealed sample showed well-crystallized material. Studies of crystallization under uni-axial stress now will be undertaken on these samples.

Studies of the factors that control grain growth and grain morphology are continuing in order to gain an understanding of how to produce gain aligned nano-grained magnets. Annealing experiments with holding times from 0-11 min were chosen for an isothermal study to slow the diffusion kinetics and to probe the phase evolution to the thermodynamically stable phase field. The analysis of the atom probe tomography (APT) results on ribbon sample of WT147 melt-spun at 25m/s and then annealed at 638˚C for 8 min. using DSC gave clear information about the local microstructure and chemical information along grain boundaries, as reported previously. The nominal composition of the WT147 alloy is $[(Nd_{4.5}(Y_2Dy_1)_{1/3*0.55})_{(2.3-y)}Zr_{0.3}Co_1Fe_{13}B]_{1-2x}+Zr_xC_x$, x=0.01, y=Zr. We found that Zr, C, B and RE are enriched and that Fe and Co are depleted within a 10nm region at the grain boundary indicating the second phase on the boundary is already formed after the 8 minute anneal. In order to gain further

understanding of the devitrification behavior of the elements at the initiation of the nucleation stage, samples annealed for 2 minutes were chosen for investigated using both TEM and APT (atom probe tomography, with a 3DAP, LEAP 3000Si) techniques. The annealing temperature was chosen based on DSC analysis (20 ˚C below the onset of the first crystallization event in the DSC). The annealing of these samples has been completed and the preparation of TEM and APT samples is underway.

Conclusions

An independent analysis was received of the total manufacturing cost for advanced electric drive motors. Based on the recommendations, the project research emphasis was focused on anisotropic sintered and anisotropic bonded MRE permanent magnets with capability for high temperature operation. To enable anisotropic sintered MRE magnet development, the processing steps needed to make particulate with an average particle size of ~3μm and a reduced oxygen content were developed, allowing excess rare earth in the MRE alloy to be significantly reduced to reduce alloy cost and to help enhance final energy product. In subsequent progress, a new high temperature sintering and annealing process was developed specifically for MRE magnet alloys that produced sintered anisotropic magnets with a density of 7.35 g/cm^3 and an energy product of 25.4 MGOe, about 5X stronger than isotropic bonded MRE magnets. Unfortunately, the high sintering temperatures developed for intrinsic consolidation/densification of the MRE magnet alloys also were discovered to produce a deleterious "core-shell" segregation pattern in the 2-14-1 phase grains in the finished magnets with Y-enrichment around the rim of each grain. This RE segregation tendency appears to increase the negative temperature coefficient of the magnetic properties of these MRE sintered anisotropic magnets, which is a critical problem to solve to make such magnets useful. Alternatively, preliminary results indicated that Al is a promising extrinsic sintering aid, especially if used for controlled solid-state transformation (forming Al-Fe intermetallic phase) bonding at a low temperature (<600˚C) that leaves residual Al phase in the interparticle region. To enable anisotropic bonded MRE magnet development, a review of literature revealed that 3 approaches should be pursued for making anisotropic nano-crystalline particulate. These approaches include a modified melt spinning method and two devitrification methods that use either a large temperature gradient or a uni-axial pressure gradient on ribbon samples during crystallization. Preliminary experiments with these approaches were conducted and analysis is in-progress. In response to a request to initiate a new research thrust that goes beyond rare earth permanent magnets, prospective partners were selected and a workshop was organized at Ames Lab to be held on November 5-6, 2009.

Publications

I. E. Anderson, R. W. McCallum, W. Tang, *Alloy design and microstructure of advanced permanent magnets using rapid solidification and powder processing,* International Journal of Powder Metallurgy (Princeton, New Jersey) (2008), 44(6), 19-37.

W. Tang, Y. Q. Wu, K. W. Dennis, N. T. Oster, M. J. Kramer, I. E. Anderson, R. W. McCallum, *Magnetic properties and microstructure of gas atomized $MRE_2(Fe,Co)_{14}B$ powder with ZrC addition (MRE = Nd + Y + Dy),* Journal of Applied Physics (2009), 105(7, Pt. 2), 07A728/1-07A728/3.

Y. Q. Wu, W. Tang, M. J. Kramer, K. W. Dennis, N. T. Oster, R. W. McCallum, I. E. Anderson, *Correlation of the energy product with evolution of the nanostructure in the Y,Dy,Nd-(Fe, Co)-B magnetic alloy,* Journal of Applied Physics (2009), 105(7, Pt. 2), 07A720/1-07A720/3.

References

1. D. Dadon, Y. Gefen, and M. Dariel, "The texture of melt spun $Fe_{76}Nd_{16}B_8$ ribbons," *Magnetics, IEEE Transactions on,* vol. 23, pp. 3605-3606, 1987.
2. M. J. Kramer, N. Yang, R. W. McCallum, K. W. Dennis, and L. H. Lewis, "In situ determination of Nd-Fe-B crystallization pathways," *J. Appl. Physics*, vol. 91, pp. 8156-8158, 2002.

3. W. B. Kamb, "Theory of Preferred Crystal Orientation Developed by Crystallization under Stress," *The Journal of Geology,* vol. 67, pp. 153-170, 1959.

Patents

1. R. W. McCallum, Y-W. Xu, I. E. Anderson, K. W. Dennis, and M. J. Kramer, U.S. Patent Application (PCT) filed November 18, 2002, “Permanent Magnet Alloy with Improved High Temperature Performance,” under examination.

Agreement 13257 – High Performance Embedded Capacitors

U. (Balu) Balachandran, Beihai Ma, Manoj Narayanan, and Stephen Dorris
Argonne National Laboratory
9700 S. Cass Avenue
Argonne, IL 60439-4838
(630) 252-4250; fax: (630) 252-3604; e-mail: balu@anl.gov

DOE Technology Manager: Jerry L. Gibbs
(202) 586-1182; fax: (202) 586-1600; e-mail: jerry.gibbs@ee.doe.gov
ANL Technical Advisor: U. Balu Balachandran
(630) 252-4250; fax: (630) 252-3604; e-mail: balu@anl.gov

Contractor: Argonne National Laboratory, Argonne, Illinois
Contract No.: DE-AC02-06CH11357

Objective

- The purpose of this effort is to develop ceramic capacitors that have excellent high temperature performance and meet most of the Vehicle Technologies Program specifications for power electronic systems in hybrid electric vehicles. This project is jointly funded by the Advanced Power Electronics and Propulsion Materials Technology programs.

Approach

- Fabricate a high permittivity ferroelectric material, $(Pb,La)(Zr,Ti)O_3$ (abbreviated as PLZT) on a base-metal foil in controlled environment.

Accomplishments

- Fabricated and characterized PLZT dielectrics on nickel metal foils with self-clearing electrodes. The key to large-area yield is to electrically isolate the defect spots that compromise the integrity of the dielectric layer.
- Reduced the defects and succeeded in increasing the capacitance of the dielectric films.

Future Direction

- Continue to fabricate high quality PLZT on larger area substrates. Using small area (250 μm diameter) top electrodes, the R&D effort has demonstrated that the properties of PLZT film-on-foils are suitable for power electronics operating at under-the-hood temperatures. The next step is to optimize the processing and fabrication conditions to make large area capacitors with the desired dielectric properties. Important processing issues such as substrate polishing, defects in the films, clean room processing, pyrolysis and crystallization temperatures have been identified.
- Characterize the dielectric properties of PLZT film-on-foils using larger area top electrodes.
- Develop chemical solution technique for adaptation by capacitor industry.

Introduction

Power inverter modules are a critical subsystem within HEVs, PHEVs, and FCVs, and their performance directly affects fuel efficiency and battery life. Capacitors occupy about 35% of the inverter volume in current designs. Thus, even if all other components in the inverter are reduced significantly, the capacitor requirement is a serious impediment to achieving the required volume and weight reduction. In addition, the use of high-temperature coolants further exacerbates the situation because existing film capacitors lose their capability to absorb ripple currents at elevated temperature, necessitating the addition of extra capacitors. Increasing the volumetric performance (capacitance per unit volume) of DC bus capacitors is required, and their maximum operating temperature also must be increased to assure reliability requirements. Theoretically, ceramic capacitors have the greatest potential for volume reduction; they could be as small as 20% of the volume of an aluminum electrolytic capacitor. Ceramics offer high dielectric constants and breakdown fields and, therefore, high energy densities. They also can tolerate high temperatures with a low equivalent series resistance (ESR), enabling them to carry high ripple currents even at elevated temperatures, although the capacitance may vary strongly with temperature.

The objective of this R&D program is to utilize ceramics with high capacitance density in developing capacitors that meet, if not surpass, DOE's OVT goals for higher operating temperatures, improved packaging and reliability, and reduced size, weight, and cost. Our approach uses ferroelectric thin films (PLZT) on base-metal foils (film-on-foils) that are either stacked on or embedded into printed wire boards (PWBs). Embedded film-on-foil capacitors reduce the component footprint area, shorten interconnect lengths, and reduce parasitic inductive losses and electromagnetic interference. Reliability is improved because the number and size of interconnects are reduced. Solder joints that are most susceptible to failure are no longer needed. Our R&D efforts focus on examining the underpinning issues of film-on-foil capacitor performance and reliability, developing low cost capacitor designs, making multilayer film-on-foil capacitors, embedding the film-on-foils into the PWBs, fabricating high-voltage-capable film-on-foil capacitors defined by the inverter application requirements, establishing robust fabrication protocols that are commercially and economically viable, and transferring the technology to industry for manufacturing. This R&D effort is funded jointly by the Advanced Power Electronics and Propulsion Materials Technology programs. The goal of the activity funded by the Propulsion Materials Technology program is to explore fabrication processes to make large-area capacitors for application in a hybrid electric vehicle. As a first step, we investigated a process based on "graceful failure" for preparing film-on-foil capacitors with large diameter-to-thickness aspect ratio ($>10^4$). The key to large-area yield is to electrically isolate the defect spots that compromise the integrity of the dielectric layer. This can be accomplished by applying high-voltage short pulses to self-clear the top electrode around the defect spot. Work done on large-area film-on-foil ferroelectric capacitors with self-clearing electrodes is presented in this report.

Approach

Nickel substrates (25 mm × 25 mm, 0.5 mm thickness, 99.8% pure, ESPI Metals) were polished to 1-μm finish (~0.4 mm final thickness) and ultrasonically cleaned in acetone and methanol prior to coating. Stock solutions of 0.3M $LaNiO_3$ (LNO) and 0.5M $Pb_{0.92}La_{0.08}Zr_{0.52}Ti_{0.48}O_3$ (PLZT) were prepared by modified sol-gel synthesis using 2-methoxyethanol as the solvent. The detailed procedure is reported elsewhere.[1-4] The LNO solution was spin-coated onto the substrate at 3000 rpm for 30 sec, pyrolyzed at 450°C for 5-10 min, and crystallized at 650°C for 2-5 min. This process was repeated five times to build the desired thickness with a final annealing at 650°C for 20 min. The PLZT stock solution was spin-coated onto the LNO-buffered substrate at 3000 rpm for 30 sec. Films were then pyrolyzed at 450°C for 10 min and crystallized at 650°C for 2-5 min, followed by a final annealing at 650°C for 20 min after deposition of ten layers. The final thicknesses of the LNO and PLZT films were ~0.4 μm and ~1.15 μm, respectively. Platinum top electrodes were then deposited by electron beam evaporation using a shadow mask. These electrodes had diameters of 250 μm, 750 μm, and 12 mm and thickness of 100 nm.

High-voltage triangular wave pulses (1 ms) were applied with a Radiant Technologies Precision Premier II tester to measure the hysteresis loops. Increasing voltages were applied until self-clearing started to occur, and the highest voltage was applied 3-4 times until self-clearing terminated. In this case, we applied voltages up to 80 V with increments of 10 V. Dielectric measurements were made with an HP 4192A impedance analyzer using an oscillator level of 0.1 V at 10 kHz before and after self-clearing.

Results

The properties of such PLZT capacitors on nickel and copper foils with aspect ratios (electrode diameter/film thickness, d/t) less than 500 have been extensively reported[1-3, 5-7], but for practical purposes, capacitors with larger aspect ratios are required. The yield of a capacitor decreases drastically with an increase in electrode diameter (or area) because the probability of encountering a defect spot (pinhole, dust, microcrack, contaminant particles, etc.) increases significantly and the defect density determines the dielectric permittivity and loss values of the capacitor. The defects are formed by various factors in the processing of the film. These factors include the environment in which the film is made (particulate level, humidity, etc.), temperature, time used for pyrolysis, and crystallization. Therefore the formation of these defects cannot be completely avoided, although the defect density can be minimized. Because the probability of depositing an electrode over such defects increases with capacitor area, the functionality, properties, and yield can be traced to the defect density of the dielectric film. Daniels et al.[8] have reported that co-firing the electrodes with the dielectric ceramic increases the yield of ultra-large-area capacitors by electrode dewetting at defect spots. We used "self-clearing" electrodes to improve the functionality and yield of large-area capacitors. The theory behind this process exploits the difference between the electrical behavior of defective regions and defect-free regions of the dielectric film. In self-clearing, the electrode directly above a defect (area most likely to have a breakdown event) vaporizes due to the rapid discharge of energy stored in the dielectric layer during a dielectric breakdown event, thus isolating the defective region from the remainder of the capacitor.[9] Self-clearing can be viewed as a selective-deposition process in which the top electrode is deposited only onto defect-free regions over a large area on the dielectric film.

Figure 1 shows the dielectric permittivity (ε) and loss of a PLZT capacitor with 250 μm diameter electrode as a function of bias voltage. A dielectric permittivity of ~1250 and loss (tan δ) of ~0.06 were typically observed at 10 kHz. Similar values were observed for 750 μm diameter electrodes. Although the area of the two electrodes differed by a factor of nine, their dielectric properties did not differ appreciably, indicating comparable defect densities over such small scales (d/t <1000).

Similar testing on a large-area capacitor (12-mm diameter electrode) was not possible because it has lower voltage tolerances (<10 V) compared to its smaller counterparts. Also, the typical ferroelectric loop (double bell curves shown in Fig. 1) was not observed for this capacitor, even within the tolerable voltage limits. Therefore, we determined the performance of the large-area capacitor at 10 kHz with zero bias prior to self-clearing. The dielectric permittivity was ~700, and the loss tangent was high (tan δ ~ 3), suggesting that the dielectric layer was leaky and conductive. We attributed this reduction in dielectric constant and increase in dielectric loss to the large number of defects that occurred under the electrode. To isolate these defective areas, we applied short pulses of incremental high voltage and the hysteresis loops were measured in the process. Figure 2 shows the hysteresis loops measured in 10 V increments over the voltage range of 10 V to 80 V. It can be noted that well-saturated hysteresis loops were measured until 70 V. At 80 V, breakdown events at defect spots started to initiate the self-clearing process.

Figure 3 presents an optical image of a representative self-cleared top electrode after breakdown at a defect spot. In a breakdown event, the dielectric discharges all its stored energy in the defect site, causing it to vaporize, sinter, or physically break the dielectric material and vaporize the electrode in that spot. This event forms a typical aperture or hole in the electrode and/or the dielectric material. As seen in Fig. 3, the Pt electrode has vaporized in and around the defect spot where the breakdown occurred as a result of micro-arcing. While voltage is no longer maintained in that defect region, because of the absence of the overlying electrode, the voltage is still maintained across the

rest of the capacitor.[9] The capacitor was cycled 3-4 times at 80V until self-clearing events terminated.

Figure 4 shows the permittivity and loss as a function of bias voltage for the large-area capacitor after self-clearing at 80V. The important features that the curves illustrate are the typical ferroelectric nature, permittivity, and the voltage tolerance of the capacitor. Prior to self-clearing, dielectric measurement on the capacitor did not indicate typical ferroelectric behavior (double bell curve) even within the tolerable voltage limits (±10 V). Since a well-saturated dielectric permittivity loop was measured after self-clearing, we believe that defects caused by the inclusion of foreign particles may have compromised the ferroelectric nature of the film at high frequencies. This hypothesis is supported by Fig. 2, where the ferroelectric nature of the material is clearly evident in the hysteresis loops measured at 1 kHz before self-clearing.

The permittivity for the large-area capacitors was ~1020 after self-clearing, compared to ~700 before self-clearing. This difference suggests the isolation or removal of low-permittivity and conductive defect spots during self-clearing. This permittivity for large-area capacitors approaches the high values observed for small-area capacitors (ε~1260) if we account for the capacitive area lost during self-clearing. While measuring the area of individual self-cleared spots is tedious, a first-order approximation of the capacitive area lost during self-clearing can still be calculated on the basis of the measured capacitance and ε ~1260 (observed for 250 μm electrodes). Preliminary calculations show a loss of ~18% in the capacitive area due to self-clearing.

Table I shows the measured dielectric permittivity, area, and capacitance density for capacitors of different electrode size. High capacitance density of ~0.97 μF/cm^2 was measured for the ~1.15 μm thick PLZT films, which is comparable to ~1.5 μF/cm^2 for a 0.7 μm thick film of the same chemical composition reported by Kaufman et al.[2] Capacitors with larger aspect ratios also approach this high capacitance density after self-clearing, as indicated in Table I.

Self-clearing also helps in improving the voltage tolerance of the capacitors by removing the low-tolerance defect spots, which is evident in Fig. 4. Although the loss values in Fig. 4 are higher than expected, we believe that this result is due to impedance matching and not a material response.[8] A frequency sweep from 0.1 to 10 kHz, illustrated in Fig. 5, showed a flat response for both the capacitance and loss until 1 kHz. A capacitance of ~1.15 μF and tan δ ~0.12 were measured at 1 kHz.

Summary

In summary, we have investigated a self-clearing process that allows the fabrication of functional capacitors with aspect ratios >10^4. Large-area devices with capacitance densities approaching ~0.97 μF/cm^2 were fabricated by this process. This process eliminates the need to use ultra-clean processing and sophisticated deposition equipment to reduce defects in the dielectric thin film, thus reducing the manufacturing costs. The principle behind the process is to electrically isolate the defective regions from the remainder of the capacitor by vaporizing the thin electrode directly above the defects using high electric fields.

References

[1] B. Ma, D.-K. Kwon, M. Narayanan, and U. Balachandran, J. Electroceram. 22, 383, (2009).
[2] D.Y. Kaufman, S. Saha, and K. Uprety, Proc. 12th US-Japan Seminar on Dielectric and Piezoelectric Ceramics, Annapolis, MD, 305-308 (2005).
[3] B. Ma, D.-K. Kwon, M. Narayanan, and U. Balachandran, Mater. Lett. 62, 3573 (2008).
[4] Q. Zou, H. E. Ruda, and B. G. Yacobi, Appl. Phys. Lett. 78, 1282 (2001).
[5] A. I. Kingon and S. Srinivasan, Nat. Mater. 4, 233 (2005).
[6] M. D. Losego, L. H. Jimison, J. F. Ihlefeld, and J.-P. Maria, Appl. Phys. Lett. 86, 172906 (2005).
[7] M. Narayanan, D.-K. Kwon, B. Ma, and U. Balachandran, Appl. Phys. Lett. 92, 252905 (2008).
[8] P. Daniels, J. Ihlefeld, W. Borland, and J.-P. Maria, J. Mater. Res. 22, 1763 (2007).
[9] D.Y. Kaufman and S. Saha, US patent 7,099,141 (2006).

Acronyms

FCV	Fuel cell vehicle
HEV	Hybrid electric vehicle
LNO	Lanthanum nickel oxide
PHEV	Plug-in hybrid vehicle
PLZT	Lead lanthanum zirconium titanate
PWB	Printed wire board

Table I. Measured capacitance and calculated capacitance density of Pt/PLZT/LNO/Ni capacitors of different sizes at 10 kHz.

Electrode Size, μm	Capacitance, μF	**ε**	Area, cm^2	Capacitance Density, $\mu F/cm^2$
250	0.000477	1260	0.00049	0.973
750	0.004227	1240	0.00442	0.956
12,000	0.891100	1020*	1.131	0.788*

(*) Note the actual area is less than the 1.131 cm^2 used in calculations due to self-clearing. Therefore, the actual ε and capacitance density are expected to be higher than calculated.

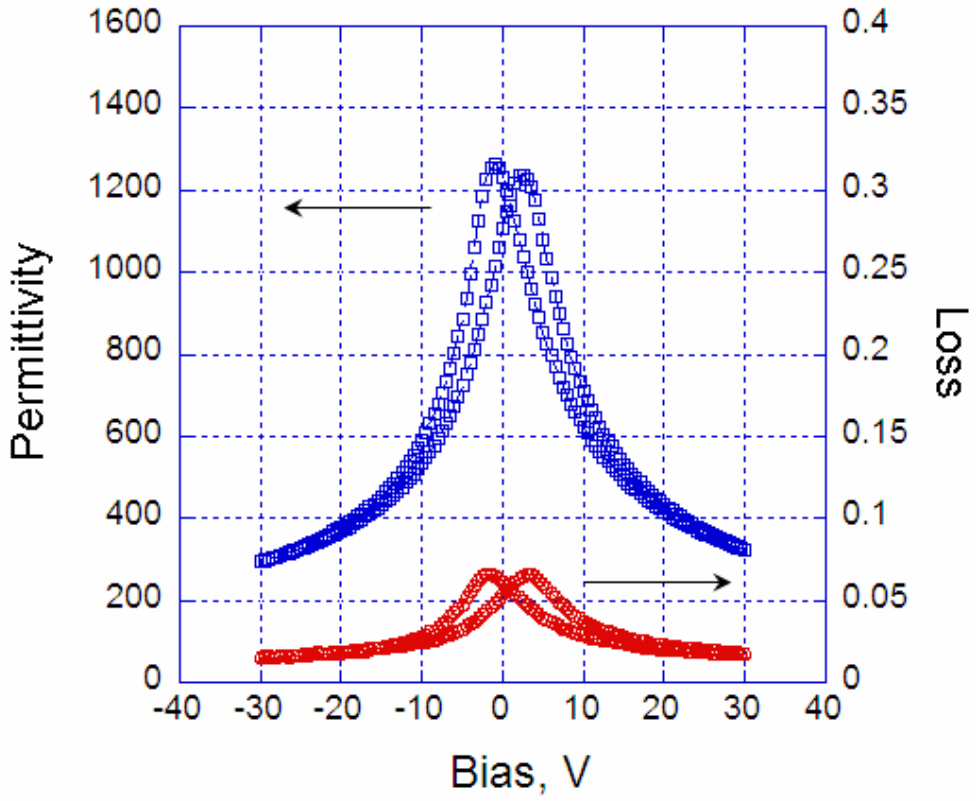

Figure 1. Dielectric permittivity and loss versus bias voltage measured at 10 kHz on Pt/ PLZT/LNO/Ni film-on-foil capacitors with 250 µm diameter electrodes. Similar values were observed for 750 µm diameter electrodes.

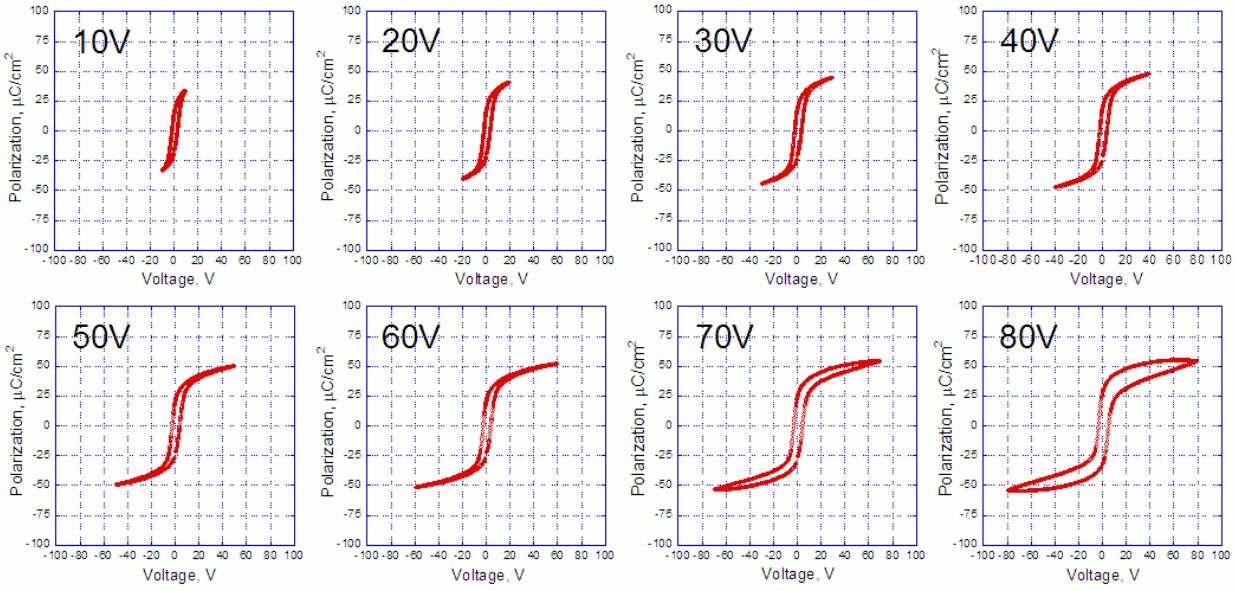

Figure 2. Hysteresis loops measured at different voltages on a 12 mm diameter capacitor to self-clear the weaker spots. Self-clearing of weaker spots started to occur at 80 V.

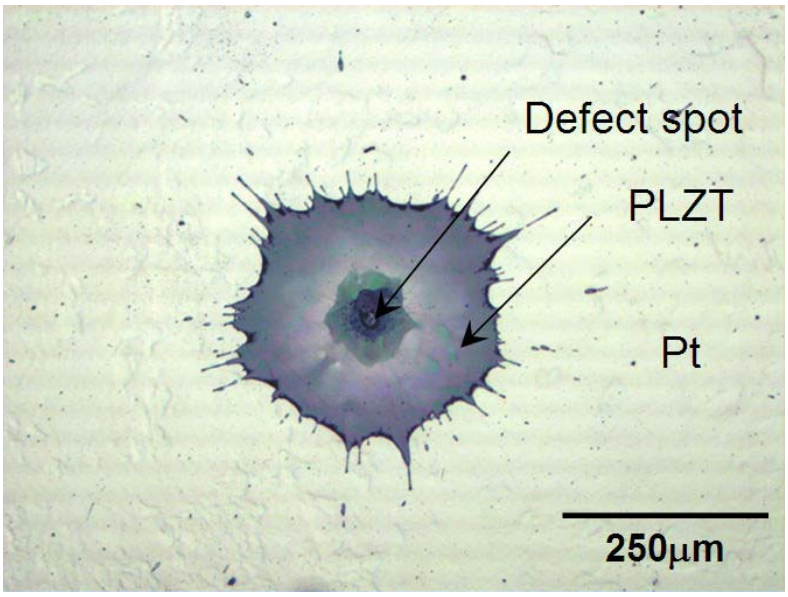

Figure 3. Typical optical image of a defect spot with top platinum (Pt) electrode self-cleared at 80 V. Figure illustrates the vaporization and clearing of Pt around the defect spot due to rapid discharge of energy during breakdown, thus separating the defective area from the remainder of the capacitor.

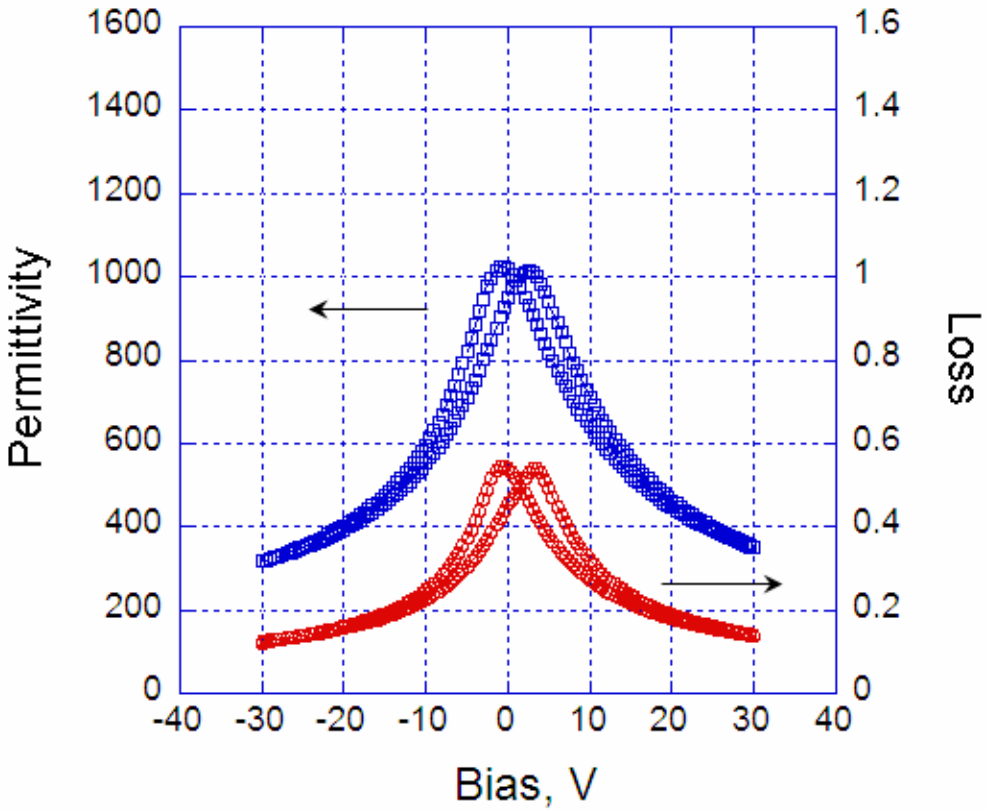

Figure 4. Dielectric permittivity and loss versus bias voltage measured at 10 kHz on a large-area Pt/ PLZT/LNO/Ni film-on-foil capacitor after self-clearing at 80 V.

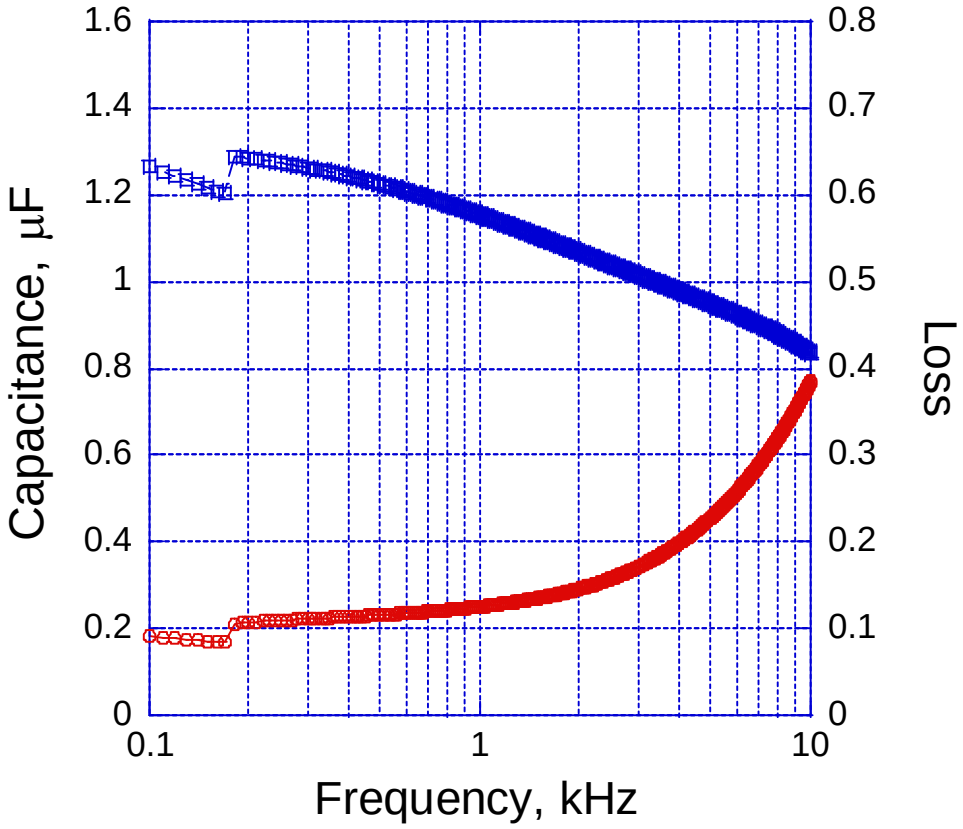

Figure 5. Capacitance measured as a function of frequency on the large-area capacitor (12 mm dia.) after self-clearing.

Agreement 17955 - Lithium Battery Recycling Issues

(This project is co-funded by the Energy Storage Program)

Linda Gaines
Center for Transportation Research
Argonne National Laboratory
9700 S. Cass Ave.
Argonne, IL 60439
630/252-4919, Fax: 630/252-3443; E-mail: lgaines@anl.gov

DOE Technology Manager: Jerry L. Gibbs
(202) 586-1182; fax: (202) 586-1600; e-mail: jerry.gibbs@ee.doe.gov

---

Contractor: Argonne National Laboratory, Argonne, Illinois
Contract No.: DE-AC02-06CH11357

Objectives

- Estimate material demands for Li-ion batteries
  - Identify any potential scarcities
- Calculate theoretical potential for material recovery
- Evaluate real potential for recovery using current recycling processes
- Determine potential for recovery via process development
- Develop improved process(es) to maximize material recovery

Barriers

- Scarcity could increase costs for battery materials
  - Recycling could increase effective material supply and keep costs down
  - Current processes recover cobalt, use of which will decline
  - Recycling economics in doubt
- Process data are not published

Technical Goals

- Characterize current battery recycling processes
- Determine current production methods for other materials
- Estimate impacts of current recycling processes
- Estimate energy use/emissions for current material processes
- Estimate energy use/emissions for current battery processes
- Evaluate alternative strategies for additional material recovery
- Develop improved recycling processes

Accomplishments

- Selected promising battery chemistries
- Designed battery packs for each chemistry and vehicle type
- Estimated materials use for optimistic EV demand scenario
- Compared US and world lithium demand to reserves
- Presented lithium demand estimates at battery and plug-in vehicle conferences
- Determined current production methods for lithium and batteries

---

Introduction

Use of vehicles with electric drive, which could reduce our oil dependence, will depend on lithium-ion batteries. But is there enough lithium? Will we need to import it from a new cartel? Are there other materials with supply constraints? We project the maximum demand for lithium and other materials if electric-drive vehicles expanded their market share rapidly, estimating material demand per vehicle for four battery chemistries. Total demand for the United States is based on market shares from an Argonne scenario that reflects high demand for electric-drive vehicles, and total demand for the rest of the world is based on a similar International Energy Agency scenario. Total material demand is then compared to estimates of production and reserves, and the quantity that could be recovered by recycling, to evaluate the adequacy of supply. We identify producing countries to examine potential dependencies on unstable regions or future cartels. As plug-in hybrid vehicles and possibly pure electrics enter the automotive market, use of lithium in batteries will rise rapidly. Recovery of material from spent batteries will be a key factor in alleviating potential material supply problems. We examine battery recycling processes that are available commercially now or have been proposed. The processes will be compared on the basis of energy saved and emissions reductions, suitability for different types of feedstock, and potential advantages.

Approach

We are answering these questions to address material supply issues.

- How many electric vehicles will be sold in the U.S. and world-wide?
- What kind of batteries might they use?
  - How much lithium would each use?
- How much lithium would be needed annually?
- How does the demand compare to the available resources?
  - How much difference can recycling make?
  - What recycling processes are available?
  - Could other materials become scarce?

Results

Vehicle Demand

To estimate U.S. sales of vehicles with electric drive, we extended the Energy Information Administration (EIA) projections of light vehicle sales for the United States from 2030 to 2050. Only moderate growth is projected between now and 2050, and most of that is in the light truck market. We took the most optimistic scenario for the penetration of vehicles with electric drive into the U.S. market from the DOE Multi-Path Study (Phase 1). In this scenario, 90% of all light-duty vehicle sales are some type of electric vehicle by 2050. This is an extreme-case scenario, not a projection, representing the maximum percent of U.S. sales that could be accounted for by hybrid and electric vehicles.

We relied on an IEA scenario for world demand. IEA is developing scenarios of what would need to be done to meet IPCC CO_2-reduction goals, based on World Bank economic and UN population projections, and the relationship between these and car ownership. Figure 1 shows our U.S. scenario, as well as IEA's projection of world LDV sales.

Batteries

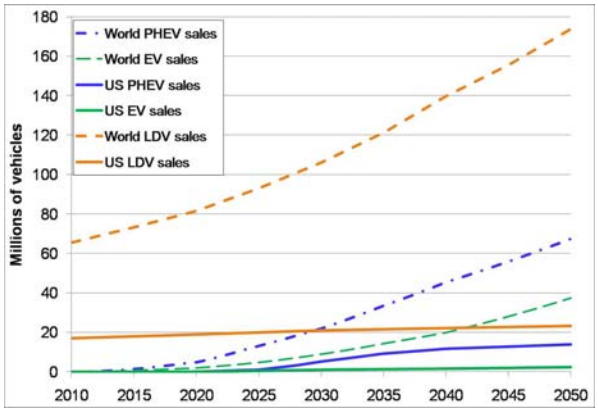

Figure 1. Light-Duty Vehicle Sales Projection to 2050

We chose three promising chemistries, in addition to the current NCA graphite, to compare on the basis of material usage. These are defined in Table I. All contain lithium in a salt for the cathode active material and a lithium salt ($LiPF_6$) in the electrolyte solution. One also uses a lithium titanate salt, instead of the standard graphite, in the anode. For each battery chemistry analyzed, all materials in the electrodes and the electrolyte were tabulated to give total material required.

From (1) the mass percent of each element in the active compounds and (2) the mass required of each compound in the batteries, we calculated the quantities of lithium and other materials required per battery pack. For lithium, the total is the sum of lithium from the cathode, the electrolyte, and the anode (for the cells with titanate anodes). The total requirement of lithium (on an elemental basis) for each car is shown in Table II. The electric vehicle battery requirement is based on

an assumed 100-mile range. Four batteries were designed — one for each of the chemistries chosen — for each of three automobile all-electric ranges.

Total Lithium Requirements and Reserves

Once the total quantities of material required per vehicle by type were determined, they were multiplied by the annual vehicle sales by type to provide an estimate of the material demanded. Figure 2 shows the U.S. results for lithium, assuming that all vehicles used the current NCA-Graphite chemistry. It also shows how potential U.S. demand compares to historical world production and U.S. consumption. The U.S. consumption is perhaps misleading, since it only accounts for direct purchases of lithium compounds by U.S. firms and omits indirect consumption in imported batteries and products containing batteries. U.S. demand for lithium for automotive batteries has a very long way to go before it strains current production levels, with U.S. demand, even under this aggressive penetration scenario, not reaching current production levels until after 2030.

We then considered the potential impact of recycling on net demand for materials. Figure 2 also shows the demand curve lagged by 10 years (assumed average battery life) to approximate material that would be available for recycling if all lithium were recycled. Finally, the graph shows the difference between the gross material demand and the potentially recyclable material. This represents the net quantity of virgin material that would be required if all battery material could be recycled. This curve turns over, meaning that the quantity of virgin material required actually declines after about 2035. This demonstrates the importance of recycling.

Table I. Battery Chemistries Included in the Analysis

System→ Electrodes	NCA Graphite	LFP (phosphate) Graphite	MS (spinel) Graphite	MS TiO
Positive (cathode)	$LiNi_{0.8}Co_{0.15}Al_{0.05}O_2$	$LiFePO_4$	$LiMn_2O_4$	$LiMn_2O_4$
Negative (anode)	Graphite	Graphite	Graphite	$Li_4Ti_5O_{12}$

Table II. Total Lithium Required per Passenger Automobile

	Battery Type															
Parameter	NCA-G				LFP-G				LMO-G				LMO-TiO			
Range (mi) @ 300 Wh/mile	4	20	40	100	4	20	40	100	4	20	40	100	4	20	40	100
Total Li in pack (kg)	.4	1.5	3.0	7.4	.2	.9	1.9	4.7	.2	.7	1.4	3.4	0.6	2.5	5.1	12.7

World demand could be considerably lower than the maximum shown in Figure 3. Smaller cars with smaller batteries than IEA assumed (12–18 kWh) are likely to be used. And, it can be argued that hybrids are more attractive than battery electric cars. Further, many of the vehicles could be electric bicycles or others that require less than 10% as much lithium per vehicle. With smaller batteries and recycling, net world demand in 2050 can be kept to 4 times current production.

We estimated cumulative battery demand for lithium under the assumption that all batteries were produced from only one chemistry. Total potential world lithium demand is shown in Table III. (This was done for each of the four chemistries; NCA graphite is shown.) This total was then compared to several estimates of the world reserve base. The maximum demand (double the quantity shown) would occur if all batteries were made by using titanate anodes, since this chemistry uses the most lithium per battery. Only in that case does total demand exceed the USGS conservative reserve base estimate. However, by taking care with battery size and taking advantage of material that could be made available from recycling, enough lithium is available to use while we work toward an even more efficient, clean, and abundant means of supplying propulsion energy.

Chile dominates current production, with Australia second. Bolivia has huge untapped reserves, and China is rapidly developing its production capacity.

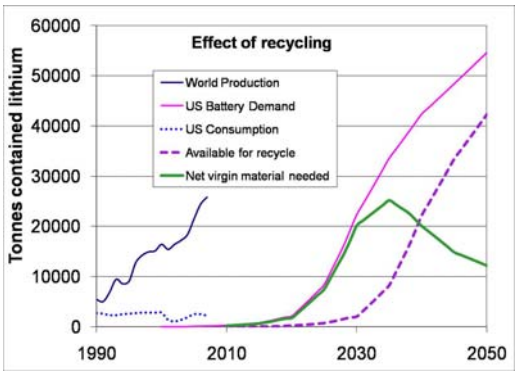

Figure 2. Future U.S. Lithium Demand Compared to Historical Production

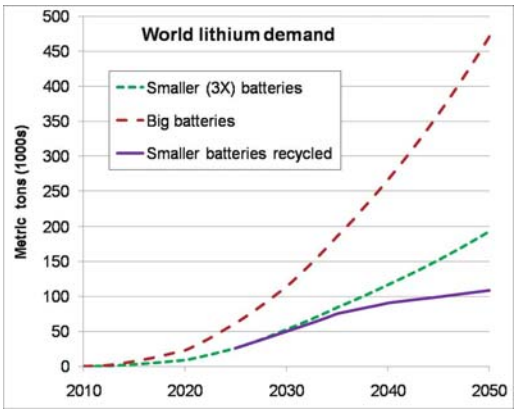

Figure 3. Future World Lithium Demand Scenarios

Table III. World Lithium Demand and Reserves

Item	Cumulative Demand to 2050 (contained lithium, 1,000 metric tons)
Large batteries, no recycling	6,474
Smaller batteries, no recycling	2,791
Smaller batteries, recycling	1,981
USGS Reserves	4,100
USGS Reserve Base	11,000
Evans and others	30,000+

The United States has limited reserves, and so it is likely to remain a materials importer, although batteries could certainly be produced here from these imported materials. The United States has relatively stable relationships with the major lithium-producing countries, and so significant supply problems are not anticipated.

Other Materials

We also estimated the potential demand for nickel, cobalt, and aluminum for NCA-graphite batteries; iron and phosphorus for LFP batteries; manganese for either the LMO-G or LMO-G; and titanium for the LMO-TiO. These quantities were then compared to USGS reserve data for each material, if appropriate. For some materials, such as iron, the quantity available is sufficiently large that another measure was used for comparison. Table IV compares material availability to potential cumulative U.S. light-duty battery demand[1] to 2050 and estimates the percent that could be required. A potential constraint was identified for cobalt. If NCA-G were the only chemistry used, batteries use could impact the reserve base by 2050. Approximately 9% of the world reserve base could be required for U.S. light-duty vehicle batteries. World demand would be a factor of 4 larger. Of course, recycling would significantly alleviate this pressure, as would the expected shift away from NCA-G to other chemistries.

The U.S. does not produce any cobalt, and so we must depend entirely on imports[2]. Cobalt is produced in many other countries, so it is unlikely that any one country or group could manipulate supply or price. Similarly, the U.S. does not produce any nickel, except for a small amount as a by-product of copper and platinum/palladium mining, so we import from a diversity of producers that suggests security of supply. The remaining battery materials are all abundant.

Recycling Processes

Recycling can recover materials at different production stages, all the way from basic building blocks to battery-grade materials. At one extreme are smelting processes that recover basic elements or salts. These are operational now on a large scale and can take just about any input, including different battery chemistries (including Li- ion, Ni-MH,

Table IV. Comparison of U.S. Light-Duty Battery Demand to Material Availability

Material	Availability (million tons)	Cumulative Demand	Percent Demanded	Basis
Co	13	1.1	9	World reserve base
Ni	150	6	4	World reserve base
Al	42	0.2	0.5	U.S. capacity
Iron/steel	1320	4	0.3	U.S. production
P	50,000	2.3	~0	U.S. phosphate rock production
Mn	5200	6.1	0.12	World reserve base
Ti	5000	7.4	0.15	World reserve base

etc.) or mixed feed. Smelting takes place at high temperature, and organics, including the electrolyte and carbon anodes, are burned as fuel or reductant. The valuable metals (Co and Ni) are recovered and sent to refining so that the product is suitable for any use. The other materials, including lithium, are contained in the slag, which is now used as an additive in concrete. The lithium could be recovered by using a hydrometallurgical process.

At the other extreme, recovery of battery-grade material has been demonstrated. Such processes require as uniform feed as possible, because impurities in feed jeopardize product quality. The components are separated by a variety of physical and chemical processes, and all active materials and metals can be recovered. It may be necessary to purify or reactivate some components to make them suitable for reuse in new batteries. Only the separator is unlikely to be usable, because its form cannot be retained. This is a low-temperature process with a low energy requirement. Almost all of the energy and processing to produce battery-grade material from raw materials is saved. Large volumes are not required.

Conclusions

Shortages have often been forecast without adequate exploration or consideration of incentives rising prices might provide. In the case of materials for lithium-ion batteries, it appears that even an aggressive program of vehicles with electric drive can be supported for decades with known supplies, if recycling is instituted. Reliance on pure electrics could eventually strain supplies of lithium and cobalt.

[1] Assumes all batteries use the chemistry requiring the material

[2] Some current supply comes from the stockpile and recycling, but any new supply will be imported.

Presentations and Publications FY2009

Presentations

Potential Demand for Lithium in Automotive Batteries, IEA Annex 10 Meeting on Lithium Supply, Charlotte, NC (December 4, 2008).
Lithium-Ion Batteries: Possible Material Demand Issues, 13th Battery Materials Recycling Seminar & Exhibit, Fort Lauderdale, FL (March 17, 2009).
Lithium-Ion Batteries: Material Demand and Recycling Issues, Plug-In 2009, Long Beach, CA (August 2009).

Papers

L. Gaines and P. Nelson, *Lithium-Ion Batteries: Possible Materials Issues*, proceedings of the 13th Battery Materials Recycling Seminar & Exhibit, Fort Lauderdale, FL (2009).

Project 18517 – Combustion System Materials

Agreement 11752 – Materials for HCCI Engines

G. (Murali) Muralidharan, and Rick Battiste
(865)574-4281: fax: (865) 574-4357; e-mail: muralidhargn@ornl.gov

Bruce G. Bunting
Engineering Science and Technology Division
(865) 946-1512; fax: (865) 946-354; e-mail: buntingbg@ornl.gov

DOE Technology Manager: Jerry L. Gibbs
(202) 586-1182; fax: (202) 586-1600; e-mail: jerry.gibbs@ee.doe.gov
ORNL Technical Advisor: D. Ray Johnson
(865) 574-4556; fax: (865) 241-0411; e-mail:

Contractor: Oak Ridge National Laboratory, Oak Ridge, Tennessee
Prime Contract No.: DE-AC05-00OR22725

Objectives

- Identify and catalog the materials operating conditions in homogeneous charge compression-ignition (HCCI) engines and use computational design concepts to develop advanced materials for such applications.
- Interact with designers of HCCI engines and manufacturers of components in order to identify the components that will be affected by the harsh operating conditions resulting from the HCCI design.

Approach

- Identify engine components, currently used materials, and current operating conditions and compare them with the expected component operating conditions for HCCI engines.
- Demonstrate the feasibility of the "materials-by-design" approach for the highest-priority item. Improve material performance for HCCI applications through computational modeling and experimental validation.

Accomplishments

- Using data from fully reversed fatigue tests and rotating beam tests, commercial alloys with required fatigue life have been down-selected
- Several new alloys with potential for better price/performance ratio have been designed
- Selected compositions have been prepared in small heats, their high temperature tensile properties have been evaluated, and promising alloys have been identified

Future Direction

- Continue to communicate with automotive companies, valve manufacturers, Diesel Cross-Cut Team, FreedomCAR, and 21st Century Truck on the progress made through computational design.
- Promising down-selected new alloy/s with desirable tensile properties and appropriate price/performance ratios will be optimized and tested for valve applications

Introduction

There has been an increasing interest in HCCI combustion in recent years because of its potential to increase engine combustion efficiency and reduce emissions. However, the use of HCCI combustion will subject the engine components to significantly higher temperatures and pressures. The temperatures for diesel engines will reach over 1600°F, and pressure may reach > 2000 psi, which is approximately four times that of the normal combustion engine.

Such severe engine operating conditions will require a significant improvement in materials performance in order to take advantage of the HCCI engine concept. This project deals with identifying materials requirements for HCCI engines for automotive and truck applications and the development of advanced, yet cost-effective, materials through computational design.

"Materials-by-design" is an Oak Ridge National Laboratory (ORNL) concept that encompasses a collection of materials-related techniques including modeling, correlation, and materials modification. The premise behind materials-by-design is that mechanical properties are correlated to microstructure and phase chemistry. The phase composition and microstructure can be achieved through thermodynamic equilibrium or through non-equilibrium techniques such as quenching, rapid casting solidification, or mechanical working. These characteristics can then be correlated to desired mechanical properties through equilibrium thermodynamics or through a variety of correlation techniques. The correlations allow untested compositions or treatments to be modeled so that desired trends can be rapidly established. Small heats of targeted materials can then be processed to confirm the modeled properties and to broaden the correlation data base.

Finally, there are several techniques, such as magnetic processing or low-temperature carburizing, that can be applied to allow further modification and optimization of desired properties. Materials-by-design is ideally suited to cast materials and heavily thermally processed materials (e.g., stainless steels, Ni alloys, cast irons, alloy steels, and brazed wrought aluminum alloys), and the concept has been successfully applied in such diverse areas as high-temperature furnace components, exhaust valves, exhaust manifolds, and tube fittings. Figure 1 and Table 1 provide an outline of the materials-by-design approach and a summary of the techniques that can be applied.

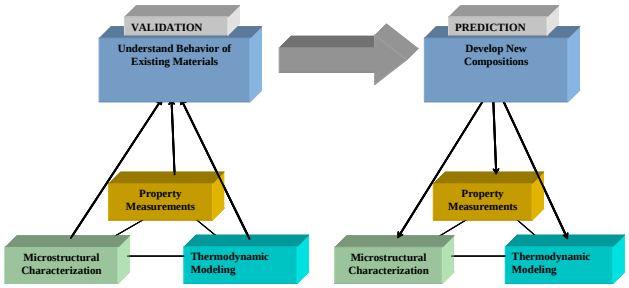

Figure 1. Overall approach for materials-by-design.

In our approach, we examined critical heavy-duty diesel engine materials and identified means to reduce their cost for acceptance in HCCI applications. This was accomplished through the following tasks:

Task 1. Identify critical material requirements for HCCI engines based on their operating conditions. This task will be accomplished through interactions with advanced engine and component designers. The interactions will include personal visits to six companies: Caterpillar, Cummins Engine, Deer, International Truck, Eaton Corp., and General Motors. Visits will be supplemented by a literature search, a review of advanced engine design studies, and follow-up discussions afterward. The key outcomes from this task will include (1) identifying operating conditions for advanced engine concepts, with a focus on the HCCI concept; (2) identifying components most affected by these operating conditions; (3) identifying currently used materials, new requirements, and performance targets; and (4) ranking the highest-priority items for study by the materials by design approach.

Task 2. Demonstrate the feasibility of materials-by-design approach for the highest-priority item. In this task, we will identify the details of the currently used material for the highest-priority item. Specifically, we will examine material compositions, processing methods, mechanical properties, corrosion properties, and cost.
Based on the available mechanical properties data, microstructural analysis, and thermodynamic phase stability calculations, we will identify the underlying mechanism that delivers the current properties.

Table 1. ORNL materials-by-design toolbox

Modeling	Experimentation	Characterization
Thermodynamic modeling of material properties vs alloy composition	Ultra-high-gauss magnetic stabilization of alloy steels	Advanced microscopy techniques
Neural-network modeling of diverse, nonlinear materials properties and process variations	Low-temperature gas carburization of finished components	X- ray and neutron scattering
Detailed microstructure based empirical modeling	Ability to produce small quantities of materials and fabricate them into test bars for property measurements and production of prototype components by a variety of methods, including sand and die casting, extrusion, forging and rolling	Surface and bulk property measuring techniques
Non-equilibrium modeling of solidified structures		
Extrapolation of properties from simple alloy systems to complex systems using interaction parameters		

Task 3. Improve materials performance for HCCI application through computational modeling and experimental validation. In this task, we will use computational modeling (key basis for the material-by-design concept) to identify compositions that will deliver the desired phases for two purposes: (1) improving property performance and (2) finding alternatives to reduce cost for both current and improved performance. The outcome of the analysis will be validated through experimentation. The validation will be carried out in the following steps:

1. Prepare compositions identified based on computational design in 1-lb heats for microstructural analysis and very limited property determination; compare the results with output based on computational analysis for validation.
2. Scale up the validated composition into 20-lb to 100-lb heats and cast them into ingots for processing trials. In most cases, the material is expected to be used in the wrought condition. However, if it is to be used in the cast condition, we will save part of the ingots for analysis of as-cast properties.
3. Subject cast ingots to processing steps that are currently used by industry. Develop optimum processing and heat-treatment conditions to obtain the desired microstructure.
4. Carry out microstructural analysis and mechanical properties analysis on the material processed and heat-treated with optimum conditions.
5. Prepare prototype components for HCCI engine tests.

Extensive interaction with industrial partners will occur during all three tasks. This collaboration is expected to result in the rapid transfer of materials improvement from this project to industry for use in HCCI and other advanced engine concepts.

Results

Materials Development through Computational Design

Ni-based alloys have been identified as potential candidates for improved valve materials. There is particular interest in increasing the operating temperature of exhaust valves to about 1600°F (870°C). High temperature fatigue strength has been identified as a critical factor in determining the performance of these alloys in the valve application. An evaluation of the microstructure of various Ni-based alloys and correlation with limited information on the fatigue properties that are available show that the volume fraction of the γ' phase is likely to be a dominant factor in determining the performance of these alloys at high temperatures. Since the size of the strengthening precipitates is also

critical, it is anticipated that the kinetics of coarsening this phase would also be influential in the long-term performance of the alloys in this application. Based upon discussions with various users and suppliers, a range of Ni-based alloys with potentially varying weight fractions (or volume fractions) of γ' have been identified in efforts to correlate the fatigue properties with the microstructure of the alloys. To obtain initial information on the microstructures of these alloys at equilibrium, thermodynamic calculations have been carried out using JMatPro V4. Comparison of the results of the calculations showed that all alloys have a matrix of γ with the major strengthening phase as γ'. One or more carbide phases such as $M_{23}C_6$, MC, and M_7C_3 may also be present in different alloys. The primary difference between the microstructures of the various alloys is in the weight percent of the γ' phase at a given temperature and the highest temperature at which the γ' phase is stable in the different alloys.

Fatigue Property Measurement

In order to develop relationships between the microstructures of the alloys and their mechanical properties, high-temperature fatigue property data were obtained on all down-selected alloys as a part of the project. Load-controlled, fully-reversed fatigue tests were conducted *in-situ* at a temperature of 870°C. Stresses of 21.8 (150) Ksi (MPa), 29 (200 MPa), 39.9 (275 MPa), 43.5(300 MPa), 50.8(350 MPa), and 54.4(375 MPa) were used to investigate the fatigue performance of the alloy. Since rotating beam tests are commonly used to specify required materials properties for applications in valves, a new rotating beam testing equipment was installed at ORNL. Initial tests were performed in Alloy 751 (which is currently used in valve applications) at ORNL to compare the fatigue life obtained in fully reversed fatigue tests with that obtained in rotating beam fatigue tests. Figure 2 shows a summary of results obtained from IN 751 obtained using the two techniques. It is clear from these results that the fatigue life observed in fully reversed tensile fatigue tests is lower than that in rotating beam tests at the same temperature and stress levels.

Using the approximate correlation between the fatigue lives obtained using the two techniques as described above, and the existing fatigue life data for commercial down-selected alloys measured at ORNL using fully reversed techniques, several alloys have been identified as candidates for high temperature valve

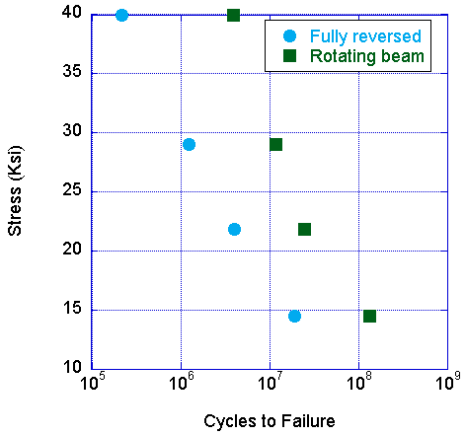

Figure 2. Comparison between fatigue life obtained using fully reversed fatigue tests and rotating beam fatigue test for a temperature of 870°C for IN751.

applications as illustrated in Figure 3. Rotating beam fatigue testing has been carried out in Alloys A and B and superior rotating beam fatigue properties have been confirmed in these alloys and project milestone has been achieved.

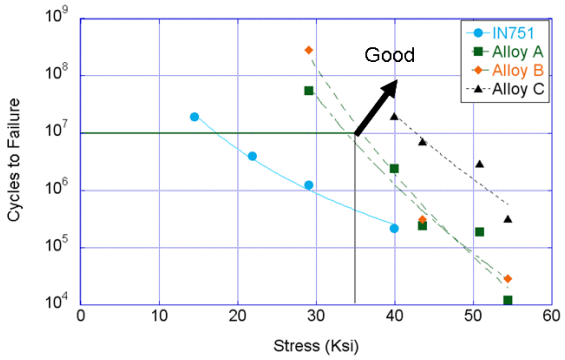

Figure 3. Several commercially available alloys with desired fatigue properties were identified as possible candidates for use in higher temperature exhaust valve applications.

Development of Improved Alloys through Computational Modeling

Using the microstructures of these alloys as a guide, computational thermodynamics was used to identify additional alloys with microstructure similar to the commercial alloys with desirable properties. In contrast to the commercially available alloys with Ni-contents in the range of 50 wt.% to 60 wt. %, the Ni-content in these alloys

ranges from about 30 wt. % to 45 wt. % with the potential to achieve comparable properties. This implies that the alloys will be of lower cost but comparable mechanical properties.

Figure 4 shows a typical small heat of alloy HCCI-2 that was cast at ORNL. Subsequent to casting, these alloys were homogenized, and rolled at high temperatures. Small tensile specimens were machined from these alloys and tensile tests were conducted *in-situ* at 870^{o}C. Figure 5 shows a typical stress-strain curve obtained from alloy HCCI-2. Note that the yield strength at 870^{o}C for this alloy was measured to be about 47 ksi. Further optimization of alloy composition and heat-treatment procedure will be performed in FY 2010.

Figure 4. Small heats of alloys were melted and cast in a vacuum arc furnace, homogenized, aged, and specimens were machined for high temperature tensile tests.

Conclusions

- Several commercial alloys that have the required fatigue properties have at 870^{o}C for use in valve applications have been identified using fully reversed fatigue tests and rotating beam fatigue tests
- Computational thermodynamics models have been used to identify alternate promising compositions, small batches of alloys have been prepared, and tensile properties of selected alloys have been evaluated
- Optimization of alloy composition will be pursued to further improve alloy performance

Publications/Presentation

G. Muralidharan, "Computational Design of Alloys For Energy Efficiency in High Temperature Applications," Gordon Conference on Integrating Computational Materials Science And Engineering, held August 2-7, 2009, Proctor Academy, Andover, NH.

Agreement 8697 - NO_x Sensor Development

Leta Y. Woo and Robert S. Glass
Lawrence Livermore National Laboratory
P.O. Box 808, L-184
Livermore, CA 94551-9900
(925) 423-7140; fax: (925) (423-0153); e-mail: glass3@llnl.gov

DOE Technology Manager: Jerry L. Gibbs
(202) 586-1182; fax: (202) 586-1600; e-mail: jerry.gibbs@ee.doe.gov

Contractor: Lawrence Livermore National Laboratory, Livermore, California
Prime Contract No.: W-7405-Eng-48

Objectives

- Develop an inexpensive, rapid-response, high-sensitivity and selective electrochemical sensor for oxides of nitrogen (NO_x) for compression-ignition, direct-injection (CIDI) exhaust gas monitoring
- Explore and characterize novel, effective sensing methodologies based on impedance measurements
- Explore designs and manufacturing methods that could be compatible with mass fabrication
- Collaborate with industry in order to (ultimately) transfer the technology to a supplier for commercialization

Approach

- Use an ionic (O^{2-}) conducting ceramic as a solid electrolyte and metal or metal-oxide electrodes
- Correlate NO_x concentration with changes in impedance by measuring the cell response to an ac signal
- Evaluate sensing mechanisms using electrochemical techniques
- Characterize aging mechanisms and the effects on long-term performance of candidate sensor materials
- Understand and develop methodology to eliminate interferences
- Collaborate with the Ford Research Center to optimize sensor materials, operating parameters, and performance and perform dynamometer on-vehicle testing

Accomplishments

- Improved design to address mechanical stability by mounting sensor on a heated alumina substrate that is suitable for packaging into a commercial sensor housing and directly attaching to the exhaust manifold for engine dynamometer tests
- Completed long-term evaluation of more advanced prototype demonstrating over 3000 h of continuous operation and stability with thermal cycling from operating temperatures (~600°C) to room temperature
- Evaluated H_2O and O_2 cross-sensitivity, successfully demonstrating the potential for O_2 compensation using a dual-frequency method that allows the background O_2 signal to be subtracted out
- Publications/Presentations/Patents:
- Submitted Record of Invention (ROI) and filed a provisional patent

- Presented poster at the 2008 Fall Meeting of the Materials Research Society Meeting
- Oral presentation at the 2009 DOE Hydrogen Program and Vehicle Technologies Program Annual Merit Review and Peer Evaluation Meeting
- Oral presentation at the 215th Electrochemical Society Meeting
- Manuscript submitted to the Journal of the Electrochemical Society

Future Directions

- Develop more advanced prototypes using processes suitable for cost-effective, mass manufacturing
- Evaluate performance of prototypes, including long-term stability and cross-sensitivity, in laboratory, dynamometer, and on-vehicle tests
- Initiate the technology transfer process to a commercial entity

Introduction

NO_x compounds, specifically NO and NO_2, are pollutants and potent greenhouse gases. Compact and inexpensive NO_x sensors are necessary in the next generation of diesel (CIDI) automobiles to meet government emission requirements and enable the more rapid introduction of more efficient, higher fuel economy CIDI vehicles.[1-3]

Because the need for a NO_x sensor is fairly recent and the performance requirements are extremely challenging, most are still in the development phase.[4-6] Currently, there is only one type of NO_x sensor that is sold commercially, and it seems unlikely to meet more stringent future emission requirements.

Automotive exhaust sensor development has focused on solid-state electrochemical technology, which has proven to be robust for in-situ operation in harsh, high-temperature environments (e.g., the oxygen stoichiometric sensor). Solid-state sensors typically rely on yttria-stabilized zirconia (YSZ) as the oxygen-ion conducting electrolyte and then target different types of metal or metal-oxide electrodes to optimize the response.[2-6]

Electrochemical sensors can be operated in different modes, including amperometric (a current is measured) and potentiometric (a voltage is measured), both of which employ direct current (dc) measurements. Amperometric operation is costly due to the electronics necessary to measure the small sensor signal (nanoampere current at ppm NO_x levels), and cannot be easily improved to meet the future technical performance requirements. Potentiometric operation has not demonstrated enough promise in meeting long-term stability requirements, where the voltage signal drift is thought to be due to aging effects associated with electrically driven changes, both morphological and compositional, in the sensor.[7]

Our approach involves impedancemetric operation, which uses alternating current (ac) measurements at a specified frequency. We have described this approach in last year's report and in several publications (See Ref. 8-10). Impedancemetric operation has shown the potential to overcome the drawbacks of other approaches, including higher sensitivity towards NO_x, better long-term stability, potential for subtracting out background interferences, total NO_x measurement, and lower cost materials and operation.[8-10]

Past LLNL research and development efforts have focused on characterizing different sensor materials and understanding complex sensing mechanisms.[8-10] Continued effort has led to improved prototypes with better performance, including increased sensitivity (to less than 5 ppm) and long-term stability, with more appropriate designs for mass fabrication, including incorporation of an alumina substrate with an imbedded heater.

Remaining challenges include mechanical stability and sensor accuracy, which depends on cross-sensitivity to interfering gases and temperature dependency. Our most recent efforts have focused on improving two of the more advanced prototypes by addressing mechanical stability and materials processing limitations while evaluating potential trade-offs in sensor performance and accuracy.

The ultimate goal is the transfer of this technology to a supplier for commercialization. Due to the recent economic downturn, suppliers are demanding

more comprehensive data and increased performance analysis before committing their resources to take the technology to market. Therefore, our NO_x sensor work requires a level of technology development more thorough and extensive than ever before.

Background

For an electrochemical cell with two electrodes, impedancemetric sensing requires that at least one of the electrodes act as the "sensing" electrode. The sensing electrode will have a preferable response to NO_x over other gas phase components. However, in impedancemetric sensing, both electrodes can nevertheless have an appreciable response. This contrasts to the case in potentiometric sensing where differential measurements are much more important. Therefore, the sensor design is flexible and can either contain one sensing electrode and one counter (i.e., non-sensing) electrode, or two sensing electrodes. It opens up the opportunity to use a greater variety of materials.

Previous work at LLNL focused on the role of electrode composition and microstructure and provided criteria for higher sensitivity electrodes, which depended on limiting the oxygen reaction on the electrode so that the NO_x reaction could be resolved.[9-10] Our previous work suggested that impedancemetric sensing was possible with a variety of electrode materials, both metal and metal oxides, that meet general sensor criteria, which include a dense microstructure and appropriate composition to limit the catalytic activity towards oxygen.[10]

In more recent work, the impedancemetric sensing behavior of two compositions, gold and strontium-doped lanthanum manganite (LSM), were compared using asymmetric cell designs. LSM is an electronically conducting metal oxide. While similar overall NO_x sensitivity was observed for the two different materials and designs, differences in NO and NO_2 selectivity were noted due to influence of specific cell design characteristics on surface reactions.

Gold sensing electrodes have demonstrated stable electrochemical performance for over 500 h of operation, the potential for low water cross-sensitivity, and a convenient wire geometry that allows the inclusion of a heated substrate. However, drawbacks of gold wire electrodes include poor mechanical performance, where the thermal mismatch with the YSZ electrolyte leads to wire delamination, and poor processing flexibility, where the melting temperature of gold requires separate low-temperature processing steps.

Another potential drawback of gold sensing electrodes is its poor performance at higher frequencies (~1 kHz), which is used in the dual-frequency measurement strategy to mitigate oxygen cross-sensitivity and increase accuracy. In previous LLNL work, we demonstrated the possibility for using a separate high-frequency signal (~1 kHz) that is selective for oxygen (i.e., not sensitive to NO_x) in addition to the low-frequency signal (~5-10 Hz), which is sensitive to both NO_x and oxygen. The oxygen contribution can then be conveniently subtracted out.[8]

Compared to gold, LSM sensing electrodes have demonstrated the potential for better performance at higher frequencies for oxygen compensation and better processing flexibility and mechanical stability due to higher melting temperatures and better thermal expansion match with the YSZ electrolyte. However, drawbacks of LSM electrodes include potential water cross-sensitivity, including water-induced drift/aging, and pose more difficult geometric considerations for incorporating a heated substrate.

Our current work focuses on addressing the drawbacks of both materials and developing more advanced prototypes that incorporate alumina substrates with imbedded heaters. The top of Fig. 1a shows the alumina substrate with an imbedded heater, which is provided by our collaborators at Ford Motor Company. The sensing electrode/electrolyte/counter electrode (i.e., cell) is located at one end of the substrate, as shown in the bottom of Fig. 1a. Leads are located on the opposite end of the substrate. This design is appropriate for packaging into a commercial sensor housing (provided by a U.S. supplier) with protective cap, as shown in Fig. 1b. The packaged sensor can then be mounted directly into the exhaust manifold during engine dynamometer testing.

(a)

(b)

Figure 1. Picture of (a) alumina substrate with imbedded heater provided by Ford Motor Company without (top) and with (bottom) sensing electrode/electrolyte/counter electrode that is suitable for packaging into a (b) commercial sensor housing.

Experimental

Two different sensing materials, Au and LSM, were investigated. Figure 2 shows a schematic of a prototype using Au wire as the sensing electrode and alumina with an imbedded Pt resistive heater as the substrate (70 mm × 4 mm × 1 mm, see Fig. 1a). The substrate has a total of four leads, two leads for the Pt resistive heater located on one side, and two leads for the sensor located on the opposite side.

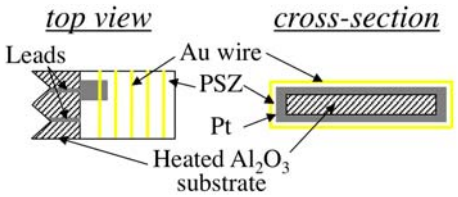

Figure 2. Schematic of more advanced NO_x prototype sensors using Au wire as the sensing electrode.

The end of the substrate was coated with Pt paste on the top, bottom, and side surfaces and fired at 1200°C. One of the substrate leads contacted the Pt counter electrode. Yttria partially-stabilized zirconia (PSZ, 3 mol % yttria doping) slurry was then applied on top of the fired Pt. Au wire was tightly wrapped around the prototype and additional PSZ slurry was applied on top of the wires and the assembly fired at 1000°C to produce the porous PSZ electrolyte. The second substrate lead for the sensor housing contacted the Au wire.

Figure 3 shows a schematic of the prototype using a dense ceramic oxide as the sensing electrode. LSM was used as the electronically conducting oxide sensing electrode. A dense pellet was prepared with commercial $(La_{0.85}Sr_{0.15})_{0.98}Mn$ oxide powder (Praxair) by pressing in a uniaxial die and sintering at 1250°C. Two pieces of LSM (6 mm × 2 mm × 1 mm) were machined and attached to the top of the substrate using Pt paste and fired to 1200°C. Yttria fully-stabilized zirconia (FSZ, 8 mol % yttria doping) slurry was applied on top of the dense LSM pieces and the assembly fired at 1000°C.

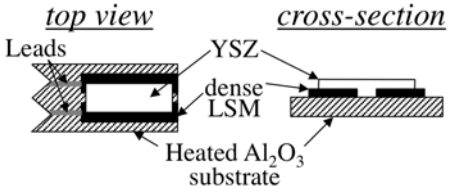

Figure 3. Schematic of more advanced NO_x prototype sensors using dense LSM as the sensing electrode.

Laboratory gas sensing experiments of sensors on heated alumina substrates were performed in a quartz tube with both electrodes exposed to the same environment. A specialized attachment (provided by Ford Motor Company) was used to make contact with the sensor and heater leads. Based on previous testing protocols and the role of the differing catalytic activity of Au and LSM in NO_x sensitivity, the prototypes with the Au wire sensors were maintained at a higher temperature (the heating element operated at a higher voltage) than the LSM sensors, 10.5 and 8.5 V, respectively.

The exact temperature corresponding to the heater voltage was not known, but was correlated with the behavior of similar prototypes that underwent furnace testing. Future prototypes may incorporate resistive temperature detectors to more accurately determine temperature. Nevertheless, Au wire and LSM sensors were previously tested at 650°C and 575°C, respectively, with similar type behavior seen in the sensors operated at 10.5 and 8.5 V, respectively.

A more detailed study of the LSM sensor and water cross-sensitivity was performed using electrodes attached to a square alumina substrate (10 mm × 10 mm × 0.5 mm) without imbedded heaters. The alternative sensor geometry was more suitable for controlled temperature testing in a tube furnace. The sensor geometry was similar to that shown in Fig. 3.

Gas composition was controlled in laboratory testing by mixing air, N_2, and a 1000 ppm NO/NO_2 feed using a standard gas handling system equipped with thermal mass flow controllers. Electrochemical measurements were performed using a Solartron 1260 Impedance Analyzer with a Solartron 1287 Electrochemical Interface.

Results and Discussion

Sensing behavior using the Au wire prototype – Previous designs for the Au wire sensor lacked the necessary mechanical robustness for mounting into the sensor housing and attaching directly to the exhaust manifold for engine dynamometer testing. Au wire delamination was responsible for the mechanical degradation.

Previous designs used a 2D geometry and Au wire electrodes were located on only the top surface of the heated substrate. To improve adhesion of the Au wires, an improved design used a 3D geometry utilizing the top, bottom, and side surfaces of the substrate and Au wire electrodes wrapped around the entire substrate.

Previous designs also used yttria fully-stabilized zirconia (FSZ, 8 mol % yttria doping) as the electrolyte material, which has a thermal expansion coefficient of ~10.5 × 10^{-6} K^{-1}. The thermal mismatch between the FSZ electrolyte and Au wire electrode (~14 × 10^{-6} K^{-1}) likely contributes to the mechanical degradation. To improve the thermal match, yttria partially-stabilized zirconia (PSZ, 3 mol % yttria doping) was used instead, which has an increased thermal expansion coefficient (~11 × 10^{-6} K^{-1}) compared to FSZ and better matches the thermal expansion of the Au wire electrode. In addition to the increase in thermal expansion coefficient, PSZ exhibits higher toughness and lower ionic conductivity than FSZ.

Figure 4 shows the impedancemetric sensing behavior for the improved Au wire prototype in laboratory testing. The sensing signal is the phase angle response of the cell to a 100 mV ac signal at 5 Hz. In Fig. 4a, the background oxygen concentration was changed from 2 to 18.9%, as indicated at the top of the graph, and the NO concentration was changed at each oxygen level: 100, 50, 20, 10, and 0 ppm. For all changes in gas concentration, the sensor responds quickly and recovers quickly to the original baseline value (< 10 s).

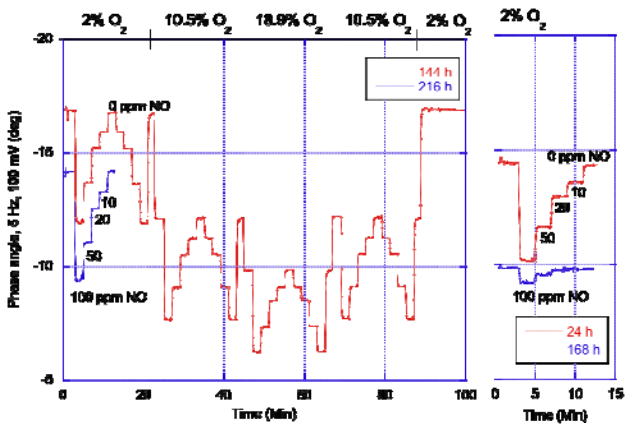

(a) (b)

Figure 4. Sensing behavior of Au wire sensor with changes in oxygen and NO concentration at (a) 144 and 216 h of testing and (b) after a single cycle from the operating temperature to room temperature and testing at 24 and 168 h. The sensing signal shown is the phase angle response of the cell to a 100 mV ac signal at 5 Hz.

In Fig. 4a, the upper red curve shows the sensing behavior after continuous testing for 144 h using a heater voltage of 10.5 V. The lower blue curve shows the initial data (from 0 to 12 min) collected at 216 h for 2% oxygen. Only the initial data is shown at 216 h because a more compact testing protocol was used for these data and displaying the full data set would detract from figure clarity. However, similar behavior was noted for the other concentrations of oxygen at 216 h as that observed at 2% oxygen. The main point to the figure is that there was a baseline shift in going from the data set at 144 h and 216 h. The baseline shift may indicate an initial "aging" effect, which is common for electrochemical sensors. At all oxygen levels, the NO sensitivity was relatively unaffected in going from 144 to 216 h of continuous testing.

Despite the efforts to improve mechanical robustness by incorporating a 3D design strategy to improve Au wire adhesion and changing the electrolyte material for better thermal expansion matching, the performance of this sensor also degraded after thermal cycling. After the initial continuous testing of the sensor to 216 h (as shown in Fig. 4a), the sensor temperature was subsequently decreased to room temperature before returning to the testing temperature using a heater voltage of 10.5 V.

In Fig. 4b, after this single thermal cycle and holding at the operating temperature for 24 h, the upper red trace shows both a shift in the baseline and a decrease in NO sensitivity compared to the data

shown in Fig. 4a. After testing at 24 h, the sensor continued to be held at the operating temperature. At 168 h, the lower blue trace in Fig. 4b shows that the baseline continued to drift and the NO sensitivity was significantly reduced with the sensor no longer able to resolve NO concentrations less than 20 ppm. This degradation in the sensor signal indicated the need for improved materials and/or designs. As discussed in the following, the LSM prototype showed significantly better performance.

Mitigating O_2 cross-sensitivity using the Au wire and LSM prototypes – As mentioned above, we are employing a dual-frequency approach to compensate for oxygen cross-sensitivity and improve sensor accuracy.[8]

The gas flow profile for oxygen and NO compositions that was used to evaluate the phase angle response to a 100 mV ac signal at 1 kHz is shown in Fig. 5a. The high-frequency behavior (1 kHz) of the Au wire prototype is shown in Fig. 5b. The upper blue trace shows the response when only the oxygen is changing. The lower red trace shows the response when both oxygen and NO composition change. This demonstrates sensitivity towards oxygen with relatively small response to changes in NO at this frequency. However, both a considerable shift in the baseline (note beginning and end response at 2% O_2) and drift in the signal were noted. Furthermore, the amount of drift seems to increase during the course of testing. The unstable high-frequency signal with the Au wire prototype shows that this design is not suitable for compensating for oxygen cross-sensitivity.

Fig. 5c shows the high-frequency response of the LSM prototype. In contrast to the behavior noted for the Au wire prototype, the sensor responds identically to either changing both oxygen and NO (red trace) or when only changing the oxygen composition (blue trace). Furthermore, the response of the LSM prototype is much more stable and reproducible. Therefore, this prototype appears to be much more suitable for potentially mitigating oxygen cross-sensitivity and improving sensor accuracy.

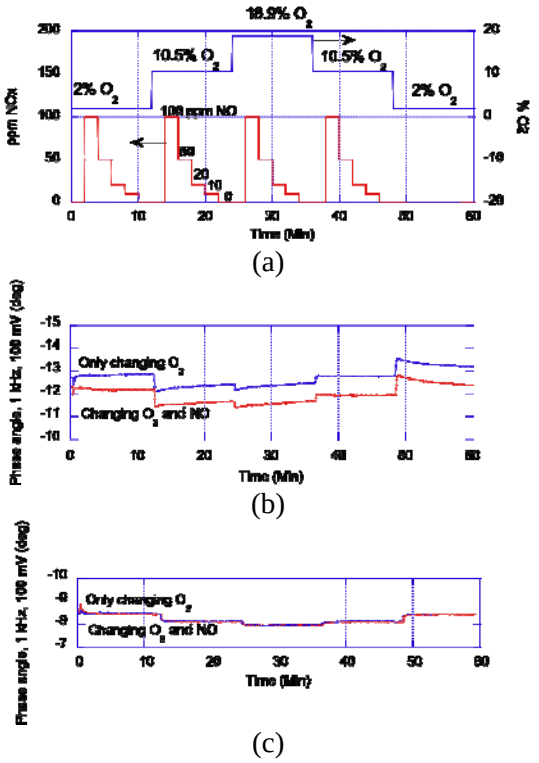

Figure 5. (a) Gas flow profile of oxygen and NO composition used for evaluating phase angle response to a 100 mV ac signal at 1 kHz. (b) Au wire prototype shows unstable signal while (c) LSM prototype shows much more stable signal suitable for potentially mitigating oxygen cross-sensitivity.

Sensing behavior using the LSM prototype – Previous designs for the LSM sensor utilized a dense sintered LSM pellet that was then dip coated with YSZ slurry. A second counter electrode (either metal or metal oxide) was typically applied as a porous slurry and the assembly was then fired at 1000°C. Unlike the Au wire prototype, the LSM sensing electrode can not be fabricated as wires and easily attached to alumina substrates. Furthermore, in the Au wire design, the porous Pt counter electrode is processed at a higher temperature than the YSZ slurry (1200°C vs. 1000°C), which is thought to stabilize the Pt microstructure and minimize drift. However, due to the constraints of the LSM pellet design, the porous counter electrode was fired at the same temperature as the YSZ slurry (1000°C), leading to a less stable microstructure and additional aging.

To improve the LSM sensor design, pieces of LSM were machined that could then be directly attached to the alumina substrate. Furthermore, by directly attaching the LSM electrode, a symmetric

electrode design was possible (both sensing and counter electrodes were LSM) that eliminated instabilities associated with the previous porous Pt counter electrode.

Figure 6 shows the impedancemetric sensing behavior for the improved LSM prototype in laboratory testing. The sensing signal is the phase angle response of the cell to a 100 mV ac signal at 5 Hz. Similar to the experimental protocol used previously for the Au wire prototype (see Fig. 6a), the background oxygen concentration was changed from 2 to 18.9%, and the NO concentration was changed at each oxygen level: 100, 50, 20, 10, and 0 ppm. For all changes in gas concentration, the sensor responds quickly and recovers quickly to the original baseline value (< 10 s).

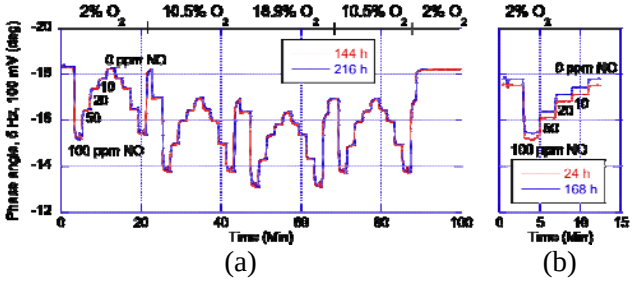

(a) (b)

Figure 6. Sensing behavior of LSM prototype with changes in oxygen and NO concentration at (a) 144 and 216 h of testing and (b) after two cycles from the operating temperature to room temperature and testing at 24 and 168 h. The sensing signal shown is the phase angle response of the cell to a 100 mV ac signal at 5 Hz.

In Fig. 6a, there was no noticeable shift in the baseline signal after continuous testing at 144 and 216 h indicating stable sensor performance. The sensor was initially tested continuously up to 408 h (data at 144 and 216 h shown in Fig. 6a) using a heater voltage of 8.5 V. At this point, the sensor temperature was reduced to room temperature before returning to the operation temperature for another 216 h of continuous testing, at which point the sensor temperature was again cycled.

In Fig. 6b, after the two thermal cycles and holding at the operating temperature for 24 h, the lower red curve shows both a shift in the baseline and a decrease in NO sensitivity. After testing at 24 h, the sensor continued to be held at the operating temperature. At 168 h additional NO sensing data were obtained. At this point, the upper blue curve in Fig. 6b shows a slight increase in the baseline, but the NO sensitivity remained relatively unchanged, again indicating better sensor stability than the previous Au wire prototype.

To evaluate long-term stability, the sensor performance of the LSM prototype, after the two thermal cycles discussed above, was monitored after testing in various water, oxygen, and NO_x concentrations. Figure 7 shows the sensing behavior of the LSM prototype with changes in oxygen and NO levels at a fixed water concentration of ~1.2% after 3120 h of total varied environment testing. All NO concentrations from 100 to 10 ppm are still clearly resolved at all oxygen levels from 2 to 18.9%. Future work includes compiling the performance data obtained over the lifetime of the sensor at various water, oxygen, and NO_x levels and improving the design and materials to enhance further the temperature control and sensor stability.

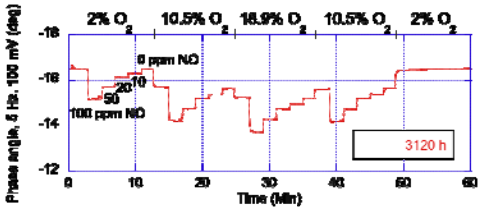

Figure 7. Sensing behavior of LSM prototype with changes in oxygen and NO levels in ~1.2% H_2O after 3120 h of continuous testing at various water, oxygen, and NO levels. The sensing signal shown is the phase angle response of the cell to a 100 mV ac signal at 5 Hz.

A more detailed study of the water cross-sensitivity of the LSM sensor was performed using a square alumina substrate (10 mm × 10 mm × 0.5 mm) without imbedded heaters onto which the LSM electrodes and FSZ electrolyte had been fabricated. The alternative sensor design was more suitable for controlled temperature testing in a tube furnace (525°C). The sensor geometry was similar to that shown in Fig. 3.

The square LSM sensor was initially tested continuously to 192 h, then thermal cycled to room temperature before returning to the operation temperature, tested continuously for another 216 h, and then thermal cycled again. In Fig. 8a, after the two thermal cycles and holding at the operating temperature (525°C) for 72 h, the lower red trace shows the sensing behavior. After testing at 72 h, the sensor continued to be held at the operating temperature. At 168 h, the upper blue trace in Fig. 8b shows almost no change in response indicating good sensor stability.

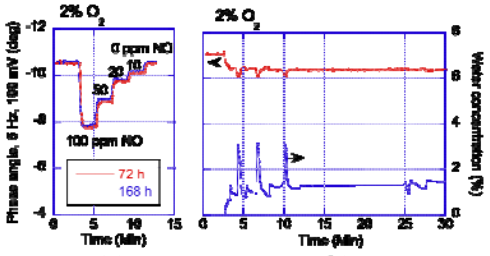

(a) (b)

Figure 8. Sensing behavior of LSM prototype on non-heated alumina substrate at 525°C in 2% O_2 (a) with changes in NO concentration after testing for 262 h and two cycles from the operating temperature to room temperature and then additional testing at 72 and 168 h and (b) sensor response (upper red trace, values on left axis of Figure 7a) with changes in water concentration (lower blue trace, values on right axis). The sensing signal shown is the phase angle response of the cell to a 100 mV ac signal at 5 Hz.

Figure 8b shows how the sensor signal changes with water concentration. In Fig. 8b, the lower blue trace shows changes in water concentration with time (values given on the right y-axis) and the corresponding sensor signal given by the upper red trace (values given on the left y-axis in Fig. 7a). Increases in water concentration have a similar directional response in the phase angle as increases in oxygen and NO concentration.

Previous work on Au wire prototypes found that optimizing temperature significantly decreased water cross-sensitivity. Future work includes a detailed analysis of water cross-sensitivity for the LSM prototype at different temperatures.

Conclusions

Work in FY2009 has focused on more advanced NO_x sensor prototypes that incorporate an alumina substrate with an imbedded heater and modifications for improving mechanical stability. Mechanical stability is crucial for packaging into a commercial sensor housing and direct testing in the exhaust manifold. The current work builds on previous work directed at understanding sensing mechanisms and the role of material composition/microstructure. From this understanding we developed criteria that has been used to guide continuous improvements in sensor performance and design, including sensor platforms more suitable for mass manufacturing.

Although previous work demonstrated an operating NO_x prototype packaged in a sensor housing, subsequent testing revealed insufficient long-term stability due to mechanical failure, in particular due to wire delamination in gold-based sensor prototypes. We attempted to improve the mechanical stability of the gold wire prototype by increasing the wire adhesion through geometry modification and improving the thermal expansion match between the gold electrode and zirconia electrolyte. Despite the improvements, the sensor still exhibited poor mechanical performance, especially after cycling from the high operating temperature to room temperature.

An advance to the Au wire sensor has been made by moving to LSM metal-oxide based electrodes directly attached to the alumina substrate. In addition to excellent stability and sufficient tolerance towards temperature cycling, the LSM prototype also exhibited stable high-frequency (1 kHz) oxygen selectivity, and this permits compensating for oxygen cross-sensitivity and improving sensor accuracy. Furthermore, the LSM prototype has undergone continuous testing in a variety of oxygen, water, and NO_x conditions for 3120 h and still showed good NO_x sensitivity.

References

1. N. Yamazoe, *Sens. Actuators, B*, **108**, 2 (2005).
2. R. Moos, *Int. J. Appl. Ceram. Technol.*, **2**, 401 (2005).
3. S. Akbar, P. Dutta, and C. Lee, *Int. J. Appl. Ceram. Technol.*, **3**, 302 (2006).
4. F. Menil, V. Coillard, and C. Lucat, *Sensors and Actuators B*, **67**, 1 (2000).
5. S. Zhuiykov and N. Miura, *Sens. Actuators, B*, **121**, 639 (2007).
6. J. W. Fergus, *Sens. Actuators, B*, **121**, 652 (2007).
7. S. -W. Song, L. P. Martin, R. S. Glass, E. P. Murray, J. H. Visser, R. E. Soltis, R. F. Novak, and D. J. Kubinski, *J. Electrochem. Soc.*, **153**, H171 (2006).
8. L. P. Martin, L. Y. Woo, and R. S. Glass, *J. Electrochem. Soc.*, **154**, J97 (2007).
9. L. Y. Woo, L. P. Martin, R. S. Glass, and R. J. Gorte *J. Electrochem. Soc.*, **154**, J129 (2007).
10. L. Y. Woo, L. P. Martin, R. S. Glass, W. Wang, S. Jung, R. J. Gorte, E. P. Murray, R. F. Novak, and J. H. Visser. *J. Electrochem. Soc.*, **155**, J32 (2008).

Publications/Presentations

Record of invention (IL-2048) entitled "Frequency Technique for Operating Electrochemical Sensors" submitted to the Department of Energy, November 2008. Provisional Patent Application (IL-12048, S114,480 Provisional) filed on December 18, 2008.

Poster presentation entitled "Sensing Behavior in Diesel Exhaust of Impedancemetric NO_x Gas Sensor Based on Porous YSZ/Dense Electrode Interface" at the 2008 Fall Meeting of the Materials Research, Dec. 1-5, 2008, in Boston, MA.

Oral project presentation at the 2009 DOE Hydrogen Program and Vehicle Technologies Program Annual Merit Review and Peer Evaluation Meeting, May 18-22, 2009 in Washington, D.C.

Oral presentation entitled "Impedancemetric NO_x Sensing Based On Porous Yttria-Stabilized Zirconia (YSZ) Electrolyte: Effect of Electrode Materials on Total-NO_x Sensing and Stability" at the 215th Electrochemical Society Meeting, May 25-29, 2009.

Manuscript entitled "Effect of Electrode Material and Design on Sensitivity and Selectivity for High Temperature Impedancemetric NO_x Sensors" submitted to the Journal of the Electrochemical Society, Sept. 2009.

Agreement 9440 - Fabrication of Micro-orifices for Diesel Fuel Injectors

George R. Fenske and Nicholaos Demas
Argonne National Laboratory
9700 South Cass Avenue
Argonne, IL 60439
(630)252-5190; fax (630)252-4798; e-mail: gfenske@anl.gov

DOE Technology Manager: Jerry Gibbs
(202) 586-1182; fax: (202) 586-1600; e-mail: jerry.gibbs@ee.doe.gov

Contractor: Argonne National Laboratory, Argonne, Illinois
Prime Contract No.: DE-AC02-06CH11357

Objectives

- Develop a methodology for reducing the diameters of fuel injector orifices to 50 μm by applying material to the internal diameter (ID) of the orifice. Micro-orifices should improve fuel distribution, increase efficiency, and reduce emissions in compression-ignition, direct-injection (CIDI) engines.
- Characterize the spray and combustion properties of the fuel injector system coated with electroless nickel (EN) and other advanced ID coating processes.
- Transfer the developed technology to DOE industrial partners.

Approach

- Evaluate the potential of EN plating for improving the surface finish and reducing deposit formation on injector nozzles.
- Evaluate the potential of vapor deposition processes to form uniform nickel (Ni) coatings.
- Evaluate the potential of laser micro-drilling processes to form uniform orifices in high length-to-diameter configurations.

Accomplishments

- Devised a new approach for preparing test nozzles in concert with the U.S. Environmental Protection Agency–National Vehicle and Fuel Emissions Laboratory (EPA-NVFEL). Also initiated collaboration with a major fuel injector manufacturer for further engine testing of plated nozzles for deposit mitigation.
- In concert with Imagineering, Inc. (a commercial plating company), developed a method for improving the surface finish of commercial-scale plated nozzles.
- Developed an X-ray phase contrast imaging technique for nondestructive examination of thin EN coatings applied to the interiors of diesel injectors.
- In collaboration with the U.S. EPA, characterized the spray characteristics of EN-coated commercial nozzles.
- Examined the microstructure and micro-hardness of commercial nozzles.
- Characterized EN-coated commercial nozzles from Imagineering; the thickness of the coatings was between 43 and 48 μm.
- Evaluated coating integrity by examining the variation of coating thickness as a function of depth; coating was uniform and adhesion was excellent

Future Direction

- Characterize spray properties of EN-coated nozzles using advanced x-ray analytical techniques.

- Provide coated injector tips to EPA-NVFEL personnel for spray characterization and combustion tests.
- Explore establishing a consortium with industrial partners to integrate EN process into a production setting.

Introduction

In 2007, EPA regulations mandated reduction in diesel engine emissions to 0.01 grams of particulate matter (PM) per engine horsepower per hour and 0.2 grams of nitrogen oxide (NO_x) per engine horsepower per hour. Further reductions are expected for 2010. To achieve these levels, CIDI engines are being redesigned to reduce in-cylinder soot production. One design change under consideration is the reduction of the diameter for the fuel injector orifice.

Pickett and coworkers[1,2] demonstrated significant reductions of soot in a test cylinder using experimental injectors with orifice diameters of 50 μm, even with high levels of exhaust gas recirculation and concomitant reduction in NO_x emissions. NVFEL researchers have observed reduced PM emissions from a light-duty diesel engine equipped with 75-μm-diam injector orifices. These reductions arise from increases in fuel atomization efficiency, leading to more complete combustion.[3] Although 100-μm-diam orifices can now be economically mass produced by electrodischarge machining, further reductions in hole size are accompanied by unacceptable fabrication error rates.

Reducing the orifice diameter (e.g., from 150 to 50 μm) carries with it a number of other penalties. It will reduce the amount of fuel that can be delivered to the combustion chamber without increasing the number of spray holes, the injection pressure, and/or the discharge coefficient. The potential impact of coking on smaller orifices is also much greater, as smaller holes will be more readily blocked by coking deposits on the injector tip and in the spray holes themselves. Coking deposits are a particular problem with tapered-orifice nozzles, another technique for increasing fuel atomization and thus reducing PM emissions.

Another issue is alternative fuels. One method to minimize dependence on foreign oil is the increased use of bioderived fuels, such as vegetable oil esters. Because of the presence of carbon-carbon double bonds in the carboxylic acid chain precursors, these fuels readily form coking deposits in the combustion chamber—a major problem in concert with smaller spray holes. Other alternative fuels include alcohols such as methanol or ethanol. These are not typically used neat but are blended with conventional diesel fuel. One emissions reduction strategy is to inject an ethanol/water mixture along with conventional fuel, reducing the combustion temperature and NO_x emissions. However, alcohol partial oxidation products can include corrosive carboxylic acids, which will damage the steel nozzles over time.

In concert with more commonly used fabrication techniques, EN plating has been used to prepare fuel injector nozzles with orifice diameters as small as 50 μm. EN plating promises to mitigate or solve all of the difficulties described above. The plated surface is corrosion-resistant and smoother, and the discharge coefficient of the plated orifices is higher. This method can be used to deposit a wide variety of alloys, offering the possibility of tailoring surface chemistry to reduce or eliminate deposit formation.

Approach

As described in previous progress reports, the diameter of the orifice can be reduced by coating its interior with EN plating. This technique has been used to deposit nickel/phosphorus or nickel/boron alloys onto metallic surfaces from aqueous solutions. It has been successfully used in previous years to reduce the orifice diameter from 200 to 50 μm on a bench scale, and from 180 to 75–80 μm on a commercial

scale. Other metal alloys have been deposited by the same technique.

Having demonstrated that EN plating reduces the orifice diameter to the desired size, we next sought to demonstrate the usefulness of EN-plated nozzles for solving the challenges described in the Introduction: improving spray properties and discharge coefficient, reducing deposit formation, and resisting corrosion. To this end, the use of phase-contrast x-ray imaging at Argonne's Advanced Photon Source (APS) was explored for nondestructive examination of plated nozzles. This technique is capable of measuring coating thicknesses on internal passages and was applied as a quality check on nozzles that were sent to the EPA for engine tests.

In collaborative studies with the EPA, fuel sprays produced with EN-coated commercial nozzles yielded encouraging results, and during FY09, we explored the application of EN plating to produce multi-sized orifices (e.g., 50 μm and 125 μm) on a given nozzle. Research also continued to evaluate the use of EN coatings as an approach to mitigate erosive wear.

Results

In FY09, activities were continued to develop/demonstrate the ability to fabricate multi-sized orifices (to improve the ability to direct fuel to a broader range of the combustion chamber) as well as to evaluate the potential of EN platings for mitigating orifice erosion. These activities involved the use of nozzles from multiple partners. Figure 3 shows microscope images of the tips of the four nozzles, while Figure 2 shows boroscope images of the inside view of same tips. Nozzle N1 (Figure 2a) is a standard baseline six-orifice nozzle with an approximate diameter of 200 μm. Nozzle N2 (Figure 2b) is a six-orifice nozzle with an orifice diameter of 125 μm. Nozzle N3 is a seven-orifice non-nitrided experimental nozzle, and nozzle N4 is an eight-orifice nitrided high-pressure experimental nozzle; both nozzles have an approximate diameter of 200 μm.

It was soon realized that the alloys and heat treatments used by the different vendors were not identical. Information on the alloy composition and heat treatments was not available, and thus it was necessary to characterize the microstructure and composition of the nozzles. The four nozzles were cross sectioned and used for microscopy and energy dispersive x-ray (EDX) analysis to determine their microstructure and composition. Microscope images and secondary electron microscope (SEM) images are shown in Figures 3 and 4, respectively.

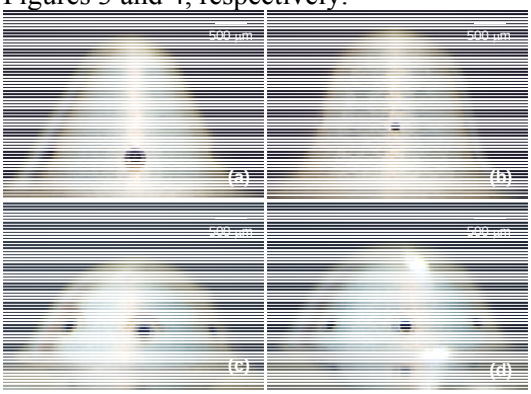

Figure 1 – Four types of fuel injector nozzles examined:
(a) N1, (b) N2, (c) N3, and (d) N4

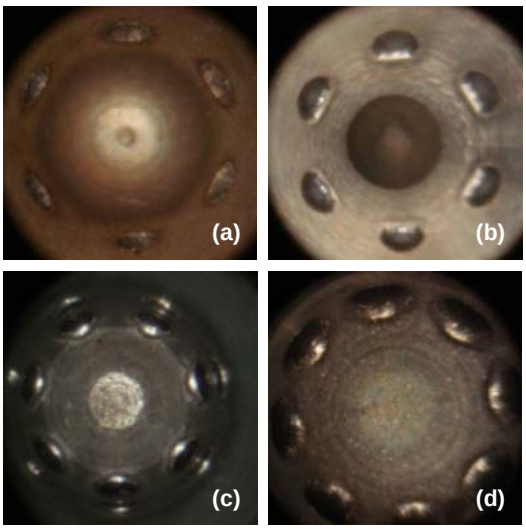

Figure 2 – Boroscope images of the four types of fuel injector nozzles:
(a) N1, (b) N2, (c) N3, and (d) N4

Analysis of the nozzle microstructures indicated that N1 consists of martensite, N2 consists of tempered-martensite, N3 contains bainite and fine pearlite, and N4 consists of tempered martensite with nitride precipitates located along prior austenitic grain boundaries. EDX analysis of N1 showed levels of Cr and Fe and lack of significant levels of other elements. These results suggest an AISI H13 alloy. N2 had levels of Cr, Mn, and Ni that suggest an alloy comparable to AISI 4340. N3 showed levels of Cr and Fe that suggest an AISI H11/H13 alloy. Finally, N4 showed levels of Cr and V that suggest an AISI H11/H13 alloy. N4 also exhibited a nitride-rich surface that is consistent with nitriding.

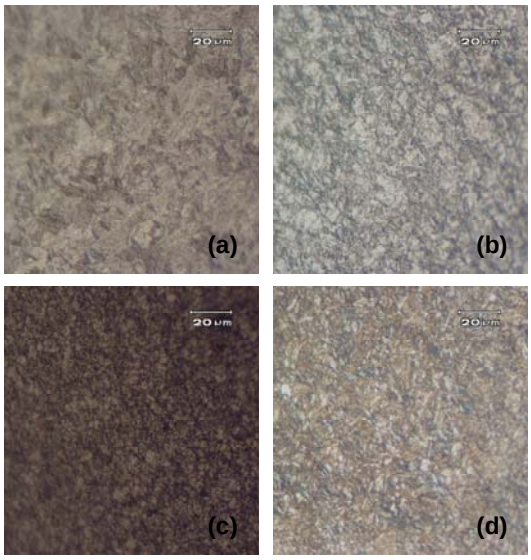

Figure 3 – Microscope images showing the microstructure of nozzles:
(a) N1, (b) N2, (c) N3, and (d) N4

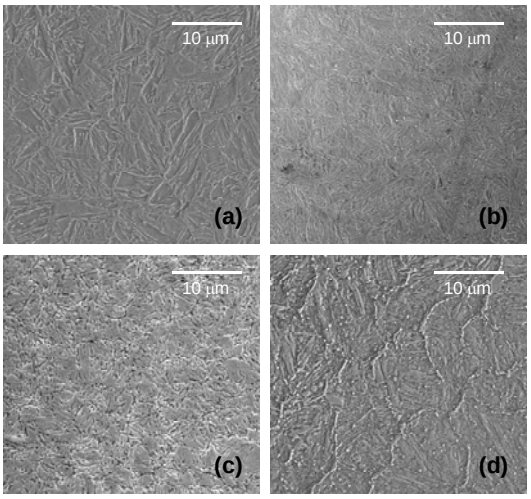

Figure 4– SEM images showing the microstructure of nozzles:
(a) N1, (b) N2, (c) N3, and (d) N4

The four types of nozzles were sent to Imagineering for plating. After plating, pitting was evident on the surface of the nozzles, especially around the orifices, as seen in Figure 5.

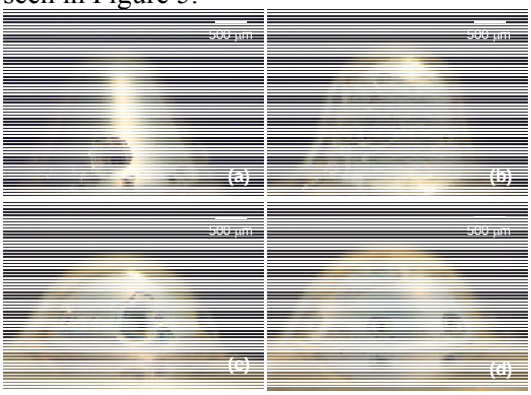

Figure 5 – Four types of fuel injector nozzles after EN plating:
(a) N1, (b) N2, (c) N3, and (d) N4

Figure 6 shows boroscope images taken after the plating process, respectively. From this perspective, the coating was uniform.

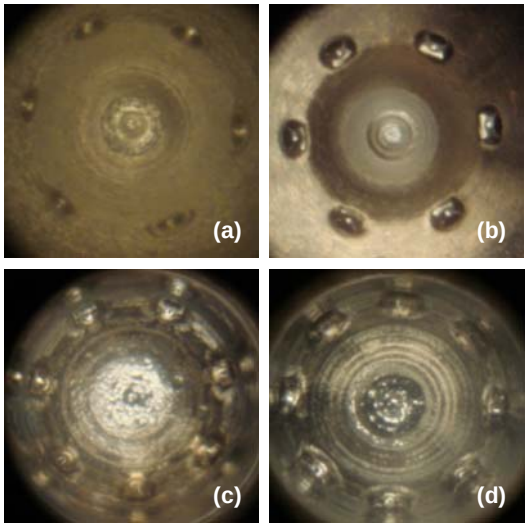

Figure 6 – Boroscope images of the four types of fuel injector nozzles after plating: (a) N1, (b) N2, (c) N3, and (d) N4

To determine the variable responsible for the blemishes and other imperfections on the surface of the nozzles, we performed EDX analysis around the holes. Nozzle N1, as received, had some darkening around the orifices. The dark area on N1 is shown in Figure 7. EDX at two locations, corresponding to locations away from the dark area (1) and inside the dark area (2), revealed the presence of W (see Figure 8). The presence of W prevented the uniform plating noted initially. Therefore, W was mechanically removed by polishing in a different batch of samples sent to Imagineering.

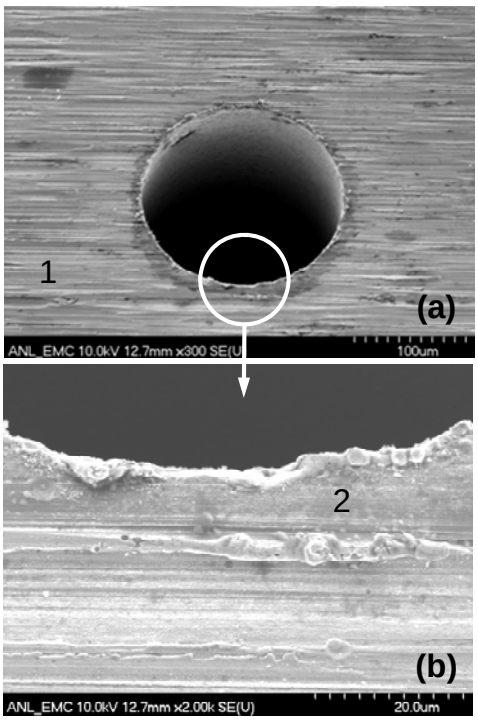

Figure 7 – SEM images showing two locations (1 and 2) where EDX analysis was performed: (a) close-up around the hole at 300× and (b) close-up around the hole at 2000×

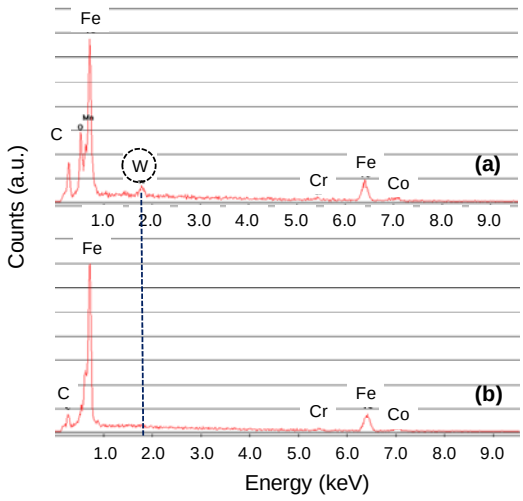

Figure 8 – EDX spectra at (a) Location 1 and (b) Location 2 from Figure 7

Mechanical polishing was performed on the rest of the samples to remove this contamination. The plating of the second batch of N1 samples was uniform. There were no pitting, blemishes, or other surface imperfections around the holes. Figure 9

shows the improved surface finish, while the reduction in orifice diameter is shown in Figure 10.

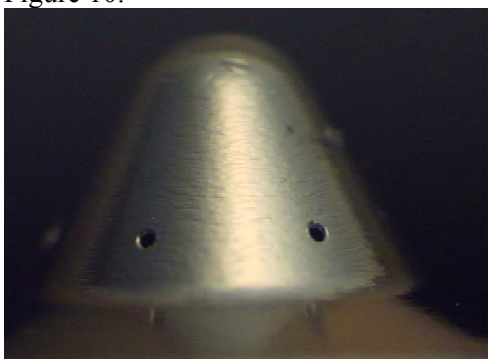

Figure 9 – Nozzle N1 after plating

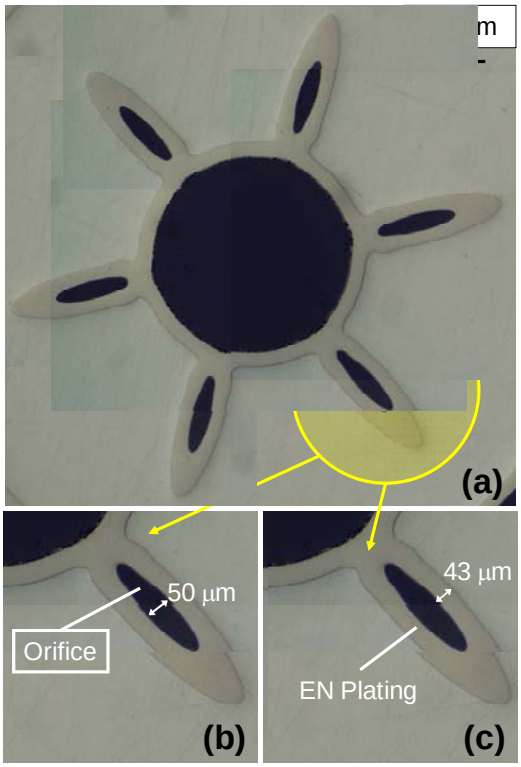

Figure 10 – Microscope images showing (a) coating uniformity for all orifices, (b) orifice reduction, and (c) coating thickness within the orifice

Adhesion, confirmed by Vickers indentation on the substrate-coating interface, was excellent, as seen in Figure 11.

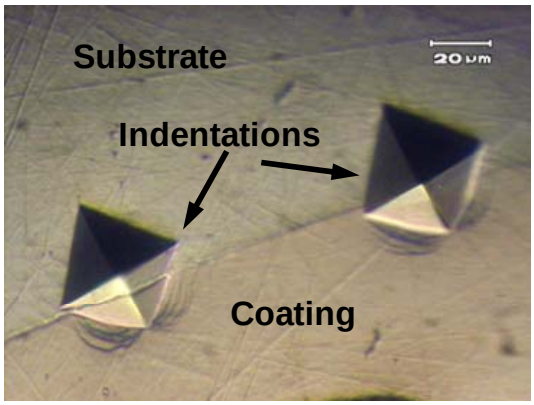

Figure 11 – Vickers indentations on the substrate/coating interface

The rest of the nozzles are under investigation to ensure that the same results as observed with N1 can be obtained.

Conclusions

Several candidate methods are being evaluated and developed for fabricating nozzles with small (50-μm diam) micro-orifices. Development of the EN aqueous-based plating process has been advanced to the stage where commercial nozzles were treated and characterized with an advanced phase-contrast x-ray imaging technique, which confirmed uniform coating deposition along the orifice. Preparations were initiated to fabricate multi-sized orifices (50 and 125 μm) on a commercial nozzle. The plating process has been optimized, and analysis of the coating uniformity on sibling nozzles confirmed that the coating was uniformly deposited along the orifices. Effort will continue in FY10 to fabricate the multi-sized orifices in preparation for flow-spray studies at the EPA.

References

1. Lyle M. Pickett and Dennis L. Siebers, Paper No. 2001-ICE-399, ICE Vol. 37-1, ed. V. W. Wong, *2001 Fall Technical Conference*, American Society of Mechanical Engineers, 2001.
2. L. M. Pickett, D. L. Siebers, A. F. Morales, J. Hachman, and A. K. Sinensky, "An Investigation of Diesel Soot Formation Processes Using High

Aspect Ratio Micro-Orifices," presented at HARMST 2003 High-Aspect Ratio Micro-Structure Technology Workshop, Monterey, CA, 2003.
3. John B. Heywood, *Internal Combustion Engine Fundamentals*, McGraw-Hill, New York, 1988.
4. John B. Woodford and George R. Fenske, "Fabrication of Small Fuel Injector Orifices," *2005 Annual Progress Report, Automotive Propulsion Materials*, U.S. Department of Energy, Washington, D.C., 2005.
5. John B. Woodford and George Fenske, "Fabrication of Micro-orifices for Diesel Fuel Injectors," *2006 Annual Progress Report, Automotive Propulsion Materials,* U.S. Department of Energy, Washington, D.C., 2006.
6. George Fenske, "Fabrication of Micro-orifices for Diesel Fuel Injectors," 2007 *Annual Progress Report, Automotive Propulsion Materials*, U.S. Department of Energy, Washington, D.C., 2007.
7. Kamel Fezzaa, Wah-Keat Lee, Seong-Kyun Cheong, Christopher F. Powell, Jin Wang, and Ming-Chia Lai, "Ultrafast X-ray Phase-Enhanced Microimaging for Visualizing Fuel Injection Process," SAE 2005-24-093, Society of Automotive Engineers, 2005.
8. R. Schaefer, US EPA-NVFEL, private communication, July, 2007.
9. G. Fenske, J. Woodford, J. Wang, and R Schaefer, "Fabrication and Characterization of Micro-orifices for Diesel Fuel Injectors," SAE 2008-01-1595, 2008.

Publications and Presentations

J. Woodford and G. Fenske, "Fabrication of Small Orifice Fuel Injectors," DEER (Diesel Engine Emissions Reduction) Conference, August 2005.

J. B. Woodford and G. R. Fenske, *Fabrication of Small-Orifice Fuel Injectors for Diesel Engines*, Argonne National Laboratory Report, ANL-05/06, March 2005.

J. B. Woodford, G. R. Fenske, and J. M. Perez, "Deposit Formation on Electroless Nickel," submitted to *Energy & Fuels*.

G. Fenske, J. Woodford, J. Wang, and R Schaefer, "Fabrication and Characterization of Micro-orifices for Diesel Fuel Injectors," submitted for presentation at the 2008 SAE International Powertrains, Fuels and Lubricants Congress, June 23-25, 2008, Shanghai, China, SAE paper 2008-01-1595.

G. Fenske, J. Wang, and E. El-Hannouny (ANL), R Schaefer and F. Hamady (NVFEL), "Fabrication of Micro-orifices for Diesel Fuel Injectors," DEER (Diesel Engine Emissions Reduction) Conference, August 2008.

Agreement 11754 - Hydrogen Materials Compatibility

Principal Investigator: Stan Pitman
Kyle Alvine, Joe Ryan
Pacific Northwest National Laboratory
P.O. Box 999
Richland, Washington 99354
(509) 376-0356; fax: (509) 376-0418; e-mail: stan.pitman@pnl.gov

Alan Welch
Westport Innovations; email awelch@westport.com
Brad Boyer
Ford Motor Company; email bboyer1@ford.com

DOE Technology Manager: Jerry L. Gibbs
(202) 586-1182; fax: (202) 586-1600; e-mail: jerry.gibbs@ee.doe.gov
Field Technical Manager: Mark T. Smith
(509) 375-4478; fax: (509) 375-4448; e-mail: mark.smith@pnl.gov

Contractor: Pacific Northwest National Laboratory
Contract No.: DE- AC05- 76RL01830

Objective

- Evaluate failure modes for piezoelectric actuators in hydrogen gas.
- Develop model for hydrogen diffusion, absorption and damage in piezoelectric ceramics, and develop methods for controlling or remediating the hydrogen damage to prolong actuator life.
- Measure the friction and wear characteristics of injector materials in hydrogen environments, including *in-situ* and *ex-situ* materials characterization.
- Measure the performance of piezoelectric actuators and actuator materials in hydrogen environments.
- Develop a design approach to hydrogen injectors based on material behavior and performance in hydrogen based on experimental data.

Approach including partner/collaborator and path to technology transfer and commercialization

- Working with our industrial partners, the overall approach is to improve the performance and endurance of piezoelectric actuators. These actuators are used in an internal combustion hydrogen test engine to improve output, efficiency, and endurance.
- A major milestone was achieved in engine efficiency (45% Brake Thermal Efficiency) by the Ford Motor Company team, using actuators designed by Westport. These efficiencies are comparable to those that may ultimately be achieved by fuel cell technologies, at significantly lower cost.
- Further advances in efficiency and reliability require prolonged actuator lifetime. This requires the development of piezoelectric actuators that are robust in the required service conditions and meet the stringent requirements for actuator speed and accuracy.
- Hydrogen diffusion in the piezoelectric materials and associated hydrogen damage are the limiting factors for actuator life. These issues are being addressed using experimental and modeling methods.
- Using advanced neutron scattering techniques at the National Center for Neutron Research

(NCNR) within the National Institute of Standards and Technology (NIST), we were able to measure the hydrogen diffusion in both lead zirconium titanate (PZT) and barium titanate ($BaTiO_3$) over a range of temperatures.

Milestones, Metrics and Accomplishments

- Milestone: Complete material failure analysis on sliding impact and wear samples. (Completed September 2009).
- Milestone: Complete operation of the Oak Ridge National Laboratory (ORNL) sliding impact wear apparatus; quantify procedures specific to these materials. (Completed September 2009).
- Milestone: Fully isolate the piezo failure mechanism from specially produced small, 3-disk assemblies, a continuation of the full injector testing. Completed. (September 2009). The failure mechanism in piezoelectric materials has been isolated, and efforts are underway to isolate the piezoelectric material from hydrogen gas (especially in PZT actuators), or to thermally mitigate the effect of hydrogen on the actuator materials (especially in $BaTiO_3$ actuators).
- Complete material diffusion model and correlate with long-term sliding and sliding-impact data. 70 percent completed. The material diffusion model is more complex than anticipated, but it appears that substantive improvements in actuator reliability may be achieved through a better understanding of the diffusion and damage processes.
- Complete full accelerated test method procedures that can transfer to other hydrogen related programs. (Completed September 2009).

Future Direction

- Complete tribological evaluation of nanolaminates, and propose the optimal nanolaminates for use in hydrogen injectors.
- Evaluate the kinetics of hydrogen absorption and diffusion in piezoelectric ceramics. Use a modeling effort to determine the mechanism of hydrogen absorption, diffusion and piezoelectric property changes (damage) in these materials.
- Evaluate Paralyne polymer coatings as a hydrogen barrier for piezoelectric films.
- Evaluate possible means to reverse piezoelectric hydrogen fouling such as oxygen annealing.
- Develop accelerated test methods and durability procedures for materials/coatings used on hydrogen injectors.

Introduction

For the transportation sector, hydrogen internal combustion engines using direct injection can be viewed as a high efficiency / low emission technology for bridging the transition process to the hydrogen economy based upon fuel cell technology. It has been estimated that a hydrogen direct injection (DI) engine can be integrated into a hybrid vehicle system which would demonstrate fuel consumption (fuel energy used per unit distance) that is only about 15% to 20% greater than a hybridized fuel cell vehicle of similar mass. Significantly lower hardware cost (as compared to present fuel cell systems) and use of existing manufacturing facilities for conventional reciprocating engines makes this an attractive consideration. Some engine manufacturers have identified robust fuel injection technology as one of the key enablers for commercialization of advanced hydrogen DI engines.

Originally, the basic hydrogen injector architecture was designed and developed for earlier direct injection natural gas engine programs. Fundamental issues limiting injector durability were expected and potential engineering solutions have been evaluated by Pacific Northwest National Laboratory (PNNL) with their partners Westport Innovations and Ford Motor Company. Overall, the injectors used in the research have been useful tools for developing engine combustion strategies and assessing fuel system technology. If there

was a significant level of interest in this type of engine technology, the long-range intention is to advance the injector technology to the point where it could enter limited production.

Compared to liquid hydrocarbon fuels, hydrogen is a challenging fluid to use in precision injectors because it has very low viscosity, low density, and can alter material properties through atomic diffusion or chemical reduction. The goal of this work is to understand the basic mechanisms that limit injector life and identify promising strategies to provide significant improvements for the next phase of research and development.

Technical Challenges

Two issues are critical to the success of the hydrogen direct injector technology (Fig. 1):

1. Hydrogen diffusion into piezoelectric actuator.
2. Impact and sliding wear between the needle and the jacket.

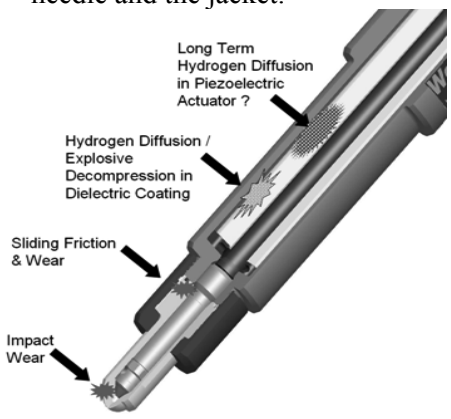

Figure 1: Critical Technical Challenges of the H-ICE Direct Injector.

Hydrogen Diffusion and Damage in Piezoelectrics (background): From recent research at PNNL and conversations with industry representatives, it is known that industrial piezoelectric devices, such as actuators for fuel injectors, tend to fail rapidly in high-pressure hydrogen atmospheres. Literature *[1-3]* indicates that piezoelectric thin films for the emerging field of Ferroelectric Random Access Memory (FRAM) lose their ferroelectric properties during exposure to low-pressure hydrogen gas during the hydrogen passivation of the underlying silicon. There does not appear to be any scientific studies on the effects of high- pressure hydrogen on piezoelectric materials most likely because the application is a recent discovery.

There are, however, several studies on the low-pressure hydrogen effects on piezoelectric materials. Thin films exposed to low pressure H_2 and high temperatures in excess of 400°C were found to turn from yellow to black with decreased resistivity and ferroelectric properties*[4]*. Surprisingly this effect could be reversed by annealing of the samples in air possibly via replenishment of oxygen vacancies created during hydrogen charging*[5]*. The degradation was found to be dependent on the electrode material on the piezoelectric film with Pt inducing the most damage*[6]*. This was thought to be due to a catalytic effect of the Pt atomizing the H_2 into H prior to diffusion into the ceramic. Additionally, it is thought that hydrogen can either form hydroxyls within the piezoelectric or recombine at grain boundaries, which can lead to significantly reduced fracture toughness and cycle lifetime*[7]*.

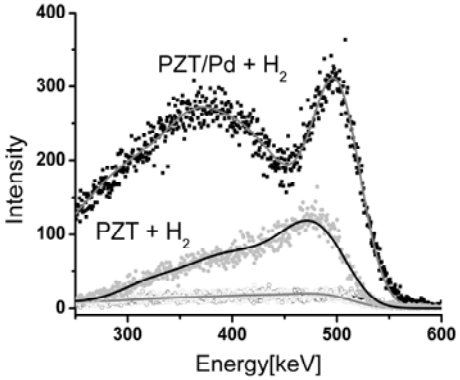

Figure 2: Comparison Plot of ERDA data for PZT and PZT/Pd Films. Uncharged films for both overlap and show little ERDA intensity. Hydrogen - charged films show large increase in intensity.

While the detrimental effects of low pressure hydrogen in piezoelectrics have been investigated to some degree, a systematic investigation into the absorption,

desorption, and diffusion of hydrogen (especially high-pressure hydrogen) as a function of pressure, temperature, and metal electrode is lacking from the literature. Also missing is a systematic investigation into the possible mechanisms to restore the piezoelectric properties and how this relates to hydrogen desorption. Such studies are critical to addressing solutions to the failure of the piezoelectric device in a hydrogen atmosphere.

Hydrogen Absorption in Piezoelectrics (Experimental Efforts- Ion Scattering)

This section discusses experimental measurements on the pure piezoelectric materials. This has the important advantage of being a much simpler system to study than the full piezoelectric stack device from the working actuator studied in the past. The project has demonstrated successful preliminary results on the hydrogen absorption in piezoelectric materials with ion scattering methods, specifically Elastic Recoil Detection Analysis (ERDA) and Nuclear Resonance Analysis (NRA) *[8]*. Measurement techniques that are actually sensitive to hydrogen, due to its small mass, are especially limited. In ERDA, high-energy He ions cause the forward recoil of absorbed hydrogen, which is collected by an energy dispersive detector. NRA is a similar technique where high-energy Fluorine ions combine with absorbed hydrogen to form an excited state and then decays, emitting gamma rays which are detected. Both methods are extremely sensitive to hydrogen and can offer concentration depth profiles.

ERDA measurements on several PZT and $BaTiO_3$ samples with various metal electrodes have been performed. Films were made via magnetron sputtering on silicon with low roughness and high purity. Bulk commercial PZT samples were also tested and were found to have higher background hydrogen contamination levels that prompted a switch to cleaner sputtered films. Films were charged in a 100% hydrogen atmosphere at 100°C at 16.5 MPa for 24 hours to mimic injector operation conditions.

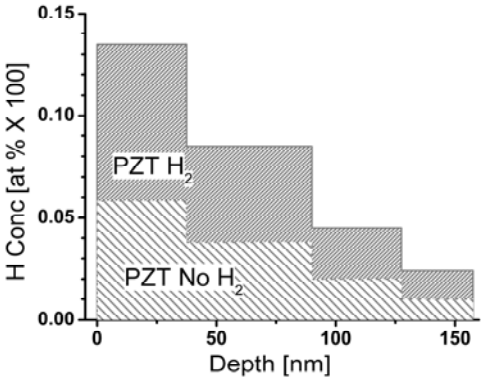

Figure 3. Hydrogen Concentration Profiles from ERDA Data for PZT Films (charged and uncharged).

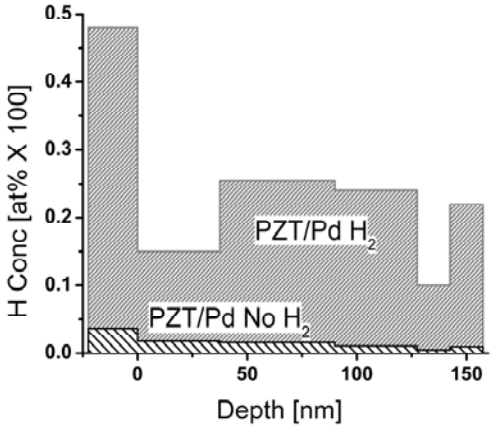

Figure 4: Hydrogen Concentration Profiles from ERDA Data for PZT/Pd Films (charged and uncharged).

ERDA measurements (confirmed with NRA) indicate a significant H_2 absorption in the piezoelectrics charged at 16.5 MPa and 100 °C. ERDA spectra and corresponding depth profiles for PZT and PZT/Pd films are shown in Figures 2-4. Hydrogen absorption is highly dependent on material and electrode composition. For example PZT absorbs more H_2 than comparably charged films of $BaTiO_3$. Additionally samples with Pd electrodes showed significantly higher H_2 absorption than samples with Cr or Al electrodes or without electrodes for both PZT and $BaTiO_3$ films. Results are being prepared for publication in a scientific journal.

Neutron reflectivity*[9]* studies were also conducted to yield complementary hydrogen absorption data however, the data is still being analyzed.

Hydrogen Diffusion in Piezoelectrics (Experiments – Neutron Scattering):

Using advanced neutron scattering techniques at the National Center for Neutron Research (NCNR) within the National Institute of Standards and Technology (NIST) the hydrogen diffusion in both PZT and BaTiO3 over a range of temperatures are measurable. This is a direct measurement of the diffusion not dependent on sample geometry or other factors as with more traditional diffusion measurements.

The neutron scattering technique used here is called quasi-elastic neutron scattering, QENS*[10]*. "Cold" neutrons have energy near k_BT and are of similar energy to diffusing hydrogen atoms. Thus when neutron-hydrogen collisions occur, the neutron may loose or gain a large amount of energy relative to its incident energy. Additionally hydrogen is one of the strongest neutron scatterers and can provide strong signal even from small amounts. This difference from the incident energy (elastic peak) is called the quasi-elastic contribution. For these measurements the incident neutron energy is known and the change in energy due to neutron-hydrogen collisions is measured to determine the hydrogen energy and thus diffusion constant. From literature *[3, 11]* the hydrogen is bound to the oxygen in the configuration shown in Figure 5.

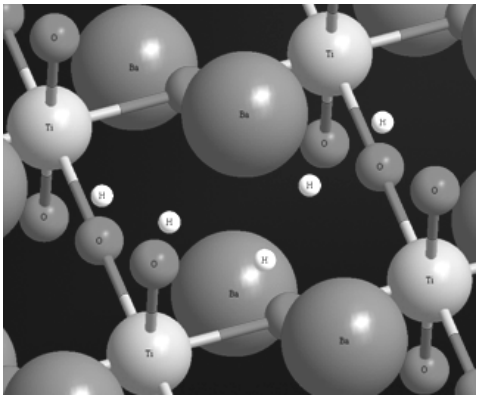

Figure 5: Illustration of Possible Locations for Hydrogen in the Perovskite Lattice.

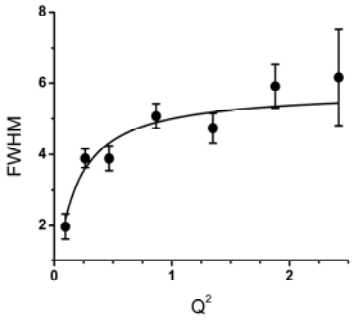

Figure 6: QENS Data for $BaTiO_3$ at 300K.

Figures 6–7 show QENS data taken at 300K and 250K for bulk powders of $BaTiO_3$ charged for 24 hours under 100% hydrogen at 16.5 MPa and 100 °C using the High Flux Back-Scattering (HFBS) instrument at the NCNR, NIST*[12]*. Plotted is the full width at half maximum (FWHM) of the quasi-elastic peak as a function of Q^2. The solid lines are a fit to the data with the standard jump-diffusion model *[10]*,which can yield the diffusion coefficient and the jump time between sites in the lattice. The fit parameters for 300K are: $D = 5.5 \times 10^{-10}$ m^2/s, and $\tau = 1.1 \times 10^{-10}s$. The fit parameters for 250K are: $D = 3.6X10^{-11}$ m^2/s, and $\tau = 3.1 \times 10^{-11}s$. Recently, additional QENS data has been generated on hydrogen–charged $BaTiO_3$ and PZT for a broader range of temperatures to get the full temperature dependence for both materials. These new results are in the process of being analyzed.

Additionally, vibrational spectra with neutron scattering of PZT charged with hydrogen under the same conditions as above was compared to uncharged hydrogen. This data is taken from the NCNR Filter Analyzed Neutron Spectrometer (FANS) instrument*[13]*.

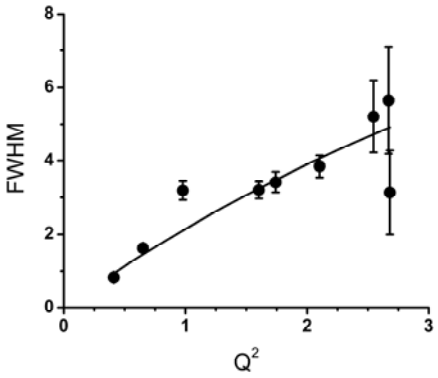

Figure 7: QENS data for BaTiO3 at 250K

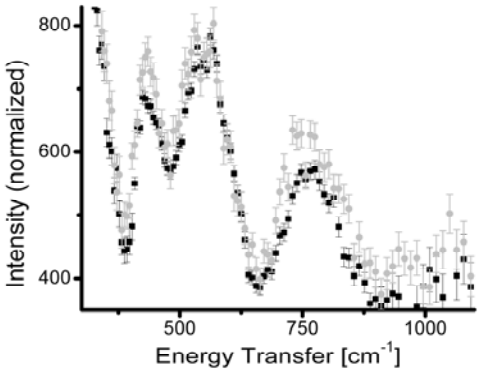

Figure 8: Vibrational Spectra from H_2 charged PZT (gray data) and Uncharged PZT (black data) from Neutron Scattering (FANS data).

From the data shown in Figure 8, there are several vibrational peaks corresponding to the motions of the oxygen atoms in the lattice that are enhanced in the hydrogen-charged sample. Since hydrogen is a much stronger scatterer than other materials this implies that the hydrogen is bound to the oxygen in the lattice and enhances the oxygen vibrations by "riding" along with their vibrations.

Hydrogen Absorption in Nanolaminates:

Preliminary ERDA measurements on the hydrogen absorption in nanolaminates (Figure 9) showed low amounts of uptake for a particular charging temperature and pressure, namely 100 °C and 14 MPa. This is encouraging because it demonstrates that detrimental hydrogen interactions are highly unlikely in the studied nanolaminates, but there is still a need to check a wide range of temperature and higher pressures as well as checking the permeability in FY 2010.

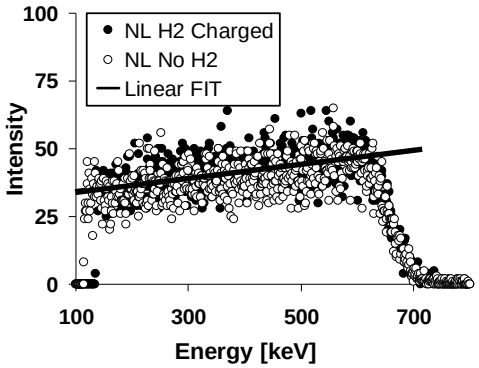

Figure 9: ERDA data from Nanolaminates. Closed circles (●) and open circles (○) represent hydrogen charged and uncharged nanolaminates respectively.

Hydrogen in Piezoelectrics (Modeling)

A first-principles study of hydrogen in $PbZr_{0.5}Ti_{0.5}O_3$ and related piezoelectrics was started to provide correlation with the experimental work described above, and to identify, if possible, methods which may be used to reduce the rate of hydrogen diffusion or to reverse the damage associated with hydrogen absorption in piezoelectric materials. The study began with bulk calculations on $BaTiO_3$, $PbZrO_3$ and $PbTiO_3$ confirming the ability of density functional theory (DFT) specifically the Generalized Gradient Approximation, (GGA)*[14]*, to reproduce lattice constants and other basic properties. All materials were treated in the cubic perovskite phase, since ferroelectric distortions are not expected to have a large effect on hydrogen interstitial energies, oxygen vacancies etc. that will be considered initially. The model was then set up as 2x2x2 (40 atom) supercells of these bulk materials. This is a convenient size to begin treating alloying and point defects, although larger cells also will have to be tested at some point.

A key point is how to distribute Zr and Ti atoms on the "B" sublattice (generic compound ABO_3, in this case $PbZr_{0.5}Ti_{0.5}O_3$) to simulate PZT. The few other theoretical studies to date seem to assume an "average atom" of "Zr/Ti" (the so-called Virtual Crystal Approximation*[15]*), but here it is desirable to have half the B sites occupied by actual Zr atoms and half by Ti. This is

important because an interstitial H (or any other localized defect) sees a local environment that may differ depending on the proportion and arrangement of nearby Zr and Ti atoms. Choosing a particular arrangement of Zr and Ti in supercells amounts to assuming a particular ordering of these atoms on the B sublattice of the infinite crystal. There does not appear to be experimental evidence of such long-range order in PZT, but some degree of short-range correlation of Zr and Ti occupancy may exist. Our approach may provide some insight about such short-range order and its effects.

Three representative orderings of Zr and Ti atoms on the B sublattice were chosen: one in which they alternate along the "z" axis (Zr and Ti layers in the xy plane), one in which they alternate along both the "x" and "y" axes (columns of Zr and Ti along the z-axis), and one in which Zr and Ti alternate along all three Cartesian axes, so there are Zr and Ti planes along the {111} directions. The three arrangements of Zr and Ti are (100), (110), and (111), respectively. Supercells of pure $PbZrO_3$ and $PbTiO_3$ were also considered as a reference. A comparison of total energies per 40 atoms of these lattices is shown in Table 1; the reference for relative energies is the average of $PbZrO_3$ and $PbTiO_3$.

It is possible to observe a trend in these results: the energy goes down as the Zr and Ti mix more "intimately" (Zr has the most Zr nearest neighbors on the B lattice in the 100 configuration, and has only Ti nearest B-lattice neighbors in the 111 configuration.) In fact, the mixing of PZ and PT is energetically unfavorable in the 100 configuration but is strongly favored in 111. Thus, the formation of PZT from PZ and PT is not only driven by entropy, but also by enthalpy in its equilibrium form, where Zr has mostly Ti neighbors on their shared sublattice and vice versa (even if not to the extent of long-range compositional order, in reality.)

Table 1. Total Energies Chart

System	Total Energy (eV)	Relative Energy δ (eV)
$PbZrO_3$	–312.9	
$PbTiO_3$	–300.2	
Average of $PbTiO_3$ + $PbZrO_3$	–306.6	0.0
$PbZr_{0.5}Ti_{0.5}O_3$ (100)	–305.8	0.8
$PbZr_{0.5}Ti_{0.5}O_3$ (110)	–307.1	–0.5
$PbZr_{0.5}Ti_{0.5}O_3$ (111)	–307.7	–1.1

The next question is of hydrogen absorption into the perovskite lattice of PZT, PZ and PT. To date this has been treated only for the case of a neutral hydrogen interstitial atom, but the plan is to begin investigating at least the donor (+1) state (i.e. an interstitial proton) in the next phase of the study. From the previous theoretical literature, the lowest-energy location for the hydrogen was identified. This position is in the Pb-O plane, about 0.95Å from the oxygen (forming a hydroxyl) and with the O-H line pointing at the midpoint of the nearest Pb-Pb line. The reference energy for H was taken to be one-half the computed energy of an H_2 molecule, and energy differences for incorporation of an interstitial H were calculated for PZ, PT and the three different PZT configurations already described. Note that there are three different local environments possible for this H atom, depending on whether the Pb-O plane containing the H atom separates two Zr atoms ("Zr-Zr"), two Ti atoms ("Ti-Ti") or one Zr and one Ti ("Zr-Ti"). Obviously PZ can only have H in a Zr-Zr environment, and only Ti-Ti in PT. In PZT with the 111 ordering only the Zr-Ti environment of H can occur, while in the 100 and 110 orderings of PZT all three chemical environments for H can occur. The energy cost to remove an H atom from a hydrogen molecule and place it in the lattice is then as follows (Table 2):

Table 2. Energy Cost to Remove H Atom

System	H environment	Defect Energy (eV)
$PbZrO_3$	Zr-Zr	-0.1
$PbTiO_3$	Ti-Ti	0.7
$PbZr_{0.5}Ti_{0.5}O_3$ (100)	Zr-Zr	0.2
	Ti-Ti	0.3
	Zr-Ti	-0.05
$PbZr_{0.5}Ti_{0.5}O_3$ (110)	Zr-Zr	1.5
	Ti-Ti	0.8
	Zr-Ti	1.1
$PbZr_{0.5}Ti_{0.5}O_3$ (111)	Zr-Ti	2.2

These results predict that hydrogen is much more soluble in lead zirconate than in lead titanate. In PZT, the solubility would be greatest with the 100 layered Ti-Zr ordering, but this structure itself was the highest in energy in pure PZT, so it is unlikely to exist. In the most stable model of PZT, the "maximally mixed" 111, the solubility of H is very low, so it might be advantageous to try to grow PZT under well-annealed conditions that might lead to such uniform alternation of Zr and Ti cells, from the standpoint of minimizing H uptake. For the intermediate case of the 110 ordering, hydrogen shows a tendency to segregate to Zr-rich locations, suggesting that hydrogen transport might involve a percolation through Zr-rich regions.

Diffusion modeling studies of H in these materials using the Nudged Elastic Band method*[16]* have been initiated with the expectation of useful results in late FY10. Similar calculations on $BaTiO_3$ are also planned.

Impact Wear and Sliding Friction Technical Challenges: Nanolaminates: The project has addressed the issues of lubrication and wear resistance by exploring the use of nanotechnology. Low-dimensional structures have shown to exhibit electrical, chemical, and mechanical properties that are not possible in bulk materials or single layer thin films. In nanolaminate structures, the alternating layers result in improved mechanical properties, such as strength, hardness, and toughness. Many nanoscale layers with alternating composition or crystal phase create the nanolaminate structure. These structures work to improve upon the mechanical properties of the component materials by several mechanisms. The most important of these is through the interruption of crack propagation at the interface of each layer. When a crack reaches this interface, the stress at its tip is dissipated into the stress field created by the lattice mismatch between the two phases. This stress field also can be used to create areas of localized compression in some layers which will serve to increase the effective yield strength in that medium.

Another proposed benefit of nanolaminate structures is the proposed combination of properties that may be achieved. In this case, nanolaminate structures were produced with alternating layers of a hard material and one with lubricating qualities. In addition, the coatings were designed to be at least inert to the presence of hydrogen and possibly protective to the metal underneath.

The materials that were explored are as follows:

1. CrN / BN
2. Cr-2N / BN
3. SiC4 / SiCxNy
4. B4C / BCxNy

Magnetron sputtering was used to produce these coatings. In most cases two targets have been used, with the deposition rate of each source individually controlled by applied power. Conditions have been chosen such that the correct stoichiometry is produced with an identical ratio of reactive gas. Substrate rotation speed was adjusted to produce the correct nanolaminate period with the substrate heated to 300°C to confirm production of desired phase.

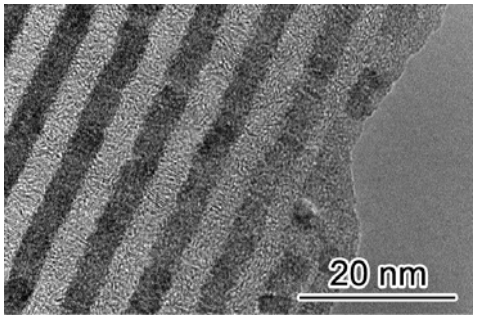

Figure 10: TEM Micrograph Showing the Uniform Nature of the Laminate Layers.

Transmission electron microscopy (TEM) was used to characterize the laminates. Figure 10 illustrates the control achieved over the layer thickness. Film performance, however, has been more inconsistent. Linear sliding wear tests produced widely varying results, even when performed on different areas of the same film. Many samples performed well, withstanding long cycle times at higher-than-anticipated stress levels. The coefficients of friction (COF) for these durable areas were typically between 0.1 and 0.3. Other tested areas, however, rapidly reduced to scuffing and wore quickly at a high COF.

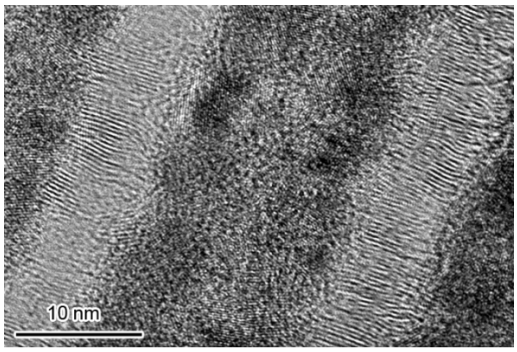

Figure 11: TEM Micrograph Showing Fluctuations in Crystallinity Within Each Layer (dark layer is CrN and light layer is BN).

Further examination of the films by TEM (Figure 11) revealed nanometer-scale inconsistencies in the film crystallinity. Attempts to correct this by ion-assisted deposition showed promise. Several peer-reviewed papers on these topics are in draft form and will be submitted shortly. Further efforts will determine the potential of laminate systems as hydrogen barriers, to improve the reliability of successfully designed films, and to explore new film combinations which are anticipated to also be successful in the proposed environment.

Conclusions

The diffusion of hydrogen in piezoelectric materials and in nanolaminates was evaluated using advanced analytical and modeling techniques. The following conclusions were obtained:

- Significant absorption of H_2 was observed in the piezoelectrics charged at 16.5 MPa and 100 °C. This absorption is highly dependent on material and electrode composition.
- Lead Zirconate Titanate (PZT) absorbs more H_2 than comparably charged films of Barium Titanate ($BaTiO_{3)}$. In addition, samples with Pd electrodes showed significantly higher H_2 absorption than samples without electrodes for both PZT and $BaTiO_3$ films.
- Only very limited diffusion of hydrogen occurred in the nanolaminates that were studied. This is encouraging regarding the potential use of nanolaminates in hydrogen environments and suggests they may be useful for protecting susceptible substrate materials from hydrogen damage.
- Evaluation of the defect energy associated with interstitial hydrogen in PZT has concluded that the PZT atomic structure (uniform alternation of Zr and Ti cells) may affect the defect energy, and thus affect the ability of hydrogen to diffuse in the lattice. In other words, it may be possible to fabricate PZT that is more resistant to hydrogen.

Presentations/Publications/Patents

- Alvine K, S Pitman, W Bennett, C Brown, M Tyagi, and T Jenkins. In Press. "Hydrogen Diffusion in Piezoelectrics: a Quasi-Elastic Neutron Scattering Study."
- Alvine K, S Pitman, V Shutthanadan, and W Bennett. In Press. "Hydrogen Absorption in Piezoelectrics: an Elastic Recoil Detection Analysis Study."
- Alvine K, S Pitman, V Shutthanadan, W Bennett, C Brown, M Tyagi, and T Jenkins. In Press. "Hydrogen Materials Compatibility in Piezoelectrics." March 2010, Portland, Oregon. American Physical Society.

References

[1] Huang HY, WY Chu, YJ Su, KW Gao, J X Li, and LJ Qiao. 2007. *J. Am. Ceram. Soc. 90*, 2062.
[2] KushidaAbdelghafar K, H Miki, K Torii, and Y Fujisaki. 1996. *Appl. Phys. Lett. 69*, 3188.
[3] Aggarwal S, SR Perusse, CW Tipton, R Ramesh, HD Drew, T Venkatesan, DB Romero, VB Podobedov, and A Weber. 1998. *Appl. Phys. Lett. 73*, 1973.
[4] Wu M, HY Huang, B Jiang, WY Chu, YJ Su, JX Li, and LJ Qiao. 2009. *J. Mater. Sci. 44*, 5768.
[5] Aimi M, M Arik, J Bray, T Gorczyca, D Michael, and S Weaver. 2007. Medium: ED.
[6] Shimamoto Y, K KushidaAbdelghafar, H Miki, and Y Fujisaki. 1997. *Appl. Phys. Lett. 70*, 3096.
[7] Peng X, YJ Su, KW Gao, LJ Qiao, and WY Chu. 2004. *Mater. Lett. 58*, 2073.
[8] Avasthi DK. 1996. *Bull. Mat. Sci. 19*, 3.
[9] Kramer EJ. 1991. *Physica B 173*, 189.
[10] Ishikawa A, H Maekawa, T Yamamura, Y Kawakita, K Shibata, and M Kawai. 2008. *Solid State Ion. 179*, 2345.
[11] Park CH and DJ Chadi. 2000. *Phys. Rev. Lett. 84*, 4717.
[12] Meyer A, RM Dimeo, PM Gehring, and DA Neumann. 2003. *Rev. Sci. Instrum. 74*, 2759.
[13] Pivovar AM, MD Ward, T Yildirim, and DA Neumann. 2001. *J. Chem. Phys. 115*, 1909.
[14] Perdew JP, K Burke, and M Ernzerhof. 1996. *Phys. Rev. Lett. 77*, 3865.
[15] Bellaiche L and D Vanderbilt. 2000. *Phys. Rev. B 61*, 7877.
[16] Henkelman G, BP Uberuaga, and H Jonsson. 2000. *J. Chem. Phys. 113*, 9901.

Acronyms

PZT: Lead Zirconate Titanate
BaTiO3: Barium Titanate
QENS :Neutron, Quasi-elastic Neutron Scattering
ERDA: Elastic Recoil Detection Analysis
NRA: Neutron Resonance Analysis
FWHM: Full-Width at Half Maximum
HFBS: High-Flux Back Scattering
FANS: Filter Analyzed Neutron Spectrometer
PNNL: Pacific Northwest National Laboratory
NIST: National Institute of Standards and Technology
NCNR: National Center for Neutron Research

Project 18518 – Materials for High Efficiency Engines

Agreement 16304 – High Performance Valve Materials (HPVM)

P. J. Maziasz and N. D. Evans
Materials Science and Technology Division
Oak Ridge National Laboratory
P.O. Box 2008, MS-6115
Oak Ridge, TN 37831-6115
(865) 574-5082; fax: (865) 754-7659; e-mail: maziaszpj@ornl.gov

N. Phillips
Advanced Materials Technology
Caterpillar Technical Center
14009 Old Galena Rd.
Mossville, IL 61552
(309) 578-5788; fax: (309) 578-2953; e-mail: phillips_nate@cat.com

DOE Technology Manager: Jerry L. Gibbs
(202) 586-1182; fax: (202) 586-1600; e-mail: jerry.gibbs@ee.doe.gov
ORNL Technical Advisor: D. Ray Johnson
(865) 576-6832; fax: (865) 574-6098; e-mail: johnsondr@ornl.gov

---

Contractor: Oak Ridge National Laboratory, Oak Ridge, Tennessee
Contract No.: DE-AC05-00OR22725

Objectives

- Characterize current engine exhaust seats and valves to define and understand temperature, performance and durability limitations
- Use understanding of the behavior of current valves and seats to enable advanced designs and/or selection of advanced materials and processing to upgrade temperature capability and performance/durability limitations.

Approach

- Work as a team with Caterpillar (CAT) diesel engine valve and seat suppliers to validate temperature/performance limitations of current technology, and facilitate upgraded seat and valve options that are commercially viable, and which can be supplied as prototype modified components for testing and evaluation.
- Analyze (at ORNL) the various seat and valve components from simulation-rig or engine testing to provide microanalysis to define the nature and causes of wear/degradation of exhaust valve/seat pairs, and compare to fresh components.
- Perform critical mechanical properties testing (at ORNL) to determine the benefits of Ni-based superalloys for exhaust valves with more temperature capability and performance than standard Pyromet 31V.
- Use detailed data and analyses to guide component manufacturers in producing prototype valves and seats with upgraded performance and capability.

Accomplishments

- Caterpillar completed upgrading and expansion of its thermo-mechanical valve & seat-insert test rig facility, and began testing solutions identified last year to mitigate premature seat-wear issues.

- ORNL and Caterpillar suggested processing modifications of the Co-superalloy seats designed to mitigate lower temperature wear, based on microcharacterization and root-cause analyses. Caterpillar's valve seat supplier produced modified seats, and confirmed reduced wear rates with testing at Caterpillar.
- ORNL and Caterpillar identified the oxidation-enhanced sub-surface degradation of the valve-seating surface of standard Pyromet 31V valves, based on microcharacterization and root-cause analyses. ORNL and Caterpillar identified several commercial Ni-based superalloy upgrade candidates, based on these analyses, and worked with the valve supplier to obtain new materials for critical mechanical testing and valve prototyping.

Future Direction

- Complete testing of modified seats with standard Pyromet 31V valves (CAT) and provide rig-tested specimen for microanalysis (ORNL).
- Perform critical tensile, creep and fatigue testing (ORNL) to measure the performance benefits of upgrade alloys relative to standard Pyromet 31V.
- Rig-test modified seat-inserts and upgraded exhaust valves to verify mitigation of degradation mechanism and evaluate upgraded capabilities (CAT).
- Extend CRADA Project for 12 months due to expanded work scope due to technical success.

Introduction

This is a continuing ORNL CRADA project with Caterpillar, NFE-07-00995 and DOE, OVT Agreement 16304, which began in 2007, and scheduled to last for about 2.5 years. However, due to expanded work scope based on technical success to date, this CRADA was extended for 12 months more. This CRADA project has addressed the wear and failure modes of current on-highway heavy-duty diesel exhaust valves and seats, and then evaluated changes in seat-insert processing and advanced exhaust-valve alloys that will enable higher temperature capability, as well as better performance and durability. The need for such upgraded valve-seat alloys is driven by the demands to meet new emissions and fuel economy requirements, which then continue to push diesel exhaust component temperature higher. Requests for more detailed information on this project should be directed to Caterpillar, Inc.

Approach

Caterpillar has provided and analyzed the baseline wear and mechanical behavior characteristics of engine-exposed valves and seats, and similar exposure of those components to laboratory simulation-rig testing at Caterpillar. ORNL completed more in-depth characterization and microanalysis of those valves and seats over the past year. These data enabled root-cause analyses that provided the basis for modifying seat processing last year, and selecting Ni-based superalloys with upgraded performance relative to standard Pyromet 31V this year. Caterpillar and ORNL have been working as a team with Caterpillar's various component suppliers to implement these solutions on prototype components, which can be tested in test rigs or diesel engines.

Upgrading temperature capability of the various critical exhaust components should enable the increased engine temperatures needed to allow a 3% decrease in fuel consumption for on-highway trucks.

Technical Progress

Caterpillar

Previously, Caterpillar provided exhaust valve and seat materials of standard materials that had been wear-tested at various temperatures on the Caterpillar "Buettner" Rig. Seats were a Co-based superalloy. Exhaust valves are standard Pyromet 31V Ni-based superalloy. ORNL and Caterpillar identified modified seat-insert processing designed to mitigate low-temperature wear, and have obtained trial seats with modified processing to verify the improved wear-resistance.

During the first part of this year, Caterpillar completed an upgrade of its original thermo-mechanical valve and seat-insert testing rig for better alignment and control of conditions during testing, and added two similar new rigs to expand their wear-testing facility, as shown in Fig. 1.

Caterpillar confirmed the initial wear-resistance tests of the modified seat inserts this year, and began longer-term testing to determine the durability of that wear-resistance.

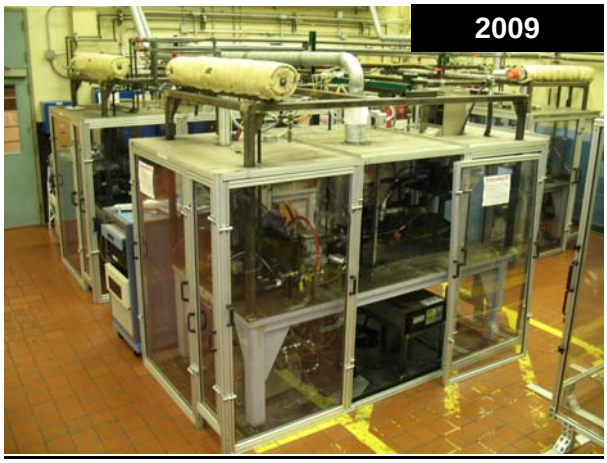

Figure 1. Thermo-mechanical valve and seat-insert test rigs for simulating high-temperature wear and performance of exhaust valves and seats for diesel engines, at the Caterpillar Technical Center. Caterpillar completed expanding facility from one to three test rigs this year, and began wear-testing of new modified seat-inserts.

An example of the typical wear data generated on sets of exhaust valves and seat-inserts on the Caterpillar wear-test rig are shown in Figure 2.

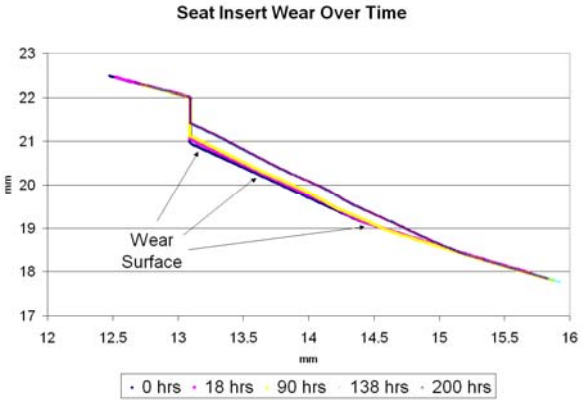

A

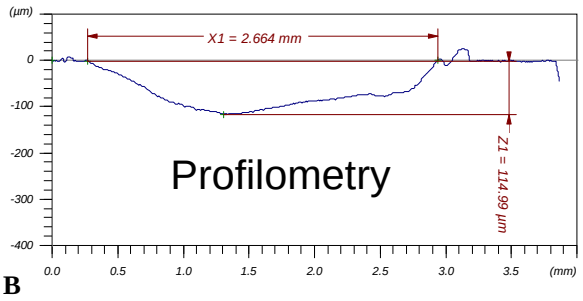

B

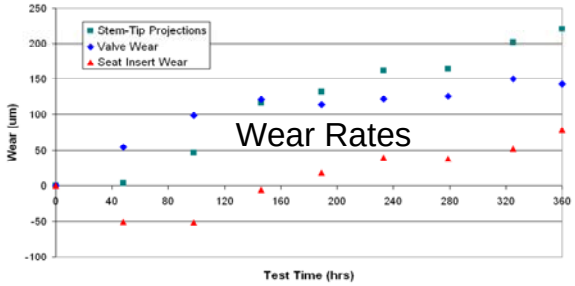

C

Figure 2 – Examples of data obtained from Caterpillar test rig for a) seat wear as a function of time, b) the profile of wear on the seating surface of the exhaust valve, and c) the individual wear recessions on valve and seat-inserts, and the combined change as reflected in valve stem-tip projection, when the worn components are in contact.

ORNL

ORNL completed thorough microstructural and microcompositional characterization studies of the valve and seat components this year, to define the detailed changes occurring at the oxidation-surfaces. Analysis included surface oxides as well as the underlying metal interface and bulk regions (including fresh and aged, non-wear control specimens). Figures 3 and 4 shows the SEM-BS imaging and X-ray EDS elemental mapping of an unworn portion of the Pyromet 31V valve surface tested in the CAT wear-rig for 360h at 850°C, while Fig. 5 shows SEM-BS imaging of an adjacent region in the wear-scar of the valve-seat face. Wear between the valve and seat removes the soft material shown in Fig. 3 and replaces it with Co-rich and Cr-rich metal and oxide debris. The X-ray EDS elemental maps in Figure 4 show that surface has a Cr-oxide layer, and that dark features beneath the surface in the gamma-prime denuded zone (Fig. 3) are internal

Ti- and Al-oxides. Clearly the dissolution of gamma-prime and the formation of internal oxidation weaken the subsurface region relative to the underlying base metal. These would be root-cause microscopic mechanisms related to the wear-removal of this layer of material on the valve-seat surface (Figs. 3 and 5).

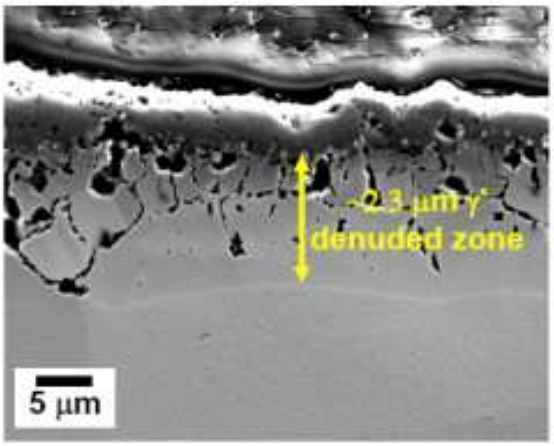

Figure 3 – Pyromet 31V exhaust valve wear-rig tested at CAT at 850°C for 360 h, and then analyzed at ORNL. Back-scattered (BS) SEM analysis reveals the surface oxide layer, and a gamma-prime denuded zone and internal oxides beneath the surface. Figure 4 shows detailed X-ray EDS elemental maps to illustrate the compositional nature of the various microstructural regions and features.

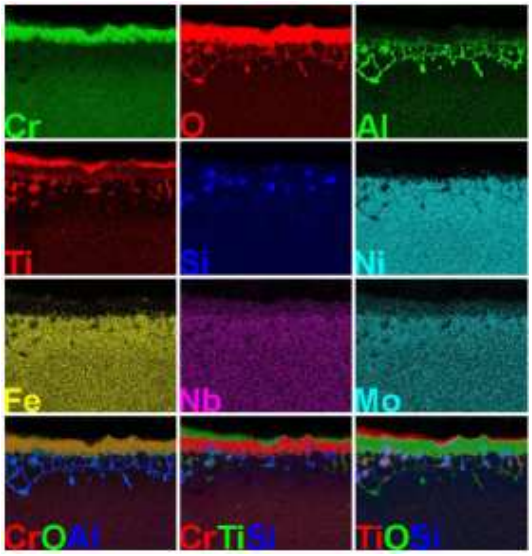

Figure 4 - SEM X-ray EDS maps and elemental images of the same region show in Fig. 3, for each of the elements or the elemental combinations indicated in the lower left-hand corner of each image. The Cr-map shows Cr-oxide on the valve surface, while the Al- and Ti-maps show internal oxidation beneath the surface.

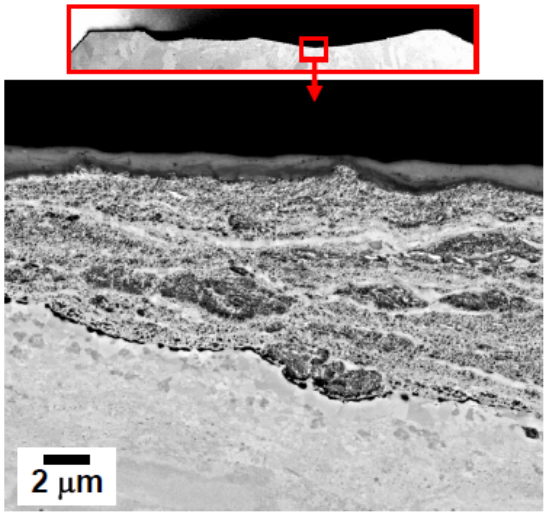

Figure 5 – SEM-BS analysis of the same Pyromet 31V exhaust valve shown in Fig. 3, but taken from the wear-scar on the valve seating surface, as indicated in the low-magnification optical image inset above. The oxide debris above the worn metal is Co- and Cr-rich oxides, indicating material transfer from the seat-insert to the valve.

Similarly, ORNL also conducted detailed microcharacterization and analysis of the seat-inserts, both fresh and worn. SEM and XPS microcompositional depth profiling of a Co-based alloy seat insert are shown in Figure 6, comparing fresh and aged components. Analysis of the surface oxides and sub-surface regions were completed this year. Based on this detailed analysis of wear-tested seat inserts, processing modifications were to the seat-inserts, which were found to mitigate some of the wear being experienced between seats and valves at lower temperatures. Caterpillar's valve seat supplier has processed seats and Caterpillar has completed short-term wear-rig testing to validate the wear-resistance. Caterpillar is currently performing longer term testing that will continue next year.

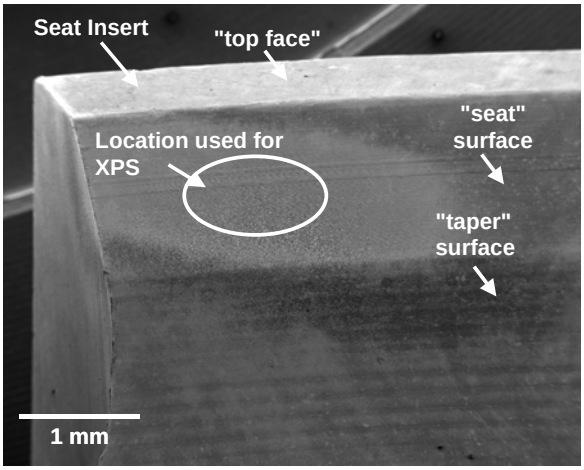

A

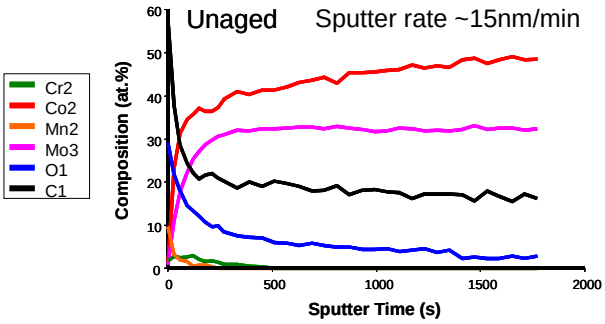

B

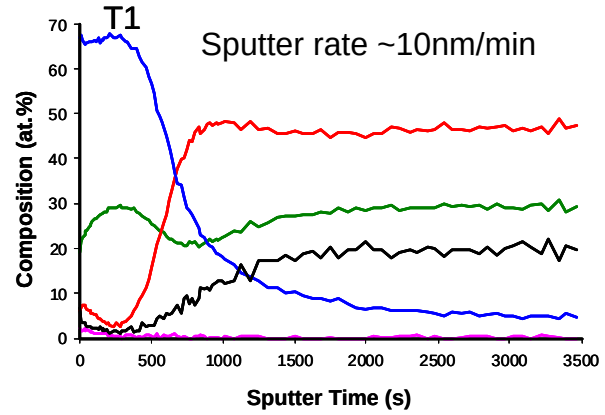

C

Figure 6 – Microcompositional analysis of a fresh and aged Co-based seat inserts. A) SEM of seat-insert, showing the face that makes contact with the valve, and the location of subsequent XPS depth profiling for compositional analysis. B) XPS profile of a fresh component, with no surface oxide present, which C) is the XPS profile of an aged (air) component showing the thickness of the Cr-oxide on the surface

Finally, ORNL and Caterpillar have identified several commercial Ni-based superalloys as upgrade materials with more temperature capability and performance than Pyromet 31V for exhaust valve applications. Caterpillar's valve supplier has obtained the new alloys, and is currently making test specimens for mechanical properties and oxidation testing at ORNL, and prototype valves for wear-rig testing at Caterpillar. Such testing will be done next year.

Conclusions

Caterpillar and their seat insert supplier have obtained seat-inserts with modified processing for increased wear-resistance. Caterpillar has conducted short-term wear-resistance tests and validated the wear-resistance benefits. Caterpillar is currently performing longer-term testing, which will continue next year.

ORNL completed in-depth micro-characterization studies of fresh and worn valve and seat components. Combined SEM and XPS studies of surface oxides and sub-surface regions were completed on the seat inserts earlier this year. ORNL completed similar microanalysis of worn valve surfaces this year of Pyromet 31V, clearly identifying the subsurface softening due to gamma-prime dissolution and internal oxidation as a root-cause in the valve seating surface wear. ORNL and Caterpillar have identified commercial Ni-based superalloys with more temperature capability and performance than Pyromet 31V. ORNL will perform mechanical testing of such alloys next year, while Caterpillar will begin wear-rig testing of prototype valves.

Publications/Presentations

None

Special Recognitions and Awards/Patents Issued

None

Caterpillar confirmed the initial wear-resistance tests of the modified seat inserts this year, and began longer-term testing to determine the durability of that wear-resistance.

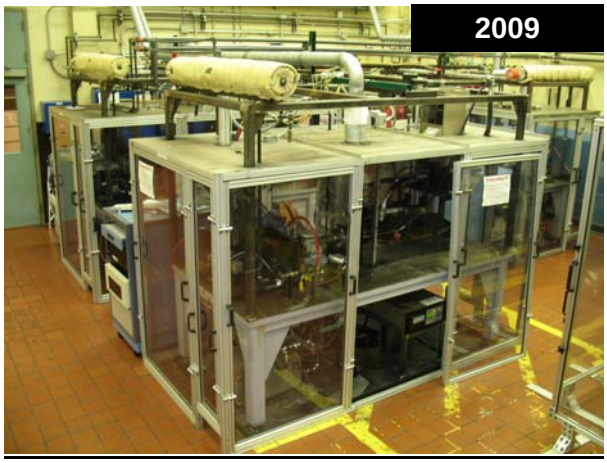

Figure 1. Thermo-mechanical valve and seat-insert test rigs for simulating high-temperature wear and performance of exhaust valves and seats for diesel engines, at the Caterpillar Technical Center. Caterpillar completed expanding facility from one to three test rigs this year, and began wear-testing of new modified seat-inserts.

An example of the typical wear data generated on sets of exhaust valves and seat-inserts on the Caterpillar wear-test rig are shown in Figure 2.

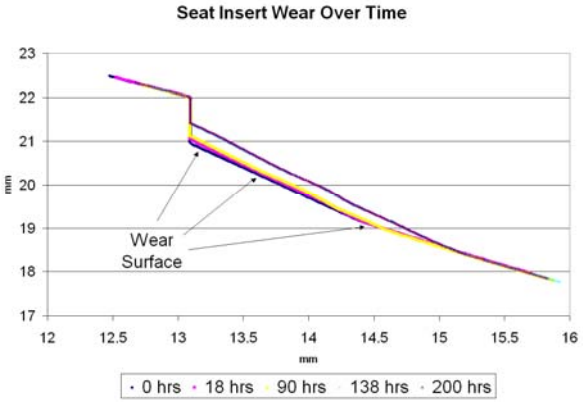

A

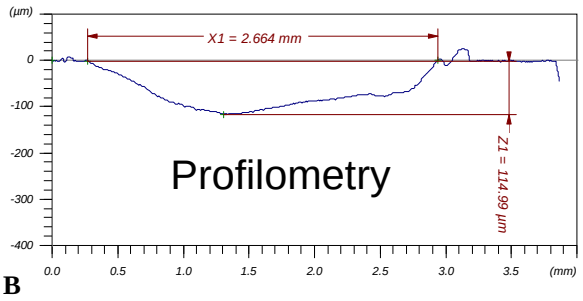

B

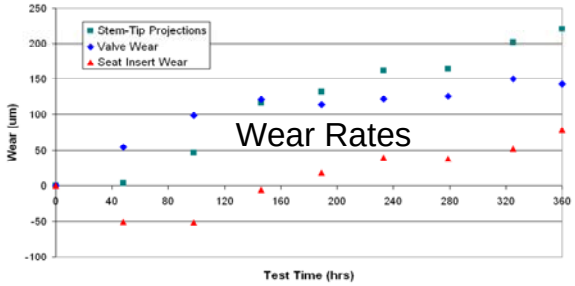

C

Figure 2 – Examples of data obtained from Caterpillar test rig for a) seat wear as a function of time, b) the profile of wear on the seating surface of the exhaust valve, and c) the individual wear recessions on valve and seat-inserts, and the combined change as reflected in valve stem-tip projection, when the worn components are in contact.

ORNL

ORNL completed thorough microstructural and microcompositional characterization studies of the valve and seat components this year, to define the detailed changes occurring at the oxidation-surfaces. Analysis included surface oxides as well as the underlying metal interface and bulk regions (including fresh and aged, non-wear control specimens). Figures 3 and 4 shows the SEM-BS imaging and X-ray EDS elemental mapping of an unworn portion of the Pyromet 31V valve surface tested in the CAT wear-rig for 360h at 850°C, while Fig. 5 shows SEM-BS imaging of an adjacent region in the wear-scar of the valve-seat face. Wear between the valve and seat removes the soft material shown in Fig. 3 and replaces it with Co-rich and Cr-rich metal and oxide debris. The X-ray EDS elemental maps in Figure 4 show that surface has a Cr-oxide layer, and that dark features beneath the surface in the gamma-prime denuded zone (Fig. 3) are internal

Ti- and Al-oxides. Clearly the dissolution of gamma-prime and the formation of internal oxidation weaken the subsurface region relative to the underlying base metal. These would be root-cause microscopic mechanisms related to the wear-removal of this layer of material on the valve-seat surface (Figs. 3 and 5).

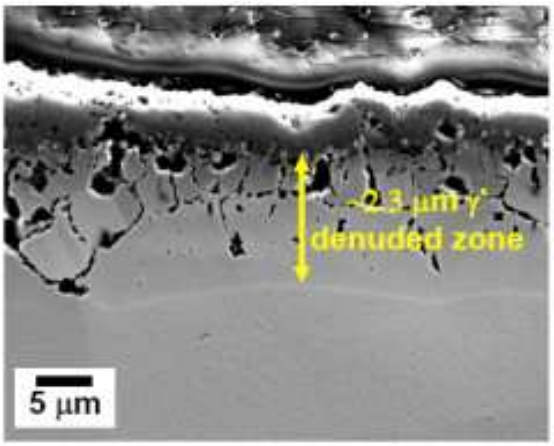

Figure 3 – Pyromet 31V exhaust valve wear-rig tested at CAT at 850°C for 360 h, and then analyzed at ORNL. Back-scattered (BS) SEM analysis reveals the surface oxide layer, and a gamma-prime denuded zone and internal oxides beneath the surface. Figure 4 shows detailed X-ray EDS elemental maps to illustrate the compositional nature of the various microstructural regions and features.

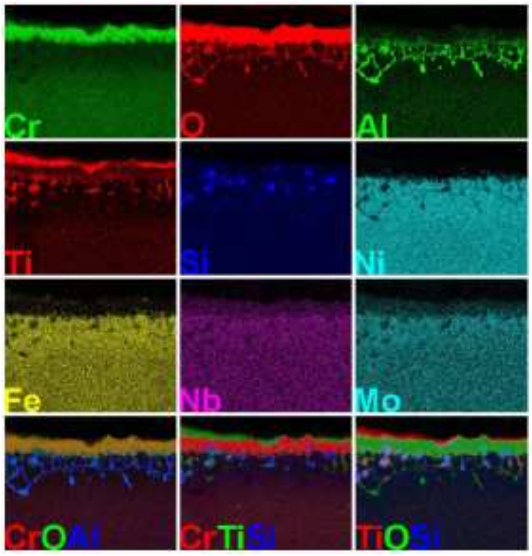

Figure 4 - SEM X-ray EDS maps and elemental images of the same region show in Fig. 3, for each of the elements or the elemental combinations indicated in the lower left-hand corner of each image. The Cr-map shows Cr-oxide on the valve surface, while the Al- and Ti-maps show internal oxidation beneath the surface.

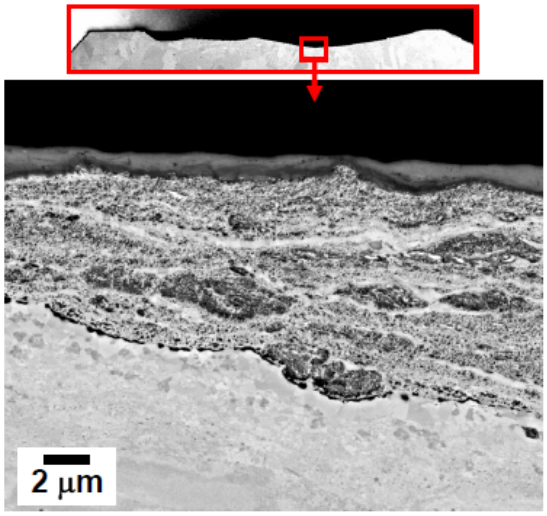

Figure 5 – SEM-BS analysis of the same Pyromet 31V exhaust valve shown in Fig. 3, but taken from the wear-scar on the valve seating surface, as indicated in the low-magnification optical image inset above. The oxide debris above the worn metal is Co- and Cr-rich oxides, indicating material transfer from the seat-insert to the valve.

Similarly, ORNL also conducted detailed microcharacterization and analysis of the seat-inserts, both fresh and worn. SEM and XPS microcompositional depth profiling of a Co-based alloy seat insert are shown in Figure 6, comparing fresh and aged components. Analysis of the surface oxides and sub-surface regions were completed this year. Based on this detailed analysis of wear-tested seat inserts, processing modifications were to the seat-inserts, which were found to mitigate some of the wear being experienced between seats and valves at lower temperatures. Caterpillar's valve seat supplier has processed seats and Caterpillar has completed short-term wear-rig testing to validate the wear-resistance. Caterpillar is currently performing longer term testing that will continue next year.

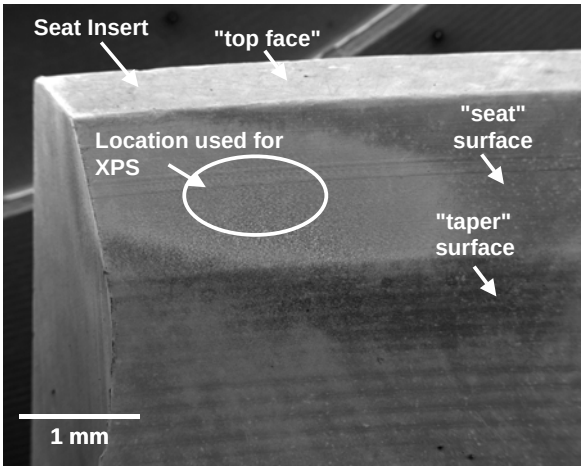

A

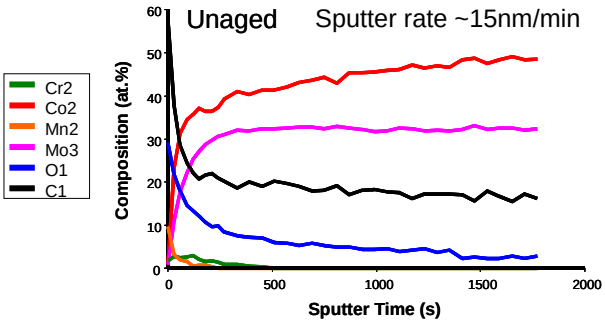

B

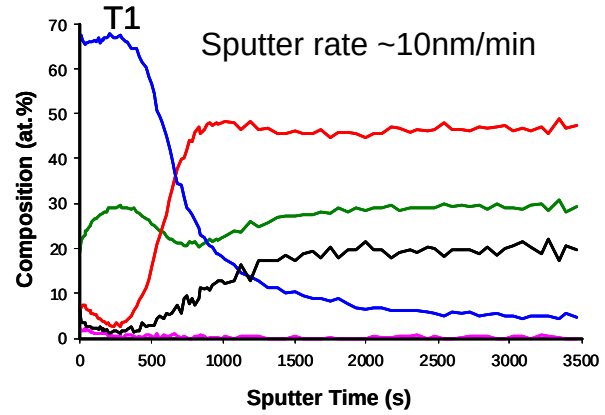

C

Figure 6 – Microcompositional analysis of a fresh and aged Co-based seat inserts. A) SEM of seat-insert, showing the face that makes contact with the valve, and the location of subsequent XPS depth profiling for compositional analysis. B) XPS profile of a fresh component, with no surface oxide present, which C) is the XPS profile of an aged (air) component showing the thickness of the Cr-oxide on the surface

Finally, ORNL and Caterpillar have identified several commercial Ni-based superalloys as upgrade materials with more temperature capability and performance than Pyromet 31V for exhaust valve applications. Caterpillar's valve supplier has obtained the new alloys, and is currently making test specimens for mechanical properties and oxidation testing at ORNL, and prototype valves for wear-rig testing at Caterpillar. Such testing will be done next year.

Conclusions

Caterpillar and their seat insert supplier have obtained seat-inserts with modified processing for increased wear-resistance. Caterpillar has conducted short-term wear-resistance tests and validated the wear-resistance benefits. Caterpillar is currently performing longer-term testing, which will continue next year.

ORNL completed in-depth micro-characterization studies of fresh and worn valve and seat components. Combined SEM and XPS studies of surface oxides and sub-surface regions were completed on the seat inserts earlier this year. ORNL completed similar microanalysis of worn valve surfaces this year of Pyromet 31V, clearly identifying the subsurface softening due to gamma-prime dissolution and internal oxidation as a root-cause in the valve seating surface wear. ORNL and Caterpillar have identified commercial Ni-based superalloys with more temperature capability and performance than Pyromet 31V. ORNL will perform mechanical testing of such alloys next year, while Caterpillar will begin wear-rig testing of prototype valves.

Publications/Presentations

None

Special Recognitions and Awards/Patents Issued

None

Agreement 13329 - Design Optimization of Piezoceramic Multilayer Actuators for Heavy Duty Diesel Engine Fuel Injectors

Hua-Tay Lin, Hong Wang, and Andrew A. Wereszczak
Ceramic Science and Technology Group
Oak Ridge National Laboratory
P.O. Box 2008, MS 6068
Oak Ridge, TN 37831-6068
(865) 576-8857; fax: (865) 574-6098; e-mail: linh@ornl.gov

Jesus Camona-Valdes and Randy Stafford
Cummins Inc.
Columbus, Indiana 47201
(812) 377-3279; fax: (812) 377-2040; e-mail: randy.j.stafford@cummins.com

DOE Technology Manager: Jerry L. Gibbs
(202) 586-1182; fax: (202) 586-1600; e-mail: Jerry.gibbs@ee.doe.gov
ORNL Technical Advisor: D. Ray Johnson
(865) 576-6832; fax: (865) 574-6098; e-mail: johnsondr@ornl.gov

Contractor: Oak Ridge National Laboratory, Oak Ridge, Tennessee
Contract No.: DE-AC05-00OR22725

Objectives

- Apply established structural ceramic probabilistic design and reliability analysis to piezoelectric multilayer actuators (PMLAs).
- Generate required micromechanical property data on lead zirconate titanate (PZT) piezoceramics and macromechanical property data on PMLAs for input into the design and reliability analysis of the latter.
- Identify minimum mechanical performance requirements for fuel injector PMLAs.
- Adapt these strategies to improve reliability of PMLAs under candidacy for use in diesel engine fuel injectors.

Approach

- Evaluate PMLA reliability under representative service conditions.
- Link constituent piezoceramic micro-mechanical and PMLA macro-mechanical responses.

Accomplishments

- Characterized the mechanical strength of Kinetic Ceramics PZT ceramic using various test configurations and indentified the strength-limiting flaw through size-scaling analysis. Investigated the electric field effect on the strength of PZT ceramic under the applied coercive field level.
- Modified the current ORNL piezo stack fatigue facility for testing EPCOS stacks. Evaluated the accelerated fatigue response of EPCOS from different sources under unipolar and semi-bipolar mode with the recommended preload.
- Developed the sequential polishing technique for characterizing the fatigue-induced microstructure damage.

Future Direction

- Develop database for candidate piezoceramics and PMLAs of Cummins with the suggested environmental factors included.
- Measure and compare piezoelectric and mechanical reliabilities of tape-cast and pressed PZT piezoceramics.
- Fabricate additional PMLA fatigue test frames.

Introduction

The use of piezoelectric multilayer actuators (PLMAs) as diesel fuel injectors has the potential to reduce injector response time, provide greater precision and control of the fuel injection event, and lessen energy consumption. Compared to conventional solenoid operation of an injector, the alternative use of a PMLA can enable precise rate shaping of the entire injection cycle that accurately controls injection timing and fuel quantity. Piezoelectric multilayer actuators (or piezo-stacks) fuel injectors contain a solid-state ceramic actuator (or "piezostack") that converts electric energy into linear motion precisely controlling the needle's opening and closing. This capability results in an engine with outstanding performance, improved fuel economy, low noise, and low emissions. Though their use is very attractive for the reasons mentioned above, uncertainty continues to exist over how reliable piezo-actuated fuel injectors will be in the challenging environment of a heavy diesel vehicle engine. Though piezoelectric function is the obvious primary function of lead zirconate titanate (PZT) ceramic PMLAs for fuel injectors, their reliability can be a performance and life limiter because the PZT ceramic within them is brittle, lacks high strength, and may exhibit fatigue susceptibility. That brittleness and relatively low strength can be overcome with proper probabilistic component design methodology.

This project undertakes the reliability characterization of candidate PMLAs used in these fuel injectors and the piezoceramics used in the PMLAs. Technical communications have been established with Cummins as a result of the execution of CRADA in the FY2009. Tests and characterizations on the piezoceramics and piezo stacks have been initiated based on recommendations from Cummins Inc. At the same time, the involved facilities have been modified accordingly at ORNL to accommodate the requirements for testing related materials and devices. The products manufactured by Kinetic Ceramics, Inc. (KCI) and EPCOS have been the focuses of the CRADA.

Approaches

Piezoceramic Characterization

Characterization on the mechanical strength of KCI PZT has been conducted. The data generated in this task will serve as the input for the subsequent reliability design study on the multilayer actuator. As a result of that, factors to be studied include strength-limiting flaw, electric field, temperature, and humidity. Both the as-extracted and as-received single-layer PZT materials were examined in this study. For the former, the specimens were obtained from a supplied KCI PZT stack (named as type A) by dissolving bond epoxy using a recommended chemical solution. Use of extracted materials not only provides the quantity of specimens for testing, but also enables the investigation of PZT material that has been laminated and experienced the same history as that of the parent stack. Each PZT specimen was a circular plate with two opposite cuts or flats in the same size. Its nominal diameter was 15.00 mm, flat-to-flat distance 12.26 mm, and thickness 0.500 mm.

Both the ball-on-ring (BoR) and 4-point bend tests were used to study mechanical strength of as-extracted PZT, strength-limiting flaw, and size-scaling of the strength. Two combinations of loading ball and supporting ring were studied in the BoR tests. The first combination was a polymer-ceramic pair consisting of a 10 mm polymer ring and 2 mm Si_3N_4 ball. The second combination was a steel-steel pair consisting of a 9.5 mm steel ring and 6.35 mm steel ball. Testing was performed in a displacement-controlled mode with a rate of 0.01 mm/s. Test data were processed with a method described in reference [1,2].

A semi-articulated 4-point bend setup was used to further investigate the flexure strength of as-extracted single-layer PZT. The loading and supporting spans were 3.175 mm and 6.35 mm, respectively. The crosshead speed was same as that in ball-on-ring testing, namely, 0.01 mm/s. The data were processed using the bending plate theory [3].

Sizable scratches could be seen on surfaces of as-received PZT plates. The surface condition of specimen was characterized subsequently using a laser profilometer. An area of 2 mm x 2 mm was scanned in each measurement. 5 specimens randomly selected from the specimen box were scanned and measured; a *Ra* range of 0.8 to 1.4 μm was found along with the roughness depth mentioned above.

Characterization of single-layer PZT necessitates the investigation on the response of PZT under a characteristic electric field, especially, coercive field (E_c). However, the relevant data sheet

does not provide any information about the *Ec*. A piezodilatometer developed at ORNL has been used for this purpose. A 0.1 Hz triangular wave was employed to load the PZT plate in thickness direction (x_3). The mechanical displacement in the plate plane (x_1 direction) was measured using a linearly varying capacitance (LVC) sensor and the electric displacement (charge) in the thickness (x_3 direction) with a modified Sawyer-Tower circuit.

Effect of electric field on the flexure strength of as-received PZT was studied by using BoR setup. 4 electric conditions were considered: open circuit, positive and negative coercive field ($\pm E_c$) and two times the positive coercive field ($+ 2E_c$). The electric loading took the same approach as reported in reference [4].

PMLA Characterization

Fatigue testing and characterization on EPCOS piezo stack (type B) were conducted. Tested piezo stacks had an overall size of 6.5 x 6.5 x 30mm, a capacitance of 2.9 μF, and two outstanding electrode-pins. This configuration of stack is different from that we tested before, and the test facility was modified and calibrated.

Prefatigue tests have been conducted with a variety of mechanical and electric loading conditions, especially, unipolar electric waveform with constant mechanical preload. During this process, dielectric breakdown was observed in 4 stacks (Nos. 01 - 04) and breakdown voltages ranged from 320 V to 480 V. The fatigue testing on type B stacks thus began with an electric loading condition of 50 Hz, 0/160V sine wave with a 766 N mechanical preload. The measurements during a fatigue test were carried out at specified cycles using 2 Hz, 0/ 160 V sine wave with two preload levels, 16 N and 766 N. Data processing and evaluation were conducted by following the procedures given in reference [5]. In later stage of the project, change of electric cycling condition from unipolar (50 Hz, 0/160 V) to semi-polar (50Hz, -40/160 V) was proposed. As a result of that, the measurement conditions in evaluation were also modified to investigate the sensitivity of actuator's response to the driving condition. Particularly, the measurements using 2 Hz, -40/160 V sine waves with two above-mentioned preloads were added. Measurements and data processing followed the procedures described in references [6,7]. Unipolar and semi-bipolar cyclic fatigue tests have been conducted in 2 recently-purchased stacks (Nos. 05 to 06) and 1 Cummins-supplied stack (No. 07), respectively.

Following accelerated fatigue test, cross section was prepared for stack No. 05 after 10^8 cycles of fatigue to investigate involved damages and controlling mechanisms. This section passed the electrode termination such that the inactive and active regions can be observed. The interfaces between neighboring multilayer actuator (MLA)

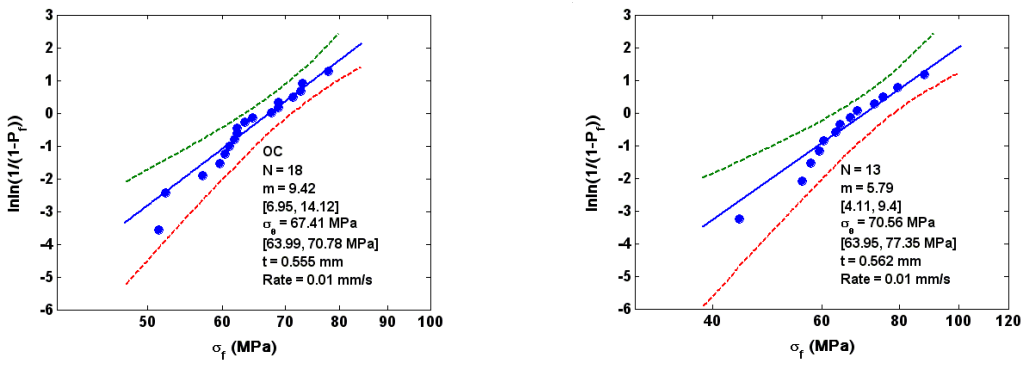

(a) (b)

Fig. 1. Weibull plots of single-layer PZT obtained using ball-on-ring setup with (a) 9.5 mm steel ring with 6.4 mm steel ball, and (b) 10 mm polymer ring with 2 mm steel ball. PZT plates were extracted from a PZT stack.

plates appeared as dark linear thick zones under optical microscope.

Results

Piezoceramics Characterization

The results for BoR tests on the as-extracted KCI specimens are given in Fig. 1 using both mentioned combinations. The characteristic strength (67 to 70 MPa) and Weibull modulus (5.8 to 9.4) were observed to be independent of loading and supporting parameters within the testing range. Fractography revealed that intergranular fractures dominated the fracture surface and surface-located volume pores were strength-limiting. One representative failure surface with failure origin is shown in Fig. 2.

The results obtained from 4-point bend are shown in Fig. 3. The flexure strength had a significantly lower value than those obtained using BoR setup. This was expected because 4-point bend sampled a larger stressed volume and surface-area than BoR flexure, which resulted in a lower characteristic strength.

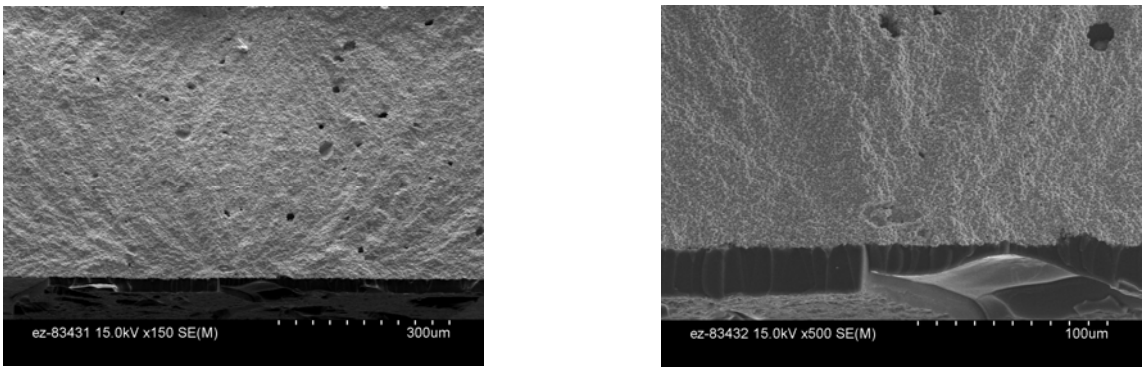

(a) (b)

Fig. 2. Fracture surface (a) and failure origin (b) featuring surface-located volume pore. Ball-on-ring setup was used with a 10 mm polymer ring and 2-mm steel ball; the rate was 0.01 mm/s and failure stress was 60 MPa.

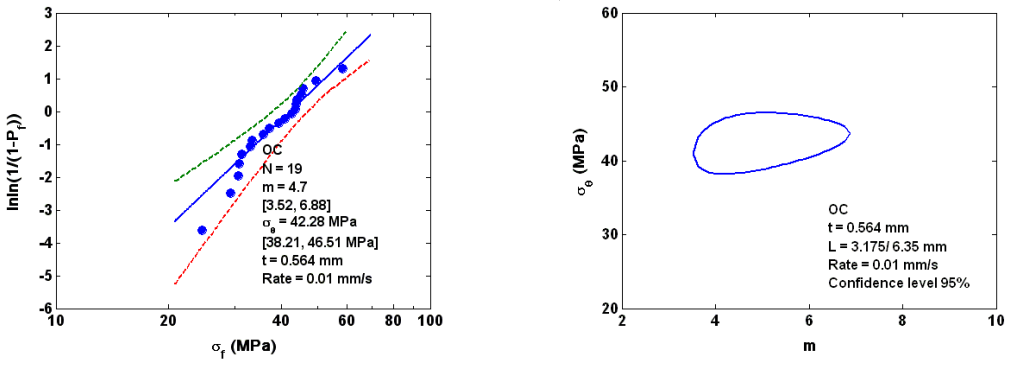

(a) (b)

Fig. 3. (a) Weibull plot and (b) confidence ratio ring (95% confidence level) of flexure strength for single-layer PZT obtained using semi-articulated 4-point bend setup with 3.175 mm of loading span and 6.35 mm of supporting span; specimens were extracted from a stack.

Extensive fractographical studies have been conducted on fracture surfaces using optical and scanning electron microscopes. Surface-located volume pore, porous region, agglomerate, inclusion, and surface void were revealed as related to identified failure origins (Fig. 4).

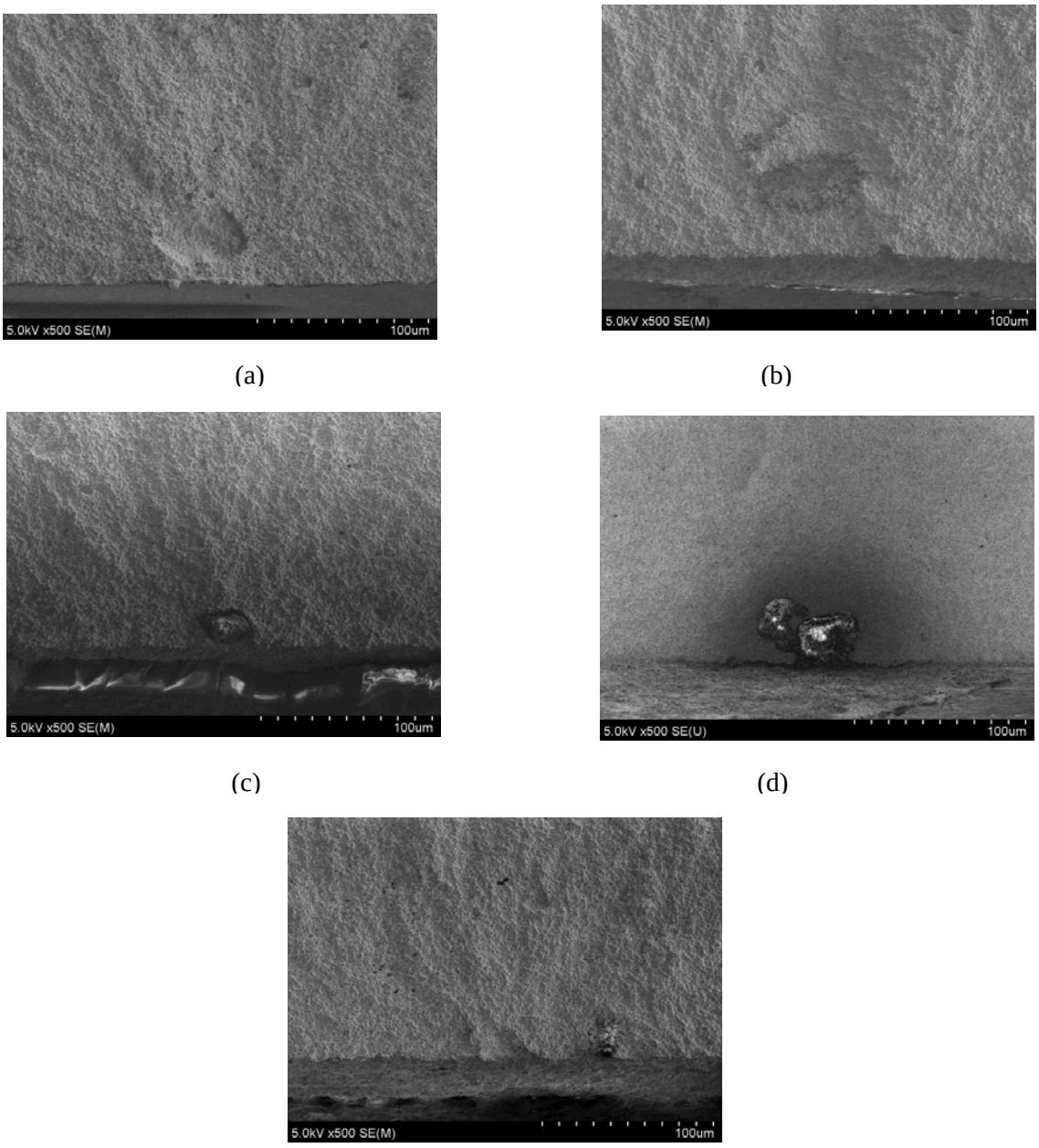

Fig. 4. Failure origins featuring (a) volume pore, σ_f = 58.5 MPa, (b) porous region, σ_f = 42.8 MPa, (c) agglomerate, σ_f = 40.9 MPa, (d) inclusion, σ_f = 33.1 MPa, and (e) surface void, σ_f = 37.1 MPa. Semi-articulated 4-point flexure setup was used with loading span 3.175 mm and supporting span 6.35 mm; the cross head rate was 0.01 mm/s.

The strength-limiting flaw type in BoR and 4-point bend tests was mostly a volume flaw located at or near the PZT plate's tensile surface. A couple of them can be viewed as a surface void; they were inherently a volume type of flaws intersecting the plate surface though. Therefore, the strength of PZT can be scaled in terms of the effective volume. The analysis [8] showed the effective volumes were 1.950 and 0.028 mm^3 for the 4-point bend and BoR, respectively. By taking account of the average *m* value of 7.1, the expected strength of the BoR would be 1.82 times that of 4-point bend. On the other hand, the observed strength ratio of two cases was actually 1.60. Nevertheless, the fact that the amount of size scaling in the strength correlated to the predicted based on Weibull scaling distribution suggested the paramount role of volume flaw, particularly, the volume pore.

Porosity of PZT materials were thus characterized particularly using back scattering scanning electron microscopy. The back scattering image was generally sized with 178 x 254 μm. Area and size distributions of pores were obtained through analysis using image analysis software (Image J). 6 images were acquired and processed. Analyzed sections suggested that the mean pore area and volume fraction of pore were around 14 μm^2 and 3%, respectively.

These raw data obviously did not take account of any sampling errors. However, the maximum of pore size (2*c*) based on a specific image (sub-region

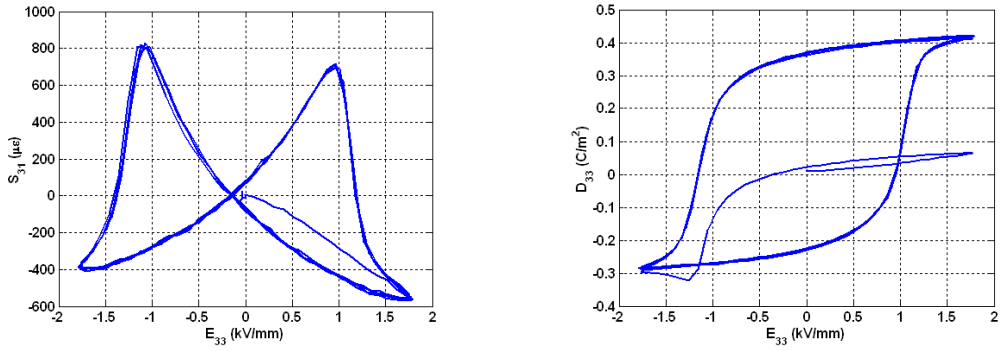

(a) (b)

Fig. 5. (a) Mechanical strain (S_{31}) – electric field (E_3) loop and (b) charge density (D_{33}) – electric field (E_3) loop for as-received single-layer PZT. A 0.1 Hz triangular wave was used.

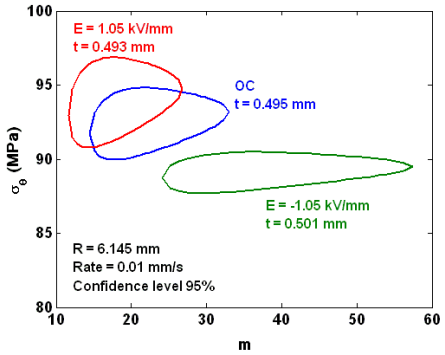

Fig. 6. Confidence ratio rings (95% confidence level) of flexural strength for as-received single-layer PZT under open circuit (OC) and E = ±1.05 kV/mm; Data were obtained using BoR setup with 9.5 mm steel ring and 6.4 mm steel ball.

of the section) was found to be distributed around 20 to 33 μm. This range fell within a wider range of strength-limiting flaws revealed by fractographic studies, 9 to 39 μm. Moreover, this range also corresponded to the surface roughness depth (12 to 20 μm of R_z) of as-received specimens measured by a profilometer, considering the R_z reflects the size of flaw (c).

A 0.1 Hz triangular wave was employed to load the PZT plate in thickness direction (x_3). The mechanical displacement in the plate plane (x_1 direction) was measured using a linearly varying capacitance (LVC) sensor and the electric displacement (charge) in the thickness (x_3 direction) with a modified Sawyer-Tower circuit. A set of loops is shown in Fig. 5. Three PZT plate specimens were tested; the averaged E_c obtained for this PZT material was 1.05 kV/mm [8].

Effect of electric field on the flexure strength of PZT showed that the electric loading to $+2E_c$ led to dielectric breakdown with the current setup. Thus, this report will focus on the open circle and $\pm E_c$ conditions. The PZT material exhibited an asymmetrical response of flexure strength with respect to the electrical field. The negative electric loading at coercive level resulted in a lower value of strength than in open circle; and the positive electric loading at the corresponding level did not cause significant difference in strength value as shown in Fig. 6. It is worth noting that a similar asymmetrical response of mechanical strength to electric loading

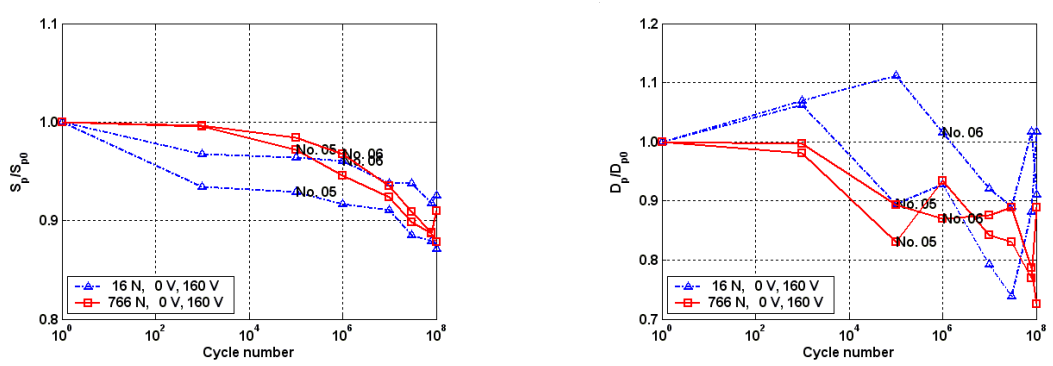

(a) (b)

Fig. 7. Variations of mechanical strain (a) and charge density (b) of type B stacks during the unipolar electric cycling with mechanical preload

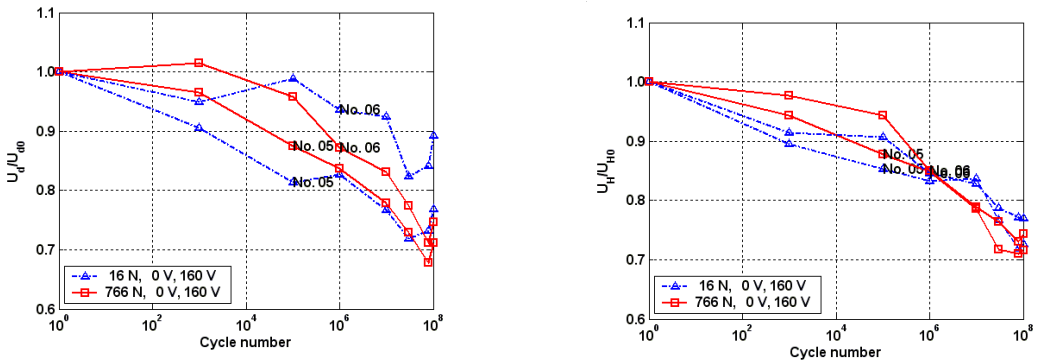

(a) (b)

Fig. 8. Variations of (a) piezoelectric and (b) dielectric hystereses of the same stacks as in Fig. 7 during the unipolar electric cycling with mechanical preload.

was also observed in another study on PZT using a 3-point bending setup [9]. However, the asymmetry in this study is obviously different from those on a similar soft PZT material but processed differently [1,2,4]. The involved controlling mechanism is being investigated [8].

PMLA Characterization

For the 2 stacks in unipolar testing, variations of mechanical strain and charge density are given in Fig. 7 (Nos. 05 and 06), and those of piezoelectric and dielectric hystereses in Fig. 8 (No. 07). Overall, both the mechanical strain and charge density reduced approximately 10- 20% at 10^8 cycles; and the piezoelectric and dielectric hystereses decreased about 20- 30%. On the other hand, the stack with semi-bipolar electric cycling exhibited about 10 to 20% increases in the mechanical strain and charge density, although same magnitude of decrease occurred in dielectric hysteresis (Figs. 9 and 10). The increase observed for No. 07 in semi-bipolar cycling seemed related to the deaging effect of electric driving on the responses of the stack and the involved mechanism is being investigated.

An extended crack was revealed near one end of the stack along with a number of other micro-cracks developed near the transition between above-mentioned inactive and active regions as shown in

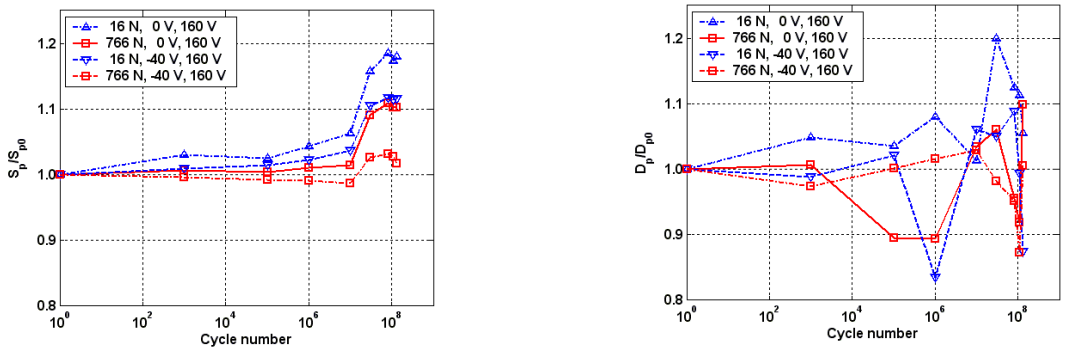

(a) (b)

Fig. 9. Variations of mechanical strain (a) and charge density (b) of type B stack No. 07 during the semi-bipolar electric cycling with mechanical preload.

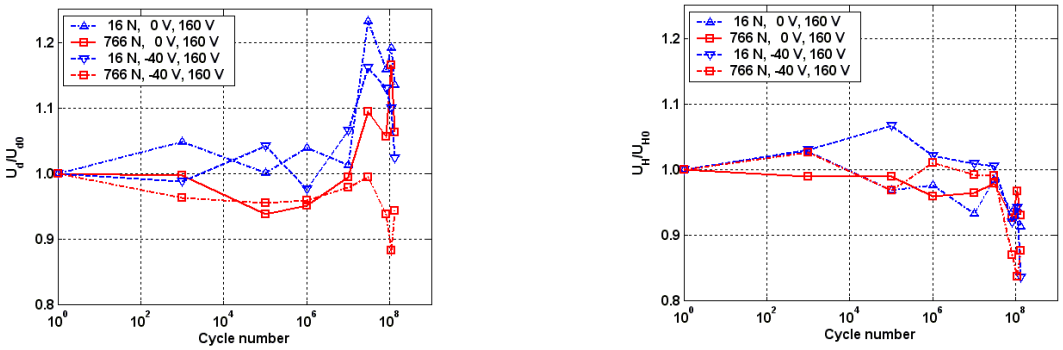

(a) (b)

Fig. 10. Variations of (a) piezoelectric and (b) dielectric hystereses of the same stack as in Fig. 9 during the semi-bipolar electric cycling with mechanical preload.

Fig. 11. Moreover, the transition near the MLA plate interface appeared to be the favorable place for these micro-cracks to occur. It is still under investigation how much the cutting procedure affected the observed microstructure of stack. For this reason, the contribution of the section preparation on the extended cracks will be examined next by using special technique such as sequential polishing developed in reference [7].

Conclusion and Future Work

Testing and characterization were focused on the candidate piezoceramics and piezo stacks that are currently considered in the use of heavy diesel engine fuel system in the first year of CRADA between ORNL and Cummins, Inc. Extensive mechanical tests were conducted on the KCI PZT by both BoR and 4-point bend fixtures in both the as-extracted and as-received. Strength limiters were characterized using the fractography. Electric field effect and temperature effect on the flexure strengths were studied and evaluated at the same time. Responses of EPCOS piezo stacks were conducted with both the breakdown and fatigue observed. Locating a safe working envelop of operation to appropriately drive a piezo actuator appears to be a main challenge for the application. With the careful prefatigue tests, this project was able to identify the operational parameters for subsequent accelerated fatigue testing. Under the unipolar cyclic fatigue with full range of the recommended voltage, 10 to 20% reduction of mechanical strain and charge density were observed on the 2 of tested stacks upon 10^8 cycles. Work in the coming year will be directed more on introducing the environmental factors into the test matrix. Specially, the following will be focused.

For KCI PZT, characterization of mechanical or flexure strength will be continued with the effects of high electric field ($2E_c$), high temperature (200^{o}C) and/ or high humidity (80%) included. Weibull parameters will be considered as they are the important input to the reliability design study. For EPCOS PZT, an alternative approach for mechanical strength characterization and data explanation will be explored because the stand-alone single-layer PZT plates are not readily available for testing. Especially the extracted MLA plate will be used in the following study for this purpose. The effects of electric field and temperature will be pursued as well.

Fatigue response of PZT materials will be tested and characterized by using the piezodilatometer, especially KCI PZT plate specimens. This test will be an important component to evaluate and explain the fatigue response of stack to be investigated.

Test setup will be designed or modified to test KCI actuator to accommodate the following requirements: 1) inclusion of stack stiffness in baseline evaluation; 2) mechanical preload more than 6,000 N; 3) temperature more than 150^{o}C; and

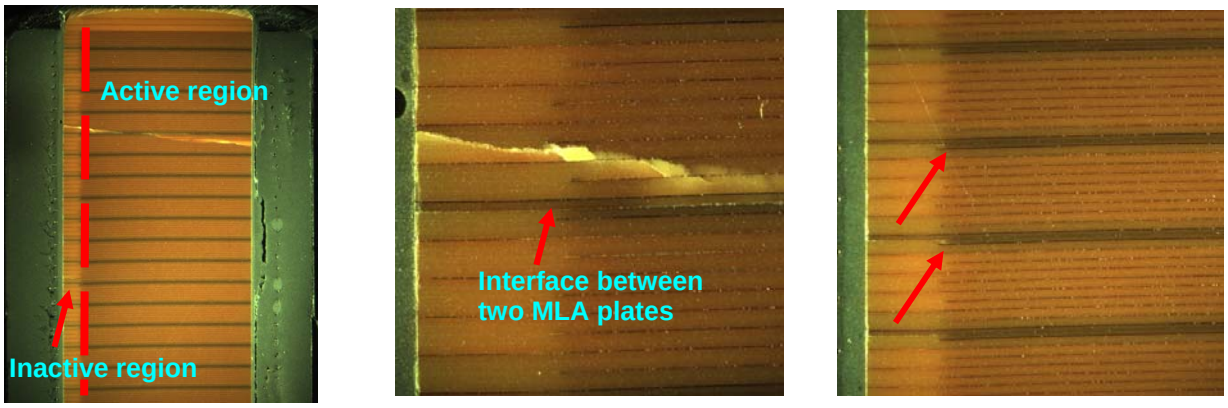

(a) (b) (c)

Fig. 11. (a) Optical micrograph of the cross section of stack No. 05 fatigued 10^8 cycles, (b) local area near interface between two MLA plates and the extended crack, and (c) micro-cracks developed around the transition between inactive and active regions near the relevant MLA plate interfaces.

4) humidity around 80% (depending on the recommendation from Cummins).
The fatigue facility for testing EPCOS will be modified also to include the corresponding requirements, especially the effect of temperature more than 150^{o}C and humidity around 80%, and the tested humidity level again depends on the recommendation from Cummins.
At the same time, the microstructure analysis will be performed on the failed (supplied by Cummins) and fatigued stacks using the sequential polishing technique developed at ORNL [7].
Finally, the work will be initiated on the finite element analysis to include the above generated data into the probabilistic design for one of recommended stack configurations.

References

1. Wang, H. and Wereszczak, A. A., Effects of electric field on the biaxial strength of poled PZT, *Proc. 31st Int. Conf. on Adv. Ceramics and Composites*, Jan. 21-26, 2007, Daytona Beach, FL; also on Advances in Electronic Ceramics, *Ceram. Eng. Sci. Proc.*, 28 (8), 2007, 57-67.
2.Wang, H. and Wereszczak, A. A., Effects of electric field and biaxial flexure on the failure of poled lead zirconate titanate, *IEEE Trans. Ultrasonic, Ferroelectrics, and Frequency Control*, 55 (12), 2008, 2559-2570.
3. Timoshenko, S. P. and Goodier, J. N., Theory of Elasticity, McGraw-Hill Int. Editions, 1970. p. 288-290.
4. Wang, H., Lin, H.-T., and Wereszczak, A. A., Strength properties of poled PZT subjected to biaxial flexural loading in high electric field, submitted to *J. Am. Ceram. Soc.*, 2009.
5. Wang, H., Wereszczak, A. A., and Lin, H.-T., Fatigue response of a PZT multilayer actuator under high-field electric cycling with mechanical preload, *J. Appl. Phys.*, 105 (1), 2009, 014112.
6. Wang, H., Lin, H.-T., Cooper, T. A., and Wereszczak, A. A., Mechanical strain and piezoelectric properties of PZT stacks related to semi-bipolar electric cyclic fatigue, *Proc. 33rd Int. Conf. on Adv. Ceramics and Composites*, Jan. 18-23, 2009, Daytona Beach, FL; also on Advances in Electronic Ceramics II, *Ceram. Eng. Sci. Proc.*, 30 (9), 2009, 53-63.
7. Wang, H., Cooper, T. A., Lin, H.-T., and Wereszczak, A. A., Fatigue responses of PZT stacks under semi-bipolar electric cycling with mechanical preload, to be submitted to *J. Appl. Phys.*, 2009, in review.
8. Wang, H., Matsunaga, T., and Lin, H.-T., Characterization of poled single-layer PZT for piezo stack in fuel injection system, to be submitted to *Proc. 34th Int. Conf. on Adv. Ceramics and Composites*, Jan. 24-29, 2010, Daytona Beach, FL.
9. Makino, H. and Kamiya, N., Effect of dc electric field on mechanical properties of piezoelectric ceramics, *Jpn. J. Appl. Phys.*, 33, 1994, 5323–5327.

Presentations and Publications

Presentations

1. Lin, H.-T., Wang, H., Wereszczak, A. A., Memering, D., Carmona-Valdes, J., and Stafford, R., Design optimization of piezoceramic multilayer actuators for heavy duty diesel engine fuel injectors, *1st Meeting on ORNL-Cummins CRADA*, Aug. 10, 2009, Oak Ridge, TN.
2. Wang, H., Lin, H.-T., Wereszczak, A. A., and Cooper, T. A., Mechanical strain and piezoelectric properties of PZT stacks related to semi-bipolar electric cycling fatigue, *33rd Int. Conf. on Adv. Ceramics and Composites*, Jan. 18-23, 2009, Daytona Beach, FL.

Publications

1. Wang, H., Cooper, T. A., Lin, H.-T., and Wereszczak, A. A., Fatigue responses of PZT stacks under semi-bipolar electric cycling with mechanical preload, to be submitted to *J. Appl. Phys.*, 2009.
2. Wang, H., Lin, H.-T., and Wereszczak, A. A., Strength properties of poled PZT subjected to biaxial flexural loading in high electric field, submitted to *J. Am. Ceram. Soc.*, 2009.
3. Wang, H., Lin, H.-T., Cooper, T. A., and Wereszczak, A. A., Mechanical strain and piezoelectric properties of PZT stacks related to semi-bipolar electric cyclic fatigue, *Proc. 33rd Int. Conf. on Adv. Ceramics and Composites*, Jan. 18-23, 2009, Daytona Beach, FL, also on Advances in Electronic Ceramics II, *Ceram. Eng. Sci. Proc.*, 30 (9), 2009, 53-63.
4. Wang, H., Wereszczak, A. A., and Lin, H.-T., Fatigue response of a PZT multilayer actuator under high-field electric cycling with mechanical preload, *J. Appl. Phys.*, 105 (1), 2009, 014112.

5. Wang, H. and Wereszczak, A. A., Effects of electric field and biaxial flexure on the failure of poled lead zirconate titanate, *IEEE Trans. Ultras., Ferroelec., and Freq. Contr.*, 55 (12), 2008, 2559-2570.

Agreement 17058 – Compact NO_x Sensor with Built in Reference– (formerly Agreement 9010 – Joining of Advanced Materials by Plastic Deformation)

Principal Investigator: J. L. Routbort (co-workers: D. Singh, Kristen Pappacena)
Argonne National Laboratory
9700 S. Cass Avenue
Argonne, IL 60439-4838
(630) 252-5065; fax: (630) 252-5568; e-mail: routbort@anl.gov

DOE Technology Manager: Jerry L. Gibbs
(202) 586-1182; fax: (202) 586-1600; e-mail: jerry.gibbs@ee.doe.gov

Contractor: UChicago Argonne LLC
Contract No.: DE AC03 06CH11357

Objective

- Join advanced materials such as ceramics, cermets, intermetallics, composites, biomaterials, etc. by plastic deformation, collaborate with industry and universities to produce sensors
- Investigate grain rotation that is assumed to occur during grain–boundary sliding resulting in deformation bonding
- Use joining technique to produce compact oxygen and NO_x sensors with internal reference

Approach

- Apply a modest compressive load to two pieces of similar or dissimilar materials that have had little surface preparation in the temperature region where the materials are known to deform by grain-boundary sliding
- Measure strength of the interface by 4-point bend tests and compare to theory
- Use electron back-scattered diffraction to measure grain rotation as a function of strain
- Perform Advanced Photon Source experiment to measure grain rotation as a function of strain
- Use joining technique to produce gas sensors with sealed internal references
- Produce gas-tight seals to isolate a metal/metal-oxide powder inside a yttria-stabilized zirconia container to produce oxygen and NO_x sensors

Accomplishments

- Strong, pore-free joints have been made with various ceramics, cermets, intermetallics, composites, and biomaterials, with and without various interlayers, fracture occurs away from interface at the region of maximum residual stress
- Demonstrated that grains in $SrTiO_3$ rotate during deformation
- Published 25 journal papers, 2 patents issued for plastic joining process, patent applications filed for oxygen and NO_x sensor, negotiations for licensing of oxygen sensor started
- R&D 100 Award for oxygen sensor
- Developed initial NO_x sensor
- Developed electrically conducting ceramic to replace Pt connections that will bond directly to sensor removing need for glass seal and providing a more robust, higher temperature sensor

Future Direction

- Program transitioned from deformation joining to applications to produce sensors, initially concentrating on improvements of the preliminary NO_x sensor reported in FY08.

Introduction

Monitoring gas composition, like O_2, NO_x, CO, CO_2, in the combustion environment with good accuracy has been of great importance since the advance of combustion heat engines in the last century. For instance, controlling the oxygen level in boilers carefully can maximize energy output and minimize pollutant emissions. It is estimated that yearly savings of $409 million from coal-fired power plants could be saved through combustion optimization. NO_x ($NO + NO_2$) sensing has also been considered as one of the key elements of next generation internal combustion engines. A reliable and accurate NO_x sensor is needed to monitor NO_x and trigger the regeneration of NO_x adsorption catalysts, or control the injection of reductants for continuous NO_x reduction.

Previously we have demonstrated that it is possible to form pore-free, high-strength joints in yittria-stabilized zirconia (YTZP) by applying a small stress at elevated temperatures ($T/T_m \approx 0.5$, where T_m is the melting temperature in K [1,2]. This technique has been used to produce oxygen sensors by encapsulating a metal/metal oxide powder in a container consisting of a lower YTZP disk, joined to an YTZP cylinder [3]. A metal/metal oxide powder is placed in the cavity that is then sealed by plastic joining to another YTZP disk to which is attached a thin Pt electrode top and bottom side. When placed in a combustion environment, the metal/metal oxide powder decomposes to produce oxygen. The difference between the internal oxygen activity (the reference) and that of the activity of the gas to be measured produces an emf that is proportional to $\ln(a_O/a_{Oref})$ where a_o is the oxygen activity of the gas to be measured and a_{oref} is the activity of the reference gas.

This technique has been applied to produce NO_x sensors [4] that could enable simultaneous measurements of NO_x and O_2 in a combustion environment. The Pd/PdO-containing reference chamber was sealed within the stabilized zirconia superstructure by a high pressure/temperature bonding method that initiated grain boundary sliding between the ceramic components. NO_x sensing was conducted in both amperometric and potentiometric modes. Pt-loaded zeolite Y was used to obtain total NO_x capacity and to cover Pt electrodes for detecting oxygen in the presence of NO_x. Both amperometric and potentiometric type sensors will eventually be tested for signal stability, total NO_x response, and NO_x-O_2 cross interference.

The glass that was used to seal the internal Pt wire limited the operating temperature of the O_2 and the NO_x sensor. This FY we have developed an electrically conducting ceramic $La_{0.77}Sr_{0.20}Al_{0.9}Mn_{0.1}O_3$ (LSAM) that can be directly joined to the YTZP eliminating the need for the internal Pt wire and producing a much more robust sensor with higher temperature capabilities.

In the present work, a highly Al doped polymorph of LSAM is joined to YTZP by plastic flow without any special preparation of the mating surfaces. The microstructure of the interface is examined by electron microscopy. Raman spectroscopic maps of the joining planes are employed to look for chemical reactions between the starting materials and the possible creation of new phases at the interlayers. In this manner, a method of bonding wholly dissimilar components for use in high-temperature environments is enabled. While this highly Al-doped perovskite may be unsuitable as an electron carrier [3], successful joining of LSAM to YTZP sets the stage for using more conducting forms of LSAM as an alternative to conventional electrodes in high-temperature applications.

Experimental Details and Results

Preparation and characterization of sensor materials

Details of the preparation and characterization of the LSAM and joining to YTZP can be found in ref. [5] and hence only the highlights will be summarized in

this annual report. The sensor with the LSAM electrode is shown in Fig. 1.

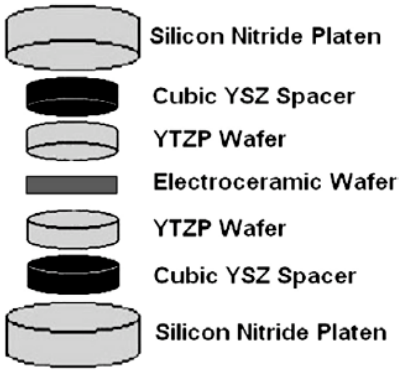

Figure 1. YTZP/LSAM/YTZP joint fabrication scheme. Cubic YSZ spacers and Si_3N_4 platens were removed following joining.

The $La_{0.77}Sr_{0.20}Al_{0.9}Mn_{0.1}O_3$ as determined from XRD of the powders indicated that there were no major impurity phases and that the material was a single phase ceramic. Joining was best achieved between the YTZP and the LSAM 92% theoretical dense pellet between 1250°C and 1350°C at a stress of 3-6 MPa as shown in Fig. 2.

SEM was performed on the joint to determine the effectiveness of the joining procedure. Fig. 3 indicates that joining LSAM to YTZP produces a good gas-tight bond. The crack in the figure deviates away from the joint and was the result of sectioning the sample for SEM with the perovskite structure.

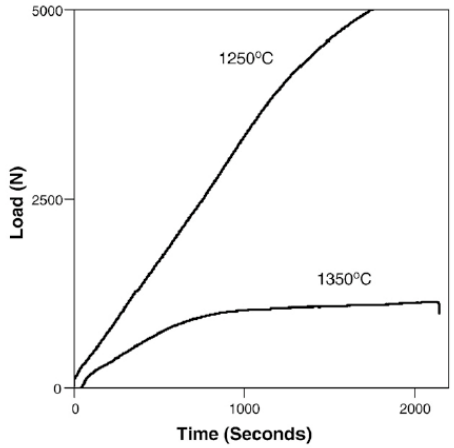

Figure 2. Load-deflection data for joining LSAM to YTZP.

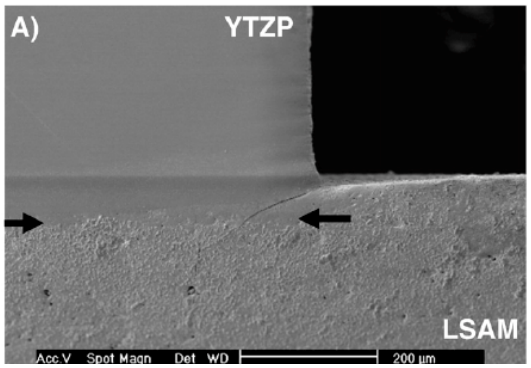

Figure 3. Joining plane of LSAM to YTZP at 1250°C. Arrows denote joining plane. Note crack does not go through the joining plane.

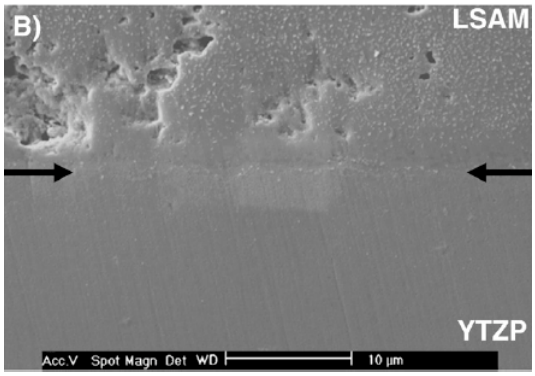

Figure 4. Joining plane of LSAM to YTZP at 1350°C. Arrows denote joining plane.

Raman spectral maps of the joining planes obtained with 2-D Raman microscopy were used to determine if there were any detrimental reactions between the LSAM and the YTZP. Results are shown in Figure 5 demonstrate that there the absence of any new phases at the interface.

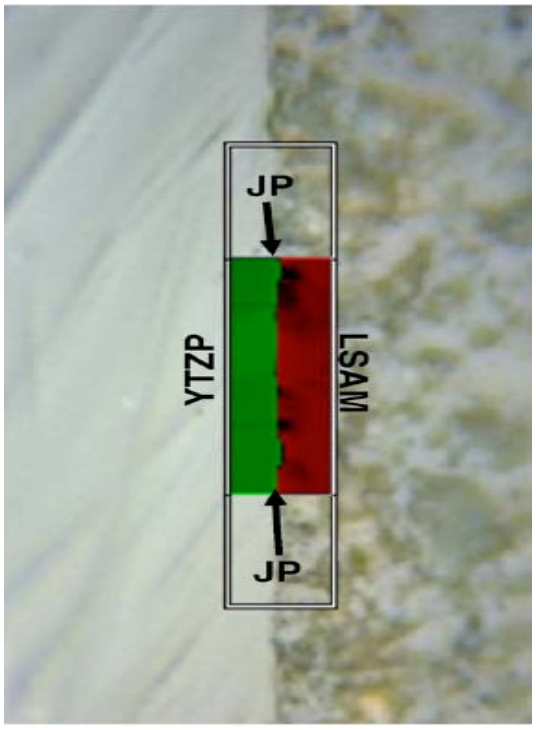

Figure 5. Raman map of YTZP/LSAM interface formed by joining at 1350°C.

Raman peaks from the LSAM bulk that match that of the unjoined LSAM are highlighted in red. The spectrum is shown in the top of Fig. 6. The joining plane spectrum is shown in the middle of Fig. 6. The laser focus is 1 µm and moved along the joining plane in 0.5 µm increments. Therefore, it is possible to identify new compounds at the interface by changes in spectral features. Based on the sharp Raman spectral transition and the absence of any new Raman bands, we conclude no $La_2Zr_2O_7$ or other phases are present in the joining plane. The lack of $La_2Zr_2O_7$ in the joining plane is important in the creation of durable joints as $La_2Zr_2O_7$ exhibits a significantly different thermal expansion coefficient than that of stabilized zirconia and would limit the operating temperature of the sensor.

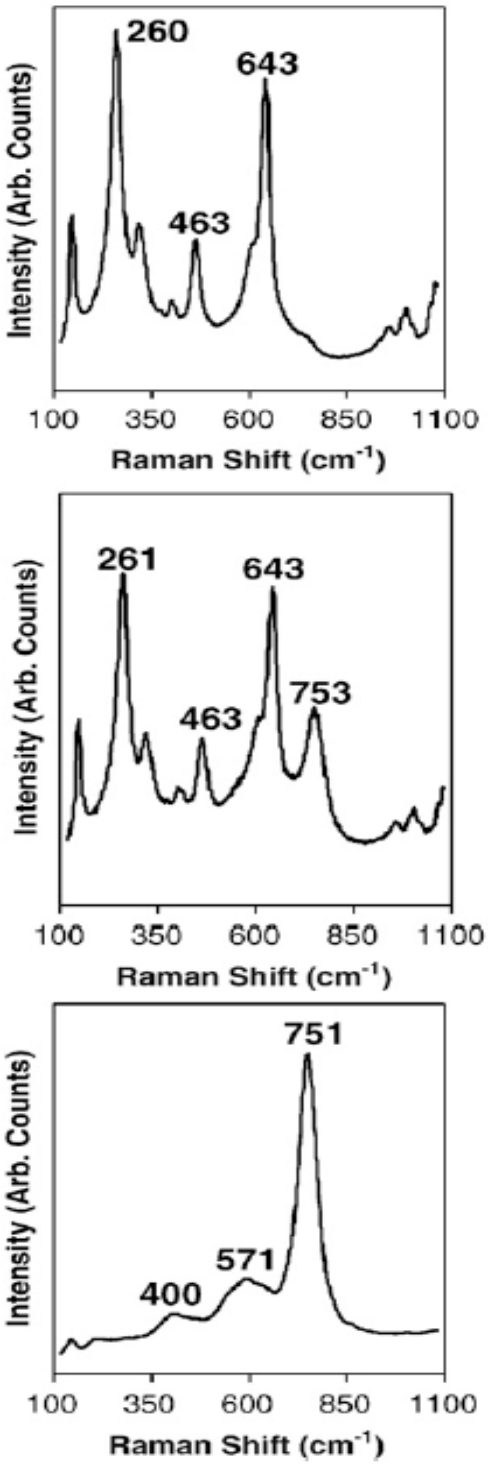

Figure 6. Representative spectrum of the joining plane denoted by JP in Fig 5.

Conclusion

$La_{0.77}Sr_{0.20}Al_{0.9}Mn_{0.1}O_3$ exhibits plasticity in the same temperature and stress region as the YTZP allowing for the creation of pore-free joints via a lower-temperature alternative to diffusion bonding. Additionally, no surface preparation is necessary. The coefficient of thermal expansion of the LSAM is similar to that of YTZP allowing higher temperature operations and thermal cycling without crack formation. The high aluminum content of LSAM inhibits reaction with YTZP and therefore the production of an interlayer that would serve to diminish the quality of the joint.

Future Directions

The use of $La_{0.77}Sr_{0.20}Al_{0.9}Mn_{0.1}O_3$ as an electrode in place of Pt will simplify the construction of the NOx sensor in that the external wires can be placed on the outside of the sensor eliminating the glass seal. A postdoc who did her Ph.D. at Northwestern University has been hired to assist in the development of the NO_x sensor to the point of commercialization. There are several improvements to make, in particular the choice and optimization of the catalytic filter, metal/metal oxide reference, and materials that give maximum sensitivity. The LSAM has not yet been incorporated in the construction of a sensor and the Al content must be optimized to give maximum electrical conductivity without resulting in deleterious phase formation.

A controlled NO_x test chamber will also be required for testing sensitivity, establishing cross-interference in O_2 and NOx signals, and evaluating long-term drift and stability of the sensors.

Acknowledgements

This work formed part of a Ph.D. thesis, by Jiun-Chan Yang and John Spirig at Ohio State University. Their supervisor was Professor Prabir Dutta of the Chemistry Department of OSU.

References

1. F. Gutierrez-Mora, A. Dominguez-Rodriguez, J. L. Routbort, R. Chaim, and F. Guiberteau, "Joining of Yttria-tetragonal Stabilized Zirconia Polycrystals using Nanocrystals," Scripta Mater. **41** 455-60 (1999).
2. F. Gutierrez-Mora, K. C. Goretta, S. Majumdar, J. L. Routbort, M. Grimdisch, and A. Domínguez-Rodriguez, "Influence of Internal Residual Stresses in Superplastic Joining of Zirconia Toughened Alumina," Acta Mater. **50** 3475-3486 (2002).
3. J. V. Spirig, R. Ramamoorthy, S. Akbar, J. L. Routbort, D. Singh, and P. K. Dutta, "High-temperature Zirconia Oxygen Sensor with Sealed Metal/Metal Oxide Internal Reference", Sensors and Actuators B **124**, 192-201 (2007).
4. Jiun-Chan Yang, John V. Spirig, Dale Karweik, J. L. Routbort, Dileep Singh, and P. K. Dutta, "Compact electrochemical bifunctional NO_x/O_2 sensors with metal/metal oxide internal reference for high-temperature applications" Sensors and Actuators, B **131**(2), 448-454 (2008) ***Patent application pending***
5. J. V. Spirig, J. L. Routbort, D. Singh, G. King, P. M. Woodward and P. K. Dutta, "Joining of highly aluminum-doped lanthanum strontium manganese oxide with tetragonal zirconia by plastic deformation, Solid State Ionics **179**, 550-557 (2008) ***Patent application pending***.

Agreement 13332 - Friction and Wear Reduction in Diesel Engine Valve Trains

Peter J. Blau
Oak Ridge National Laboratory, P. O. Box 2008, Mail Stop 6063
Oak Ridge, TN 37831-6063
(865) 574-5377; fax: (865) 574-6918; e-mail: blaupj@ornl.gov

DOE Technology Manager: Jerry L. Gibbs
(202) 586-1182; fax: (202) 586-1600; e-mail: Jerry.gibbs@ee.doe.gov
ORNL Technical Advisor: D. Ray Johnson
(865) 576-6832; fax: (865) 574-6098; e-mail: johnsondr@ornl.gov

---

Contractor: Oak Ridge National Laboratory, Oak Ridge, TN
Prime DOE Contract Number DE-AC05-00OR22725

Objectives

- To provide an improved understanding of wear processes in valves that will better enable the selection and use of materials for exhaust valves and seats in energy-efficient diesel engines.
- To design a specialized high-temperature, repetitive impact (HTRI) apparatus and use it to investigate the combined effects of mechanical contact, high temperatures, and oxidizing environments on the durability of high-performance diesel engine valve materials.
- To design and develop a wear model for exhaust valves.
- To develop consensus-based testing standards that enable more realistic bench-scale measurements of diesel engine component durability and energy efficiency.

Approach

- Identify exhaust valve operating conditions; then design a high-temperature repetitive impact valve materials testing system to simulate that type of contact damage. The system should be capable of testing actual valves as well as simpler specimens of candidate valve materials.
- Conduct experiments to investigate the oxidation and re-oxidation of high-performance metallic alloys when subjected to wear at temperatures experienced by diesel engine valves.
- Develop an exhaust valve wear model which reflects the conjoint, non-linear effects of wear, deformation, oxidation, and high temperature.

Accomplishments

- A high-temperature, repetitive impact (HTRI) testing system was designed and built. It is capable of operating at temperatures up to 850^{o}C. Using several different geometric configurations, the HTRI can be used to test actual valves or simple test coupons.

- Research on Fe-, Ni-, and Co-based alloys demonstrated that prior abrasion damage affects the ability of contacting surfaces to form protective scales at high temperatures.

- To provide data for the valve wear model, the friction coefficient was measured as a function of temperature up to 850^{o} C for a commercial exhaust valve material against a seat material.

- Based on past literature, experiments conducted over the course of this work, and examinations of used valves, an exhaust valve wear model was developed. It involves the conjoint effects of deformation and abrasion of mechanically-mixed oxide layers.

- Assembled test materials, recruited participants, and worked with ASTM International to lead an interlaboratory study on ASTM standard test method G 181, whose development was supported by OVT. The standard measures friction of piston rings against cylinder materials in oil conditions simulating diesel engine environments.

Future Directions

- This project concluded in FY 2009. Additional presentations and publications on this work are planned.

Introduction

Currently, heavy truck diesel engine designers face two important challenges: (a) to improve overall fuel efficiency, and (b) to meet increasingly strict emissions regulations while keeping manufacturing and maintenance costs affordable to owners and operators. Concepts like homogeneous charge compression ignition, advanced engine control systems, and exhaust gas after-treatment are being employed, but such approaches affect the mechanical, thermal and chemical environments to which engine materials are exposed. Current materials and surface treatments may fall short of meeting those needs, leading to decreased durability.

The objective of this effort was to enable the selection and use of durable moving parts in diesel engine components: specifically exhaust valves. The approach draws on past studies, wear-oxidation experiments, the simulation of valve wear conditions in a custom-designed laboratory system, and finally, the development of a multi-parameter valve-seat wear model.

Past tribology research has documented the complexity of surface degradation processes that occur on engine valves and seats (for example, see Fig. 1). A literature study was conducted to support the rationale employed in the current work, and especially, to facilitate the development of a valve wear model, described in this report.

Figure 1. Used diesel engine exhaust valve sealing surface showing the combined effects of corrosion, deformation, and wear.

Over the course of this project, three journal articles and four presentations were produced. In addition, a final report

describing the wear model, to be published as an ORNL technical report, is under final review. ASTM G 181 a standard test method for piston ring on liner friction under also was developed as a consequence of DOE/OVT support, and is briefly described.

Approach

A three-task approach was undertaken over the course of this project. The first two tasks were described in previous annual reports and publications, and will be briefly highlighted. The third task, a wear model, was completed during FY 2009, and is outlined in this report.

Task 1) Investigation of the effects of prior contact damage on high-temperature oxidation. Experimental work showed that high-temperature oxides that form on mechanically-damaged surfaces of alloys differ from those that form on the same surface in the absence of mechanical damage. Using Fe-based, Ni-based, and Co-based alloy as model materials, elevated temperature exposure of abraded surfaces was performed. Energy-dispersive x-ray elemental mapping revealed that the oxidation of wear-damaged surfaces does not produce the same scales as non-damaged surfaces (FY 2008 Annual Report). This work included micro-gravimetric oxidation studies on the same alloys, by B.A. Pint, Corrosion Science and Technology Group, ORNL.

Experimental findings on the role of surface damage on oxidation rates have implications for engine valves, where these processes occur in combination. Details may be found in References 2 and 3.

Task 2) Development of a high-temperature repetitive impact test system. In order to simulate the mechanics and oxidation of valves and seats, a high-temperature, repetitive impact (HTRI) testing system was designed and built. The system is described in the FY 2008 annual report, and will be presented at an international conference in October 2009 (see Ref. 5). The test system consists of a variable-speed drive motor with a roller-follower that raises and lowers a valve specimen onto two counterface blocks. The furnace chamber can produce temperatures up to 900^{o} C.

Task 4) Development of a valve wear model. The physical concept on which the model is based was predicated on (a) a literature review (provided as an Appendix in Ref. 6), (b) experimental work, and (c) examination of used exhaust valves and seats provided by an engine manufacturer. Output from the model is the cross-sectional area of the wear profile on a valve-seat interface, as shown schematically in Figure 2.

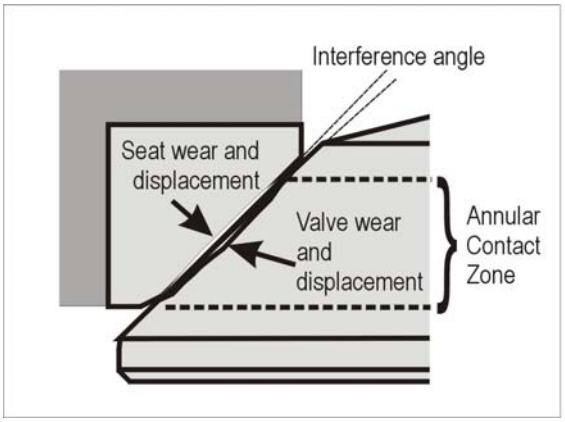

Figure 2. Profiles of the interface between the seating surface of a valve and its seat.

The form of the model is based on the observation that valves experience a combination of repetitive impact with slip. The impact causes deformation and the slip, abrasion. Complications enter because tribo-chemical factors (i.e., oxidation and exposure to corrosive gases), alloy aging, and temperature cycling can alter the contact surface conditions over the lifetime of the components. Since the profile of wear can differ at different circumferential locations even on the same valve, it was impractical to predict a specific shape of wear profile, but rather to present results in terms of the

cross-sectional area of material that has been lost or displaced in the valve-seat contact region from the conjoint action of deformation and abrasive wear.

In the course of valve operation, tribolayers can form. These, in effect, add material to the profile (compared with wear processes that simply subtract from the profile). Consequently, the model consists of four terms which describe the cycle-dependent deformation and abrasion of the valve and the seat, respectively. In recognition that different engines perform differently, the rate of surface displacement and wear can be varied during the initial wear-in process, by using adjustable rate constants and incubation periods. In addition, the insert angle can be varied in the model to accommodate that design variable. The seat angle is known to affect the contribution of sliding wear to valve seat recession.

The general form of the model is:

$$A_p(n) = A_{disp}(n)]_{valve} + A_{disp}(n)]_{seat} + \mu_T p c_{a4} \{k^*_{valve}[S(n)]_{valve} + k^*_{seat}[S(n)]_{seat}\}$$

where,

$A_p(n)$ = area of the profile after n cycles

$A_{disp}(n)]_{valve}$ = area of the profile due to valve surface deformation

$A_{disp}(n)]_{seat}$ = area of the profile due to seat deformation

μ_T = interfacial friction coefficient as a function of temperature

p = cylinder pressure

c_{a4} = a geometrical constant related to the seat angle and the annular contact area of the seating face

k^*_{valve} = the post run-in abrasive wear rate of the valve face with a 45° seat angle

$[S(n)]_{seat\ or\ valve}$ = cumulative slip distance in the interface

k^*_{seat} = the post run-in abrasive wear rate of the seat face with a 45° seat angle

In order to provide realistic data for the friction coefficient as a function of temperature, experiments were conducted in the high-temperature sliding friction and wear testing system at ORNL up to 850°C using two typical valve component alloys, Pyromet 31V and a Co-based seat alloy. The friction versus temperature response of this alloy couple could be represented as a polynomial function for use in the model. Further details on the individual terms in the model, and their rationale, will be described in the final report (Ref. 6).

A sample plot of number of kilocycles of contact versus the worn cross section is shown in Figure 3. Individual contributions from the seat and valve face are shown. This case assumes a temperature of 750°C with a 45 degree seat angle and no contribution from the deformation of the seat. The abrasion rate of the seat was assumed to be 1/3 that of the valve, and the incubation period for abrasion for the seat was twice that of the valve. The reason for the different in incubation periods for seat and valve presume that the seat is more abrasion resistant than the valve, and would begin to abrade only after wear particles from the valve built up to a sufficient concentration to have an effect on the seat surface wear.

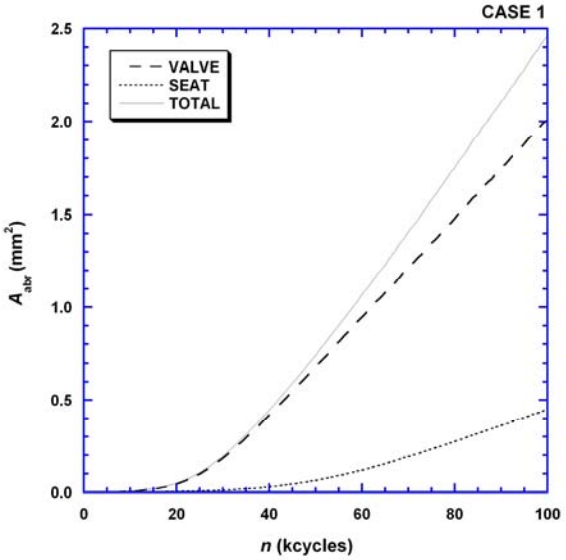

Figure 3. Cross-sectional area of valve wear as a function of thousands of cycles.

Wear Test Methods and Standardization. An ASTM inter-laboratory study (ILS), to complete the development of a consensus standard (ASTM G181) for friction testing of oil-lubricated piston ring and liner materials, was organized with support from this project. A quantity of used diesel engine test oil was obtained from Southwest Research Institute. International participants in the study include a diesel engine maker, an oil company, three tribology testing machine makers, a British university, and ORNL. Completion of the study is expected by the end of CY 2009, after which ASTM G 181 will be re-balloted for final approval. Even in its pre-approval form, this test is being used by diesel engine makers.

Summary and Conclusions

- This project used a three-pronged approach to understand and model the wear-oxidation-deformation processes involved in exhaust valve wear.
- A high-temperature repetitive-impact diesel engine valve material testing system was been constructed and used to generate mechanically-mixed metal-oxide layers like those observed on valves.
- Research demonstrated the effects of mechanical damage on the re-oxidation of model Fe-, Ni-, and Co-based alloys.
- A model for the effects of abrasive wear, deformation, and high-temperature frictional contact on exhaust valves and seats was developed.
- A new ASTM standard is being completed for measuring the friction of candidate materials for piston rings and cylinder liners under engine-conditioned lubricants..

Publications/Presentations

1) P. J. Blau: “The Many Faces of Scuffing: Mechanisms, Measurements, and Control,” invited paper, Annual Meeting of the Society of Tribologists and Lubrication Engineers (STLE), May 8, 2008.

2) P. J. Blau and T. M. Brummett: “High-Temperature Oxide Regrowth on Mechanically-Damaged Surfaces,” *Tribology Letters*, Vol. 32 (3) (2009) pp. 153-157

3) P. J. Blau, T. M. Brummett, and B.A. Pint: “Effects of prior surface damage on high-temperature oxidation of Fe-, Ni-, and Co-based alloys,” pres. at the 2009 International Conference on Wear of Materials, April 19-22, 2009, and published in *Wear*, Vol. 267 (2009) pp. 380-386.

4) P. J. Blau: “Elevated Temperature Tribology of Metallic Alloys,” invited presentation 2nd Intl. Conf. on Tribo Corrosion, Wiener Neustadt, Austria, March 17-18, 2009 (paper to be published in a special issue of *Tribology International*.)

5) P. J. Blau and B. C. Jolly: “Development of a High Temperature, Repetitive Impact Apparatus for Valve Material Testing,” accepted for pres. at the International Joint Tribology Conference Memphis, TN, October 19-22, 2009.

6) P. J. Blau: “A Wear Model for Diesel Engine Exhaust Valves,” ORNL Tech Report, 31 pp. (draft under review).

Agreement 15050 – MaterialsTesting with ACERT Engine (CRADA with Caterpillar)

M. D. Kass, T. J. Theiss, R. Wagner, and N. Domingo
Fuels, Engines and Emissions Group
Oak Ridge National Laboratory
NTRC Building
2360 Cherahala Blvd.
Knoxville, TN 37932
(865) 946-1241; fax: (865) 946-1354; e-mail: kassmd@ornl.gov

H. T. Lin
Ceramic Science and Technology Group
Oak Ridge National Laboratory
P.O. Box 2008, MS 6068, Bldg. 4515
Oak Ridge, TN 37831-6068

DOE Technology Manager: Jerry L. Gibbs
(202) 586-1182; fax: (202) 586-1600; e-mail: Jerry.gibbs@ee.doe.gov
ORNL Technical Advisor: D. Ray Johnson
(865) 576-6832; fax: (865) 574-6098; e-mail: johnsondr@ornl.gov

Contractor: Oak Ridge National Laboratory, Oak Ridge, Tennessee
Prime Contract No.: DE-AC05-00OR22725

Objectives

- Improved diesel engine performance, efficiency, and emissions through the applications of materials enabled technologies.
- Evaluate material/component performance on a heavy-duty diesel engine platform.

Approach

- Install 2004 Caterpillar C-15 ACERT instrumented for thermal and combustion analysis and modified for dynamometer experimentation.

Accomplishments

- Commissioned test cell infrastructure, engine, and dynamometer.
- Completed engine break-in..

Future Direction

- Install and commission power-factor correction system
- Perform engine baseline experimentation to confirm operating parameters with Caterpillar.
- Evaluate component/material performance and durability for at least one critical component.

Introduction

The purpose of this Cooperative Research and Development Agreement between UT-Battelle, Inc. and Caterpillar, Inc. is to improve diesel engine performance, efficiency, and emissions through the application of materials-enabled technologies. The demands of meeting new emissions and fuel economy goals are continuing to push heavy-duty diesel engine components to higher temperatures and pressures and improved durability. Engine manufacturers have recognized several key needs that need to be addressed in order for heavy duty diesel engines to achieve an national efficiency goal of 55% by the year 2012. These include 1) improved structural materials to accommodate higher cylinder pressures and temperatures (associated with advanced combustion methodologies), 2). improved thermal management and waste heat recovery technologies, 3) improved durability, 4) improved transient performance, and 5) better aftertreatment performance. These needs address barriers associated with high parasitic losses, high-efficiency clean combustion and thermal management of the cylinder and exhaust.

This CRADA brings together expertise and facilities from the ORNL Materials Science & Technology and Engineering & Transportation Science Divisions. Similarly, materials and engine research staff at Caterpillar are also working together. In anticipation of this CRADA, Caterpillar provided ORNL with two 600 hp motoring dynamometers and C15 ACERT engine. Caterpillar (working with ORNL) will develop and provide components to be evaluated on the engine platform. ORNL engine research staff will evaluate the engine performance with emphasis on combustion diagnostics, optimization and modeling. Materials scientists at ORNL will examine material performance and provide guidance to materials development.

Results

The original Cell 7 infrastructure was removed and modification commenced immediately afterwards. A control room was installed to separate the operators from the operating machinery. Cooling water and room ventilation capable of handling large heavy duty diesel engines was installed along with the bedplates. The dynamometer was placed on the bedplates and the wiring to the control panel was completed. At the completion of the research cell infrastructure, the engine was mounted and aligned with the dynamometer as shown in Figure 1.

Figure 1. *Photograph showing mounted engine and dynamometer. The control room is on the other side of the wall on the left of the photograph and behind the dynamometer.*

The calibration gas rack and accompanying plumbing were completed and two fuel tanks have been setup outdoors as shown in Figure 2.

Figure 2. *Photograph showing fuel tanks (left) and the calibration gas racks (right) used for engine and cell operation.*

The engine and exhaust system were instrumented for temperature and pressure measurement. This instrumentation is necessary to perform the detailed thermodynamic analysis necessary to identify areas of potential efficiency gains. The engine and dynamometer were successfully commissioned in April and the engine was operated according to the Caterpillar break-in cycle to degreen the engine. During high-load operation, the electrical feedback was found to be out-of-phase with the utility power. A power-factor correction system has been procured

and is currently being installed. After the power-factor correction has been demonstrated, engine baseline operation will begin.

Conclusions

The test cell infrastructure, engine, and dynamometer were successfully commissioned. Once the power-factor correction system has been installed and operational, engine baseline experimentation will commence.

Agreement 15054 - Fatigue Enhancements by Shock Peening

Principal Investigators: Curt A. Lavender and Elizabeth V. Stephens
Energy Materials Group
Pacific Northwest National Laboratory
PO Box 9998, MS K2-44
Richland, WA 99352
(509) 372-6770; fax: (509) 375-2186; e-mail: curt.lavender@pnl.gov
(509) 375-6836; fax: (509) 375-4448; e-mail: elizabeth.stephens@pnl.gov

Yong-Ching Chen
Cummins Inc.
(812) 377-8349; e-mail: yong-ching.c.chen@cummins.com

DOE Technology Manager: Jerry L. Gibbs
(202) 586-1182; fax: (202) 586-1600; e-mail: jerry.gibbs@ee.doe.gov

Field Technical Manager: Mark T. Smith
(509) 375-4478; fax: (509) 375-4448; e-mail: mark.smith@pnl.gov

---

Contractor: Pacific Northwest National Laboratory
Contract Number: DE-AC05-76RL01830

Objective

- Evaluate the capability for surface modification techniques such as laser shock peening (LSP), water jet peening (WJP), and friction stir processing (FSP) to improve the fatigue performance of steel, aluminum, and cast iron engine components.
- Evaluate the fatigue performance impact offered by these surface treatments to induce compressive residual stresses and to modify microstructure in the surface of aluminum, steel, and cast iron engine components.
- Compare fatigue performance and thermal stability of these novel surface treatment approaches to traditional shot peening methods.

Approach including industrial partner/collaborator and path to technology transfer and commercialization

Industrial Cooperative Research and Development Agreement (CRADA) Participant: Cummins Inc., Columbus, IN (Dr. Yong-Ching Chen; Jeffrey Cooper)

Technology Development

- Demonstrate that surface treatments can induce deep subsurface compressive residual stresses in test specimens
- Characterize the stress distributions in test specimens as well as the surface roughness after treatments and compare to control specimens.
- Evaluate the mechanical properties of surface-treated bar specimens using rolling contact fatigue and rotating beam fatigue tests methods.
- Perform thermal stability tests of surface-modified specimens.
- Develop a cost model for process deployment.

Technology Transfer and Commercialization

- Cummins to demonstrate LSP and WJP surface modification approaches on a full-scale steel and/or aluminum components using engine systems qualification tests.
- Cummins/PNNL to develop and demonstrate a cost effective process sequence for LSP/WJP of a relative high-volume production.
- Cummins to disseminate technology benefits to product design and development groups.

Milestone, Metrics and Accomplishments

- **Milestone 1 –** Complete evaluation of improvements to M50 steel alloy fatigue life and distribute to DOE a progress report on results. (Milestone Complete). The material alloy of interest changed to a 52100 steel alloy (as recommended by the CRADA industrial partner) due to it being a more common material found in the fuel system. Further evaluation and characterization is currently being performed on this alloy. All limited work on the M50 alloy was documented and presented in the 2009 DOE Hydrogen Program and Vehicle Technologies Program Annual Merit Review
- Completed an additional population of LSP surface treatments with a ground finish for A354 aluminum specimens and characterized the surface stress distributions.
- Began parameter development for water jet peening of A354 cast aluminum.
- Fabricated and characterized friction welded cast iron bars to aid friction stir processing development of cast iron components.
- Completed selection of relevant test articles for friction stir processing/joining of cast iron.
- Continued with rotating beam fatigue tests of surface-modified specimens for both A354-T6 specimens and 52100 steel specimens.
- Continued with rolling contact fatigue tests of surface-modified 52100 steel specimens (Cummins).
- Identified potential component applications using LSP surface treatments and initiated prototype development (Cummins).

Future Direction

- Complete mechanical testing evaluations of specimens with novel surface treatment techniques to establish fatigue enhancement capability.
- Continue development of surface treatment techniques of cast iron material via friction stir processing/joining.
- Initiate thermal stability studies of surface modified 52100 steel.

Introduction

The primary objective of this project is to evaluate the impact of laser shock peening (LSP), water jet peening (WJP), and friction stir processing (FSP) on the fatigue performance of aluminum, cast iron, and steels. Fatigue performance is an important factor in propulsion materials, especially for fuel system components, cylinder heads and blocks, etc. With the advent of faster injector response and higher pressures for better control of combustion events, cam stresses are significantly increased leading to reduced contact and flexural fatigue life. Cyclic fatigue improvements of forming dies made from tool steels have been achieved by selectively applying compressive residual stresses at the surface. Methods to apply these stresses vary, but among them, LSP has been used successfully. Laser shock peening not only induces compressive residual stresses at the surface, improving cyclic fatigue life more than five times, but it has also been shown to decrease the susceptibility of steels to stress corrosion cracking. However, there are some uncertainties with the application of the LSP process for engine components: 1) knowing exactly where to

optimally apply the process based on part starting condition and ultimate performance requirements, and 2) the parameters required to effectively improve performance based on failure modes encountered.

For softer metals like aluminum, a lower-energy option that operates similarly to LSP is high-pressure WJP. This process is still in its infancy, but it has shown promise for improving fatigue performance in aluminum castings and wrought products with better control of residual stress distribution. Like that of LSP of high strength steels, the fatigue life enhancement mechanisms of WJP and optimum processing parameters are not yet well defined. Further understanding of the effects of LSP on aluminum alloys is also needed.

A cost and energy-efficient way of localized processing of metals to improve their fatigue life and wear resistance is by using FSP. This process is known to increase fatigue life by refining grain structure and homogenizing the microstructure of the metal, eliminating defects, if any, within the processed area. Porosity is inherent to a cast metal, and its strength is always lower than that of a forged metal. By friction stir processing the area of interest, forged properties can be attained in a cast component and low cost, high-strength castings can still be produced. This is ideal for applications like cylinder heads and blocks, where high strength and wear properties are desired in localized areas such as the combustion chamber, bolt hole bosses, etc. This process can deliver high strength in aluminum, cast iron, and steel. Significant challenges exist in understanding the effect of FSP process parameters on mechanical properties of high-temperature materials like steel and cast iron.

This project is a three-year development and demonstration effort and will include active participation by Cummins, Inc. In October 2007 (FY2008), a formal Cooperative Research and Development Agreement (CRADA) was established with Cummins. This fiscal year, work continued on evaluating the fatigue enhancements in steel and aluminum, process development of WJP surface modifications of aluminum, and FSP/joining of cast iron.

Experimental Characterization of A354-T6 Cast Aluminum

Laser Shock Peening Evaluation

During this reporting period, rotating beam fatigue testing of the A354 cast aluminum specimens continued. An additional LSP population with a stress-free/low-stress ground surface finish was added to the test matrix. Preliminary fatigue test results are shown in Figure 1. No surface finish was applied to the as-LSP specimens.

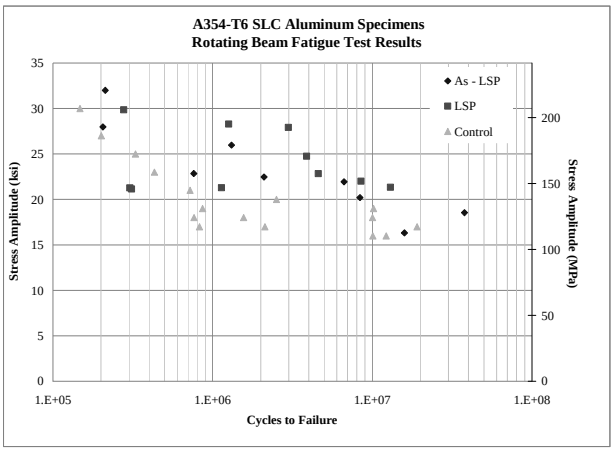

Figure 1. Preliminary fatigue test results of the A354-T6 aluminum specimens.

A slight improvement in fatigue life was observed when comparing the LSP specimens (regardless of surface finish) to the control specimens. Preliminary statistical analysis of the fatigue data was performed by Cummins utilizing their proprietary fatigue analysis software. The analysis indicated that the LSP and as-LSP specimens exhibited a significantly better fatigue strength at 10 million cycles in comparison to the control specimens at the 95% confidence level. However, no statistically significant difference was observed among the three populations at 100 million cycles. Much scatter in the LSP fatigue data was observed. Further evaluation of the failed specimens is needed to determine whether dispersed shrinkage porosity from the sub-liquidus casting process may be influencing the fatigue results.

As previously reported, the residual stress measurements (Figure 2) indicated deep stresses at nearly 70% of the compressive and tensile yield strength of A354. At depths of 0.5 mm

(millimeter), greater than 140 MPa (megapascal) compressive residual stress was observed in the as-LSP specimens. During this reporting period, stress distributions were determined for the LSP treated specimens with a surface finish. Figure 2 shows that much of the residual stress was retained in an LSP specimen when a low-stress ground finish was applied.

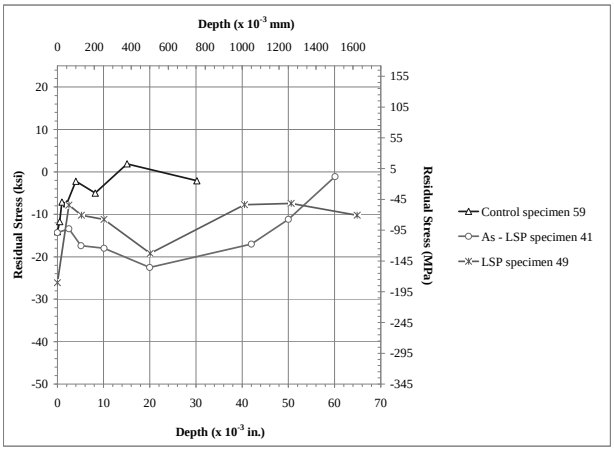

Figure 2. Comparison of the longitudinal residual stress distributions of A354 cast aluminum specimens.

Water Jet Peening Evaluation

Task 1 of the WJP evaluation was completed, and Task 2 is currently in progress. The WJP evaluation uses water jet technology for peening the A354 cast alloy to enhance its fatigue life. In Task 1, a screening of three water jet methods (methods A, B, and C) was performed. Similar processing conditions were applied to all specimens with the exception of increasing the supply pressure in the second processed specimen from each method. Figure 3 compares the overall visual appearance of the specimens processed. Comparable compressive surface stresses (~240 MPa) and similar surface roughness (<1 μm (micrometer) R_a) were observed in specimens from methods A and C. Based on overall visual appearance, surface roughness, and residual stress results, these two methods were subjected to further evaluations in Task 2.

In Task 2, a quadratic model design of experiments (DOE) was applied where the supply pressure, air pressure, stand-off distance, and traverse rate was varied to determine the optimum processing parameters from the promising methodologies determined in Task 1. Twenty-six runs were conducted, and residual stress measurements and 3-D surface profilometry was performed on each specimen processed. The maximum compressive stresses observed among the specimens ranged from 75 to 275 MPa, and the average R_a surface roughness measurements observed ranged from 0.8 to 7 μm.

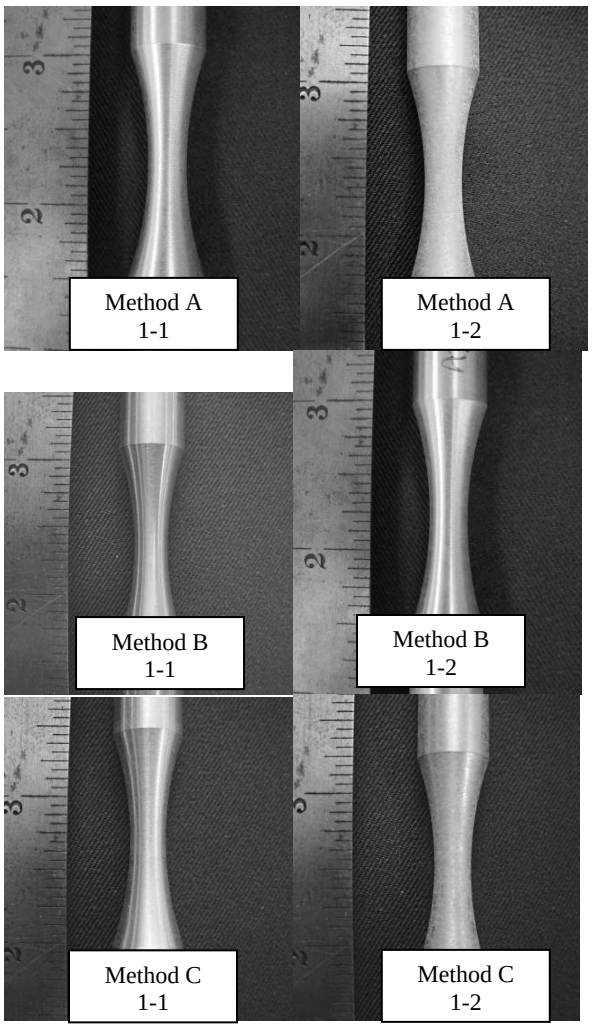

Figure 3. Surface finish comparisons of the WJP specimens processed by varying water jet methods.

Further DOE analysis is needed to evaluate the water jet methods applied. All results will be entered into the DOE to determine which method and process parameters produce an optimum finish and deep compressive stresses. Once the most promising method and processing parameters have been established, a set of rotating beam fatigue

specimens will be fabricated and processed with the parameters determined from Task 2.

Experimental Characterization of 52100 Steel

Rotating beam fatigue tests and rolling contact fatigue tests of 52100 steel specimens continued in FY09. As previously reported, four populations of 52100 steel rotating beam fatigue specimens were fabricated for evaluation. The populations consisted of baseline control specimens, LSP specimens, shot peened specimens, and shot peened specimens evaluated in the as-peened condition. A stress-free/low-stress ground surface finish (with an 8 μin. R_a value) was applied to the control specimens, LSP specimens, and shot-peened specimens. No surface finish was applied to the as-shot peened specimens.

A significant difference in fatigue life was observed particularly at high stresses when comparing the LSP specimens to the other populations (Figure 4). Further analysis of the data by Cummins indicated approximately a 12% improvement in high-cycle fatigue life of the LSP rotating beam specimens and approximately a 50% improvement in fatigue life of the LSP rolling contact fatigue specimens. These promising results have led Cummins to explore potential applications and to produce prototype components for further evaluations.

Thermal stability tests of the 52100 surface-treated specimens have also been initiated. One specimen from each processed condition, including the control, was held for two hours at each test temperature, 141°C and 246°C. The stress distributions will be characterized.

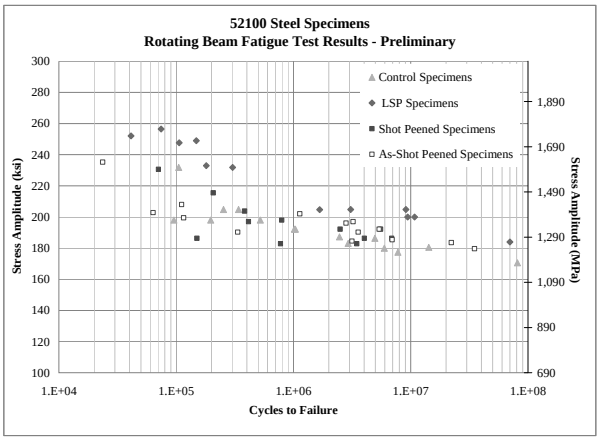

Figure 4. Preliminary fatigue test results of the 52100 steel specimens. No surface finish was applied to the as-shot peened specimens

Friction Stir Processing Development of Cast Iron

Round, grade 40 cast iron bars were friction welded together to further aid the FSP development of cast iron components. The friction welded rods were characterized to have a better understanding of the microstructural changes and property changes that may occur during welding. Three weld processing conditions were evaluated with two specimens prepared for each condition. Figure 5 shows a representative image of a friction welded rod and its respective cross section. Solid state bonding was observed between the two cast iron bars. Specimens were cut in half lengthwise for characterization.

Microhardness measurements were performed on one-half of each welded rod, and tensile specimens were prepared from the remaining half. Similar hardness measurements and comparable tensile strengths were observed in the friction welded rods in comparison to the parent material. Greater tensile strengths were observed in three of the welded specimens. Two of the welded rods (with similar processing conditions) both failed away from the weld centerline at the heat-affected zone/parent material interface.

(a)

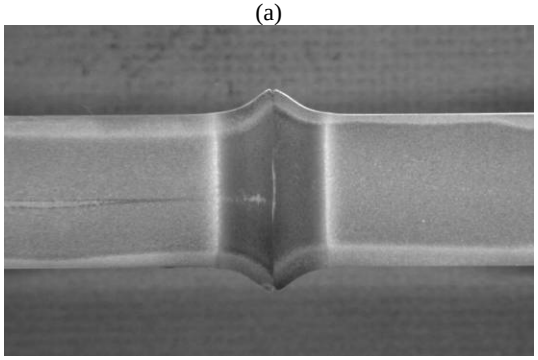

(b)

Figure 5. Representative image of two, round cast iron bars friction welded together to produce a welded specimen (a). Image (b) is an etched cross section of a welded rod.

Properties observed indicate that if we can successfully friction stir process cast iron, strength properties should be comparable or greater than the parent material.

Development of friction stir processing cast iron is currently ongoing. It is proving to be a difficult material to work with; however, development is focusing on achieving plasticization of the material.

Conclusions

During this reporting period, the following conclusions were derived:

- Water jet peening of A354 aluminum can produce surface compressive residual stresses while maintaining a required surface finish.
- Significant increase in fatigue life of the laser shock peened and ground 52100 steel specimens was observed in comparison to the shot-peened, as-shot peened, and control specimen populations.
- Promising results of the LSP 52100 steel specimens in both rotating beam fatigue and rolling contact fatigue have prompted Cummins to evaluate LSP prototype components.

The friction stir processing development of cast iron is ongoing, and further investigation of the water jet peening of A354 aluminums is under way.

Presentations/Publications/Patents

Cummins Internal Project Review, October 2008 and December 2008.

DOE Materials Technologies Project Review, January 2009.

DOE Hydrogen Program and Vehicle Technologies Program Annual Merit Review, May 2009.

Acronyms

CRADA: Cooperative Research and Development Agreement
DOE: Design of Experiments
FSP: Friction Stir Processing
LSP: Laser Shock Peening
mm: Millimeter
μm: Micrometer
MPa: Megapascal
WJP: Water Jet Peening

Agreement 15055 - Tailored Materials for High Efficiency CIDI Engines (CAT)

Principal Investigator: Glenn J. Grant
Energy Materials
Pacific Northwest National Laboratory
902 Battelle Blvd.
Richland, Washington 99356
(509) 375-6890; fax: (509) 375-4448; email: glenn.grant@pnl.gov

Nate Phillips
T&SD AMT–High Temp Materials
M. Brad Beardsley
Technology Leader–Surface Engineering
Caterpillar, Inc.
Technical Center Bldg. C-13, PO Box 1875
Peoria, Illinois 61656-1875
(309) 578-5788; cell: (309) 361-8309; email: Phillips_Nate@cat.com

DOE Technology Manager: Jerry L. Gibbs
(202) 586-1182; fax: (202) 586-1600; email: Jerry.gibbs@ee.doe.gov

Field Technical Manager: Mark T. Smith
(509) 375-4478; fax (509) 375-4478; email: Mark.smith@pnl.gov

---

Contractor: Pacific Northwest National Laboratory
Contract No.: DE-AC05-76RL01830

Objective

- To develop friction stir processing (FSP) to tailor the properties of conventional, low-cost engine materials (cast iron, alloy steels, and aluminum alloys) with the goal of increasing their high temperature performance, durability, and thermal properties.
- To deploy friction stir processed components that can enable energy efficient combustion strategies, especially those that will require higher peak combustion pressure or higher temperature operation.

Approach including partner/collaborator and path to technology transfer and commercialization

- This project will develop surface modification techniques, modified materials, and components. The project is a Cooperative Research and Development Agreement (CRADA) with Caterpillar, Inc., but also involves input from diesel piston suppliers.
- The project is primarily investigating FSP, a new technology that can produce functionally graded surfaces with unique and tailored properties that will allow propulsion materials to withstand higher temperatures and pressures without losing appreciable strength, hot hardness, or wear resistance, and exhibit improved resistance to thermal fatigue.
- FSP treated components will be evaluated and tested by the industry collaborators to demonstrate efficiency benefits and potential commercial applications

Milestones, Metrics and Accomplishments

- Milestone (Dec 2008): Demonstrate property improvements from FSP that can reach metrics established by project team: minimum 2 times improvement in fatigue life, significant reduction in thermal fatigue crack initiation and growth rate, 20% improvement in average failure stress level at N cycles. (Completed)
- FSP was found to produce significant improvement in fatigue performance when compared to as-cast aluminum alloy 356. Depending on stress ratio and stress level, the FSP-processed materials showed from 5 to 15 times fatigue life improvement over as-cast material. In addition, FSP-processed materials showed up to 80% improvement in fatigue strength across a wide range of maximum stress levels.
- FSP also was used to modify the surface of an aluminum alloy analog to a production piston alloy. Tooling was developed, and process parameters were explored that allow for processed regions showing very fine-grained, homogeneous microstructure.
- FSP was used to physically "stir-in" multi-wall carbon nanotubes and several different carbon nanofiber compositions into aluminum surfaces to a depth of 5.8 mm.
- Milestone (Sept 2009): Demonstrate consolidated FSP regions in a ferrous piston alloy, and establish process window to successfully stir particulate into the surface of steel.
- The tooling and process parameter space for accomplishing thick section (up to 13 mm thick) FSP of steel materials was investigated. Fully consolidated process zones were demonstrated, but tool survivability must be improved.

Future Direction

- FSP of aluminum alloys will continue in 2010 with the goal of improving high-temperature fatigue resistance and modifying thermal conductivity.
- In preparation for prototype part testing, develop the process and equipment needed to create two dimensional (2-D) curved FSP regions on piston blanks.

Introduction

The overall goal of the project is to enable the implementation of new combustion strategies, such as homogeneous charge compression ignition (HCCI), that have the opportunity to significantly increase the energy efficiency of current diesel engines and decrease fuel consumption and environmental emissions. These strategies, however, are putting increasing demands on conventional engine materials, either from increases in peak cylinder pressure (PCP) or from increases in the temperature of operation. The specific objective of this project is to investigate the application of a new material processing technology, friction stir processing (FSP), to improve the thermal and mechanical properties of engine components. The concept is to modify the surface of conventional, low-cost engine materials. The approach is to produce components with functionally graded surfaces that are optimized for thermal properties and better in-service performance without suffering the cost penalty of using exotic or expensive materials. Low-cost, higher-performance materials will allow new combustion strategies to be implemented that can increase energy efficiency. This project is a Cooperative Research and Development Agreement (CRADA) in partnership with Caterpillar, Inc.

Background

Almost since the inception of internal combustion engines, there has been a steady rise in specific power (SP) output, or the power per liter of engine displacement. SP is correlated with efficiency and is the combined effect of better optimization of combustion, fuels, engine materials and design, reduction in parasitic losses, and improved heat management. Figure 1 shows that from 1970 to 2001, there has been a steady increase in SP. After 2001, the SP levels dropped due to emission and after-treatment devices and controls mandated by federal legislation (primarily increased exhaust gas recirculation (EGR) rates and particulate filters). The drop in SP from 2001 to about 2003 would have been even greater were it not for significant advances in engine management, computer control, higher injection pressures, etc., made during this period to compensate for the power losses. However, around 2003, a different

restriction on the optimization of the combustion process was beginning to force diminishing returns. The restriction is illustrated in Figure 1 as the plot of the PCP. The higher the peak pressure, the more work that can be done by the piston as it is forced downward in the bore and the higher the specific power.

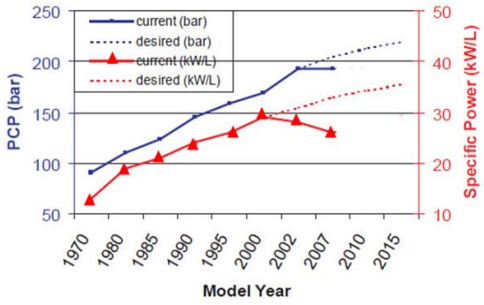

Figure 1. Plot showing the increase in SP and PCP for Typical Heavy-duty Diesel Engines over the Last 38 Years (*Figure modified from Southwest Research Institute: www.swri.org)*

Since 2003, PCP has plateaued around 190 to 200 bar because above this, conventional engine materials in pistons, cylinder liners, and heads will be beyond strength and fatigue limits[1]. In order to increase efficiency further, either unconventional, expensive materials (i.e., Ni alloys, titanium, compacted graphite iron, nodular Fe, or micro-alloyed steels) must be used or conventional materials must be modified in a way that increases their durability. New energy-efficient combustion strategies, especially HCCI, will increase PCP potentially above 220 bar. As such, to enable this process, materials must be improved.

One of the major challenges for conventional materials under increasing peak pressure environments is resistance to thermal fatigue failure. Pistons and cylinder heads are particularly vulnerable to this failure mode due to the cyclic nature of the loading and temperature changes in the combustion chamber. Figure 2 shows failures of pistons in the bowl rim area when subjected to high PCP over time.

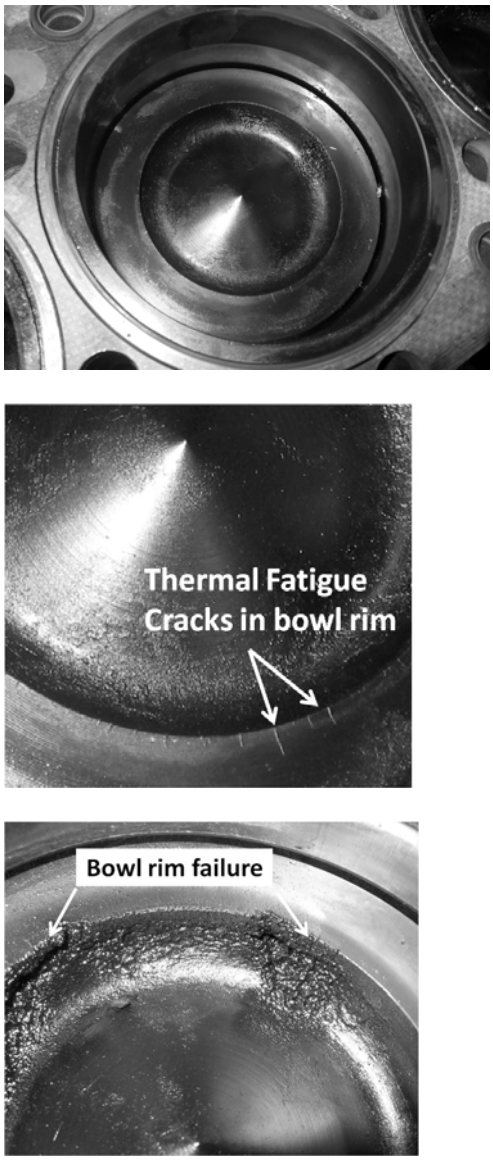

Figure 2. a) Piston in Bore; b) Cracks on Inside Edges of Bowl Rim; c) Bowl Rim Failure

Rather than substitute a potentially high-cost, high-temperature, monolithic material, one low-cost strategy to enable higher PCP involves using techniques to improve the thermal fatigue performance of current materials. In the case of thermal fatigue in the bowl rim area, the technique need only be applied to the narrow area around the

[1] Figure 1 represents data primarily from medium- to heavy-duty diesel engines. Production automotive diesel engines (light-duty, high-speed) now achieve SP levels up to 75kW/L in turbocharged and intercooled configurations.

bowl rim itself since failures of this area drive the overall material selection.

FSP is a new technology that can be used to create engineered regions on selective areas on a part. In recent years, PNNL has worked on developing techniques and tools that allow FSP to be accomplished in steels, cast iron, and aluminum.

FSP is an outgrowth of friction stir welding (FSW), invented 18 years ago by TWI, Ltd. (Figure 3). It has been recognized that the same techniques and processes used to make a friction stir weld could be used to process a material for enhanced properties. The process can be selectively applied to the surface of a material and it alters the microstructure by the severe plastic deformation that occurs in the processed zone. FSP can create a robust and graded structure with fundamentally different properties than the underlying surface and has been shown to produce surface regions with improved fatigue life, ductility, and strength.

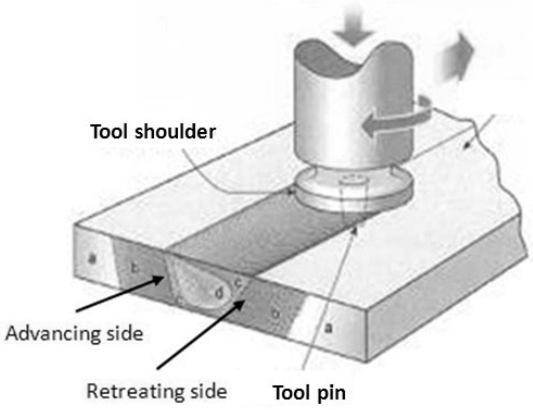

Figure 3. Friction Stir Process Illustration (top) and Typical Friction Stir Tools

FSP produces a surface modified region that is different from a coating. Commonly, surface treatments designed to enhance wear or thermal performance include various coating methods or fusion-welded hard facings. Most of these processes are liquid state and often involve detrimental temperature effects on the base material. Heat-affected zones in the base metal and various deleterious high temperature reactions can create a coated part with less-than-desirable properties.

Also, traditional thin coatings can suffer from issues involving the nature of the interface between the coating and the base material (spalling, debonding, and cracking on the interface), especially under high-stress, gouging wear conditions or under cyclic-thermal conditions where coefficient of thermal expansion (CTE) mismatch is an issue. Also, failure of a coating under high-loading conditions can occur when the substrate below a thin, hard coating fails by plastic deformation. Friction stir processed regions can show significant robustness over traditional coatings for two reasons: 1) FSP produces a modified region that transitions to the base material without a sharp interface (Figure 4), and 2) the modified region is generally thicker and the transition region wider than traditional coating because the plasticized region depth is related to the tool geometry, specifically the depth and size of the pin.

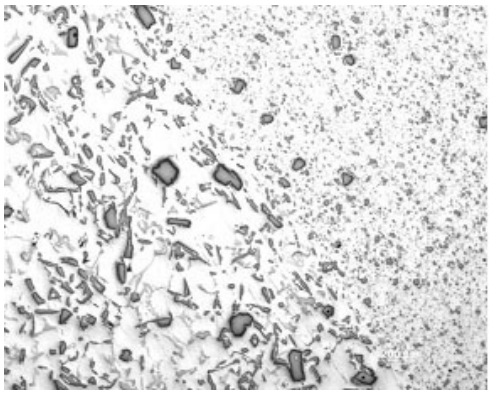

Figure 4. Micrograph Showing Edge of Stirred Zone Showing Particle Refinement in Processed Region (FSP can close porosity in castings and decrease both size and aspect ratio of particles, producing better fatigue performance.)

It is also possible to use FSP to "stir" insoluble particles from the surface into the substrate to depths limited only by the FSP tool geometry (Figure 5). This engineered metal matrix composite layer can create unique surface properties, including increased hardness, wear resistance, and thermal characteristics. To date, the addition of up to 20% ceramic to aluminum has been demonstrated and approximately 10% addition to steel has been achieved.

FSP can be used to alter the original microstructure, create surface composites and new alloys, and has the potential to produce selective areas of improved material performance. This project will investigate several opportunities for FSP to improve engine materials in order to enable increases in engine efficiency.

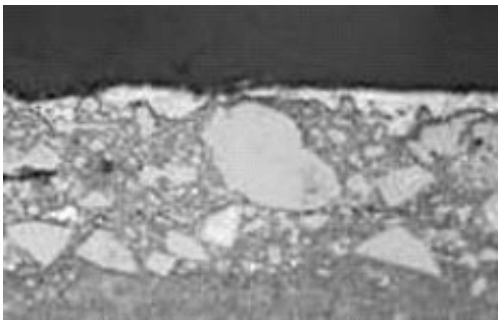

Figure 5. Ceramic Particulate can also be Stirred into the Surface to Produce Functionally Graded Surfaces and Near-Surface MMCs.

Approach

This project proposes to experimentally develop the FSP processes and technologies required to engineer the surface of propulsion materials for improved properties. The application focus is to tailor the mechanical properties and thermal conductivity of engine materials, both ferrous and non-ferrous, by using FSP techniques. This microstructural modification is expected to lead to a set of materials with enhanced surface properties that can handle increased combustion pressure and exhaust temperatures, resulting in improved engine efficiency.

The project scope will involve developing the FSP manufacturing parameters, as well as selecting and evaluating proper tool materials and techniques to produce defect-free FSP regions. Coupon-level testing and evaluation of the thermal and mechanical properties will be conducted, focusing on specific performance targets identified by project partners. If performance metrics are met for sample materials enhanced by FSP, additional research will include developing and demonstrating the appropriate method to apply this process to 2-D and 3-D geometry. If successfully developed, this class of engineered materials can significantly impact the efficiency and durability of compression ignition direct injection (CIDI) and potentially address some of the technical barriers to implementing HCCI engines.

In 2009, the primary focus of project work was on FSP of aluminum piston materials used for light- and medium-duty compression ignition direct injection (CIDI) engines. The work is intended to improve the thermal fatigue performance of typical piston alloys in order to allow them to be used in higher peak stress environments without suffering premature bowl rim failure. The concept is illustrated in Figure 6. If FSP were applied to the area of a piston blank (prior to final machining) that will be the bowl rim area, then, after final machining, the bowl rim will be composed entirely of fine-grained FSP "nugget" material that will have improved fatigue performance. Adjacent areas of the piston will remain unmodified.

The project approach is to first develop the techniques (process parameters, friction stir tools and methods) to create robust process zones, then physically perform the FSP process on full-sized piston blanks, machine them to shape, and test them in actual operating conditions on test cell engine dynamometers or single-cylinder test engines.

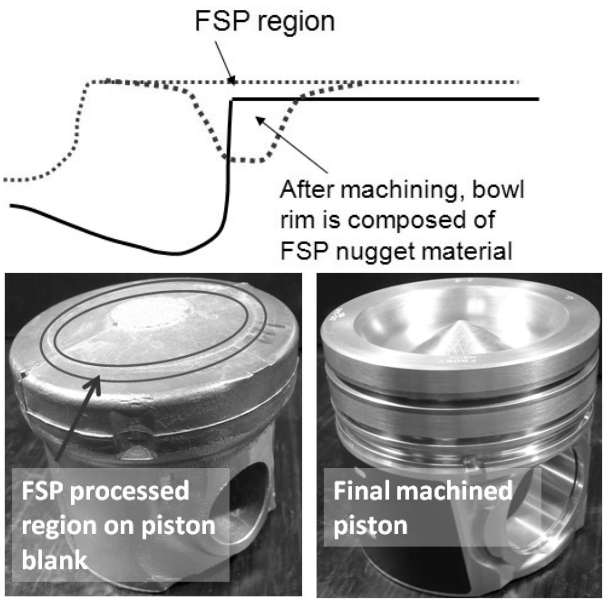

Figure 6. Cast Piston Blank (The area in the bowl rim after machining will be friction stir processed for improved microstructure.)

Results

In 2009, the project focused primarily on FSP in aluminum materials that are compositional analogs to the typical piston and head alloys seen in small- to mid-sized CIDI engines. Investigations were primarily of two types: 1) FSP of cast hypo-eutectic aluminum (Alloy 356/357) with no introduction of any new component materials, and 2) FSP of aluminum alloys involving physically "stirring-in" various quantities of carbon nanotubes and nanofibers. The two investigations are summarized as follows.

FSP of Alloy 356

FSP significantly refines microstructure, closes casting porosity, and reduces the aspect ratio of the Si particles in cast Al-Si alloys. These three features produce a dramatic improvement in fatigue life. Figure 7 shows the S/N curves for both tensile and bending fatigue performance comparing the as-cast to the FSP-processed material. A 90% improvement in maximum tensile stress at the fatigue limit and improvements in bending fatigue lifetime up to an order of magnitude can be shown for this alloy.

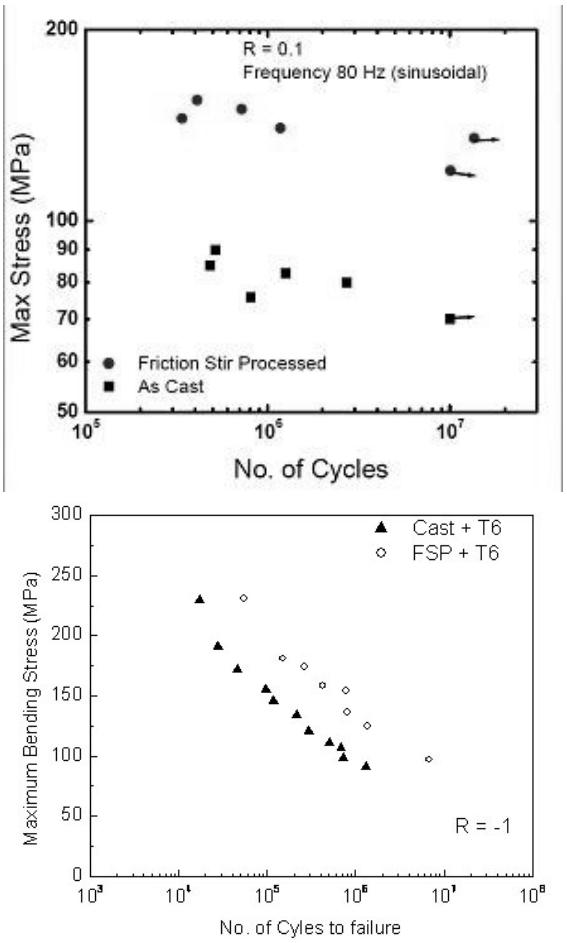

Figure 7. SN Curve for Tensile Loading (top) at R=0.1 (showing as-cast 356 versus FSP-processed 356) and SN Curve for Bending (bottom) at R=-1 (showing as-cast 356 versus FSP-processed 356 [1,2,3])

In current applications of these alloys, especially for pistons and cylinder heads, fatigue, particularly thermal fatigue, is the primary limiting condition on part life. As CIDI engines go to lean burn and potentially more HCCI-like conditions (i.e., maximum stress in bowl rim edges, ring landings, bridge areas between valves, etc.) will all likely see much higher stress levels than current designs. The improvements offered by selective FSP of these regions may enable these energy-efficient combustion strategies.

FSP—"Stirring-in" Carbon Nanotubes and Nanofibers

The primary failure at high PCP in service is fatigue and thermal fatigue at several locations on the piston and head. Our goal is to use FSP to improve the microstructural and mechanical

properties that most influence thermal fatigue (i.e., CTE, conductivity, and, to a lesser extent, high temperature strength). Primarily, the goal is to reduce CTE and increase conductivity. Table 1 shows candidate materials that could be stirred into the base metal to selectively modify mechanical properties.

Table 1. Potential Additions to 339 Base Material

Material	Modulus	CTE	Conductivity
Aluminum	80 GPa	25 μm/m°C	180 W/m-K
SiC	410 GPa	4.4 μm/m°C	150 W/m-K
Al_2O_3	370 GPa	8.5 μm/m°C	13 W/m-K
Carbon Nanotubes	>600 GPa	Low or Can be negative !	> 1000 W/m-K

Of these, carbon nanotubes and fibers offer the best potential to improve thermal fatigue due to their very low CTE and high conductivity. The bulk of the experimental effort in 2009 was devoted to developing the methods, procedures, FSP tools, and process parameters needed to create processed regions with even distributions of particulate. This work continues efforts from 2008 to find the best methods of stirring in particulate into the aluminum substrate while producing the most homogeneous and highest particulate loading possible.

In 2009, experimental work consisted of cutting 6.4 mm. wide longitudinal slots in base plates of aluminum. These slots were approximately 76- to 154 mm long. Then, 100% nanotube powders were packed in the slot and covered with an aluminum square section rod that was press-fit and staked into place (Figure 8). The nanotubes used in this study were Bayer Baytubes C150P, a multi-walled nanotube with O.D. 13–16 nm and a length from 1 to 10 micron.

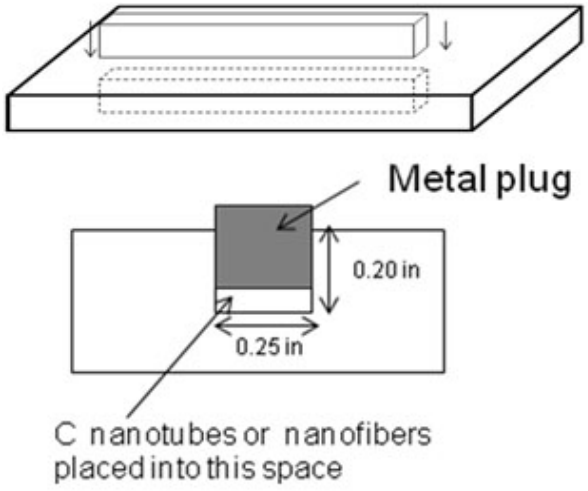

Figure 8. Nanotubes are Packed into Grooves and a Cap Plug is Installed Prior to FSP

The metal plug and groove then was processed by multiple overlapping passes of a friction stir tool at a wide range of different parameters and conditions. Variables investigated included RPM, travel speed, normal load, tool design, number of passes, and order of passes with respect to the advancing and retreating side of the tool. To explain this latter concept, Figure 9 shows a multi-pass overlay FSP run. These overlays can be run so the first pass over the nanotube reservoir is under the advancing or retreating side of the shoulder, and each successive pass can be rastered either with the same or opposite rotation and travel direction. The effect of these differences places the advancing or retreating side of the processed zone in the path of the tool on each run and different flow patterns develop. For example, one result of this work (shown in Figure 10) is that a much better particulate distribution can be obtained if each pass consumes the advancing side of the previous pass. If the retreating side is consumed, there will be a discontinuity in particle loading seen as the interrupted dark areas in Figure 10 (top).

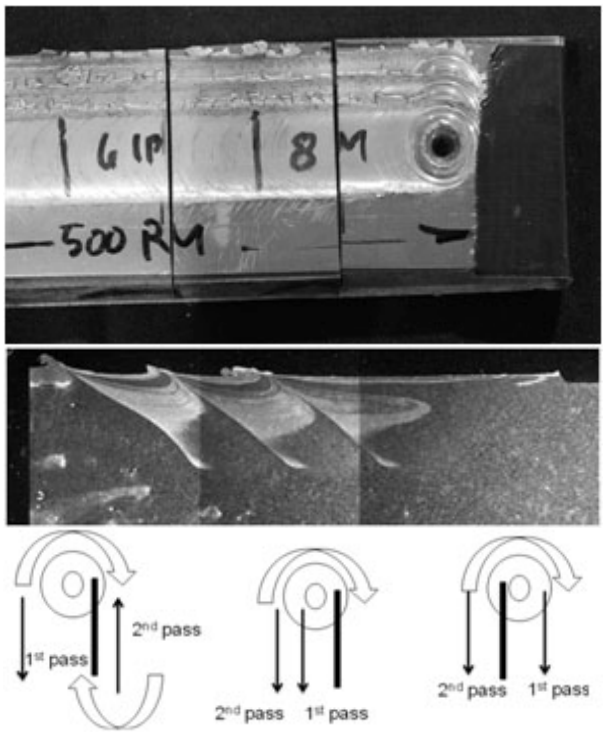

Figure 9. Illustration of Variables Around Multipass FSP (Each successive pass can overlap the previous pass in different ways as determined by rotation direction and travel direction of the tool.)

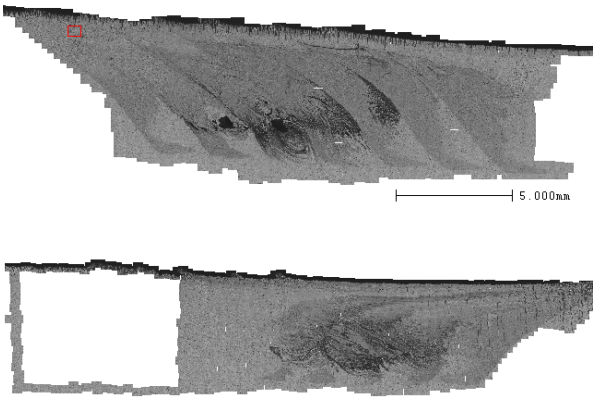

Figure 10. Overlap Pattern that Consumes Retreating Side of Nugget (top) and Overlap Pattern that Consumes Advancing Side of Nugget (bottom)

Another important influence on homogeneity of particulate distribution is the rotation and travel speed of the tool. In 2009, several studies were undertaken to understand these variables and their fundamental effect on material flow and mixing. One result determined mixing of particulate is enhanced by using process parameters that allow the tool to rotate many times while covering some fixed distance. This is analogous to thread pitch on a screw. In the case of FSP, the quantity varied is advance per revolution (APR), or how far the tool travels during each rotation. To improve the degree to which a particle is mixed with a base material, the tool needs to move slowly and rotate quickly so more plastic work is introduced to the base material for each unit length of tool travel.

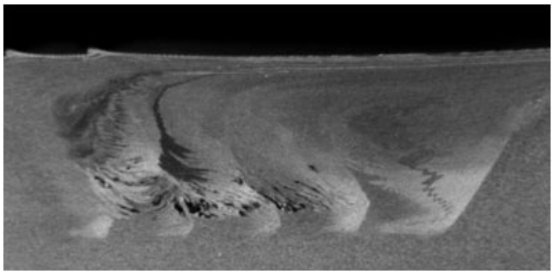

Figure 11. Processed Region at the Highest APR Showing Uneven Distribution of Nanotubes and Some Void Spaces

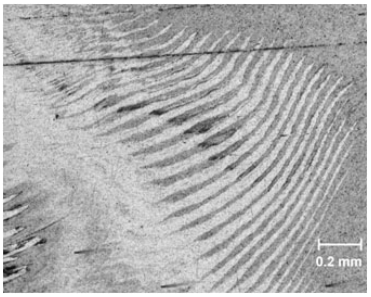

Figure 12. Higher Magnification View of Figure 11 Showing Relatively Wide Banding and Segmenting of Nanotube-rich Areas (dark spots)

Figures 11 through 14 illustrate the effects of decreasing APR. FSP takes place by shearing and deforming small slices of material from the front of the tool and moving them to the back. As the tool progresses forward, these slices are forged together, leaving behind a characteristic spacing between bands of material. The bands are defined by alternating regions of differing grain size and grain boundary angle that are the result of varying amounts of shear, recrystallization, and grain growth in each band. Lower APR produces thinner banding, reflecting more slices were sheared per inch of travel. The number of slices per inch affects the degree of mixing and homogeneity attained in the processed region. Figure 11 shows a macrograph cross section of the processed region at the highest APR. Dark areas

are rich in agglomerated nanotubes and contain open void space.

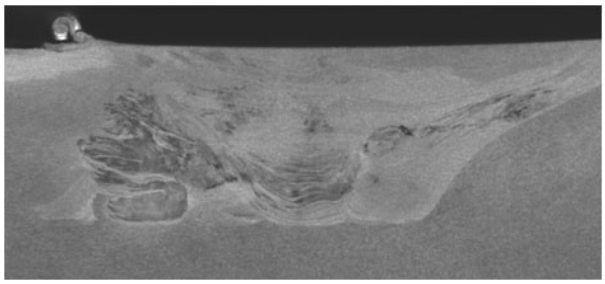

Figure 13. Processed Region at the Lowest APR

Figure 13 shows a cross section macrograph of a processed region at very low APR. In this case, the processed region shows improved consolidation and less indication of visible agglomerated nanotube-rich regions. At increased magnification (Figure 14), the processed region shows very fine banding and interleaving of the layers. From the perspectives of the agglomeration of nanotubes and weld consolidation, the very low APR parameters show much more promise for creating even nanotube distribution in the processed region.

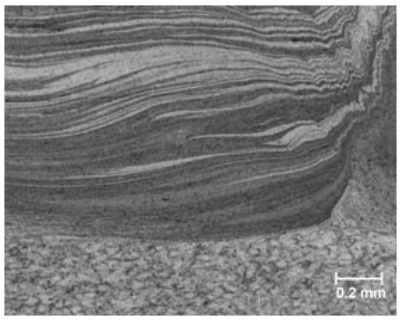

Figure 14. Higher Magnification View of Figure 13 Showing Fine Banding

One of the problems when dealing with nanoparticles (as opposed to micron-size particulate) is understanding when the process has led to a good particle distribution in the processed zone. In cases where the nanoparticulate is significantly agglomerated, the clumps are easily seen, but when finely divided, nanoparticles are not visible by optical methods. For best property improvement, it is anticipated that well-dispersed nanotubes, at the nanoscale, will be important. One of the analytical techniques explored in this project to determine the fine distribution of nanotubes is Raman spectroscopy.

This technique was used to determine whether or not nanotubes were present in a processed zone and to determine a qualitative sense of distribution by surveying numerous locations. Two samples were analyzed by these methods—a high APR case and a low APR case. In the high APR case it was found that outside the regions identified optically where nanotubes were agglomerated there was no evidence of nanotube dispersion. In the low APR case, where the tool created finer macroscopic bands, it was found that the nanotubes were much more evenly distributed. Nanotubes were even located by Raman methods in areas at significant distance away from agglomerated areas. We interpret this data to indicate that low APR will produce the best particle mixing. Thus, as we proceed into coupon testing, the process parameters that produce low APR will be emphasized.

This project will also investigate FSP in steels and cast iron. Trails in steel began during the last quarter of 2008 and continued in 2009. The tooling and process parameter space for accomplishing thick section (up to 13 mm thick) FSP of steel materials was investigated. Much of the efforts involved equipment development for induction pre-, and, more importantly, post-heating of the FSP region. Steel and cast-iron FSP can require additional heat during the plunging phase of the processing run because drastic tool wear can occur when a cold tool is driven down into a cold substrate. In earlier work by PNNL and South Dakota School of Mines and Technology, induction heating of the plunge zone was found to be necessary to preserve the life of the tooling. Induction heating also was used to accomplish post-processing heating to effectively slow the cooling rates after processing. In fusion welding, it has been shown that *in situ* or trailing heating can significantly increase weld region ductility, affect the final microstructure, and may be able to positively affect fatigue performance as well.

Figure 15 shows a macrograph of a 13 mm thick processed area in low-carbon steel. Micrographs of the nugget region (Figure 15-bottom) and the parent metal (Figure 15-middle) show the microstructure is similar but with a large degree of very fine-grained acicular ferrite in the nugget of

the processed zone. This microstructure may be especially favorable for fatigue life improvement. Testing of this concept will begin in early 2010.

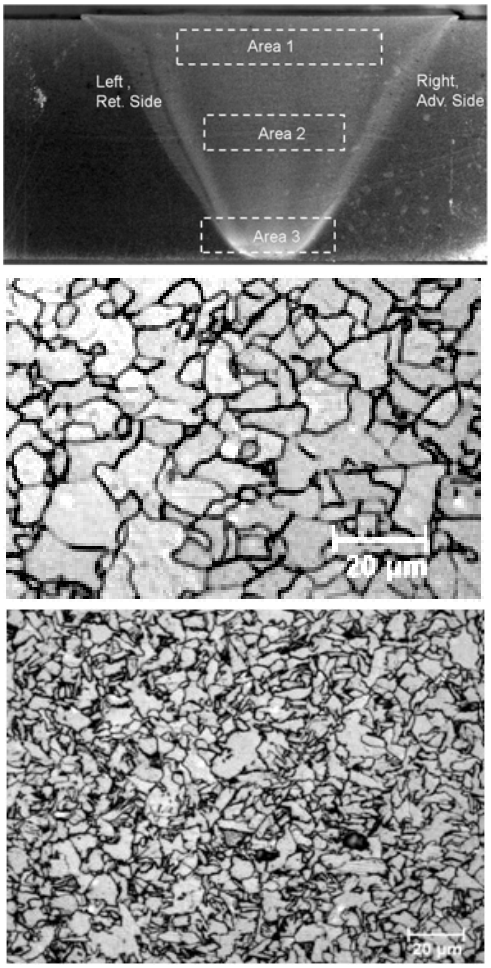

Figure 15. Macrograph of a FSP-processed Region in Low-carbon Steel (top); Micrograph of Parent Material Microstructure (middle); Micrograph of Nugget Material from Area 2 Showing Fine-grained Acicular Ferrite (bottom)

Conclusions

The goal of this project is to deploy friction stir processed components that can enable energy-efficient combustion strategies, especially strategies that will require higher PCP or higher temperature operation. FSP produces selected, graded structures that have shown increased strength and durability in fatigue. Surface modification through FSP may have an opportunity to address some emerging material problems seen in very high combustion pressure systems such as HCCI engines. Additionally, the process allows for the incorporation of particulate into the surface, potentially selectively modifying the properties of materials to alter the thermal environment for increased thermal efficiency. Experimental work to date on aluminum systems has shown significant increases in fatigue lifetime and stress-level performance in aluminum-silicon alloys using friction processing alone, and ongoing work has shown the potential to create new mechanically mixed alloys of aluminum and carbon nanotubes and fibers that may provide unique thermal fatigue resistant surface regions to fatigue failure prone CIDI engine components. Future work includes quantifying property improvements and fabrication of prototype parts for engine durability testing.

Presentations/Publications/Patents

Jana S, RS Mishra, JB Baumann, and G Grant. 2009. "Effect of stress ratio on the fatigue behavior of a friction stir processed cast Al-Si-Mg alloy." *Scripta Materialia* 61(10):992-995.

Jana S, RS Mishra, JB Baumann, and G Grant. In Press. "Effect of friction stir processing on fatigue behavior of an investment cast Al–7Si–0.6 Mg alloy." *Acta Materialia (2009), doi:10.1016/ j.actamat.2009.10.015*

Jana S, RS Mishra, JB Baumann, and G Grant. In Press. "Effect of friction stir processing on microstructure and tensile properties of an investment cast Al-7Si-0.6 Mg alloy." *Metallurgical and Materials Transactions*.

Agreement 16303 – Materials for High Pressure Fuel Injection Systems

Peter J. Blau, Camden R. Hubbard, and Amit Shyam
Oak Ridge National Laboratory, P. O. Box 2008, Mail Stop 6063
Oak Ridge, TN 37831-6063
(865) 574-5377; fax: (865) 574-4913; e-mail: blaupj@ornl.gov

and

Michael J. Pollard
Caterpillar Inc.
Technical Center Bldg. E-854
P.O. Box 1875
Peoria, IL 61656-1875

DOE Technology Manager: Jerry L. Gibbs
(202) 586-1182; fax: (202) 586-1600; e-mail: Jerry.gibbs@ee.doe.gov
ORNL Technical Advisor: D. Ray Johnson
(865) 576-6832; fax: (865) 574-6098; e-mail: johnsondr@ornl.gov

---

Contractor: Oak Ridge National Laboratory, Oak Ridge, TN
Prime DOE Contract Number DE-AC05-00OR22725

Objectives

- To critically evaluate current and future material choices for high pressure fuel injector nozzles indented for energy-efficient, low-emissions diesel engines.

- To provide metallurgical analysis, fatigue test data, hole metrology information, and residual stress measurements that will aid in the selection of alternative high-performance alloys for advanced, high-pressure diesel engine fuel injection systems.

Approach

- Working through a Cooperative Research and Development Agreement (CRADA) between ORNL and Caterpillar, characterize the metallurgical structure, hardness of candidate high-pressure fuel injector nozzle alloys.

- Develop methods to characterize injector spray holes shapes, sizes, and internal bore morphology.

- Evaluate alternative x-ray and neutron-based methods, as means to determine the residual stress states of materials in the ‘sack’ (nozzle tip) of fuel injectors.

- Develop and use appropriate methods to determine the fatigue life and reliability of ferrous alloys for fuel injectors in the presence of spray-hole-like features and in fuel environments.

Accomplishments

- A means to cross-section fuel injector holes and measure the interior surface features, and roughness, of 200 μm-diameter fuel spray holes was demonstrated.

- X-ray and neutron-based experiments were run at four different facilities to determine the feasibility of using various methods to quantify the residual stresses in fuel injector nozzles, in the region surrounding the sacks (tips). Results were unsatisfactory for the sacks, and future residual stress work will mainly focus on fatigue test specimens.

- After the establishment of a fatigue testing plan and calibration of load frames, a series of baseline tests were conducted on smooth specimens of heat-treated fuel injector steel provided by Caterpillar. Two regimes of fatigue crack initiation and propagation were revealed in tests lasting for as many as 36 million stress cycles. A high-resolution optical system was purchased to observe the propagation of small fatigue cracks *in situ*.

- A potential supplier of advanced, highly fatigue-resistant steels has been brought into discussions regarding an alterative to the current fuel injector alloy. Plans are to test these materials in FY 2010.

Future Directions

- Continue to characterize of current and potential fuel injector alloys using metallurgical studies, hardness studies, and residual stress methods applied to fatigue test specimens.

- Introduce controlled flaws into fatigue specimens and study their effects on crack propagation.

- Design and install a 'wet-cell' to enable fatigue testing in diesel fuel environments.

Introduction

In order to improve fuel efficiency while controlling emissions, diesel engine designers have raised the pressures imposed on the fuel injectors (see Figure 1). Repetitive pressurization exceeding 25,000 psi could stress the walls of the tips of the fuel injector nozzles above the endurance limit, leading to fatigue cracking and fracture. The consequences of these events can significantly affect engine performance, and the ability of nozzle materials to resist these effects becomes extremely important.

The objective of this work is to ensure the durability of high-pressure fuel injector nozzle materials through a three-pronged approach, described in the next section.

Figure 1. Fuel injector nozzles showing the sacks at the tips, where spray holes are located.

Approach

A three-pronged approach is being used: (a) metallurgical characterization and hole metrology, (b) residual stress measurements of material near of spray holes, and (c) fatigue testing of smooth and notched specimens, dry and in the presence of fuel.

During FY 2009, a trip was made to the Caterpillar Tech Center in Peoria, Illinois, to discuss approaches to the work. The visit included a tour of the Waterloo, Illinois, facility where spray holes are produced. In addition, used fuel injector nozzles were provided to evaluate their condition after engine service.

Metallurgical characterization and hole metrology. Mounting and sectioning methods were developed to enable the preparation of cross-sections of spray holes. The features of the interiors of the holes and the hole walls were investigated using optical microscopy, scanning electron microscopy, and scanning optical interference imaging.

The holes in an unused sack are shown in Figure 2. Figure 3 shows a 3-D optical scanning interference image of the interior of one of the holes. A scanning electron micrograph of the hole wall (Fig. 4) shows splat-like features remaining from the hole-forming process. Such features could initiate fatigue cracks under favorable conditions.

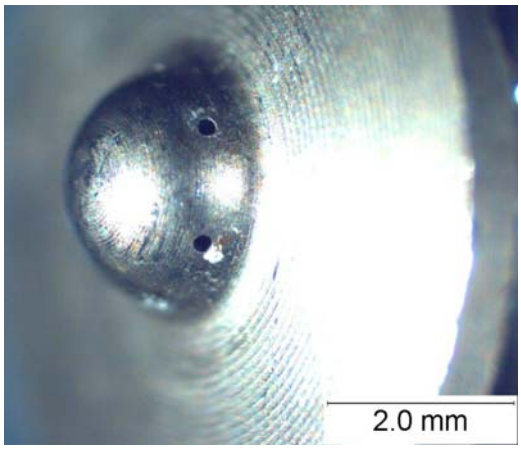

Figure 2. Spray holes in the sack of an unused fuel injector nozzle.

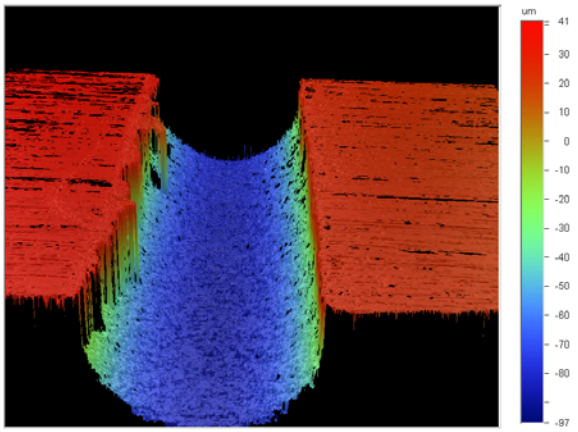

Figure 3. 3-D reconstruction of the interior of a spray hole. Associated software also allowed measurement of the arithmetic average roughness along the bore axis.

Irregularities in the hole walls may not be problematic for current fuel injectors, but they may become an issue the for next-generation of high-pressure injectors. Fatigue tests in FY 2010 will investigate the effects of such defects on fatigue life.

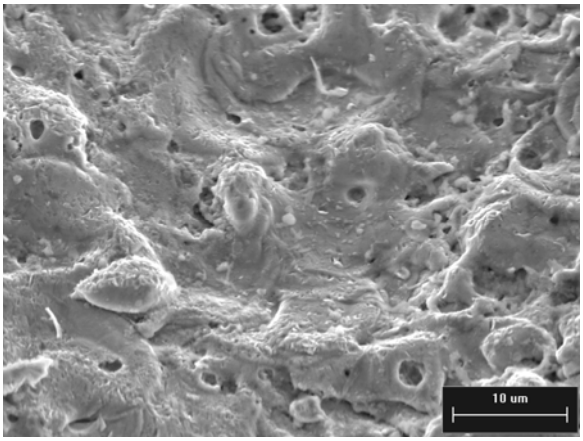

Figure 4. Features remaining from the spray hole finishing process.

Polished sections of new and used nozzles were etched to study their microstructure. Low-load Vickers microindentation tests indicated a variation in micro-mechanical properties in the radial direction through the nozzle wall. Due to exposure to engine conditions, the hardness of the sack walls of used injectors was noticeably decreased.

Residual stress studies. Four different instruments, at three national laboratories, were used in an attempt to measure residual stresses in fuel injectors and test samples provided by Caterpillar. They were:

(i) x-ray diffraction (ORNL)
(ii) synchrotron (low-energy) x-ray diffraction (Brookhaven National Laboratory, NSLS)
(iii) synchrotron (high-energy) x-ray diffraction (Argonne National Laboratory, APS)
(iv) neutron diffraction (ORNL, High Flux Isotope Reactor)

Due to constraints of beam size, specimen shape, and gauge volumes, none of these techniques provided acceptable measurements of residual stresses near the spray holes. Therefore, residual stress studies may need to be limited to test specimens in which the geometries and volumes of material that can be probed are better suited for such analyses.

Fatigue testing. Fatigue testing was performed on uniform diameter gage specimens in an MTS 810 servo-hydraulic machine at a frequency of 20 Hz. The tests were performed at a load ratio of -1 under stress control. The maximum stress in the cycle was varied to obtain the stress-life (S-N) response of the material.

Figure 5 represents the S-N response of the steel used in injector nozzles. A two-stage fatigue life diagram was observed with clear separation in the fatigue lifetime of specimens that failed due to surface crack initiation (σ_{max} > 900 MPa) and subsurface crack initiation (σ_{max} < 900 MPa). The fatigue lifetimes for the two separate failure modes are separated by nearly two orders of magnitude. This can also be observed in the fracture surface SEM images (Fig. 5, inset).

The multi-stage S-N curve has practical implications for design in that the endurance limit for conventional failure lifetimes ($<10^6$) is about 900 MPa, but is reduced to below 800 MPa if the ultra-high cycle regime failures (10^6-10^9) are considered.

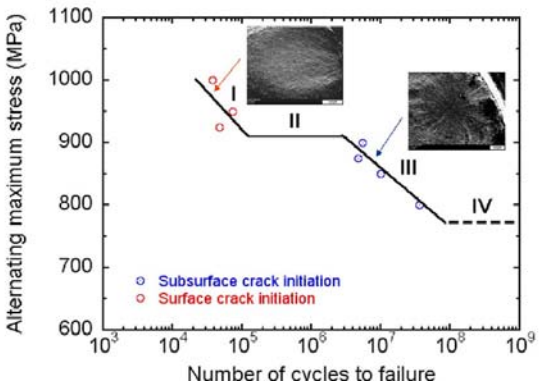

Figure 5. Two-stage fatigue life diagram for an alloy steel that is used in fuel injectors.

Summary and Conclusions

- Metallurgical studies were performed on fuel injector nozzles. Methods were developed to cross-section spray holes. Bore wall surface roughness and fine-scale surface features were studied.
- Microindentation tests indicated that the hardness in nozzle alloys decreased during service, potentially changing their durability and cracking resistance.
- Neither x-ray nor neutron-based methods were satisfactory for measuring residual stresses in materials adjacent to spray holes. Further residual stress work will focus on test specimens.
- A two-stage fatigue lifetime diagram was constructed for the steel used in fuel injector nozzles.

Publications/Presentations

1) P. J. Blau, M. J. Pollard, C. R. Hubbard, and A. Shyam (2009) “Materials for High-Pressure Fuel Injectors,” poster at the DOE Transportation Merit Review, May 21-22, 2009, Washington, DC.

Agreement 17257 – Materials for Advanced Turbocharger Designs

P. J. Maziasz, A. Shyam, and S. Das
Materials Science and Technology Division
Oak Ridge National Laboratory
P.O. Box 2008, MS-6115
Oak Ridge, TN 37831-6115
(865) 574-5082; fax: (865) 754-7659; e-mail: maziaszpj@ornl.gov

K. Pattabiraman
Global Materials Engineering Manager
Honeywell – Turbo Technologies
3201 W. Lomita Blvd.
Torrance, CA 90505
(310) 571-1616; fax: (310) 539-7061; e-mail:kalathur.pattabiraman@honeywell.com

DOE Technology Manager: Jerry L. Gibbs
(202) 586-1182; fax: (202) 586-1600; e-mail: jerry.gibbs@ee.doe.gov
ORNL Technical Advisor: D. Ray Johnson
(865) 576-6832; fax: (865) 574-6098; e-mail: johnsondr@ornl.gov

---

Contractor: Oak Ridge National Laboratory, Oak Ridge, Tennessee
Contract No.: DE-AC05-00OR22725

Objectives

- CRADA NFE-08-01671 – Provide the critical test data for new, improved materials, which in turn will enable the design of advanced turbocharger systems with upgraded performance, and more durability and reliability relative to conventional systems.
- CF8C-Plus Economics Study – Materials behavior data, and component casting and component finishing processes are evaluated to determine the cost benefits of CF8C-Plus cast stainless steel relative to standard materials for diesel and automotive exhaust components, and larger gas-turbine casing/end-cover components.

Approach

- CRADA NFE-08-01671 – This is a 3 year project designed to consider all materials and components for the turbine and compression sections, and to consider turbochargers for both passenger/gasoline and commercial/diesel engines. Honeywell will assess and prioritize the components that would benefit most from materials upgrades or alloy development. ORNL will work with Honeywell materials/component suppliers to obtain new materials for testing and evaluation.
- CF8C-Plus Economics Study – Plant visits or phone interviews with various steel and stainless foundries, and component makers were used to provide processing, properties and cost information for comparison of CF8C-Plus cast stainless steel with standard exhaust component or gas-turbine casing/cover alloys.

Accomplishments

- CRADA NFE-08-0171 was executed on July 31, 2009, so the project just began at the end of FY2009. ORNL and Honeywell began the initial task of assessing component/materials priorities, and took the first steps to define neutron-scattering residual stress measurements for turbine wheel/shaft components, and to continue evaluation of CF8C-Plus stainless steel as a cost-effective performance upgrade relative to HK30Nb steel for turbine housings.

- A draft report on analysis of cost-effectiveness of CF8C-Plus stainless steel in automotive applications was completed, based on visits to 4 stainless steel foundries and phone interviews with 9 other foundries or component manufacturers.

Future Direction

- CRADA – Performance-limiting behavior will be assessed by comparing new and used components for turbine and compressor parts of the turbocharger system, and the properties benefits for upgrade materials for the various components will also be determined. Turbocharger systems will range from those for gasoline engine passenger vehicles to those for heavy-duty truck diesel engines.
- CF8C-Plus Economic Study – The potential for CF8C-Plus to displace more expensive heat-resistant alloys in a wider range of applications will be assessed.

Introduction

This is a new ORNL CRADA project with Honeywell, NFE-08-01671 (DOE/EERE/OVT Agreement 17257), that began in August, 2009, and is scheduled to last for about 3 years. This CRADA project will address the limitations of lifetime or use-temperature for the various components (casing, wheel, shaft, bearings) of both the turbine and compressor parts of the turbocharger system. Requests for more detailed information on this CRADA project should be directed to Honeywell, Inc.

Agreement 17257 also included an economic assessment of CF8C-Plus for automotive applications. More information can be obtained from Sujit Das at the National Transportation Research Center (NTRC) at ORNL.

Approach

CRADA Project

The new CRADA project, which began at the end of FY2009, will extend for 3 years, and cover several different tasks. The first will be to assess and prioritize the various components that need or would most benefit from materials upgrades to increase temperature capability and performance, as well as durability and reliability. The next tasks will examine current performance and degradation modes of wheel/shaft assemblies for turbines and compressors, housings for turbines and compressors, and bearings. They will then obtain and test new materials with upgraded performance, and provide the results to Honeywell for designing advanced turbocharger systems, or manufacturing new prototype components for testing and evaluation.

CF8C-Plus Cost-Analysis

Cost-analysis was be based on gathering extensive information on commercial exhaust component manufacturing, including automotive exhaust manifolds, and other exhaust components for both automotive gasoline and on-highway truck diesel engines. Commercial manufacturing information included making exhaust components out of cast-irons, austenitic stainless steels and Ni-based superalloys. It also included visits or phone interviews with a variety of U.S. foundries.

Technical Progress

Figure 1. Caterpillar Regeneration System (CRS) burner housing, made of CF8C-Plus cast stainless steel, for regenerating ceramic diesel particular filter (DPF) components. Commercial application began in late 2006, and to date over 450 tons of CF8C-Plus steel have been cast. CRS units, attached to the turbocharger, must endure rapid thermal cycling for maximum temperatures close to 900^{o}C. No CRS units have failed, with the longest service being 3 years or more.

Figure 2 – Typical Honeywell turbocharger system for passenger vehicles. Cut-away shows turbine wheel inside the cast-iron casing (nearest end) of the turbine end, an aluminum housing on the compressor side, and the transition region in between, containing the steel shaft connecting both wheels and bearings.

CRADA Project

This new CRADA project began at the beginning of August, 2009, and is comprised of six tasks, which will span the 3y duration of this project. Activity began with ORNL and Honeywell discussing the priority of the various turbocharger components for materials upgrades.

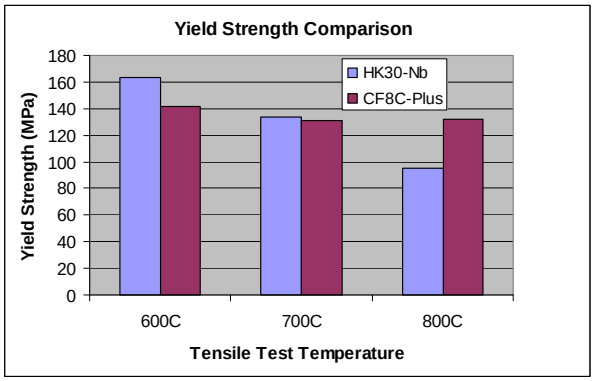

Figure 3 – Comparison of yield strength (YS) measured by elevated temperature tensile testing of both cast CF8C-Plus and cast HK30-Nb austenitic stainless steels. While the HK30-Nb has slightly higher YS at 600°C, both materials have similar strength at 700°C, and the CF8C-Plus steel is stronger at 800°C.

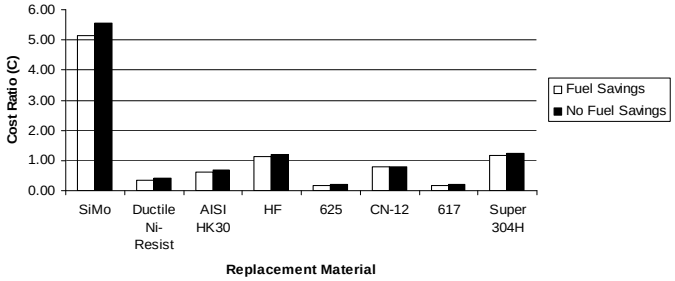

Figure 4 – Cost comparison of the new CF8C-Plus cast stainless steel to alternative heat-resistance materials that could be used for automotive exhaust manifold components, ranging from cast-irons (SiMo and Ni-resist), to austenitic stainless steels (Super 304H, CN-12, HK-30 and HF), to Ni-based superalloys (625 and 617). Ratios greater than 1 indicate CF8C-Plus steel costs more, while ratios less than 1 represent a cost-benefit for CF8C-Plus steel.

The turbine wheel-shaft assembly was chosen as the first component for consideration, with analysis of residual stresses near the weld-joint of the Ni-based superalloy wheel to the steel shaft being the focus. This new CRADA project also continues previous work between ORNL and Honeywell on testing of the new CF8C-Plus cast stainless steel as a significant performance upgrade for the turbine housing relative to standard SiMo cast iron.

Figure 1 shows a Caterpillar Regeneration System burner housing made from CF8C-Plus cast stainless steel, for initiating the regeneration cycle for ceramic diesel particulate filters (DPF), mandated on all on-highway diesel engines to clean up exhaust in January, 2007. The CRS unit is subject to rapid and severe thermal cycling for such service, with maximum temperatures being close to 900°C. This was the first commercial application of the new CF8C-Plus steel, developed earlier by ORNL and Caterpillar, and to-date over 450 tons of steel have been cast for this single application. No CRS units have failed, with the initial components deployed having over 3 years of service.

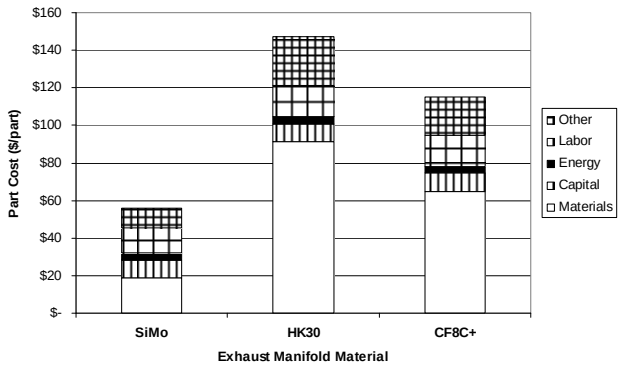

Figure – 5 - A more detailed cost-analysis, showing the various components that comprise the finished cost of an exhaust component for commercial SiMo cast-iron and HK-30 cast stainless steel, and for CF8C-Plus steel.

Figure 2 shows a typical Honeywell turbocharger system used for passenger vehicle engine applications. It is cut-away, so that the internal rotating components (wheels, shaft) for the turbine (hot-end) and compressor (cold-end) can be seen. Figure 3 shows some results from previous work by ORNL and Honeywell comparing the new CF8C-Plus steel to HK30-Nb, a standard commercially available upgrade material for turbochargers for heavy-duty truck diesel engines when temperatures exceed the limitations of SiMo cast iron. For comparison of elevated temperature tensile properties at 600-800^{o}C, CF8C-Plus cast stainless steel has similar yield-strength at 700^{o}C, and higher strength at 800^{o}C than HK30-Nb stainless steel. One task of this new CRADA project for turbine housings will continue this work for a broad range of other high temperature properties, including creep and fatigue strength, and expand it to turbine housing applications for passenger vehicle gasoline engines.

CF8C-Plus Cost-Analysis

A detailed cost analysis for automotive exhaust manifolds and other exhaust components for other engine systems, comparing the new CF8C-Plus cast stainless steel to a wide of range of conventional heat-resistant materials that are (or could be) used for exhaust components, was conducted by S. Das at the NTRC. The materials ranged from conventional SiMo ductile cast iron and Ni-resist austenitic cast iron, to austenitic stainless steels (CN12, Super 304H (wrought), HF and HK30), to more expensive Ni-based superalloys (alloys 625 and 617). It included visits to U.S. foundries with experience or licenses for casting CF8C-Plus, including MetalTek International (Carondelet Division, Pevley, MO, and Wisconsin Centrifugal Division, Waukesha, WI) and Stainless Foundry & Engineering (Milwaukee, WI), and telephone interviews with many others. Figure 4 shows ratios of cost of conventional materials to CF8C-Plus steel, with 1 being the same, less expensive being greater than 1, and more expensive being less than 1. CF8C-Plus has cost-benefits relative to alloys with high Ni and other more expensive alloying elements (i.e. Mo, W, Nb), including Ni-resist austenitic cast-iron, stainless steels like HK30 and CN12, and Ni-based superalloys. Figure 5 shows a more detailed cast analysis for the various manufacturing steps involved in making automotive exhaust manifolds, for CF8C-Plus steel compared to commercial SiMo cast-iron and HK30 cast stainless steel.

Conclusions

CRADA – not applicable, new project started in August, 2009.

CF8C-Plus Economics Study – CF8C-Plus cast stainless steel has significant performance benefits, but costs more than conventional SiMo cast iron or Super 304H or HF stainless steels. However, CF8C-Plus cast stainless steel has significant cost benefits relative to Ni-resist austenitic cast-iron, HK30 cast stainless steel, and particularly compared to Ni-based superalloys.

Publications/Presentations

A draft of an ORNL Report on Cost-Effectiveness of CF8C-Plus Cast Austenitic Stainless Steel in Automotive Applications was prepared for DOE/EERE/OVT by Sujit Das in August, 2009.

Special Recognitions and Awards/Patents Issued

None

Agreement 17894 - NDE Development for ACERT Engine Components

Jiangang Sun
Argonne National Laboratory
9700 South Cass Avenue
Argonne, IL 60439
630-252-5169; fax: 630-252-2785; e-mail: sun@anl.gov

DOE Technology Manager: Jerry L. Gibbs
(202) 586-1182; fax: (202) 586-1600; e-mail: Jerry.gibbs@ee.doe.gov
ORNL Technical Advisor: D. Ray Johnson
(865) 576-6832; fax: (865) 574-6098; e-mail: johnsondr@ornl.gov

Contractor: Oak Ridge National Laboratory, Oak Ridge, Tennessee
Contract No.: DE-AC05-00OR22725
Subcontractor: Argonne National Laboratory, Argonne, Illinois

Objectives

- Develop rapid, reliable, and repeatable nondestructive evaluation (NDE) methods for inspection of advanced materials and processing technologies to support the material-enabled high-efficiency diesels program.
- Establish NDE methods and test procedures for characterization of advanced materials and components being tested in an ACERT experimental engine at ORNL.

Approach

- Develop infrared thermal imaging methods for quantitative measurement of thermal barrier coating (TBC) properties and 3D imaging of TBC structures to determine TBC degradation and detect delamination.
- Evaluate optical imaging methods for detection of TBC delaminations and for characterization of subsurface crack geometry in advance ceramics.
- Investigate synchrotron x-ray CT technologies for NDE characterization of microstructural flaws in ceramics and welding quality of light-weight metallic components for diesel engines.

Accomplishments

- Developed thermal imaging technology for NDE characterization for as-processed and thermally-cycled TBCs.
- Demonstrated capability of optical NDE technologies for high-resolution detection of delaminations in TBCs.
- Developed and evaluated synchrotron x-ray CT technologies for NDE inspection of advanced materials and components for diesel engines. In particular, microCT can detect submicron cracks in ceramics and high-energy CT may be used to inspect large metallic engine parts.

Future Direction

- Continue development and evaluation of optical and thermal imaging NDE technologies for characterization of TBCs applied on diesel engine components.
- Develop/evaluate x-ray and ultrasonic imaging NDE technologies for inspection of jointed components for diesel engine.

Introduction

Application of advanced materials in diesel engines may enhance combustion and reduce parasitic and thermal losses, thereby improving engine efficiency while meeting the emission standard. Engine components developed from advanced materials and processing technologies, however, require rigorous assessment to assure their reliability and durability in higher temperature and pressure operating conditions associated with advanced engine systems. To address these materials challenges, selected materials/components are being prepared and tested in a Caterpillar heavy-duty C15 ACERT experimental diesel engine located at ORNL. The engine tests will provide crucial information on the material performance and durability and on their effects to engine efficiency and parasitic losses in combustion and thermal management systems[1]. In collaboration with materials scientists and engine engineers from Caterpillar and ORNL, these engine materials and components are being characterized by nondestructive evaluation (NDE) technologies at ANL to determine their reliability and durability for engine applications. The objective of this work is to develop and assess various NDE methods for characterization of advanced materials and components for ACERT engine systems. NDE technologies established at ANL, including optical scanning, infrared thermal imaging, ultrasonic imaging, and x-ray computed tomography (CT), are being further developed for detection of volumetric, planar, and other types of flaws that may limit the performance of these components. NDE development is focused on achieving higher spatial resolution and detection sensitivity. The primary effort in FY 2009 was focused on developing infrared thermal imaging and optical scanning technologies for thermal barrier coatings (TBCs) to be utilized in engine exhaust systems. Another effort was directed on development and evaluation of synchrotron x-ray CT technologies for 3D structural characterization of engine components made from advanced materials. This research is collaborated with Caterpillar Inc. and ORNL.

Approach

Advanced TBC is a key enabling material technology to allow for diesel engines to achieve higher fuel efficiency and reduce emission. A TBC material typically has drastically lower thermal conductivity and superior oxidation resistance, which may significantly reduce heat losses and at the same time prevent corrosion and facilitate utilization of cost-effective metals in engine systems because of the decreased component temperature. In the gas turbine industry, ceramic TBCs have become an integral part of high-temperature components in hot-gas paths. TBCs have also been developed for diesel-engine components such as pistons and exhaust systems. These TBCs have wide variations in composition and thickness, ranging from tens of microns to a few millimeters. The challenge for TBC characterization has been on developing NDE methods that can (1) accurately measure TBC properties to allow for quantitative determination of TBC quality and degradation and (2) detect TBC cracks and delaminations that cause TBC spallation. The most used NDE technologies for TBCs are pulsed thermal imaging and optical methods. ANL has been active in developing both technologies. A pulsed thermal imaging system (see Fig. 1) consists of an infrared camera, one and more photographic flash lamps, and a data acquisition and processing PC. Two data-processing methods are being developed: a thermal tomography method and a multilayer modeling method. The thermal tomography method can construct 3D images of material's thermal effusivity in an entire specimen volume, and the multilayer modeling method may quantitatively determine thermal properties (conductivity) of the TBC layer; both can be used for NDE characterization of multilayer TBC materials of various thickness. On the other hand, optical methods are suitable to detect cracks and delaminations in thin translucent TBCs. ANL has developed and evaluated laser backscatter and optical coherence tomography (OCT) for TBC characterizations. The laser backscatter is based on cross-polarization detection of optical scattering originated from subsurface discontinuities (i.e., TBC delaminations), and the OCT may image 3D microstructure variation of the TBC layer. These NDE methods are utilized to evaluate TBCs developed for diesel exhaust system application.

NDE development may also lead to quantitative prediction of mechanical properties for advanced materials and components. For advanced ceramics, geometric parameters of subsurface flaws have been identified to affect material strength because they determine the fracture initiation stress. These

parameters, e.g., crack size and depth, can be measured using 3D optical imaging methods such as confocal microscopy and OCT. Synchrotron x-ray microCT technology, developed at the advanced photon source (APS) at ANL, was also investigated for detection of small cracks in ceramics. Figure 2 shows the microCT experimental system at APS. In addition, in collaboration with APS beamline scientists, a prototype high-energy x-ray CT system was developed for examination of industrial metallic components up to 2-inches in size. The synchrotron x-ray source has high peak energy (>250keV) and flux than conventional industrial source, and the spatial resolution may reach to ~40μm. This system is being evaluated to examine metallic joints and other diesel engine components.

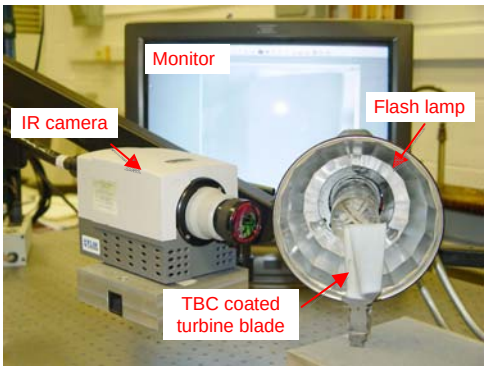

Figure 1. One-sided flash thermal imaging system.

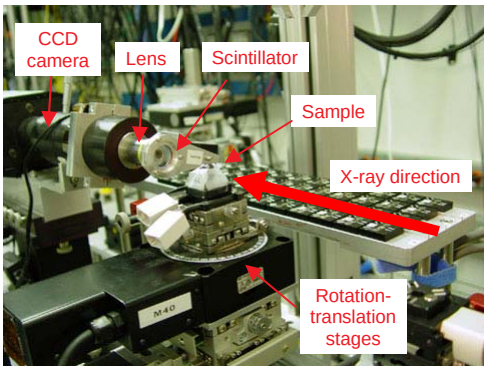

Figure 2. Synchrotron microCT system at APS.

Results

Thermal Imaging Analysis of As-Processed TBCs

Ten as-processed TBC specimens, six (6) 2-inch-squared and four (4) 1-inch-squared, see Fig. 3, were supplied by Caterpillar for NDE analysis. They consist of a ceramic TBC coat produced by a conversion process from slurry deposition and a cast Fe-steel substrate.

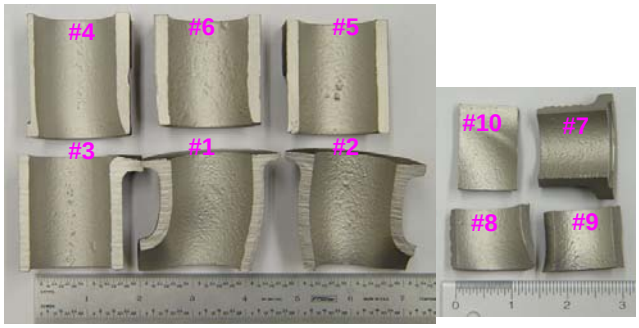

Six 2"-squared Four 1"-squared

Figure 3. Photos of 10 as-processed TBC specimens.

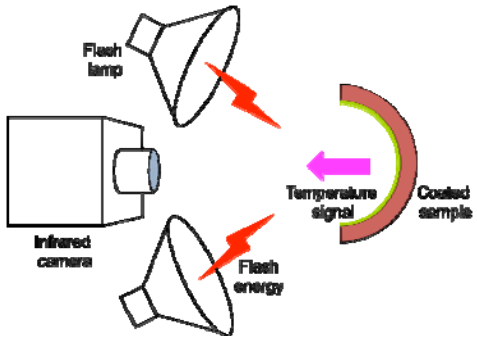

Figure 4. Schematic top view of thermal imaging setup.

Figure 4 shows a schematic of the thermal imaging test setup. Because the specimens have deep concave surfaces, two flash lamps, operated at their highest power of 6.4kJ per flash, were used to supply adequate heating on the entire coating surface. However, because the coating surface has very low absorption (or high reflection as seen in Fig. 3), the flash heating efficiency was poor. The high surface reflection also necessitated the use of an optical filter on flash lamps. Incidentally, ANL has invented such a filter that was granted a US patent in FY2009. The maximum temperature increase on coating surface during the flash was found to be only about 13°C, which is much smaller than needed for such test (by at least 5X smaller). As a result, the NDE data are generally noisier.

Each TBC specimen was tested individually. The infrared camera was operated at a speed of 1068Hz and 3000 frames of the surface temperature evolution after the flash heating were acquired. The recorded thermal images (frames) were processed off-line using the thermal tomography method, which constructs 3D images of material's thermal effusivity in the entire TBC specimen volume. The thermal tomography results are generally presented in 100 plane slices that corresponds to various

depths from the imaged surface, with plane 1 on the surface and plane 100 at the deepest depth. The 3D data can also be sliced in the cross-sectional directions, which display the depth distributions of the material's thermal effusivity. The pixel size in the plane slice is ~0.4 mm for 2" TBCs and ~0.2 mm for 1" TBCs and, in depth direction, on the order of tens of microns.

Figure 5 shows plane and cross-section slice images for TBC specimen #5, a 2-inch-squared specimen (see Fig. 3). From the cross-section images in Fig. 5c, the coating layer was identified to have a lower thermal effusivity and a thickness represented by 5 plane slices (the thickness of each slice can be determined if the thermal properties of the coating material are known). Accordingly, Fig. 5a shows 3 plane coating slices (1, 3, and 5) and Fig. 5b shows 3 plane substrate slices (6, 8, and 10) that are just below the coating. The plane slice #1 on the surface is generally darker, which is an artifact likely due to the effect of flash characteristics. This darker tone gradually diminishes as the depth increases (or slice number increases). There appears a "crack" feature running along the axis (top to bottom) in the middle of the curved specimen (see Fig. 5a). This feature is not a defect, because defective features generally show much darker grayscale (lower effusivity), but likely a wrinkle on substrate surface as it is also seen in the substrate images (Fig. 5b). In addition, there are a few large bumps on surface (see Fig. 5a and also Fig. 3). Because heat transfer was not one dimensional around these bumps, they generate some artifacts in the tomographic images (note that the two cross-section images in Fig. 5c cut though the two bigger bumps). Except the artifacts due to surface features, no apparent defects were identified for TBC specimen #5.

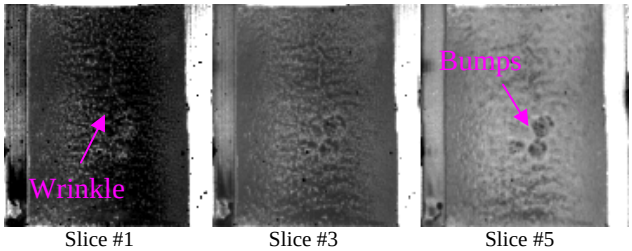

Figure 5a. Plane slices within the coating layer of TBC specimen #5.

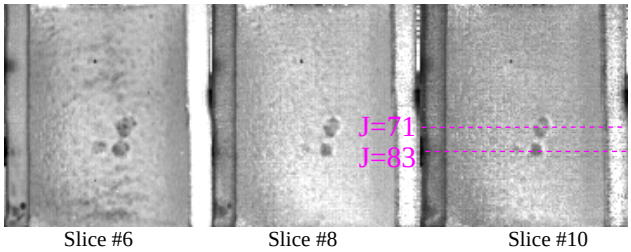

Figure 5b. Plane slices within the substrate layer of TBC specimen #5.

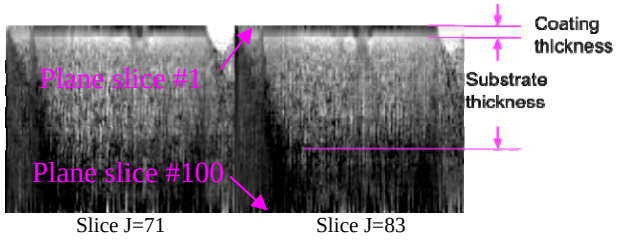

Figure 5c. Cross-section slices at locations indicated in Fig. 5b for TBC specimen #5.

Figure 6 shows plane and cross-section slice images for TBC specimen #8, a 1-inch-squared specimen (see Fig. 3). This specimen has a relatively smooth surface, so the NDE results are generally uniform. Again, the cross-section image in Fig. 6c indicates that the coating thickness is represented by 5 plane slices. From the plane slices in Figs. 6a and 6b, no apparent defects were found in this specimen. In general, thermal imaging data suggested that there is no apparent defect in all as-processed TBC specimens.

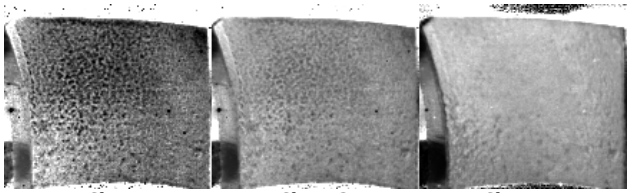

Figure 6a. Plane slices within the coating layer of TBC specimen #8.

Figure 6b. Plane slices within the substrate layer of TBC specimen #8.

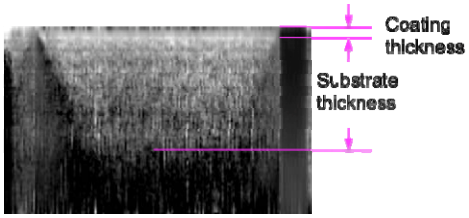

Figure 6c. Cross-section slice at location indicated in Fig. 6b for TBC specimen #8.

Thermal Imaging Analysis of Thermally-Cycled TBCs

Six TBC and two reference Fe-steel specimens were subjected to thermal-cycling tests at ORNL, with a total of 500 cycles between 300 and 760ºC. Microscopic examination of TBC surfaces at ORNL identified severe TBC delaminations as well as considerable porosity due to oxidation[2]. The TBC cracking and delamination appeared to initiate at individual sites; many are linked together to form large delaminated areas. Figure 7 shows the thermally-cycled TBC specimens when received at ANL for NDE analysis. The TBC surfaces exhibit two distinct colors, light gray and dark brown. The gray areas are oxidized TBC surface and the brown areas are where the TBCs had spalled. This becomes apparent when examining the photographs of TBC specimen #7 taken at ORNL after the cycling test and at ANL, see Fig. 8. Many new brown surface areas are shown in the ANL photograph, a result of spallation due to handling (bubble wrap packaging) during shipment. This also indicates that many TBC surfaces were completely delaminated; they still remained on surface because of lateral support.

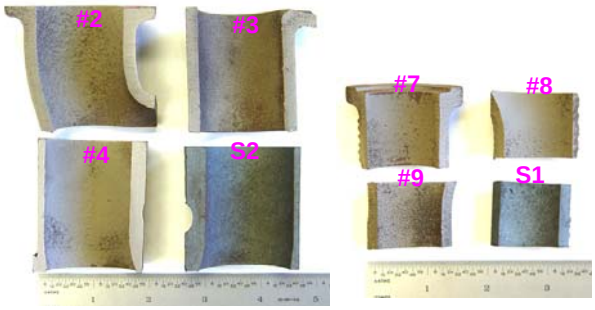

2”-squared 1”-squared

Figure 7. Photographs of thermally-cycled TBC and Fe-steel (S1 and S2) specimens.

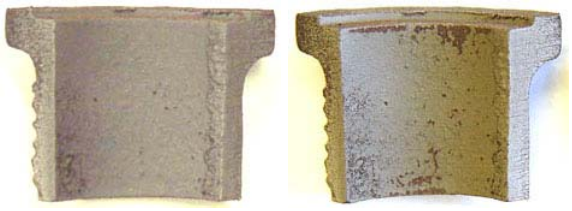

Taken at ORNL Taken at ANL

Figure 8. Photographs taken at ORNL and ANL for thermally-cycled TBC specimen #7.

Figure 9 shows plane and cross-section slice images of thermally-cycled TBC specimen #7. The delaminated TBC areas have low thermal effusivity and are displayed with darker grayscale in the images. The delaminated TBC top layer was not resolved as seen in the cross-section image Fig. 9c, indicating that the layer is very thin (~20μm[2]) that would require a higher thermal imaging frequency to resolve it. The cross-section image data in Fig. 9c also indicate that subsurface material in the TBC-spalled areas is generally free of damages. The plane slice data in Figs. 9a and 9b suggest that delaminations took place initially in individual sites and linked together later to form larger sizes. Similar results, although “lesser” damage severity, were found for other thermally-cycled TBC specimens. In Fig. 10, thermal imaging data for TBC #8, the individual delamination sites are more segregated and smaller in size.

Slice #1 Slice #3 Slice #5

Figure 9a. Plane slices within the coating layer of TBC specimen #7.

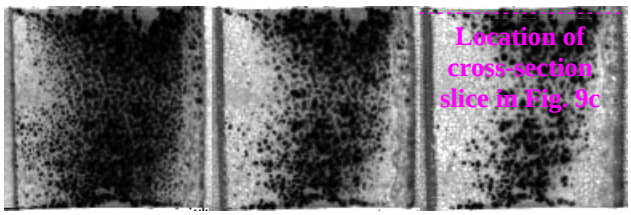

Slice #6 Slice #8 Slice #10

Figure 9b. Plane slices within the substrate layer of TBC specimen #7.

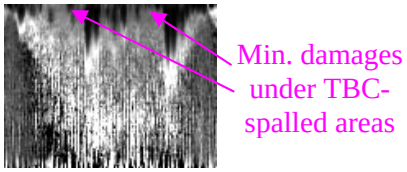

Figure 9c. Cross-section slice at location indicated in Fig. 9b for TBC specimen #7.

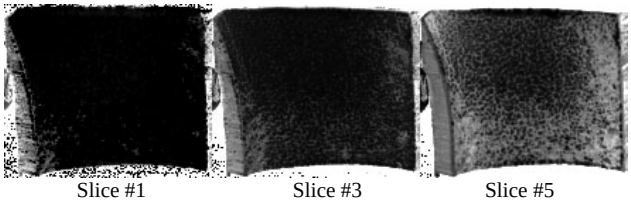

Figure 10a. Plane slices within the coating layer of TBC specimen #8.

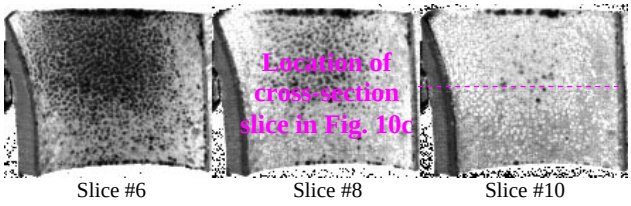

Figure 10b. Plane slices within the substrate layer of TBC specimen #8.

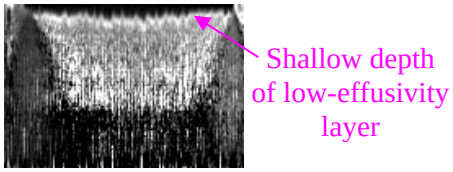

Figure 10c. Cross-section slice at location indicated in Fig. 10b for TBC specimen #8.

Optical Imaging Analysis of TBCs

Although thermal imaging provides NDE data for the entire TBC surface, its lateral resolution is limited by the pixel size which is ~0.2mm when testing 1"-squared specimens. To obtain higher resolution, optical scanning methods can be used because ceramic TBCs are optically translucent. Two optical methods were evaluated for NDE inspection of TBCs at both as-processed and thermally-cycled conditions, the laser backscatter for surface imaging and the OCT for cross-sectional imaging.

Figure 11 is a photomicrograph of an as-processed TBC surface; it consists of raised circular features of various sizes. In high-magnification SEM images[2], many cracks and pores up to a few tens of microns in size are visible mostly around the boundaries of large circular features. These cracks/pores are detected in the laser-backscatter surface-scan image Fig. 12, shown with higher scatter intensities. Because the detected backscatter mostly came from subsurface, the data indicate that these cracks/pores may penetrate for a considerable depth under the surface.

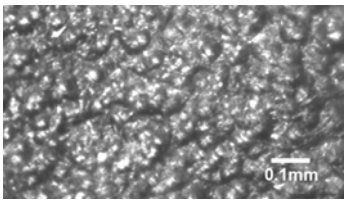

Figure 11. Photomicrograph of as-processed TBC.

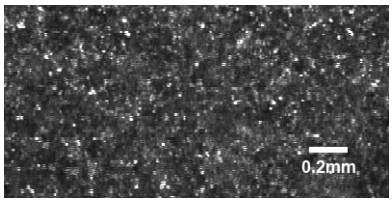

Figure 12. Laser-backscatter scan image of as-processed TBC surface.

Figure 13 is a photomicrograph of a thermally-cycled TBC surface. Many delamination features of various sizes and shapes are clearly visible on the surface. The delaminations can be confirmed using OCT. Figure 14 shows two OCT cross-sectional scan images. The delaminated regions are typically raised and cracked at the peaks. The sizes and shapes of the delaminated areas can be determined from laser-backscatter scan of the TBC surface, as shown in Fig. 15. Compared with scan image for as-processes TBC surface in Fig. 12, large areas of the TBC surface were delaminated as represented by higher scatter intensities in Fig. 15. In general, optical NDE data provided detailed configuration of the TBC crack and delamination, down to ~10μm spatial resolutions with current systems. The correlation of optical NDE data with TBC microstructure is being further investigated.

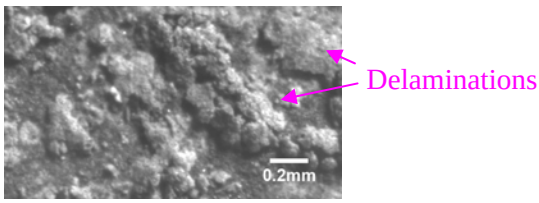

Figure 13. Photomicrograph of thermal-cycled TBC.

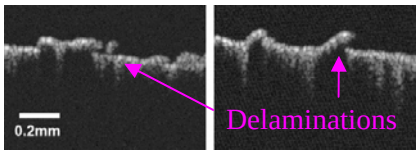

Figure 14. Cross-sectional OCT scan images of thermal-cycled TBC.

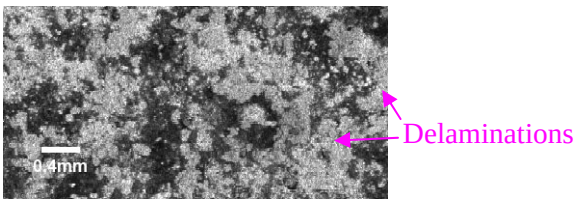

Figure 15. Laser-backscatter scan image of thermal-cycled TBC surface.

Synchrotron X-Ray MicroCT for Ceramic NDE

Synchrotron x-ray microCT at APS (see Fig. 2) was evaluated for NDE inspection of subsurface cracks in Si_3N_4 ceramics. These cracks typically have small crack openings, say <1µm, and dimensions <1mm, and they are the strength limiters in many applications of structural ceramics. MicroCT can reconstruct 3D structures with voxel size of ~1µm, and has been reported to be capable of detecting features at one tenth of the voxel size when a high quality x-ray source like the one from synchrotron is used. The microCT system at APS may perform data acquisition and construct all slices of entire 3D volume of a specimen within an hour. Figure 16 shows a microCT slice within the subsurface of a Si_3N_4 ceramic specimen with two surface-breaking cracks (sample curtsey of Dr. C. Vieillard of SKF). The voxel size in this image is 0.74µm. It is clear that microCT detected and resolved the dimensions of both cracks, with the small crack having an opening of <0.1µm. This result demonstrates that microCT can be a valuable NDE technology to characterize the microstructure of ceramic materials.

Synchrotron X-Ray CT for Metallic Components

ANL has developed advanced x-ray imaging systems and software for 3D CT reconstruction. These systems have been widely used for NDE inspection of advanced materials and components. For large metallic components, however, industrial x-ray sources don't have sufficient intensity (flux) to produce high-quality images with good signal-to-noise ratio. This has limited their application to examine metallic diesel-engine components made from advanced materials and processing technologies such as friction welding for light-weight TiAl materials. Synchrotron x-ray CT, with its high peak energy and beam intensity, can produce high-resolution images for NDE inspection. Figure 17 shows a preliminary cross-sectional CT slice of a nickel-based superalloy turbine blade. Volumetric features with sizes in the order of the voxel size ~60µm may be identified. This system is still being optimized.

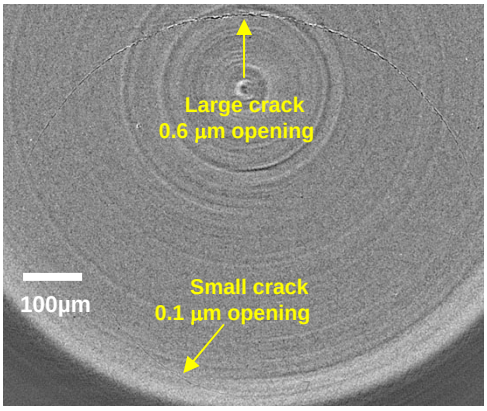

Figure 16. Synchrotron microCT slice of the subsurface of a ceramic specimen with two cracks.

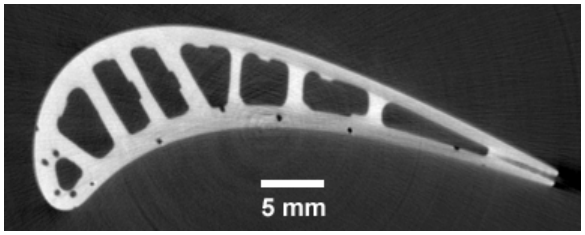

Figure 17. Typical synchrotron CT slice of a superalloy turbine blade.

Conclusions

Thermal imaging and optical scanning methods were developed for NDE inspection of TBCs consisting of a top ceramic coat produced by a conversion process from slurry deposition and a cast Fe-steel substrate. The thermal tomography method was used to image the entire specimen volume including the coating and the substrate, and the results were displayed in plane and cross-section slice images. For as-processed TBCs, although various surface features were observed, such as large

wrinkles/bumps and small micro-scale cracks/pores, no apparent TBC defect was detected. After thermal-cycling test at ORNL, significant delamination in the coating was detected. The thermal tomography data suggest that delaminations initiated in individual sites with small sizes and they linked together as thermal cycling proceeded. Below the surface areas where TBC has spalled, the subsurface material is generally free of damages. However, because thermal imaging has limited lateral resolution determined by the pixel size (~0.2mm) used in imaging, optical laser-backscatter and OCT methods were also used to examine the TBC coating layer because it is optically translucent. The optical methods were demonstrated to have better spatial resolution, in the order of 10μm, and revealed further details of the coating flaws that further confirmed the findings from thermal imaging. These NDE results are being correlated and optimized.

Synchrotron x-ray CT at APS was investigated for NDE characterization of advanced materials and components developed for diesel engines. Two technologies were examined: microCT and high-energy CT. X-ray microCT was used for detection of subsurface cracks in Si_3N_4 ceramics. It was demonstrated that cracks of 0.1μm opening size can be detected and complete crack geometry can be determined. Such result cannot be obtained by other NDE methods. One the other hand, in collaboration with APS beamline scientists, a high-energy synchrotron CT system was developed for NDE of large metallic components. It has produced high-sensitivity and high-resolution images than those from conventional CT systems, and can be used for characterization of diesel engine components made with advanced materials and processing technologies.

References

1. M.D. Kass, et al., "Materials Testing with ACERT Engine," *Annual Report for FY2008, Heavy Vehicle Propulsion Materials Program.*

2. H.T. Lin, et al., "Durability of ACERT Engine Components," *Quarterly Report for April-June 2009, Heavy Vehicle Propulsion Materials Program.*

Presentations and Publications

J.G. Sun, E.R. Koehl, S. Steckenrider, C. Vieillard, and T. Bayer, "Nondestructive Inspection of Ceramic Bearing Balls Using Phased Array Ultrasonics," in Ceramic Eng. Sci. Proc., eds. D. Singh and J. Salem, Vol. 30, no. 2, pp. 233-240, 2009.

J.G. Sun, "Measurement of Thermal Barrier Coating Conductivity by Thermal Imaging Method," in Ceramic Eng. Sci. Proc., eds. D. Singh and J. Salem, Vol. 30, no. 3, pp. 97-104, 2009.

J.G. Sun, "Optical Filter for Flash Lamps in Pulsed Thermal Imaging," U.S. Patent No. 7,538,938, issued May 26, 2009.

Budong Yang, Jiangang Sun, Elizabeth Frink, Shuting Lei, and Kevin Lease**, "**Assessment of Part Quality in Laser Assisted Milling of Silicon Nitride Ceramic," paper submitted to ICALEO 2009 conference.

J.G. Sun, "Thermal Conductivity Measurement for Thermal Barrier Coatings Based on One- and Two-Sided Thermal Imaging Methods," paper presented at the 36th Annual Review of Progress in Quantitative Nondestructive Evaluation, Kingston, Rhode Island, July 26-31, 2009.

Agreement 18571 – Materials Issues Associated with Exhaust Gas Recirculation Systems

M. J. Lance, C. S. Sluder, and J. M. E. Storey**
Ceramic Science and Technology Group
Oak Ridge National Laboratory
P.O. Box 2008, MS 6068, Bldg. 4515
Oak Ridge, TN 37831-6068
(865) 241-4536; fax: (865) 574-6098; e-mail: lancem@ornl.gov
* *National Transportation Research Center, ORNL*

DOE Technology Manager: Jerry L. Gibbs
(202) 586-1182; fax: (202) 586-1600; e-mail: Jerry.gibbs@ee.doe.gov
ORNL Technical Advisor: D. Ray Johnson
(865) 576-6832; fax: (865) 574-6098; e-mail: johnsondr@ornl.gov

---

Contractor: Oak Ridge National Laboratory, Oak Ridge, Tennessee
Prime Contract No.: DE-AC05-00OR22725

Objectives

- Provide information to industry specialists about fouling deposit properties so as to enable improved models and potential design improvements to reduce fouling and its impact on the performance of EGR (exhaust gas recirculation) coolers.

Approach

- Assemble EGR engineers from member companies of the Diesel Crosscut Team to serve as an advisory board for this project.
- Purchase and set up a diesel engine as an exhaust generator with a sampler system that will allow for the formation of controlled particulate matter (PM) deposits on model cooler tubes.
- Obtain and evaluate representative (half-useful-life) EGR coolers from industry members,

Accomplishments

- An EGR Team consisting of nine diesel engine OEMS was assembled and survey as to what the greatest materials issues are facing EGR systems. The main problem was high pressure EGR cooler fouling.
- A GM 1.9 L engine on a Drivven controller is operational in standard and PCCI modes.
- Seven companies have provided eleven real-world coolers for analysis. Deposits have been analyzed using a variety of experimental techniques to identify common features that will help to guide future research.

Future Direction

- Complete chemical and microstructural characterization of industry provided coolers.
- Use exhaust sampler system to generate PM deposits that will be aged in controlled conditions using a bench-flow reactor so as to evaluate the effect of water, hydrocarbon and cycling on deposit properties.

Introduction

High-pressure exhaust gas recirculation (HP-EGR) is the dominant NO_x-reduction technology used by the diesel engine community today. High-pressure EGR systems extract a portion of the exhaust gases upstream of the exhaust turbine, pass the gases through a compact heat exchanger (EGR cooler) and then introduce them to the intake downstream of the compressor and charge-air cooler (intercooler). As the exhaust gas flows through the EGR cooler, particulate matter (PM) will migrate from the hot exhaust gas to the cooled heat exchanger surface forming a porous deposit that has a thermal conductivity comparable to Styrofoam making it a nearly ideal thermal insulator. As the thickness of the deposit increases, the effectiveness of the EGR system goes down due to the inability to cool the exhaust gas. This is known as cooler fouling. Despite its importance for (HP) EGR, there do not appear to be many investigations of the effect of fouling from diesel particulate matter on the performance of EGR cooling devices or heat exchangers.

In February of 2009, a team consisting of engineers responsible for EGR systems was assembled from nine diesel engine manufacturers: Caterpillar, Cummins, Detroit Diesel, Ford, GM, John Deere, Navistar, PACCAR and Volvo/Mack. They were surveyed to identify the biggest problem facing EGR systems. The clear winner was EGR cooler fouling. The EGR Team then recommended the purchasing of a traditional engine-on-dynamometer to generate fouling deposits on model tubes. They also agreed to send a real-world cooler from an actual engine that had seen enough operation to categorize it as 'half-useful-life'. Of the 9 team members, the 7 companies that currently use HP-EGR all sent at least one cooler for analysis with the data obtained to be shared with the entire team. The results of this survey will be discussed below.

Experimental Approach

A GM 1.9 L engine on a Drivven controller is operational in standard and PCCI modes. The EGR team recommended this set-up as opposed to the proposed genset as an exhaust generator. Most of the sampler system parts have arrived and are ready to be assembled. This system is based on a previous sampling system designed at ORNL that directs exhaust gas through square tubes that are externally cooled to temperatures similar to those existing in actual EGR coolers. Additionally, a bench flow reactor is being built for accelerated aging of deposits at controlled temperatures and gas composition. This will allow for the characterization of microstructural changes that occur in the deposits due to engine transients.

Results

The results presented here are for the real-world cooler deposits obtained from 7 out of 9 of the GER Team members. A total of 11 coolers were obtained and all underwent the same forensic analysis. Figure 1 shows all the information that was provided by the engine companies about these coolers. Coolers #5, #6 and #9 (and likely #1 and #7) came from actual engines in use whereas coolers #2, #8 and #10 (and probably #3 and #4) came from a dyno-cell. Coolers #10a and #10b were the 1st and 2nd pass from the same EGR loop. All had seen hours that would be infeasible to reproduce at ORNL given our single-shift environment. Each cooler was cut open with a band saw and two of the tubes from within the shell were selected to be further cut into ¾ inch segments so they could fit into 2 inch mounts for machining and polishing. The sawing was done without water and slowly so as to minimize vibration and local heating of the deposit. Most of the cooler deposits were tacky enough such that the deposit easily survived the cutting. Tapping the cooler segments didn't release much deposit.

Figure 2 shows the approximate total surface area of the coolers. Larger coolers like #7, which weighed 37 lbs., likely came from off-road trucks whereas coolers #3 and #10a&b came from light-duty engines. Other coolers fell in between these two extremes. This shows that the samples analyzed here represent a cross-section of all EGR cooler platforms.

Figure 3 shows the deposit mass per unit area for the inlet, middle and outlet of each cooler. The mass of the deposit was measured by heating ¾ inch long sections of tube near the inlet, middle and outlet to 600°C, cleaning them and measuring weight change. Coolers #3 and #4 both exhibited significant clogging whereby entire channels were blocked with deposit which accounts for the high mass/area of these coolers. #5 was very wet and

smelled of oil which likely increased the deposit mass significantly. Cooler #7 exhibited silicates and clays which likely increased the deposit mass over what would be expected from just carbonaceous material.

The trends in deposit mass/area along the length of the cooler were independently confirmed using optical microscopy, with the exception of coolers #4 and #7. There was no consistent trend between all of the coolers in the change in deposit mass along the length.

The elemental compositions of the deposits were measured using energy dispersive spectroscopy (EDS) in a scanning electron microscope (SEM), see Figure 4. X-ray Fluorescence (XRF) wasn't used because it is insensitive to oxygen and carbon. Also, using the SEM allows one to avoid metal debris produced during cutting when collecting spectra. Coolers #1 & #9 had large amounts of sulfur and iron. These two were the only coolers that exhibited clear evidence of corrosion. Cooler #5 had significant amounts of Fe & Cr (metal debris) from cutting since this deposit was very wet and tacky which allowed metal chips to stick to it. Cooler #7 had elements common in dirt (Si, Na, Ca, K, P).

The phases present in each cooler was measured suing X-ray Diffraction (XRD) (Figure 5). Coolers #1 and #9 showed the presence of metal sulfate and cooler #7 showed silicates which confirms the EDS results. Some of the coolers showed trace amounts of steel presumably from the cutting process and nearly all showed amorphous carbon peaks.

Two methods were developed to image the microstructure of the deposit. The first was to mount the deposit in epoxy and polish the cross-section. Epoxy mixed with a fluorescent dye was poured over a ¾" section of tube without pulling a vacuum to remove pores. The mount is then ground on one side until the outer tube is gone. A second epoxy infiltration, this time with a vacuum infiltration, is then done. The sample is then ground and polished. The technique is useful for seeing the interaction between the tube geometry and the deposit (Figure 6) and seeing where the hydrocarbon (HC) is distributed throughout the deposit cross-section (Figure 7). As the black soot is covered in HC, its reflectivity increases, providing contrast when using optical microscopy. This technique is NOT useful for determining deposit thickness since the epoxy tends to collapse the soot microstructure.

The second method for imaging the microstructure is to look at the fracture surface (Figure 8). The metal substrate is milled to the thickness of Al-foil and then broken open revealing the deposit fracture surface. This method allows one to see the pristine microstructure and thickness of the deposit.

Many common features were observed across all 11 coolers. First mudcracking was observed on many deposits (Figure 8) which suggest that the deposit is shrinking in the plane of the substrate. Moreover, the mudcracks can lead to spallation of the deposit as flakes defined by mudcracks often absent. Spallation seems to occur near turbulators on many of the coolers. Spallation of the deposit may be a source of spontaneous regeneration of the cooler which has been reported by many EGR team members.

Another common feature is that the HC concentration in the deposit increases near the metal substrate. This reflects the large temperature gradient that exists across the deposit during operation owing to the very low thermal conductivity of the PM. The deposit near the metal will be colder and hence will allow for the condensation of HC on it. This HC condensation will in turn cause the deposit to densify which can be seen in Figure 9. The deposit near the metal appears much coarser and the fine PM is hard to find. The density of the dry PM-composed deposit has been measured at ORNL to be ~2%. The condensing of HC on the PM appears to collapse the porous structure of the deposit causing it to be denser and therefore more thermally-conductive. Since HC will be concentrated at the metal surface, it will also greatly influence the adhesion of the deposit.

Figure 10 shows the surface of one of the fins of cooler #2 shown in cross-section in Figure 6. The left side of the image is a valley of the sinusoidal wave and the right side is a peak. The deposit is being eroded on the leading edge of the sinusoidal peak of each fin. The erosion is uneven and forms channels or grooves in the deposit, presumably from the action of the flowing exhaust gas. This microstructure has been observed on most of the coolers suggesting that erosion is a significant regeneration mechanism.

Conclusions

A team of industry advisors has been assembled that will help guide future research directions of this pre-competitive research.

An engine and a sampler tube system for laying down controlled PM deposits is being designed and purchased. A portable gas manifold for controlled post-deposition aging is being built.

Hydrocarbon condensation plays a pivotal role in EGR fouling and will affect clogging, densification, heat transfer, mud-cracking and adhesion.

Corrosion was observed on two coolers but didn't appear to present a large problem.

Microstructures indicating deposit erosion were observed on most coolers.

Microstructural analysis of EGR cooler deposits may reveal degradation mechanisms that can be easily prevented.

Cooler #	*Miles*	*Hours*	*Condition*
1	280000		
2			Dyno-cell
3			
4			
5	89478		Field Aged
6	113764		Field Aged
7	249128		
8		315	Dyno-cell
9		1389	Field Aged
10a	140000		Dyno-cell
10b	140000		Dyno-cell

Figure 1: Industry-provided cooler descriptions.

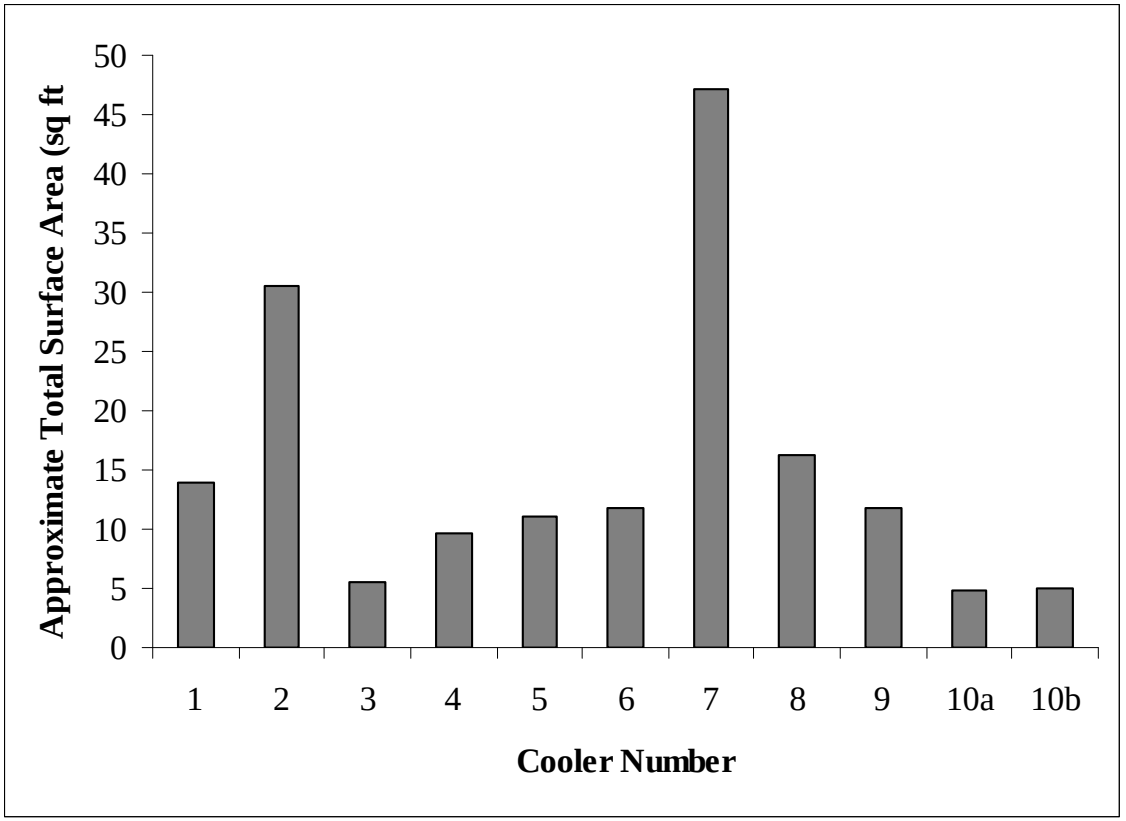

Figure 2: Total approximate surface area of coolers.

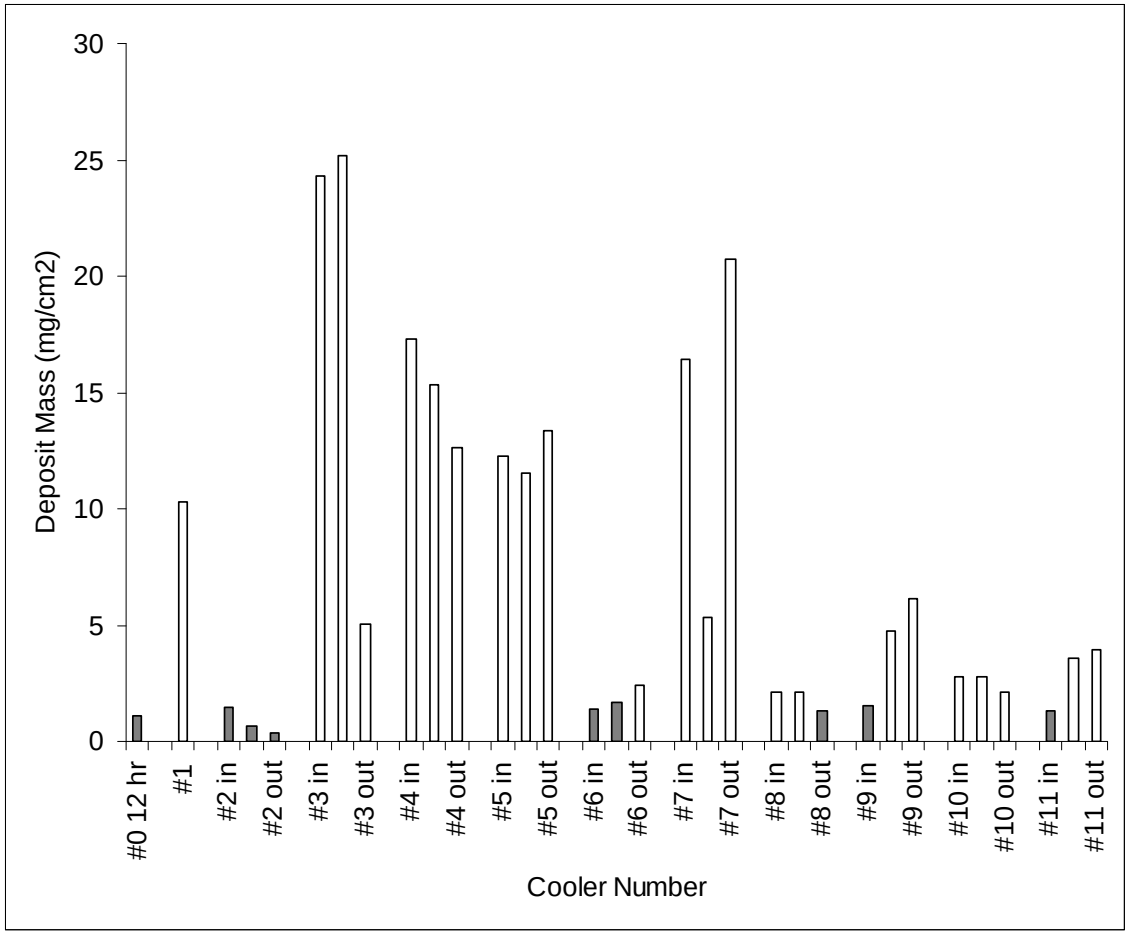

Figure 3: Deposit mass/area for each cooler measured near the inlet, middle and outlet.

Cooler #	*C*	*O*	*S*	*Fe*	*Si*	*Cr*	*Na*	*K*	*P*	*Ca*
1	50.1	32.4	10.7	4.9						
2	87.0	12.1								
3	82.3	17.3								
4	85.7	12.8								
5	76.1	11.0	0.2	9.0	0.1	2.8				
6	83.5	15.3			0.3					
7	14.0	44.0	0.2		29.5		6.7	2.0	0.6	1.3
8	83.7	13.9	0.4		0.1					0.7
9	32.8	39.0	14.3	10.8	0.4	1.2				
10a	85.8	13.3	0.3							
10b	83.5	16.0								

Figure 4: Energy Dispersive Spectroscopy (EDS) for Element Concentration. All values are in standardless weight percent.

Cooler #	*Amorphous C*	*Steel*	*Metal Sulfate*	*FeS*	*Na2SO4*	*Silicates*	*Graphite*
1	X		X	X			
2	X						X
3	X						
4	X						
5		X					
6	X						
7	X				X	X	
8	X	X					
9	X	X	X				
10a	X	X					
10b	X						

Figure 5: Phases present in each cooler deposit measured by X-ray Diffraction (XRD).

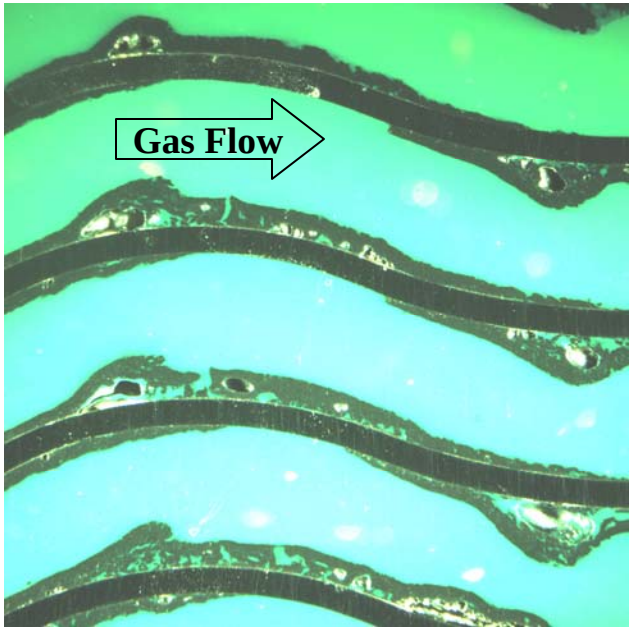

Figure 6: Cooler #2 in cross-section demonstrating the epoxy-mounting method for microstructural analysis. Here, the deposit is thicker on the peaks of the sine wave than in the valleys.

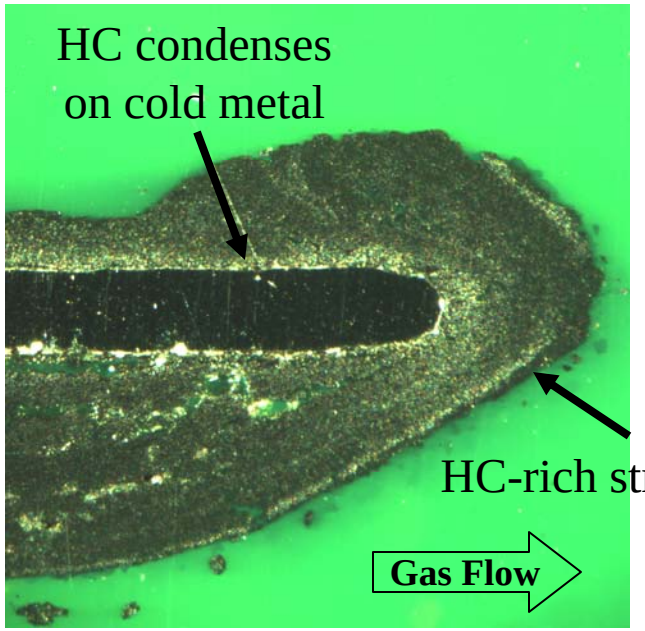

Figure 7: Cooler #3 in cross-section. HC rich strata can be observed which show up as shiny bands in the deposit.

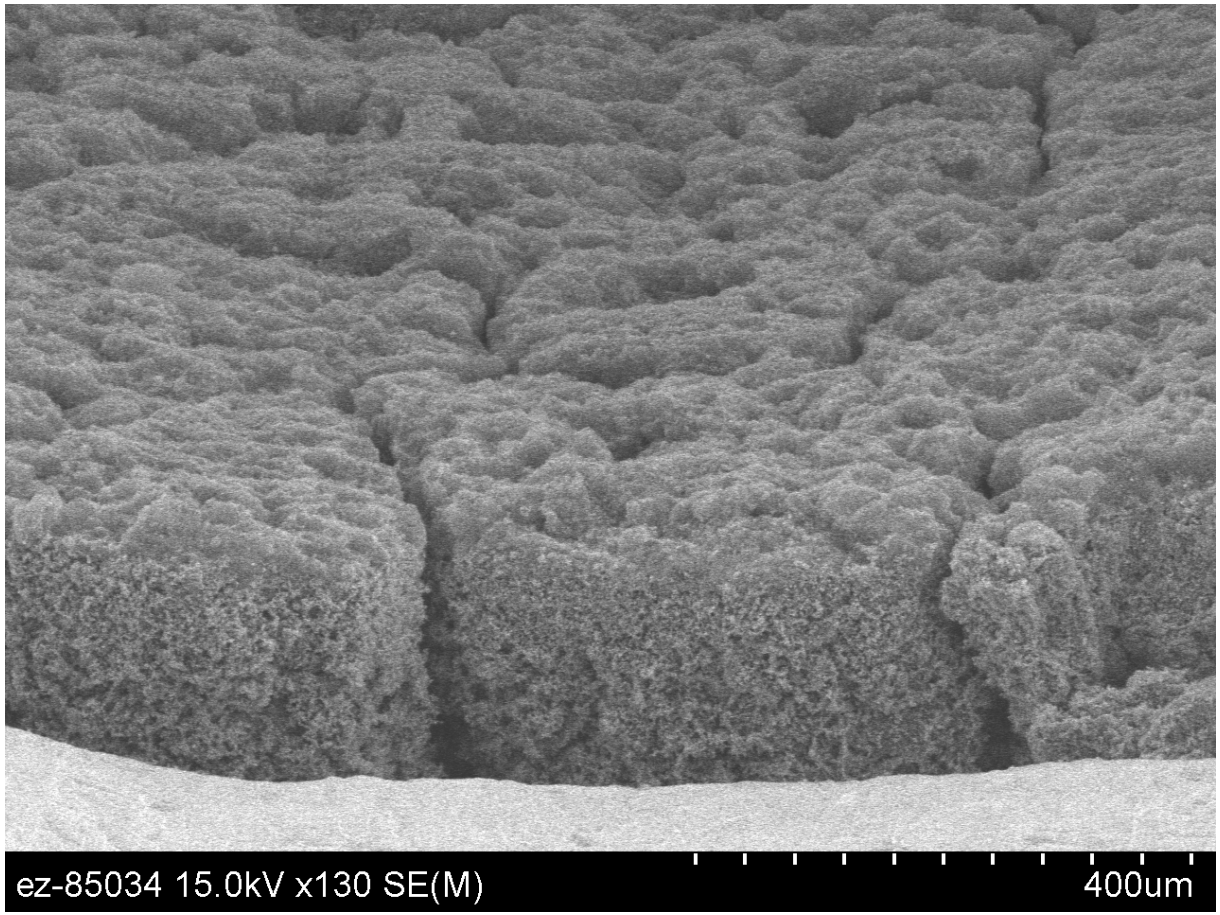

Figure 8: Cooler #1 showing mudcracking.

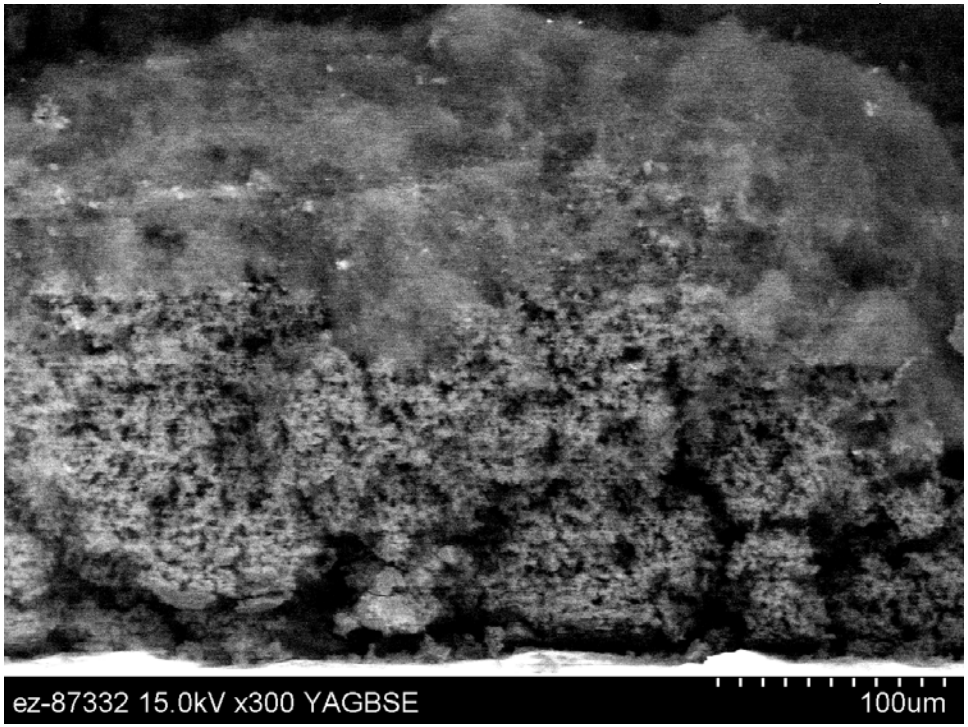

Figure 9: Back-scattered electron image of the fracture surface of the deposit from cooler #6.

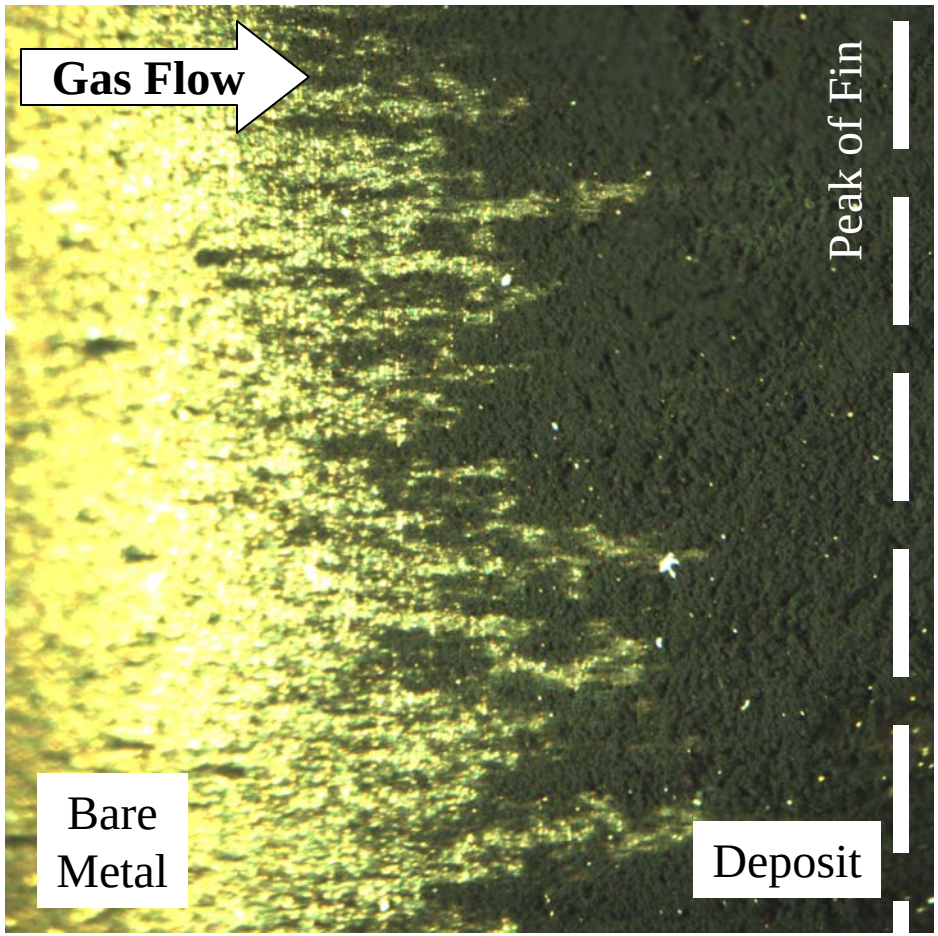

Figure 10: The surface of a fin of Cooler #2. Lines in the deposit suggest that erosion of the deposit is occurring due to the action of the exhaust gas.

Project 18519 - Materials for Control of Exhaust Gases and Energy Recovery Systems

Agreement 9130 - Development of Materials Analysis Tools for Studying NO_x Adsorber Catalysts (CRADA No. ORNL-02-0659 with Cummins Inc.)

Thomas Watkins, Larry Allard, Michael Lance, and Harry Meyer
Oak Ridge National Laboratory
P.O. Box 2008
Oak Ridge, TN 37831-6064
(865) 574-2046; fax: (865) 574-4913; e-mail: watkinstr@ornl.gov

DOE Technology Manager: Jerry L. Gibbs
(202) 586-1182; fax: (202) 586-1600; e-mail: jerry.gibbs@ee.doe.gov
ORNL Technical Advisor: D. Ray Johnson
(865) 576-6832; fax: (865) 574-6098; e-mail: johnsondr@ornl.gov

Contractor: Oak Ridge National Laboratory, Oak Ridge, Tennessee
Contract No.: DE-AC05-00OR22725

Objective

- The purpose of this effort is to produce a quantitative understanding of the process/product interdependence leading to catalyst systems with improved final product quality, resulting in diesel emission levels that meet the 2010 emission requirements.

Approach

- Characterize lab-engine tested samples with X-ray diffraction (XRD), spectroscopy, and microscopy. Correlate findings with Cummins data and experience.

Accomplishments

- Complete evaluation of feasibility of the advanced tools available at ORNL for quantitative analysis of the materials changes underlying the SCR catalyst performance degradation with age.
- Assembled portable gas manifold system. This system will provide varied atmospheres for in-situ studies using XRD, TEM and Raman.

Future Direction

- Initiate evaluation of feasibility of the advanced tools available at ORNL for quantitative analysis of the materials changes underlying the AMOX catalyst performance degradation with age.
- Assist Cummins to competitively produce engines which attain the required emission levels for 2010 and beyond while maintaining the advantage of the diesel's inherent energy efficiency.
- Continue to characterize the soot, coke and ash formed on the catalyst from different fuels, including biodiesel.

Introduction

In order to meet the 2010 US Environmental Protection Agency (EPA) emission requirements for diesel exhaust, aftertreatment in diesel engines may be necessary. The technology necessary for 2010 will need to integrate aftertreatment with engine control systems. Currently, no commercial off-the-shelf technologies are available to meet these standards. Consequently, Cummins Inc. is working to understand the basic science necessary to effectively utilize these catalyst systems. ORNL is assisting with the materials characterization effort. This report will focus on the study of materials used in selective catalytic reduction.

Selective catalytic reduction (SCR) is one possible method to reduce NOx emissions. Here, a gaseous or liquid reductant is added to the exhaust gases and adsorbed on to the catalyst, sometimes a zeolite. The reductant reduces NOx to H_2O and N_2.[1] Urea is a typical reducing agent which can operate under lean or oxygen rich conditions as follows:[2] $(NH_2)_2CO + 2NO + 1/2O_2 \Rightarrow 2N_2 + 2H_2O + CO_2$.

A zeolite is classically defined as a crystalline, porous aluminosilicate. More recently, zeolites are defined as porous oxide structures with well-defined pore/channel structures and a high degree of crystallinity. There are an unlimited number of structures possible, making them particularly useful as molecular sieves.[3] There are many chemical interactions with zeolites which center around $Si\text{-}O_4$ and $(Al\text{-}O_4)^{-1}$ tetrahedra and the cations within the pores, supplying charge compensation. Zeolites are often used as ion exchangers in water softeners and shape selective catalysis. The cation with H+ becomes a strong acid, which is catalytically active.

Approach

A commercial Fe zeolite powder is being examined with diagnostic tools developed previously under this CRADA. The crystal structure, morphology, phase distribution, particle size, and surface species of catalytically active materials supplied by Cummins were characterized using transmission electron microscopy (TEM), X-ray diffraction (XRD), X-ray photoelectron spectroscopy (XPS), and Raman Spectroscopy. These materials will come from all stages of the catalyst's life cycle: raw materials, as-calcined, sulfated, regenerated, etc. Both ORNL and Cummins personnel have participated in this work to understand zeolite degradation.

Samples

A commercial Fe zeolite powder was hydrothermally aged at 500, 700, or 900°C for 12 hours in a gas composed of 10 H_2O, 72 N_2 and 18 O_2 v% with a space velocity of ~ 42,000 h^{-1}.[4]

Results

The above samples were examined with microscopy, XRD and Raman from October 2007 to September 2008, are summarized in reference 4. The information below completes the characterization of the hydrothermally aged samples.

Microscopy

Electron microscopy of most of the samples in this study was very difficult, as even short exposures of the zeolite material to the electron beam resulted in amorphization and often disintegration of the region of interest. Powder samples were prepared typically by dry-dipping a TEM grid covered by a holey carbon film into the provided powder, shaking off the excess, and loading the grid into the TEM specimen holder.

High-resolution electron microscopy studies continued on the suite of hydrothermally aged Fe-zeolite samples, utilizing HTML's aberration-corrected JEOL 2200FS STEM/TEM instrument (the "ACEM", see Figure 1). A major goal of our study has been to try to identify by imaging and possibly elemental microanalysis the location of Fe species within the cage structure of the zeolite material, which has been shown to be consistent with the basic structure of H-beta zeolite by XRD techniques. The ACEM, however, has not, until very recently, been equipped with an energy-dispersive x-ray analysis system, so intermediate results were obtained at first using the new cold-field emission 300kV Hitachi HF-3000 TEM/STEM instrument, which is an advanced capability analytical electron microscope equipped with a Noran energy-dispersive spectrometer. The HF-3000 can provide annular dark-field images similar to those obtained on the ACEM, but with a resolution of about 0.5 nm at best, using beam conditions suitable to also give reasonable x-ray imaging results.

Figure 2a shows an annular dark-field (ADF) image, recorded at 300kx, of the as-received Fe-zeolite material "before" simultaneous acquisition of a series of x-ray maps for the elements Al, Fe, and Si. Figure 2b is the same sample area "after" the analysis. The x-ray images were obtained with a scanning time of about 40 minutes, so the changes in the morphology of the zeolite in the "after" images are indicative of the effects of the electron beam on the structure. In Figure 3a, the characteristic structural feature seen is a distribution of bright patches in the ADF images that we have supposed are consistent with concentrations of Fe species, since annular dark-field contrast is essentially directly proportional to Z^2, where Z is the atomic number. Figures 3b, c and d show the results of the x-ray mapping of this area. The Al and Si maps are essentially uniform in counts, as expected, whereas the Fe map shows an overall uniform distribution with several indications of concentrations (arrowed) consistent with corresponding bright patches in the ADF image. It is expected that higher magnification maps, as are soon to be possible with the new detector on the ACEM, will clarify further the Fe distributions.

A new x-ray detector was recently installed on the ACEM (see Figure 4). The detector was provided by Bruker AXS Inc. (Madison, WI), and is a new design of Silicon Drift Detector (SDD), which is typically used in high-count rate environments such as found on scanning electron microscopes and electron microprobes. The new SDD is designed to give good results on a TEM instrument, which, because of the typical thin sample (or nanoparticle) morphology will inherently give low count rates. Our Bruker SDD is the first of its kind to be commercially installed on a TEM in the US (only 3 currently in the world). We are testing this detector and will report on the efficacy of its use for analysis of catalytic materials in general, and our zeolites in particular, in a future report.

Portable Gas Manifold

Figure 5 shows the assembled potable gas manifold system. This system will provide varied atmospheres for in-situ studies using XRD, TEM and Raman. Presently, The starting gases mixtures need to be reformulated. Before collecting in-situ data, the safety paperwork has to be generated, followed by preliminary testing.

Overall Summary

Based on the FY2008 [4] and FY2009 work, XRD, TEM, DRIFTS, NMR and XPS all showed the effect of hydrothermal aging after 900°C exposure. Dealuminization was observed with NMR, DRIFTS and XPS as hydrothermal aging temperature increased.

The Team consensus is that spectroscopic techniques and NMR provide important information about hydrothermal degradation of Fe-zeolites. In contrast, XRD and TEM do not provide enough insight into the early stages of the hydrothermal aging process. As such, one future focus of this work will be to shift some of the characterization to AMOX catalysts while continuing to support SCR-zeolite work

References

[1] Internet: en.wikipedia.org/wiki/Selective_catalytic_reduction

[2] I. Chorkendorff and J. W. Niemantsverdriet, Concepts of Modern Catalysis and Kinetics, Wiley-VCH Verlag GmbH & Co. KGaA, Weinheim, 2003, p. 400.

[3] Internet: www.personal.utulsa.edu/~geoffrey-price/zeolite/zeo_narr.htm.

[4] Propulsion Materials, 2008 Annual Progress Report, Vehicle Technologies Program, US DOE, Energy Efficiency and Renewable Energy, Office of Vehicle Technologies, Advanced Materials Technologies, E. J. Wall, R. A. Sullivan, J. L. Gibbs, Jan. 2009, www.ornl.gov/sci/propulsionmaterials/Reports.html , pp. 137-151.

Acronyms

ACEM	aberration-corrected electron microscope
BF	bright-field
DRIFTS	Diffuse reflectance infra-red Fourier transform spectroscopy
EDS	Energy dispersive spectroscopy
EPA	Environmental Protection Agency
HA-ADF	high-angle annular dark-field
NMR	Nuclear Magnetic Resonance
NO_x	Nitrogen and Oxygen containing compounds
ORNL	Oak Ridge National Laboratory
SCR	selective catalytic reduction
STEM	Scanning Transmission Electron Microscopy
XPS	X-ray photoelectron spectroscopy
XRD	X-Ray Diffraction

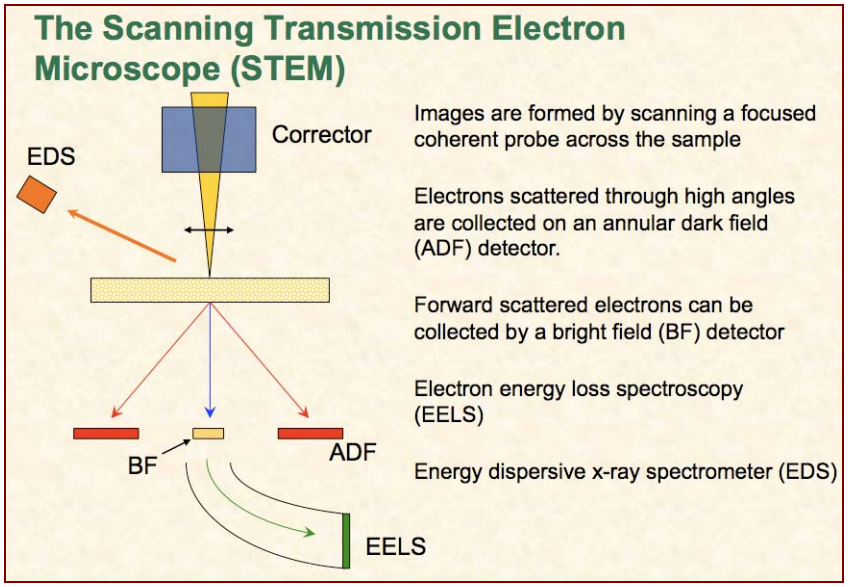

Figure 1. A schematic showing imaging modes for the aberration-corrected electron microscope (ACEM). Dark-field and bright-field images are acquired simultaneously, providing complementary information. ADF images show heavy elements (e.g., Fe) in bright contrast relative to the light element composition (alumino-silicate) of the zeolite structure.

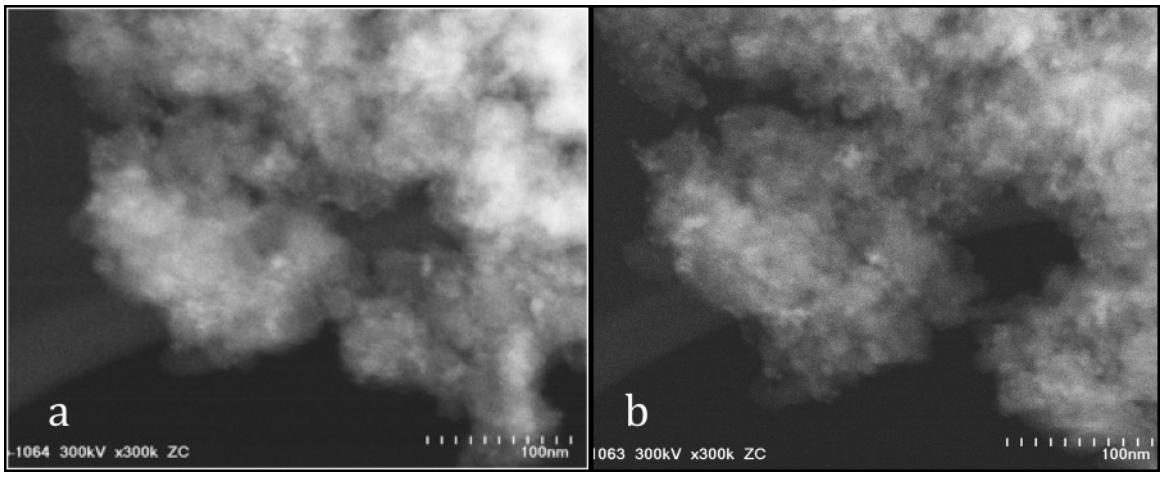

Figure 2. ADF images obtained a) before and b) after a scanning time of about 40 minutes.

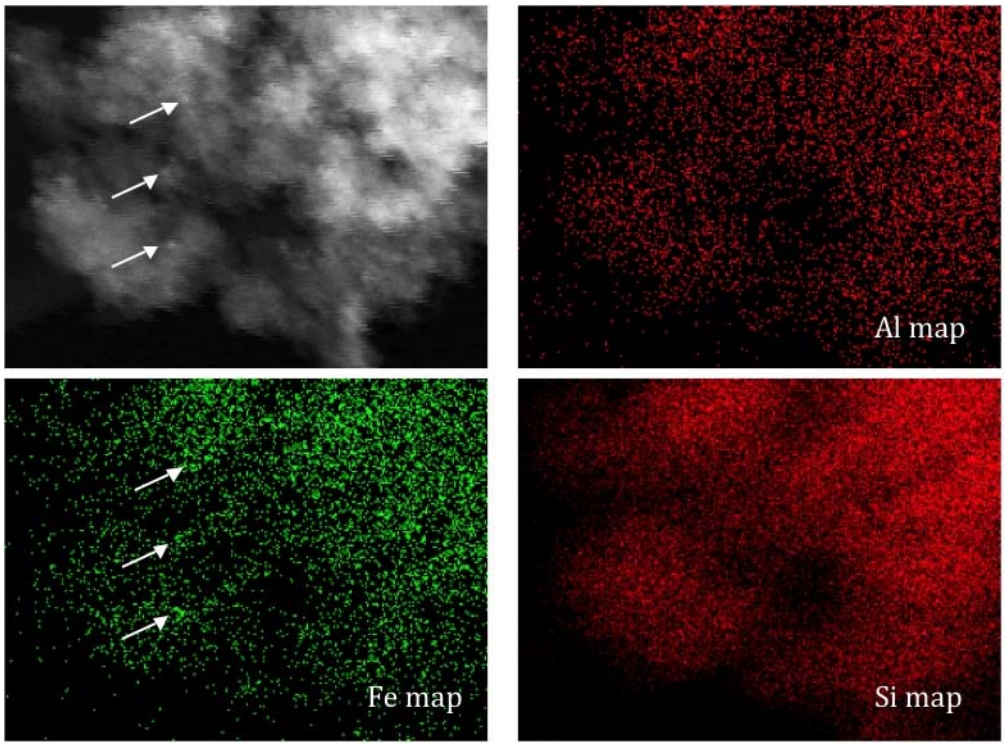

Figure 3. a) ADF image and corresponding X-ray images mapping out the b) Al, c) Fe and d) Si elements.

Figure 4. A new silicon drift x-ray detector, desired for inherently give low count rate environments, was installed on the ACEM.

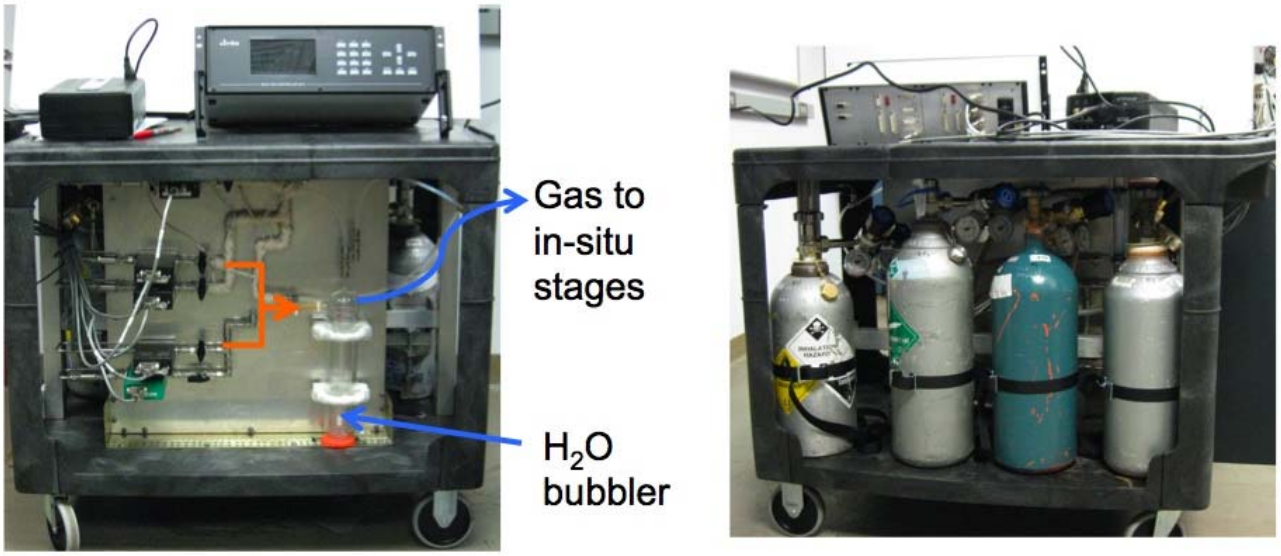

Figure 5. Portable gas manifold system a.) front view: showing the controller, mass flow controllers and piping and b.) back view: showing the gas cylinders.

Agreement 10461 - Durability of Diesel Particulate Filters (CRADA with Cummins Inc.)

Thomas R. Watkins, Hua-Tay Lin and Amit Shyam
Oak Ridge National Laboratory
P.O. Box 2008, MS-6064
Oak Ridge, TN 37831-6064
(865) 574-2046; fax: (865) 574-4913; e-mail: watkinstr@ornl.gov

DOE Materials Engineer: Jerry Lee Gibbs
(202) 586-1182; fax: (202) 586-1600; e-mail: jerry.gibbs@ee.doe.gov
ORNL Technical Advisor: D. Ray Johnson
(865) 576-6832; fax: (865) 574-6098; e-mail: johnsondr@ornl.gov

Contractor: Oak Ridge National Laboratory, Oak Ridge, Tennessee
Contract No.: DE-AC05-00OR22725

Objective

- Implement test techniques to characterize the physical and mechanical properties of ceramic diesel particulate filters (DPFs) and develop analysis and inspection tools for assessing their reliability and durability.

Approach

- Characterize the properties of and rank the thermal shock resistance of candidate DPF substrates.
- Application of probabilistic design tools and non-destructive evaluation (NDE) techniques to DPF ceramic substrates.
- Refinement of DPF service lifetime prediction models based on characterization of field returned filters.

Accomplishments

- Participated in ASTM round robin testing, wherein the strengths of the SiC DPF materials were a least a factor of three stronger than those of the cordierite.
- Young's moduli of the aluminum titanate were found to be stiffer in the rim region than the core region.
- Dynamic fatigue testing showed that the mullite DPF material has excellent resistance to the susceptibility of slow crack growth.

Future Direction

- Detailed examination field returned DPF substrates and other alternate substrates that meet or exceed the mandated Environmental Protection Agency (EPA) 2010 regulations.

Introduction

The EPA regulates the emissions of nitrogen oxides (NO_x) and particulate matter (PM) from diesels engines. Stringent regulation on PM went into effect in 2007. There are many technologies designed to reduce emissions from diesel engines; prominent among the technologies for PM control are DPFs. A DPF is often a ceramic device that collects particulate matter in the exhaust stream. The high temperature of the exhaust heats the ceramic structure and allows the particles inside to break

down (or oxidize). DPFs reduce emissions of PM, hydrocarbons, and CO by 60 to 90%.

Most DPFs consist of a ceramic honeycomb with hundreds of cell passages partitioned by walls (Figure 1). Each cell passage has a square cell opening at one end and is closed at the other end so that the cell passages are alternately closed at each end. The so-called checkerboard plugging structure forces the exhaust gases through the porous, thin ceramic honeycomb walls. When the gases carrying the PM flow through the fine pores of the walls, the PM is filtered out. High porosity values, in the range of 40-70%, heighten filtration efficiency to more than 90% and reduce gas-flow resistance for better engine performance.

The process of diesel PM collection continues while the engine is operating. The particles are collected on the ceramic walls and as a result, the backpressure of the system increases. The back pressure is reduced by oxiding the trapped PM, aided by a catalytic reaction using exhaust gas heat at 400°C or more, into CO_2 and water vapor. This process, called regeneration, results in a cleaner filter. The regeneration process is dependent upon exhaust temperature, oxygen, NO_x content, time, and PM levels.

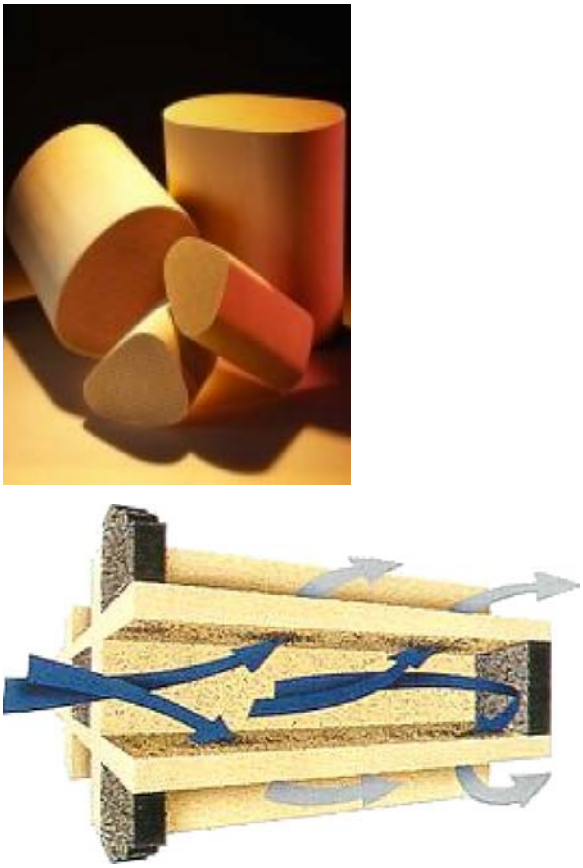

Figure 1. Cordierite-based DPFs.

The key to the successful application of DPFs is to reliably regenerate the filter (e.g., to clean up the PM that the filter continues to trap or collect). Traditionally, combustion of soot is done in an oxygen atmosphere (air). In air, the soot will oxidize at about 500°C. However, this is not a typical operating temperature for diesel engine exhaust. Therefore, to oxidize soot in air, an active system—i.e., one that increases the temperature of the exhaust using some external heat source—is required. But if an active system is not carefully controlled, or if too much PM collects on the filter walls, the filters can experience an "uncontrolled regeneration" where the temperature increases to 600°C or more, resulting in damage to the filter element.

A useful conceptual model for the prediction of reliability is the bathtub curve, which describes reliability-related phenomena of a component over its life cycle.[1] A schematic of the reliability bathtub curve is represented in Figure 2. It consists of three stages: the infant mortality phase is characterized by premature failures due to improper manufacturing or assembly, poor workmanship, or defects introduced during processing. The second stage of the curve corresponds to the useful life of the component and is characterized by a constant failure rate. In this regime, failures are typically associated with random, excessive loads. If sufficiently high safety factors are used during the design process, the magnitude of this failure rate should be negligible. The third stage of the bathtub curve is known as the wear-out phase, wherein the failure rate increases with time as a result of aging phenomena. Aging phenomena include thermal and mechanical fatigue, corrosion, creep deformation and environmentally assisted crack growth. The time at the onset of wear-out is often regarded as the useful life of the component.

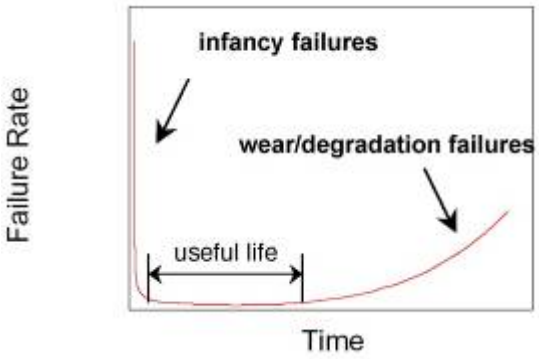

Figure 2. Reliability bathtub curve.

The reliability bathtub curve can be used as a descriptor of how the failure rate of DPFs evolves over time. Infancy failures of DPFs could be related to manufacturing or process defects (large pores, inclusions, cracking) or defects introduced during assembly. Failures of DPFs during their useful life will be dictated by the intersection between the spectrum of thermomechanical loads and the distribution of DPF strengths. Such failures could result from excessive vibration, for example, or unwanted thermal excursions during transients associated with regeneration. Wear-out and degradation failures of DPFs could also be associated with the growth of microcracks by thermal fatigue, and assisted by the chemistry of the environment, and/or by chemical and microstructural changes in the material due to long-term exposure to elevated temperatures in the exhaust environment.

The objective of this project is to implement test techniques to characterize the physical and mechanical properties of ceramic DPF substrates and to develop analysis and inspection tools for assessing the reliability and durability of DPFs. The developed tools and methods would allow the design of more durable and reliable DPFs. An important outcome of the development of the test methods is the ability to rank the relative thermal shock resistance of substrates in different conditions (catalyzed, soot loaded, field returned etc.) and of different candidate substrate materials.

Approach

The design process for making DPFs that are durable and reliable includes a complex materials property optimization and selection process.[2] For example, the porosity of DPFs, which allows them to remove PM from the exhaust gas stream, has a deleterious effect on their mechanical and fracture strength. A higher porosity also decreases the engine backpressure and increases efficiency of the diesel engine. Designing mechanically reliable DPFs is important because these components will experience demanding thermo-mechanical conditions during service. These include, for example, thermal shock resulting from rapid heating/cooling and thermal stresses that arise from temperature gradients.

Techniques to assess the elastic and fracture properties of virgin or unexposed DPF substrates have been identified, implemented and reported earlier.[3] The test techniques were applied to rank the suitability of common candidate substrates for application in DPFs. The developed test techniques were applied to characterize field returned DPFs. The material properties responsible for the thermal shock resistance and mechanical property degradation in the various stages of the bathtub curve were determined. These properties include thermal expansion, thermal conductivity, heat capacity, density, porosity, elastic properties, strength, fracture toughness, and environmentally assisted crack growth at ambient and elevated temperatures, in air and in relevant environments.

The information generated will be used in turn to implement probabilistic design tools. Such probabilistic design methodologies are based on a combination of experimentally determined strength data, stress analyses of the component using a finite-element analysis, and selection of appropriate failure criteria. The durability (service life) of the component can also be predicted using this framework by considering the mechanisms that are responsible for the degradation of material strength, such as slow crack growth or creep. In addition, the service life predictions are refined based on the properties of the field returned filters.

Results

In FY 2007, the comparative mechanical properties and relative thermal shock resistance of several DPF substrates were assessed and reported.[3] This ranking system was populated continuously in FY 2008 by testing several available candidate DPF substrates.[4] Procedures for characterizing DPF substrates were reported in a journal article[5] and in earlier reports and will not be repeated here. In

2009, ORNL participated in a round robin testing program to quantify the repeatability and reliability of a new ASTM test standard for honeycomb flexural testing of cordierite based DPF. Dynamic fatigue test continued for the mullite DPF material. Also, ORNL began characterization of another DPF material: aluminum titanate (Al_2TiO_5 or Al_2O_3•TiO_2).

The interlaboratory study (ILS) on flexure testing of commercially available honeycomb ceramics for applications such as diesel particulate filters had the following stated objectives:

- Determine the repeatability and reproducibility for the new ASTM test method - ASTM C1674 -- Flexural Strength of Advanced Ceramics with Engineered Porosity (Honeycomb Cellular Channels) at Ambient Temperatures.
- Validate the honeycomb structure strength calculation and the linear cell count requirements in ASTM C1674.
- Determine the statistical distribution of flexure strength for the honeycomb ceramics, considering variations in test specimen size, materials, and architecture.

The following three compositions were tested as a part of the round robin testing program:

1) Cordierite material -- 300 cpsi/12 mil wall thickness

2) Cordierite material -- 600 cpsi/4 mil wall thickness

3) Silicon Carbide material -- 300 cpsi/12 mil wall thickness

The flexural specimens were cut and prepared by Cummins, and the details of the five test specimen geometries are included in Table I. Two different outer loading spans of 130 mm (method A) and 90 mm (method B) were applied in the four point bend flexural tests. The failure loads and the corrected moment of inertia (MOI) calculations were utilized to calculate the nominal beam strength and wall fracture strength of the honeycomb. The strength values were calculated by application of a commercial reliability analysis software available at ORNL called Weibull++® 7. The materials for Test set E experienced crushing under the load points, and, as such, these values are not reported. The characteristic strength and Weibull modulus of data sets A-D (for both corrected and uncorrected MOI strength values) are summarized in Table II.

It can be concluded from Table II that the SiC specimens (data set D) have higher strength values compared to the cordierite specimens (data set A-C) by a factor of 3 to 4. The effect of correcting for the moment of inertia of the honeycomb structure for data set A is shown in Figure 3. Whereas, the nominal beam characteristic strength for data set A is 2.09 MPa, the strength values corrected for the MOI leads to a wall characteristic strength of 5.13 MPa. It is recommended that analyses involving honeycombs should report the wall strength values since these are intrinsic to the material and not a function of the cell architecture.

The effect of specimen size on the Weibull parameters of honeycombs can be understood with the help of data presented in Figure 4. Even though two different sizes (and different outer spans) are represented in Figure 4, the characteristic strength of specimens from data set A and B are within ~ 1% of each other. This indicates that in the size range of specimens tested, there is no discernible size effect on the characteristic strength of the honeycomb specimens. The absence of a size effect may be a function of the multitude and uniformity of defects available to initiate cracks in the porous ceramic substrates. Detailed analysis of the results from all the labs in the ILS will be reported in the future.

A new aluminum titanate filter was received for characterization. The sample possessed a cross-section with two different sized channels (see Figure 5). The samples were carefully machined and the corrected MOI was determined[7] for each end of the 4 cell x 2 cell x 60 mm samples. The MOIs from each end of a typical sample differed by as much as 25% due to slight machining differences and the small thicknesses involved. The samples underwent dynamic mechanical analysis (DMA)[6] to determine the Young's modulus. DMA is typically applied to polymers and deforms a material and measures its response (force and deflection). Table III shows the results indicating that the modulus of the core is significantly less than that of the rim of the DPF monolith. The origin of this difference is suspected to be due to a difference in density and will be investigated in the future. This particular filter was produced early in the production line set up, and as such, the property difference in the cross section may be due to initial variations in the processing. Interestingly, these modulus values are comparable to those of cordierite reported previously (10-15 GPa at RT).[4]

Dynamic fatigue testing was carried out on the mullite and aluminum titanate materials. The objective of the dynamic fatigue testing is to develop a statistical mechanical database for verification of probabilistic DPF component design and prediction of long-term reliability and durability. This testing continued for the mullite DPF and provided insight into the performance limiting factors.

This testing occurred at temperatures of 600, 800, and 900°C and at stressing rates of 30, 0.0003, and 0.000003 MPa/s in air per ASTM C1465. The 30 MPa/s is used to evaluate the inert characteristic strength as a function of temperature, and both 0.0003 and 0.000003 MPa/s were applied to measure the slow crack growth (SCG) susceptibility at temperatures. Two specimen sizes (3 cell x 4 cell and 4 cell x 6 cell) were machined from the as-received DPF components and evaluated under the stated test conditions to understand the effect of specimen size on the dynamic fatigue response. The dynamic fatigue procedures carried out for DPF materials are similar to those employed for monolithic ceramic specimens as specified in ASTM C1465. Further detailed electron microscopy analysis was carried out to provide insight into the strength degradation process that limits the lifetime and reliability of materials.

Figure 6 show the fracture strength versus stressing rate curves for two different sizes of specimens for mullite DPF specimens extracted from the component manufactured by Dow Automotive. The specimen size of 3 cell x 4 cell showed little or no stressing rate effect on the measured fracture strength at the temperature range used in this study. Also, the 6 cell x 3 cell samples exhibited high fatigue exponent values (~ 70-126) under the same test conditions. Dynamic fatigue strength data plus the high fatigue exponent values suggest that the mullite DPF exhibits excellent resistance to the susceptibility of slow crack growth (SCG) at temperatures. Figure 7 compares the fracture surface features of samples test at room temperature and 800°C. Both surfaces show distinctive acicular grains of mullite that presumably provide unique filtration function of particulate matters as well as mechanical performance. Stress rupture tests under the selected stress levels will be initiated and carried out in FY 2010.

The study of dynamic fatigue behavior of Al_2TiO_5 DPF material was initiated in FY2009 using the same test conditions employed as those employed for both mullite and cordierite DPF materials. The preliminary mechanical results show that the Al_2TiO_5 DPF exhibits the lowest mechanical strength among the three candidate DPF materials. Also, the scatter of the mechanical strength measured for the Al_2TiO_5 DPF material exhibits a larger variation as compared to those obtained for mullite and cordierite DPF materials. The root cause of the observed large scatter in the strength values of Al_2TiO_5 DPF material was not clear at the moment, but it could result from the differences in the localized flaws like pores and microstructure (see Figure 8). The dynamic fatigue data obtained so far did not reveal a reasonable statistical trend as a function of stressing rate (and temperature) due to the large scatter of data obtained (as shown in Figure 9). Therefore, more tests will be continued in FY2010 to provide a better insight into the dynamic response of Al_2TiO_5 DPF material.

Summary

Mechanical and thermal shock characterization test procedures developed earlier were employed to measure properties in cordierite, aluminum titanate and mullite DPF materials. In ASTM round robin testing, the strengths of the SiC DPF materials were a least a factor of three stronger than those of the cordierite. Correcting the moment of inertia for the empty channels resulted in a factor of 2 increase in all strengths. The Young's modulus of the aluminum titanate varied from the core to the rim with the rim region being stiffer. Finally, dynamic fatigue testing showed that the mullite DPF material has excellent resistance to the susceptibility of slow crack growth. The aluminum titanate material possessed a lot of strength variability requiring more testing before a conclusion can be drawn.

Table I: Details of the five set of test specimens provided for the honeycomb flexural ILS.

Test Set	A	B	C	D	E
Composition	Cordierite	Cordierite	Cordierite	Silicon Carbide	Silicon Carbide
Cell Architecture (cpsi/wall mils)	300 /12	300 /12	600 /4	300 /12	300 /12
Test Method Geometry & Linear Cell Count for *d* dimension	Method B – 9 cells	Method A – 15 cells	Method B – 12 cells	Method B – 9 cells	Method A - 15 cells
Specimen Size (mm)	**13-25-116**	**22-25-150**	**13-25-116**	**13-25-116**	**22-25-175**
Outer Test Span (mm)	**90**	**130**	**90**	**90**	**130**

Table II: The two parameter Weibull analysis results for specimens from dataset A-D. The specimen with a Weibull modulus value greater than 50 indicates that Weibull analysis is not suitable for this dataset.

Data Set	Characteristic Strength (MPa)	Weibull Modulus
Flex A	2.09	31
Flex Corrected MOI A	5.13	24
Flex B	1.97	26
Flex Corrected MOI B	5.19	19
Flex C	2.79	35
Flex Corrected MOI C	7.57	>50
Flex D	8.43	21
Flex Corrected MOI D	19.68	17

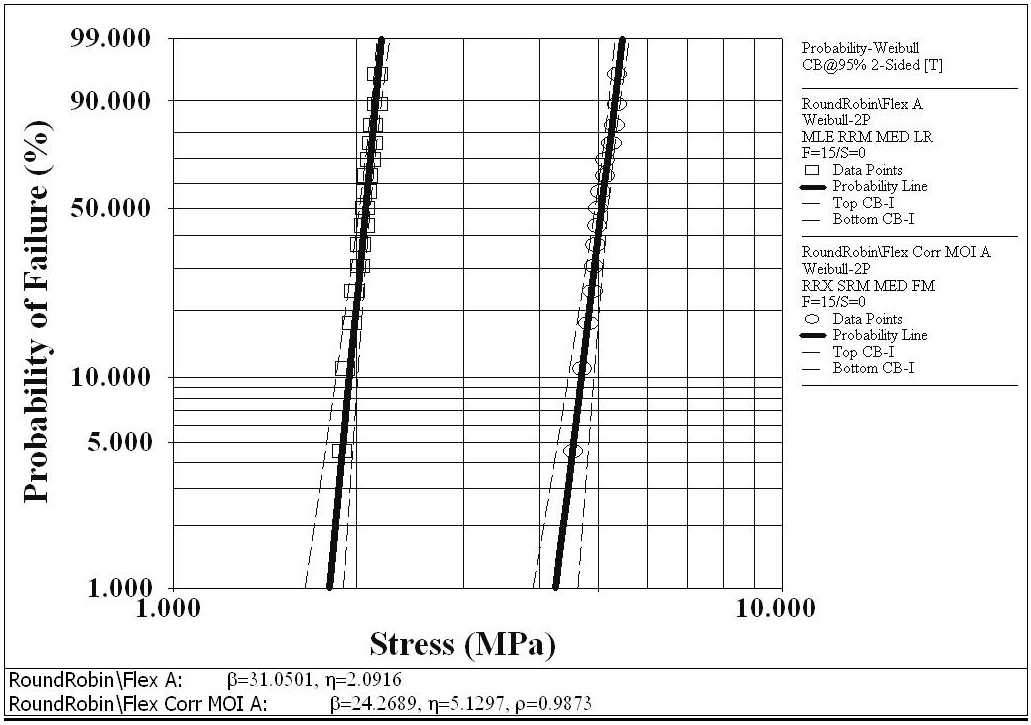

Figure 3: The effect of correcting for moment of inertia (right most data) on the Weibull parameters of a cordierite honeycomb specimen. Correcting for the wall architecture leads to computation of the wall strength of the honeycomb.

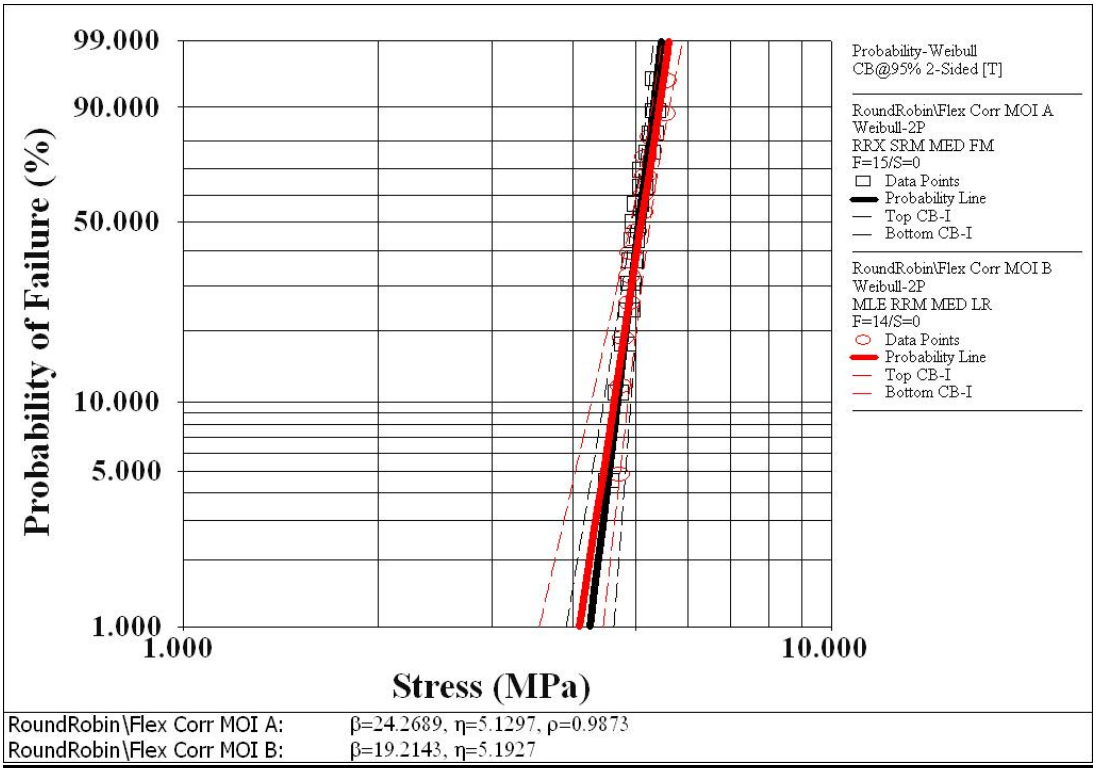

Figure 4: The effect of specimen size on the Weibull parameters of a cordierite honeycomb specimen. Larger specimens B (22-25-150 mm) are in red and the smaller specimens (13-25-116 mm) are in black.

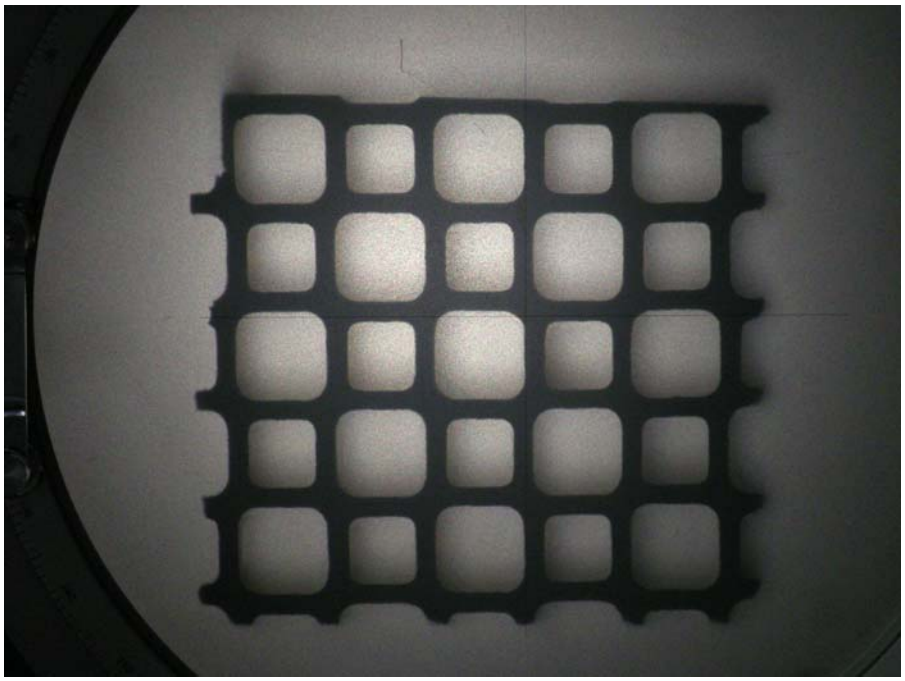

Figure 5 - Image of the aluminum titanate filter cross section in an optical comparator. Length dimension is ~7 mm.

Table III: The corrected MOI and Moduli for the aluminum titanate samples.

Sample	Region	MOI side 1 (mm^4)	MOI side 2 (mm^4)	Ave MOI (mm^4)	Modulus (GPa)	ESD†
A0001	core	3.505	4.324	3.915	4.84	0.29
A0002	core	2.931	4.091	3.511	4.85	0.24
A0003	core	3.011	3.060	3.036	4.70	0.19
A0005	rim	3.782	4.267	4.025	6.69	0.04
A0006	rim	4.001	3.343	3.672	7.29	0.04
A0007	rim	3.668	4.693	4.180	7.59	0.05
A0008	rim	4.896	4.506	4.701	6.46	0.16

† Each sample was tested 5-7 times.

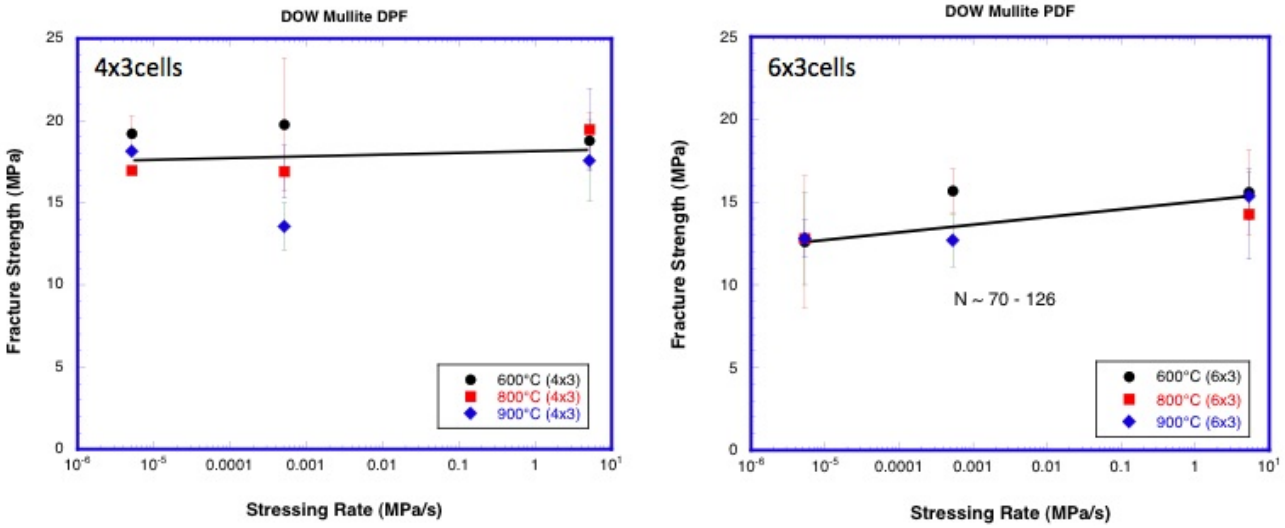

Figure 6: Fracture strength versus stress rate curve of mullite DPF material.

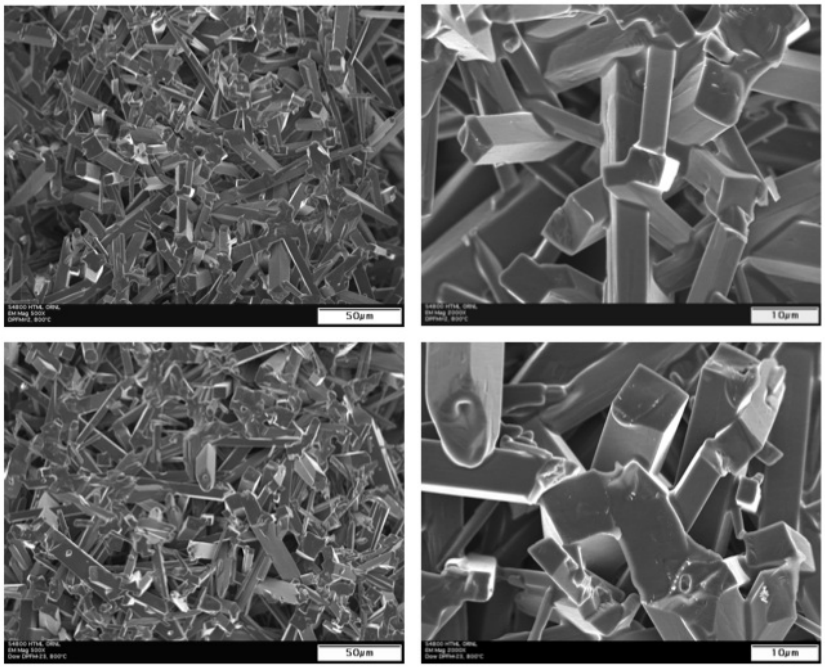

Figure 7: Fracture surface of mullite DPF material tested at RT (top row) and 800°C (bottom row).

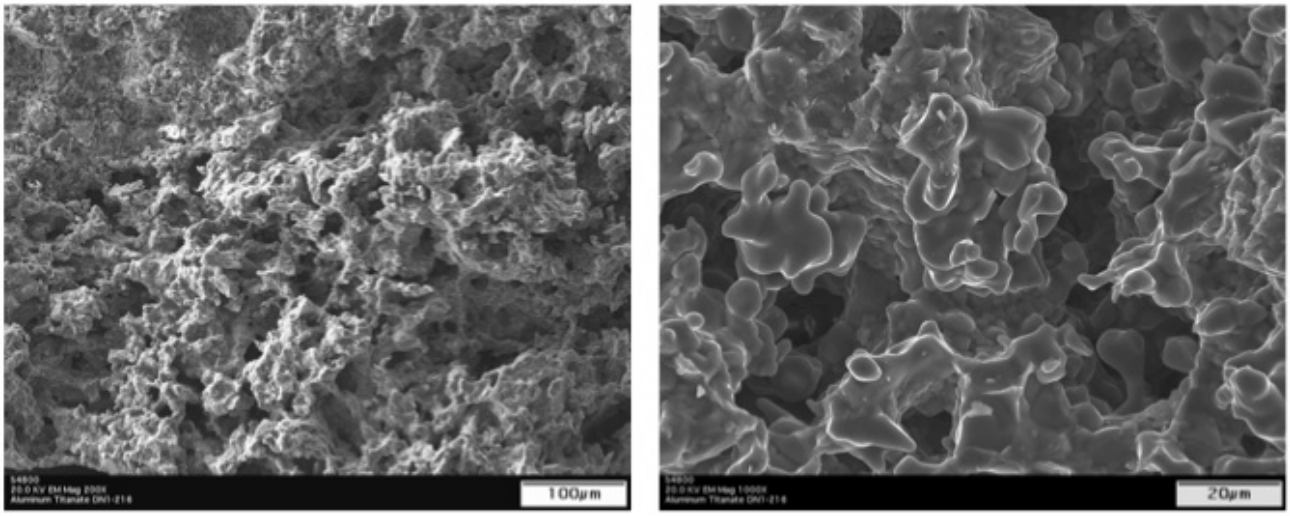

Figure 8: Fracture surface of Al_2TiO_5 DPF material tested at 600°C.

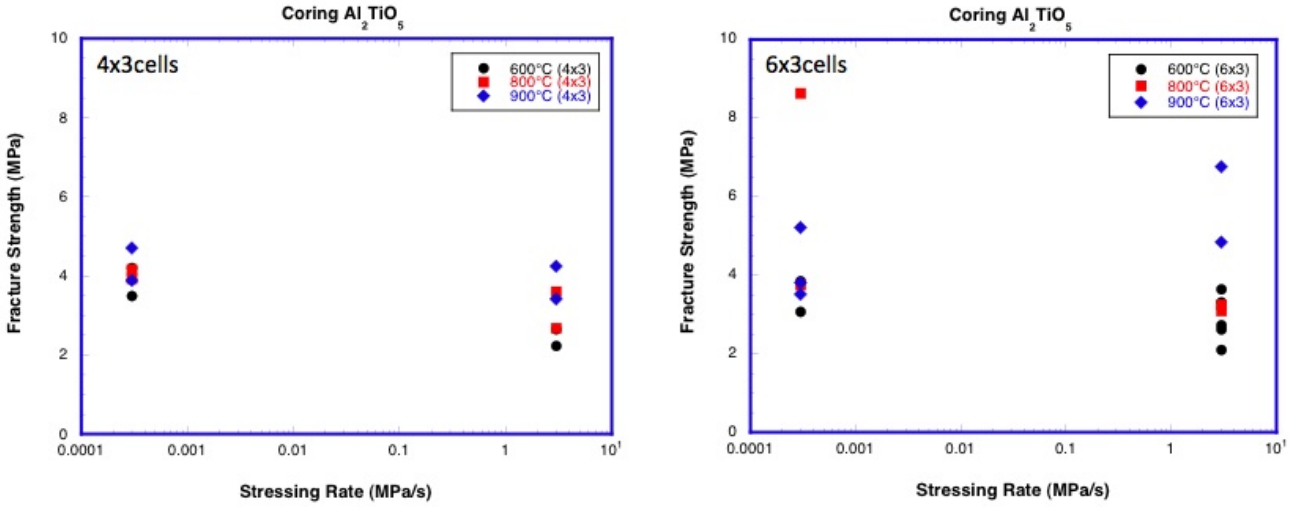

Figure 9: Fracture strength versus stress rate curve of Al_2TiO_5 DPF material.

References

1. G. S. Wasserman, *Reliability Verification, Testing and Analysis in Engineering Design*, Marcel Dekker, New York, 2003.

2. J. Adler, "Ceramic Diesel Particulate Filters," International Journal of Applied Ceramic Technology, vol. 2, no. 6, pp. 429-439, 2005.

3. Propulsion Materials, 2007 Annual Progress Report, Vehicle Technologies Program, US DOE, Energy Efficiency and Renewable Energy, Office of Vehicle Technologies, Advanced Materials Technologies, E. J. Wall, R. A. Sullivan, J. L. Gibbs, Jan. 2008, www.ornl.gov/sci/propulsionmaterials/Reports.html.

4. Propulsion Materials, 2008 Annual Progress Report, Vehicle Technologies Program, US DOE, Energy Efficiency and Renewable Energy, Office of Vehicle Technologies, Advanced Materials Technologies, E. J. Wall, R. A. Sullivan, J. L. Gibbs, Jan. 2009, www.ornl.gov/sci/propulsionmaterials/Reports.html.

5. A. Shyam, E. Lara-Curzio, T.R. Watkins and R. J. Parten, "Mechanical characterization of diesel particulate filter (DPF) substrates" Journal of the American Ceramic Society, vol. 91, no. 6, pp. 1995-2001, 2008.

6. Q800 DMATA, Instruments, New Castle, DE.

7. E. P. Popov, *Mechanics of Materials*, 2nd. Ed. Prentice Hall, Englewood Cliffs, NJ, 1976, pp. 119-34, 144-49.

Presentations, Publications and Patents

A. Shyam, E. Lara-Curzio, T. R. Watkins, R. J. Stafford and T. M. Yonushonis, "Effect of Porosity on the Properties of Cordierite Diesel Particulate Filters," presented by A. Shyam at the *33rd International Conference and Exposition on Advanced Ceramics and Composites*, Daytona Beach, FL, January 21, 2009.

Agreement 10635 - Catalysis by First Principles

C. K. Narula, L. F. Allard, M. Moses-DeBusk, M. Stocks
Oak Ridge National Laboratory
P.O. Box 2008, MS 6116
(865)574-8445, narulack@ornl.govl

DOE Technology Manager: Jerry L. Gibbs
(202) 586-1182; fax: (202) 586-1600; e-mail: Jerry.gibbs@ee.doe.gov
Field Technical Manager: D. Ray Johnson
(865) 576-6832; fax: (865) 574-6098; e-mail: johnsondr@ornl.gov

---

Contractor: Oak Ridge National Laboratory, Oak Ridge, Tennessee
Contract No.: DE-AC05-00OR22725

Objective

The objective of this work is to search for durable emission treatment catalysts (LNT, TWC, OC) from a protocol based on

- an integrated approach between computational modeling and experimental development,
- design and testing of new catalyst materials to rapidly identify the key physiochemical parameters necessary for improving the catalytic efficiency of these materials.

Approach

- Theoretical Modeling
  - Density functional theory-based first-principles calculations
  - Optimization of Pt clusters supported on alumina
  - Interaction of CO, NO_x, and HC with Pt clusters supported on alumina
- Experimental System
  - Synthesize Pt Nanoclusters on morphologically diverse alumina supports
  - Evaluate systems for CO, NO_x, HC oxidation individually and in combination
  - Understand non-structural changes in catalyst under operating conditions and correlating the changes to performance.

Accomplishments

- We have previously shown by theoretical models that nano-particles of Pt are stable as oxides and metallic particles are poorer catalysts than oxides. In this report, we describe theoretical studies of platinum supported on θ-alumina.
  - First, we carried out DFT optimization of θ-alumina and found that the calculated structural parameters are comparable to experimentally observed ones.
  - We optimized a 180 atom charge neutral 010 slab which is 2-cell wide and 4 cell deep and a 420 atom slab made by combining 2 x 3 x 3 cells and found that the preferred position of Pt supported on either of the two slabs is identical. We found that Pt, Pd, Au, and Ag single atom adsorption is in the order of Pt>Pd>Au>Ag. The surface mapping and nudged elastic band method allowed us to find the lowest energy location for platinum and its reaction pathway to highest energy site.
  - The bonding of platinum with θ-alumina is different from that reported for α- or γ-alumina. Pt is a d9s1 atom and after interaction with θ-alumina, it does not show an unpaired electron suggesting d8 structure with dπ – pπ backbonding where 2 electron pairs from two adjacent oxygen atoms is donated to platinum.
- Previously we have shown that platinum supported on γ-alumina or θ-alumina exhibit identical CO, NOx, and HC oxidation behavior. We found that under lean burn conditions,

- CO and NO_x conversion became quantitative at ~170ºC while NO_x conversion reached a maximum of 45% at ~250ºC.
- TEM analysis on the sample after lean burn testing showed an average particle size of 7.1nm and predominately ranging from 1.8-20nm with random large Pt particle in the 51-71.2nm range.

Future Direction

- Understanding of the structures of nano-clusters on support.
  - Theoretical models to understand cluster oxidation state (oxidized, reduced, in equilibrium), dependence on cluster size, and the kinetics of oxidation
  - Experimental studies on the structures of these systems using ACEM
- Support interaction with clusters and its impact on the structure and reactivity
  - Cationic or zero-valent metals or both
  - Cationic metals at the metal–support interface
- Reactivity of the clusters
  - Theoretical studies of CO, NOx, and HC reaction on supported clusters
- Guided by our results, the synthesis and evaluation of new durable supported catalysts for lean NO_x catalysts and other systems such as TWC, OC for diesel etc.

Introduction

This research focuses on an integrated approach between computational modeling and experimental development, design and testing of new catalyst materials, that we believe will rapidly identify the key physiochemical parameters necessary for improving the catalytic efficiency of these materials.

The typical solid catalyst consists of nano-particles on porous supports. The development of new catalytic materials is still dominated by trial and error methods, even though the experimental and theoretical bases for their characterization have improved dramatically in recent years. Although it has been successful, the empirical development of catalytic materials is time consuming and expensive and brings no guarantees of success. Part of the difficulty is that most catalytic materials are highly non-uniform and complex, and most characterization methods provide only average structural data. Now, with improved capabilities for synthesis of nearly uniform catalysts, which offer the prospects of high selectivity as well as susceptibility to incisive characterization combined with state-of-the science characterization methods, including those that allow imaging of individual catalytic sites, we have compelling opportunity to markedly accelerate the advancement of the science and technology of catalysis.

Computational approaches, on the other hand, have been limited to examining processes and phenomena using models that had been much simplified in comparison to real materials. This limitation was mainly a consequence of limitations in computer hardware and in the development of sophisticated algorithms that are computationally efficient. In particular, experimental catalysis has not benefited from the recent advances in high performance computing that enables more realistic simulations (empirical and first-principles) of large ensemble atoms including the local environment of a catalyst site in heterogeneous catalysis. These types of simulations, when combined with incisive microscopic and spectroscopic characterization of catalysts, can lead to a much deeper understanding of the reaction chemistry that is difficult to decipher from experimental work alone.

Thus, a protocol to systematically find the optimum catalyst can be developed that combines the power of theory and experiments

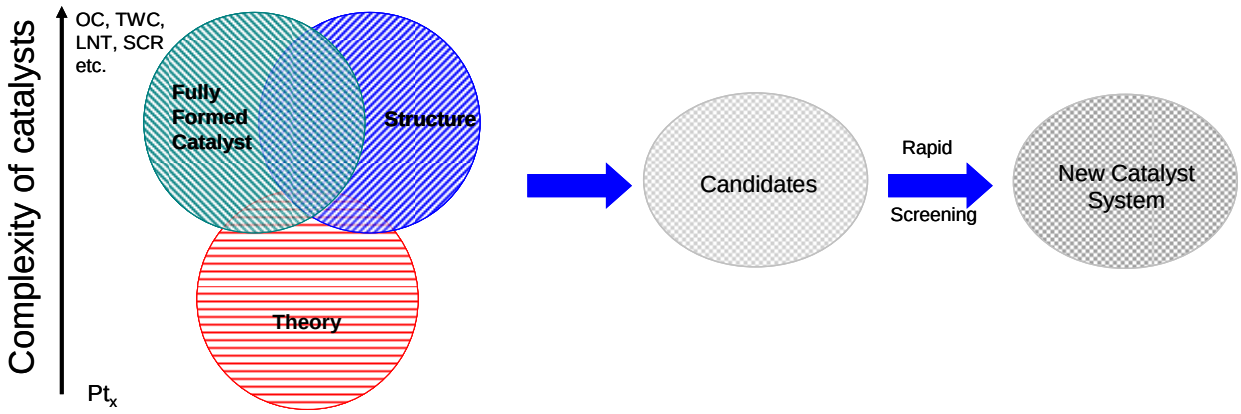

for the atomistic design of catalytically active sites and can translate the fundamental insights gained directly to a complete catalyst system that can be technically deployed.

Although it is beyond doubt computationally challenging, the study of surface, nanometer-sized, metal clusters may be accomplished by merging state-of-the-art, density-functional-based, electronic-structure techniques and molecular-dynamic techniques. These techniques provide accurate energetics, force, and electronic information. Theoretical work must be based on electronic-structure methods, as opposed to more empirical-based techniques, so as to provide realistic energetics and direct electronic information.

A computationally complex system, in principle, will be a model of a simple catalyst that can be synthesized and evaluated in the laboratory. It is important to point out that such a system for experimentalist will be an idealized simple model catalyst system that will probably model a "real-world" catalyst.

Thus it is conceivable that "computationally complex but experimentally simple" system can be examined by both theoretical models and experimental work to forecast improvements to obtain optimum catalyst systems.

Approach

The theoretical modeling is based on DFT studies of Pt supported on θ-alumina. We have completed the study of single atoms of Pt, Pd, Au, and Ag supported on 010 surface of θ-alumina. We have initiated the DFT study of larger clusters of Pt supported on θ-alumina. Our experimental studies suggest that CO oxidation is identical on both Pt supported on γ-alumina and θ-alumina. This suggests that the catalyst site structure is probably identical in both catalysts.

Experimentally, we have synthesized a series of Pt clusters/particles of different sizes supported on γ-alumina and evaluated the catalysts NO oxidation activity. We monitored the microstructural changes throughout the NO oxidation process to correlate microstructure and activity. We have also carried out preliminary study of HC oxidation processes.

Guided by the theoretical models and experimental results of our study, we will anticipate that we will initiate our work on the synthesis of a new set of catalyst materials with higher durability under operating conditions in FY10.

Results

Over the last year, we have carried out experimental studies on Pt nanoclusters and nanoparticles to correlate their CO, NO and HC oxidation activity with nanostructural changes.

We employed ORNL *ex-situ* reactor[1] and scanning transmission electron microscopy (STEM) using the HD-2000 and HF-3300 to study the nanostructural changes in catalysts upon exposure to CO and NO oxidation condition. It is important to note that the *ex-situ* reactor permits duplication of the oxidation conditions obtained on the bench-top reactor.

The results show the correlation between nanostructural changes and their impact on the catalytic activity and are summarized in the following subsections:

THEORETICAL STUDIES OF Pt/θ-Al_2O_3

We employed Vienna *Ab Initio* Simulation Package (VASP) to carry out first principle total energy calculation within the supercell DFT framework.[1-3] Generalized gradient approximation (GGA) in the Perdew-Wang-91 form was employed for electron exchange and correlations.[4,5] The Kohn-Sham equations were solved using the projector augmented wave (PAW) approach for describing electronic core states. [6,7] The plane-wave basis set was truncated at a kinetic energy cut-off of 500eV.

The bulk θ-alumina structure was described as a monoclinic system crystallized in C2/m (12) space group with a=11.85 Å, b=2.904 Å, c=5.622 Å, β =103.8º and Z = 4. For reference, we have calculated the bulk θ-alumina. A 6 x 6 x 4 Monkhorst-Pack k-point mesh is used for bulk calculations. The kinetic energy cut-off of 600eV was used. These parameters are sufficient for the total energy to converge to a few meV. The calculated lattice parameters exceed the experimental values by approximately 1% which is typical for GGA. The calculated lattice constants were used in all calculations. Calculations were performed in the slab geometry to describe the [010] surface of θ-alumina. The slab geometry is defined by a charge neutral supercell of 180 atoms which is 2-cell wide and 4 cell deep. The slabs are separated by 15 Å vacuum to minimize spurious interactions by periodic images. Both sides of the slab were relaxed. The surface energy is defined as energy excess between bulk alumina and a slab with relaxed surfaces per surface area [$\gamma_0 = E_{bulk} - E_{surf}) A^{-1}$]. The adsorption energy of metal atoms is defined as the energy difference between systems of metal-alumina and a separated metal atom and relaxed surface of alumina [$E_{ad} = E_{surf} + E_{metal} - Emetal\text{-}_{surf}$]. We also repeated our calculation using a charge neutral supercell of 420 atoms combining 2 x 3 x 3 cells and found the location of platinum to optimize in an environment identical to the one in 180-atom supercell.

We now consider the Pt, Pd, Au, and Ag single atom (M) adsorption on θ-alumina (010) surface. All atoms adsorb at oxygen sites in the order of Pt>Pd>Au>Ag [Figure 1]. While the adsorption of Pt and Pd is exothermic, that of Au and Ag is endothermic. Platinum placed initially between two parallel layers of surface oxygen relaxes to one layer of oxygen and occupies a bridging position between 2 oxygen atoms from adjacent layers and is located above aluminum. For these atoms, the M-O distances are 2.18 and 2.13 Å with an O-M-O angle of 140.55º. The distance from sub-surface Al is 2.41 Å and nearest surface Al is 2.93 Å. The platinum atom is located 0.728 Å above the cell surface. The adsorption energies for Pt, Pd, Au, and Ag are -62.29, -42.54, 5.87, and 13.25 Kcal/mole, respectively.

The optimized structure is different from the one reported for Pt on α-alumina or γ-alumina. For Pt, Pd, and Au atoms supported on α-alumina, the preferred site is atop surface oxygen while Ag prefers hollow sites. The calculated M-O bond distances for Pt, Pd, and Au are 2.02, 2.15, and 2.41 Å, respectively. The Ag atom which occupies the hollow site has Ag-O bond distance of 2.37 Å. The adsorbed platinum atom is paramagnetic and the interaction of Pt with surface is summarized as localized covalent bonding between Pt and O enabled by nearly Al-centered electron-accepting empty states available to accept excess electron density. The Pd and Au atoms also exhibit a bonding pattern which is quite similar to Pt bonding but Ag interacts with alumina surface in a largely ionic fashion.

For Pt supported on γ-alumina, a recent report suggests that platinum atoms anchor on Al^{3+}_{penta}

sites. When the Pt loading exceeds Al^{3+}_{penta} sites, the platinum forms 2D PtO rafts anchored on Al^{3+}_{penta} sites. DFT studies found that O-terminated PtO(101) structure on the γ-alumina surface was the most stable structure and interacts strongly with γ-alumina surface via four O- Al^{3+}_{penta} bonds with a binding energy of 7.1 eV. Previous theoretical study on a 3 atom Pt cluster on γ -alumina suggested that the structure is –OH capped Pt atom trimer on oxygen terminated 110 surfaces. Authors also suggest that –OH group receives electron density from Pt-Pt bonds making the Pt-Pt bond distances to be anomalous.

In order to ensure that our Platinum is indeed optimized at lowest energy position we carried out systematic surface mapping of platinum by fixing x and z coordinate and allowing y-coordinate to vary. The resulting map is shown in Figure 2. The highest deviation from optimized energy was for location 1 and the lowest was for position 13 which is closes to the optimized position. We used Nudged Elastic Band (NEB) method to find the reaction pathway for platinum to go from lowest energy location to location 1 which has highest deviation from optimized location. The minimized energy images between initial and final state of the reaction path are shown in Figure 3. The energy barrier of 5.352 eV is obtained for this reaction pathway.

We also carried out calculations using a charge neutral supercell of 420 atoms combining 2 x 3 x 3 cells. The platinum atom was placed at various locations on the 010 surface and all atoms were allowed to relax. In the lowest energy location, platinum occupies a bridging position between 2 oxygen atoms from adjacent layers and is located above aluminum [Figure 4]. The Pt-O distances are 2.186 and 2.132 Å with an O-M-O angle of 142.66º. The distance from sub-surface Al is 2.399 Å and nearest surface Al is 2.89 Å. The adsorption energy for the platinum atom is -68.89 kcal/mole. Thus, it is not necessary to employ a large supercell for studying the single atom absorption on 010 surface of θ-alumina.
The analysis of projected local density of state [LDOS] leads to a different bonding picture than that reported in literature for α-alumina or γ-alumina. Since platinum is a d^9s^1 atom, the d and s states are close in energy. The interaction of platinum orbitals with Op states results in O p_y orbitals shifting to lower energy [Figure 5]. A dπ-pπ overlap with both oxygen atoms result in no upaired electron on the platinum atom.

EXPERIMENTAL STUDIES

CO Oxidation: 1nm 2%Pt/Al_2O_3 catalyst, prepared by the traditional impregnation method from H_2PtCl_6 • xH_2O, were exposed to CO oxidation conditions. Previously reported batch studies of both 2%Pt/γ-Al_2O_3 and 2%Pt/θ-Al_2O_3 samples were tested on a bench-top reactor under CO oxidation condition, 5%CO, 5%O_2 and 90%N_2. The batch testing studies included testing two samples of each catalyst for CO oxidation efficiency as a function of temperature. Testing of one sample was stopped after oxidation was initiated and the Pt particles were imaged by scanning transmission electron microscope (STEM). The second samples were allowed to achieve quantitative CO oxidation before cooling to room temperature and repeating for a total of 3 cycles before imaging the particles by STEM. Temperature profiles for both catalysts (γ and θ) were identical after 3 cycles, initiating at 180°C and reaching quantitative conversion at 210°C.

While batch testing provides valuable data regarding conditions necessary for CO oxidation, nanostructural changes of the Pt particles observed after these tests are subject to sample-to-sample variation. In order to get a better understanding of how the nanostructures of certain particles change during CO oxidation, *ex-situ* reactor studies were carried out. The *ex-situ* reactor allows the exact same area of alumina to be imaged under each condition noted during the batch reactor tests. Figure 6 shows the exact same area from the 2%Pt/γ-Al_2O_3 catalyst as a fresh sample, after it was exposed to initiation conditions (180°C) and after exposure to 3 cycles of quantitative CO oxidation conditions (210°C).
Visual inspection of the images in Figure 6 suggests some particle growth after exposure to CO oxidation condition compared to the fresh sample. A graphical program designed for

measuring particle sizes of images obtained by electron microscopy was used to quantitatively evaluate the changes in the Pt particles nanostructure. Figure 7 shows the changes in particles size distribution for multiple areas followed on a 2%Pt/γ-Al_2O_3 catalyst sample throughout the CO oxidization *ex-situ* study described above. The distribution curves show that while the average particle size changes little throughout the *ex-situ* study and the size range increases only slightly after both the initiation-testing and quantitative conversion cycles, the quantity of particles towards the higher end of the size range begins to increase. When compared to the results obtained by batch testing, the effect of sample-to-sample variation can be seen.

A similar batch/*ex-situ* set of studies was also done for the 2%Pt/θ-Al_2O_3 catalysts to show any effect the catalysts' substrate morphology would have on nanostructural changes. Figure 8 shows the exact same area from the 2%Pt/θ-Al_2O_3 catalyst as a fresh sample, after it was exposed to initiation conditions (180°C) and after exposure to 3 cycles of quantitative CO oxidation conditions (210°C).

Visual inspection of the images in Figure 8 suggests some particle growth after exposure to CO oxidation condition compared to the fresh sample. Figure 9 shows the quantitative changes in the particles size distribution for multiple areas followed on the 2%Pt/θ-Al_2O_3 catalyst sample throughout the CO oxidization *ex-situ*. The distribution curves show that while the bulk of the particles show little change in size throughout the *ex-situ* study, the size range increases after both the initiation-testing and quantitative conversion cycles.

Lean Burn Conditions: 1nm 2%Pt/γ-Al_2O_3 catalyst, prepared by the traditional impregnation method from $H_2PtCl_6 \cdot xH_2O$, was exposed to lean burn conditions to begin looking at how the Pt clusters behave in more complex systems. The lean burn conditions refers to exposing the catalyst to a gas composition of 5%CO, 500ppm NO, 500ppm hydrocarbons (2:1 mix of propene and propane), and 10%O_2. A space velocity of 50,000 h^{-1} was obtained using N_2 as a balance gas to reach the required flow rate of 3L/min. The oxidation of each gas was monitored by analyzers attached to our bench-top exhaust reactor.

CO oxidation reached 100% conversion quickly at 167°C, and remained completely oxidized throughout the remainder of the test [Figure 10]. At this temperature, the C_3 hydrocarbon mix reached 95% conversion. NO oxidation to NO_2, which is equilibrium limited, reached a maximum conversion of 45.5% at a slightly higher temperature of 251.5°C before the reverse NO_2 reduction reaction became favored. Interestingly, at the same temperature that NO oxidation reached its maximum conversion (251.5°C), a small drop in the hydrocarbon oxidation was observed. Oxidation of the hydrocarbon gases began approaching completion by the next temperature monitored (306.5°C) and reached ~97% by 420.5°C.

Microstructure analysis using microscopy was performed on a sample of the lean burn tested catalyst. Most areas analyzed resembled figure 11 with an average particle size of 7.1nm and predominately ranging from 1.8-20nm with random large Pt particle in the 51-71.2nm range, see figure 8 for distribution curve. However, an area with extremely large particles which was difficult to properly quantify was also observed. These extra large Pt particles are not spherical or semi-spherical as is often observed for the smaller particles. While this area shows some smaller particles, like those seen in other sample areas, the large particles appear to range from 31-135nm. An *Ex-situ* study of the catalyst under the lean burn conditions is necessary to determine whether the large particles seen can be attributed to Pt particle density, as was seen in *ex-situ* studies under NO oxidation conditions, or a product of sample-to-sample variation

Conclusions

Theoretical studies on single atom show that the bonding of platinum with θ-alumina is different from that reported for α- or γ-alumina. Pt is a d9s1 atom and after interaction with θ-alumina, it does not show an unpaired electron

suggesting d8 structure with dπ – pπ backbonding where 2 electron pairs from two adjacent oxygen atoms is donated to platinum. The reported structure for single atoms supported on α-alumina is quite different. The adsorbed platinum atom is paramagnetic and the interaction of Pt with surface is summarized as localized covalent bonding between Pt and O enabled by nearly Al-centered electron-accepting empty states available to accept excess electron density. The Pd and Au atoms also exhibit a bonding pattern which is quite similar to Pt bonding but Ag interacts with alumina surface in a largely ionic fashion.

Previously we have shown that platinum supported on γ-alumina or θ-alumina exhibit identical CO oxidation behavior. We propose that that the local catalyst environment of platinum sites in both catalysts could be identical. Thus, theoretical studies of platinum supported on γ-alumina need to be reinvestigated with realistic structure of γ-alumina as input in theoretical studies.

Experimentally, we found that CO and NO_x conversion becomes quantitative at ~170ºC while NO_x conversion reached a maximum of 45% at ~250ºC on a Pt/ γ-alumina catalyst. A rapid growth in particle size is also observed which is quite consistent with Oswald ripening under oxidizing conditions.

References

1. Kresse, G.; Hafner, J.; Phys. Rev. B, **1993**, *47*, 558.
2. Kresse, G.; Hafner, J.; Phys. Rev. B, **1993**, *48*, 13115.
3. Kresse, G.; Hafner, J.; Phys. Rev. B, **1194**, *49*, 14251.
4. Perdew, J.P., Chevary, J.A.; Vosko, S.H.; Jackson, K.A.; Pederson, M.R.; Singh, D.J. *Phys. Rev. B*, **1992**, *46*, 6671.
5. Perdew, J.P., Chevary, J.A.; Vosko, S.H.; Jackson, K.A.; Pederson, M.R.; Singh, D.J. *Phys. Rev. B*, **1993**, *48*, 4978.
6. Bloch, P.E. *Phys. Rev. B*, **1994**, *50*, 17953.
7. Kresse, G.; Joubert, D. *Phys. Rev. B*, **1999**, *59*, 1758.

Presentations and Publications (FY 09)

1. Narula, C.K.; Chen, X.; Stocks, M.G.; "First-Principles Studies of the Structural Properties of Metal Atoms Supported on θ-Alumina" Phy. Rev. Lett. (Manuscript in preparation).
2. Moses-DeBusk, M.; Narula, C.K., "Catalyst by design: Combining the power of theory, experiments, and nanostructural characterization for catalyst development." *Prepr. Pap.-Am. Chem. Sco., Div. Fuel Chem.* **2009**, *54 (1)*.
3. Moses-DeBusk, M.; Narula, C.K., Stocks, M.G, Chen, X.; "Catalyst by design: Combining the power of theory, experiments, and nanostructural characterization for catalyst development," 227th National American Chemical Society Meeting, March 2009 (invited).
4. Narula, C.K.; DeBusk, M.M.; Allard, L.F.; Chen, X.; Stocks, M.G.; 'Catalyst by Design – Theoretical, Nanostructural, and Experimental Studies of Catalyst for Diesel Engine Emission Treatment', DEER 2009, Detroit, MI.

Figures

Figure 1: Side view of Pt atom on θ-alumina surface model and charge density transfer isosurface for metal adsorption on θ-alumina.

Figure 2: Surface contour plot for platinum locations.

Figure 3: Minimized energy images of reaction path for Pt atom on θ-alumina to go from lowest to highest energy location.

Figure 4: Top view of Pt atom on θ-alumina surface 2 x 3 x 3 slab.

Figure 5: Projected O p_x, p_y, and p_z LDOS of surface oxygen atoms within (black) and outside green) bonding distance from platinum.

Figure 6: DF-STEM images of 2%Pt/γ-Al_2O_3 fresh (left), the exact same area after initiation conditions, 180°C (middle), and again after 3 cycles of quantitative

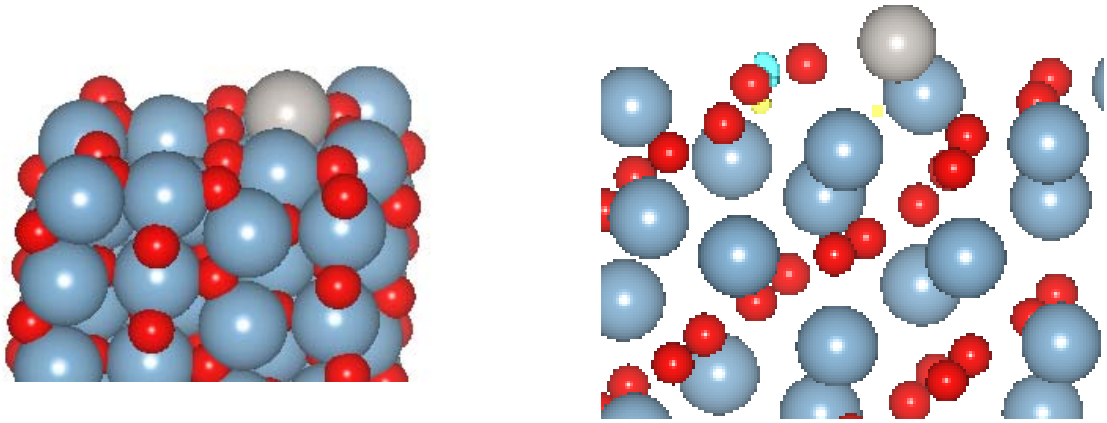

Figure 1: Side view of Pt atom on θ-alumina surface model and charge density transfer isosurface for metal adsorption on θ-alumina.

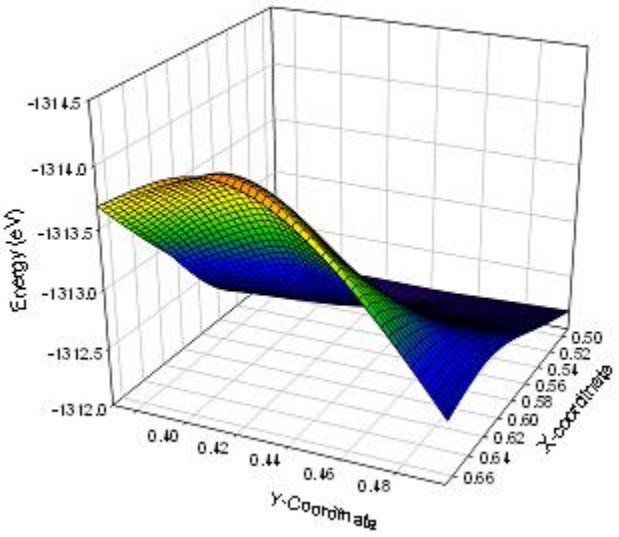

Figure 2: Surface contour plot for platinum locations.

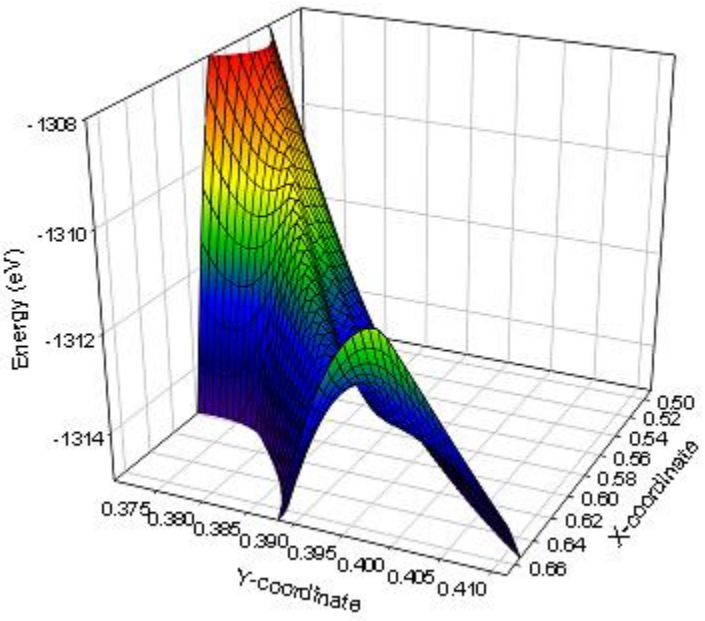

Figure 3: Minimized energy images of reaction path for Pt atom on θ-alumina to go from lowest to highest energy location.

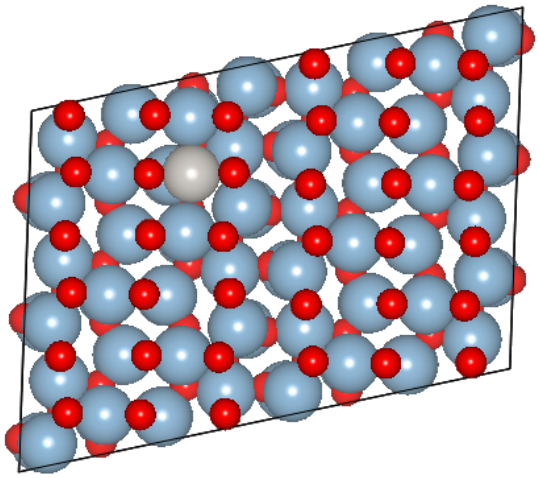

Figure 4: Top view of Pt atom on θ-alumina surface 2 x 3 x 3 slab.

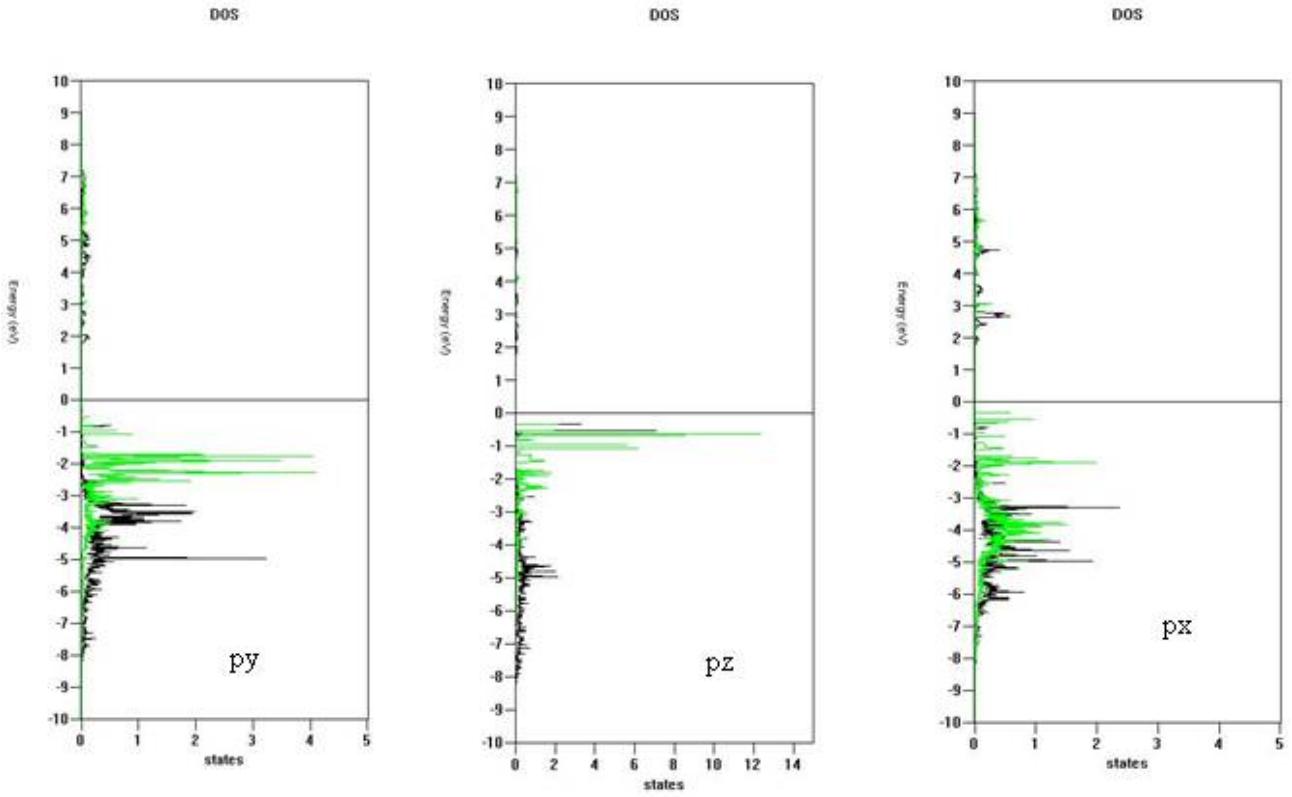

Figure 5: Projected O p_x, p_y, and p_z LDOS of surface oxygen atoms within (black) and outside green) bonding distance from platinum.

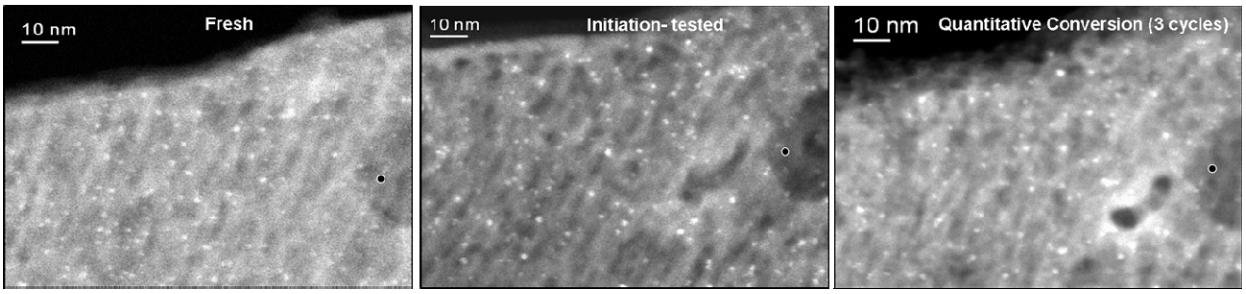

Figure 6: DF-STEM images of 2%Pt/γ-Al_2O_3 fresh (left), the exact same area after initiation conditions, 180°C (middle), and again after 3 cycles of quantitative CO oxidation conditions, 210°C (right). The black circles rimmed in white are used to show the same spot in each image.

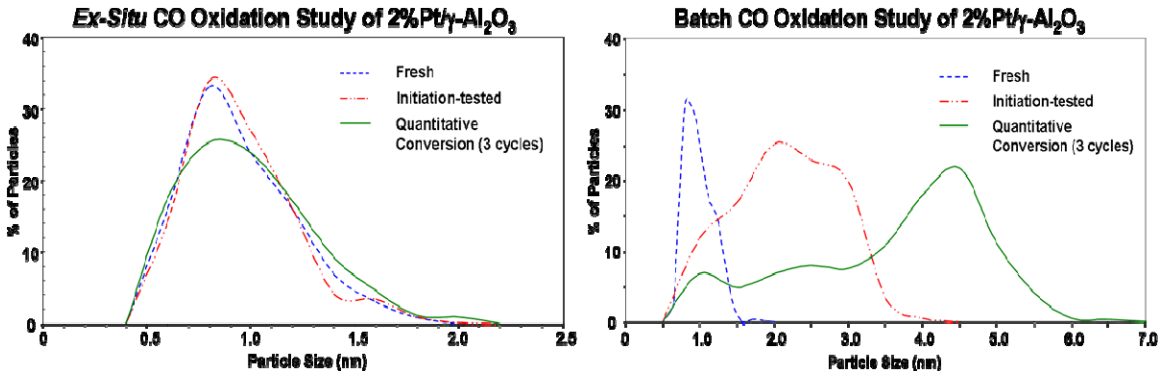

Figure 7: Pt particle size distribution curves obtained from STEM images of 2%Pt/γ-Al_2O_3 taken in the course of an *ex-situ* reactor study (left) and a batch reactor study (right) under CO oxidation conditions.

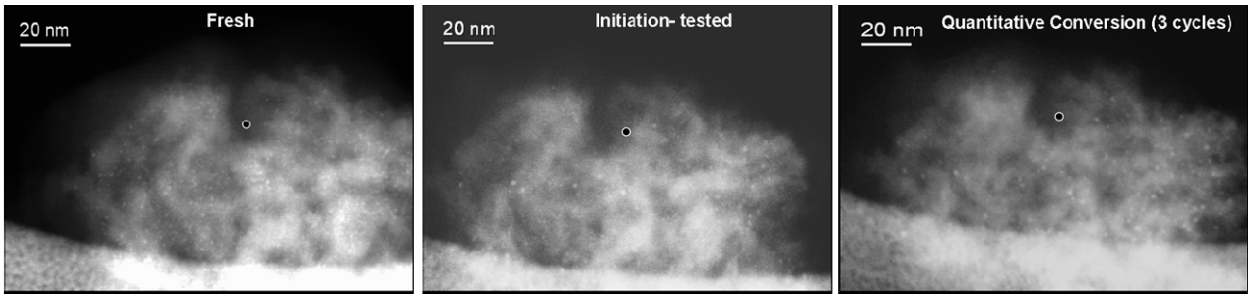

Figure 8: DF-STEM images of 2%Pt/θ-Al_2O_3 fresh (left), the exact same area after initiation conditions, 180°C (middle), and again after 3 cycles of quantitative CO oxidation conditions, 210°C (right). The black circles rimmed in white are used to show the same spot in each image.

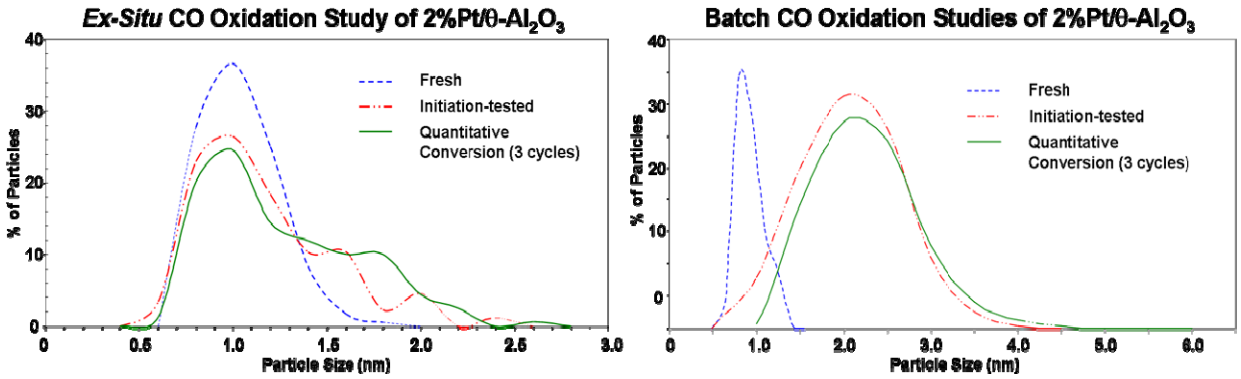

Figure 9: Pt particle size distribution curves obtained from STEM images taken in the course of an *ex-situ* reactor study (left) and a batch reactor study (right) under CO oxidation conditions.

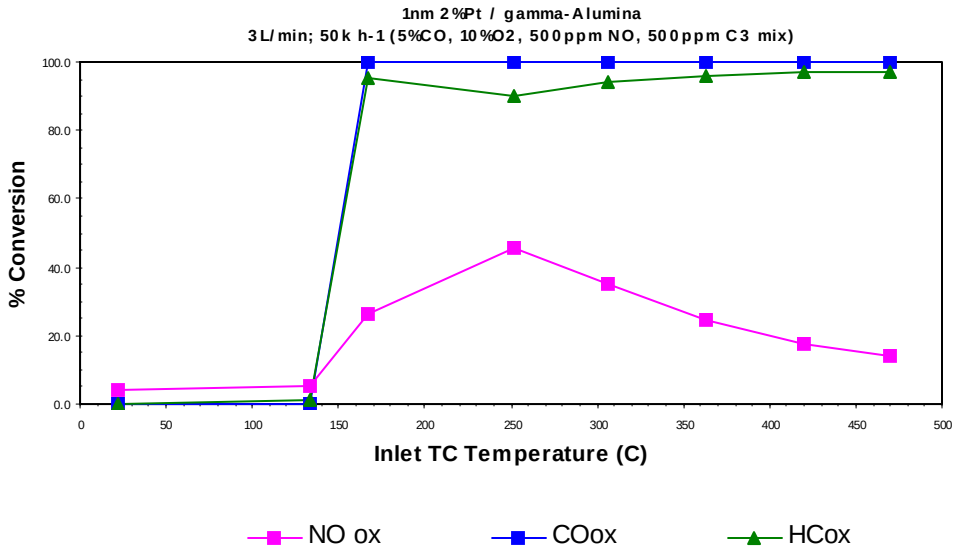

Figure 10: Conversion graph depicting CO, NO and hydrocarbon (HC) oxidation over 1nm Pt/2%Pt/Al_2O_3 catalyst as a function of inlet gas flow temperatures of 133.5°C to 465.5°C.

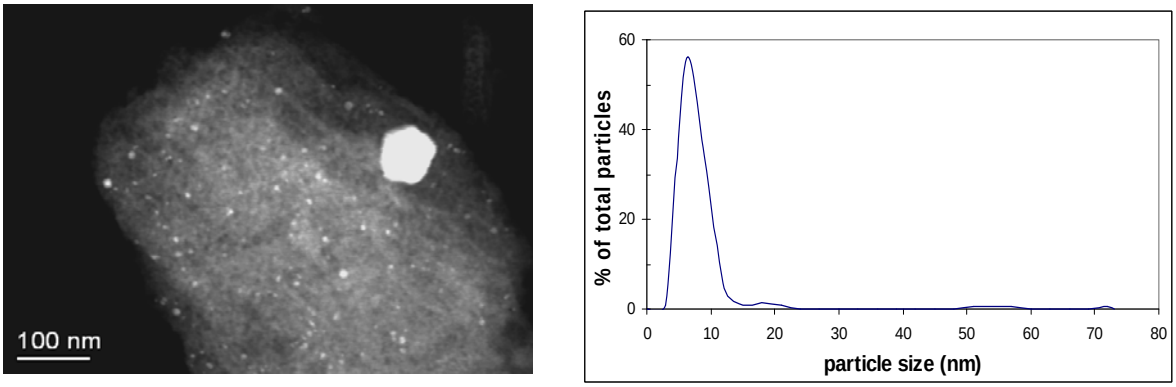

Figure 11: STEM image (left) and particle size distribution (right) of 2%Pt/γ-Al_2O_3 after testing under lean burn conditions.

Agreement 19214 - Effects of Biodiesel Fuel on Diesel Particulate Filter Materials

*M. J. Lance and T. J. Toops**
Ceramic Science and Technology Group
Oak Ridge National Laboratory
P.O. Box 2008, MS 6068, Bldg. 4515
Oak Ridge, TN 37831-6068
(865) 241-4536; fax: (865) 574-6098; e-mail: lancem@ornl.gov
* *National Transportation Research Center, ORNL*

DOE Technology Manager: Jerry L. Gibbs
(202) 586-1182; fax: (202) 586-1600; e-mail: Jerry.gibbs@ee.doe.gov
ORNL Technical Advisor: D. Ray Johnson
(865) 576-6832; fax: (865) 574-6098; e-mail: johnsondr@ornl.gov

---

Contractor: Oak Ridge National Laboratory, Oak Ridge, Tennessee
Prime Contract No.: DE-AC05-00OR22725

Objective

- To characterize changes in the microstructure and material properties of diesel particulate filters (DPFs) in exhaust gas produced by biodiesel blends.

Approach

- Measure the chemical composition and pH of condensate and PM generated by a diesel engine running with ULSD and biofuel blends.
- Age filter samples (cordierite, mullite and SiC) in solutions identical to condensate composition.
- Monitor microstructural changes in the DPF substrate with SEM and electron-probe microanalysis (EPMA). Additionally, x-ray photoelectron spectroscopy (XPS), x-ray diffraction (XRD) and vibrational spectroscopy (Raman and FT-IR) will be used to determine any changes in the crystal structure or possible phase changes. Mechanical property degradation will also be characterized by machining bend bars out of the DPF and fracturing them.

Accomplishments

- Since this project is a new start, we have no results to report at this time.

Agreement 20091 - Electrically-Heated Diesel Particulate Filter Regeneration

M. J. Lance, J. E. Parks, A. A. Wereszczak, B. J. Bunting*, and W. P. Partridge**
Ceramic Science and Technology Group
Oak Ridge National Laboratory
P.O. Box 2008, MS 6068, Bldg. 4515
Oak Ridge, TN 37831-6068
(865) 241-4536; fax: (865) 574-6098; e-mail: lancem@ornl.gov
* *National Transportation Research Center, ORNL*

DOE Technology Manager: Jerry L. Gibbs
(202) 586-1182; fax: (202) 586-1600; e-mail: Jerry.gibbs@ee.doe.gov
ORNL Technical Advisor: D. Ray Johnson
(865) 576-6832; fax: (865) 574-6098; e-mail: johnsondr@ornl.gov

Contractor: Oak Ridge National Laboratory, Oak Ridge, Tennessee
Prime Contract No.: DE-AC05-00OR22725

Objectives
Study efficiency benefits and materials issues associated with the electrically-heated diesel particulate filter (EHDPF) device developed by General Motors (GM). Specific objectives are:

Task 1: FEERC-NTRC
- Characterize potential fuel savings of the approach and related benefits to other emission control devices.
- Measure gas and substrate temperatures to obtain accurate picture of conditions experienced during regeneration.

Task 2: CerSaT-HTML-MST
- Resolve current disconnect between cordierite substrate model predictions and actual substrate durability.
- Use data and results to develop general design rules on heater geometries to optimize substrate durability.

Task 3: CS-MST
- Conduct a high-level discussion on the durability of the heater alloy.

Accomplishments
- Since this project has yet to be approved by the DOE and General Motors, no accomplishments can be reported at this time.

Discussion
New advanced diesel vehicles have been commercialized in the U.S. and Europe for passenger car applications. Particulate matter (PM) emission regulations are met via DPF technology. Although these vehicles meet emissions regulations, a substantial amount of operating time is spent performing DPF regeneration. This leads to several disadvantages including fuel efficiency loss, prolonged exposure to high operating temperatures for other exhaust system components, and potential customer acceptance issues (especially for cases where customers drive for short time frames which causes repeated launch into DPF regeneration modes).

GM has developed a novel approach to DPF regeneration that is electrically-based. As opposed to traditional DPF regeneration strategies that use combustion exhaust heat and supplemental fuel injected into the exhaust for exothermic heating of the DPF, the GM approach utilizes resistive heat-

ing elements to raise the DPF temperature to a point where PM oxidation will occur. This approach can potentially alleviate the disadvantages associated with the traditional approach.

GM has demonstrated durability of the electric-based DPF device in engine dynamometer aging studies. Although the device proved durable, concerns regarding the substrate durability still remain because the actual durability shown was greater than the durability predicted by substrate models based on the exposure temperatures. Thus, a greater understanding of the accuracy of the models for this approach is desired. Furthermore, more thorough and accurate temperature measurements are desired to better characterize the gas, substrate surface, and substrate bulk temperatures which greatly affect the substrate durability. A better understanding of these issues will enable the development of rules of design for the location of the heaters to optimize substrate durability.

Experimental Approach

A new CRADA project is proposed in collaboration with GM. Three tasks at ORNL comprise the technical approach and the detail of each follows. Task 1 will be conducted within the Fuels, Engines, and Emissions Research Center (FEERC) at the National Transportation Research Center (NTRC), Task 2 by the Ceramic Science and Technology (CerSaT) Group within High Temperature Materials Laboratory (HTML) and the Materials Science and Technology (MST) Division, and Task 3 by the Corrosion Science (CS) Group within the MST Division. Key barriers addressed by these proposed activities are: cost-effective emission control, minimizing emission control fuel penalty, enabling market penetration of fuel-efficient vehicles.

Task 1. Thermal Characterization of Diesel Particulate Filter Regeneration

Jim Parks and Bill Partridge
Fuels, Engines, and Emissions Research Center at the National Transportation Research Center (FEERC at the NTRC)
Oak Ridge National Laboratory

General Motors has developed a diesel particulate filter (DPF) system that utilizes an electrically energized element to start ignition of particulate loaded on the DPF for enabling active regeneration of the DPF for improved particulate filtering. GM's technology has demonstrated the capability of actively regenerating the DPF over multiple loading cycles; however, concerns still remain regarding the durability of the technology over the number of cycles representative of product life. Furthermore, insight into the fundamental mechanisms of the particulate ignition and material durability impacts is desired. The following proposed research sub-tasks are designed to add insight into the fundamentals of this DPF technology and contribute to its development.

Task 1.a. Install Electrically-Heated DPF on 1.9-liter GM Diesel Engine

A 1.9-liter, 4-cylinder GM diesel engine is presently operational at ORNL in cell 2 of the engine cells located at the National Transportation Research Center (NTRC). The engine is operated with a Driven-based controller that allows full control of the engine including the ability to add post-combustion fuel injection in-cylinder. The engine is used for emissions and catalyst related research projects that are public in nature (funded by DOE). The intent is leverage this engine capability for the work detailed here as a more cost effective option compared with installing a specific engine for these tasks.

An electrically-heated DPF from GM will be installed on the 1.9-liter GM engine. A power supply will be acquired and appropriate controls for operation will also be added. At this stage, basic temperature measurement will be added (upstream and downstream temperature). The engine will be operated to load the DPF with soot, and regeneration (desoot) of the device will be conducted per guidance from GM.

Deliverable: Electrically-heated DPF installed and operational (desoot event conducted successfully).

Task 1.b. Fuel Penalty Comparison of Electrically-Heated DPF with Conventional DPF Desoot Technique

An experiment will be conducted to compare the fuel penalty for the electrically-heated DPF with a conventional fuel-based heated DPF. The experi-

ment will be conducted by loading each DPF to a similar level by using specific engine modes for soot loading and monitoring backpressure to achieve a starting backpressure level. Then, each DPF will be regenerated with its standard protocol for desoot. During both loading and regeneration stages, fuel consumption will be recorded so that a fuel penalty for DPF operation can be obtained. For the electrically-heated DPF, electrical energy use will be recorded, and the total electrical energy will be converted into a fuel penalty based on efficiencies for combustion to electrical power.

Deliverable: Fuel penalty measurement for both Electrically-Heated DPF and conventional approach (fuel-heated).

Task 1.c. Fiber-Optic Based Temperature Measurement Downselection and Design Based on Bench Experiments

In order to acquire the critical accurate temperature measurements necessary to fully understand the impact of desoot operation on the durability of the substrate, fiber-optic based temperature measurements will be employed. Standard thermocouple measurements will also be made during the studies, but thermocouples may suffer from slow response time and conductive heat transfer along the thermocouple sheath. The two fiber optic technologies of interest are: phosphor thermography and pyrometry. Phosphor thermography is conducted by exciting a phosphor and monitoring the decay time of the fluorescence which is a function of temperature. Typically, the phosphor is placed at the end of a fiber optic to form a temperature probe. In pyrometry, the ratio of colors of light emitted from a hot body are analyzed to determine the temperature of the hot body; so, a fiber optic is used primarily to collect light emission. The analysis of pyrometry is based on blackbody radiation theory which is well understood.

In this task, bench experiments will be conducted to select and design the appropriate fiber-optic technologies that will be used in the engine-based experiments (Tasks 1.e. and 1.f.). A furnace or other element will be used as a steady and controllable heat source. For phosphor thermography, various phosphor materials will be evaluated to determine their sensitivity in the temperature range of interest for DPF regeneration (nominally 500-1000ºC). Degradation of the phosphor due to heat will also be evaluated. For pyrometry, various fiber end geometries will be explored to selectively probe the temperatures of surfaces for spatial temperature measurements. Also, the specific wavelengths of interest will be investigated so that the appropriate spectrometer equipment can be used for the experiments (multiplexing expected to be required).

Deliverable: Selection of fiber-optic probe technology for use in the engine experiments.

Task 1.d. Development of Fiber-Optic Temperature Probes for Engine Study

The fiber-optic technologies selected in Task 1.c. will be developed for the engine study and installed in the DPF system. Activities in this task will focus on addressing the technical and practical issues associated with transferring from the bench environment to the engine exhaust environment. Example issues to be addressed include: positioning of fiber optics in DPF, feedthrough and guiding of fiber optics into DPF and "can" and into spectrometers/detectors, and multiplexing opportunities for fiber optics (to enable more than one measurement point for a given regeneration). Standard thermocouples will also be installed in the DPF system for reference and comparison to the fiber optic probe data.

Deliverable: Rigged DPF system with fiber-optic and thermocouple probes ready for engine use.

Task 1.e. Experiments to Characterize Temperature During Desoot of Electrically-Heated DPF

The electrically-heated DPF outfitted with fiber optic and thermocouple temperature probes in Task 1.d. will be studied on the 1.9-liter diesel engine platform. Experiments will be conducted to characterize the gas, surface, and substrate temperatures during DPF regeneration. Spatiotemporal variations in temperature will be measured, and various parameters for the regeneration operation will be changed to understand their affect on the spatiotemporal temperature variations. Specific parameters of interest are space velocity (linear flow velocity), soot loading, initial substrate and

gas temperature, desoot temperature, and electric power.

The data from these experiments will be analyzed to determine the critical gas and surface temperatures experienced during the desoot operation. Comparisons between the temperature data from the fiber optic probes and thermocouples will be made. Also, experimental data will be compared with model results as supplied by the DPF substrate vendor. This important task in the work scope will be directed at understanding the current mismatch between model predictions and experimental results.

Deliverable: Data with comprehensive analysis of gas and surface temperatures during electrically-heated DPF desoot events on the engine.

Task 1.f. Controlled Study of Parameters Affecting Desoot Operation of Electrically-Heated DPF with Material Analysis for Microstructure Degradation

During this project, engine-based studies will be conducted in conjunction with materials analysis studies. In Task 1.f., DPF substrates with specific exposure histories will be created and given to the materials analysis team for evaluation. In this manner, specific material changes identified by the materials analysis can be linked to specific operation parameters and conditions in the engine exhaust environment.

Early on in the project after capabilities to perform regeneration of the electrically-heated DPF are established, DPF samples will be generated by approaching and causing failure of the DPF substrate. These samples will be transferred to the ORNL HTML team for analysis.

After the results from Task 1.e. are acquired, select conditions will be defined for safe operation of the electrically-heated DPF system. A controlled study will be setup based on the data to expose substrates to a range of conditions below and above the limitations of the substrate. These substrates will be removed systematically after various exposure levels for analysis by the ORNL HTML team. In this manner, specific conditions experienced by the DPF can be related to microstructure changes. Such data will serve as a basis for failure mode and effects analysis (FMEA).

Deliverable: Substrates with defined temperature exposure history for materials analysis and failure mode and effects analysis support.

Task 2. Mechanical Durability of EHDPFs

Michael J. Lance and Andy Wereszczak
Ceramic Science and Technology - High Temperature Materials Laboratory (CerSaT - HTML)
Oak Ridge National Laboratory

Task 2 is comprised of six subtasks that support the ultimate goal to develop and refine rules of design for EHDPF regenerators. The proposed plans for subtasks 2.a.-2.d. are based on the assumption that a single combination of ceramic substrate and architecture will be evaluated. The detail of each subtask follows.

Task 2.a. Failure Analysis of Tested EHDPF Regenerators

Perform established ceramic fractographic analysis of EHDPFs that have been subjected to service or laboratory test conditions that produced surface-located crack patterns. The location and orientation of primary and secondary crack patterns will portray the combination of the direction of the maximum tensile stress and the local tensile failure stress of the EHDPFs ceramic. These observations will assist the interpretation of the thermomechanical stress state of the EHDPF (e.g., produced from existing or additional finite element analysis or FEA) and in the design of appropriate mechanical test coupons to measure relevant failure stress or strength of the EHDPFs ceramic.

Deliverable: Identify and characterize failure initiation locations of cracked EHDPFs.

Task 2.b. Design Mechanical Test Coupons

The identification of the tensile strength directionality from Task 2.a will provide a primary guide to designing mechanical strength test coupons. The results from the testing of these coupons will play an important role in the eventual development of rules of design for the EHDPFs including those associated with any strength-size-scaling. Failure

stress of the DPF is anticipated to be directional and potentially a function of size too, so the chosen test coupons needs to appropriately and conservatively capture those nuances. The CerSaT group possesses a long history of designing test coupons that are harvested from components - that is a consequence of the recognition that material strength measured from components produces the most relevant and informative results. Depending on the directionality of the maximum tensile stress that causes crack initiation, the primary axis of the (flexure) specimens could either sample hoop or axial tensile stresses and material strength in those directions. The 8-fold symmetry of the DPF will also be considered with an intent to produce as many test coupons as possible to ultimately generate reliable failure stress statistics and confident analysis. Conventional finite element analysis using ANSYS or μ-FEA softwares will assist the design of these test coupons.

Deliverable: Design test coupons that can be harvested from EHDPFs and whose testing will produce material, size-dependent, failure stress data for input for durability analysis and prediction.

Task 2.c. Fabrication/Harvesting Test Coupons from EHDPF Regenerators

Machine designed test coupons from unused and used EHDPFs. Harvest enough test coupons whose strength testing will produce the identification of any size-scaling significant failure statistics. ORNL possesses extensive experience and in-house capabilities to harvest test coupons from DPFs and ceramic honeycomb structures.

Deliverable: Produce strength test coupons from EHDPFs.

Task 2.d. Durability Testing and Strength-Size-Scaling Interpretation

Perform (tensile) strength and fatigue testing of harvested test coupons and estimate failure stress statistics as a function of size. Test coupons from EHDPFs subjected to different periods of operation. Analyze and interpret with respect to operational finite element analysis of the EHDPF and reconcile with those examples where cracking was produced.

Deliverable: Database of strength-size-scaling statistics of ceramic used in EHDPF.

Task 2.e. FEA Design/Reliability Sensitivity Analysis

Use probability design sensitivity analysis to identify which ceramic properties and which EHDPF geometrical parameters have the largest effect on produced tensile stresses. Propose material improvements or practical architectural redesigns to that will lessen produced tensile stresses.

Deliverable: Rank properties and geometrical parameters that most affect tensile stresses in EHDPFs.

Task 2.f. Develop and Refine Rules of Design for EHPDF Regenerators

Develop a protocol that General Motors could use with their suppliers to determine what operational conditions a given or arbitrary EHDPF can sustain or what minimum properties a hypothetical ceramic would need to sustain a given or arbitrary operating condition of an EHDPF. The protocol would involve the marriage of FEA and specific mechanical strength data (i.e., tests which adhere to Tasks 2.a.-2.c). Prospective proof testing conditions would be an outcome as well. ANSYS (FEA) input files and spreadsheet analysis would be provided that GM could use to guide their own iterative design concepts using the accumulated results from Task 2.

Deliverable: Rules of design for EHDPF regenerators.

Task 3. Durability of EHDPF Heater Materials

Mike P. Brady and Michael J. Lance
Corrosion Science and Technology Group
Oak Ridge National Laboratory

We will conduct a high-level discussion on the durability of the heater alloy with experts in the Materials Science and Technology Division.

Deliverable: Recommendations for the best commercial alloy for this application.

Project 18865 - Materials by Design

Agreement 13723 - Residual Stresses in Thin Films*

*(This project is jointly funded by Propulsion Materials and Heavy Vehicle Systems Optimization)

Principal Investigators: D. Singh and J. L. Routbort coworkers: Kristen Pappacena
Argonne National Laboratory
9700 S. Cass Avenue, Argonne, IL 60439-4838
630-252-5009 dsingh@anl.gov

DOE Technology Manager: Jerry L. Gibbs
(202) 586-1182; fax: (202) 586-1600; e-mail: jerry.gibbs@ee.doe.gov

Contractor: UChicago Argonne LLC
Contract No.: DE AC03 06CH11357

Objective

- Measure residual stresses in thin films and coatings as a function of film thickness and relate stresses to film properties such as hardness, fracture toughness, and adhesion energy to relate to film processing variables and to predict durability
- Use techniques developed for measurements of residual stresses in thin films and coatings to measure residual stresses in bulk layered structures produced by joining by high-temperature deformation and to improve their mechanical properties

Approach

- Develop X-ray technique to measure change of lattice parameter of coating constituents as a function of depth and hence to calculate the lattice strains and stresses
- Develop indentation and/or scratch techniques to measure hardness, fracture toughness, and adhesion energy of films and coatings
- Relate stresses, properties, and processing conditions to film durability

Accomplishments

- Procured ZrN and TiC commercial coatings deposited on steel substrates with varying processing conditions: high-rate reactive sputtering (HRRS) & activated reactive evaporation (ARE)
- Advanced Photon Source (APS) used to measure residual stresses in ZrN and TiC coatings as a function of processing conditions
- Stresses were found to be sensitive to deposition conditions
- A commercial scratch tester procured and installed for adhesion energy measurements

Future Directions

- Develop indentation and/or scratch approaches to measure film adhesion
- Develop correlations between processing, residual stresses, adhesion energy for the coating systems studied: MoNCu, ZrN, and TiC. These correlations will help develop processing approaches for the development of coating systems with enhanced durability for applications on heavy vehicle engine components.

Introduction

Because of their unusual structural, mechanical, and tribological properties, superhard, nanocrystalline coatings can have an immediate and far-reaching impact on numerous advanced transportation applications including FreedomCar and 21st Century Truck Programs of DOE by reducing parasitic friction losses (hence increasing fuel economy) and wear (hence increasing durability/reliability). They can also be used to overcome toxic emission problems associated with exhaust gas recirculation in diesel engines. Durability of hard coatings is a critical property. The durability is determined by the surface adhesion energy, but is the result, in a large part, of the residual stresses that form as a result of materials, and processing parameters such as deposition bias voltage, ion flux, and temperature.

The approach for this effort is to use the high-brilliance X-rays produced by the Advanced Photon Source (APS) at Argonne National Laboratory, and a microfocus beam, to measure the residual stresses/strains of MoN based thin films and commercial coatings such as ZrN and TiC as a function of depth from the surface through the interface to the substrate. Subsequently, residual stress profiles will be correlated with the film processing conditions, and the resulting film/substrate adhesion and the films tribological properties.

During the past year, focus has been on two coating/substrate systems: (a) ZrN on steel and (b) TiC deposited on steel. Residual stresses as a function of depth in both in-plane and out-of-plane directions have been measured. Mechanical properties evaluation of these coatings was conducted to study the variation of properties as a function of position on the coating. Finally, a scratch tester system was procured and installed. This system will be used for the determination of the adhesion energy of the coatings for correlations with the processing and residual stresses.

Experimental Procedures

Samples

Samples of ZrN and TiC coatings deposited on steel were obtained from a commercial source. These coatings were deposited on tool steel (T-15). Two different processes of deposition were used to fabricate samples of ZrN and TiC: (a) high rate reactive sputtering (HRRS) and (b) activated reactive evaporation (ARE).

HRRS coatings were deposited below 300°C at deposition rates between 2300 Å/min and 4400 Å/min with reactive partial pressures ranging from 0.2-0.5 mTorr and a dc substrate bias of -100V. On the other hand, ARE coatings were deposited between 350-500 °C with deposition rates between 2000-5000Å/min. Carbide samples were fabricated using methane (in Ar carrier gas) in the HRRS process and acetylene in the ARE process. For the nitride samples, nitrogen gas was used in both the processes. Typical sample size was 0.5 in x 0.5 in square with the deposited coatings approximately 5μm thick.

Residual stresses measurement

X-ray microdiffraction was performed on beamline 34-ID-E at the Advanced Photon Source (Argonne National Laboratory) [1]. The x-ray beam was focused by Kirkpatrick-Baez mirrors down to 0.4 (horizontal) × 0.6 (vertical) μm^2. A high-resolution charged coupled device (CCD) x-ray detector was used to collect x-ray diffraction (XRD) patterns from the x-ray microbeam with energy of 8.9 keV (1.39308 Å). Strains and stresses were evaluated from the change in the lattice spacing determined from diffraction pattern of specific diffraction planes of coating materials and their respective stress free states.

The sample was aligned such that one of the edges was perpendicular to the x-ray

beam. A schematic of the set-up is shown in Figure 1. The sample was aligned by an x-ray fluorescence method so that the film surface (perpendicular to the page in Figure 1) was parallel to the x-ray beam. The sample was then scanned with respect to the x-ray beam with a step size of 0.25 μm. Similarly, by rotating the detector or the sample by 90°, out-of-plane strains were determined.

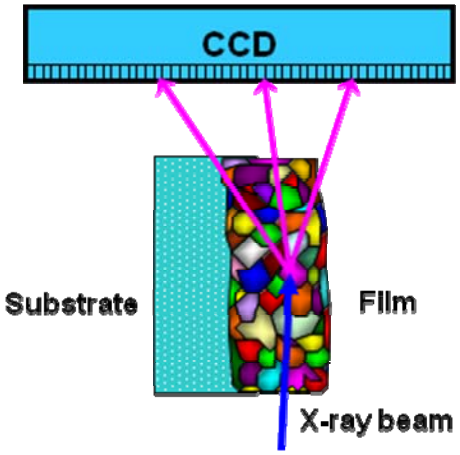

Figure 1. Experimental set-up for residual stress (strain) measurements

Nano-indentation

Nano-indentation on the ZrN coated sample was conducted to ascertain the variability of the coating properties at various locations, especially near sample edges. Nano-indentation tests were conducted at University of Illinois at Urbana Champaign. The sample surface was divided into four quadrants. Within each quadrant several measurements were made for hardness and elastic modulus as a function of depth of penetration.

Results and Discussion

Figure 2 shows the diffraction patterns obtained from TiC and ZrN coatings, respectively. The diffraction patterns at various detector orientations are shown for the two cases. The (111) diffraction planes for both coatings were used for the strain measurements. Figures 3 and 4 show the corresponding lattice parameters of TiC and ZrN coatings determined from x-ray diffraction as a function of coating depth. In-plane and out-of-plane values of lattice parameters are plotted as a function of coating depth. The strain-free lattice parameter is calculated from $\sin^2\psi$ approach [2]. The calculated strains are plotted in Figures 5 and 6 for TiC and ZrN coatings, respectively.

Three major observations can be made from the residual strain measurements: (a) For TiC coatings, in-plane residual strains are compressive and out-of-plane strains are tensile and their magnitudes decreases from coating surface to the substrate interface, (b) for ZrN coatings, strain profiles are quite similar to those observed for TiC samples, i.e., in-plane strains are compressive and out-of-plane are tensile, and (c) For both ZrN and TiC coatings, the strain variation as a function of coating depth is much steeper for the high deposition rate process, i.e., HRRS, as compared to the ARE process.

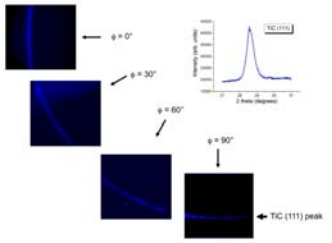

(a)

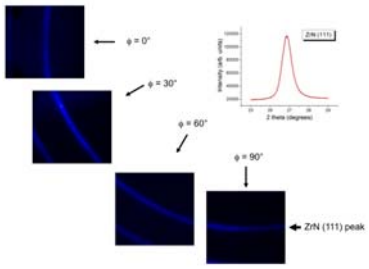

(b)

Figure 2. Diffraction patterns from (111) reflections of (a) TiC and (b) ZrN coatings as a function of detector orientation.

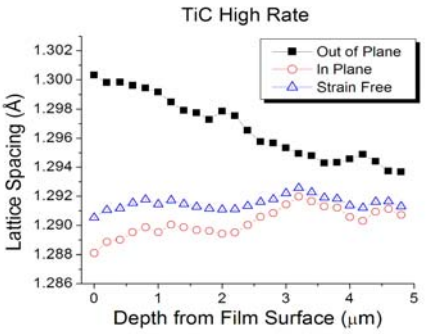

(a)

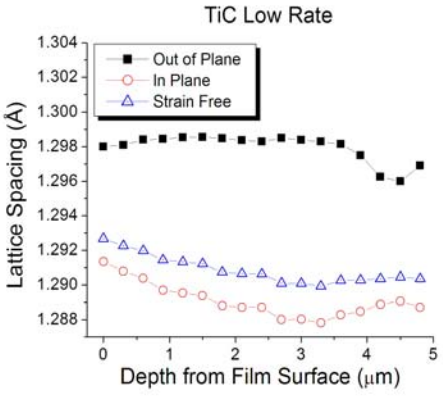

(b)

Figure 3. Lattice spacings of TiC coatings as a function of coating depth in in-plane and out-of-plane modes for (a) HRRS and (b) ARE processes.

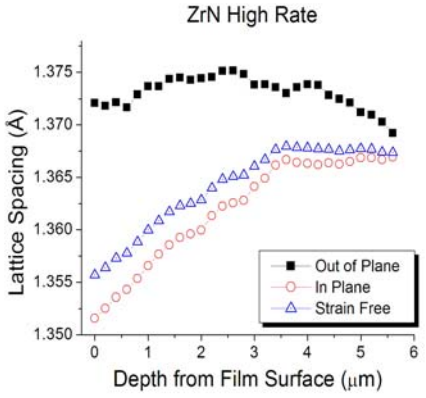

(a)

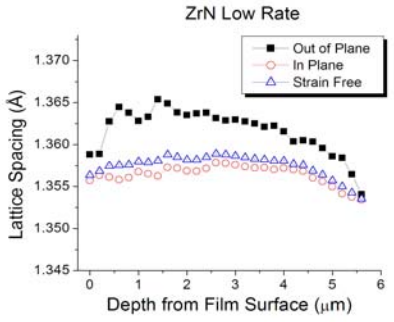

(b)

Figure 4. Lattice spacings of ZrN coatings as a function of coating depth of in-plane and out-of-plane modes for (a) HRRS and (b) ARE processes.

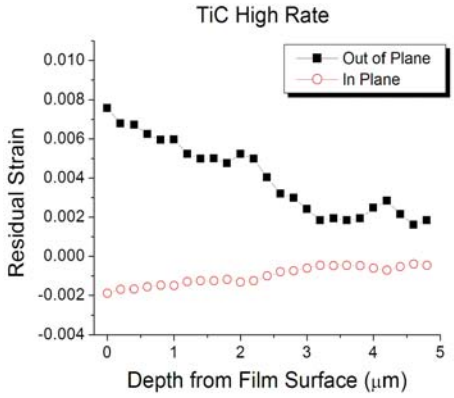

(a)

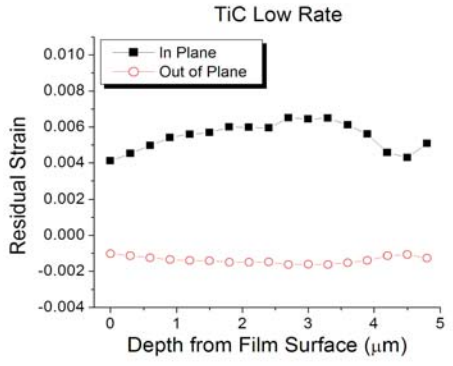

(b)

Figure 5. Residual strains of TiC coatings as a function of coating depth in in-plane and out-of-plane modes for (a) HRRS and (b) ARE processes.

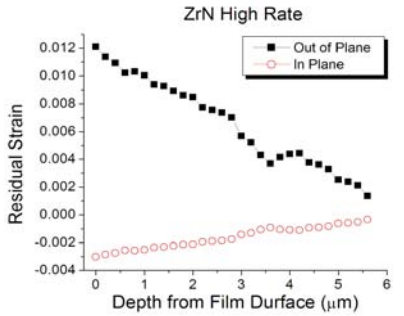

(a)

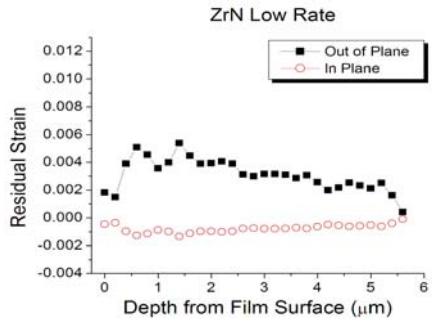

(b)

Figure 6. Residual strains of ZrN coatings as a function of coating depth in in-plane and out-of-plane modes for (a) HRRS and (b) ARE processes.

As shown in Figure 7, there is significant variability in the measured elastic moduli and hardness as a function of location for the ZrN coating. This figure corresponds to a quadrant in which the lower and right sides correspond to the sample edges. Elastic moduli values vary from 200 GPa to 350 GPa. It is interesting to note that the two lowest elastic moduli (locations 13 and 12) are on the sample edge, whereas, higher elastic moduli are observed for locations (6 and 5) that are away from the sample edge. Similar observations are made in the hardness measurements. These results confirm that there could be processing related local variations in the mechanical properties of the coatings which could contribute to the reduction of the coating durability under service conditions.

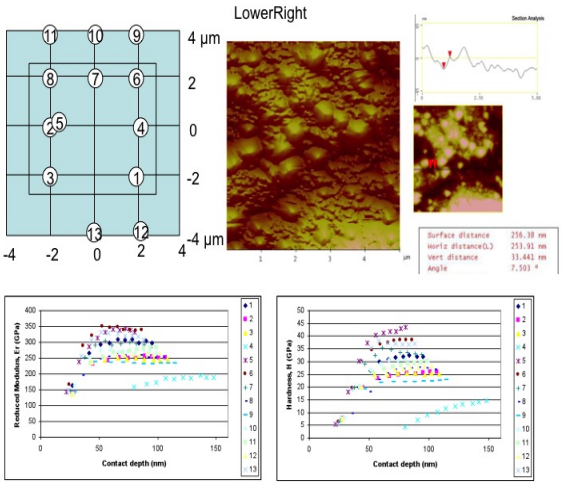

Figure 7. Location of nano-indents on ZrN coating and the measured elastic moduli and hardness values.

Scratch tester

We have now procured and installed a Romulus scratch tester with stylometer attachment, manufactured by the Quad Group (Spokane, WA). Figure 8 shows a photograph of the scratch tester. The procedure involves scratching the sample surface using a stylus (125-533 μm radius) at a fixed loading rate that is computer controlled. The system has a built in acoustic transducer that picks up any coating delamination or fragmentation events. The system also has a microscope that allows one to examine the scratch path (Fig. 9) and visually confirm the coating delamination. The load at which the coating delamination occurs is used to determine the adhesion energy of the coating [3].

Figure 8. Computer controlled scratch tester for coating adhesion energy measurements.

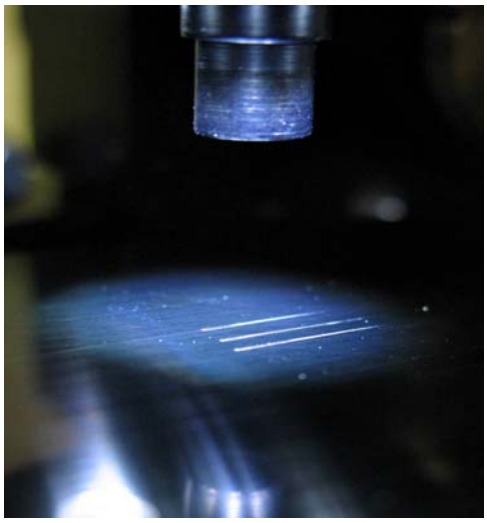

Figure 9. Typical scratches generated during the scratch test.

Conclusions

In conclusion, we have applied cross-section x-ray micro-diffraction technique to study depth-resolved residual strain in two commercial coatings: ZrN and TiC, deposited on steel substrates. These coatings were fabricated using two different processing conditions. The nano-indentation technique has been demonstrated as a tool for establishing the variability in the mechanical properties of the coating as a function of the location from the edges to the center of the coatings. To determine the adhesion energy of the coatings, a scratch tester has been procured and installed.

Future Directions

We will continue to develop the scratch test technique to measure surface adhesion energies. Further, residual stress measurements will be correlated to processing conditions and the adhesion energy to develop a protocol for fabricating coatings with long-term durability. Finally, collaboration(s) will be established with a coatings manufacturer for heavy vehicle engine OEM and technology will be transferred.

References

1. 1. G. E. Ice, B. C. Larson, W. Yang, J. D. Budai, J. Z. Tischler, J. W. L. Pang, R. I. Barabash, and W. Liu, J. Synchrotron Rad. **12**, 155 (2005).
2. V. Hauk, *Structure and Residual Stress Analysis by Nondestructive Methods*, (Elsevier, Amsterdam, 1997), Chapter 2.
3. S. T. Gonczy and N. Randall, An ASTM Standard for Quantitative Scratch Adhesion testing of Thin, Hard Ceramic Coatings, Int. J. Ceram. Technl., 2 [5] 422-428 (2005).

Agreement 9105 - Ultra-High Resolution Electron Microscopy for Characterization of CatalystMicrostructures and Deactivation Mechanisms

L. F. Allard, C. K. Narula, J. Howe, J-H. Kwak, C.H.F. Peden,* and A.K. Datye***
Oak Ridge National Laboratory
P.O. Box 2008, MS-6064
Oak Ridge, TN 37831-6064

** PNNL, Richland, WA*
*** Univ. of New Mexico, Albuquerque, NM*

DOE Technology Manager: Jerry L. Gibbs
(202) 586-1182; fax: (202) 586-1600; e-mail: jerry.gibbs@ee.doe.gov
ORNL Technical Advisor: D. Ray Johnson
(865) 576-6832; fax: (865) 574-6098; e-mail: johnsondr@ornl.gov

Contractor: Oak Ridge National Laboratory, Oak Ridge, Tennessee
Contract No.: DE-AC05-00OR22725

Objectives

- Develop and utilize new capabilities and techniques for ultra-high resolution transmission electron microscopy (UHR-TEM) to characterize the microstructures of catalytic materials of interest for reduction of NOx emissions in diesel and automotive exhaust systems.
- Relate the effects of reaction conditions on the changes in morphology of heavy metal species on “real” catalyst support materials (typically oxides).
- Continue project with Protochips Co. (Raleigh, NC) to demonstrate the utility of a robust MEMS-based heating technology (i.e. "AduroTM" chips) for the ACEM, that allows the behavior of catalytic materials to be studied *in situ* as a function of temperature and time, and under gaseous environments with the development of an environmental cell (E-cell) specimen holder and gas-handling apparatus.
- Develop procedures for calibration of Protochips AduroTM heating chip temperature profiles in the low-temperature regime (RT to 300°C), to correlate to calibrations from a nominal 400°C provided by Protochips Co.
- Have fabricated, install and test a glove box assembly with integrated video system and specimen pass-through to enable air-sensitive ACEM catalyst specimens to be loaded and transferred to the microscope under a protective, inert atmosphere.
- Collaborate with Bruker-AXS Co. to evaluate efficacy of new design of energy-dispersive x-ray detector system utilizing silicon-drift technology (SDD) on the ACEM (the first such commercial unit in the nation).

Approach

- Utilize Oak Ridge National Laboratory ACEM to characterize the atomic morphology and behavior of heavy-metal species such as platinum and rhenium on oxide (and other) support materials (alumina, silica, titania, carbon) as a function of *in situ* heating procedures.
- Utilize heater holder fabricated for Hitachi HF-3000 TEM to characterize behavior of catalyst species on oxide support via bright-field TEM imaging, coupled with secondary electron imaging in scanning transmission mode.

- Demonstrate ability to image at the atomic level through E-cell window materials, an essential milestone for final development of full E-cell capability.
- Utilize ACEM high-angle annular dark-field (HA-ADF) imaging to characterize the structure and chemistry of a series of model bimetallic nanoparticle comprising controlled compositions in the gold/palladium, platinum/zinc, and platinum/rhenium systems, on oxide supports such as ZnO "nanobelts."
- Utilize new SDD x-ray analysis capability to characterize chemistry of bimetallic catalyst nanoparticles as demonstration of new capability for microchemical analysis at near-atomic levels.

Accomplishments

- Developed and began testing of a Gen 2 E-cell holder, with Protochips Co. colleagues. Demonstrated ability to image atomic structure and even single atoms of heavy metal species (e.g. gold) on oxide support.
- Worked out testing and calibration procedures using HTML's special infra-red camera system to profile behavior of Protochips AduroTM chips in the low-temperature regime.
- Utilized Protochips heating holder for Hitachi TEM to characterize behavior of gold species in iron oxide support using both bright-field and secondary electron imaging techniques available on the Hitachi instrument. Special benefits of high-resolution secondary electron imaging to visualize behavior of catalyst nanoparticles on the support surface have been demonstrated.
- New glove box to allow air sensitive catalysts samples for the ACEM to be loaded into the specimen holder under a protective atmosphere was acquired and installed. System uses CCD camera system to facilitate the sample loading procedure.
- ACEM analysis of Pt/alumina and BaO/alumina NOx reduction catalysts in a collaboration with PNNL colleagues provided information to support a mechanism of binding of heavy metal species to sites on the alumina surfaces.
- ACEM experiments using Protochips heating showed mechanisms of formation of PdZn bimetallic nanoparticles at elevated temperatures via Pd particle growth and reactions with ZnO surface on novel nanobelt model support.

Future Directions

- In a cooperative project with Protochips Co., continue to develop techniques for *in situ* heating experiments, especially the development of a reliable environmental cell (E-cell) capability for gas reaction experiments.
- Perform precisely controlled *in situ* thermal experiments using *in situ* heating capabilities to understanding the interaction of Pt atoms with catalyst supports, and the development of catalyst nanoparticles and subsequent coarsening kinetics.
- In collaboration with colleagues at Ford Motor Co. and the University of Michigan, undertake a systematic study of a new class of “intelligent” catalyst materials, comprising heavy metal species such as Pd and Rh in perovskite structures like LaFePdO3 and CaTiRhO3, and their behavior in oxidation-reduction cycles. These catalysts are candidates for HC and NOx reduction in automotive exhausts, and are ideal subject materials for study with the advanced in-situ techniques we are developing.

Technical Progress

Our development of a new research thrust into in-situ microscopy studies of catalytic materials continued this year. We are working in collaboration with Protochips Co. (Raleigh, NC) which provides a novel heating technology called Aduro™, comprising heating elements fabricated utilizing semiconductor micro-fabrication techniques that have proven to have outstanding properties and behavior ideal for *in-situ* electron microscopy studies at the sub-Ångström level. A variety of methods for conducting heating experiments have been developed and tested, and used in several studies that have resulted in publications and presentations as listed at the end of this report. Work to extend the standard heating capability into an environmental cell (E-cell) capability continued, with the development of a second generation (Gen 2) E-cell holder that fits more reliably into the narrow objective lens pole-piece gap of the JEOL 2200FS ACEM. This holder has been tested in a fully configured mode and shown (as detailed herein) to provide atomic structure imaging at elevated temperature under a gaseous environment. To meet a milestone, we have specified and acquired a new glovebox with a pass-through chamber, to allow air-sensitive catalyst samples (e.g. reduced catalysts) to be loaded into ACEM specimen holders without exposure to the ambient atmosphere. This is facilitated by installing inside the glovebox a specially designed CCD camera system that is coupled to an external monitor.

Our catalyst studies also continued, in collaboration with a number of colleagues in industry, national laboratories and academia, including colleagues at Eastman Chemical Co. (Kingsport, TN), ORNL, and PNNL, the universities of Texas-Austin, Michigan, New Mexico and Missouri-St. Louis, and MIT. These projects have also resulted in significant publications. Examples of the most recent results obtained in selected studies are given in the sections that follow.

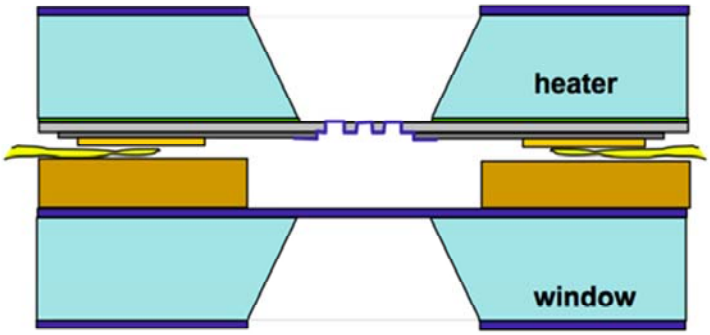

Fig. 1 Cross-section of Gen 2 E-cell design. Lower window is 50nm amorphous silicon nitride. Upper "window" is heater chip with continuous amorphous film over holes in low-conductivity ceramic heating membrane.

Development of the Gen 2 Environmental Cell Holder

As mentioned earlier, we have utilized several heating scenarios over the past year of use of the Protochips heating technology that have all been successful to one extent or another, depending on the requirements of the heating experiment. A principal goal was to design and fabricate a new specimen holder with a closed-cell heating capability that would fit more easily into the narrow gap of the ACEM objective lens. The new idea was to eliminate the upper 'window' of thin amorphous silicon nitride, and instead use a heater chip, mounted into a removable plate, with a

heater membrane that had a thin amorphous film over it that still allowed imaging through holes in the heater membrane, but with the holes covered by the thin film. Figure 1 shows the "Gen 2" cell geometry, and Fig. 2 shows an enlarged sketch of the center part of the cell, with the deposition of the catalyst powder specimen material indicated on the interior surface of heater chip.

microscope column. In a recent vacuum test, an actual heater chip was coated with a 25-30nm thick carbon film, made by deposition of carbon onto a cleaved salt crystal surface, floated off the salt by immersion in water, and then picking up the carbon film on the upper surface of a heater chip that had been mounted into the upper plate of the E-cell holder. The upper plate/heater window was then sealed into the E-cell, and the holder was

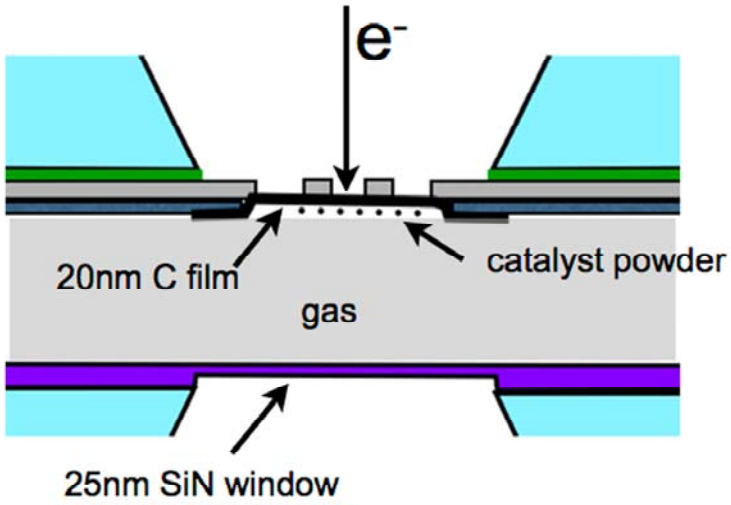

Fig. 2 Enlarged view of central part of Gen 2 E-cell design. Catalyst powder is deposited on the inside surface of the heater, supported by a thin continuous film of amorphous carbon or silicon nitride.

The primary question that arises is whether or not it is possible to achieve atomic level, single-atom imaging resolution when the electron probe has to pass through a window material prior to incidence on the specimen material. In the prior quarterly, we demonstrated that resolution of crystal lattice structure of gold nanoparticles and even single atoms of gold could be imaged through a 25nm amorphous silicon nitride window material. This demonstration offered great promise for the eventual test of the E-cell in a fully configured mode, i.e. fully sealed with an amorphous film covering holes in the heater membrane, and with a catalyst sample material deposited on the interior surface. Prior to a final geometry test, we are proceeding in an incremental fashion, to assure that we can produce a closed cell with an amorphous coating layer that will in fact hold pressure against the vacuum of the electron

inserted in our special external test chamber that allows pumping of the holder by a clean turbomolecular pump to a pressure of low 10^{-6} Torr, with a full atmosphere inside the cell. The cell did not show any significant leak tendency in the external test, so the holder was inserted into the ACEM, but with the interior of the cell pumped to a low pressure with our special pumping manifold that allows control of the pressure in the cell at the milliTorr level. We showed we could easily control the pressure in the cell in the microscope up to the several Torr level, and there was no evidence of vacuum degradation whatsoever. Further tests of the fully configured E-cell, showing imaging of catalyst nanoparticles through a gas phase at elevated temperature (i.e. an operational experiment) will be reported in the next quarterly report.

In-Situ Heating in the Hitachi TEM/STEM

In a prior quarterly, we described the fabrication of a heater holder compatible with Protochips Aduro™ devices that would fit into the Hitachi HF-3300 STEM/TEM instrument. This heater holder was aimed at doing in-situ studies at elevated temperatures during which EDS spectra could be collected using the standard energy dispersive spectrometer fitted onto that instrument's column. In addition, it was of interest to be able to do TEM imaging with reasonable facility at elevated temperatures, and to then be able to switch to the scanning mode, again with facility, and collect not only annular dark-field (ADF) images, but also secondary electron images (standard SEM imaging, but at high incident beam voltage). The latter capability coupled with the phase contrast images available in TEM mode provide a view of the sample structure and behavior at elevated temperature that is not achievable in the ACEM, which does not have a secondary electron imaging capability.

To test heating in the TEM/STEM, we again used the Au/FeOx sample as a test specimen, because of its know structure and behavior at high temperature. Figure 3 shows two BF images from a lengthy series acquired at 600°C. Faceted gold nanoparticles are seen on Fe oxide support particles. In the time between images, the FeOx particle shows the development of extended faceting (arrows). For comparison, Fig. 3c shows an image of a similar Au/FeOx particle in high-angle annular dark-field (HA-ADF) mode on the ACEM, also acquired at 600°C.

For comparison, Fig. 3c shows an image of a similar Au/FeOx particle in high-angle annular dark-field (HA-ADF) mode on the ACEM, also acquired at 600°C. The Au particles in this image show comparable structures, but faceting is not seen clearly on the oxide in the HA-ADF image. This faceting phenomenon is seen in better detail using the secondary imaging mode on the HF-3300, when the sample is treated at higher temperature. Figure 4 shows an image of an FeOx particle acquired at

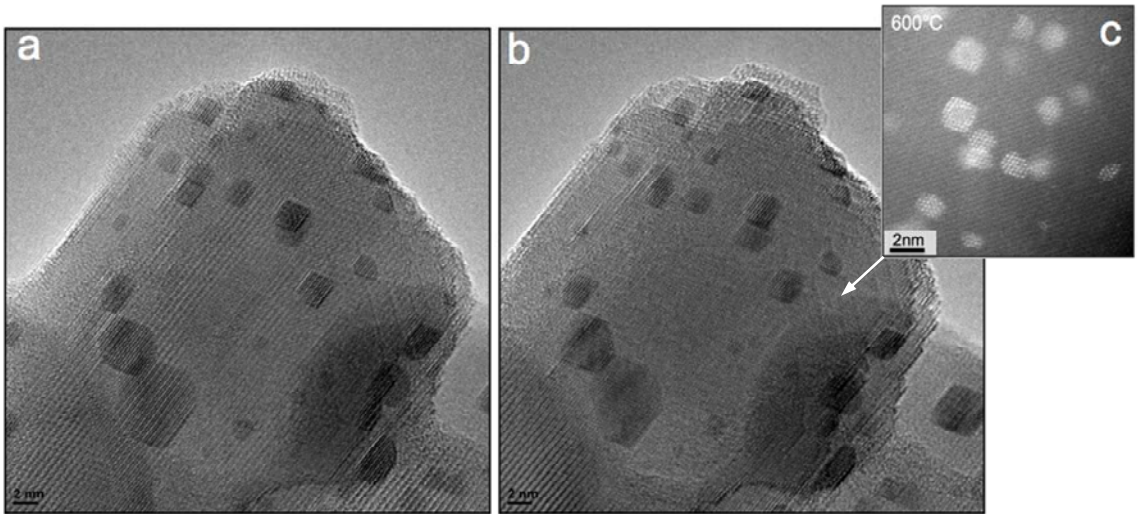

Fig. 3 a,b) Bright-field images of an Fe/Ox support particle showing the development of Au nanoparticles during heating at 600°C. Note the apparent increase in faceting after a short time (minutes) of additional heating in (b) vs (a) (arrows). c) HA-ADF images from the ACEM at 600°C shows similar shapes of Au nanoparticles, but little evidence of faceting.

600°C, compared with 4 sequential images of the same particle acquired at 800°C. Very small Au nanoparticles are seen on the surface, and surface faceting in the FeOx support particle develops at the higher temperature. In the sequence of images, gold particles are seen to coalesce, and then move along the developing facets in the oxide to further coalesce. These images show the remarkable information that can be obtained by in-situ heating, using the full range of techniques available with our advanced electron microscopes.

Implementation of Glove Box for ACEM Sample Loading Under Protective Atmosphere

Many catalyst samples we investigate are provided to us in e.g. a reduced state, and are

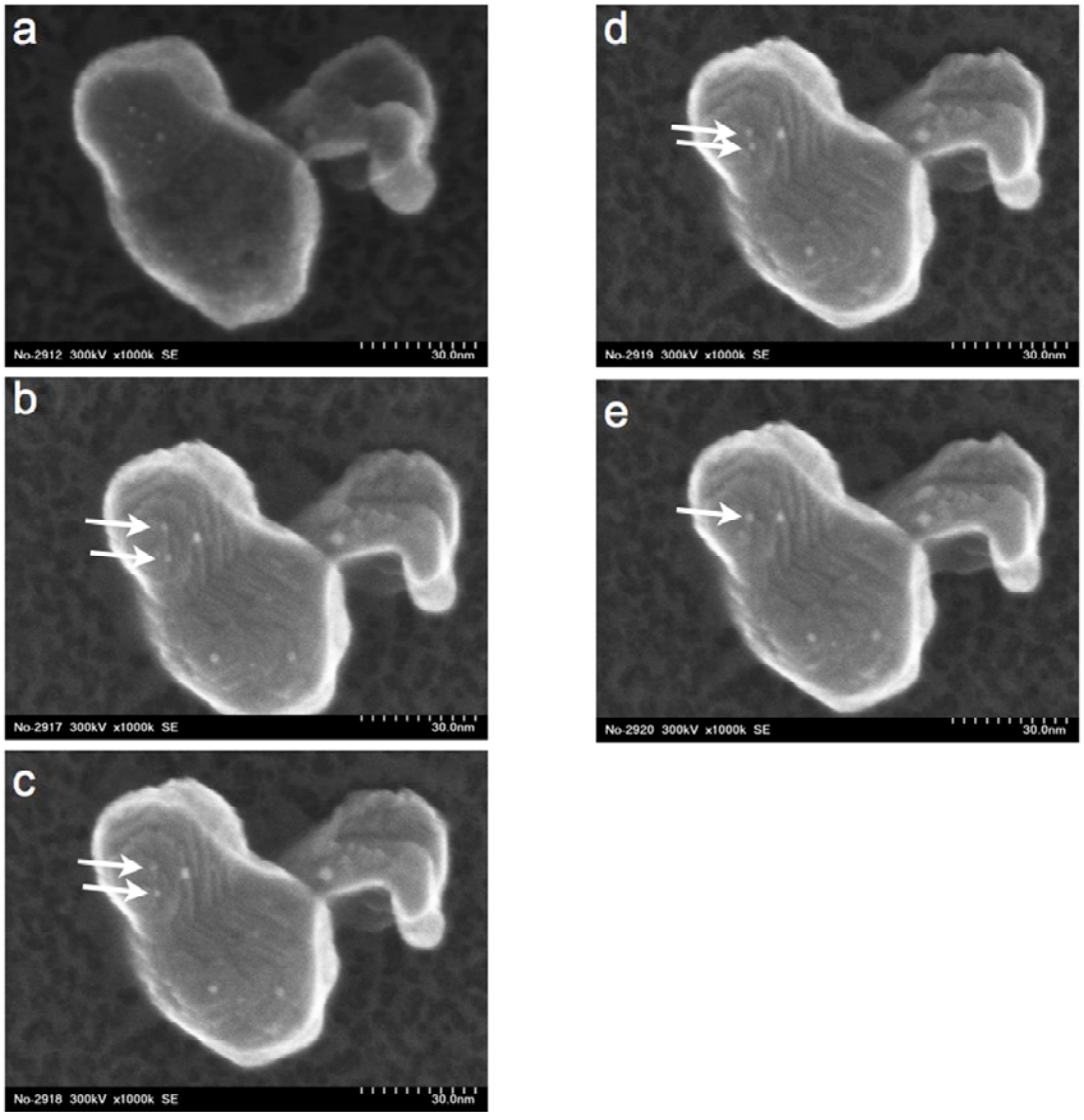

Fig. 4 a) Au/FeOx catalyst particle imaged with secondary electrons in the Hitachi HF-3300 STEM/TEM. After heating at 600°C, a few Au nanoparticles in the 1nm range are seen, and little surface faceting. b,c,d,e) time sequence at 800°C, showing surfce faceting, additional Au particle growth, and movement of Au particles over the surface with further coalescence (arrows).

stored under protective atmospheres, typically an inert gas such as nitrogen or argon. It is usually desired to examine these materials as-received, with no or little exposure to the atmosphere. In the past we have used plastic glove bags fixed around a stereomicroscope, into which we put the samples, the ACEM's specimen rod, and assorted tools and specimen grids as needed. This method, while workable, is tedious and time-consuming, since it requires time for flushing the bag for every use, and does not provide any mechanism for passing items in and out of the bag with facility. To overcome many of these difficulties, we decided to install a glove box that could be kept permanently sealed in an inert atmosphere, and that would have an appropriate pass-thru chamber attached to allow the specimen holder, samples, and other tools to be put into the box as desired for loading the holder. The other requirement was the equivalent of the stereomicroscope to be available, to facilitate the loading procedure. This was accomplished by using a CCD camera attached to a special lens system to allow a long working distance, and the appropriate magnification range for easy loading. Another feature of the new glove box is the novel design of the sleeves for the operator; instead of bulky rubber gloves, the present sleeves have rubber cuffs that seal tightly to the operator's wrist, an leave the hands free (with surgical gloves) to handle the delicate sample loading operation. Early tests showed that the new glove box works very well, giving us an improved capability, and meeting a defined milestone. Figure 5 shows the glove box in operation, and Fig. 6 is a view of the external monitor showing the holder for in-situ heating, with a heater chip in place. A cylindrical cover is placed over the end of the

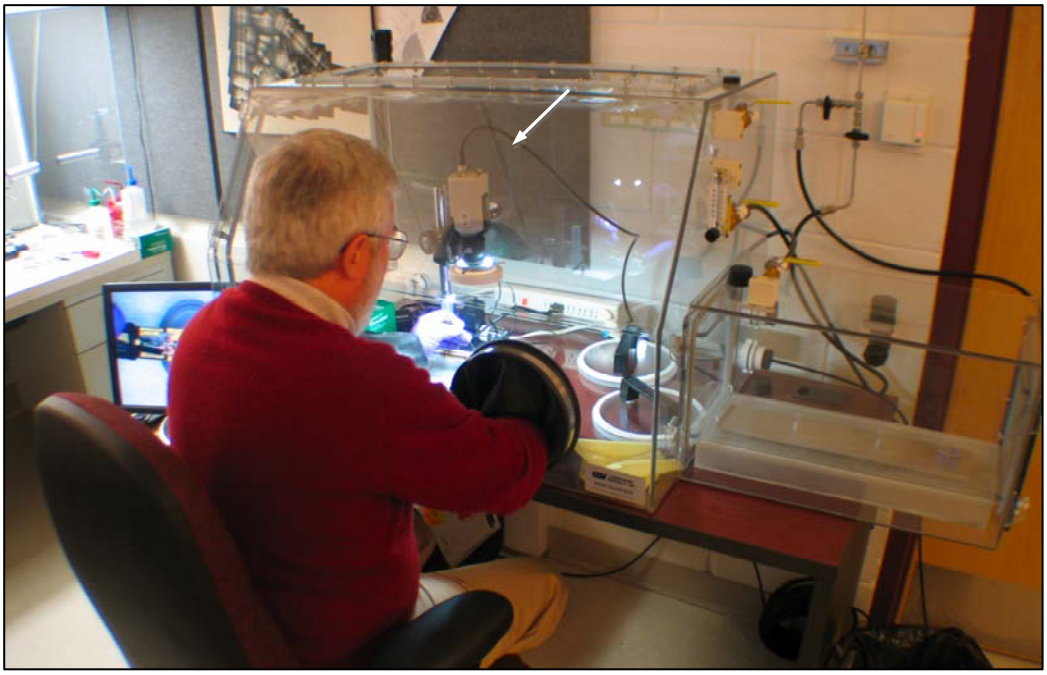

Fig. 5 Larry Allard using the new glove box for catalyst sample loading into the ACEM specimen holder under protective atmosphere. The CCD camera is arrowed, and the pass-thru chamber is seen on the right side of the box.

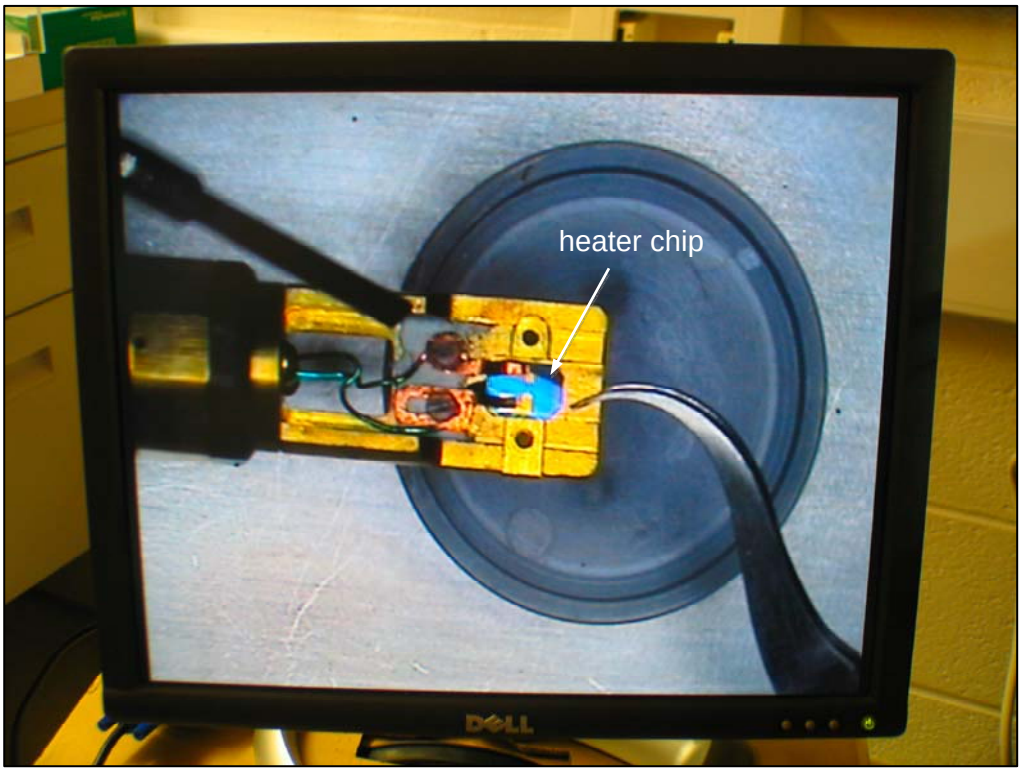

Fig. 6 Monitor view of the Protochips specimen holder inside the glove box, showing installation of a heater chip with air-sensitive catalyst material.

rod, so it can be removed for transfer to the microscope. A final requirement is a way to pass the rod into the microscope airlock for pumping with minimal or no air exposure; at present, we remove the cover cylinder and quickly insert the rod into the airlock, but we would like to eliminate even this short exposure. A couple of potential solutions to this problem are under consideration, and will be discussed in the next quarterly.

Concluding Remarks:

Our research activities on the forefront studies of the behavior of catalyst clusters and nanoparticles with reaction treatments, imaged at ultra-high resolution with the aberration-corrected electron microscope, are building a foundation towards a better understanding of the phenomena, which control performance in real systems. The implementation of novel methods for conducting these studies on specimens heated inside the electron microscope is the primary thrust of our research. Significant progress has been made in further development of an integrated heating technology for high-resolution electron microscopy, extending heating capabilities to an environmental cell capability for studying gas reactions on catalytic materials. Our work is in support of a variety of catalyst materials studies supported by DOE and the HTML national user program. New studies centered on a recently introduced class of "intelligent" catalysts for HC and NOx reduction in vehicle exhaust systems are being undertaken in collaboration with Ford Motor Co. and the University of Michigan; first results will be reported in an upcoming quarterly.

Publications and Presentations:

1. **Understanding the nature of surface nitrates in BaO/γ -Al_2O_3 NO*x* storage materials: A combined experimental and theoretical study;** Ja Hun Kwak, Donghai Mei, Cheol-Woo Yi, Do Heui Kim, Charles H.F. Peden, Lawrence F. Allard and János Szanyi, *Journal of Catalysis* **261** (2009) 17–22.

2. **Co-ordinatively unsaturated $^{Al3+}$ centers as binding sites for active catalyst phases on γ-Al_2O_3,"** Ja Hun Kwak, Jianzhi Hu, Donghai Mei, Cheol-Woo Yi, Doheui Kim, Charles H.F. Peden, Lawrence F. Allard and Janos Szanyi; *Science*, 325, 25 Sept. 2009, 1670-73.

3. **A New MEMS-Based System for Ultra-High-Resolution Imaging at Elevated Temperatures**; L.F. Allard, W.C. Bigelow, M. Jose-Yacaman, D.P. Nackashi, J. Damiano and S.E. Mick; Micros. Res & Tech, 72(3), pp. 208-215, March 2009

4. **A novel heating technology for ultra-high-resolution imaging in electron microscopes**; L. F. Allard, W. C. Bigelow, S. A. Bradley and J. Liu, Microscopy Today, pp.50-55, July 2008

5. L. F. Allard, Invited Seminar, University of South Carolina Interdisciplinary Mathematics Institute series on Imaging in Electron Microscopy. Seminar title: *Imaging the behavior of atoms, clusters and nanoparticles during elevated temperature experiments in an aberration-corrected electron microscope,* March 16-18, 2009

6. **Specific role of alumina surfaces for BaO anchoring and nitrate formations in BaO/γ-Al_2O_3 NO_x Storage Materials**, Ja Hun Kwak, Donghai Mei,Cheol-Woo Yi, Do Heui Kim, Charles H.F. Peden, Lawrence F. Allard, and János Szanyi, 21st North American Catalysis Soc., San Francisco, June 7-12, 2009

7. L. F. Allard, et al., **Developments in Aberration-Corrected Imaging at Elevated Temperatures Using a New MEMS-Based Heating Technology,** ORNL-Hitachi Workshop on "Advanced Electron Microscopy in Materials Science," Oak Ridge National Laboratory, November 2008

8. **Characterization of Pt-Pd Bimetallic NO Oxidation Catalysts with Advanced Electron Microscopy,** Obiefune K. Ezekoye, Andrew R. Drews, Robert W. McCabe, George W. Graham , Jane W. Howe, Lawrence F. Allard and Xiaoqing Pan

9. **Novel Synthesis and Atomic Level Characterization of PtSn/C Nanocatalysts for Direct Ethanol Fuel Cell Applications** Jingyue Liu, Janet Braddock-Wilking and Lawrence F. Allard, 21st North American Catalysis Soc., San Francisco, June 7-12, 2009

10. **In-situ elevated temperature electron microscopy of catalysts with single-atom resolution using a novel MEMS-based heater technology**; L. F. Allard, W. C. Bigelow, S. J. Overbury, M. Flytzani-Stephanopoulos, V. Ortalan, N. D. Browning, B. C. Gates, A. Uzun, D. P. Nackashi and J. Damiano, American Chemical Soc., Salt Lake City, March 22-26, 2009

11. **Performance and Applications of Protochips Aduro™ Heater Technology for In-Situ Ultra-High Resolution Imaging at Elevated Temperatures;** L. F. Allard, W. C. Bigelow, J. Liu, S. A. Bradley, J. E. Wittig, J. Bentley, D. P. Nackashi and J. Damiano, Frontiers of Electron Microscopy in Materials Science, Nagasaki, Japan, Sept 27-Oct 2, 2009

Communications and Visits

1. JEOL Ltd. factory visit, Akishima, Japan, Sept. 25, 2009; meeting with JEOL engineers, managers and designers to discuss collaboration with Protochips to formally integrate AduroTM heating technologies into JEOL electron microscopes

2. Hitachi Naka factory visit, Mito City, Japan, Oct. 2, 2009; meeting with Hitachi engineers, managers and designers to discuss collaboration with Protochips to formally integrate AduroTM heating technologies into Hitachi electron microscopes

Agreement 17895 - Durability of ACERT Engine Components

H. T. Lin, T. P. Kirkland, and A. A. Wereszczak
Oak Ridge National Laboratory
P.O. Box 2008, MS-6068
Oak Ridge, TN 37831-6068
(865) 576-8857; fax: (865) 475-6098; e-mail: linh@ornl.gov

Nate Phillips and Jeff Jenson
Caterpillar, Inc.
Peoria, IL 61656-1875
(309) 578-2969; fax: (309) 578-2953; e-mail: Jensen_Jeff_A@cat.com

DOE Technology Manager: Jerry L. Gibbs
(202) 586-1182; fax: (202) 586-1600; e-mail: jerry.gibbs@ee.doe.gov
ORNL Technical Advisor: D. Ray Johnson
(865) 576-6832; fax: (865) 574-6098; e-mail: johnsondr@ornl.gov

---

Contractor: Oak Ridge National Laboratory, Oak Ridge, Tennessee
Contract No.: DE-AC05-00OR22725
Subcontractor: Caterpillar, Inc., Peoria, Illinois

Objective

- Generate a database and characterize damage mechanisms of candidate advanced ceramics and intermetallic alloys.
- Apply and verify probabilistic life prediction and component design and verification methods for advanced diesel engine components.

Approach

- Evaluate the long-term mechanical performance and reliability of candidate advanced light-weight high-temperature metallic alloys and ceramics at elevated temperatures in air before and after long-term exposure to simulated engine environments, as well as engine field tests.
- Characterize the evolution and role of damage mechanisms, and changes in microstructure and chemistry, linked to the long-term mechanical performance and reliability of ceramics and intermetallic alloys.
- Predict the failure probability and reliability of complex-shaped diesel engine components subjected to application conditions via the use of life prediction codes.

Accomplishments

- Completed thermal cycle fatigue tests on the as-casted ferrictic ductile iron steel substrates with and without alumina-based thermal barrier coating deposited via polymer precursor processing approach.
- Completed post characterization of coated ferrictic ductile iron steel substrates after 500 thermal cycles to provide insight into the microstructure stability and durability of coating under the simulated engine operation condition.
- Completed generation of long-term tensile creep database for Howmet TiAl alloys under the test matrix defined by the heavy-duty (HD) diesel company. The database has been successfully employed by end users to confirm

the probabilistic life prediction of TiAl components under the engine operation condition and thus resulting in the commercialization of the components in HD diesel engines.

Future Direction

- Characterize the thermal stability and durability of both candidate and developmental thermal barrier coating materials aiming to significantly improve the thermal management via the reduction of heat rejection of high efficiency and clean HD diesel engine.
- Develop mechanical and physical database for candidate heat recovery materials to meet the challenge of increased high pressure and temperature combustion condition in high efficiency and clean HD diesel engine.

Introduction

There has been considerable interest in the potential for extensive use of advanced ceramics and intermetallic alloys in advanced diesel engine systems because of their superior thermomechanical properties at elevated temperatures. The implementation of components fabricated from these advanced materials would lead to significant improvement in engine efficiency and long-term durability and reduced nitrogen oxides (NO_x) and CO exhaust emissions as required in the 21st Century Truck Program. Interest has focused primarily on research into characterization and design methodology development (life prediction) for advanced silicon nitride ceramics and TiAl alloys to enable the manufacture of consistent, reliable complex-shaped components for diesel engine. The valid prediction of mechanical reliability and service life is a prerequisite for successful use of these materials in internal combustion engine components.

This research project has three primary goals: the generation of a mechanical engineering database, from ambient to high temperatures, of candidate advanced materials before and after exposure to simulated engine environments; the microstructural characterization of failure phenomena in these advanced materials and in components fabricated from them; and the application and verification of probabilistic life prediction methods using diesel engine components as test cases. For all three stages, results will be provided to both material suppliers and component end-users for use in refining and optimizing processing parameters to achieve consistent mechanical reliability, and in validating the probabilistic design and life prediction of engine components made from these advanced materials.

Approach

Three types of thermal barrier coatings (TBCs), which provide the thermal and oxidation/corrosion protection, have been proposed by the end user for durability and reliability evaluation. Two types of coatings will be applied onto the as-cast Fe steel substrates (6.4 mm thick) via air plasma spray (APS) process and the third one will be applied using the ceramic conversion process deposited via the slurry approach. The thermal cycle test would be carried out between 760°C (1400°F) and 20°C (68°F) in air to simulate the temperature cycling condition encountered during the heavy-duty (HD) diesel engine operation. Two sizes of substrates (e.g., 25 mm x 25 mm and 50 mm x 50 mm), machined from the as-casted exhaust component, would be evaluated to understand the effect of surface area on the thermal cycle response due to the difference in the extent of heat dissipation and thus stress generation during testing. A NDE characterization of these as-coated steel coupons would be completed by ANL prior to the thermal cycle test to identify the pre-existing flaws and/or delamination after the oxide coating conversion process. The post NDE analysis would then also be carried out to further characterize the newly formed cracks and/or delamination after the thermal cycle test. In addition, both of the detailed optical and electron microscopy analysis were carried out to confirm the results of NDE analysis and failure mechanisms of the coating.

Studies of long-term creep behavior in air of TiAl alloy (designated as 45XD) manufactured by Howmet were completed in FY2009. The creep specimens are cylindrical buttonhead type. The test conditions specified (temperatures: 600-750°C, stress levels: 120-390 MPa) are importantly relevant to the temperature and first principle tensile stress

profiles encountered by TiAl turbo wheel under the application conditions based on the FEA modeling. The database generated will then be used by the end users to verify probabilistic component design and life prediction of turbo wheel under engine operation conditions, and could also provide important feedbacks to material suppliers for process modification to further improve its high-temperature mechanical performances.

Results

Materials technologies for high-efficiency HD diesel engines

The objective of this study is to provide important material support to address multiple key barriers to enable the design of high-efficiency and clean HD diesel engines. There key technological barriers identified are 1) parasitic, friction, and heat transfer losses accounts for > 30% of the available energy in internal combustion engines, 2) High Efficiency Clean Combustion (HECC) peak pressures challenge structural limits of current materials and designs, and 3) improvements in thermal management will require the incorporation and evaluation of new materials concepts. This may also lead to additional opportunities in managing exhaust energy. The materials technologies taken to address each barrier will be described as follows.

Reduction in heat rejection could be achieved by the application of durable, cost-effective thermal barrier coatings (TBCs) for piston and exhaust port, and exhaust manifold, and also development of advanced TBCs resistant to thermal cycling. The increase in waste heat recovery could be accomplished via 1) the enhancement of gear strength and wear resistance for turbocompounding, 2) development of light weight, high strength, and efficient heat exchanger materials, and 3) application of thermoelectric generation systems. Also, optimization of internal combustion engine can be achieved by 1) the application of lighter, corrosion resistant high-temperature valves, 2) enhanced fuel injector designs and materials, 3) high-strength cylinder heads and engine blocks, and 4) reduced heat rejection in cylinder head. In addition, the high-efficient aftertreatment (and thus NOx reduction) could be accomplished by the significant improvement in ceramic DPF properties and design and also the catalyst systems. The reduction in friction can be achieved by the development of low friction, durable liner/ring ceramic coatings and surfacing technology. Lastly, high engine efficiency and clean emission engine can be achieved by the employment of high efficiency cooling systems via the development of advanced corrosion resistant resistance aluminum alloys and coatings and cost-effective stainless steels.

Thermal cycle test of oxide thermal barrier coating

Instrumentations of thermal cycling and thermal shock test facilities were successfully designed and fabricated for planed thermal durability test. The objective this thermal testing is to provide a baseline data and also insight into durability and integrity of thermal barrier coating (TBC) designed and employed on ductile ferritic Fe steel alloys with high Si content similar to the Grades defined in SAE J2582. The ferritic Fe steel alloy is the current production material used for the exhaust components in the HD diesel engines. The application of TBCs would allow end users to significantly reduce the heat rejection and also prevent the oxidation/corrosion degradation process encountered in the current production materials. Ultimately it thus could avoid the application of the very high-cost stainless steel materials for the exhaust port and manifold components. This is one of the key enabling materials technologies that would allow end users to achieve 55% engine efficiency by 2012 as set under the 21st Century Truck Program.

Figure 1 shows the photos of the as-received coated coupons with two sizes of 25mm x 25mm x 6.4mm and 50mm x 50mm x 6.4mm. The 500 thermal cycle test was carried out between 300° and 760°C in ambient air that provided a simulated thermal cycle condition similar to that encountered during the diesel engine operation. The use of 300°C instead of 20°C was due to the need to significantly shorten the time of heating and cooling period. The typical surface features of these coated coupons after 500 thermal cycles were shown in Fig. 2. Note that there were some regions especially near the edges exhibiting some kind of spallation and crack formation along with oxidation feature (and color). Electronic microscopy study of surface of the as-received coupons showed a relative dense but uneven surface feature of the as-coated surfaces (as shown in Fig. 3). At higher magnification an

individual and detailed microstructure (and grains) could be further observed and distinguished.

After 500 thermal cycle between 300° and 760°C in air in some regions the coating, which was still intact, became relative porous (Fig. 4). The porous feature, unlikely due to the sintering process because of relative low temperature, might result from the oxidation and recession of some unstable phase(s) present after the coating conversion process. In addition, features of spallation and cracking were observed on surface of all of the coupons (Fig. 5). The observed features of coating spallation and crack formation were confirmed by the NDE analysis carried out at ANL. Upon the completion of the NDE characterization selected coupons were metallographically polished for subsequent SEM examinations to provide important insight into the mechanisms that lead to the porous feature as well as coating delamination and spallation. Figure 6 shows the polished cross section of coated ferritic Fe coupon after the 500 thermal cycles. Observations again confirmed the porous feature of coating that still remained intact to the substrate and also the delamination of the coating after the thermal cycle testing. The porous coating was identified to contain Al-Si-O with minor elements of Fe, Mg, and P. The dense layers underneath the porous oxide coating are the reaction products formed during the coating conversion process as well as the thermal cycle test. These reaction layers contain chemical elements of Al-Fe-Si-O. Note that a dense oxide layer (~ 200 μm) with Fe-Si-O composition formed on the as-casted side of coupons without the oxide coating (as seen in Fig. 7). It is interesting to see that the dense oxide layer remained intact after 500 thermal cycles and no crack formation was observed as well. In addition, the typical spheroidal graphite nodules were observed in the ferrite matrix region.

An effort to develop oxide-based coating for the HD hot-section components will be initiated in FY2010. The effort would aim to provide adequate long-term thermal and oxidation protection for those hot-section components based on the temperature and environment parameters encountered during the engine operation. Following the screening step the exhaust components coated with the down-selected TBC will be tested in C15 ACERT engine located at NTRC under the specified engine test condition. Variables such as component chamber temperature, exhaust flow rate, transients, and exhaust chemistry as well as the increased efficiency gained would be closely monitored during the engine field test.

High-temperature creep response of TiAl alloys

Studies of long-term creep behavior in air of TiAl alloys manufactured by Howmet were successfully completed in FY2009. The purpose of this long-term tensile creep study was to generate the database and to provide insight into the creep response and mechanisms as a function of temperature and stress level for probabilistic component design and life verification. Note that the test matrix of temperature and applied stress states employed in the present study was based on the conditions that the TiAl components will encounter under the engine operation conditions as predicted by the FEA model. Note that all of the tensile creep tests were discontinued when the specimen fractured or the test time reached more than 6000-h of test time without failure. Efforts of this year were placed on the generation of long-term creep database, especially under the lower stress levels at lower temperatures, of Howmet TiAl alloy. These Howmet TiAl specimens were all tested for more than 6000-h and did not exhibit any sign of tertiary creep stage or fracture. Thus, these creep testes were terminated for subsequent data and microstructure analysis. In general, these creep data indicated that the Howmet TiAl exhibited creep rates that were about 20-30 times faster than Daido HIP TiAl under similar test conditions, especially under high stress level regime and at lower test temperature; i.e. 650°C (Fig. 8). The difference in creep response between Diado and Howmet TiAl alloy was probably due to the difference in microstructure (i.e., domain size and lamellar thickness) and compositions. Also, at 650°C the Howmet TiAl exhibited a higher creep exponent valve (n~ 11-13) than that obtained for the Daido TiAl (n ~ 2-4) under the similarly applied stress range (240-390 MPa). However, the trend and values of creep exponents obtained at temperatures ≥ 700°C for both TiAl alloys were quite similar, and both exhibited a transition to a higher n valve at stress level of > 200 MPa. The higher creep exponent values were in general attributed to the occurrence of creep cavitation and micro crack formation.

References

1. H. T Lin et al, "Life Prediction of Diesel Engine Components," 2008 Annual Report for Heavy Vehicle Propulsion Materials.

2. S. M. Wiederhorn, B. J. Hockey, and T. J. Chuang, "Creep and Creep Rupture of Structural Ceramics," pp. 555-575 in Toughening Mechanisms in Quasi-Brittle Materials, Kluwer Academic Publishers, Norwell, MA 1991.

Presentations and Publications

Presentation

1. H.-T. Lin, "Implementation Methodology of Silicon Nitride Ceramics for Heavy-Duty Diesel Engine Applications," **Invited paper**, presented at the 6th International Conference on Nitrides and Related Materials, Karlsruhe (ISNT 2009), March 15-18, 2009, Karlsruhe, Germany.

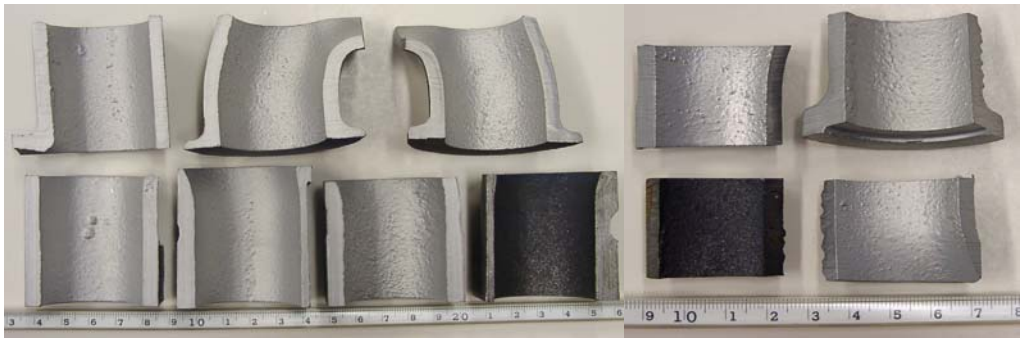

Figure 1. *Photos show as-received oxide-based coating on ferritic Fe-steel substrates with two different sizes (25mm x 25mm x 6.4mm and 50mm x 50mm x 6.4mm).*

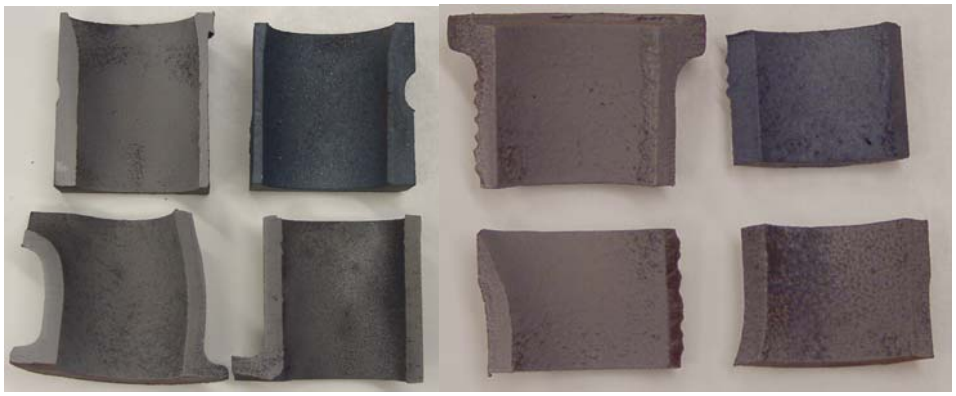

Figure 2. *Photo shows oxide-based coating on ferritic Fe-steel substrates after 500 thermal cycles between 300 and 760°C in air..*

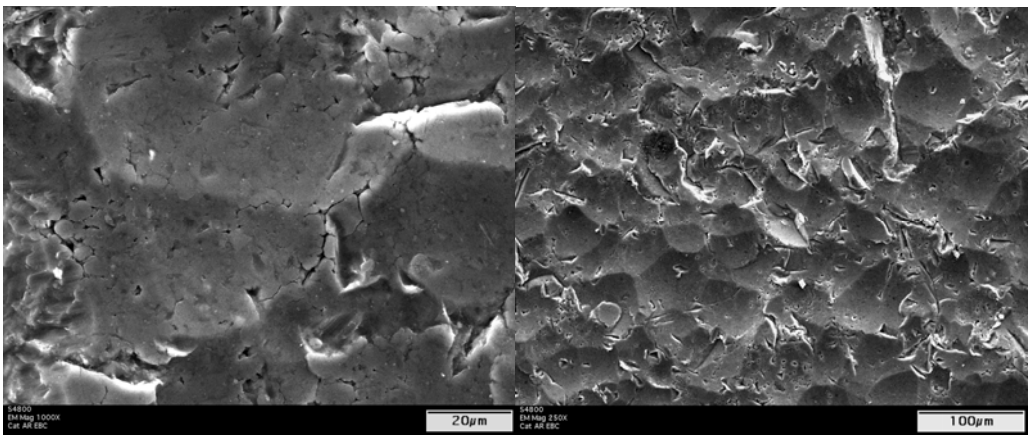

Figure 3. *SEM of surface of as-received oxide-base coating on Fe-steel substrates*

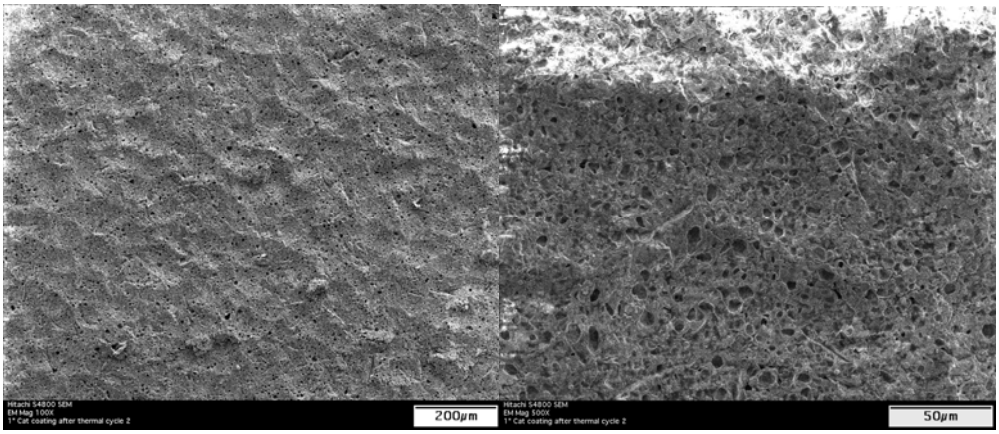

Figure 4. *SEM of surface of oxide-base coating on Fe-steel substrates after 500 thermal cycles between 300 and 760°C in air. Observations very porous microstructure after thermal cycle testing.*

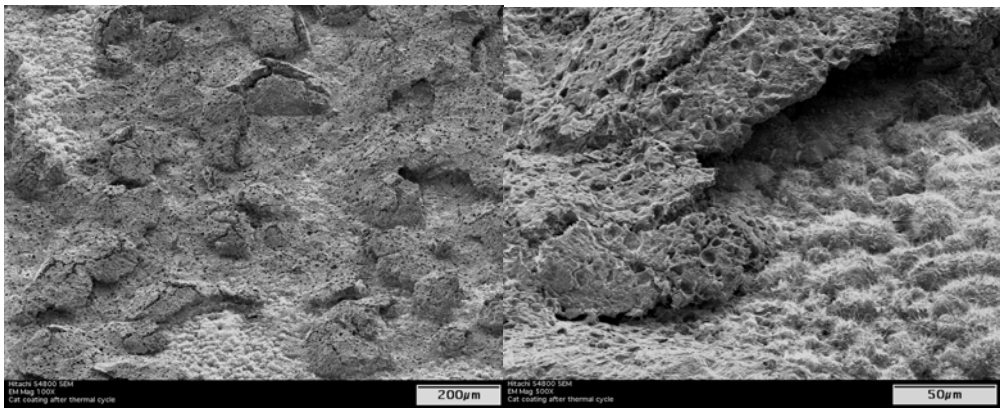

Figure 5. *SEM of surface of oxide-base coating on Fe-steel substrates after 500 thermal cycles between 300 and 760°C in air. Observations show spallation and crack formation after thermal cycle testing.*

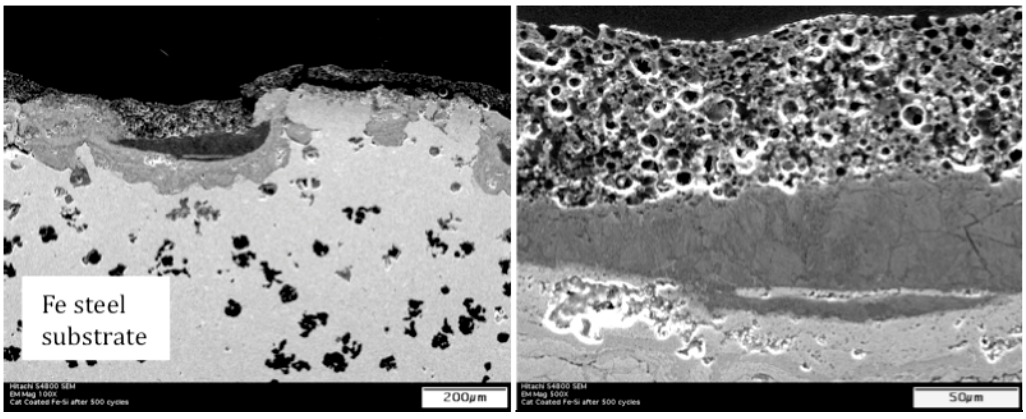

Figure 6. *SEM of polished cross section of oxide-base coating on Fe-steel substrates after 500 thermal cycles between 300 and 760°C in air.*

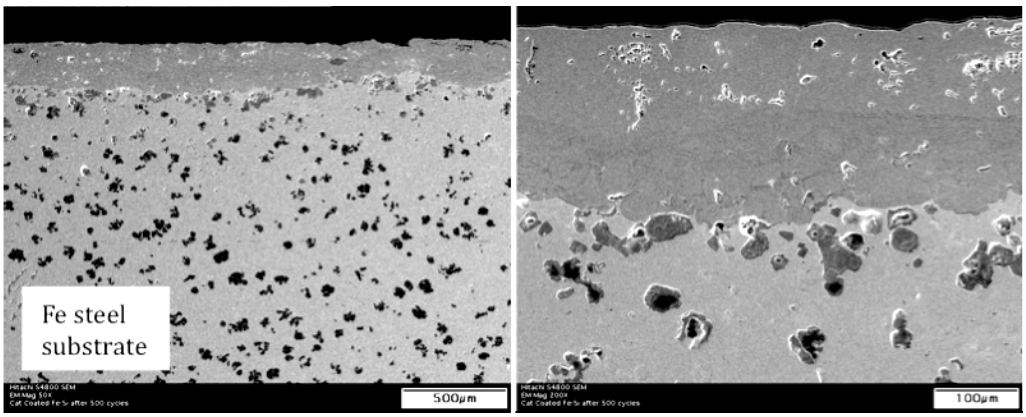

Figure 7. *SEM of polished cross section of as-casted side of Fe-steel substrates after 500 thermal cycles between 300 and 760°C in air.*

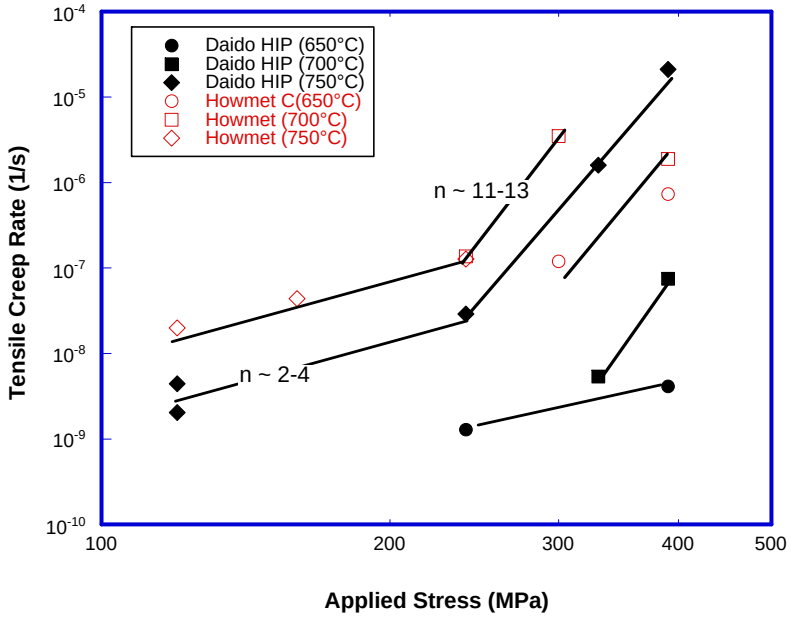

Figure 8. *Tensile creep rates versus applied stress curves of Howmet TiAl alloy. The data of Daido TiAl alloys tested under the same condition were used for reference.*

Agreement 14957 - Modeling of Thermoelectrics

A. A. Wereszczak and H. Wang†*
* *Ceramic Science and Technology Group*
† *Diffraction and Thermophysical Properties Group*
Oak Ridge National Laboratory
P.O. Box 2008, MS 6068, Bldg. 4515
Oak Ridge, TN 37831-6068
(865) 576-1169; fax: (865) 574-6098; e-mail: wereszczakaa@ornl.gov

R. McCarty and J. Sharp
Marlow Industries, Inc.
10451 Vista Park Road
Dallas, TX 75238-1645
(214) 342-4287; fax: (214) 341-5212; e-mail: rmccarty@marlow.com

DOE Technology Manager: Jerry L. Gibbs
(202) 586-1182; fax: (202) 586-1600; e-mail: jerry.gibbs@ee.doe.gov
ORNL Technical Advisor: D. Ray Johnson
(865) 576-6832; fax: (865) 574-6098; e-mail: johnsondr@ornl.gov

Contractor: Oak Ridge National Laboratory, Oak Ridge, Tennessee
Prime Contract No.: DE-AC05-00OR22725

Objectives

- Non-CRADA sub-project: Measure thermomechanical and thermophysical properties of candidate thermoelectric (TE) materials (TEMats) under consideration for waste heat recovery and cooling in vehicular applications. Develop and refine test methods where needed to advance TEMats and devices (TEDs).
- CRADA sub-project: Support Marlow with their development of high temperature TEMats and TEDs for use in vehicular waste heat recovery applications.

Approach

- Non-CRADA sub-project: Measure elastic modulus, Poisson's ratio, strength, coefficient of thermal expansion, heat capacity, thermal conductivity, electrical resistivity, and Seebeck coefficient as a function of temperature of candidate high temperature TEMats. Execute finite element and design sensitivity analyses to model thermomechanical stresses in TEMats and TEDs.
- CRADA sub-project: Measure properties of proprietary Marlow materials and provide development support.

Accomplishments

- Non-CRADA sub-project: Measured thermomechanical and thermophysical properties of bismuth telluride and skutterudite TEMats and developed new fixturing to enable high temperature testing of the latter.
- CRADA sub-project: Initiated project (May09), performed initial testing of Marlow materials, and examined alternative methods for TED non-destructive analysis.

Future Direction

- Non-CRADA sub-project: Measure properties of additional high-temperature capable TEMats, and refine and perform thermal-gradient strength tests directly on thermoelectric legs.
- CRADA sub-project: Perform thermomechanical and thermophysical properties of proprietary Marlow TEMats and assist in development of Marlow TEDs.

Introduction

Potential next generation thermoelectric devices (TEDs) comprised of p- and n-type materials enjoy strong interest for implementation in high temperature and oxidizing environments because their waste heat could be used to generate electricity. However, the intended thermoelectric function of these devices will only be enabled if the TED is designed to overcome the thermomechanical limitations (i.e., brittleness) that are usually inherent to these materials. A thermoelectric material (TEMat) with a combination of poor strength and low thermal conductivity can readily fail in the presence of a thermal gradient thereby preventing the exploitation of the desired thermoelectrical function.

This seemingly insurmountable problem can be overcome with the combined use of established probabilistic design methods developed for brittle structural components, good thermoelastic and thermomechanical databases of the candidate TEMat comprising the TED, and iteratively applied design sensitivity analysis. This project executes this process to involve TEDs.

This project has two parts. The first sub-project focuses on the thermomechanical and thermophysical evaluation of candidate TEMats that are of interest to the entire TE community for high temperature waste heat recovery. The development of appropriate strength test fixturing and methods are required as there are no widely accepted strength test practices (e.g., ASTM) for thermoelectric materials. The second sub-project involves a CRADA with Marlow Industries and the thermomechanical and thermophysical characterization of their proprietary TEMats.

There will be several outcomes from this work. It will benefit TEMat and TED developers and end-users of these potentially high temperature TEDs, mechanical reliability of prototypical TEDs will be evaluated from a structural brittle-material perspective and suggested redesigns will be identified, thermomechanical reliability of developmental TEMats will be assessed, and minimum required thermomechanical properties of hypothetical TEMats would be identified that produce desired reliability in a TED.

Results

Non-CRADA sub-project

This effort focuses on the thermomechanical and thermophysical evaluation of candidate TEMats that are of interest to the entire TE community for high temperature waste heat recovery. As a reference, mature and lower-temperature-capable TEMats were characterized to facilitate comparison. Additionally, the development of appropriate strength test fixturing and methods are required as there are no widely accepted strength test practices (e.g., ASTM) for thermoelectric materials.

Bismuth Telluride

The uncensored Weibull flexure strength distributions of n- and p-type bismuth telluride as a function of several variables (orientation, temperature, and how machined) were determined. The intent of this was to establish a reference database to be used for later comparisons of measured responses of high-temperature TEMats. Proprietary bismuth telluride were both purchased and cut into shape by Marlow Industries, Inc., Dallas, TX. A large number of specimens enabled the generation of statistically significant data. Uniaxial and biaxial flexure strength test methods enabled the censorship of the data according to edge-type and surface-type, and perhaps even volume-type flaws.

There is transverse isotropy in bismuth telluride owing to the method it is fabricated. Therefore, uniaxial flexure (3-pt-bend) strength coupons were harvested in a manner to enable the study of strength-dependence on orientation. This was examined for both n- and p-type bismuth telluride alloys. For both the n- and p-type, the RZ orientation strength was approximately twice that of the RR orientation as shown in Fig. 1. For the stronger RZ orientation, the strengths of the n- and p-type were equivalent though the former showed more scatter in its strength distribution. For the RR orientation, the n-type was slightly stronger than the p-type.

The effect of temperature was explored by testing uniaxial flexure specimens at room temperature and 225°C. Those results are illustrated in Fig. 2. Compared to room temperature, the strength decreased by approximately 15% at 225°C. This strength decrease occurred for both the n- and p-types and within both orientations for each.

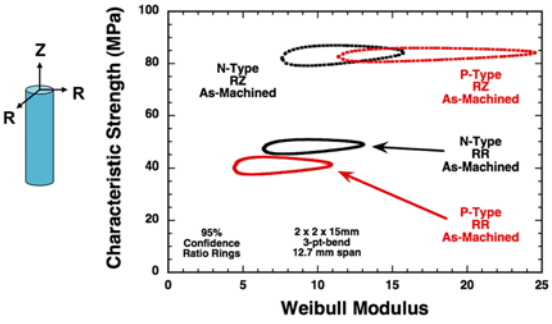

Figure 1. Weibull uniaxial flexure strength distributions for n- and p-type bismuth telluride as a function of orientation at 25°C.

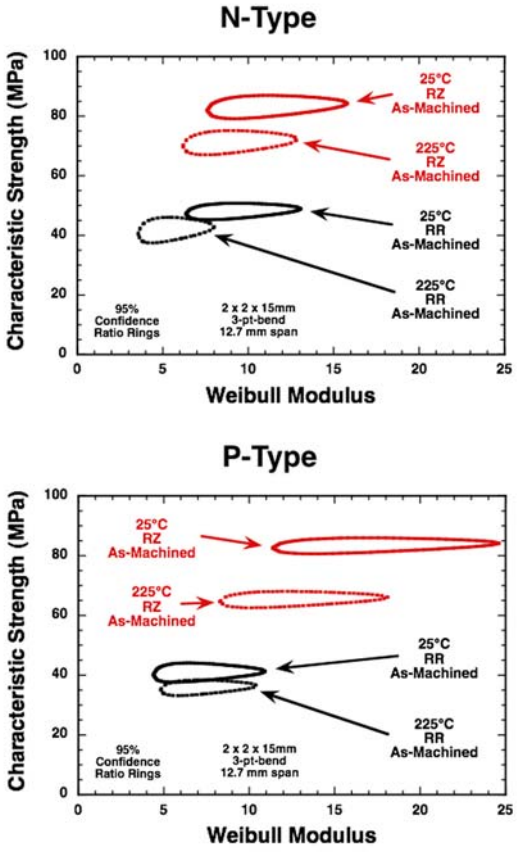

Figure 2. Weibull uniaxial flexure strength distributions for n- and p-type bismuth telluride as a function of orientation and temperature.

The effect of surface preparation method on strength was examined. One pair of parallel surfaces was ground while the other pair was produced through a slicing process. The comparison of their strengths is shown in Fig. 3. There was a not significant difference in their strengths though the strength distributions for the ground surfaces tended to exhibit more scatter. This trend was independent of the type and orientation.

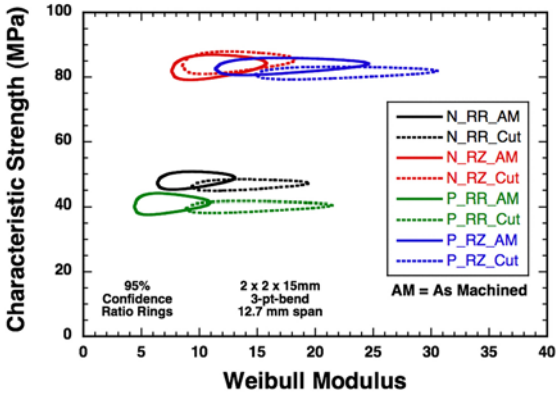

Figure 3. Weibull uniaxial flexure strength distributions for n- and p-type bismuth telluride as a function of orientation and method of surface preparation at 25°C.

Polishing some specimens and then measuring their strength explored the "potential" strength of the bismuth tellurides. These results are shown in Fig. 4. Specimens of this geometry were only available for the p-type, so the n-type was not tested in this fashion. As expected, the biaxial flexure strength was higher for polished specimens, and these values (in reference to the effective area) provide a high end bound of the strength potential of this material.

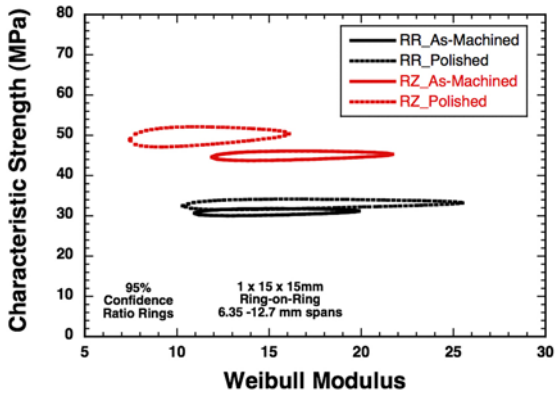

Figure 4. Weibull biaxial flexure strength distributions for p-type bismuth telluride as a function of orientation and method of surface preparation at 25°C.

Electrical resistivity and Seebeck coefficient of n-type and p-type materials were tested from room temperature to 250ºC to understand the effect of orientation on heat and electric current flows. Three RZ, 2 mm x 2 mm x 15 mm, bars and three RR bars

with similar dimensions were prepared. Measurements were conducted at 25ºC steps. At each temperature, three differential temperatures were used to calculate Seebeck coefficient. As shown in Figs. 5 and 6, the electrical resistivity and Seebeck coefficient showed different behavior as a function of temperature. The results are similar to the materials tested earlier in this project using an ULVAC-Riku ZEM-2 system in which K-type thermocouples were used. The newly upgraded ZEM-3 system uses R-type thermocouples.

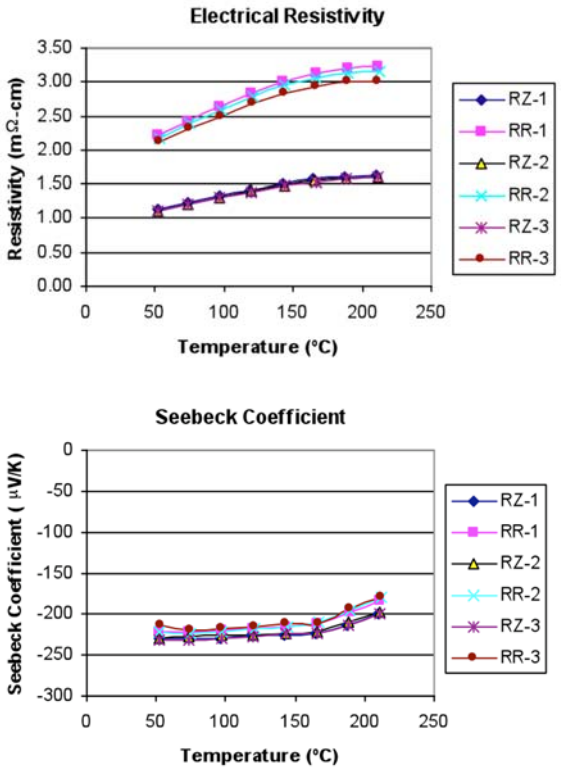

Figure 5. Electrical resistivity (top) and Seebeck Coefficient (bottom) of n-type bismuth telluride in RR and RZ directions.

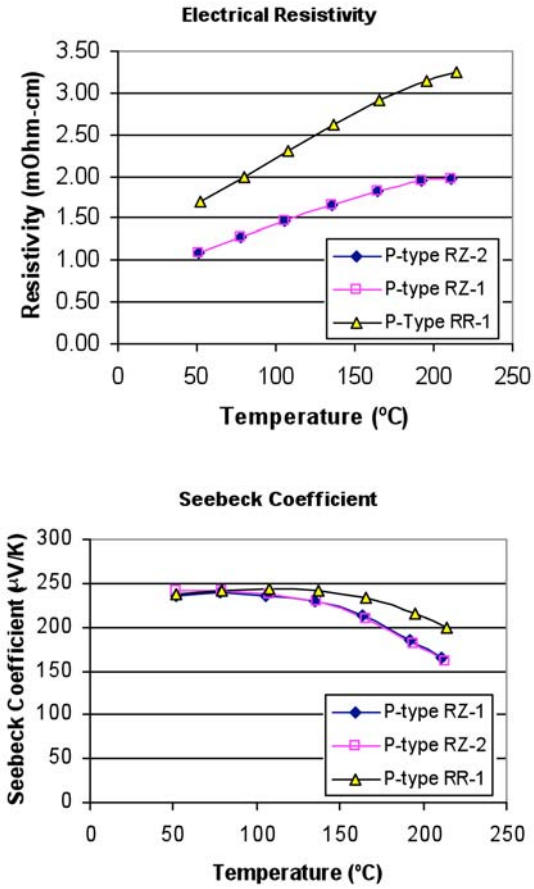

Figure 6. Electrical resistivity (top) and Seebeck coefficient (bottom) of p-type bismuth telluride in RR and RZ directions

Skutterudites

Bismuth telluride modules are used for waste heat recovery at lower temperatures from room temperature to 250ºC. Skutterudites are candidate materials for high temperature power generation modules. Their transport properties are desirable for waste heat recovery between 250-500ºC. These two materials can be used together to maximize power output.

A high temperature fixture was developed to enable flexure strength testing up to at least 500°C. It is shown in Fig. 7. The fixture is self-contained, has built-in provisions for semi-articulated loading (i.e., self-alignment), and made of alumina ceramic. It has an oxygen gettering material reservoir that lessens the oxidation rate of the prismatic bend bars. Lastly, its simple design allows for rapid insertion

and extraction of the test specimen, so an attractive testing rate can be achieved.

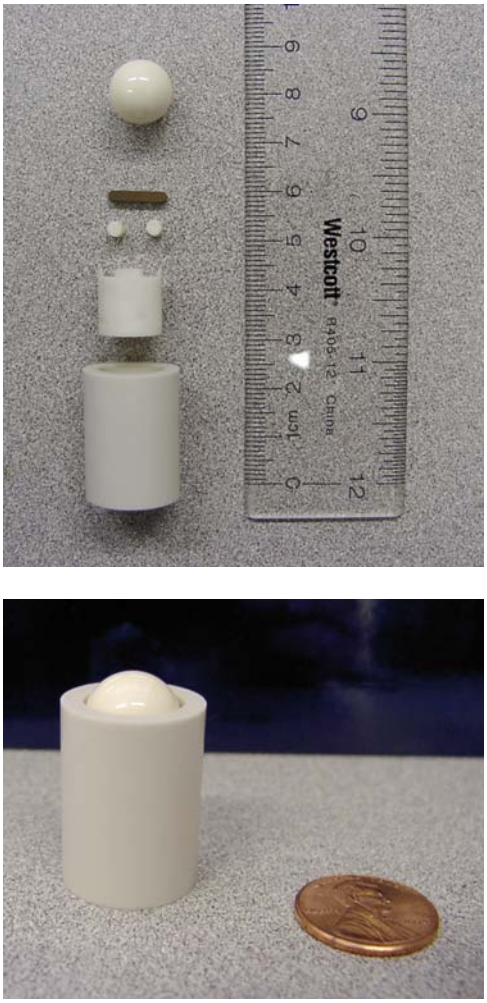

Figure 7. High temperature three-point bend fixture designed for testing small prismatic bars of thermoelectric specimens.

The room temperature and 200°C strength distributions of n- and p-type skutterudites, provided by General Motors (GM), were measured. The resulting strength distributions are shown in Fig. 8. Characteristic strength was equivalent for the n- and p-type skutterudites and independent of temperature between 25 and 200°C.

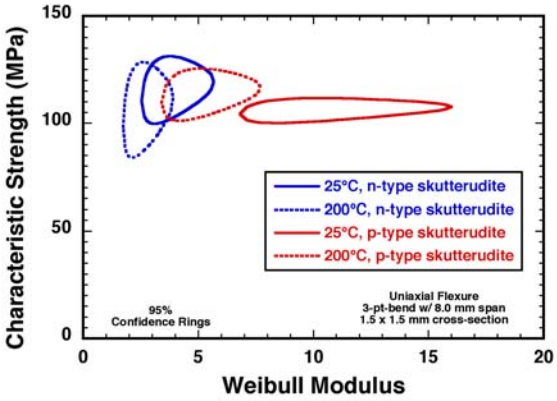

Figure 8. Strength distributions as a function of temperature for an n- and p-type skutterudite.

N- and p-type skutterudite specimens were scaled up at General Motors to produce ingots for prototype modules using the spark plasma sintering (SPS) technique. One of the most important issues requiring resolution with SPS is the improved homogeneity of the ingots. Three ingots produced by SPS are show in Figure 9. The ingots were 12.7 mm in diameter and 13-15 mm tall. Four to five disks, each about 1.5 mm thick, were sliced from the ingots. As demonstrated in the mechanical properties, the skutterudites were easy to machine and none of the disks were damaged in the sample preparation process.

Figure 9. N-type and p-type Skutterudite ingots produced by the SPS method.

Electrical resistivity (4-point in-line probe) and thermal diffusivity (xenon flash method) were measured. As shown in Figure 10, electrical resistivity values of the two p-type ingots showed about 10% difference. Within the same ingots the top and bottom slices sometimes showed variation from the middle slices. The n-type ingot showed much lower resistivity and relatively uniform values among the 5 slices. The end-slice variability might be a consequence of the graphite die used in the SPS or loss of Sb from the near-surface volume.

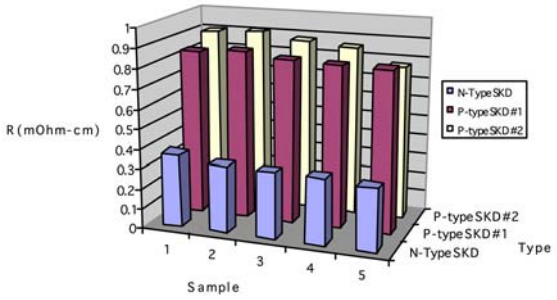

Figure 10. Electrical resistivity of 5 slices cut from n-type and p-type skutterudites.

Thermal diffusivity was measured using a laser flash system from room temperature to 500ºC. The thermal diffusivity values of 5 p-type skutterudite samples as a function of temperature are shown in Fig. 11. The largest error among 5 slices was 4.2% at room temperature. At higher temperature, the errors ranged from 2.3% to 3.8%. This indicates uniformity exists with thermal transport properties among the 5 slices.

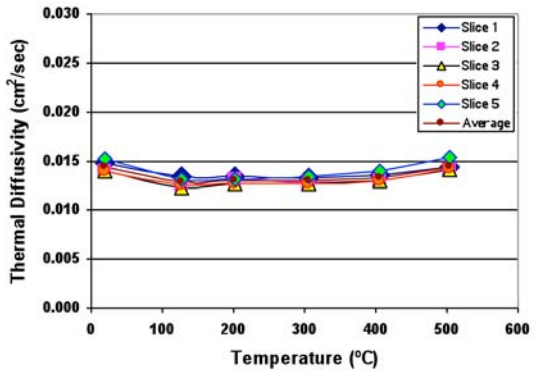

Figure 11. Thermal diffusivity of 5 p-type skutterudites from room temperature to 500ºC.

CRADA sub-project

A CRADA with Marlow Industries was initiated in May 2009 with the primary intent to thermomechanically and thermophysically characterize their proprietary TEMats. Initial testing of their materials commenced and alternative non-destructive test methods to evaluate Marlow TEDs were examined. Transport properties of Marlow production and research thermoelectric materials were evaluated.

Conclusions

Bismuth telluride (low-temperature capable) TEMats were thermomechanically and thermophysically characterized. The intent of this testing was to establish a database of a properties of a mature TEMat that will provide comparisons against measured responses of high-temperature TEMats.

High temperature bend fixturing was developed for testing of high-temperature capable TEMats.

Preliminary strength testing of a high-temperature-capable TEMat (skutterudite) was initiated.

Transport properties of skutterudites were also evaluated. The materials used for module production showed fairly good homogeneity. Electrical conductivity of skutterudites showed some variation among end pieces while thermal transport properties showed very uniform values among 5 slices obtained from an ingot.

Publications

- J. R. Salvador, J. Yang, X. Shi, H. Wang, and A. A. Wereszczak, "Transport and Mechanical Property Evaluation of $(AgSbTe_2)_{1-x}(GeTe)_x$ (x=0.80, 0.82, 0.85, 0.87 and 0.90)," *Journal of Solid State Chemistry*, 182:2088-2095 (2009).
- J. R. Salvador, J. Yang, X. Shi, H. Wang, A. A. Wereszczak, H. Kong, and C. Uher, "Transport and Mechanical Properties of Yb-Filled Skutterudites," *Philosophical Magazine*, No. 19, 89:1517-1534 (2009).
- A. A. Wereszczak, T. P. Kirkland, O. M. Jadaan, and H. Wang, "Strength of Bismuth Telluride," in press, *Ceramic Engineering and Science Proceedings*, (2009).
- O. M. Jadaan and A. A. Wereszczak, "Probabilistic Design Optimization and Reliability Assessment of High Temperature Thermoelectric Devices," *Ceramic Engineering and Science Proceedings*, 29, [3], 157-172 (2008).
- ORNL/TM-2009/133 Report: "Probabilistic Mechanical Reliability Prediction of Thermoelectric Legs," O. M. Jadaan and A. A. Wereszczak, May, 2009.

Agreement 15529 - Erosion of Materials in Nanofluids

(This project is jointly funded by Propulsion Materials and Heavy Vehicle Systems Optimization)

Principal Investigators: J. L. Routbort and D. Singh
Argonne National Laboratory
9700 S. Cass Avenue, Argonne, IL 60439-4838
(630) 252-5065; fax: (630) 252-5568; e-mail: routbort@anl.gov

DOE Technology Manager: Jerry L. Gibbs
(202) 586-1182; fax: (202) 586-1600; e-mail: jerry.gibbs@ee.doe.gov

Contractor: UChicago Argonne LLC
Contract No.: DE AC03 06CH11357

Objective

- Determine if the use of fluids containing a variety of nanoparticles result in erosive damage to radiator materials and coolant pumps.
- If damage occurs, then develop models to predict the erosive damage.

Approach

- Develop an experimental apparatus to measure erosive loss.
- Conduct experiments to study erosive damage of fluids containing various types and sizes of nanoparticles on typical radiator materials.
- Develop methods to characterize nanofluids and analyze erosion results.

Accomplishments

- Little erosion damage to a typical radiator material, aluminum Al3003, was observed in experiments performed using CuO nanoparticles in ethylene glycol having impact angles of 30 and 90° and velocities up to 10m/s for impact for a total time of 3620 hrs. Particle concentration varied between 0.1 and 0.85 vol %.
- Utilized small-angle x-ray scattering, dynamic light scattering, and surface area measurements to measure nanoparticle size, distribution, and shape.
- Determined that polymeric gears are degraded by a SiC/water nanofluid
- Determined that a 130 nm, 2 vol. % SiC/water nanofluid does not degrade aluminum Al3003 in over 700 hours of accelerated testing at 8 m/s for 30° and 90° impacts
- Designed, built, and calibrated a new erosion apparatus to measure wear in an automotive water pump and the torque required to pump nanofluids

Future Direction

- Erosion of typical radiator materials using fluids containing a variety of well-characterized nanoparticles will be measured, varying the angle, size of the nanoparticles, impact velocity, nanoparticle volume percent, and temperature.
- If erosion occurs, a predictive model will be developed.
- Determine wear of nanofluids on automotive pump cast aluminum impeller.
- Measure the pump power of nanofluids and compare to base fluids

Forward

Efforts have shifted away from the in-house production of nanofluids, to development of advanced characterization techniques and establishment of working relationships between companies that produce nanofluids. Our principal partner on a related project for the Industrial Technology Program is Saint Gobain. They have been supplying SiC/water nanofluids for industrial cooling. ANL has been characterizing the nanoparticles, adding ethylene glycol to produce a nanofluid suitable for radiator cooling, and reducing the viscosity by changing the pH. Fluids that show promise from a heat transfer perspective will then be characterized by measuring the viscosity, thermal conductivity, and heat transfer coefficients while particle sizes will be measured by small-angle X-ray scattering (SAXS) and Dynamic Laser Scattering (DLS). Finally, liquid erosion tests will be performed to determine the pumping power and if the nanofluid will cause deleterious damage to radiator materials.

Introduction

Many industrial technologies face the challenge of thermal management. With ever-increasing thermal loads due to trends toward greater power output for engines and exhaust gas recirculation for diesel engines, cooling is a crucial issue in transportation. The conventional approach for increasing cooling rates is use of extended surfaces such as fins and microchannels. Reducing radiator size will reduce the frontal area and hence the aerodynamic drag. However, current radiator designs have already stretched these approaches to their limits. Therefore, an urgent need exists for new and innovative concepts to achieve ultra-high-performance cooling. Nanofluids seem to show enormous potentials as a coolant for radiators. Literature has many examples of increased thermal conductivity of fluids by the addition of nanoparticles (see review by Yu, et al. [1]. Enhanced thermal conductivity could lead to enhanced heat transfer. A CFD calculation of a Cummins 500 hp diesel engine using an ideal nanofluid as coolant has shown that the radiator size could be reduced by 5% [2], reducing weight and size, and hence aerodynamic drag.

In order for the enhanced thermal conductivity to be utilized it must be shown that liquid erosion of typical radiator materials will be tolerable and that the increased pumping power resulting from higher viscosity will not exceed the gain in parasitic energy losses from enhanced cooling. If nanofluids result in excessive erosive wear or very high increased pumping power, they cannot be used. Hence, the Vehicle Technologies program funds an investigation on liquid erosion of radiator materials using nanofluids.

Results and Discussion of Erosion

A photograph of the recently build and calibrated liquid erosion apparatus is shown in Fig. 1.

Figure 1. Photograph of the liquid erosion apparatus.

The apparatus consists of a reservoir containing the fluid and an automotive pump with a cast aluminum impeller attached to a motor controlled electronically to ± 5 RPM. The pump can be isolated and drained and the impeller removed to measure any possible weight loss resulting from erosion. A very accurate, calibrated strain gauge is mounted on the shaft of the motor so that the torque required to pump the nanofluids can be measured and compared to the base fluid.

The flow is measured by a magnetic flow meter that has been calibrated by measuring the weight of fluid/unit time. It is accurate to ± 2% and the voltage that is linearly proportional to the flow is measured by a voltmeter. Flows of about 27 liters/minute are readily achievable. The specimen chamber remains the same as was pictured in the FY07 annual report but is also shown in Fig. 2. The fluid temperature in the reservoir and the specimen chamber are monitored by thermocouples. The velocity in the specimen chamber can easily reach 10m/s for accelerated erosion testing.

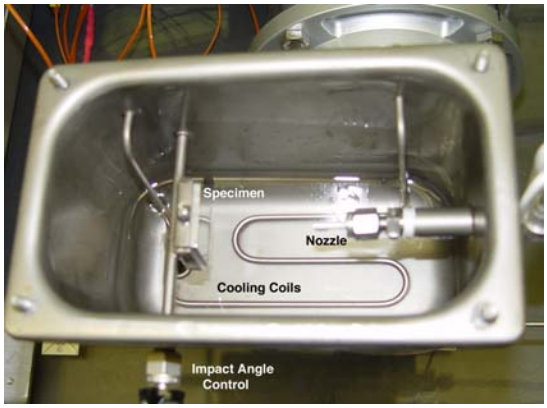

Figure 2. View of specimen chamber with cover removed.

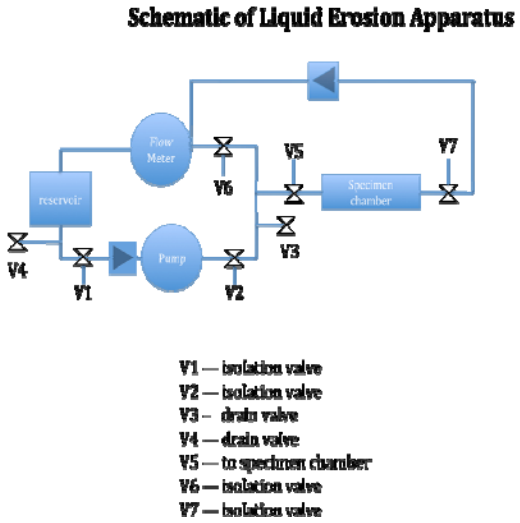

Figure 3. Schematic of new liquid erosion apparatus, torque meter and motor are included in the pump.

A schematic of the pumping system is shown in Fig. 3.

Results of the torque measurements for the base fluids and three concentrations of nominal 170nm SiC in water nanofluids are presented in Fig. 4. The 170 nm is believed to represent the agglomerated size. Surface area measurements reported in the section "Nanofluid Development for Engine Cooling Systems" of the FY09 Annual Report for Heavy Vehicle Systems Optimization) indicates that the actual individual particle size is 29 nm [3]. The nanofluids have not been modified for reduced viscosities. The results are as expected, increasing concentration of nanoparticles increases the torque required to pump them.

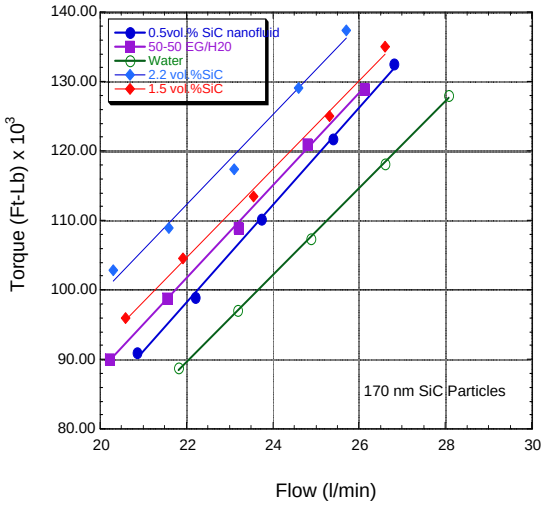

Figure 4. Measurement of the torque as a function of flow rate for water (green), 50% ethylene glycol- 50%water, (purple) and three different concentrations of SiC-water based nanofluids. Each point is the average of between 4 and 6 datum.

However, while the torque increases with increasing nanoparticle concentration it should be realized that 1. Water has a very low viscosity, 2. A mixture of ethylene glycol and water has a much higher viscosity, and 3. Changing the pH and using surfactants can modify the viscosity in alumina [4] or SiC based nanofluids [5].

Additionally, and equally as important, the size can affect both the thermal conductivity, viscosity, and heat transfer [4,5]. Larger sizes have a reduced interfacial resistance and hence have a higher thermal conductivity [5]. The above observations open the way of engineering the properties of nanofluids by selection of particle sizes and controlling the chemistry.

SiC is a very promising nanoparticle. It will not oxidize and has a relatively high thermal conductivity, over 5 times greater than CuO. Also after 750 hrs of testing the 2 vol.% SiC/water nanofluid at 8 m/s and at an impact angle of 30°, there was no erosion damage to the aluminum 3003 target. This is most encouraging from an engineering viewpoint.

The above observation was obtained at one condition and does not represent the most severe conditions. Hence, it would be premature to conclude that nanofluids will cause no damage in cooling systems.

Issues & Future Direction

The new liquid apparatus will allow several important parameters to be determined. First, we will be able to measure the increased pumping power resulting from the higher viscosity of the nanofluid. This is extremely important from an energy efficiency point of view. Furthermore, the measurements can be compared to theory and hence can be extrapolated for other nanofluid viscosities.

The new apparatus will allow continued measurements of the erosion of nanofluids on targets made from radiator materials at controlled impact angles and velocities. If erosion occurs, we will use this data, in conjunction with microscopy to model and predict erosion by nanofluids.

The targets represent conditions that are easy to model. However, we will also be able to measure the erosion of the impellers of the commercial water pump. The water pump is used for a racing vehicle and is not representative of the sealed centrifugal pump units, but it chosen because the pump can be disassembled to measure the weight of the impellers.

Experiments planned for FY10 include an investigation of the torque and erosion of SiC nanoparticles in a 50% ethylene glycol-50% water fluid. The largest sized particles and highest concentration will be used because they represent a combination of the best thermal conductivity and heat transfer properties, with the lowest viscosity increase. Furthermore, if erosion depends on the kinetic energy or critical particle size, they will cause the most damage.

Conclusions

We have built an apparatus that not only allows continuation of well-controlled tests designed to develop the data required to model erosive damage, but will closely replicate "real world" conditions in an automotive water pump and measure the torque required to pump the fluids.

References

1. W. Yu, D. M. France, J. Routbort, S.U.S. Choi, "Review and Comparison of Nanofluid thermal Conductivity and Heat Transfer Enhancements, Heat Transfer Engineering, **29**, 432-460 (2008).

2. S. K. Saripella, W. Yu, J. L. Routbort, D. M. France, and Rizwan-uddin, " Effects of Nanofluid Coolant in a Class 8 Truck Engine, SAE Technical Paper 2007-01-21413.

3. Annual Report (FY09), Heavy Vehicle System Optimization, in press

4. E. Timofeeva, J. Routbort, and D. Singh, "Particle shape effects on thermophysical properties of alumina nanofluids", JAP **106**, 014304 (2009)

5. D. Smith, E. Timofeeva, W. Yu, D. France, D. Singh, and J. Routbort, "Particle Size and Interfacial Effects on Heat Transfer Characteristics of Water-based α-SiC Nanofluids", submitted

Agreement 16308 – Science Based Approach to Thermoelectric Materials

D.J. Singh
Materials Theory Group
Oak Ridge National Laboratory
P.O. Box 2008, MS 6114, Bldg. 4500S
Oak Ridge, TN 37831-6114
(865) 241-1944; fax: (865) 574-7659; e-mail: singhdj@ornl.gov

DOE Technology Manager: Jerry L. Gibbs
(202) 586-1182; fax: (202) 586-1600; e-mail: Jerry.gibbs@ee.doe.gov
ORNL Technical Advisor: D. Ray Johnson
(865) 576-6832; fax: (865) 574-6098; e-mail: johnsondr@ornl.gov

Contractor: Oak Ridge National Laboratory, Oak Ridge, Tennessee
Prime Contract No.: DE-AC05-00OR22725

Objectives

- Find ways to optimize existing thermoelectric materials and discover new families of high performance thermoelectrics for waste heat recovery applications using modern science based materials design strategies.
- Find low cost materials with high thermoelectric figures of merit suitable for application in vehicles.

Approach

- First principles calculations based on quantum mechanics are used to calculate electronic structure and thermoelectric properties of materials.
- Boltzmann transport equations are solved to obtain electrical transport properties.
- Vibrational properties are obtained using linear response and mechanisms for thermal conductivity reduction are assessed.

Accomplishments

- Performed first principles calculations of transport and other properties of potential thermoelectric materials.
- Investigated the doping dependence of thermoelectric properties of PbSe – WSe_2 intergrowth compounds. The doping levels needed for high thermoelectric performance were identified.
- The high thermoelectric performance of La-Te was shown to be due to a combination of heavy and light bands in the electronic structure. This provides a design principle that may be used to identify other promising thermoelectrics.

Future Direction

- Identify new oxide and chalcogenide thermoelectric compositions suitable for vehicle applications.
- Calculate doping level dependence of thermoelectric properties to guide optimization.

Introduction

The use of thermoelectric devices to convert waste heat in vehicle exhaust to electricity offers potentially significant energy savings. Among the requirements for the effective use of such devices is the availability of high performance thermoelectric materials, with low cost and other properties needed for application in vehicles. The dual requirement for both high performance and low cost has constrained thermoelectric applications in the automotive industry, although thermoelectrics

have been effectively inserted in the context of seat cooling.

We are therefore developing improved materials using a science-based approach. In particular, we are using materials design strategies based on first principles calculations of electronic, vibrational and transport properties to identify potentially low cost, high performance thermoelectric materials suitable for application in vehicles. We are also calculating properties of existing materials as a function of doping and other parameters to obtain information needed for optimization of these materials. The emphasis is on the thermoelectric figure of merit, *ZT* at temperatures relevant to waste heat recovery, as well as materials properties of importance in engineering thermoelectric modules, for example anisotropy and mechanical properties. High $ZT=\sigma S^2T/\kappa$ requires a combination of high thermopower (S), good electrical conductivity (σ), and low thermal conductivity (κ). Finding materials with the needed combination of properties is challenging because for example high thermopower and high conductivity most commonly occur in different doping regimes. [1] We use state-of-the-art computational tools such as the linearized augmented planewave method [2] and the BoltzTraP code [3] for these calculations.

Results

(1) Lanthanum-Tellurium Thermoelectrics:

We completed our investigation of $La_{3-x}Te_4$. [4] This material is a known excellent thermoelectric at high temperature. The goals were (1) to identify the origin of the high thermoelectric performance in terms of the electronic structure and (2) to determine whether the high *ZT* behavior can be shifted to lower temperatures appropriate for waste heat recovery by altering the doping level. We performed first principles calculations of the band structure, and then used it to obtain electrical transport properties that we then systematically compared with experimental data. We found that there are two sets of bands that are active in determining the electrical transport in this compound. These are light bands that form the band edge for n-type material and heavier bands that become active at the doping levels where high thermoelectric performance occurs. This is as shown in Fig. 1. The signature of the heavy bands in transport is an increase in the thermopower when the doping level reaches its onset. The net result is an enhanced thermopower while maintaining high conductivity. This leads to a high power factor and thermoelectric performance at high doping levels. However, it also means that the high *ZT* cannot be shifted to lower temperature by reducing the doping level. On the other hand, the finding that the high thermoelectric performance of this compound originates in this particular combination of heavy and light bands may be useful in finding other thermoelectrics more appropriate for waste heat recovery. This may be done by searching for materials having such a band structure but with heavy and light features that are closer together in energy. As discussed below this is useful in finding new PbSe based compositions.

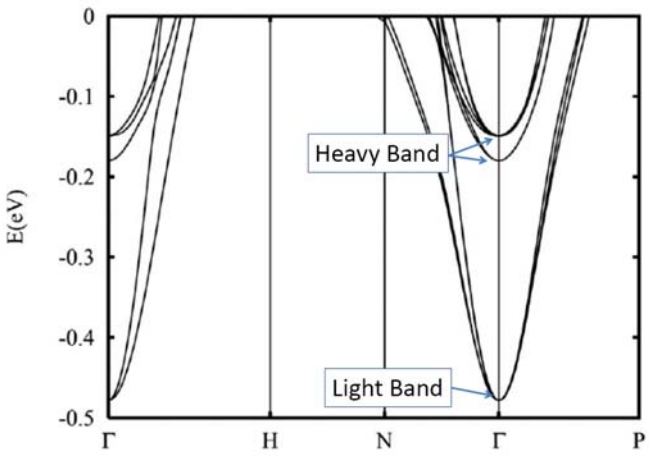

Figure 1: *Band structure of La-Te from first principles calculations. Note the heavy and light bands. The light band provides high conductivity while the heavy band enhances the thermopower.*

(2) Manganese Pnictide Phases

Thermoelectric materials are much more likely to be useful in vehicular waste heat recovery if high performance low cost compositions are identified. In this regard, we studied two newly proposed low cost materials, $BaMn_2Sb_2$ and $BaMn_2As_2$. These compounds occur in the so-called $ThCr_2Si_2$ structure. Intermetallic compounds with this structure type often have low anisotropy in their transport properties. This is highly desirable in a thermoelectric material for applications. Earlier experimental work had shown high values of the thermopower in ceramic samples of $BaMn_2Sb_2$ although the conductivity was not high enough to yield high *ZT*. It is not known if this was an issue that resulted from inappropriate doping, the microstructure of the samples or intrinsic behavior of the material.

We calculated the electronic structure and magnetic properties of these phases and analyzed these in relation to experimental data. [7] The calculated electronic density of states for $BaMn_2As_2$ is shown in Fig. 2. It does have heavy bands, which account for the measured high thermopowers. However, we found the material to be an

antiferromagnetic semiconductor with strong spin dependent hybridization and a strong coupling of the electronic states near the band edges to the magnetic order. We found a very similar result for $BaMn_2Sb_2$.

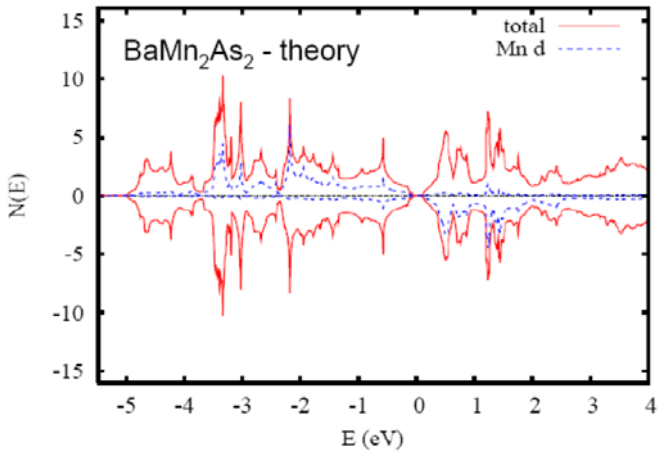

Figure 2: *Calculated electronic density of states of antiferromagnetic $BaMn_2As_2$. Note the strong spin dependent hybridization in this semiconducting compound. The implication is that the carrier mobility is intrinsically low.*

The implication of these results is that while high thermopowers at reasonable doping levels will occur in the magnetic state, the mobility is intrinsically low. Therefore, while $ThCr_2Si_2$ structure intermetallics may be useful thermoelectric materials, compositions other than the manganese pnictides should be explored.

(3) PbSe-WSe_2 Intergrowth Compounds

We used first principles methods to calculate the electronic structure and transport properties of PbSe and PbSe-WSe_2 intergrowth compounds. This was motivated by recent experimental results showing extremely low thermal conductivities in thin films of WSe_2 and also in PbSe-WSe_2 layered materials. [5] These compounds consist of layers of PbSe and WSe_2 with various layer thicknesses (see Fig. 3). The key questions are (1) to what extent are the electronic properties similar to those of PbSe (2) whether these materials can have high thermoelectric performance when suitably doped and (3) whether bulk nanostructured materials based on PbSe are likely to have performance comparable to or better than PbTe. This latter question is important because supply constraints on Te could be a barrier to the widespread deployment of vehicular thermoelectric waste heat recovery based on Te compounds if the device designs require large quantities of thermoelectric material. We performed structure relaxations, electronic structure calculations and Boltzmann transport calculations to address these issues.

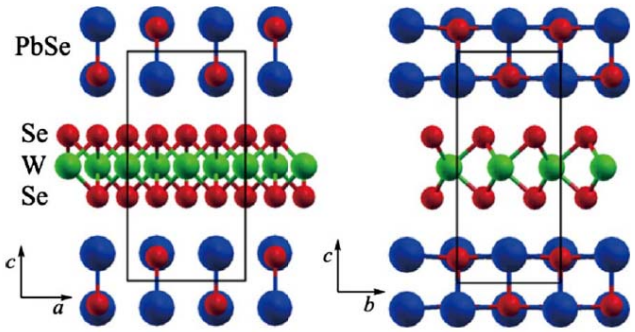

Figure 3: *Relaxed structure for a coherent approximant structure of the simplest 1:1 PbSe-WSe_2 intergrowth compound as obtained from density functional calculations.*

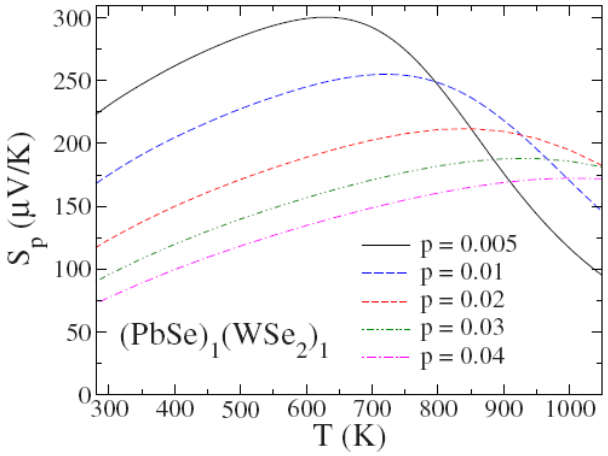

Figure 4: *Calculated thermopower of the first member of the family of PbSe-WSe_2 intergrowth compounds as a function of temperature for various doping levels given in holes per PbSe formula unit. These results imply an optimum doping level in the range 1-2% for low thermal conductivity material.*

We found [6] that the electronic states of the WSe_2 and PbSe subsystems remained independent for p-type, but not for n-type doping levels. We also found increases in the band gap for small PbSe thicknesses. This was due to quantum confinement connected with the effective nanostructuring in these intergrowth compounds. The band masses were correspondingly increased leading to enhanced thermopowers. This is illustrated in Fig. 4, which shows the calculated ther-

mopower as a function of temperature for various doping levels.

In addition to showing that this material is potentially a high performance thermoelectric at temperatures appropriate for waste heat recovery in vehicles, the calculations identified the doping levels that are most appropriate. These were in the range of 1-2% on a per formula unit basis, assuming that low thermal conductivities can be maintained. The calculations also revealed an unusual doping and temperature dependence. In particular, the thermopowers were higher than would be expected based on standard parabolic band models in conjunction with the known low temperature, low doping level behavior. Analysis of the origins of this behavior in terms of the band structure showed a mechanism related to that discussed above for $La_{3-x}Te_4$ but more complex in detail. The key is that the electrical transport is controlled by heavier bands at higher doping levels and temperature, similar to $La_{3-x}Te_4$.

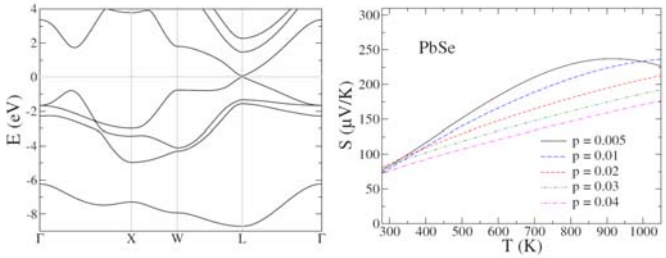

Figure 5: *Band structure including spin-orbit interactions (left) and calculated thermopower as a function of temperature and doping (right) for p-type PbSe. Note that the thermopower in the temperature regime relevant to waste heat recovery does not decrease as rapidly as might be expected with doping.*

These results led us to reexamine the transport properties of bulk p-type PbSe at high doping levels. While PbSe is a known thermoelectric material, previous work concentrated on lower doping levels, well below 1%. We found that PbSe could become a high performance thermoelectric at higher doping levels than have been previously considered, especially if the thermal conductivity can be lowered by nanostructuring. We estimated the length scales that would be effective for enhancing thermoelectric performance via nanostructuring. These results imply that PbSe doped at the 1% level and nanostructured appropriately is a promising material for waste heat recovery. This is a consequence of the non-parabolic band structure of PbSe as shown in Fig. 5. Experiments should be conducted examining heavily doped PbSe as a lower cost, potentially higher performance thermoelectric compared to PbTe. In addition, fine scale nanostructuring of PbSe, for example with WSe_2, may also provide a route to high *ZT*. The calculations show that control of the doping level will be critical.

Conclusions

New insights into thermoelectric materials performance have emerged from density functional calculations in conjunction with transport theory. Promising directions for new thermoelectrics based on PbSe and on the use of materials with both heavy and light bands were found. These results suggest new opportunities for developing high performance lower cost thermoelectrics for vehicular waste heat recovery.

References

[1] D.J. Singh and I. Terasaki, "Nanostructuring and more", Nature Materials **7**, 616 (2008).
[2] D.J. Singh, "Planewaves, Pseudopotentials and the LAPW Method, 2nd Edition", Springer, Berlin (2006).
[3] G.K.H. Madsen and D.J. Singh, "BoltzTraP: A code for calculating band-structure dependent quantities", Computer Physics Communications **175**, 67 (2006).
[4] A.F. May, D.J. Singh and G.J. Snyder, "Influence of band structure on the large thermoelectric performance of lanthanum telluride", Physical Review B **79**, 153101 (2009).
[5] C. Chiritescu, D.G. Cahill, N. Nguyen, D. Johnson, A. Bodapati, P. Keblinski and P. Zschack, "Ultralow thermal conductivity in disordered layered WSe_2 crystals", Science **315**, 351 (2007).
[6] L. Zhang and D.J. Singh, "Electronic structure and thermoelectric properties of layered PbSe-WSe_2 materials", Physical Review B **80**, 075117 (2009).
[7] J. An, A.S. Sefat, D.J. Singh and M.H. Du, "Electronic structure and magnetism in $BaMn_2As_2$ and $BaMn_2Sb_2$", Physical Review B **79**, 075120 (2009).

Agreement 16309 – Carbon Based Thermoelectrtics

Principal Investigators: D.M. Gruen, D. Singh, and J.L. Routbort
Argonne National Laboratory
9700 S. Cass Avenue, Argonne, IL 60439-4838
(630) 252-5065; fax: (630) 252-5568; e-mail: dmgruen@anl.gov

DOE Technology Manager: Jerry L. Gibbs
(202) 586-1182; fax: (202) 586-1600; e-mail: jerry.gibbs@ee.doe.gov

Contractor: UChicago Argonne LLC
Contract No.: DE AC02 06CH11357

Objective

- Develop high-temperature, high-ZT thermoelectrics

Approach

- Use nanoensembles to break the interdependence between the thermopower and the electrical and thermal conductivities. Optimize these parameters separately and systematically for high ZT. Enhance the thermopower of the materials by increasing their configurational electronic entropies that enter the expression for the figure of merit in a quadratic fashion thus powerfully affecting conversion efficiencies.

Accomplishments

- During the last year, we refined the synthesis procedure to produce ensembles that are thermally and electrically stable to 2500K. Measurement of their Seebeck coefficients and electrical as well as thermal conductivities were made as a function of temperature.
- The Seebeck coefficient increased with temperature to 1200K, the limit of our apparatus.
- The thermopowers of boron doped ensembles reached 1 mW/K^2-cm. The thermal conductivities were found to be in the 10^{-2} W/K-cm range as determined at the High-Temperature Materials Laboratory at ORNL and confirmed by Netzsch Instruments in Burlington, MA.
- These materials were exhaustively characterized using HRTEM, SEM, Raman, and XRD techniques and have been shown to preserve their nanostructures even at extremely high temperatures.
- Density functional tight binding calculations on "molecular analogue" models have provided theoretical support for the hypothesis that the configurational electronic entropies of the ensembles is largely responsible for their thermopower values and temperature behavior.

Future Direction

- The favorable high-temperature thermoelectric properties of the nanocarbon ensembles (NCE) demonstrated by the above "proof of concept" results strongly suggests an extension of this approach for the development of high ZT thermoelectrics
- The extension involves using silicon carbide as a basic constituent for the next generation of nanoensembles. This material is widely available, is not resource limited and is environmentally benign.
- Silicon carbide is known to have a large number of coexisting polytypes. By proper doping, we create in each polytype a high density of states near the Fermi level. The usefulness of this idea has been demonstrated in preliminary experiments where much larger thermopowers than in the carbon ensembles have already been measured.

Introduction

This project has shown "proof of concept" during the past year. Nanocarbon ensembles that are thermally and electrically stable at temperatures up to 2500K have been synthesized and characterized. They preserve their nanostructures at very high temperatures. Thermoelectric properties are promising but further development work needs to be done to reach the overall objective of the project that is to create materials displaying ZT values in the 4-5 range so as to reach heat to electricity conversion efficiencies of 30-40%.

Measurements of thermal conductivities give low values that are most likely due to the nanostructured nature of the nanoensembles. Support for that conclusion is provided by HRTEM, XRD and Raman characterizations.

Preliminary results on nanoensembles containing doped silicon carbide show that much higher thermopowers can be achieved with these materials than with the nanocarbons. Thus, the extension of our work for FY 2010 appears to confirm that the configurational electronic entropy hypothesis is a useful guide to the achievement of higher Seebeck coefficients.

Experimental

Thermal Conductivity Measurements

The thermal conductivities were calculated using measurements of the thermal diffusivity and specific heat together with a measurement of the nanoensembles bulk density carried out by Netzsch Instruments.

HRTEM Measurements

These measurements were performed on an FEI Tecnai F20 operating at 200 KeV. The compact bulk nanoensembles were prepared for TEM by scraping the sample and dispersing the resulting powders in ethanol. The dispersions were ultrasonicated and subsequently deposited on a holey carbon 3 mm copper grid.

Raman Measurements

An excitation wavelength of 632.8 nm was used on a Renishaw micro-Raman RM2000 using a 50X objective over the range 50-4000 cm-1 with an approximate 1 micron spot size

XRD measurements

X-ray diffraction data were collected using a Rigaku Miniflex+ diffractometer with Cu K-alpha radiation (lambda=0.154 nm) from 3 to 90 degrees 2-theta with a scan speed of 2 s/step and a step size of 0.02 degrees

Results

Thermal conductivity measurements performed at the HTML of ORNL by Hsien Wang and collaborators have been repeated by Robert Campbell at Netzsch Instruments with very similar results. They are graphically displayed in Fig. 1. A likely explanation of the low values is effective phonon scattering at the ubiquitous grain boundaries of the nanoensembles.

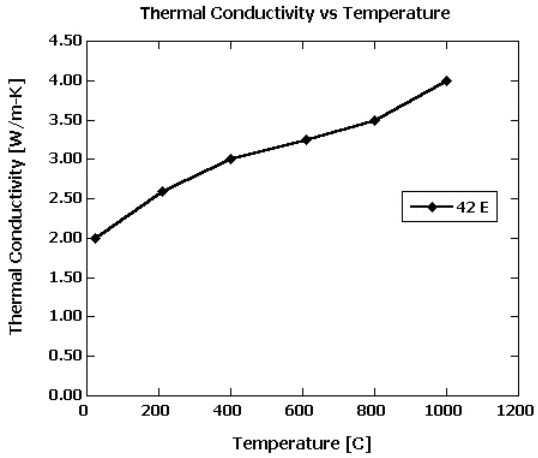

Figure 1. Variation of thermal conductivity as a function of temperature for nanocarbon ensembles.

The unusual circumstance that the nanocrystallinity of the ensembles is in fact retained even though they have undergone annealing at temperatures as high as 2500K is highly intriguing. To explore this

phenomenon, we have undertaken extensive HRTEM studies exemplified by the results shown in Fig. 2. The salient result is that 5-10 nm hollow polyhedral graphene-like structures form at the high temperatures that appear successfully to resist grain growth.

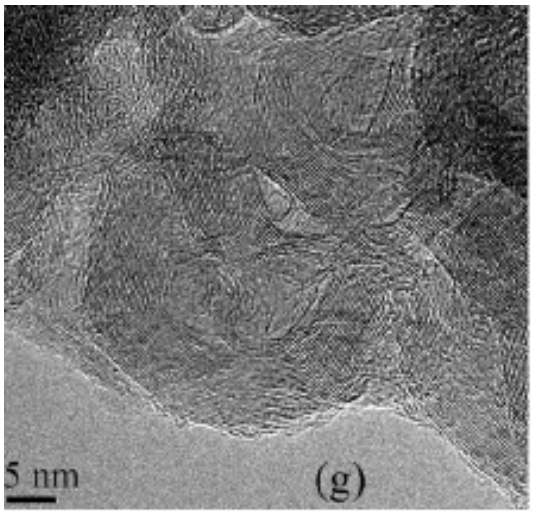

Figure 2. TEM of area showing polyhedrical nanopore structures acquired in a nanocarbon ensemble sample after annealing at 2100K.

The Raman spectra displayed in Fig. 3 shed additional light on the nature of the structural transformations that occur as a result of high temperature annealing.

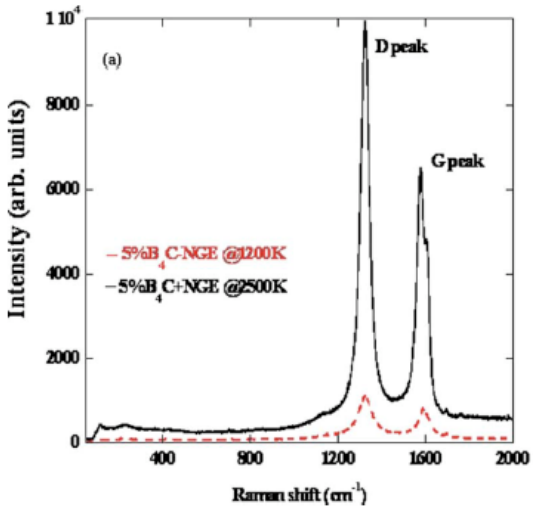

Figure 3. Raman spectra corresponding to a 5% B_4C-nanographite sample as fabricated (red) and after annealing at 2500K for 4 h.

A likely interpretation of the observed D/G peak intensity increase with annealing temperature is an increase in "aromaticity" associated with the growth of the polyhedral structures seen in the HRTEM work.

The remarkable thermal evolution of the graphene-like structure of the nano-ensembles is further evidenced by the XRD data shown in Fig. 4. The sharpening (decrease in half-width) of the diffraction peaks with annealing temperature manifests the increasing number of nanographene crystallites.

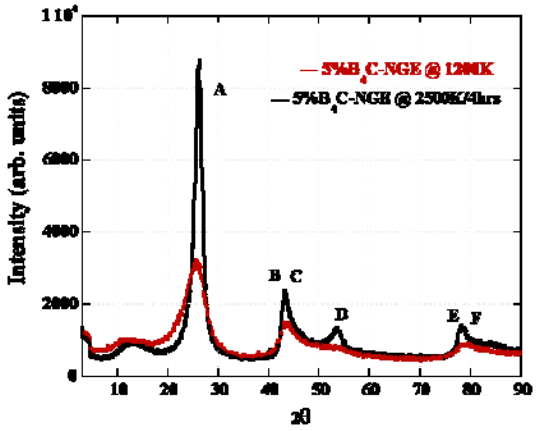

Figure 4. XRD spectra corresponding to a 5% B_4C-nanographite sample as fabricated (red) and after annealing at 2500K for 4 h.

Issues & Future Direction

Work during the past year has provided a "proof of concept" for the approach taken by us to use nanoensembles to break the interdependence of the three variables that determine the thermoelectric figure of merit. It appears, however that with nanocarbons, the thermopower cannot be increased sufficiently to achieve our ultimate objective of ZT values in the 4-5 range.

The thermopower of a material is due to electronic entropy transported by charge carriers. To maximize this quantity requires one to use materials with large electronic entropy. We have decided to concentrate on silicon carbide which has many polytypes with very similar energies of formation. Extensive density functional calculations are

under way to determine how different dopant configurations affect the density of states near the Fermi level. Preliminary data on fully dense doped spark plasma processed SiC give thermopower values near 350 microV/K. These values are high enough so that our ZT objectives could be met provided that the electrical and thermal conductivities retain the values seen with the nanocarbon ensembles. Much development work needs to be done to meet these requirements.

Conclusions

Reaching the ultimate objective of a ZT of 4-5 would have a profound impact on energy conversion technology. Single phase materials appear to be limited to ZTs of 1-2. The nanoensemble approach proposed by us may be able to overcome this limitation by independently maximizing the three parameters that determine the figure of merit.

Our work up to now provide some support for the hypothesis that configurational electronic entropy can very important in determining thermopower. We are further optimizing that quantity by using SiC as a basis for the next step in nanoensemble synthesis. Work in 2010 will concentrate on developing methodologies that increase electrical while decreasing thermal conductivities of SiC based nanoensembles.

Published Papers

1. D. M. Gruen, P. Bruno, M. Xie, Appl. Phys. Lett., 92, 143118 (2008)
2. P. C. Redfern, D. M. Gruen, L. A. Curtiss, Chem. Phys. Lett., 471, 264 (2009)
3. D. M. Gruen, P. Bruno, R. Arenal, J. Routbort, D. Singh, M. Xie, J. Appl. Phys., 105, 073710 (2009)

Agreement 18340 - Thermoelectric Materials for Advanced Vehicle Energy Recovery

Principal Investigator: Dr. Terry Hendricks
MBI Business Development Manager/Senior Program Manager
MicroProducts Breakthrough Institute
Pacific Northwest National Laboratory
1000 NE Circle Blvd., Suite 11101, Corvallis, Oregon 97330
(541) 713-1353; fax: (541) 758-9320; e-mail: terry.hendricks@pnl.gov

Professor Mas Subramanian
Department of Chemistry
Oregon State University
Corvallis, Oregon 97330
(541)-737-8235; fax (541)-737-2062; e-mail: mas.subramanian@oregonstate.edu

DOE Technology Manager: Jerry L. Gibbs
(202) 586-1182; fax: (202) 586-1600; e-mail: jerry.gibbs@ee.doe.gov

Field Technical Manager: Mark T. Smith
(509) 375-4478; fax: (509) 375-4448; e-mail: mark.smith@pnl.gov

---

Contractor: Pacific Northwest National Laboratory
Contract No: DE-AC05-76RL01830

Objective

- Develop new high-performance n-type and p-type thermoelectric (TE) material compositions to enable OVT to achieve or approach 10% fuel efficiency improvements from waste energy recovery in advanced light-duty engines and vehicles.
- Develop new, high-performance n-type and p-type TE materials compositions to enable OVT to achieve stretch thermal efficiencies of 55% in advanced heavy-duty engines by 2013.
- Improve cost-effectiveness and performance of exhaust heat recovery in light- and heavy-duty vehicles.
- Design, synthesize, and characterize p-type and n-type skutterudites and metal oxide TE materials for waste-heat-driven power generation in light-duty or heavy-duty vehicle exhaust flows or other comparable exhaust flows. Develop TE materials with operational temperatures as high as 800 K to 900 K.
- The project seeks to develop advanced n-type and p-type bulk TE materials that have peak ZT (Figure of Merit x Temperature) of approximately 1.6 or higher at 600 K and temperature-dependent properties that provide high performance in the 350 K to 820 K range.

Approach including industrial partner/collaborator and path to technology transfer and commercialization

- Pacific Northwest National Laboratory (PNNL) and Oregon State University (OSU) are systematically investigating multiple-rattler skutterudite materials and metal oxide TE materials that can perform effectively and structurally survive at temperatures from 350 K to 820 K.
- Indium (In)-based Cobalt Antimony ($In_xR_yCo_4Sb_{12}$) compounds are one targeted n-type skutterudite material. However, p-type skutterudites and metal oxides also are being investigated and developed.
- PNNL and OSU are simultaneously characterizing the temperature-dependent thermoelectric and structural properties of advanced p-type and n-type TE materials, particularly Seebeck coefficient, electrical conductivity, thermal conductivity, Young's modulus, Poisson's ratio, and the coefficient of thermal expansion up to 300°C to 400°C.
- OSU is developing and fabricating the advanced TE material compounds and measuring the TE properties using their TE measurement equipment.

- PNNL is measuring structural properties, Young's modulus, and Poisson's ratio, in resonant ultrasound (RUS) facilities and coefficient of thermal expansion at the Physical Sciences Laboratory in Richland, WA.
- PNNL is using its TE system modeling capabilities to characterize system-level benefits of the material compositions in vehicle waste energy recovery applications.

Milestones, Metrics and Accomplishments

- Various p-type $Co_{3-x}Rh_xSb_3$ compounds were investigated and characterized with x varied from 0 to 1 with the optimum p-type composition occurring at x=0.6.
- TE properties of $Co_{2.4}Rh_{0.6}Sb_3$ compounds characterized from 300 K to 500 K. Power factor as high as 7 $\mu W/cm^2$-K demonstrated at 465 K.
- Decision to discontinue work on p-type $Co_{3-x}Rh_xSb_3$ compounds because of their high cost.
- Work has continued on fabricating In-based n-type dual-rattler skutterudite materials, $In_{0.15}Ce_{0.1}Co_4Sb_{12}$ and $In_{0.1}Y_{0.1}Co_4Sb_{12}$, which show the most promising n-type TE behavior.
- Measured thermoelectric properties of $In_{0.15}Ce_{0.1}Co_4Sb_{12}$ and $In_{0.1}Y_{0.1}Co_4Sb_{12}$ compounds. **(Milestone)**
- Measured Coefficients of Thermal Expansion for several n-type Co_4Sb_{12}, $In_{0.15}Ce_{0.1}Co_4Sb_{12}$, and $In_{0.1}Y_{0.1}Co_4Sb_{12}$ compounds at temperatures from 25 °C to 400 °C **(Milestone).**
- Measured room-temperature Young's modulus and Poisson's ratios for several n-type Co_4Sb_{12}, $In_{0.15}Ce_{0.1}Co_4Sb_{12}$, and $In_{0.1}Y_{0.1}Co_4Sb_{12}$ compounds. **(Milestone)**
- Identified a refined method of fabricating $In_{0.15}Ce_{0.1}Co_4Sb_{12}$ incorporating ball milling processes, which creates dramatically reduced thermal conductivity and higher ZT.
- Designed and fabricated critical high-temperature thermal chamber and RUS transducers for high-temperature structural property measurements in PNNL RUS systems **(Milestone).**
- Performed system-level thermal/TE analyses to show the potential benefits of the PNNL/OSU skutterudites used in vehicle waste energy recovery and potential auxiliary power unit (APU) systems.

Future Direction

- Optimize synthesis procedures for n-type $(In,R)Co_4Sb_{12}$ and p-type FeSb compositions.
  - Good reproducibility
  - Fabricating highly dense samples
  - Develop hot-pressing techniques
- Develop FeSb compounds as p-type TE materials and introduce single and multiple "rattlers" (In, rare earths) for better p-type high ZT materials.
- Characterize TE properties and validate with third-party testing.
- Perform structural property measurements at high temperatures (up to 300 °C to 400 °C).
  - Young's modulus, E(T), and Poisson's ratio, υ(T)
  - Coefficient of thermal expansion (T)
  - Mechanical strength at room temperature
- Transition n-type and p-type materials to TE couples and measure performance.
- Continue evaluating system-level benefits with the new p- and n-type TE materials as they are available.

Introduction

Background

DOE's Transportation Energy Data Book: Edition 24 shows, in 2002, approximately 130 billion gallons of gasoline were used nationwide by light-duty passenger car, van, and sport-utility vehicle (SUV) segments. Some current estimates indicate that approximately 4 to 5 Quads (1 Quad = 10^{15} Btus) of the energy in this fuel ends up as waste thermal energy in the vehicle exhaust stream. The same reference also indicates another approximately 30 billion gallons of diesel fuel was used nationwide by heavy-duty vehicles in 2002. Some current estimates indicate that approximately 1.4 Quads of the energy in this fuel ends up as waste thermal energy in the heavy-vehicle exhaust stream. Other estimates indicate that another 5 to 7 Quads of thermal energy originating from the fuel energy ends up in the vehicle coolant systems of light-duty passenger cars, vans, SUVs, and heavy-duty vehicles. DOE's Office of Energy Efficiency & Renewable Energy,

Vehicle Technologies Program has initiated a Waste Heat Recovery & Utilization project with the goal of recovering enough of this waste energy to increase the vehicle fuel economy by 10%. Contractor teams are pursuing advanced thermoelectric (TE) systems, leveraging recent advanced TE materials research and development (R&D) in skutterudites, quantum well, and nano-structured materials to recover and convert this waste thermal energy into high-grade electrical energy onboard the vehicle. Advanced TE materials are critical to achieving project performance goals and introducing other potential future applications of TE power generation and advanced cooling in vehicle systems. Several researchers have reported advanced TE materials demonstrating (ZT) values of 1.6 to 2.4, with at least some of this data occurring at high temperatures of 400°C to 700°C. It is possible to expect advanced TE power conversion efficiencies of 12% to 15% with TE materials in this ZT range at high temperatures, which is two to three times the values using older bulk TE materials. Further advances in TE materials may lead to power conversion efficiencies approaching 20%.

Several technical challenges exist to developing advanced hybrid TE power systems in advanced light-duty and heavy-duty vehicle platforms, including increasing TE device conversion efficiencies through demonstrated high-performance TE materials, transferring hot-side exhaust thermal energy into the TE conversion devices, dissipating cold-side thermal energy to the environment, and optimizing advanced TE systems for a variety of nominal and off-nominal performance conditions. Tasks performed here address these new opportunities by developing the necessary advanced TE materials with ZT ~1.6 @ 600 K in bulk form that allows cost-effective engineering transition into high-performance TE power generation devices.

This project leverages recent progress in skutterudite TE materials and metal oxide materials. Skutterudite materials have a cubic crystal structure as shown in Figure 1, which contains "voids" inside the crystal. These "voids" are large enough that various elements can be inserted inside. Any inserted element has a particular resonance frequency associated with it that can be excited by thermal phonons of the proper wavelength traveling through the crystal. The complete wavelength spectrum of thermal phonons is responsible for producing the observed lattice thermal conductivity in any material. The elements inserted into the crystal voids interact with and resonate with particular wavelengths of the spectrum, thereby causing them to resonate or "rattle" at that particular wavelength and, ultimately, scatter the thermal phonon rather than allowing it to transmit through the crystal. This ultimately reduces the lattice thermal conductivity of the skutterudite. The more elements that can be put inside the crystal voids, the more wavelengths or range of wavelengths can be impacted and scattered, further reducing the lattice thermal conductivity. This ultimately increases the ZT of skutterudite materials, which already have inherently high Seebeck coefficients, through the equation (1):

$$ZT = \frac{S^2\sigma}{K_e + K_L}T \qquad (1)$$

S = Seebeck Coefficient [μV/K]
σ = Electrical Conductivity [S/cm]
K_e = Electronic Thermal Conductivity [W/m-K]
K_L = Lattice Thermal Conductivity [W/m-K]
T = Temperature [K]

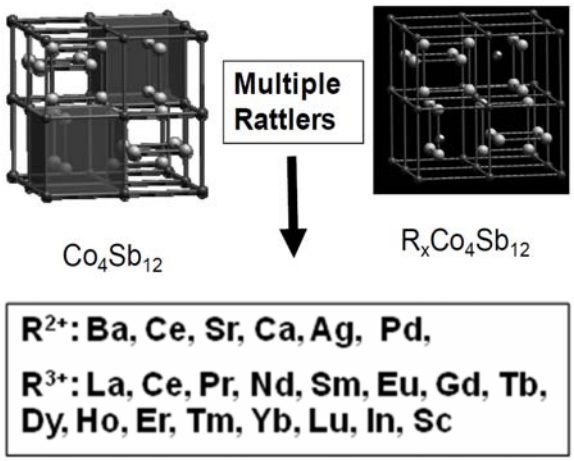

Figure 1. Skutterudite Crystal Structure and Potential Rattler Elements for Thermal Conductivity Suppression

The box in Figure 1 shows the various elements that potentially can be inserted into the skutterudite crystal voids, which are being investigated in this project. This is the basis for one approach to developing high-performance TE materials.

Project Accomplishments

This year the project has focused on investigating and developing p-type multiple-"rattler" and n-type multiple-"rattler" skutterudites. We have investigated and quantified the thermoelectric properties of various promising compounds, measured room-temperature Young's modulus and Poisson's ratio, and prepared systems for high-temperature structural property measurements in PNNL RUS systems.

Advanced Skutterudite TE Materials
This year, the work first identified interesting Rhodium (Rh)-based $CoSb_3$ compounds that could be tailored into p-type TE materials. Various $Co_{3-x}Rh_xSb_3$ compounds were investigated with x varied from 0 to 1. Figure 2 shows the resulting room temperature Seebeck coefficient and electrical resistivity of the different compounds.

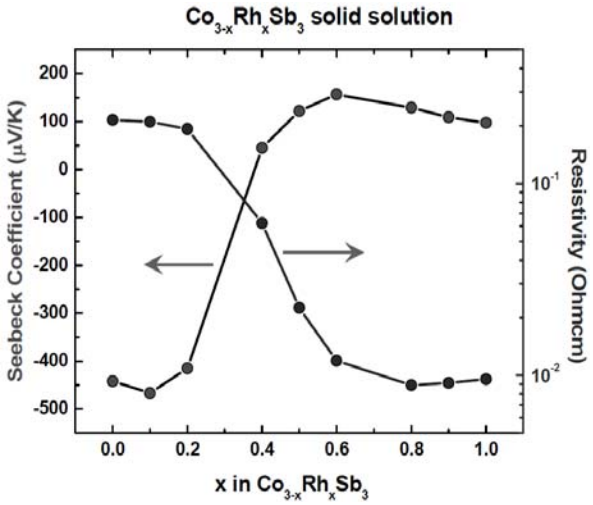

Figure 2. Seebeck Coefficient and Electrical Resistivity of Various $Co_{3-x}Rh_xSb_3$ Compounds

α = Seebeck Coefficient [μV/K]
ρ = Electrical Resistivity [Ω-cm]

The compounds showed n-type and p-type characteristics depending on the value of x, with the optimum p-type composition occurring at x=0.6. Figure 3 shows the resulting power factor (α^2/ρ) for the various $Co_{3-x}Rh_xSb_3$ compounds. The optimum p-type power factor is shown clearly at the x=0.6 composition in Figure 3. This room temperature p-type power factor is quite good. It actually is a higher room temperature power factor than the best n-type skutterudite TE materials, namely $In_{0.1}Ce_{0.15}Co_4Sb_{12}$, which have shown ZT~1.6 at 600 K. Figure 4 shows the temperature-dependent power factor for the optimum composition $Co_{2.4}Rh_{0.6}Sb_3$, with (α^2/ρ) reaching approximately 7 $\mu W/K^2$-cm at near 470 K. This early work with $Co_{3-x}Rh_xSb_3$ compounds was encouraging, but the power factor was not high enough to achieve the project goals. In addition, one major issue with $Co_{3-x}Rh_xSb_3$ compounds is the high cost of Rh. This would make any of the $Co_{3-x}Rh_xSb_3$ compounds quite expensive and, therefore, difficult to commercialize. As a result, the project focus turned toward other less expensive alternatives for p-type skutterudite materials.

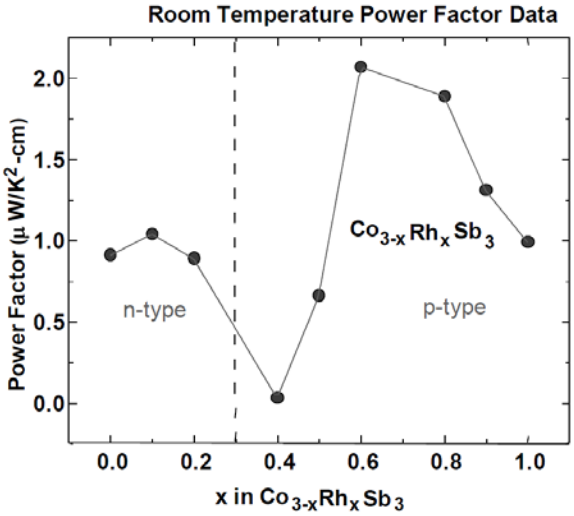

Figure 3. Power Factor of Various $Co_{3-x}Rh_xSb_3$ Compounds

Work also continued on the most promising Indium (In)-based n-type dual-rattler skutterudite materials that have shown ZT ~ 1.6 at 600 K in early work completed in 2008. Two dual rattler compounds, namely

$In_{0.15}Ce_{0.1}Co_4Sb_{12}$ and $In_{0.1}Y_{0.1}Co_4Sb_{12}$, have shown the most promising n-type TE behavior.

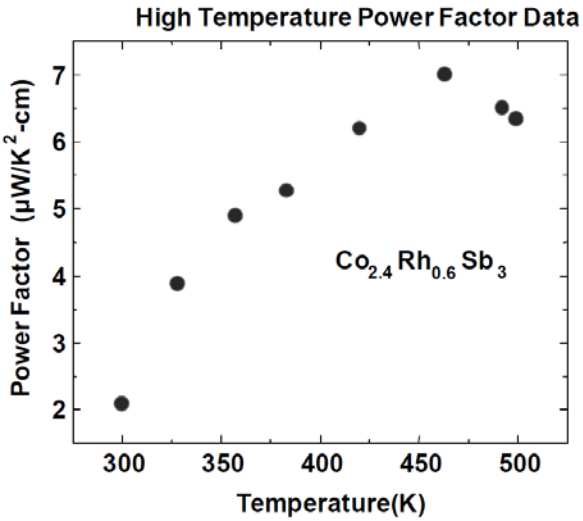

Figure 4. Power Factor as a Function of Temperature for $Co_{2.4}Rh_{0.6}Sb_3$

Samples of nominal composition $In_{0.15}Ce_{0.1}Co_4Sb_{12}$ were synthesized by two methods. In the first method, In, cobalt (Co), and antimony (Sb) were mixed together in stoichiometric ratio in a mortar and ground in air. The $In_{0.15}Co_4Sb_{12}$ sample was put into an argon atmosphere. Cerium (Ce) was then weighed, mixed, and ground with the un-reacted $In_{0.15}Co_4Sb_{12}$ sample. The In-Ce-Co-Sb mixture was reacted in a hydrogen-nitrogen environment. The resulting sample was calcined in a furnace at temperatures up to 67 ^oC for approximately 40 hours. The sample then was loaded into a quartz tube with flowing hydrogen and nitrogen gas, as noted above, and sintered in a furnace at 675^oC. The structure was characterized via powder X-ray diffraction, and the collected pattern showed evidence of the desired single-phase skutterudite structure.

The second method incorporated ball milling processes into the fabrication. In, Co, and Sb were mixed together in stoichiometric ratio in a mortar and ground in air. As in the first method, the In-Co-Sb mixture was reacted in a hydrogen and nitrogen gas environment. The sample was calcined using the same reaction conditions as in the first method. The In-Co-Sb sample was ground, then ball milled under the same conditions as in the first method. The ground and dried $In_{0.15}Co_4Sb_{12}$ sample was combined with Ce that was weighed, mixed, and ground to form the proper compound stoichiometry. The In-Ce-Co-Sb sample was reacted in a hydrogen-nitrogen environment at up to 700^oC for 24 hours at the same heating and cooling ramp rates used in the first method. The resulting sample was ground again, ball milled, and dried using the same conditions as the previous synthesis method. The resulting sample then was sintered using the same conditions as in the first method. The structure was characterized via powder X-ray diffraction, and the collected pattern showed evidence of the desired single-phase skutterudite structure.

Figure 5 and Figure 6 show the temperature-dependent Seebeck coefficient and temperature-dependent electrical resistivity, respectively, for some compound samples fabricated with the first synthesis method used early in our project. The Seebeck coefficient of these two compounds is generally high, approaching or exceeding 300 μV/K at nearly 500 K. The resistivity is generally around 3-5 x 10^{-3} ohm-cm in the temperature range of 350 K to 575 K. This information reflects early 2009 results on these particular compounds.

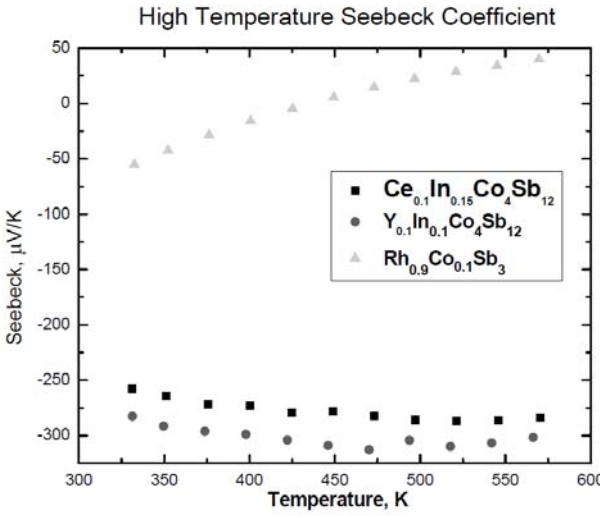

Figure 5. Seebeck Coefficient of Early $In_{0.15}Ce_{0.1}Co_4Sb_{12}$ and $In_{0.1}Y_{0.1}Co_4Sb_{12}$ Compounds Fabricated with First Synthesis Method in 2009

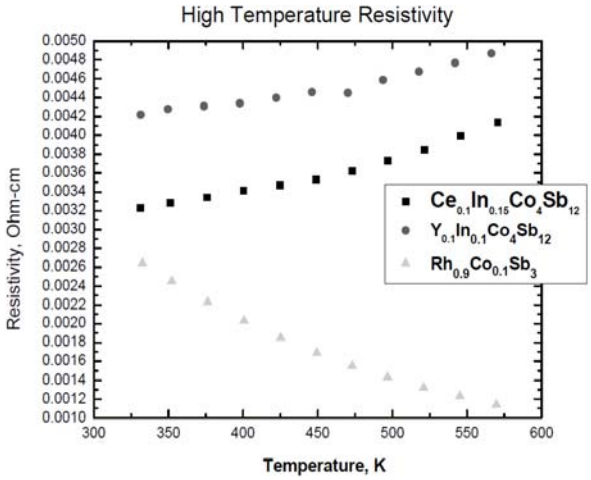

Figure 6. Electrical Resistivity of Early $In_{0.15}Ce_{0.1}Co_4Sb_{12}$ and $In_{0.1}Y_{0.1}Co_4Sb_{12}$ Compounds Fabricated with First Synthesis Method in 2009

Figure 7 shows the thermal conductivity of these early dual-rattler compound samples. Generally, these thermal conductivities were higher than expected and did not produce the high ZT behavior required. We have since transitioned to the second synthesis method of fabricating these compounds, which is providing better thermal conductivity results and higher ZT values than the earlier compound samples.

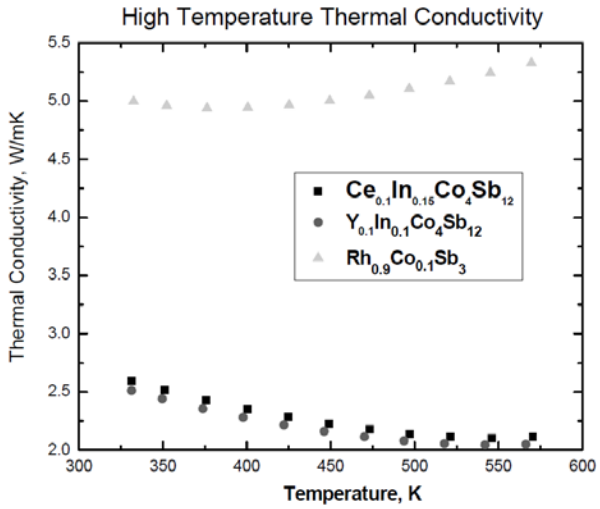

Figure 7. Thermal Conductivity of Early $In_{0.15}Ce_{0.1}Co_4Sb_{12}$ and $In_{0.1}Y_{0.1}Co_4Sb_{12}$ Compounds Fabricated with First Synthesis Method in 2009

Figures 8 and 9 demonstrate the Seebeck coefficient and thermal conductivity of a subsequent batch of $In_{0.15}Ce_{0.1}Co_4Sb_{12}$ and $In_{0.1}Y_{0.1}Co_4Sb_{12}$ compounds using the original synthesis method and a new batch of $In_{0.15}Ce_{0.1}Co_4Sb_{12}$ fabricated with the second synthesis process (i.e., triangles).

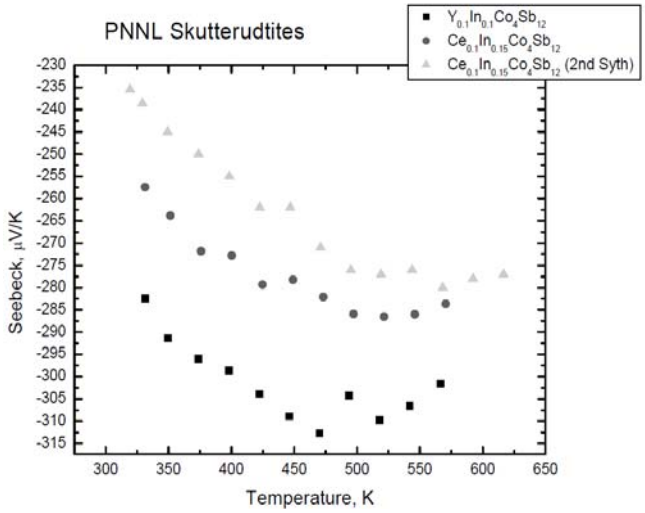

Figure 8. Seebeck Coefficient of $In_{0.15}Ce_{0.1}Co_4Sb_{12}$ Compounds Fabricated With Two Synthesis Methods and $In_{0.1}Y_{0.1}Co_4Sb_{12}$ Compounds

Figure 8 demonstrates that the Seebeck coefficient of the $In_{0.15}Ce_{0.1}Co_4Sb_{12}$ fabricated with the two synthesis methods are similar with peak values around 280–285 µV/K at temperatures of 525 K to 550 K. However, Figure 9 shows the second synthesis method dramatically decreases the thermal conductivity of $In_{0.15}Ce_{0.1}Co_4Sb_{12}$, creating much higher ZT performance in the $In_{0.15}Ce_{0.1}Co_4Sb_{12}$. This demonstrates the dual-rattler effect in these advanced skutterudite materials when the In-Ce are properly placed and manipulated into the crystal lattice voids. This is a major result and accomplishment for our work conducted in 2009. As we move forward in FY 2010, we will continue using this second synthesis process to develop the high-performance n-type $In_{0.15}Ce_{0.1}Co_4Sb_{12}$ skutterudites. All of these In-based skutterudites are bulk materials, making them much easier to integrate into TE devices and, therefore, easier to commercialize in operating devices and systems.

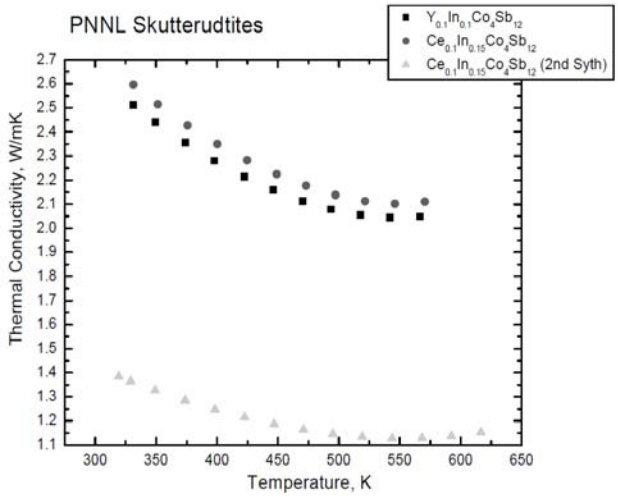

Figure 9. Thermal Conductivity of $In_{0.15}Ce_{0.1}Co_4Sb_{12}$ Compounds Fabricated With Two Synthesis Methods and $In_{0.1}Y_{0.1}Co_4Sb_{12}$ Compounds

Structural Properties

Additional work has been completed characterizing the room-temperature structural properties; Young's modulus, E; and Poisson's ratio, υ; and the coefficient of thermal expansion at high temperature for several n-type Co_4Sb_{12}, $In_{0.15}Ce_{0.1}Co_4Sb_{12}$, and $In_{0.1}Y_{0.1}Co_4Sb_{12}$ compounds. The resonant ultrasound (RUS) system used for the Young's modulus and Poisson's ratio measurement is shown in Figure 10, along with the typical sample measurement configuration between the input transducers. Generally, a vibrational signal is input to the sample, and the resulting frequency response signal then is generated from the sample, which can be measured and appropriate sample resonant frequencies identified. Then, these resonant frequencies are inversely analyzed using sophisticated sample modeling software to back out the sample's Young's modulus and Poisson's ratio. The sample dimensions, surface planarity, and accuracy of the 90-degree edges and corners are critical to this measurement technique and can greatly impact measurement accuracy. FY 2009 work has focused on producing highly accurate sample surfaces, edges, and corners, which requires great attention to detail and is quite tedious.

Table 1 shows the structural properties, E and υ, and coefficient of thermal expansion for some of n-type $CoSb_3$, $In_{0.15}Ce_{0.1}Co_4Sb_{12}$, and $In_{0.1}Y_{0.1}Co_4Sb_{12}$ compounds samples. As of this publication, the structural properties for additional samples of $In_{0.15}Ce_{0.1}Co_4Sb_{12}$ made with both fabrication methods are being measured to add to this database.

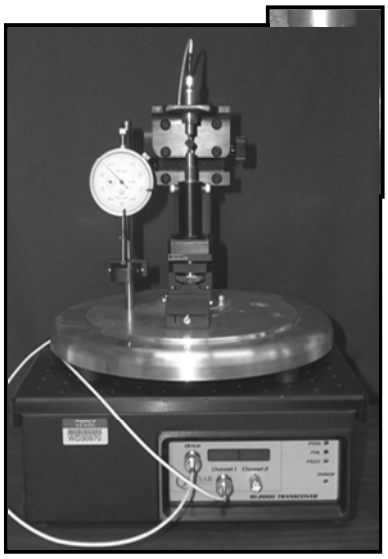

Figure 10. Resonant Ultrasound Equipment for Structural Property Measurement Used at PNNL (The typical sample mount between measurement transducers is shown.)

Table 1 also shows the measured ZT of these samples at or near 600 K, as well as some typical literature-available data. The ZT values for the In-Ce and In-Y compounds represent a work-in-progress toward our ultimate goal of ZT ~ 1.6 at 600 K. The coefficient of thermal expansion measurements in Table 1 are generally taken at 200°C, but show little variation from room temperatures to about 400 °C. Table 1 also shows comparisons to the structural and thermoelectric properties of common, more conventional TE materials, such as bismuth telluride (Bi_2Te_3) alloys and lead telluride (PbTe) alloys.

Additional FY 2009 work has focused on constructing the high-temperature thermal chamber and transducers necessary for obtaining the structural properties of TE materials up to 300°C to 400°C. Figures 11 through 14 showcase these designs, as well as the specific hardware fabricated in FY 2009 to prepare for

the high-temperature structural property measurements. The transducers shown in Figures 13 and 14 will be integrated into the high-temperature thermal chamber system shown in Figures 11 and 12. These transducers and the thermal chamber will be integrated into the RUS system (see Figure 10) to produce high-temperature structural property measurements, E and υ, in FY 2010.

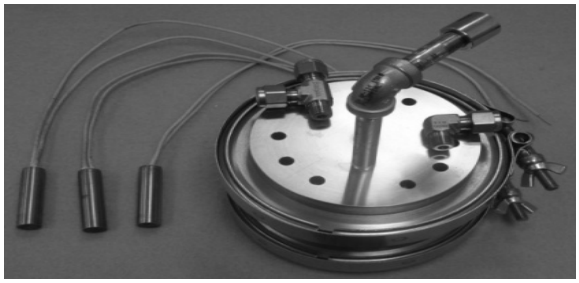

Figure 12. High-Temperature Thermal Chamber Article Fabricated in FY 2009

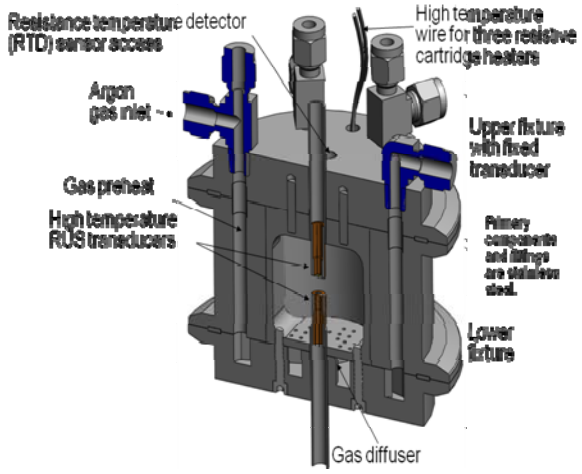

Figure 11. High-Temperature Thermal Chamber Design for High-Temperature Structural Measurements

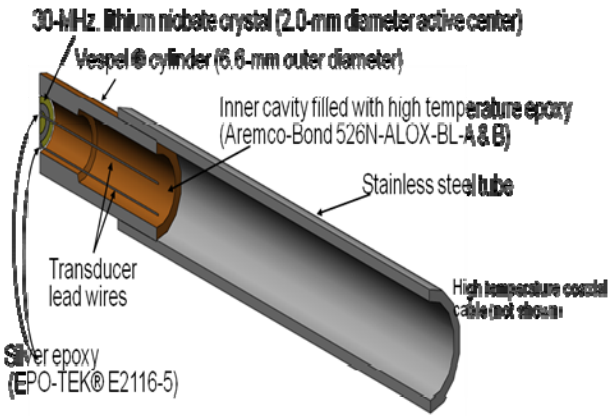

Figure 13. High-Temperature RUS Transducer Design for High-Temperature Structural Measurements

Table 1. Structural and Thermoelectric Properties for Various n-type Skutterudites

Isotropic	υ, Poisson's	*CTE [/°C]*	*E*, Young's [10^{11}] N/m^2	*ZT (@ 600 K)*
Bi_2Te_3 Alloys	0.21-0.37	(Anisotropic) 14 21	0.40-0.47	0.0-0.1
PbTe	0.26	19.8	0.58	0.7
$CoSb_3$ (literature)	0.222		1.396	0.6
$La_{0.75}CoFe_3Sb_{12}$ (literature)	0.228		1.365	
$CoSb_3$ (PNNL)	0.226	12.8×10^{-6}	1.398	
$CoSb_3$ (PNNL)	0.225		1.391	
$In_{0.1}Co_4Sb_{12}$ (PNNL)	0.227	8.37×10^{-6}	1.396	
$Y_{0.1}In_{0.1}Co_4Sb_{12}$ (PNNL)	0.247	9.26×10^{-6}	1.413	0.82
$In_{0.15}Ce_{0.1}Co_4Sb_{12}$ (PNNL – 1st Method)		$8.3 - 8.75 \times 10^{-6}$	Being Measured Now	0.52 (@ 575 K)

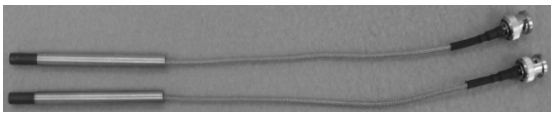

Figure 14. High-Temperature RUS Transducer Articles Fabricated in FY 2009

PNNL also has performed system-level TE analyses to show the potential benefits of the PNNL/OSU skutterudites used in vehicle waste energy recovery systems. Figure 15 shows the efficiency–power map for typical exhaust energy recovery conditions in light-duty vehicles using the PNNL/OSU skutterudites and more conventional Tellurium-Antimony-Germanium-Silver (TAGS) $[(AgSbTe_2)_{1-x}(GeTe)_x]$ alloys and PbTe alloys. This efficiency–power map shows the loci of all possible TE designs and their potential optimum TE conversion efficiency and power output using these TE material classes. This analysis shows the potential superior performance of the PNNL/OSU skutterudites with TE conversion efficiencies near 10% in the preferred TE design regime shown. It also is well known that the TAGS alloys are extremely expensive and have not been widely commercialized because of their high cost. We expect the PNNL/OSU skutterudites will be more cost-effective than TAGS and will help to surmount the cost barriers, leading to a better commercialization opportunity as their development matures.

PNNL also has performed system-level TE analyses to show the potential benefits of the PNNL/OSU skutterudites in combustion-driven auxiliary power units (APU) for heavy-duty vehicle applications (e.g., during truck stop rest periods when truck-idling constraints exist in many locals and regions). Figure 16 shows the efficiency–power map for typical combustion-driven conditions in heavy-duty APUs using the PNNL/OSU skutterudites and more conventional TAGS alloys–PbTe alloys. The TE system analysis for combustion-driven exhaust conditions shown in Figure 16 are for conservative, low-temperature conditions since the combustion gases can be well above 600°C in these systems.

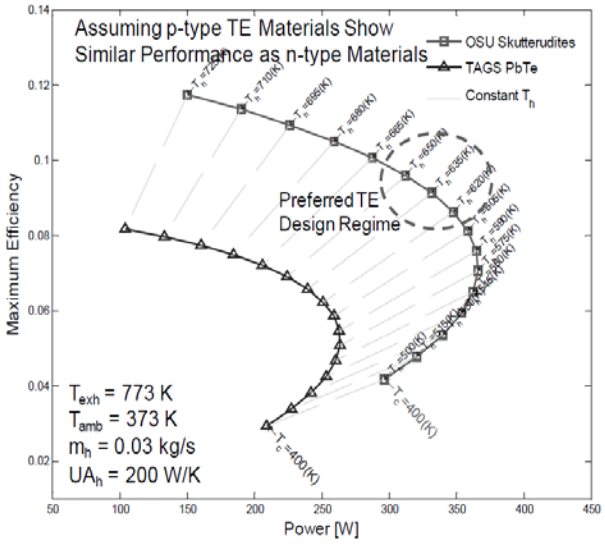

Figure 15. TE System-Level Analysis Results for Typical Light-Duty Vehicle Waste Energy Recovery Conditions (m_h=Exhaust Mass Flow Rate, UA_h=Hot-Side Heat Exchanger UA Performance Factor, T_h=TE Hot-Side Temperature, T_c=TE Cold-Side Temperature, T_{exh}=Exhaust Temperature, and T_{amb}=Ambient Temperature)

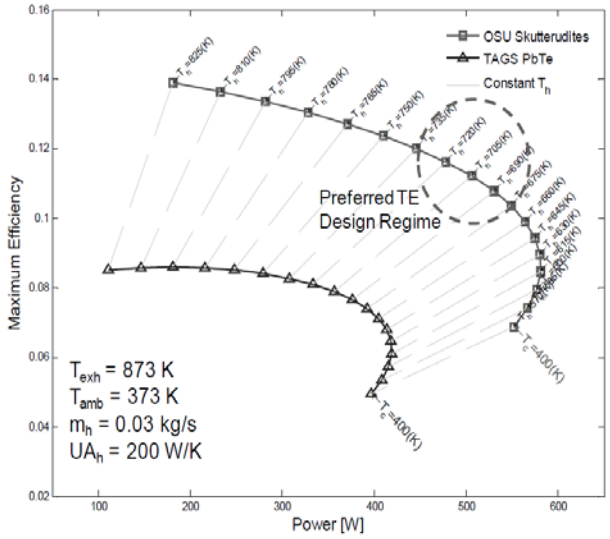

Figure 16. TE System-Level Analysis Results for Typical Light-Duty Vehicle Waste Energy Recovery Conditions (m_h=Combustion Mass Flow Rate, UA_h=Hot-Side Heat Exchanger UA Performance Factor, T_h=TE Hot-Side Temperature, T_c=TE Cold-Side Temperature, T_{exh}=Combustion Gas Temperature, and T_{amb}=Ambient Temperature)

Nevertheless, the TE system analysis in Figure 16 again shows the potential performance superiority of the PNNL/OSU skutterudites in this application compared to the more conventional TAGS-PbTe TE materials. The conversion efficiencies approach 12% in the preferred TE design regime and represent cautious estimates in this conservative TE system APU analysis. The TE conversion efficiencies using these new skutterudites in APU applications could be significantly higher in actual systems.

Conclusions

- $Co_{2.4}Rh_{0.6}Sb_3$ compounds have shown good p-type power factor behavior, but its high thermal conductivity and economics (i.e., high cost) does not justify pursuing it. Better p-type TE materials will be pursued in FY 2010 with FeSb compounds.
- Fabrication of $In_{0.15}Ce_{0.1}Co_4Sb_{12}$ compounds using ball-milling techniques provides superior TE property performance and higher ZTs.
- High Seebeck coefficients (~280 μV/K) and low thermal conductivities (~1.1 W/m-K) at 575 K have been demonstrated in fabrication of our latest n-type $In_{0.15}Ce_{0.1}Co_4Sb_{12}$ compounds.
- $In_{0.15}Ce_{0.1}Co_4Sb_{12}$ and $In_{0.1}Y_{0.1}Co_4Sb_{12}$ compounds appear to have higher Young's modulus, E, than more conventional TE materials, such as Bi_2Te_3 alloys and PbTe alloys, but comparable Poisson's ratio, υ.
- Sample preparation is critical to making structural measurements using the RUS technique. It is critical to take the time and effort to make surfaces planar and sharp 90-degree corners and edges. Therefore, it is required to have high-precision cutting and polishing equipment for making accurate structural test samples in order to obtain accurate structural property measurements. Proper sample preparation requires constant vigilance and attention to detail.
- Our high-temperature equipment is now designed and fabricated to perform high-temperature structural measurements on TE materials in FY 2010.
- PNNL/OSU skutterudites provide potentially superior system-level performance than more conventional TAGS-PbTe materials in light-duty and heavy-duty waste energy recovery and APU applications. TE conversion efficiencies of 10% to 12% appear possible if high-performance p-type skutterudite materials are developed to match the n-type skutterudite materials identified and cultivated.

Presentations/Publications/Patents

T.J. Hendricks and M. Subramanian. 2009. *Proactive Strategies for Designing Thermoelectric Materials for Power Generation*. May 22, 2009, Arlington, Virginia. DOE Vehicle Technologies Program Annual Merit Review.

T.J. Hendricks and M. Subramanian. 2009. *Proactive Strategies for Designing Thermoelectric Materials for Power Generation*. September 29–October 2, 2009, San Diego, California. DOE 2009 Thermoelectrics Applications Workshop.

Agreement 13721 – Low-friction Hard Coatings

A. Erdemir and O. L. Eryilmaz, Principal Investigators
Argonne National Laboratory
9700 S. Cass Avenue, Argonne, IL 60439-4838
(630) 252-6571; fax: (630) 252-5568; e-mail: Erdemir@anl.gov
Eryilmaz@anl.gov

DOE Technology Manager: Jerry L. Gibbs
(202) 586-1182; fax: (202) 586-1600; e-mail: jerry.gibbs@ee.doe.gov

Contractor: UChicago Argonne LLC
Contract No.: DE AC03 06CH11357

Objective

- Design, develop, and implement low-friction and hard coatings to increase the durability, fuel economy, and environmental compatibility of future engine systems.

Approach

- Optimize deposition parameters that are most effective in physical, mechanical, and tribological properties of superhard and low friction coatings. Increase bonding and reduce surface roughness, demonstrate large-scale production and cost-competitiveness, and verify durability and performance in actual engine applications.

Accomplishments

- Deposited optimized coatings on actual engine parts with strong bonding and very smooth surface finish.
- Verified their superior mechanical and tribological properties by bench-top studies.
- Completed initial screening tests by engine company partners.
- In conjunction with our industrial partners, performed field testing of optimized coatings in actual engines.
- Licensing the technology to Galleon International for large-scale production and industrial applications.
- Won an R&D-100 Award in 2009 for our technology.

Future Direction

- Validate large-scale manufacturability of optimized coatings in a commercial-scale deposition system with our coating partner.
- Demonstrate cost-competitiveness and performance and durability benefits.
- Complete engine tests.
- Concentrate on technology transfer and commercialization; finalize licensing talks.

Introduction

Higher energy efficiency, longer durability, and lower emissions are much desired attributes in future transportation systems; but, without further improvements in the surface mechanical and tribological properties of sliding, rolling, or rotating engine components, these goals will be difficult to realize. In particular, higher loads, speeds, temperatures, and other harsh operating conditions in future engines will render most traditional materials useless. Accordingly, in this project, we aim to design, develop, and implement novel superhard and low-friction coatings that can result in higher energy efficiency, longer durability, and lower emissions in future engines. A nano-structured and composite coating consisting of MoN hard phase and Cu soft phase is a typical example of the superhard coatings that we have developed over the years, while a nearly frictionless diamond-like carbon film represents the low-friction coatings that we have been working on at Argonne.

During FY 2009, we made remarkable progress toward large-scale production, field testing, and commercialization of our superhard and low-friction coating. Specifically, we worked closely with Hauzer Technocoating and Galleon International to produce these coatings on functional surfaces of numerous engine parts using a production-scale deposition system available at Hauzer. We also worked closely with several engine companies and successfully deposited our coatings on their engine parts and components for performance and durability tests in simulated and actual engines.

Experimental

During FY 2009, we accelerated our process development and coating optimization efforts to achieve much higher coating adhesion, smoother surface finish, and lower friction and wear. In particular, the surface roughness was found to be detrimental to the friction and wear resistance of most coated engine parts. Due to its ultra-hard nature, the coated surfaces were well-protected against wear, but they were causing significant wear on the opposite side or counterface materials (which were not always coated). With our industrial partners, we have tried several remedies to control the surface roughness of these coatings. These included post-deposition ion etching, adjustment of the rotational speed of part holders, optimization of bias voltage, control of the deposition rate and temperature, etc. Furthermore, we tried short-duration mechanical polishing or buffing of coated parts to achieve even smoother surface finishes.

Structurally, our hard coatings were dense and uniform, but when they were deposited at lower deposition temperatures (i.e., below 200^{o}C), occasionally, the structural morphology of the resultant coatings was somewhat columnar in nature. In actual applications, such morphology could result in coating failure due to inter-columnar fracture or de-cohesion. By changing the bias voltage to the target, adjusting the deposition rate and temperature, and adjusting the rotational speed of the parts to be coated, we were able to overcome this problem and achieve a truly dense and homogeneous coating, which also resulted in a smooth surface finish (due to much smaller grain size).

On another front, we concentrated on further improving the coating adhesion to substrate materials and actual engine parts. For most mechanical and tribological applications, strong adhesion is extremely important for achieving low friction and wear. If a coating has poor adhesion strength to its substrate, it can easily delaminate from the surface during repeated sliding or rolling contacts and thus becomes useless. In general, our hard and low-friction coatings displayed excellent adhesion to their substrates due to a functionally graded, proprietary bond or transition layer architecture that is produced on the substrate surface prior to the deposition of actual coatings.

The coating chemistry is extremely important not only for tribological performance but also compatibility with lubricants in a lubricated test environment, as we emphasized in previous reports. Accordingly, we spent a significant amount of time and effort in further optimization of the coating chemistry during the last fiscal year. Our initial laboratory-scale studies confirmed that coating chemistry was indeed important for achieving low friction under boundary-lubricated sliding conditions. With the help of expert engineers from our industrial partners, we reached a consensus on the fabrication of special sputtering targets that would possess a unique coating composition with superior tribological behavior during lubricated sliding tests.

Results

Based on the knowledge gained from the above studies, we produced a series of smooth and dense MoN-Cu and carbon coatings on representative engine parts and steel substrates. Engine parts were delivered to industrial partners for their internal evaluations, while the steel substrates were tested internally for their friction and wear performance under a wide range of lubricated sliding conditions. Figure 1 shows four tappets coated with our superhard coating while Figure 2 and 3 shows the friction coefficient and wear profiles of the same coating during a lubricated sliding test. As is clear, the friction coefficient of this coating is low from the beginning, mainly because of its smooth surface finish and optimized chemical composition. Other tests performed at Argonne were directed toward determining the scuffing behavior of coated samples. All of the tests in our laboratory were performed under severe loading conditions to achieve a boundary-lubricated sliding regime. The highly optimized coatings passed all of these tests successfully and often exceeded the load limit of the test machines.

During 2009, we worked closely with Hauzer Technocoating to scale up the deposition process and to offer our coatings to interested industrial companies for large-scale applications in the transportation field. Specifically, we held numerous conference calls to teach them how to produce our coating in their commercial-scale deposition systems. Those process parameters that are most important for high-quality film deposition (bias voltage, target configuration, deposition rate and temperature, rotational speed of sample holder, etc.) were discussed during these telephone conversations. Coatings produced according to our instructions were then sent to us for quality control and tribological evaluation. As part of this close collaboration, we met with several Hauzer representatives at technical conferences, and they also visited us at Argonne to discuss progress being made

and the range of potential industrial applications they would like to entertain first.

During the initial trials, some minor problems were noted with structural morphology and coating composition. Also, the surfaces of coated parts were not very smooth or superhard. As a result, the tribological performance of these first-generation industrial coatings was not at the desired or acceptable levels. After several rounds of corrective actions and trials, the second-generation coatings were close to the ones that we have been producing at Argonne. After each deposition trial, some of the coated samples were shipped to Argonne for chemical, mechanical, and tribological characterization. Others were subjected to the coating company's tests for hardness, adhesion, thickness, etc. The results from these studies were compared and discussed in detail during weekly teleconferences. After several rounds of coating trials, Hauzer was able to deposit films that looked almost the same as the ones that we have been producing at Argonne.

With the installation of a new high-power impulse magnetron sputtering source, our coating system at Argonne is now one of a kind and is well-suited for the synthesis of superhard coatings for industrial applications. With this new power source, the ionization efficiency of our deposition system increased by a factor of 10 to 15 (this would have a huge positive impact on the structural morphology and adhesion of coatings on the substrate materials). Figure 4 indicates the condition of the latest coating subjected to a Rockwell C adhesion test. The figure shows that this new coating remained attached to the substrate, and there was no evidence of delamination or failure, except for cone-like cracks around the indented spot.

During 2009, we performed numerous tribological tests on near-frictionless carbon coatings as well under a wide range of tribological conditions. Specifically, we tried to optimize the coating composition with the selected lubricant. Figure 5 shows the friction test results from a highly optimized carbon coating, which showed excellent compatibility with the glycerol-based lubricant that was used during these tests.

Using time-of-flight secondary ion mass spectrometry, we performed extensive surface analytical studies on the superhard and nearly frictionless carbon coatings after friction and wear tests in lubricants. Most often we found that a thin boundary film had formed on the sliding surface. Depending on the oil chemistry and/or additive package, the chemical composition of the boundary film was consistent with the type of active anti-friction and wear additives present in these oils. Specifically, the boundary films consisted of high levels of sulfur and phosphorous, suggesting that they were the key ingredients participating in the tribochemical reactions during sliding.

The test results from our industrial partners on coated engine parts were also impressive. Specifically, our superhard coatings performed extremely well in their friction, wear, and scuffing tests and resulted in huge reductions in friction and wear. Based on these remarkable results, the industrial partners are now preparing to initiate field and fleet studies. They are already working closely with our coating partner for the treatment of numerous engine

components, including tappets and piston pins and rings, which will be used in these field studies.

Conclusions

During FY 2009, we made remarkable progress in terms of scaling up and commercializing our superhard and low-friction coatings. Most of the product optimization and quality control studies have now been completed. Our industrial partner in the coating field is able to produce essentially the same quality coatings as the original ones that we had developed at Argonne. During 2009, we performed extensive tests on numerous coatings provided by them and confirmed that the latest coatings were as good as our original coatings in terms of tribological performance. Tests by the engine company partners further confirmed the impressive tribological properties of these coatings in actual engines. The surface analytical studies on tested parts revealed the formation of a protective boundary film on sliding surfaces. These findings are important for understanding the friction and wear mechanisms of our coatings.

During FY 2010, we will shift our focus onto technology transfer and licensing, cost-benefit analysis, and full-scale commercialization of our coating technology. Additional effort will concentrate on the usefulness of the newest high-power impulse magnetron sputtering method for the production of much harder, smoother, and lower-friction coatings than before. All of these attributes are important for achieving further improvements in performance and durability of actual engine parts. We will also continue to test and qualify the coatings produced by our industrial partners and provide our expert opinions on their performance.

Patents and Publications

During FY 2009, a new invention disclosure was filed, and we published and/or presented several new papers on the work that was performed under this project as listed below.

Peer Reviewed Publications:

1. Erdemir, A., and Voevodin, A., "Metallurgical Coatings for Severe Applications," in *Handbook of Thin Films*, P. Martin (Ed.), Elsevier, in press, 2009.
2. Dickrell, P.L., Argibay, N., Eryilmaz, O.L., and Erdemir, A., "Temperature and Water Vapor Pressure Effects on the Friction Coefficient of Hydrogenated Diamondlike Carbon Films," *Journal of Tribology*, 131 (2009) 032102.
3. Colaco, R., Serro, A.P., Eryilmaz, O.L., and Erdemir, A., "Micro-to-Nano Triboactivity of Hydrogenated DLC Films," *Journal of Physics D-Applied Physics*, 42 (2009) 085307.
4. Matta, C., Eryilmaz, O.L., Bouchet, M.I.D., Martin, J.M., Erdemir, A., and Nakayama, K., "On the Possible Role of Triboplasma in Friction and Wear of Diamond-like Carbon Films in Hydrogen-Containing Environments," *Journal of Physics D-Applied Physics*, 42 (2009) 075307.
5. Eryilmaz, O.L., and Erdemir, A., "On the Hydrogen Lubrication Mechanism(s) of DLC Films: An Imaging TOF-SIMS Study," *Surface and Coatings Technology*, 203 (2008) 750.
6. Donnet, C., and Erdemir, A., "New Horizon in the Tribology of Diamondlike Carbon Films," *Surface Engineering*, 24 (2008) 399.
7. Merkle, A. P., Erdemir, A., Eryilmaz, O. L., Johnson, J. A., and Marks, L. D., "In-situ TEM Studies of Structural Modifications in Near-Frictionless Carbon Films," accepted for publication in *Carbon*.

Presentations:

1. Erdemir, A., and Eryilmaz, O. L., "Tribology of Carbon Films in Hydrogen and Deuterium Gas Environments," AVS 55th International Symposium and Exhibition, Boston, MA, Oct. 19-24, 2008.
2. Erdemir, A., and Eryilmaz, O. L., "Development of MoN-Ag-Based Nanocomposites Films for Severe Tribological Applications," AVS 55th International Symposium and Exhibition, Boston, MA, Oct. 19-24, 2008.
3. Erdemir, A., "Innovative Surface Technologies for Advanced Engineering Applications: From Superhard and Low-Friction Coatings to Super-Fast Surface Treatments," Invited Colloquium Seminar, Department of Mechanical Engineering, Georgia Institute of Technology, Atlanta, GA, Jan. 27, 2009.
4. Eryilmaz, O. L., Erdemir, A., and Kartal, G., "The Effect of Methane and Acetylene in the Surrounding Test Environment of Tribological Behavior of Non to Highly Hydrogenated DLC Films," STLE 64th STLE Annual Meeting and Exhibition, Orlando, FL, May 17-21, 2009.
5. Matta, C., De Barros Bouchet, M. I., Vacher, B., Eryilmaz, O. L., Le Mogne, T., Martin, J.-M., and Erdemir, A., "Tribological Effects on Friction and Wear Behavior of ta-C Coatings in Presence of Alcohols and a-C:H Coatings in Dry Conditions," 64th Annual Meeting of the Society of Tribologists and Lubrication Engineers, Lake Buena Vista, FL, May 17-21, 2009.
6. Eryilmaz, O. L., Erdemir, A., and Kartal, G., "Tribology of Deuterated Diamond-like Carbon Films: An Imaging TOF-SIMS Study," 36th International Conference on Metallurgical Coatings and Thin Films, San Diego, CA, Apr. 27- May 1, 2009.
7. Erdemir, A., Eryilmaz, O. L., Kartal, G., Timur, S., Urgen, M., and Kazmanli, K., "Review of Innovative Surface Technologies: From Super-hard and –Low Friction Coatings to Super-fast Surface Treatments," Invited Talk, 36th International Conference on Metallurgical Coatings and Thin Films, San Diego, CA, Apr. 27-May 1, 2009.
8. Eryilmaz, O. L., and Erdemir, A., "Fundamental Tribological Mechanisms of Hydrogen-Free and Highly Hydrogenated DLC Films: An Imaging TOF-SIMS Study," Invited Talk, 4th World Tribology Congress, Kyoto, Japan, Sept. 6-11, 2009.
9. M'ndange-Pfupfu, A., Eryilmaz, O., Erdemir, A., and Marks, L., "Tribological Investigation of Amorphous Carbon Films Using In Situ TEM Nanomanipulation," 64th Annual Meeting of the Society of Tribologists and Lubrication Engineers, Lake Buena Vista, FL, May 17-21, 2009.
10. Erdemir, A., Eryilmaz, O.L., Urgen, M., and Kazmanli, K., "Ultra-low Friction and Wear of Designer Nanocomposite Coatings Enabled by the Use of a Crystal-Chemical Model," Invited Talk, World Tribology Congress–IV, Kyoto, Japan, Sept. 6-10, 2009.
11. Erdemir, A., Eryilmaz, O.L., Urgen, M., and Kazmanli, K., "Designing Hard Coatings for Ideal Tribochemistry and Superlubricity under Boundary Lubricated Sliding Conditions," Invited Keynote Talk, Presented at the International Conference on Advances in Boundary Lubrication and Boundary Surface Films, Seville, Spain, March 29-April 3, 2009.
12. Erdemir, A., "Advanced Nano-Lubricants and -Coatings for Saving Energy and Environment," Invited Keynote Talk, presented at Shell Nano Forum–2008, Houston, TX, Oct. 7-9, 2008.

13. Erdemir, A., and Eryilmaz, O.L., "On the Origins of Tribochemistry and Superlubricity in DLC Films," Invited Talk, International Tribochemistry Forum, Kyoto, Japan, Sept. 2-4, 2009.

14. Erdemir, A., Eryilmaz, O. L., Urgen, M., and Kazmanli, K., "Novel Design Approaches to the Development of Multifunctional Nanocomposite Coatings for Demanding Engine Applications," Invited Talk, SVC 52nd Annual Technical Conference, Santa Clara, CA, May 9-14, 2009.

15. Erdemir, A., Eryilmaz, O.L., Urgen, M., and Kazmanli, K., "Novel Design Criteria for the Synthesis of Superhard and Low-Friction Nanocomposite Coatings," Invited Plenary Talk, 3rd Vienna International Conference on Nano-Technology, Vienna, Austria, Mar. 18-20, 2009.

16. Erdemir, A., "On the Hydrogen Lubrication Mechanisms of Nearly-Frictionless Carbon Films: An Imaging TOF-SIMS Study," Invited Colloquium Seminar Talk at Pennsylvania State University, University Park, PA, Apr. 21, 2009.

17. Erdemir, A., and Eryilmaz, O. L., "An Imaging of TOF-SIMS Study of the Tribochemical Interactions in Diamondlike Carbon Films," AVS 56th International Symposium and Exhibition, San Jose, CA, Nov. 8-13, 2009.

18. Erdemir, A., Eryilmaz, O. L., Urgen, M., and Kazmanli, K., "Advances in Superhard and Low-Friction Coatings for Extreme Tribological Applications," Invited Talk, ASME/STLE International Joint Tribology Conference, Memphis, TN, Oct. 19-21, 2009.

19. Fontaine, J., Erdemir, A., and Donnet, C., "Fundamental Phenomena in Tribology of DLC Films: How to Reduce Friction and Wear," Invited Keynote Talk, 4th World Tribology Congress, Kyoto, Japan, Sept. 6-11, 2009.

20. Erdemir, A., "Advances in Surface Engineering for Extreme Tribological Applications," Invited Keynote Talk, 4th World Tribology Congress, Kyoto, Japan, Sept. 6-11, 2009.

21. Erdemir, A., and Eryilmaz, O.L., "Intrinsic and Extrinsic Lubrication Mechanisms of DLC Films," Invited Keynote Talk, 4th World Tribology Congress, Kyoto, Japan, Sept. 6-11, 2009.

22. Erdemir, A., Eryilmaz, O.L., Urgen, M., and Kazmanli, K., "Innovative Design Concepts for the Development of Superhard and Low-Friction Nano-composite Coatings," Invited Keynote Talk, 64th Annual Meeting of the 64th Annual Congress of the Brazilian Metallurgical, Materials, and Mining Association, Belo-Horizonte, Brazil, July 13-17, 2009.

23. Tlustochowicz, M., McNallan, M., Erdemir, A., and Sudarshan, T. S., "Tribology of Carbide-Derived Carbon Films Synthesized on Tungsten Carbide," 22nd International Conference on Surface Modification Technologies, Trollhattan, Sweden, Sept. 22-24, 2008.

24. Matta, C., De Barros Bouchet, M. I., Vacher, B., Eryilmaz, O. L., Le Mogne, T., Martin, J.-M., and Erdemir, A., "Tribochemistry of ta-C Coatings in Presence of Alcohols and a-C:h Coatings under Dry Sliding Conditions," 4th World Tribology Congress, Kyoto, Japan, Sept. 6-11, 2009.

25. Eryilmaz, O. L., Cakir, S., Kazmanli, K., Erdemir, A., and Urgen, M., "Characterization of Tribofilms Formed on Mo-N-Cu Coatings under Boundary Lubrication Conditions," 13th European Conference on Applications of Surface and Interface Analysis, Antalya, Turkey, Oct. 18-23, 2009.

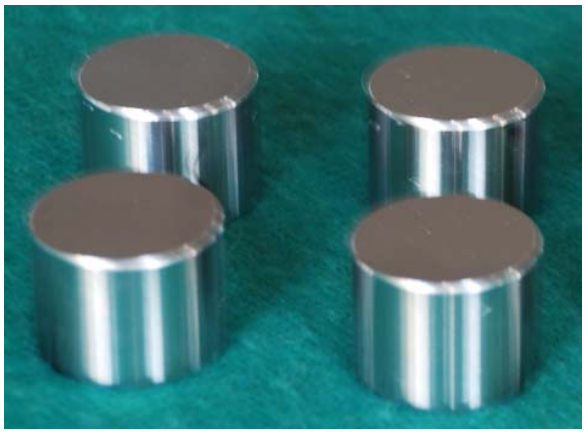

Fig. 1. Four tappets coated with superhard nanocomposite coatings.

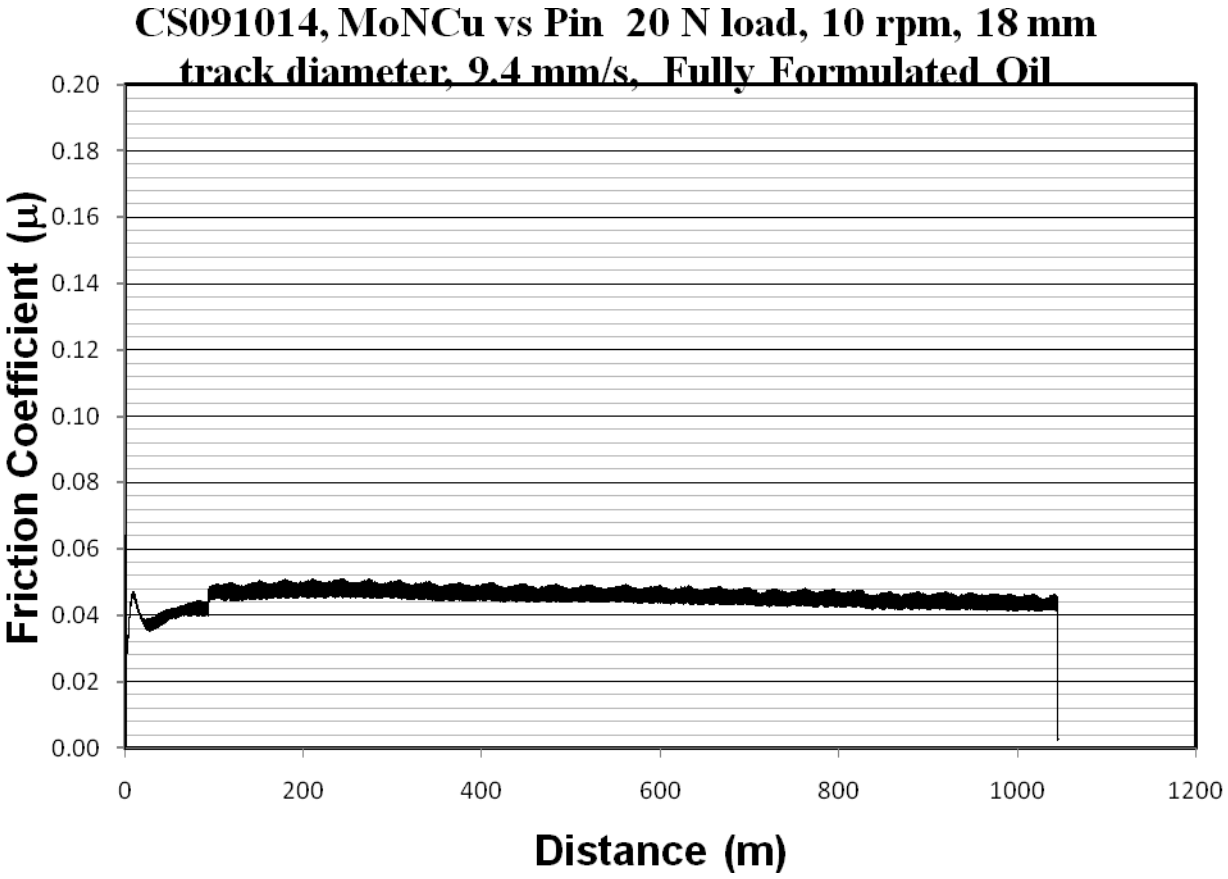

Fig. 2. Typical friction coefficient of a nanocomposite coating produced on actual tappets. The friction coefficient of an uncoated tappet would have been more than two times higher.

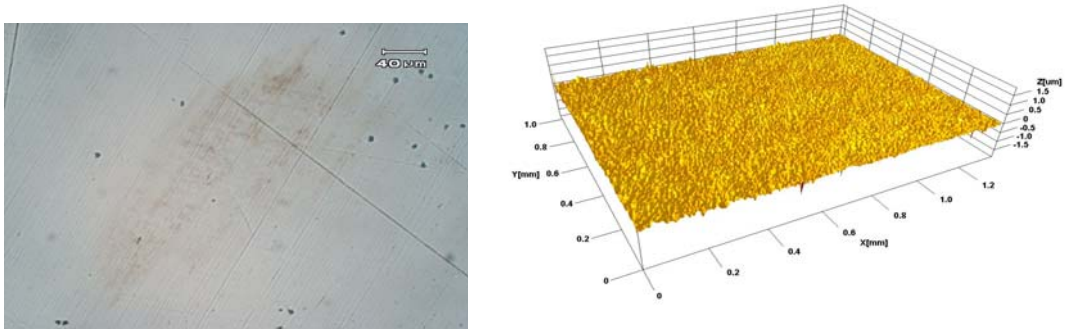

(a) (b)

Fig. 3. (a) Photomicrograph of the sliding pin surface and (b) 3D surface profile of test disk showing no evidence of wear on these sliding surfaces after the test.

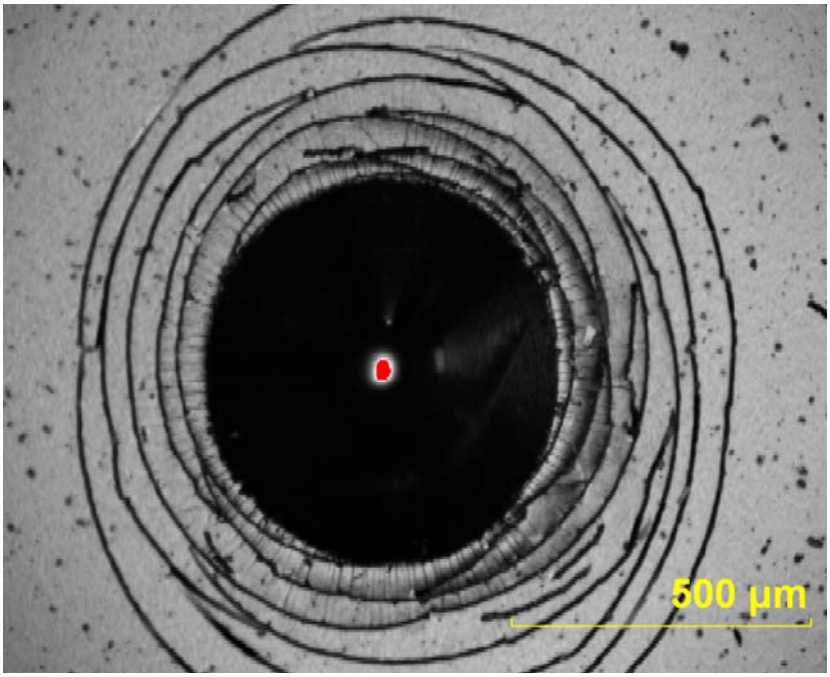

Fig. 4. Optical photomicrograph of a Rockwell C adhesion-tested superhard coating produced by high-power impulse magnetron sputtering technique.

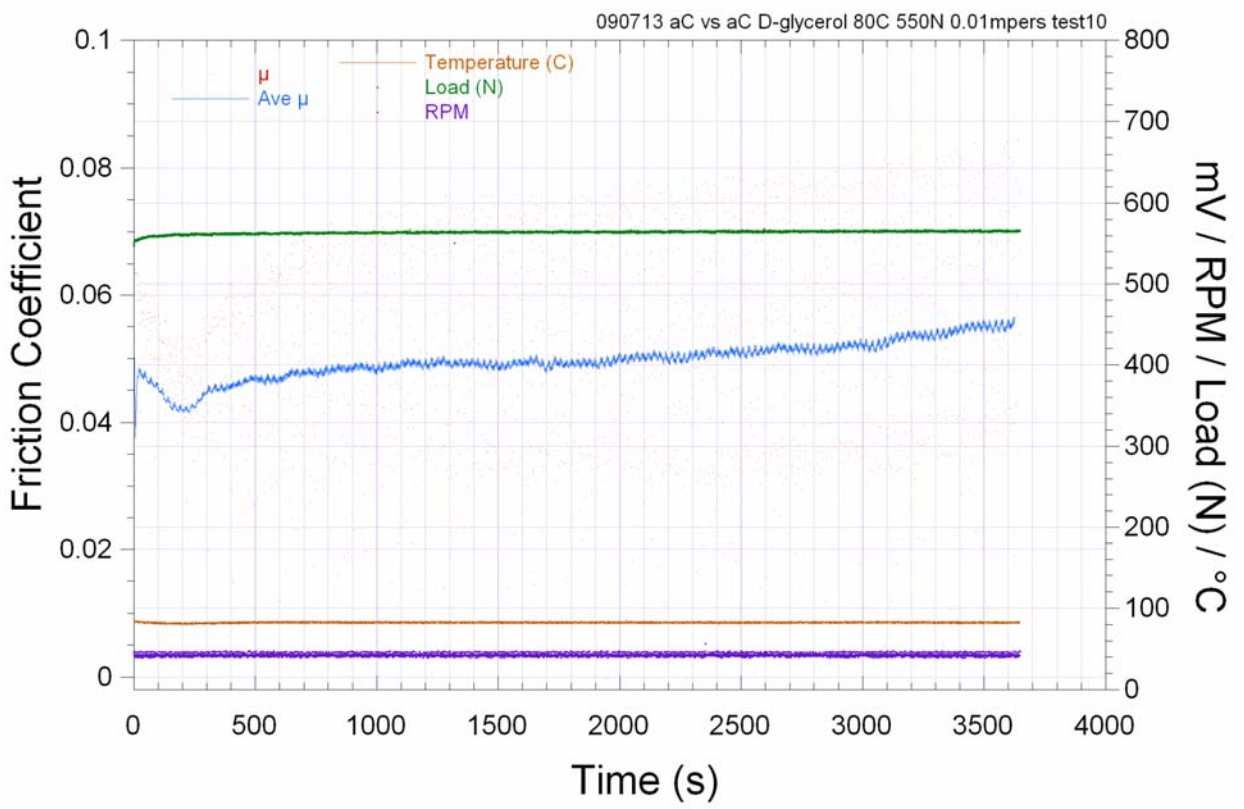

Fig. 5. Friction coefficient of the carbon film in glycerol-based lubricant.

U.S. DEPARTMENT OF ENERGY | Energy Efficiency & Renewable Energy

For more information
1-877-EERE-INF (1.877.337.3463)
programname.energy.gov